UNIVERSITÉ PARIS DIDEROT

Habilitation à Diriger Des Recherches

présentée par

SONIA FORNASIER

Maître de Conférence à l'Université Paris Diderot

CARACTÉRISATION PHYSICO-CHIMIQUE DES PETITS CORPS DU SYSTÈME SOLAIRE

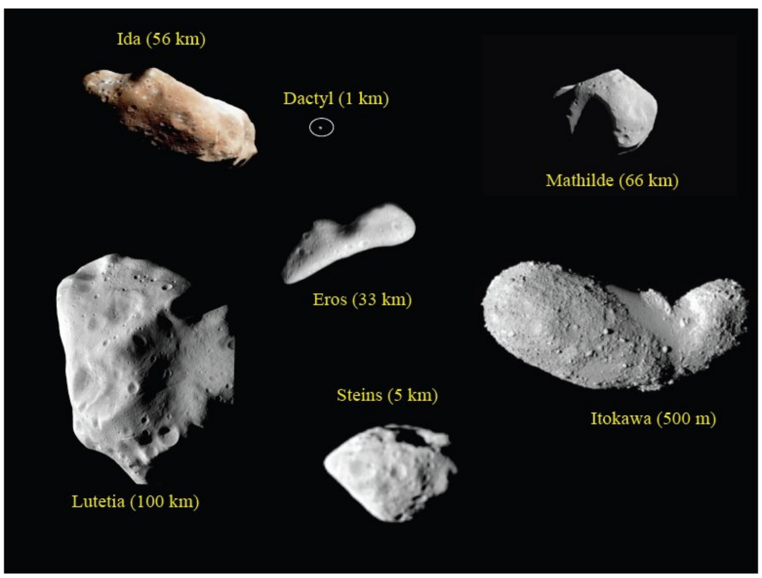

Soutenue le 25 mai 2012, devant le Jury composé de :

Anny–Chantal Levasseur-Regourd	Université Pierre et Marie Curie	Président
Alberto Cellino	INAF-Observatoire de Turin	Rapporteur
Cécile Ferrari	Université Paris Diderot	Rapporteur
Daniela Lazzaro	Observatoire de Rio de Janeiro	Rapporteur
Mirel Birlan	Observatoire de Paris	Examinateur
Fabrizio Capaccioni	INAF-IAPS	Examinateur

CARACTÉRISATION PHYSICO-CHIMIQUE DES PETITS CORPS DU SYSTÈME SOLAIRE

Résumé : L'objectif fondamental des sciences planétaires est la compréhension des phases de formation et d'évolution du Système Solaire, jusqu'aux conditions qui favorisent l'apparition de la vie. Les petits corps du Système Solaire sont très importants car ils constituent les restes des essaims de planétésimaux qui se sont formés au cours des premières phases d'accrétion des planètes. L'étude de leurs propriétés physiques et de leurs compositions de surface doit donc nous renseigner sur la formation et l'évolution du Système Solaire. L'étude des petits corps est aujourd'hui en plein essor grâce à l'exploration continue des missions spatiales et aux nombreuses campagnes observationnelles au sol.
Dans cette habilitation je décrit mon travail de recherche sur la caratérisation des propriètes physico-chimiques des petits corps du système solaire à différentes distances héliocentriques : géocroiseurs, astéroïdes, Troyens de jupiter, Centaures et transneptuniens. Mes travaux s'appuient largement sur les observations multi-longueur d'onde obtenues à partir de télescopes au sol et dans l'espace (missions Rosetta, Herchel, et Spitzer), sur la modélisation de la composition physico-chimique, sur la modélisation thermique et sur l'analyse statistique. Malgré les progrès considérables dans les études des petits corps, de nombreuses questions demeurent encore sans réponse. Mon activité de recherche a visé à comprendre la composition de surface des différents petits corps et leurs relations avec le gradient de composition dans la nébuleuse solaire, à étudier les différents processus d'altération de surface qui ont affecté leurs compositions, à identifier des régions et corps parents sources des météorites, et à étudier les interconnexions entre les différentes populations de petits corps.

PHYSICAL AND CHEMICAL CARACTERISATION OF MINOR BODIES OF THE SOLAR SYSTEM

Abstract : The aim of planetary sciences is the understanding of the formation and evolution of the Solar System, up to the conditions which support the appearance of the life. The small bodies of the solar system are very important because they constitute the left over of the planetesimals formed during the very first planets accretional phases. The study of their physical properties and surface composition shed light on the formation and evolution of our Solar System. The study of small bodies is blooming thanks to dedicated observations from the ground and from the space, with several space missions devoted to asteroids and comets. This defence will summarise my research activity on the caracterisation of the chemical and physical properties of different small bodies : near earth objects, asteroids, Jupiter troyans, Centaurs and transneptunians. This research activity is based on multiwavelength observational campaigns from groundbased and space telescopes (including data from the Rosetta, Spitzer and Herschel space missions), on the modelling of the bodies physico-chemical surface composition, on the thermal modelling, and on statistical analysis. In spite of the increasing amount of data and information, our knowledge of the minor bodies is still limited. My research activity was devoted to the understanding of the physical properties of different minor bodies, from the inner solar system up to the Kuiper belt, in particular in order to constrain their surface composition, and to relate it with the compositional gradient of the early solar nebula. My works include the analysis of the space weathering and aqueous alteration processes which affected their surfaces and changed their spectral behaviour. I applied statistical analysis on large samples of asteroids, Jupiter Troyans and Centaurs-TNOs spectra/colors, to look for possible relationships and correlations between the different classes of minor bodied, and to constrain their origin and dynamical evolution.

A ma fille Anna

le plus beau *petit*
corps de mon univers.

REMERCIEMENTS

Ce mémoire d'habilitation synthétise les activités de recherche que j'ai mené depuis 1998. Depuis ce temps j'ai eu l'opportunité de travailler avec plusieurs collègues qui m'ont initiée, guidée, conseillé et aidée dans mes recherches. Je ne peux pas tous les citer, mais je tiens à remercier mes principaux collaborateurs avec qui j'ai signé une grande partie de mes travaux scientifiques.

Je voudrais tout d'abord remercier Antonella Barucci, collègue et amie au LESIA avec laquelle j'ai mené une grand partie des mes activités de recherche en étroite collaboration, collaboration entamée bien avant mon doctorat, qu'elle a co-encadré. Merci pour ton support, ta dynamique et nos nombreuses interactions et discussions scientifiques sur différentes thématiques.

Merci également à Marcello Fulchignoni pour les conseils, le support et les échanges scientifiques et sur l'enseignement ainsi qu'à tous mes collègues du pôle de planétologie du LESIA à l'Observatoire de Paris pour leur accueil chaleureux et les nombreuses discussions enrichissantes et stimulantes.

Merci à Catherine de Bergh et à Adeline Gicquel pour avoir patiemment lu ce mémoire et en avoir corrigé le français.

Merci aux jeunes que j'ai co-encadré et aux post-doctorants avec qui j'ai travaillé (Alessandra Migliorini, Fréderic Merlin, Davide Perna, Francesca de Meo, Alvaro Alvarez, Cédric Leyrat) pour leur motivation et leur enthousiasme.

Un remerciement aux collègues de l'Université de Padoue où j'ai entamé mes études et où j'ai travaillé pendant et après le doctorat. Je remercie en particulier Cesare Barbieri pour sa disponibilité et sa curiosité, Francesco Marzari pour son expertise sur la dynamique, et les amis-collègues Vania Da Deppo, Sara Magrin et Ivano Bertini.

Je remercie toute l'équipe de l'instrument OSIRIS, avec laquelle j'ai entamé en 1998, il y a longtemps, la merveilleuse aventure de la mission Rosetta. Merci à tous pour les conseils et les nombreuses discussions scientifiques, et merci en particulier à Holger Sierks, Nicolas Thomas, Luisa Lara, Uwe Keller, Stubbe Hviik, Michael Kuppers, Rainer Kramm, Laurent Jorda, Cecilia Tubiana, Bjorn Daviddson, et Vania Da Deppo. Je ne peux pas oublier les longues campagnes de calibrations dans le bucolique Lindau, et l'émotion, partagée avec vous, des toutes premières images d'Osiris et celles obtenuées ensuite au cours des survols de Rosetta avec la Terre, Mars, et les astéroïdes Steins et Lutétia.

Merci également à toute l'équipe du programme d'observations "TNOs are Cool" avec le télescope HERSCHEL, et en particulier à Emmanuel Lellouche, Pablo Santos-Sanz, Thomas Müller et Audrey Delsanti.

Je veux remercier Elisabetta Dotto, avec qui j'ai partagé un grand nombre de campagnes d'observations pour percer les secrets des Troyens de Jupiter ou des cibles de missions spatiales.

Merci à Irina Belskaya pour sa disponibilité et pour m'avoir fait découvrir la technique de la polarimétrie, à Beth Clark pour sa précieuse collaboration sur les astéroïdes du groupe X , à

Rick Binzel pour les longues discussions sur la taxonomie et la composition des petits corps, et à G. Tozzi pour son expertise sur la spectroscopie et la polarimétrie.

Un remerciement spécial à mon mari Pasquale qui m'a toujours fait confiance et qui m'a soutenue en acceptant même de changer de pays pour me suivre. Merci pour ton écoute, ta patience et ta présence...

Je voudrais pour finir remercier les membres du jury de cette HDR de m'avoir fait l'immense plaisir et l'honneur d'expertiser ce mémoire d'habilitation et de participer à cette soutenance.

Table des matières

1 Introduction et résumé sur l'originalité des recherches 11
1.1 Le contexte scientifique . . . 11
1.2 Originalité des recherches . . . 13

2 Les astéroïdes 23
2.1 Introduction . . . 23
2.2 Techniques d'observations . . . 23
2.3 Les astéroïdes primitifs et le processus d'altération aqueuse . . . 24
2.3.1 Article : Spectroscopic comparison of aqueous altered asteroids with CM2 carbonaceous chondrite meteorites . . . 25
2.4 Les astéroïdes de la classe S et le "space weathering" . . . 35
2.4.1 Article : A portrait of 4979 Otawara, target of the Rosetta Space Mission 35
2.5 Les astéroïdes ignés : le type E . . . 43
2.5.1 Article : Visible and near infrared spectroscopic survey of E-type asteroids, including 2867 Steins, a target of the Rosetta mission . . . 44
2.6 Les astéroïdes de type M . . . 61
2.7 Les astéroïdes de type X . . . 61
2.8 Observations à partir de la Terre et de l'espace des astéroïdes 2867 Steins et 21 Lutétia, cibles de la mission Rosetta . . . 62
2.8.1 2867 Steins . . . 62
2.8.2 Article : First albedo determination of 2867 Steins, target of the Rosetta mission . . . 63
2.8.3 21 Lutétia . . . 68
2.8.4 Article : Asteroids 2867 Steins and 21 Lutétia : surface composition from far infrared observations with the Spitzer space telescope . . . 68
2.8.5 Article : Puzzling asteroid 21 Lutétia : our knowledge prior to the Rosetta fly-by . . . 68

3 La mission Rosetta 83
3.1 Introduction . . . 83
3.2 Partie instrumentale : le système d'imagerie OSIRIS . . . 84
3.2.1 La caméra WAC : le système de suppression de la lumière diffuse . . . 84
3.2.2 OSIRIS : les calibrations scientifiques faites au sol . . . 85
3.3 Les observations en vol . . . 86
3.3.1 Calibration radiométrique et vérification sur l'astéroïde Vesta . . . 87
3.3.2 Article : Photometric observations of asteroid 4 Vesta by the OSIRIS cameras onboard the Rosetta spacecraft . . . 87
3.3.3 2867 Steins . . . 92

3.3.4 Article : E-Type Asteroid (2867) Steins as Imaged by OSIRIS on Board Rosetta . . . 92
3.3.5 Article : Search for Steins' surface inhomogeneities from OSIRIS Rosetta images . . . 92
3.3.6 21 Lutétia . . . 107
3.3.7 Article : Images of Asteroid 21 Lutétia : A Remnant Planetesimal from the Early Solar System . . . 107

4 Troyens de Jupiter **113**
4.1 Introduction . . . 113
4.2 Etude des Troyens membres de familles dynamiques . . . 114
4.2.1 Article : The surface composition of Jupiter Trojans : Visible and near-infrared survey of dynamical families . . . 114
4.3 La famille d'Eurybates . . . 130
4.3.1 Article : A peculiar family of Jupiter Trojans : The Eurybates . . . 130
4.4 Analyse des nuages L4 et L5 . . . 136
4.5 Corrélations entres les Troyens et les petits corps du Système Solaire externe . . . 136
4.5.1 Article : Visible spectroscopic and photometric survey of Jupiter Trojans : final results on dynamical families . . . 136

5 Centaures et Transneptuniens **159**
5.1 Les nouvelles frontières du Système Solaire . . . 159
5.1.1 Classification dynamique . . . 159
5.2 Campagnes d'observation . . . 160
5.3 Etudes photométriques et statistiques . . . 161
5.3.1 Article : Colors and taxonomy of Centaurs and trans-Neptunian objects . 162
5.4 Polarimétrie . . . 170
5.5 Spectroscopie et composition de surface . . . 170
5.5.1 Article : Water ice on the surface of the large TNO 2004 DW . . . 172
5.5.2 Article : Visible spectroscopy of the new ESO *Large Programme* on trans-Neptunian objects and Centaurs : final results . . . 172
5.6 Observations avec le télescope spatial HERSCHEL . . . 186

6 Perspectives scientifiques **187**
6.1 Mission Rosetta : rendez-vous avec la comète 67P . . . 188
6.2 Les géocroiseurs : observations au sol et *in situ* : missions OSIRIS-REX et MARCO POLO-R . . . 189
6.3 La mission BepiColombo : la planète Mercure . . . 190
6.4 Caractérisation des propriétés physico-chimiques des OTNs et Centaures . . . 191
6.5 Mesure en laboratoire d'échantillons de météorites, de minéraux et de mélanges de glaces . . . 192
6.6 Propriétés physiques des astéroïdes primitifs . . . 193

Bibliographie **195**

Sonia Fornasier :Curriculum Vitæ **199**

Liste des publications **207**

Chapitre 1

Introduction et résumé sur l'originalité des recherches

1.1 Le contexte scientifique

Le système solaire est un des thèmes de recherche astronomique où les connaissances se développent très rapidement, grâce notamment aux missions spatiales qui ont exploré et observent actuellement beaucoup de corps du système solaire : les missions Stardust, Deep Impact, Rosetta, Cassini, Mars Express, Venus Express, Messenger, Dawn, juste pour citer les plus récentes, nous ont fourni et/ou sont en train de récolter des données exceptionnelles sur les planètes telluriques, sur les planètes géantes avec leur satellites, mais également sur les petits corps, c'est-à-dire les astéroïdes et les comètes.
L'objectif fondamental des sciences planétaires est la compréhension des phases de formation et d'évolution du système solaire, jusqu'aux conditions qui favorisent l'apparition de la vie. Dans les années 1992-1995 deux découvertes majeures ont changé les confins du système solaire et nos perspectives : la découverte de plusieurs objets trans-neptunians dans la ceinture de Kuiper (1992 QB1 fut le premier), région source des comètes à courte période dont l'existence était prévue depuis les années 1940-50, et la découverte de la première exoplanète autour d'une étoile de type solaire, 51 Peg, suivie de nombreuses autres (plus de 500 exoplanètes connues à présent). La compréhension des phases de formation et d'évolution des systèmes planétaires est donc importante non seulement pour notre système solaire mais également pour la compréhension des systèmes d'exoplanètes et pour la recherche d'éventuelles bio-signatures.

Dans ce contexte, les petits corps du système solaire, qui représentent la cible de mon activité de recherche, sont très importants car ils constituent les restes des essaims de planétésimaux qui se sont formés au cours des premières phases d'accrétion des planètes. Bien que les astéroïdes aient subi de nombreuses collisions au cours de leur existence, la plupart d'entre eux n'ont pas subi une évolution géologique et thermique significative. C'est là que réside le principal intérêt d'étudier les petits corps : en raison de leur petite taille ces corps ont pu évacuer rapidement la chaleur originelle de la nébuleuse proto-solaire figeant ainsi la composition initiale de cette dernière, à la différence des planètes où le matériel primordial a été modifié par des processus géologiques comme la différenciation, le métamorphisme, l'érosion et la fusion. En tant que témoins primitifs restés intacts, les petits corps nous donnent une indication sur la composition chimique primordiale à partir de laquelle les planètes se sont formées il y a 4,6 milliards d'années. La distribution des différentes classes taxonomiques montre qu'il existe un gradient de composition assez bien défini dans le système solaire, avec les astéroïdes les plus évolués (dits ignés)

présents dans la partie interne de la ceinture principale et les moins évolués (les classes primitives C, P et D) peuplant surtout la partie externe de la ceinture principale ou les régions encore plus éloignées, comme les Troyens de Jupiter ou les astéroïdes Hilda à 5.2 et 4 UA, respectivement, et, encore plus loin, les Centaures et les Trans-neptuniens (OTNs) (sur la Fig 1.1 on peut voir la distribution des différents petits corps dans le système solaire en fonction de leur distance héliocentrique).
Astéroïdes, Centaures et transneptuniens peuvent aussi bien contenir les éléments primordiaux du nuage proto-solaire que des éléments produits par altération (par radiation ou réactions chimiques). Les derniers modèles dynamiques de formation et d'évolution du Système Solaire tendent à montrer que ces objets ont connu un grand brassage au cours de la migration des planètes géantes et plusieurs observations récentes tendent à le confirmer. Certains astéroïdes de la ceinture principale ont récemment montré la présence de la glace d'eau à leur surface (les astéroïdes Thémis et Cybèle) alors que des objets plus froids supposés peu évolués, comme les OTNs ou les Centaures par exemple, peuvent montrer des signes d'altération aqueuse révélant un passé beaucoup plus chaud (Fig. 1.1).

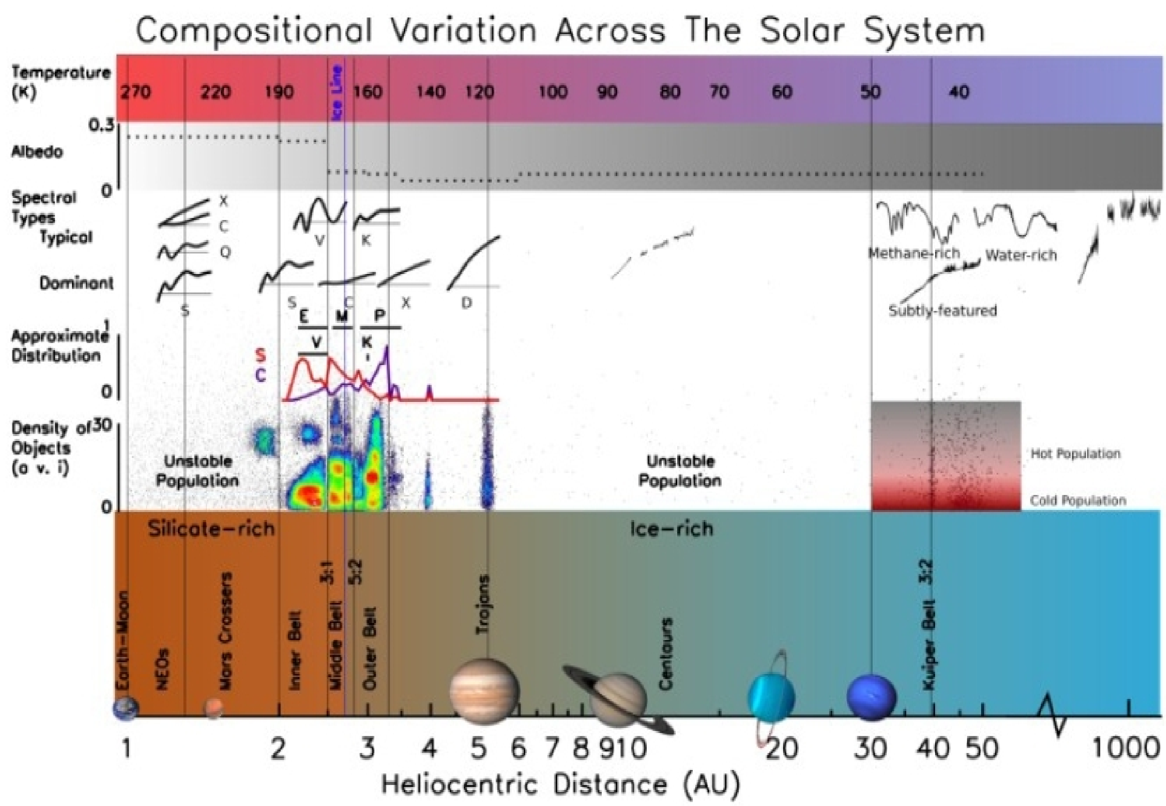

FIG. 1.1 – Vue globale des objets du Système Solaire. De bas en haut : le gradient de couleur (du brun au bleu, en bas de l'image) indique la transition entre les objets riches en silicates et ceux riches en glace. La distribution des petits corps est reportée en fonction de leur distance héliocentrique (demi grand axe). Une distribution taxonomique sommaire est affichée pour les astéroïdes de la ceinture principale ainsi que les spectres typiques des différentes familles (DeMeo, 2010, thèse de doctorat).

L'activité de découverte et de caractérisation des propriétés physiques des petits corps est

en plein essor. Les vingt dernières années ont produit une formidable moisson des données grâce à l'exploration continue des missions spatiales et aux nombreuses campagnes observationnelles au sol, de plus en plus poussées grâce à l'utilisation des grands télescopes couplés avec des instruments et des détecteurs très performants. Ceci a permis de découvrir un grand nombre d'astéroïdes dans la ceinture principale mais également dans des orbites proches de celle de la Terre (les géocroiseurs) ou dans les limites externes du système solaire (les Centaures et les transneptuniens), d'en étudier les propriétés de surfaces et les différents processus qui les ont modifiées.
Depuis la découverte du premier satellite (Dactyl) d'un astéroïde (Ida) faite par la sonde Galileo en 1993, de nombreux autres systèmes binaires ont été mis en évidence, nous donnant des contraintes fort intéressantes sur la structure interne et la densité des objets.
Les études sur le processus d'altération de surface des astéroïdes suite aux micro-impacts, à l'interaction avec le vent solaire et avec les rayons cosmiques ont fait d'énormes progrès et ont permis de résoudre le paradoxe de l'origine des chondrites ordinaires. Ces météorites, qui représentent 80% des météorites trouvées sur Terre, ont des spectres caractérisés par la présence de bandes d'absorption de silicates mais ils ne sont pas directement comparables à ceux des astéroïdes de type S, de composition également silicatée, car ces derniers ont des spectres plus rouges que ceux des chondrites ordinaires. Les études d'altération de surface ont montré que l'interaction des matériaux de surface avec le vent solaire, les rayons cosmiques et les micro-impacts produit du fer nanophase et induit un rougissement du spectre ainsi qu'une diminution de l'albédo et de la profondeur des bandes d'absorption. Le lien entre astéroïdes de type S (et Q) et chondrites ordinaires est maintenant bien établi grâce notamment aux mesures faites par les sondes spatiales NEAR pour le géocroiseur Eros (de type S) et Hayabusa pour le géocroiseur Itokawa (de type S). Hayabusa est la première sonde à avoir ramené sur Terre des échantillons d'un astéroïde (des petites quantités de poussière de la surface d'Itokawa ont été prélevées en novembre 2005). L'analyse de ces échantillons a définitivement prouvé le lien entre astéroïdes silicatés et chondrites ordinaires, car la composition et la chimie des échantillons en provenance d'Itokawa correspondent à celles de cette classe de météorites primitives qui se sont formées à l'origine du système solaire.
La découverte et la caractérisation des objets transneptuniens et des Centaures a été une des recherches phares dans le système solaire dans les 20 dernières années. En particulier, la découverte d'objets trans-neptuniens de taille comparable à celle de Pluton a remis en question la définition du terme "planète" dans le Système Solaire et a conduit l'Union Astronomique Internationale à définir une nouvelle classe d'objets, les planètes naines, dans laquelle se trouvent Pluton en même temps que Cérès et les OTNs Éris, Hauméa et Makemake.

Malgré les progrès considérables dans les études des petits corps, de nombreuses questions demeurent encore sans réponse. Mon activité de recherche a visé à répondre à des questions sur la composition des différents petits corps et sur leurs relations avec le gradient de composition dans la nébuleuse solaire, sur la compréhension des différents processus d'altération de surface qui ont affecté leurs compositions, sur l'identification des régions et corps parents sources des météorites, et sur les interconnexions entre les différentes populations de petits corps.

1.2 Originalité des recherches

Le thème fédérateur de mes travaux est l'étude des propriétés physiques des petits corps du Système Solaire à différentes distances héliocentriques, grâce à des observations obtenues à partir de télescopes au sol (VLT-NTT-1.52m de l'ESO, NASA-IRTF, TNG-ENO..), et dans l'espace (missions Rosetta, Spitzer, Herschel).

Mes outils sont principalement des observations obtenues par différentes techniques (la spectroscopie, la photométrie, la polarimétrie, la radiométrie) du domaine visible jusqu'à l'infrarouge-submillimétrique, la modélisation spectrale pour contraindre la composition de surface des objets observés, la modélisation thermique et l'analyse statistique.

Mon activité de recherche a visé à caractériser les propriétés de surfaces des petits corps, à étudier les processus qui ont altéré leur composition, à rechercher et analyser les interconnexions entre les différentes populations de petits corps.
J'ai commencé ma carrière de chercheuse en étudiant les petits corps les moins évolués comme les astéroïdes appartenant aux classes C, P, D, puis les Troyens de Jupiter, les Centaures et les trans-neptuniens (OTNs)).
Le fil rouge qui relie mes recherches sur ces différents objets primitifs est l'étude que j'ai menée sur l'eau, sous forme de glace dans les Centaures et les OTNs (à l'état amorphe et aussi cristallin, découverte surprenante et inattendue étant donné les basses températures (40-50 K) de ces objets), ou dans les minéraux hydratés présents à la surface des astéroïdes primitifs et produits par l'altération aqueuse des minéraux. Ce processus a des implication importantes sur la composition et la température de formation de ces objets car il implique que l'eau à l'état liquide était présente dans le passé. La glace d'eau est attendue aussi à la surface des Troyens de Jupiter, probablement capturés par la planète pendant la phase de migration planétaire, mais la recherche de signatures dues à la glace d'eau à leur surface a été infructueuse jusqu'à présent.

J'ai mené, en collaboration avec différents collègues, de nombreuse campagnes observationnelles sur les petits corps primitifs obtenant 110 nouveaux spectres d'astéroïdes primitifs et 80 spectres de Troyens de Jupiter pour la recherche des signatures des silicates hydratés, de la glace d'eau et l'étude du processus d'altération aqueuse. En particulier, pour les Troyens de Jupiter, mes recherches ont pour la première fois ciblé les membres de familles dynamiques de dimension relativement petite (diamètre < 50 km) par rapport aux études faites précédemment.
J'ai participé à deux Large Programme d'observation aux télescopes VLT&NTT de l'ESO dédiés à l'étude des Centaures et trans-neptuniens, opportunité qui m'a permis d'avoir accès à des données de haute qualité pour une étude ciblée de certains objets et également pour une analyse statistique de cette population d'objets du système solaire externe.

La recherche de l'eau et l'étude de l'altération aqueuse m'ont conduite à observer aussi les astéroïdes les plus évolués, appartenant aux classes E et M, sur lesquels on ne s'attendrait pas à voir des signatures dues aux silicates hydratés, étant donné qu'il s'agit d'objets évolués qui ont subi des températures élevées (> 1500 K) dans le passé. La découverte dans les années 2000 d'une bande d'absorption à 3 μm, typiquement associée aux silicates hydratés, sur des astéroïdes de type E et M (Rivkin et al. 2000) a ouvert un débat dans la communauté scientifique car cela implique que ces objets n'ont pas tous approché des températures très élevées comme supposé auparavant.

J'ai obtenu la plus complète base de données sur les astéroïdes de type E, en observant 2/3 de cette population rare d'astéroïdes, et 30 nouveaux spectres d'astéroïdes de type M. Mes recherches ont permis de découvrir et/ou confirmer la présence de bandes d'absorption associées aux sulfites et aux silicates sur leur surface ; par contre, aucune bande clairement associée aux silicates hydratés a été observée dans le visible et proche infrarouge.

Je participe à plusieurs collaborations internationales de large envergure qui ont abouti à plusieurs publications scientifiques de mes travaux de recherche. Parmi ces travaux, les résultats les plus originaux et importants sont les suivants :

1. **Etude du processus d'altération aqueuse sur les astéroïdes primitifs :** ce processus

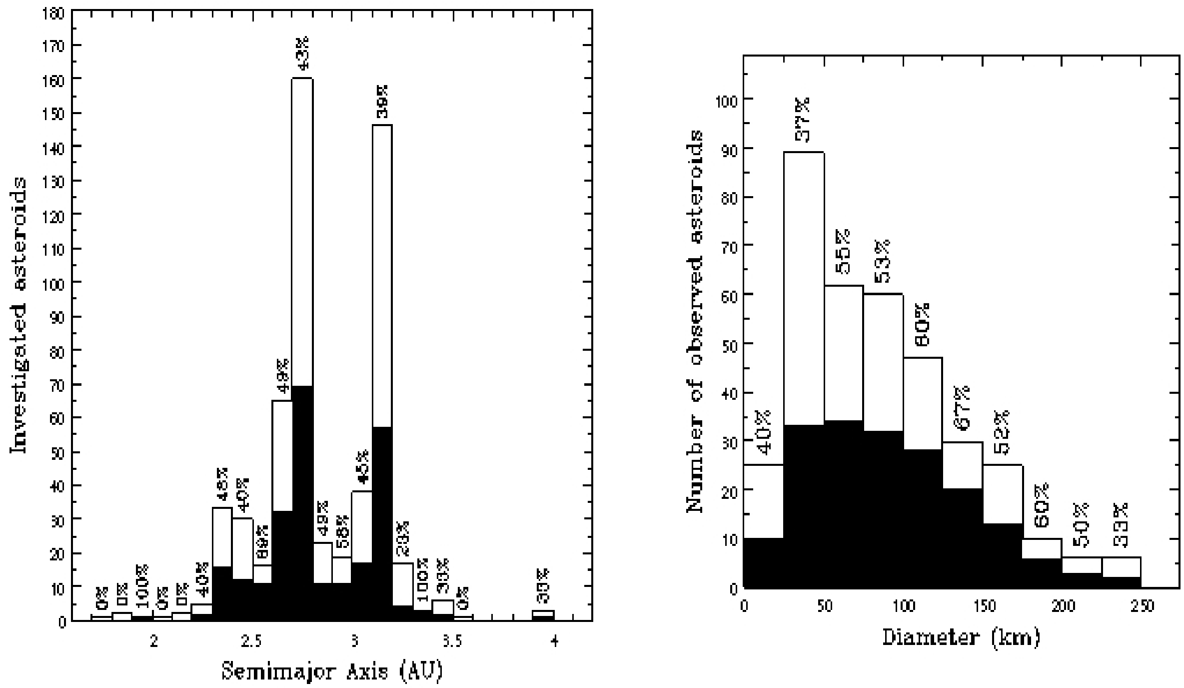

FIG. 1.2 – Distribution d'astéroïdes primitifs en fonction du demi grand axe (à gauche) et du diamètre (à droite). En noir les objets qui ont montré des bandes d'absorption associées à l'altération aqueuse.

est dû à l'eau dans l'état liquide qui agit comme solvant et produit des phylosilicates, des sulfates, des oxydes, des hydroxydes et des carbonates. Ce processus d'altération donne des contraintes sur la composition des planétésimaux (de la glace d'eau était nécessaire) et sur les processus thermiques du Système Solaire en formation.

Pour étudier les effets de l'altération aqueuse, j'ai obtenu 110 nouveaux spectres d'astéroïdes de classe C, P, F, B et G (dans la taxonomie de Tholen & Barucci 1989) et j'ai montré que ce processus agit sur la majorité des astéroïdes C (et la totalité de type G) de la ceinture principale. Par contre aucune signature due à l'altération aqueuse n'est présente sur les spectres des astéroïdes lointains comme les Troyens de Jupiter.
Combinant les nouveaux spectres avec ceux publiés dans la littérature, j'ai créé une base de données d'environ 580 astéroïdes primitifs. Ceci m'a permis de rechercher toutes les corrélations possibles entre l'altération aqueuse et les propriétés à la fois physiques et orbitales des astéroïdes observés. J'ai trouvé que le pourcentage d'astéroïdes hydratés augmente avec leur dimension (Fig. 1.2) ; par contre aucune relation ne semble exister entre l'hydratation et l'albédo.
En comparant les spectres d'astéroïdes hydratés avec ceux des météorites, nous trouvons que les chondrites carbonées de type CM2 ont des astéroïdes hydratés comme corps parents, du fait de leurs fortes similitudes spectrales (voir le paragraphe 2.3 pour plus de détails).

2. **Campagnes observationnelles des astéroïdes du groupe X (comprenant les classes E, M et P)**. J'ai obtenu une base de données unique sur les rares astéroïdes ignés de type

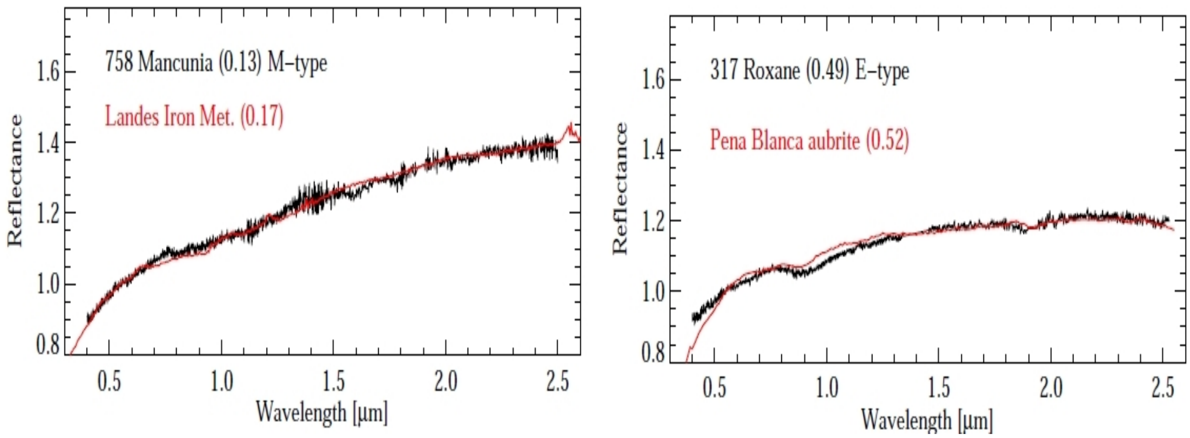

FIG. 1.3 – Spectres de réflectance des astéroïdes 758 Mancunia (à gauche, classe M), et 317 Roxane (type E, subclasse III). Leur valeur d'albédo est donnée entre parenthèses. Les spectres des météorites qui ressemblent le plus à ces spectres sont aussi tracés, avec la valeur d'albédo de ces météorites. Roxane pourrait être le corps parent de l'aubrite Pena Blanca et Mancunia de la météorite de fer Landes. Mancunia a aussi une grande valeur de l'albédo radar, ce qui indique une composition dominée par les métaux (Fornasier et al. 2008, 2010).

E, en observant plus des 2/3 de la population connue. Ces rares objets d'albédo élevé montrent 3 différentes minéralogies de surface avec des bandes d'absorption dues aux sulfites ou aux silicates. Ces bandes ont en partie été mises en évidence, pour la première fois, grâce à mes observations. Nos études confirment aussi que les astéroïdes de type E sont les corps parents les plus probables des aubrites (Fig. 1.3).

Pour les astéroïdes de type M, supposés de composition métallique, nous avons observé la présence de différentes bandes d'absorption sur leurs spectres, dont certaines pourraient être associées à l'orthopyroxène ou aux silicates hydratés. Ceci indique que la composition des astéroïdes de type M n'est pas exclusivement métallique, et aussi que les corps parents d'une partie de ces objets n'ont pas tous approché des températures très élevées ($>$ 1500 K) comme cela était supposé auparavant. Nos modèles de composition ont permis de contraindre la composition de surface des astéroïdes observés.

La comparaison avec les météorites montre que les astéroïdes de type M sont potentiellement des corps parents des météorites ferreuses, des pallasites et des chondrites à enstatite (Fig. 1.3). Les détails de mes recherches sur les astéroïdes de type E, M et X sont synthétisés dans les paragraphes 2.5-2.7 de ce mémoire.

3. **Les astéroïdes cibles de la mission Rosetta :** j'ai participé à plusieurs campagnes observationnelles internationales qui ont permis de fournir à l'ESA une liste de cibles potentielles parmi lesquelles 21 Lutétia et 2867 Steins ont été choisis. Ces observations ont permis de caractériser les propriétés de surface (la forme, l'orientation du pôle, la période de rotation, l'albédo, la composition de surface et les propriétés thermiques) de ces deux astéroïdes. Ces informations ont été très utiles pour optimiser les trajectoires de Rosetta pendant les rencontres ainsi que les séquences observationnelles.

   Mon activité d'observation au sol des cibles de Rosetta a été particulièrement importante suite au report du lancement de la mission et à la redéfinition de son orbite. Mes études en polarimétrie ont donné la toute première valeur d'albédo de 2867 Steins. Cette valeur élevée (0,45±0,10), couplée avec les observations spectroscopiques, a permis de montrer

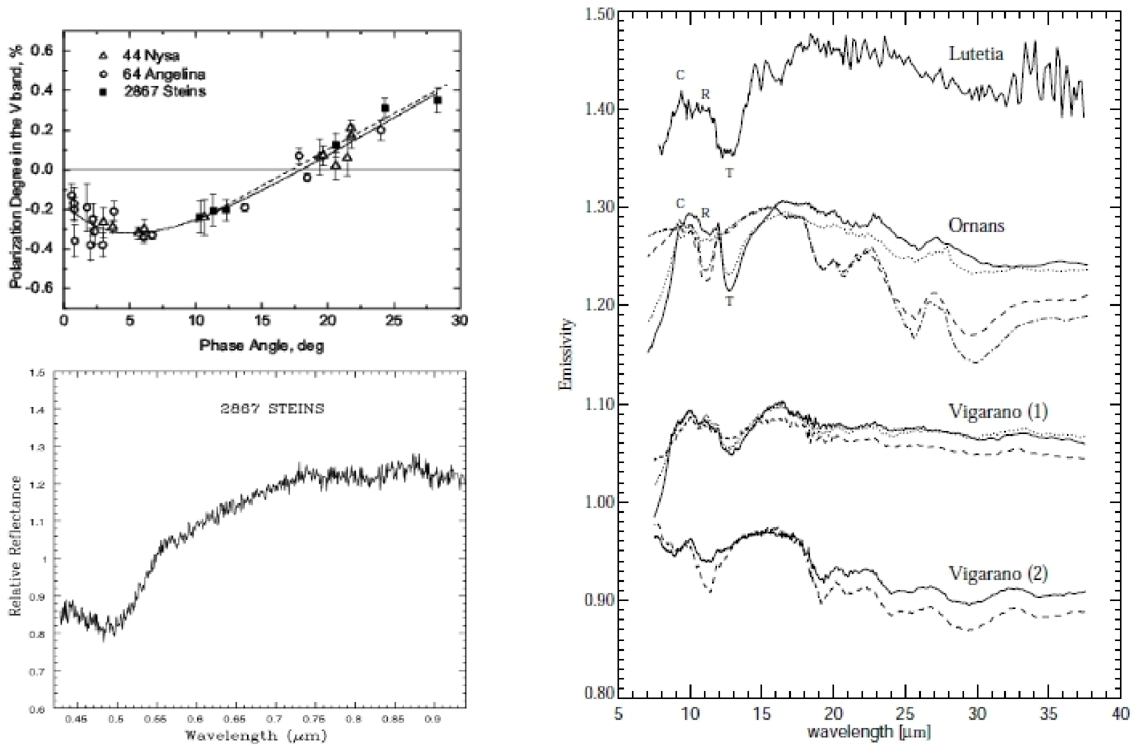

FIG. 1.4 – A gauche : courbe de polarisation (en haut) de Steins, qui ressemble à celles d'autres astéroïdes de type E comme Nysa et Angelina (Fornasier et al. 2006), et son spectre (en bas) qui est typique de la classe E(II) avec une bande d'absorption à 0,49 micron due à l'oldhamite (Fornasier et al. 2007). A droite : spectre d'émissivité de Lutétia obtenu à partir des données Spitzer (Barucci et al. 2008). Le spectre ressemble à ceux de chondrites carbonées de type CV3 (Vigarano) et CO3 (Ornans) à différentes tailles de grains (voir Fig. 4, page 76, pour les détails).

que Steins est un astéroïde évolué de la rare classe E (Fig. 1.4, voir le paragraphe 2.8.1 pour plus des détails).
Lutétia est un grand astéroïde de la ceinture principale qui était classifié comme appartenant à la classe M sur la base de ses couleurs dans la région visible et de sa valeur d'albédo. Les campagnes d'observation auxquelles j'ai participé ont prouvé que cette classification était discutable, car son spectre infrarouge est exceptionnellement plat comparé à d'autres astéroïdes de type M et aux météorites de fer, et il ressemble plutôt à ceux des chondrites carbonées.
Des observations avec le télescope SPITZER ont permis de déduire l'albédo et les propriétés thermiques de Steins et de Lutétia, ainsi que d'étudier leur spectre d'émissivité. Le spectre d'émissivité de Steins entre 5 et 38 μm, mesuré par Spitzer, est conforme à celui des aubrites et des minéraux à enstatite et confirme le classement de type E. Pour Lutétia, nous trouvons une faible valeur de l'inertie thermique et un spectre d'émissivité qui ressemble aux spectres des chondrites carbonées du type CO et CV, confirmant une composition chimique assez primitive de sa surface. Nos études en polarimétrie confirment aussi une similitude entre la courbe de polarisation de Lutétia et celle des chondrites carbonées de type CV3 et CO (Fig. 1.4, voir le paragraphe 2.8.3 pour plus des détails).

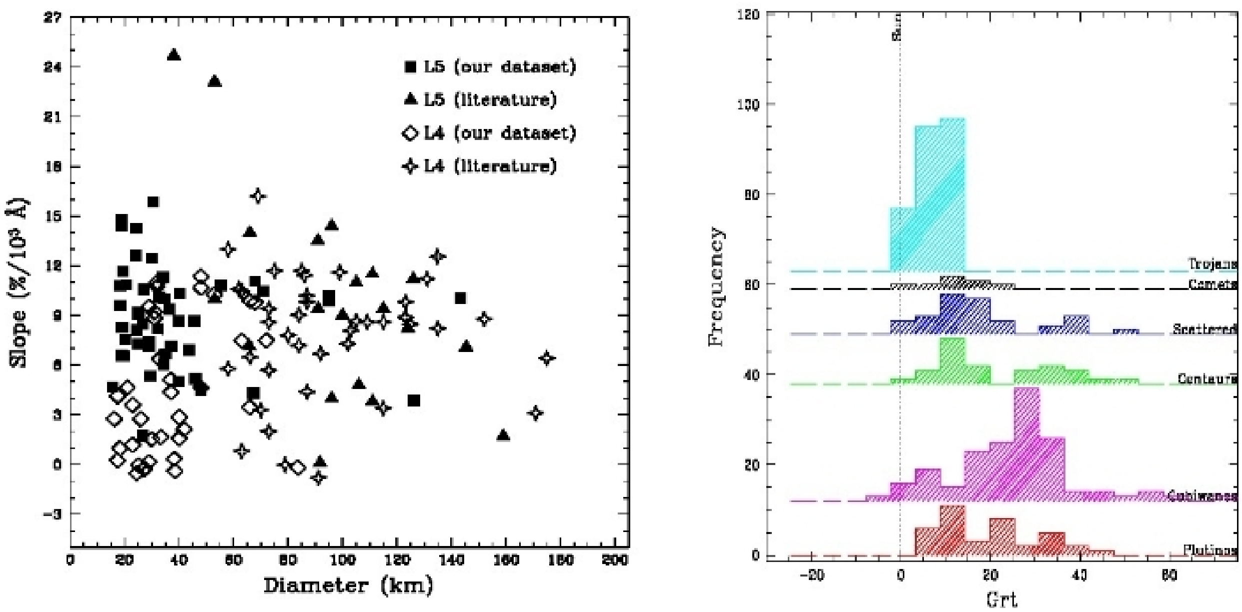

FIG. 1.5 – A gauche : distribution de la pente spectrale des Troyens des nuages L4 et L5 en fonction de leur diamètre. Les faibles valeurs de la pente spectrale pour les objets de L4 avec un diamètre < 40 km sont dues principalement aux membres de la famille d'Eurybates. A droite : distribution de la pente spectrale (Grt) pour les Troyens et les différentes classes d'objets du Système Solaire externe (les Cubiwanos sont les OTNs classiques ; Fornasier et al. 2007).

4. **Troyens de Jupiter** : j'ai entamé des collaborations internationales pour des observations des Troyens de Jupiter, observations dédiées en particulier à l'étude des membres des familles dynamiques. Il s'agit des toutes premières observations de Troyens de dimension relativement petite (diamètre < 50 km, Fig. 1.5). Nous avons ciblé des Troyens membres de familles (80 objets) car celles-ci se sont formées par destruction collisionnelle d'un corps parent, et leur étude permet donc de comprendre la nature de ces familles et de donner un aperçu sur la structure interne du corps parent, probablement riche en glace d'eau.
   Nous n'avons pas détecté de bandes d'absorption ni dans la région visible, sauf pour quelques objets de la famille d'Eurybates (Fornasier et al. 2004a, 2007b), ni dans la région infrarouge (en particulier il n'y a pas de bandes d'absorption dues à la glace d'eau, pourtant supposée abondante à ces distances héliocentriques). Le modèle de transfert radiatif appliqué à la surface des Troyens observés montre que leurs spectres et leur faible valeur d'albédo sont reproduits par des mélanges de carbone amorphe, de composés organiques et de faibles quantités de silicates (voir le paragraphe 4.2 pour plus des détails).
   La plus grande partie des Troyens observés ont des spectres rouges (réflectance qui augmente avec la longueur d'onde) semblables à ceux des astéroïdes de la ceinture principale externe, et appartiennent surtout aux classes primitives D et P. Nous avons identifié une famille particulière, celle d'Eurybates dans le nuage L4, qui est dynamiquement très robuste et dominée par des astéroïdes appartenant aux classes P et C. Des membres de la famille d'Eurybates montrent une chute de réflectivité en dessous de 5000 Å. Cette chute a été aussi observée sur les spectres d'astéroïdes de la ceinture principales soumis au processus d'altération aqueuse, où elle est associée à d'autres bandes d'absorption. Sur les spectres de

membres de la famille d'Eurybates nous n'avons pas détecté d'autres bandes d'absorption associées à l'altération aqueuse ou à la glace d'eau (les résultats de cette recherche sont résumés dans le paragraphe 4.3).
L'étude statistique menée sur les Troyens observés dans cette campagne et ceux publiés dans la littérature (échantillon de 142 Troyens) montre que les nuages L4 et L5 présentent une dominance d'astéroïdes primitifs de type D (plus de détails dans les paragraphes 4.4 et 4.5). Le nuage L4 montre une plus grande variété de types spectraux par rapport au nuage L5. En étudiant les paramètres orbitaux, nous avons trouvé que les astéroïdes avec une petite inclinaison ont des couleurs/spectres plus bleus que ceux avec une grande inclinaison. Cette corrélation est opposée à celle que l'on observe pour les autres populations de petits corps du Système Solaire externe, populations dans lesquelles les objets dynamiquement plus excités et avec une grande inclinaison ont des spectres plus neutres/bleus, par effets de collisions qui rajeunissent leur surface. La corrélation entre l'inclinaison et les couleurs de Troyens est associée principalement à la famille d'Eurybates, car elle disparait si l'on ne considère pas les membres de cette famille.
En comparant les couleurs/spectres de Troyens avec ceux d'autres objets du Système Solaire externe, nous avons trouvé que leurs couleurs moyennes sont similaires à celles des comètes et de la partie bleue de la population de Centaures et OTNs. Par contre, la distribution de couleurs de Troyens n'est pas compatible avec celle des autres classes d'objets, et elle montre que les Troyens constituent une population assez particulière (Fig. 1.5).

5. **Observations de Centaures et de transneptuniens (OTNs) :** j'ai participé à un large programme d'observation au sol à l'ESO-VLT&NTT (PI Barucci avec collaboration de différents instituts internationaux, plus de 500 heures d'observations) dédié à l'étude des Centaures et trans-neptuniens par photométrie, spectroscopie et polarimétrie, ainsi qu'à des observations ciblées de certains OTNs. J'ai participé aussi à des campagnes observationnelles multi-couleurs en photométrie menées aux télescopes CFHT et TNG. J'ai obtenu le tout premier spectre d'Orcus, spectre qui a permis de détecter la glace d'eau et de contraindre par modélisation son abondance de surface (Fig. 1.6).
Dans le large programme, plus de 40 objets du Système Solaire externe ont été observés en spectroscopie dans le visible et le proche infrarouge. J'ai découvert que quelques objets (comme 2003 AZ84) ont de faibles bandes d'absorption dans la région visible qui peuvent être associées au processus d'altération aqueuse, mais la plupart des OTNs et Centaures n'ont pas de bandes d'absorption dans ce domaine de longueur d'onde. Par contre, dans l'infrarouge, beaucoup de spectres sont caractérisés par les bandes d'absorption dues à la glace d'eau, amorphe et cristalline, au méthane, à l'azote et au méthanol (Fig. 1.6).
La présence de glace d'eau cristalline à la surface de certains OTNs donne des contraintes très fortes sur les mécanismes d'évolution (altération et/ou renouvellement) de leur surface. En effet, l'eau cristalline implique des températures supérieures à 110/120 K, nécessaires pour cristalliser la glace d'eau amorphe, alors que les températures attendues à la surface des OTNs sont certainement plus froides (20-60 K). Les processus de cryovolcanisme ou radiogéniques et les micro-impacts ont été invoqués pour expliquer la présence de la glace à l'état cristallin.
L'étude statistique sur les propriétés de surface montre que tous les objets de la classe BB (ceux qui ont des couleurs similaires à celle du Soleil), semblent posséder de la glace en surface (Fig. 1.6). Les objets intermédiaires de classe IR, associés uniquement aux trans-neptuniens résonnants et classiques, ne semblent pas présenter de surfaces riches en glace. Enfin, les objets les plus rouges (RR) et les modérément rouges (BR) sont indistinctement recouverts ou non de glace. Une partie des objets les plus rouges ont la particularité de

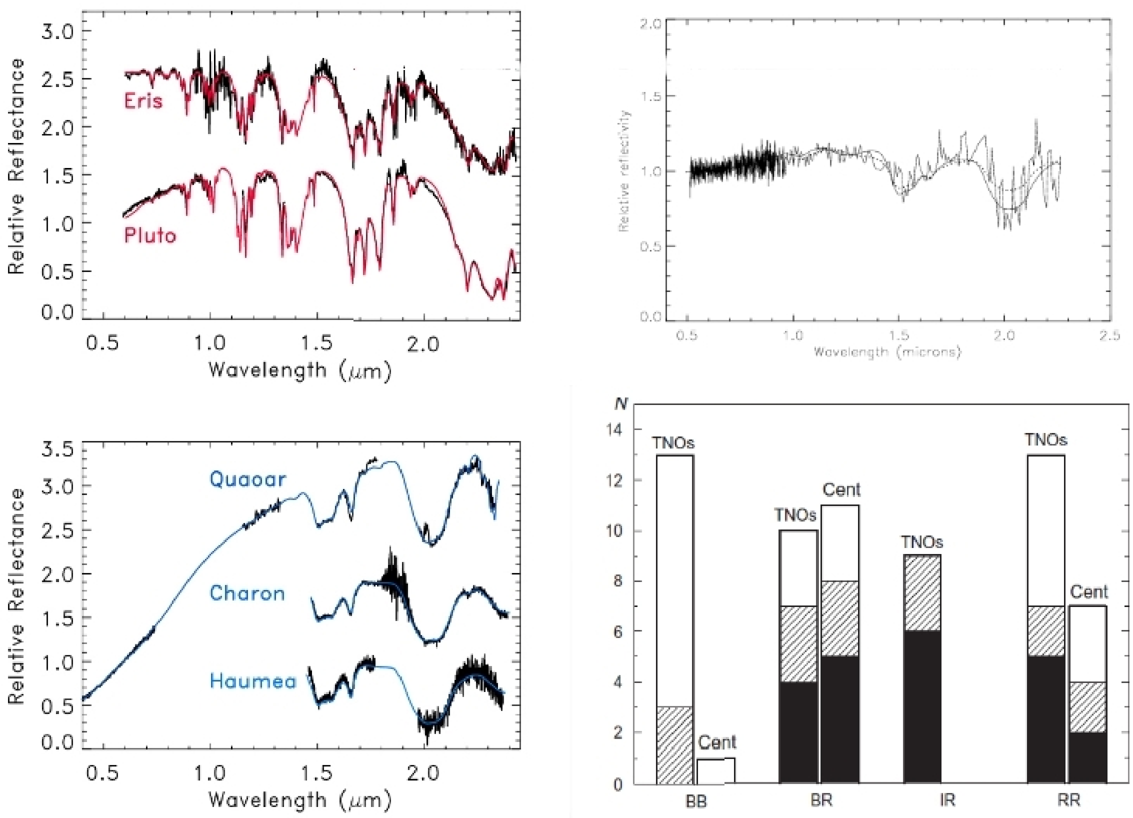

FIG. 1.6 – A gauche : Spectres des plus grands OTNs riches en méthane (haut) et en glace d'eau (bas) et leur modéles. A droite : en haut, spectres de 2004 DW Orcus obtenus au télescope TNG et les modèles de composition proposés, avec une abondance de glace d'eau allant de 10% (ligne continue) à 2% (ligne pointillée) ; en bas : nombre d'objets sur lesquels on a (en blanc) ou non (en noir) détecté de la glace en surface en fonction de la classe taxonomique. Les objets représentés par les hachures correspondent à ceux où la glace est probable en surface mais pas certaine.

posséder, dans certains cas, de la glace de méthanol. Les résultats sur les observations en spectroscopie des OTNs et Centaures sont présentés dans le paragraphe 5.5 de ce mémoire.

Nous avons observé en photométrie plus de 40 objets dans le large programme et plus de 120 dans les campagnes d'observation multi-couleurs de Meudon. Ceci a permis d'avoir des contraintes sur la composition superficielle des objets, de donner une classification taxonomique, d'étudier les propriétés rotationnelles pour une douzaine d'objets (en déterminant la période de rotation et en donnant des contraintes sur leur forme et structure interne), et de faire des études statistiques (voir le paragraphe 5.3 pour tous les détails). Ces dernières ont montré que les objets dynamiquement plus excités, ceux avec une grande inclinaison et excentricité, ont des surfaces moins rouges que les autres, ce qui semble indiquer qu'il y a un processus de rajeunissement des surfaces plus efficace dans la région des OTNs classiques. Les objets observés avec un périhélie > 40 UA sont pour la plupart très rouges. Les Centaures montrent une distribution bimodale des couleurs, c'est-à-dire une forte dichotomie entre les objets neutres et les objets très rouges.

Une dizaine d'OTNs et de Centaures ont été observés aussi en polarimétrie (voir le paragraphe 5.4). Leur courbe de polarisation montre une branche de polarisation négative qui

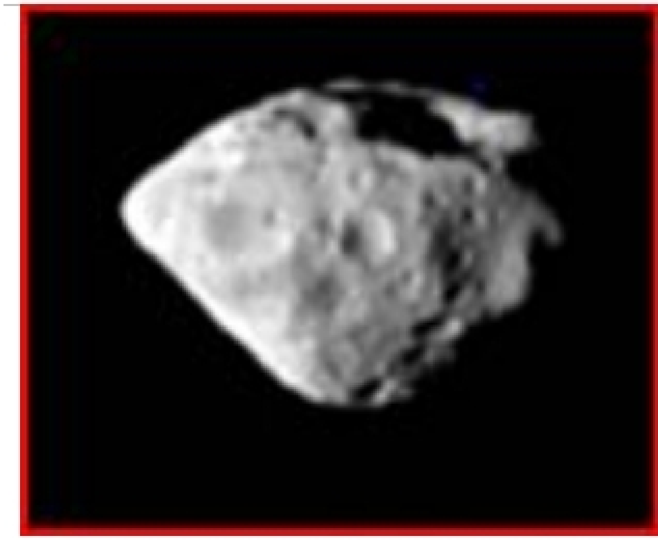 

Fig. 1.7 – A gauche : image de 2867 Steins prise le 5 Septembre 2008 par la caméra WAC d'OSIRIS à une distance de 803 km de l'astéroïde (résolution 80 m/px). A droite : image de 21 Lutétia prise par la caméra NAC d'OSIRIS à une distance de 3159 km (résolution 60 m/px).

est typique des objets sans atmosphère du Système Solaire. Les objets observés montrent deux courbes de polarisation différentes selon leur taille : ceux avec un diamètre < 1000 km montrent une polarisation négative qui augmente en valeur absolue jusqu'à -1% à l'angle de phase de 1^o ; les gros OTNs et planètes naines montrent une polarisation négative plus petite et qui reste presque constante pour les angles de phase $< 2^o$. Les modèles du comportement polarimétrique des gros OTNs observés montrent que leurs surfaces consistent en des particules transparentes, larges par rapport au domaine de longueur d'onde observé, et hétérogènes. Les OTNs et les Centaures plus petits semblent par contre être recouverts d'une couche de glace cristalline, dont les grains ont une dimension inférieure au micron, déposée sur une surface sombre

Au-delà de l'activité d'observation au sol des petits corps du Système Solaire **je suis fortement impliquée dans la mission Rosetta**, pierre angulaire de l'ESA dédiée aux petits corps. Je suis co-investigatrice de l'instrument OSIRIS, le système d'imagerie de Rosetta. Dès 1998 j'ai commencé à m'investir sur la mission Rosetta avec des activités scientifiques et instrumentales : observations au sol de ses cibles, afin d'améliorer leur connaissance et donc optimiser l'orbite de la sonde et les séquences observationnelles pendant les rencontres, participation active à la réalisation de la caméra à grand champ de vue WAC du système d'imagerie OSIRIS (travail de caractérisation de propriétés optiques des matériaux employés dans la caméra WAC et simulations de type *ray-tracing* de son complexe système de suppression de la lumière diffuse), et participation à toutes les activités de calibration scientifiques faites au MPS (Max-Planck-Institut für Sonnensystemforschung), en Allemagne.
Je suis membre de 3 groupes de travail qui gèrent les différentes phases de la mission (survol des astéroïdes, calibration et noyau cométaire).
Après le lancement de Rosetta j'ai ensuite participé à la définition des séquences observationnelles pour les observations scientifiques (les OIOR, Orbiter Instrument Operation Request), à l'activité de calibration en vol, devenant responsable des calibrations photométriques d'OSIRIS, et à l'analyse des images. Les résultats d'OSIRIS au cours des survols de Steins et Lutétia et des

observations de la comète Tempel 1 ont été très importants et ont donné lieu à des publications dans des revues prestigieuses comme Science et Nature (Fig. 1.7). Mes activités instrumentales et scientifiques sur l'instrument OSIRIS de la mission Rosetta sont présentées dans le chapitre 3 de ce mémoire.

Ce mémoire s'articule en 5 chapitres principaux. Dans le chapitre 2 je décris mes recherches sur les astéroïdes de la ceinture principale, des classes les plus primordiales aux objets ignés plus évolués, et comprenant aussi les observations des cibles de la mission Rosetta. Dans le chapitre 3 je présente la mission Rosetta, mon travail instrumental sur le système d'imagerie OSIRIS, l'activité de calibration au sol et en vol et enfin les résultats scientifiques de la mission, issus des rencontres avec les astéroïdes Steins et Lutétia. Dans le chapitre 4 on passe au-delà de la ligne de formation de la glace d'eau, et je présente les résultats issus des campagnes observationnelles dédiées aux Troyens de Jupiter membres de familles dynamiques, leur étude statistique, l'analyse des objets peuplant les deux nuages L4 et L5, et la comparaison avec les propriétés de surface d'autres objets du Système Solaire. Dans le chapitre 5 je décris mes travaux sur les Centaures et les objets Transneptuniens, issus des campagnes observationnelles de large envergure et avec de nombreuses collaborations internationales. Enfin, dans le chapitres 6, je présente les perspectives de mes recherches.

Mes recherches ont abouti à de nombreuses publications scientifiques (plus de 80 dans les revues à comité de lecture, voir page 207 la liste complète de mes publications). J'ai inclus dans ce mémoire une sélection d'une quinzaine d'articles les plus représentatifs de mes recherches.

Chapitre 2

Les astéroïdes

2.1 Introduction

Les astéroïdes sont les restes de la population de planétésimaux qui ont formé les planètes il y a 4,6 milliards d'années. Bien que les astéroïdes aient été affectés par une évolution thermique et dynamique, et par des collisions, la plupart d'entre eux n'ont pas subi une évolution géologique et thermique significative, et ils gardent donc la mémoire des conditions initiales qui ont existé dans la nébuleuse solaire.
L'étude physico-chimique des astéroïdes a montré qu'il existe une variation continue de leur composition avec la distance héliocentrique, qui reflète la présence d'un gradient thermique dans le Système Solaire. En effet, les astéroïdes les plus évolués (type E) se situent dans la partie interne de la ceinture principale, alors que les plus primitifs (type D-P), composés de matériaux carbonés et organiques, sont situés vers les régions externes de la ceinture principale ou bien au delà, comme les Troyens de Jupiter. Les différences entre les diverses classes taxonomiques d'astéroïdes sont donc le résultat des différences de conditions environnementales dans lesquelles se trouvaient les matériaux d'origine lors des premières phases de la formation. L'étude des différents types d'astéroïdes permet de mieux comprendre la formation du Système Solaire et les processus successifs d'évolution thermique et dynamique.

2.2 Techniques d'observations

Je me suis dédiée à la caractérisation des propriétés physiques des différentes classes d'astéroïdes en utilisant de nombreuses observations au sol et spatiales (Spitzer, Herschel et Rosetta), et en appliquant différentes techniques et méthodologies d'étude. La plus grande partie des observations ont été faites en spectroscopie dans les domaines visible et proche infrarouge, mais j'ai aussi effectué des études en photométrie, polarimétrie et radiométrie.
La spectroscopie dans les domaines du visible et de l'infrarouge proche constitue la technique la plus sensible et la plus largement utilisée pour la caractérisation de la surface des petits corps. Les paramètres spectraux (par exemple, la position, la profondeur, la forme) des bandes d'absorption sont liés à la composition chimique spécifique de la surface, toutefois l'interprétation est difficile, puisque les différents éléments se combinent de façon non linéaire. La manière la plus simple pour identifier les matériaux sur la surface des petits corps est la comparaison avec des spectres de laboratoire de météorites, de minéraux, et de glaces. L'étape successive nécessaire pour mieux contraindre la composition de surface est la modélisation spectrale, c'est-à-dire le calcul de spectres synthétiques basé sur des théories de transfert radiatif et des mesures en labo-

ratoire de constantes optiques. Les deux principales théories qui sont utilisées pour modéliser les surfaces des petits corps ont été développées par Hapke (1981, 1993) et Shkuratov et al. (1999).

La photométrie, en utilisant plusieurs filtres, permet d'obtenir les indices de couleurs qui fournissent une première estimation des propriétés de surface des objets. L'analyse des courbes de lumière apportent des informations sur les propriétés rotationnelles de l'objet, comme la période et l'orientation de l'axe de rotation, ainsi que sur la forme et la structure à grande échelle de la surface de l'objet. Si l'on dispose d'observations faites à angles de phase différents, l'étude de la courbe de phase (c'est-à-dire de la relation entre la magnitude et l'angle de phase) permet d'avoir des renseignements sur la porosité, la rugosité, et la taille des particules à la surface de l'objet.

La polarimétrie est une technique qui permet de contraindre certaines propriétés de surface et, en particulier, d'évaluer l'albédo des petits corps grâce à des relations empiriques entre l'albédo et les paramètres de la courbe de polarisation (pente, valeur minimum de la polarisation), relations dérivées des études polarimétriques sur des échantillons de météorites et minéraux. Tous les objets du Système Solaire qui n'ont pas d'atmosphère ont une courbe de polarisation caractérisée par une partie négative pour des angles de phases compris entre 0^o et 16-20^o, qui est liée à la relation phase-luminosité (incluant l'effet d'opposition) et expliquée par l'effet de rétrodiffusion cohérente et le *shadowing*. La polarimétrie donne aussi des contraintes sur la classe taxonomique-composition, car les matériaux primitifs et sombres ont une courbe de polarisation beaucoup plus marquée (valeur de la pente, minimum et maximum de polarisation plus grands) par rapport aux matériaux ignés et avec un albédo élevé.

2.3 Les astéroïdes primitifs et le processus d'altération aqueuse

J'ai entamé mes recherches par l'étude spectroscopique des astéroïdes primitifs appartenant aux types primitifs C-B-F et G (suivant la taxonomie de Tholen & Barucci, 1989). Cette étude était dédiée à la compréhension et aux effets du processus d'altération aqueuse. Ce processus est très important pour comprendre la composition et l'évolution chimique et physique du Système Solaire primordial. Il est dû à l'eau liquide qui agit comme solvant et produit des phyllosilicates, des sulfates, des oxydes, des hydroxydes et des carbonates (Vilas et al. 1994, Zolensky et al. 2008). Pour avoir de l'eau à l'état liquide, on suppose que des planétésimaux glacés étaient présents pendant la phase de formation des astéroïdes hydratés et qu'un processus thermique aurait produit la chaleur nécessaire pour fondre la glace et produire de l'eau à l'état liquide. Les possibles sources de chaleur sont le chauffage produit par l'induction électromagnétique de matériaux par le vent solaire pendant la phase T-Tauri du Soleil (Shimazu & Teresawa, 1995) ; la chaleur produite par la désintégration de radionucléides comme l'Al^{26} (Grimm & McSween, 1993) ; ou l'énergie produite par des collisions (Scott et al., 1989).
L'altération aqueuse produit des bandes absorption dans les régions visible et proche infrarouge. La bande la plus représentative (profondeur jusqu'à 23%) se trouve à environ 3 μm, et elle est due à la combinaison d'une bande centrée à 2,7 μm, produite par les ions OH, et d'une bande plus large centrée à 2,9 μm due aux molécules d'eau. Dans la région visible, des bandes plus faibles sont produites à 0,43, 0,60–0,65, 0,7 et 0,80–0,90 μm. La plus importante d'entre elles est la bande très large (0,3 μm de largeur) centrée à 0,7 μm (profondeur jusqu'à 7% par rapport au continuum), produite par des transitions de type $Fe^{2+} \rightarrow Fe^{3+}$ dans les phyllosilicates (la bande centrée à 0,43 μm étant due à des transition ${}^6A_1 \rightarrow^4 A_1$ du Fe^{3+} dans la jarosite (Vilas & Gaffey, 1989), celles centrées à 0,60–0,65 μm et 0,80–0,90 μm sont dues à des absorptions du fer du type ${}^6A_1 \rightarrow^4 T_1(G)$ et ${}^6A_1 \rightarrow^4 T_2(G)$).

Pour mieux comprendre ce processus, une étude spectroscopique à été menée en collaboration avec M. Lazzarin sur un échantillon de 110 astéroïdes de la ceinture principale appartenant aux classes C, G, F, B et P, ceux les plus affectés par le processus. Les données viennent d'observations en spectroscopie dans le domaine visible avec les télescopes 1.5m de l'ESO (principalement), et 1.8m d'Asiago. Les résultats obtenus sont les suivants :

1. 65% des astéroïdes observés montrent des bandes d'absorption dues à l'altération aqueuse.
2. L'analyse en détail des différentes classes taxonomiques montre que 65% des astéroïdes de type C et la totalité des astéroïdes de type G sont hydratés, alors que les astéroïdes de type B, F et P observés ne présentent pas de bandes d'altération aqueuse. Cette analyse confirme la séquence d'altération aqueuse entre les classes P $\rightarrow$ B $\rightarrow$ C$\rightarrow$ G, où les objets de type P ne subissent pas le processus alors que ceux de type G sont les plus altérés.
3. L'analyse de la distribution des astéroïdes hydratés en fonction de la distance héliocentrique confirme la présence d'une zone d'altération aqueuse entre 2,6 et 3,5 UA, comme montrée par Vilas (1994). Nos données montrent que cette région s'étend probablement aussi aux distances héliocentriques plus petites, car entre 2,2 et 2,6 UA 78% des objets observés sont hydratés.
4. L'analyse de la distribution des astéroïdes hydratés en fonction de l'albédo montre que le pourcentage des astéroïdes hydratés augmente au fur et à mesure que la valeur d'albédo dévient plus grande.
5. On ne trouve aucune corrélation entre les astéroïdes hydratés et les diamètres des objets
6. Il y a une forte corrélation entre la bande due à l'altération aqueuse à 0,7μm et celle à 3μm
7. La comparaison entre les astéroïdes hydratés et différentes météorites montrent une forte ressemblance entres ces astéroïdes et les chondrites de type CM2. Les astéroïdes primitifs de la ceinture principale qui ont subi le processus de l'altération aqueuse sont donc les corps parents les plus probables des météorites CM2.

L'analyse à été successivement étendue à un échantillon beaucoup plus important de 572 astéroïdes primitifs, incluant les spectres disponibles dans la littérature (498 astéroïdes de type C, 8 de type G, 42 de type B, 13 de type F et 11 de type P). Cette base de données a montré que l'altération aqueuse agit pour le 9% de la population observée des astéroïdes de la ceinture principale appartenant à la classe P, 8% pour le type F, 5% pour le type B, 47% pour le type C et 100% pour le type G. Avec cette échatillon nous avons aussi trouvé une faible corrélation entre le processus et les dimensions des objets, car le pourcentage d'astéroïdes hydratés augmente avec leur taille, pour des diamètres entre 50 et 225 km (Fornasier et al. 2011, conférence ORIGIN 2011)

2.3.1 Article : Spectroscopic comparison of aqueous altered asteroids with CM2 carbonaceous chondrite meteorites

ASTRONOMY & ASTROPHYSICS
SUPPLEMENT SERIES

Astron. Astrophys. Suppl. Ser. **135**, 65–73 (1999)

Spectroscopic comparison of aqueous altered asteroids with CM2 carbonaceous chondrite meteorites*

S. Fornasier[1], M. Lazzarin[1], C. Barbieri[1], and M.A. Barucci[2]

[1] Dip. di Astronomia, Vic. Osservatorio 5, I–35122 Padova, Italy
e-mail: fornasier@pd.astro.it, lazzarin@pd.astro.it, barbieri@pd.astro.it
[2] Observatoire de Paris, 92195 Meudon Principal Cedex, France
e-mail: barucci@obspm.fr

Received July 15; accepted September 23, 1998

Abstract. In the last year we have started a spectroscopic investigation of asteroids located in the region of the main-belt between about 2.2 and 3.6 AU. The aim of this work is to study the aqueous alteration process which acted in that zone, dominated by low albedo C–type asteroids, and to compare the spectra of these hydrous objects with those of CM2 carbonaceous chondrite meteorites. In fact, the spectra of these meteorites reveal features probably due to aqueous altered materials on their surfaces.

The study of the aqueous alteration process can give important information on the chemical and thermal evolution of the earliest Solar System.

More that 65% of the investigated objects have revealed features suggesting the presence of hydrous materials. The comparison of the spectra of the hydrated asteroids obtained to date with those of several CM2 carbonaceous chondrite meteorites seems to indicate that aqueous altered asteroids could be the parents of CM2 meteorites.

The data have been obtained during several observational runs at the Asiago Observatory with the 1.8 m telescope and at ESO–LaSilla with the 1.5 m telescope.

Key words: meteors, meteoroids — minor planets, asteroids — solar systems: formation

1. Introduction

The origin of most meteorite types is still a matter of debate (asteroidal, cometary or planetary origin).

In this work we attempted a comparison between hydrated asteroids and CM2 carbonaceous chondrites as they exhibit similar spectroscopic behaviour.

The distribution of asteroidal classes is dependent on heliocentric distance: objects closer to the Sun (belonging above all to S–type), appear to have been strongly heated and differentiated, while asteroids at greater distance seem to have undergone little or no heating and differentiation. These ones belong to C, P and D taxonomic types: they are low–albedo (≤ 0.05) objects, darkened by carbonaceous and organic materials on their surfaces (Gradie & Tedesco 1982). So the small bodies at great heliocentric distances ($d_\odot \geq 3$ AU) may have preserved materials which witnessed the condensation of the Solar nebula and the early phases of the formation of the Solar System. Vilas (1994), has revealed that a particular zone of the outer main belt seems dominated by objects which have undergone aqueous alteration process, that is the low temperature chemical alteration of materials by liquid water which acts as a solvent and produces materials like phyllosilicates, sulfates, oxides, carbonates, and hydroxides. The study of this process can give important information on the evolution of the earliest Solar System. It is now believed that hydrous minerals could not have condensed directly from the solar nebula, but that they have been produced by hydration of pristine anhydrous silicates. This means that water was present in the primordial asteroids, probably in the form of ice condensed together with the lithic material. Successively, an heat source, probably electric induction by the solar wind during the T-Tauri phase of our Sun (as suggested by Shimazu & Teresawa 1995; Herbert 1989) melted the ice and produced the liquid water necessary to alter superficial minerals. As liquid water can exist only under particular conditions of temperature and pressure, the study of aqueous alteration processes can help to reconstruct the

Send offprint requests to: S. Fornasier
* Based on observations carried out at the European Southern Observatory (ESO), La Silla, Chile, and at the Asiago Observatory, Italy.

different evolutionary stages of the chemical and thermal history of our Solar System.

The asteroids that show hydrated minerals on their surfaces seem to dominate the region of the main belt between 2.6 and 3.5 AU, called also "aqueous alteration zone" (Vilas 1994), and belong essentially to the C, G, F and B taxonomic classes.

Hydrated materials produce characteristic absorption features on the spectra of the asteroids: in the infrared region the 3 μm band (Lebofsky 1980; Jones et al. 1990), associated to "free" water molecules, and to OH ion bounded in the mineral crystal lattice; in the visible range there are several bands centered around 0.43 μm, $0.60 - 0.65$ μm, 0.70 μm and $0.80 - 0.90$ μm, attributed to $Fe^{2+} \rightarrow Fe^{3+}$ charge transfer transitions in oxidized iron (Vilas et al. 1993, 1994; Vilas 1994; Barucci et al. 1998).

In this context we have started a spectroscopic survey of asteroids located between about 2 and 4 AU. Moreover, we attempted a comparison of the spectra of hydrated asteroids with those of CM2 carbonaceous chondrites which show features due to aqueous altered materials, in order to obtain information about the origin of CM2 chondrites.

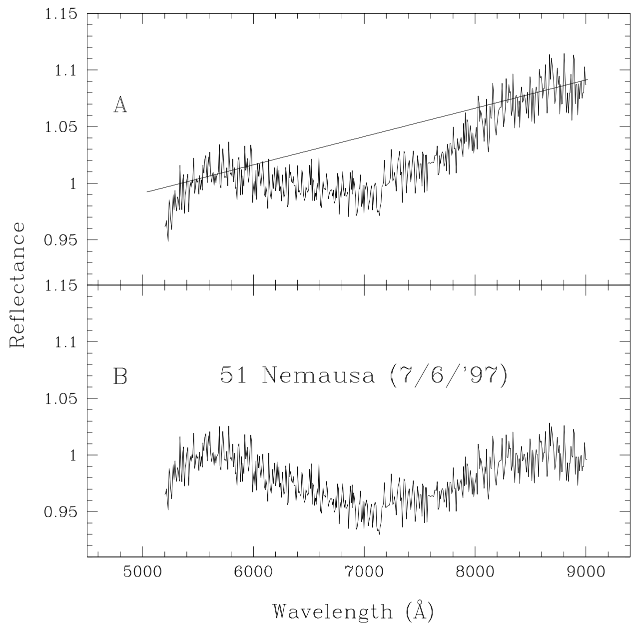

Fig. 1. a) reflectance spectrum of the asteroid 51 Nemausa with superimposed its linear continuum, computed with a linear least squares fit to the smoothed spectral data points. **b)** residual spectra of 51 Nemausa created as a result of the asteroid spectra in A being divided by the linear background. The same procedure was applied to all the other asteroids

2. Observations and data reduction

The data of the asteroids presented have been obtained during different observing runs in the course of 1997.

The observations were performed at the European Southern Observatory of La Silla (Chile) and at the Asiago Astrophysical Observatory (Italy).

At La Silla we used the 1.5 m telescope equipped with a Boller & Chivens spectrograph and a Loral Lesser CCD as detector (2048×2048 pixels). The grating used was a 225 gr/mm, with a dispersion of 331 Å/mm in the first order. The CCD has a 15 μm square pixels, giving a dispersion of about 5 Å/pixel in the wavelength direction. The spectral range is about $0.48 < \lambda < 0.92$ μm with a FWHM of about 10 Å.

At the Asiago Observatory we used the 1.82 m telescope equipped with a Boller & Chivens spectrograph and a Thomson CCD (430 × 600 pixels) as detector. The grating was a 150 gr/mm with a dispersion of 340 Å/mm in the first order. The CCD has 23 μm square pixels giving a dispersion of about 7.8 Å/pixel in the wavelength direction. The spectral coverage is about $0.5 < \lambda < 0.9$ μm with an instrumental FWHM of 15.6 Å.

Each spectrum was recorded through a slit oriented in the East–West direction. The slit was opened to about 8 arcsec in order to reduce effects due to differential refraction and the possibility of losing signal due to guiding errors of the telescopes.

In Table 1 we report the circumstances of the observations (date and site), the visual magnitude of the asteroids, the solar analog stars used for reduction and some physical characteristics of the observed objects: semimajor axis (AU), diameter (km) and albedo derived from IRAS observations, and taxonomic type (Tholen taxonomy).

During each night, we also recorded bias, flat–field, calibration lamp, spectrophotometric standard and solar analog stars spectra at different intervals throughout the night. The stars were observed at airmasses similar to those of the objects.

Solar analog stars (Hardorp 1978) are fundamental in the final step of the reduction procedure to remove the solar contribution from the spectra of the asteroids and to obtain the asteroidal reflectivities. Eight stars have been used: Hyades64, 16 Cyg B, HD 28022, HD 44594, HD 89010, HD 20630, HD 86728, HD 76151. Their choice is connected with the observational period.

The spectra were reduced using ordinary procedures of data reduction with the software packages Midas and IDL.
These procedures include: subtraction of the bias from the raw data, flattening of the data in order to remove large scale structures, cosmic ray removal, background subtraction, collapsing the two dimensional spectra, wavelength calibration, atmospheric extinction. The reflectivity of the asteroids was then obtained by dividing the spectra of the objects by the respective solar analog spectrum.

All asteroid spectra are normalized at 1 around 5500 Å.

Spectra used in these studies, even with a good signal to noise ratio, have been smoothed with a median

Table 1. Observational and physical characteristics of the observed asteroids: circumstances of the observations (date and site), visual magnitude of the asteroids, the solar analog stars used for reduction, semimajor axis (AU), diameter (km) and albedo derived from IRAS observations, and taxonomic type (Tholen taxonomy)

Asteroid	Date	Site	m_v	Solar An.	a (AU)	D (Km)	Albedo	T
1 Ceres	12/11/'97	ESO	9.0	HD28022	2.76	932	0.100	G
10 Hygiea	12/13/'97	ESO	10.2	HD44594	3.13	429	0.075	C
19 Fortuna	12/12/'97	ESO	11.5	Hyades64	2.44	192	–	G
19 Fortuna	9/3/'97	Asiago	9.7	16 Cyg B	2.44	192	–	G
24 Themis	5/3/'97	Asiago	12.2	HD 89010	3.12	234	–	C
34 Circe	9/3/'97	Asiago	13.1	16 Cyg B	2.68	118	0.054	C
38 Leda	5/3/'97	Asiago	12.8	HD 89010	2.74	120	0.062	C
41 Daphne	12/13/'97	ESO	11.9	HD20630	2.76	182	0.073	C
45 Eugenia	9/4/'97	Asiago	11.3	16 Cyg B	2.72	214	0.040	C
51 Nemausa	7/6/'97	Asiago	10.5	16 Cyg B	2.36	153	0.092	C
51 Nemausa	9/3/'97	Asiago	11.7	16 Cyg B	2.36	153	0.092	C
65 Cybele	12/13/'97	ESO	12.5	HD20630	3.42	230	0.057	P
70 Panopaea	12/12/'97	ESO	12.8	Hyades64	2.61	127	0.070	C
74 Galatea	12/13/'97	ESO	12.2	Hyades64	2.78	123	0.034	C
104 Klymene	12/13/'97	ESO	12.6	Hyades64	3.16	127	0.052	C
105 Artemis	12/13/'97	ESO	12.9	Hyades64	2.37	123	0.032	C
128 Nemesis	5/2/'97	Asiago	12.9	HD86728	3.09	194	0.050	C
130 Elektra	9/4/'97	Asiago	10.4	16 Cyg B	3.11	189	0.076	G
137 Meliboea	12/13/'97	ESO	13.1	Hyades64	3.11	150	0.048	C
144 Vibilia	12/13/'97	ESO	11.0	HD20630	2.65	146	0.059	C
145 Adeona	5/3/'97	Asiago	11.9	16 Cyg B	2.67	155	0.043	C
146 Lucina	12/13/'97	ESO	13.6	Hyades64	2.71	137	0.052	C
185 Eunike	5/3/'97	Asiago	12.4	16 Cyg B	2.73	165	0.064	C
190 Ismene	12/13/'97	ESO	12.7	Hyades64	3.97	212	–	P
200 Dynamene	12/13/'97	ESO	13.1	Hyades64	2.73	132	0.053	C
211 Isolda	5/2/'97	Asiago	13.4	HD76151	3.04	148	0.060	C
238 Hypatia	5/4/'97	Asiago	13.0	16 Cyg B	2.90	156	0.043	C
304 Olga	12/13/'97	ESO	13.4	Hyades64	2.40	68	0.047	C
410 Chloris	12/13/'97	ESO	13.5	Hyades64	2.72	128	0.054	C
444 Gyptis	7/7/'97	Asiago	11.2	16 Cyg B	2.76	170	0.051	C
488 Kreusa	5/3/'97	ESO	11.8	HD86728	3.14	158	0.059	C
490 Veritas	7/7/'97	Asiago	13.5	16 Cyg B	3.16	121	0.062	C
618 Elfreide	12/13/'97	ESO	13.6	Hyades64	3.18	124	0.058	C
712 Boliviana	12/13/'97	ESO	11.8	Hyades64	2.57	132	0.046	C
776 Berbericia	12/13/'97	ESO	12.4	Hyades64	2.93	178	–	C
1093 Freda	5/1/'97	Asiago	13.3	HD89010	3.13	120	0.038	C

filter technique. Moreover, in order to study aqueous absorption features, which may be very weak, we treated each asteroid/solar–analog–spectrum as a continuum with discrete absorption features superimposed on it, as described by Vilas et al. (1993, 1993b). For the spectra, a simple linear continuum is defined by a linear least squares fit to the smoothed spectral data points. We then divided each individual spectrum by the continuum, thus removing a sloped background (Fig. 1). If residual absorption features are present in these processed spectra, these features can then be easily recognized. In Figs. 2 and 3 we report the spectra of the observed asteroids divided by their linear backgrounds.

3. Results

3.1. Survey of asteroids

Our spectroscopic survey reveals that more than 65% of the 34 observed asteroids show the presence of absorption bands due to aqueous alteration products, in particular of the 0.7 μm band, which is the most characteristic feature of the hydrated materials in the visible.

The depth of these bands varies between 2% and 6% with respect to the continuum.

We considered only the absorption features deeper than the peak-to-peak scatter (that is ≤ 0.02) in the spectrum, which, from previous experience, seems to be a better indicator of the spectrum quality than the calculated signal to noise ratio (Vilas & Smith 1985).

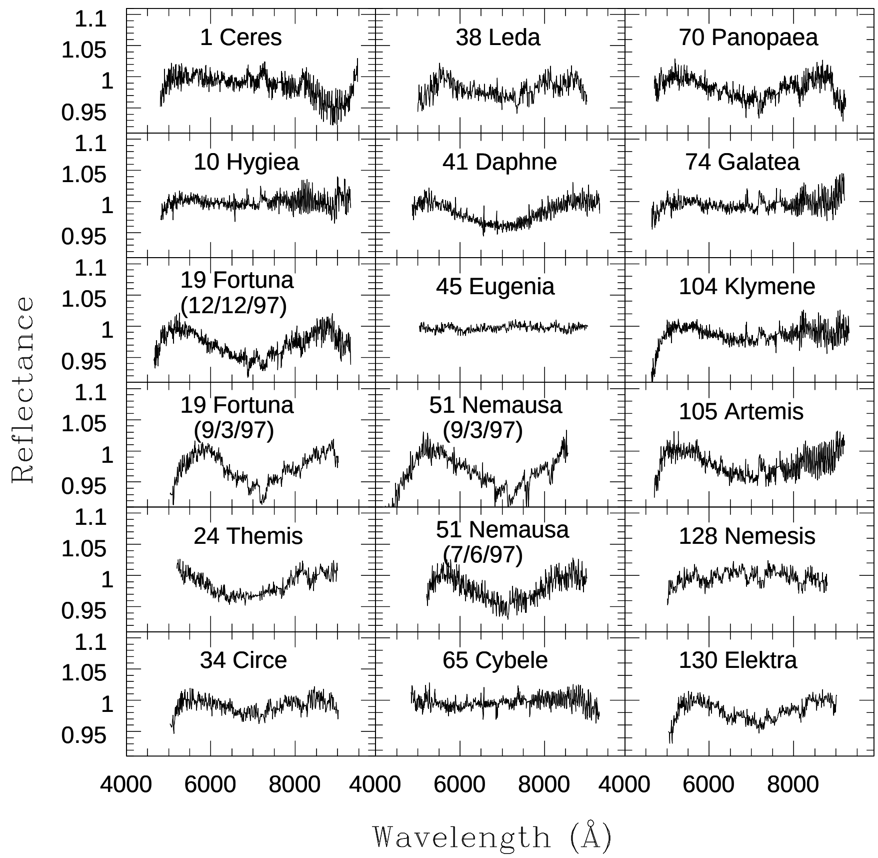

Fig. 2. Reflectance spectra of the observed asteroids. The spectra are normalized to 5500 Å and a linear continuum has been removed

The repeatability of the 0.7 μm absorption band in 19 Fortuna and 51 Nemausa, which were both observed twice on different observing runs, is a good indicator of the quality of data reduction.

Moreover the location and the extension of aqueous altered absorption characteristics do not match any atmospheric absorption band or solar analog feature.

The intense telluric water absorption beginning near 0.9 μm coupled with a drop in responsivity of the CCD detectors have affected the identification of $0.8 - 0.9$ μm features in the asteroid spectra, which we have clearly identified only on 1 Ceres.

Some spectra present spurious features due to an incomplete removal of telluric H_2O at 7300 and 8200 Å and/or to the atmospheric O_2A and O_2B bands at 7619 and 6882 Å respectively, but they do not influence the identification of aqueous altered bands.

Of six investigated objects located outside the "aqueous alteration zone", four have shown the presence of hydration features (Fig. 4). We think that more observations could help to understand the efficiency zone of the aqueous alteration process.

Our results are consistent with those obtained by Barucci et al. (1998), who found that more than 65% of their observed asteroids are hydrated. They also observed hydration features on asteroids located closer to the Sun than 2.6 AU.

Our data also confirm the existence of a relationship between the albedo of the objects and the aqueous alteration process (Fig. 5): the percentage of the observed hydrated asteroids grows as albedo increases. This relation may be explained with the progressive leaching of iron from silicates as the aqueous alteration proceeds. Leached iron (iron is the most important opaque phase in the visible range associated to aqueous alteration process) would be enveloped into magnetite and iron sulfide grains, so less material would be available to absorb the incoming sunlight and this would cause the increasing of the albedo (Vilas 1994).

All the 3 G-class observed asteroids (1 Ceres, 19 Fortuna, 130 Elektra) have features attributed to aqueous altered materials, confirming the fact that G-type objects seem to be the most aqueous altered asteroids. In fact aqueous alteration sequence seems to begin with P class objects (the least altered) and to increase through

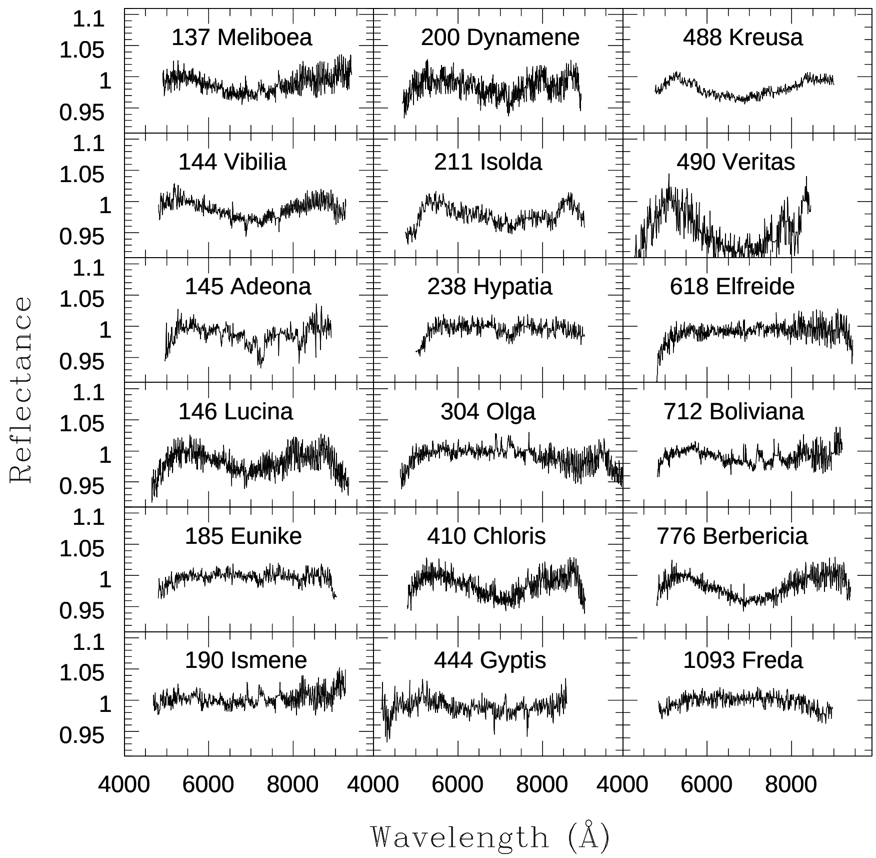

Fig. 3. Reflectance spectra of the observed asteroids. The spectra are normalized to 5500 Å and a linear continuum has been removed

F → B → C → G asteroids (Vilas 1994). Two of the G-type observed objects, 19 Fortuna and 130 Elektra show a well defined 0.7 μm absorption band, while 1 Ceres has the $0.8-0.9$ μm band and two weak absorption bands at 0.6 and 0.67 μm, as observed by Vilas & McFadden (1992) and Sawyer (1991).

Ceres has not the 0.7 μm band, that seems to be a spectral characteristic of G class objects, but, owing to its significant size, it cannot be considered typical of any asteroidal class.

3.2. Comparison between CM2 chondrites and hydrated asteroids

Finally, we have compared the spectra of the observed hydrated asteroids with those of several CM2 carbonaceous chondrite meteorites.

The spectra of the CM2 meteorites have been obtained from literature (Vilas et al. 1994) and have laboratory origin.

They reveal features probably due to aqueous altered materials on their surfaces. This investigation is important because the origin of meteorites is not well known yet.

Many factors affect the comparison between meteorites and asteroids (Pieters & McFadden 1994):

- Physical preparation of a meteorite for measurement in the laboratory may not accurately reproduce the physical form of material on an asteroid surface.
- A significant limiting factor that affects the mineralogical interpretation of meteorite and asteroid spectra includes the signal to noise ratio (so the quality of the spectra), the spectral range of the measurement and the spectral resolution. In fact signal to noise ratio of dark asteroids spectra is generally quite lower than that of meteorites spectra obtained in the laboratory environment (100 or less for asteroids, about 3000 for meteorites). Available spectra of asteroids are limited by the sensitivity of detectors and the faintness of the signal from the object combined with the atmospheric and instrumental noise contribution.
- There are significant dimensional differences, so meteorites and asteroids may have experienced different thermal and chemical processes.
- Many asteroids have not contributed to our meteorite collection and may not correspond to any meteorite class. Moreover, asteroidal observations allow only the

Table 2. Identification of absorption bands on the observed asteroids. For each band we indicate the central wavelength position, the depth and extension. We have identified only those bands whose depth is greater that the peak-to-peak scatter of the spectra due to noise. With the ? we have indicated those bands that seem to be present but are too weak with respect to the noise, so we believe that more observations are necessary to confirm them

ASTEROID	AQUEOUS PRODUCTS	OBSERVED BANDS (μm)	DEPTH	EXTENSION
1 Ceres	Y	0.8 – 0.9	5.0%	8000–9000 Å
		0.60, 0.67?		
10 Hygiea	?	0.60?		
19 Fortuna	Y	0.70	5.0%	5500–8500 Å
24 Themis	Y	0.70	4.0%	5600–8200 Å
34 Circe	Y	0.70	2.3%	5600–8300 Å
38 Leda	Y	0.70	3.4%	5600–8300 Å
41 Daphne	Y	0.70	4.6 %	5400–8400 Å
45 Eugenia	N	–	–	–
51 Nemausa	Y	0.70	4.7%	5600–8300 Å
65 Cybele	?	0.60?		
70 Panopaea	Y	0.70	4%	5600–8300 Å
74 Galatea	N	–	–	–
104 Klymene	Y	0.70	2.5%	5500–8200 Å
		0.8–0.9?		
105 Artemis	Y	0.70	4.5 %	5700–8300 Å
128 Nemesis	N	–	–	–
130 Elektra	Y	0.70	4.7%	5700–8400 Å
137 Meliboea	Y	0.70	3%	5500–8200 Å
144 Vibilia	Y	0.70	3%	5600–8300 Å
145 Adeona	Y	0.70	3.0%	5600–8400 Å
146 Lucina	Y	0.70	3.4%	5600–8000 Å
185 Eunike	N	–	–	–
190 Ismene	N	–	–	–
200 Dynamene	Y	0.70	2.5%	6000–8000 Å
		0.8–0.9?		
211 Isolda	Y	0.70	3.4%	5500–8500 Å
238 Hypatia	N	–	–	–
304 Olga	N	–	–	–
410 Chloris	Y	0.70	4.7%	5500–8000 Å
444 Gyptis	Y	0.70	2.1%	5600–8500 Å
		0.43?		
		0.50?		
488 Kreusa	Y	0.70	3.4%	5400–8300 Å
490 Veritas	Y	0.70	6.9%	5300–8300 Å
618 Elfreide	N	–	–	–
712 Boliviana	Y	0.70	3.1%	5800–8300 Å
776 Berbericia	Y	0.70	4.5%	5500–8300 Å
1093 Freda	N	–	–	–

study of their surface properties, while meteorites may be derived also from the inner parts of the parent bodies.

- Space weathering influences the surface composition, and may affect asteroid and meteorites in different manner. This is a result of studies especially on lunar meteorites, and seems to produce lower albedo, weaker absorptions and a red-sloped continuum.
- Meteorites may be deeply altered from their pristine interspace condition by terrestrial weathering (Britt et al. 1992).

We compared our hydrated asteroids(those which have the 0.7 μm band) with 7 CM2 carbonaceous chondrites (see Fig. 6), whose spectra were treated as those of the asteroids, that is they were divided by a linear continuum defined by a linear least squares fit to the spectral data points.

We used the Chi–Square Fitting method to measure the agreement between each hydrated asteroid and the 7 CM2. The Chi–Square is defined in the following way:

$$\chi^2 = \sum_{i=1}^{N} \frac{(ya_i - yc_i)^2}{\sigma_i^2}$$

Table 3. Values of the Chi-Square computed by the comparison of each hydrated asteroid with the 7 CM2 chondrites. The maximum likelihood between the asteroid and the meteorites is obtained for that CM2 which gives the least Chi-Square value (represented in boldface)

ASTEROID	**CM2 CARBONACEOUS CHONDRITES**						
	ALHA81002	ALHA83100	ALHA84029	COLDBOKK	LEW90500	MIGHEI	MURRAY
19 Fortuna	190.37	136.69	210.48	149.68	**117.56**	129.17	153.68
34 Circe	568.79	390.56	675.35	402.86	**199.63**	287.78	266.88
38 Leda	338.15	249.55	428.34	248.07	**112.96**	161.63	176.49
41 Daphne	306.68	240.04	392.20	231.73	**108.13**	153.63	183.64
51 Nemausa	305.41	214.19	360.45	239.30	**116.74**	161.04	185.02
70 Panopaea	332.80	247.67	422.52	238.06	**109.74**	163.35	180.36
104 Klymene	472.69	331.95	581.13	342.68	**160.48**	227.91	215.54
105 Artemis	218.51	179.41	297.06	173.31	**96.92**	110.62	133.86
130 Elektra	353.08	227.35	430.03	234.53	**89.75**	152.77	152.00
137 Meliboea	438.91	312.04	539.44	318.57	**144.93**	213.06	212.33
144 Vibilia	399.74	275.89	491.40	278.69	**117.76**	184.28	187.58
145 Adeona	1155.17	1034.91	1250.80	1110.81	**908.84**	988.64	958.53
146 Lucina	406.56	284.63	493.35	289.16	**136.25**	198.52	201.60
200 Dynamene	519.33	396.66	609.94	431.76	**251.69**	320.57	313.02
211 Isolda	248.50	117.01	331.12	161.86	**67.65**	97.19	116.42
410 Chloris	404.02	273.46	484.06	299.08	**128.10**	197.68	201.90
712 Boliviana	541.99	373.99	647.68	378.72	**196.35**	266.76	243.87
776 Berbericia	300.72	218.19	378.16	222.01	**94.89**	145.71	164.82

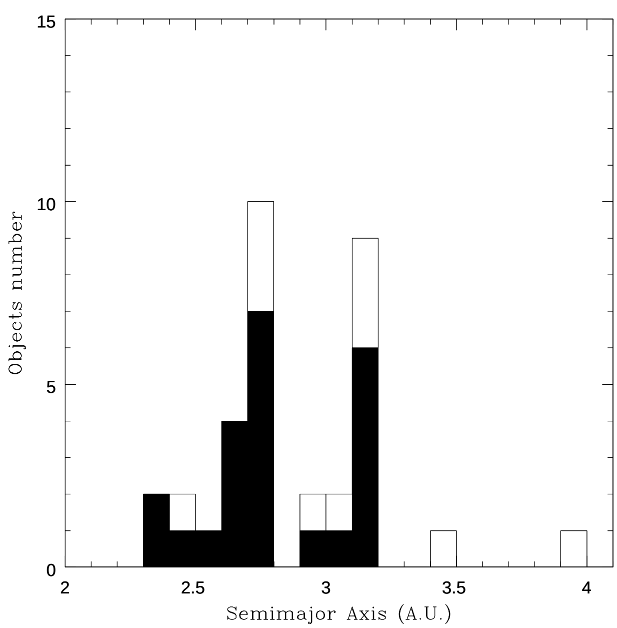

Fig. 4. Number of the observed objects as function of the semimajor axis. The black part represents the hydrated asteroids (only those which have clear and well identified hydration absorption features)

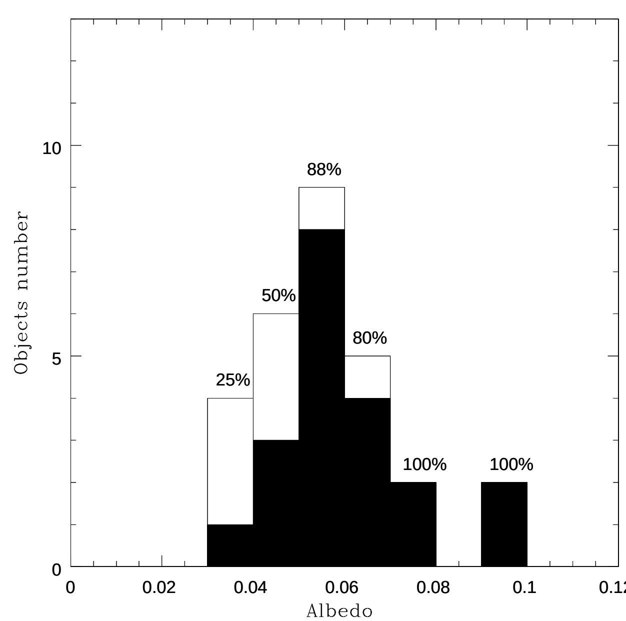

Fig. 5. Number of the observed objects as function of the geometric albedo. The black part represents the hydrated asteroids (only those which have clear and well identified hydration absorption features)

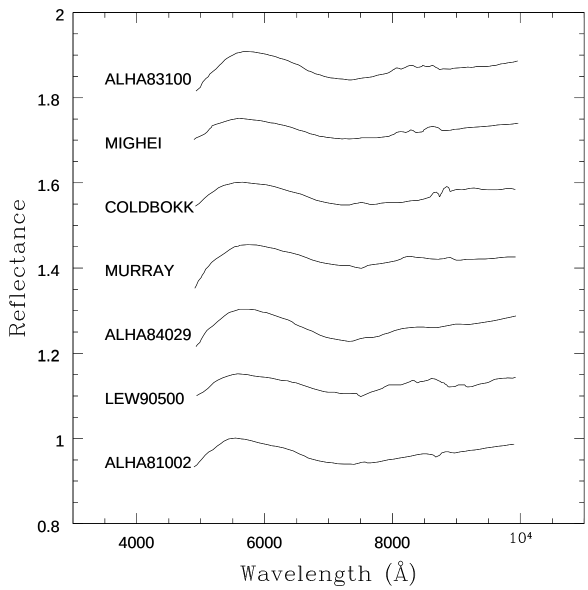

Fig. 6. Reflectance spectra of 7 CM2 carbonaceous chondrite meteorites (Vilas et al. 1993). The spectra were normalized to 5500 Å and a linear continuum has been removed. They were offset by 0.15 in reflectance for clarity

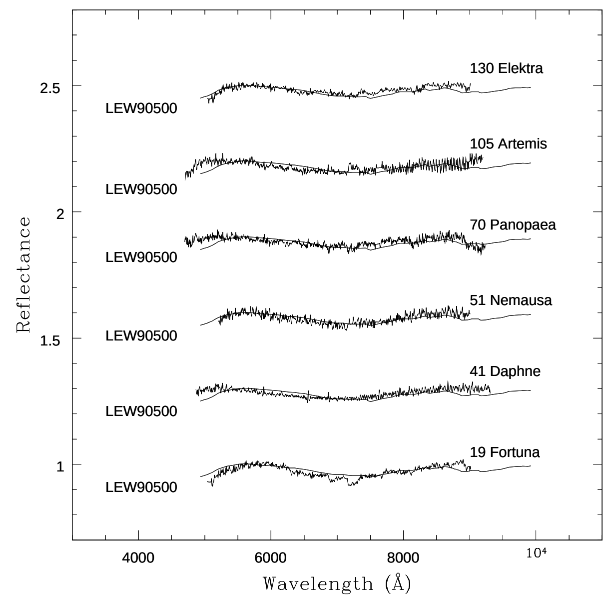

Fig. 7. Comparison between the asteroids 19 Fortuna, 41 Daphne, 51 Nemausa, 70 Panopaea, 105 Artemis and 130 Elektra with the carbonaceous chondrites LEW90500. The spectra are offset by 0.3 in reflectance for clarity

where (x_i, ya_i) are the mean data points (x = wavelength; y = reflectance) of the asteroid (i.e. a mean of the asteroidal signal, affected by noise); (x_i, yc_i) are the data points of CM2 chondrites (these spectra were obtained in laboratory, so they have pratically no noise); N = number of degree of freedom, i.e. the number of points in which we have divided the wavelength range; σ_i is the standard deviation of the asteroidal data points.
We have computed the Chi–Square on 200 points ($N = 200$).

As we have not a set of observations for each asteroid, but a single spectrum per asteroid, we have assumed σ_i = costant = 0.02, which is about the mean peak–to–peak variation of the asteroidal signal.

The maximun likelihood estimate between each asteroid and the 7 "models" represented by the 7 CM2 meteorites is obtained when the Chi–Square assumes the least value.

The results of this quantitative comparison are summarized in Table 3. The best meteoritical analog of all the hydrated asteroids is LEW90500 CM2: the other 6 CM2 have a deeper and wider 0.7 μm absorption band than that of the asteroids.

In Figs. 7 and 8 we report some examples of the comparison between hydrated asteroids and LEW90500 CM2.

The differences in depth of the band and in its extension may depend on the degree of aqueous alteration

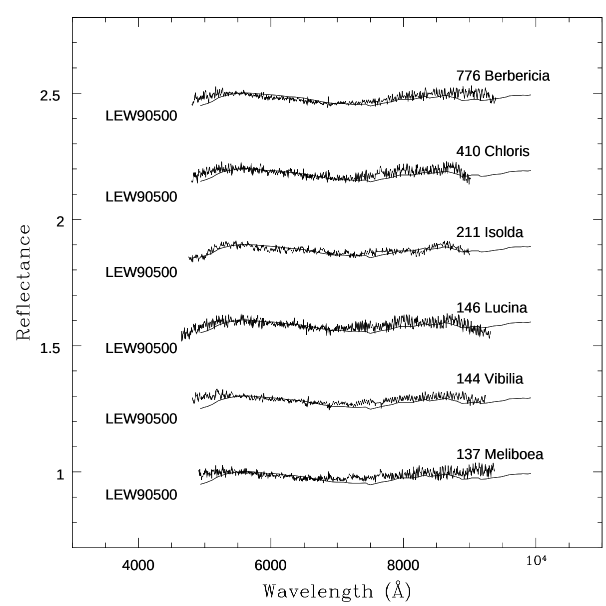

Fig. 8. Comparison between the asteroids 137 Meliboea, 144 Vibilia, 146 Lucina, 211 Isolda, 410 Chloris and 776 Berbericia with the carbonaceous chondrites LEW90500. The spectra are offset by 0.3 in reflectance for clarity

and on the presence of different amount of Fe in silicates crystal lattices. Moreover, laboratory experiments show that the reflectance of a mineral mixture is nonlinear and is a function of viewing geometry and properties of the particles such as single scattering albedo (efficiency of an average particle to scatter and not absorb light), porosity, diameters and mass fractions (Burbine et al. 1996). So small differences in composition or in particle sizes and properties are sufficient to produce a different spectral response.

The good match between several observed hydrated asteroids and CM2 meteorites, in particular LEW90500, resulting from our analysis, is a valid confirmation that aqueous altered asteroids could be the parents of CM2 carbonaceous chondrite meteorites.

4. Conclusions

We obtained visible spectra of 34 asteroids belonging to C, G, and P classes, localized between 2.2 and 3.9 AU. Our analysis reveals that more than 65% of the investigated asteroids show the presence of absorption bands due to aqueous alteration products (0.6, 0.7, $0.8-0.9$ μm, depth between 2% and 6% with respect to the continuum), in particular of the 0.7 μm band, which is the most characteristic feature of the hydrated materials in the visible. Our data also confirm the existence of a relationship between the albedo of the objects and the aqueous alteration process: in fact the percentage of the observed hydrated asteroids grows as albedo increases. We also found hydration features on 4 asteroids located outside the "aqueous alteration zone" as defined by Vilas (1994). Our results confirm those recently obtained by Barucci et al. (1998).

We compared the spectra of the observed hydrated asteroids with those of 7 CM2 carbonaceous chondrite meteorites. This comparison reveals a good match (differences $\leq 3\%$) between the meteorites and most of the observed objects, suggesting that hydrated asteroids might be the parent bodies of CM2 meteorites.

References

Barucci M.A., Fulchignoni M., Lazzarin M., 1996, Planet. Space Sci. 44, 1047

Barucci M.A., Doressoundiram A., Fulchignoni M., Lazzarin M., Florczak M., Angeli C., Lazzaro D., 1998, Icarus 132, 388

Britt D.T., Tholen D.J., Bell J.F., Pieters C.M., 1992, Icarus 99, 153

Burbine T.H., Meibon A., Binzel R.P., 1996, Meteor. Planet. Sci. 31, 607

Gradie J.C., Tedesco E.F., 1982, Sci 216, 1405

Hardorp J., 1978, A&A 63, 383

Herbert F., 1989, Icarus 78, 402

Jones T.D., Lebofsky L., Lewis J., Marley M., 1990, Icarus 88, 172

King T.V.V., Clarck R.N., Calvin W.M., Sherman D.M., Brown R.H., 1992, Sci 255, 1551

Lazzarin M., Barbieri C., Barucci M.A., 1995, AJ 110, 3058

Lebofsky L.A., 1978, MNRAS 182, 17

Lebofsky L.A., 1980, AJ 85, 573

Lebofsky L.A., Feierberg M.A., Tokunaga A.T., Larson H.P., Johnson J.R., 1981, Icarus 48, 453

Lebofsky L.A., Jones T., Owensby P.D., Feierberg M.A., Consolmagno G.J., 1990, Icarus 83, 16

Pieters C.M., McFadden L.A., 1994, Annu. Rev. Earth Planet. Sci. 22, 457

Sawyer S.R., 1991, PhD thesis, The University of Texas at Austin, A hight resolution CCD Spectroscopic Survey of Low Albedo Main Belt Asteroids

Shimazu H., Teresawa T., 1995, Jou. Geoph. Res. 100, 16923

Vilas F., Smith B.A., 1985, Icarus 64, 503

Vilas F., McFadden L.A., 1992, Icarus 100, 85

Vilas F., Hatch E.C., Larson S.M., Sawyer S.R., Gaffey M.J., 1993, Icarus 102, 225

Vilas F., Larson S.M., Hatch E.C., Jarvis K.S., 1993b, Icarus 105, 67

Vilas F., 1994, Icarus 111, 456

Vilas F., Jarvis K.S., Gaffey M.J., 1994, Icarus 109, 274

Zolensky M.E., McSween M., 1988, in: Kerridge J.F., Matthews M.S. (eds.) Meteorites and the early Solar System. Univ. of Arizona Press, Tucson, p. 114

2.4 Les astéroïdes de la classe S et le "space weathering"

Les astéroïdes de la classe S ont une composition de surface silicatée et des spectres caractérisés par des bandes d'absorption dans la région 0,9-1 μm et 2 μm dues aux olivines et pyroxènes. Ces astéroïdes sont supposés être les corps parents des chondrites ordinaires, qui représentent 80% des météorites tombées sur Terre. Pendant longtemps ce lien a été controversé car il y avait des problèmes de similitude spectrale entre les astéroïdes de type S et les chondrites ordinaires (OC). En effet, même si les bandes associées aux silicates sont bien visibles et les paramètres spectraux comparables, la pente spectrale est, elle, très différente. Aujourd'hui, grâce aux résultats des missions spatiales (NEAR, HAYABUSA) le lien entre les astéroïdes S et les OC est bien établi et la différence de pente spectrale est expliquée par les processus de *space weathering*, c'est-à-dire les phénomènes de vieillissement de la surface produits par le vent solaire et les micro impacts, qui affectent les surfaces des objets sans atmosphère et qui vont altérer les propriétés optiques, physiques et chimiques de surface. Les missions spatiales comme la sonde Galileo sur les astéroïdes du type S Gaspra, Ida et Dactyl et la sonde NEAR sur 433 Eros (type S) ont montré que les surfaces de ces objets sont effectivement modifiées par le processus de space weathering, qui cause un rougissement de la pente spectrale, une diminution d'intensité des absorptions et de l'albédo. En particulier, Eros a montré une composition chimique similaire à celle des météorites OC, même si son spectre présente le phénomène du rougissement (Clark et al. 2000 ; McFadden et al., 2001).

Un exemple d'étude du processus de vieillissement de la surface d'astéroïdes de type S et du lien météorite-astéroïde est celui de l'astéroïde 4979 Otawara (Fornasier et al., 2003), une des anciennes cibles de Rosetta avant la redéfinition de son orbite. Des campagnes observationnelles avait été menées en 2001-2002, à l'occasion de son opposition, pour une analyse complète spectroscopique et photométrique. A partir de la courbe de lumière, nous avons déterminé que l'astéroïde a une rotation rapide (P=2,707 heures) et nous avons donné une première évaluation de l'axe de rotation de l'objet.
L'analyse du spectre permet de déduire qu'Otawara est un astéroïde du type S et plus précisément, suivant la classification de Gaffey et al. (1993) sur la base du rapport entre les superficies des bandes BI (celle à environ 1 μm) et BII (celle à environ 2 μm), qu'il fait partie du sous-type S(IV). Les astéroïdes du type S(IV) sont les corps parents les plus probables des chondrites ordinaires parmi la population des astéroïdes de type S. Nous avons donc analysé le spectre d'Otawara pour voir si des corrélations avec ces météorites existaient. Suivant la méthode de Cloutis et al. (1986), nous avons trouvé une valeur de l'orthopyroxène de 25±3 %, compatible avec les valeurs typiques des chondrites ordinaires de type L et LL. Cependant le spectre d'Otawara a une pente beaucoup plus rouge que celle des chondrites ordinaires, et il est donc affecté par des processus de *space weathering*. Pour mieux étudier ces processus, nous avons simulé les effets de vieillissement de la surface avec la présence de fer nanophase, qui est un produit d'altération et induit un rougissement spectral. Nous avons donc corrigé le rougissement en divisant le spectre d'Otawara par la courbe de rougissement produite par le fer nanophase (0.05%). Après la correction et en considérant aussi l'abondance d'orthopyroxène dérivée de l'analyse spectrale, Otawara montre une forte analogie avec les chondrites ordinaires de type LL.

2.4.1 Article : A portrait of 4979 Otawara, target of the Rosetta Space Mission

A&A 398, 327–333 (2003)
DOI: 10.1051/0004-6361:20021622

Astronomy & Astrophysics

A portrait of 4979 Otawara, target of the Rosetta space mission⋆

S. Fornasier[1,2], M. A. Barucci[2], R. P. Binzel[3], M. Birlan[2], M. Fulchignoni[2], C. Barbieri[1], S. J. Bus[4], A. W. Harris[5], A. S. Rivkin[3], M. Lazzarin[1], E. Dotto[6,7], T. Michałowski[8], A. Doressoundiram[2], I. Bertini[1], and N. Peixinho[2,9]

[1] Astronomical Department of Padova, Vicolo dell'Osservatorio 2, 35122 Padova, Italy
e-mail: [fornasier; barbieri; lazzarin]@pd.astro.it, bertini@planet.pd.astro.it
[2] LESIA, Observatoire de Paris, 92195 Meudon Principal Cedex, France
e-mail: [antonella.barucci; Mirel.Birlan; Marcello.Fulchignoni; alain.doressoundiram; Nuno.Peixinho]@obspm.fr
[3] Department of Earth, Atmospheric and Planetary Sciences, Massachusetts Institute of Technology, Cambridge, 02139, USA
e-mail: [rpb; asrivkin]@mit.edu
[4] Institute for Astronomy Hilo, HI 96720, USA
e-mail: sjb@ifa.hawaii.edu
[5] Space Science Institute, 4603 Orange Knoll Ave., La Canada, CA 91011-3364, USA
e-mail: harrisaw@colorado.edu
[6] INAF-Osservatorio Astronomico di Torino, Strada Osservatorio 20, 10025 Pino Torinese (TO), Italy
e-mail: dotto@to.astro.it
[7] INAF-Osservatorio Astronomico di Roma, Via Frascati 33, 00040, Monte Porzio Catone (Roma), Italy
[8] Astronomical Observatory, Adam Mickiewicz University, Sloneczna 36, 60-286 Poznan, Poland
e-mail: tmich@amu.edu.pl
[9] CAAUL, Tapada da Ajuda, 1349-018 Lisboa, Portugal

Received 27 May 2002 / Accepted 17 October 2002

Abstract. A physical portrait based on spectral and photometric data of 4979 Otawara, the first asteroid target of the Rosetta mission, is presented. The aim of this work is to investigate the composition of 4979 Otawara and to evaluate its rotation pole orientation. The spectroscopic observations obtained at the Palomar 200″and IRTF telescopes cover the wavelength range 0.4 to 2.5 μm, and provide a definitive classification of Otawara as an S-type asteroid. An analysis of band depths and slopes places Otawara in the S(IV) subgroup, suggesting a similarity to ordinary chondrite meteorites.
Moreover we present new photometric data, obtained at the Asiago Observatory and at the TNG telescope, that allow confirmation of the fast rotational period of 2.707 ± 0.005 hours, and a first indication of the spin vector of Otawara.

Key words. planets and satelites: individual: Otawara – minor planets, asteroids

1. Introduction

Rosetta is the cornerstone mission of ESA devoted to the study of minor bodies of the Solar System. The mission will be launched in January 2003 and has as its primary target 46P/Wirtanen, a short period comet in the Jupiter family whose rendezvous will be in November 2011. During its cruise to comet Wirtanen, the Rosetta spacecraft will encounter two main belt asteroids: 4979 Otawara and 140 Siwa. Rosetta will fly by Otawara on 11 July 2006, at a heliocentric distance of 1.89 AU, with a minimum encounter distance of 2200 km and a relative velocity of about 10 km s^{-1}. The Siwa flyby will occur on 24 July 2008 at 2.75 AU from the Sun, at a minimum distance of 3500 km. The goals of the mission during the asteroid encounters will be a complete determination of their physical properties (size, shape, density, mass, rotational properties), the study of their composition, and the investigation of the neighbouring space in order to detect possible satellites.

Send offprint requests to: S. Fornasier,
e-mail: fornasier@pd.astro.it

⋆ Based on observations obtained at the IRTF Observatory, Hawaii, USA, at the Palomar Mountain Observatory, California, USA, at the TNG telescope, La Palma, Spain and at the Asiago Astrophysical Observatory, Asiago, Italy.

Table 1. Orbital and physical characteristics of 4979 Otawara. [a] data from Doressoundiram et al. (1999).

perihelion distance (AU)	1.855
aphelion (AU)	2.481
semimajor axis (AU)	2.169
eccentricity	0.144
inclination (degrees)	0.912
synodical rotation period (hrs)	2.707 ± 0.005[a]
taxonomy	S or V[a]
absolute magnitude	14.08 ± 0.04[a] (S − type)
circular effective radius	2.0 km[a] (S − type)
density	≥1.9[a]

Otawara is a small main-belt asteroid. At the time of Rosetta asteroid target definition, very little was known about the physical properties of this object. Successive international campaigns have revealed that Otawara is a very interesting target; it has a rotational period of only 2 hours and 42 min (Doressoundiram et al. 1999). It will be the first fast rotating asteroid encountered by a space mission. The fast rotation of Otawara will enable Rosetta to image and measure the asteroid's characteristics during one complete rotation.

In this paper we present the first near infrared spectrum of Otawara that definitively determines its taxonomic class. We add also a new visible spectrum of the object and new photometric data that confirm the rotational period value previously determined by Doressoundiram et al. (1999), and Le Bras et al. (2001) and allow a first estimation of the spin vector state.

This information will aid Rosetta mission planners in optimising the encounter trajectory and planning of science operations.

2. Observations and data reduction

2.1. Photometric measurements

Photometric observations of Otawara were carried out at the Asiago Astrophysical Observatory, Italy, and at the Telescopio Nazionale Galileo (TNG), La Palma, Spain. Unfortunatly, 2 nights devoted to Otawara observations at the Asiago telescope were lost due to bad weather conditions, and we could observe only partially during two other nights (one at the Asiago telescope and one at the TNG telescope) in poor photometric conditions. So for both nights only relative photometry between the asteroid and some field comparison stars was possible.

At Asiago we observed on 23 December 2001 using the 1.82 m telescope equipped with the AFOSC camera and a 1024 × 1024 pixel CCD, with a total field of view of 8.14 × 8.14 arcmin. The pixel size is 24 μm and the pixel scale is 0.473 arcsec/px. Our measurements were made with a V filter (Johnson) and 300–420 s of exposure time. At the TNG 3.5 m telescope we observed on 8 January 2002, with the OIG camera equipped with a mosaic of two thinned and back-illuminated EEV 42–80 CCDs with 2048 × 4096 pixels each (pixel size of 13.5 microns). The resulting pixel scale is 0.072 arcsec/pix for a total field of view of about 4.9 × 4.9 arcmin. We observed both in V and R filters (Johnson) and the exposure times ranged from 60 to 360 s.

Data reduction was performed in the following way: images were bias subtracted and divided by a flat field (computed as a median of several flat fields obtained during twilight), then relative magnitudes were computed using aperture photometry. We used an aperture radius of about twice the average seeing, and sky subtraction was performed using a 5–10 pixels wide annulus around the asteroid or reference stars.

2.2. Visible spectrum

The visible spectrum of Otawara was obtained at Palomar Mountain Observatory on 23 December 2001 with the 200-inch (5-m) telescope equipped with the Double Spectrograph (see Fig. 2). The instrument simultaneously obtains the blue and red halves of a long slit spectrum using a pair of CCD cameras. Different focal lengths of the two cameras give a pixel scale of 1.25 and 0.94 arcsec per pixel (the 2×2 binned mode was used) respectively for the blue and red channels. A 300 line/mm grating was used for the blue channel, covering a spectral range of 0.42 to 0.62 μm and giving a dispersion of 7 Å per binned pixel. A 158 line/mm grating was used for the red part, covering the wavelength range from 0.53 to 0.92 μm with a dispersion of 10 Å per binned pixel. The final spectrum is the mean of three blue/red pair exposures of 600 s each. A slit of 6 arcsec was used to acquire the data, oriented in a N–S direction in order to minimize effects due to differential atmospheric refraction for objects observed near the meridian. Solar analog stars were observed at airmasses close to that of Otawara.

Data were reduced following usual reduction procedures for visible spectroscopy (see Bus 1999; Xu et al. 1995). Upon extraction each spectrum was rebinned to a uniform dispersion of 25 Å/px and the solar contribution was removed by division by a solar analog star. All the spectra were normalized at 5500 Å.

2.3. Infrared spectrum

The infrared spectrum of Otawara was obtained at the NASA Infrared Telescope Facility (IRTF), Hawaii, USA, equipped with the medium-resolution infrared spectrograph SpeX and employing a 1024 × 1024 InSb array (Rayner et al. 1998). Each exposure consisted of 32 non-destructive reads providing a readout noise of about 15 e^- RMS. Otawara was observed on 12 January 2002 in remote mode from the Observatoire de Paris-Meudon. The instrument was used in the low-resolution prism mode that allows a single exposure to cover the wavelength range from 0.8 to 2.5 μm, with a dispersion of about 50 Å per pixel. The observations were made using a slit of 0.8 arcsec (oriented in the N–S direction) nodding the object along the spatial direction of the slit (offset of 7.5 arcsec), in order to obtain alternated pairs of exposures (denoted as A and B). This procedure allows a very close sky and bias measurement in the same pixel positions as the spectral measurement. A sequence of 9 cycles, each one of the type ABBA, with four exposures of

Table 2. 4979 Otawara: observational circumstances, where r and Δ are respectively the heliocentric and geocentric distances of the asteroid, α the phase angle of the asteroid at the time of observations and m_v is the predicted magnitude from the JPL ephemeris service. The date indicated is relative to the beginning of observations; the symbol * means that observations ended the following day.

Date	UT start	UT end	Telescope	Mode	Instrument	m_v	r (AU)	Δ (AU)	α
23 Dec. 01	08:54	09:18	Palomar 200″	Vis. spectrum	Double Spec.	17.27	2.480981	1.512879	5°.16
23 Dec. 01	21:48	01:43*	Asiago 1.8 m	V imaging	AFOSC	17.26	2.480928	1.511215	4°.87
08 Jan. 02	21:47	01:25*	TNG 3.5 m	$V + R$ imaging	OIG	17.15	2.478565	1.501553	3°.32
12 Jan. 02	09:55	11:21	IRTF 3.0 m	IR spectrum	SpeX	17.26	2.477813	1.509438	5°.09

2 min each, was obtained for a total integration time of 72 min. The object was observed on the meridian, with an airmass less than 1.1, in order to minimize effects due to differential refraction. A solar analog star, Hyades 64, was observed just before and after (and at very similar airmasses) as the object and was used to normalize the reflectance spectrum of the asteroid. Flat field and arcline spectra were also acquired for data calibration.

Data reduction was performed in the traditional way for IR observations: first spectra were corrected for flat fielding, then bias and sky subtraction was performed by producing A–B and B–A frames. The next step involved shift and add of the positive spectrum of (B–A) frame on the positive spectrum of A–B frame. The final spectrum (Fig. 2) is the result of the mean of all pairs of frames previously combined. The spectrum was then extracted and wavelength calibrated using the arcline spectrum of an Argon lamp. Finally, the extinction correction and solar removal was obtained by division of the asteroid spectrum with that of the solar analog star Hyades 64.

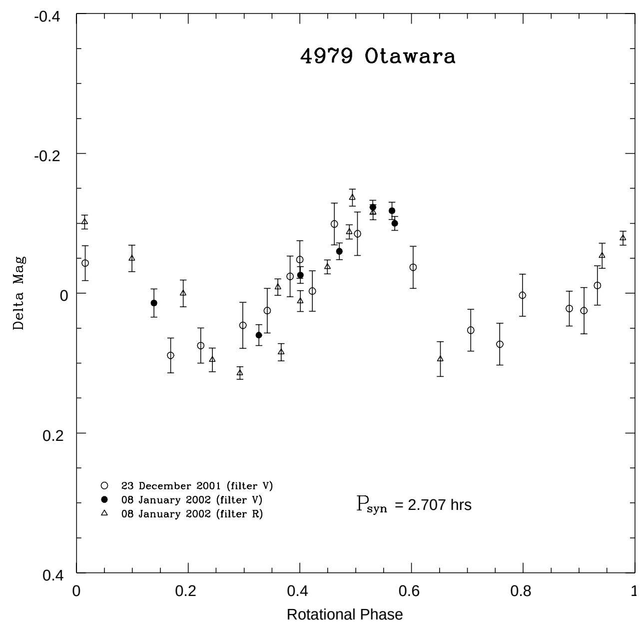

Fig. 1. Composite lightcurve of 4979 Otawara. The error bars contain the photon noise. The zero phase is at JD 2 452 276.5.

3. Analysis

3.1. Lightcurve and spin state

The synodic rotational period was determined by applying a Fourier analysis to our photometric data, as described by Harris et al. (1989). The value of the synodic rotational period that best fits our observations is $P_{\rm syn} = 2.707 \pm 0.005$ hours. This result was already found by Doressoundiram et al. (1999) and confirmed by Le Bras et al. (2001). Figure 1 shows the composite lightcurve obtained by combining in rotational phase all of our photometric data.

Since no absolute calibration was obtained, due to the non-photometric sky conditions, an offset was applied to each night of data, in order to center the lightcurve on the mean brightness of the asteroid. R-filter and V-filter composite lightcurves, which show similar behaviour, have been superimposed. The obtained amplitude is 0.22 ± 0.03 mag.

The spin vector, sidereal period, and triaxial ellipsoid model for a given asteroid can be determined using the method described by Michałowski (1993). In this method the epochs of brightness maxima, amplitudes and magnitudes are considered. The results are obtained by building a set of nonlinear equations whose solution is found by the least square fitting.

We have been able to use for Otawara the epochs, amplitudes and R magnitudes from December 1998–January 1999 (Doressoundiram et al. 1999) and July–August 2000 (Le Bras et al. 2001) and only the epochs and amplitudes obtained in December 2001–January 2002 (this paper). The ecliptic longitude (λ) and latitude (β) of Otawara during these observations are the following:

Date	λ	β
23 Jan. 1999	123.5°	+ 1.0°
06 Aug. 2000	314.3°	− 1.3°
01 Jan. 2002	101.9°	+ 0.6°

It should be noted that these observations were obtained from rather similar geometric configurations of Otawara as the difference in ecliptic longitudes between the 1998/99 and 2001/02 oppositions was smaller than 30° and the longitude difference was close to 180° between 2000 and 1998/99 apparitions. For that reason, the available observational data are far from ideal as required for the method mentioned above. The observed amplitudes of Otawara have been reduced to zero phase angle with the *amplitude-phase* relationship described by Zappala et al. (1990). The correction coefficient was found to be $m = 0.006$. The HG-magnitude system (Bowell et al. 1989) has allowed us to reduce the R magnitudes to zero phase angle and we have obtained $G_R = 0.19$.

Despite the limitation in the observational data we have obtained some preliminary results for Otawara. The sense of rotation seems to be retrograde. The sidereal period ($P_{\rm sid}$), the ecliptic coordinates of the asteroid north pole ($\lambda_{\rm p}, \beta_{\rm p}$), the a/b ratio of the triaxial ellipsoid shape, the absolute R magnitude for the aspect 90° $H_R(90,0)$, and their formal errors are as follows:

$$P_{\rm sid} = 0.112776 \pm 0.000001 \text{ (days)}$$
$$\lambda_{\rm p} = 50° \pm 5°$$
$$\beta_{\rm p} = -30° \pm 16°$$
$$a/b = 1.21 \pm 0.05$$
$$H_R(90,0) = 13.99 \pm 0.05 \text{ (mag)}.$$

A second solution with the same parameters and $\lambda_{\rm p} = 230°$ has also been obtained.

According to these results, Otawara was observed close to equatorial aspects (≈90°). Careful examination of the relation between aspect, pole and asteroid ecliptic coordinates (Eq. (4) in Michałowski 1993) shows that equatorial aspects do not practically depend on pole latitude when the asteroid latitude is close to 0°, as it is for Otawara. This is probably the reason for the large formal error in $\beta_{\rm p}$.

A spurious value of the b/c ratio (2.3 ± 0.9) of the triaxial ellipsoid shape comes out of the formal solution, but in this case it does not diminish the validity of the rest of the solution. In fact, the *amplitude–aspect* and *magnitude– aspect* relationships (Eqs. (3) and (5) in Michałowski 1993, respectively) show that observed amplitudes and magnitudes do not depend on b/c for aspects close to equatorial ones. Therefore, we can assume that the value for b/c and its formal error are solution artifacts and not real. Furthermore, because of the rapid spin rate, if the polar flattening b/c is significantly greater than 1.0, a state of tensile stress would be implied. This is highly unlikely for an asteroid of this size, thus we expect b/c is not greater than about 1.2.

In order to obtain the full model for Otawara we need further observations carried out for aspects far from equatorial ones. The best observations will be during the oppositions when the ecliptic longitudes of Otawara are in the range 0°–70° or 180°–250°.

The next oppositions of Otawara will be in June 2003, with an ecliptic longitude (λ) of 263°, in December 2004 with λ = 81°, in April 2006 with λ = 216°, in November 2007 with λ = 58°, in March 2009 with λ = 180°. So the oppositions from 2006 to 2009 fall in the desirable ecliptic longitude range.

Further ground observations are needed to improve the spin vector of Otawara, even if only the opposition in April 2006 seems to have an orbital configuration suitable for a better pole determination before the spacecraft flyby in July 2006.

3.2. Spectral analysis

In Fig. 2 the combined visible and infrared spectra of Otawara are shown. The visible data are normalized at 5500 Å and the overlap between visible and infrared spectra was performed by shifting the infrared data with a scaling factor derived by minimizing the chi-squared value of polynomial fitting to both visible and IR data. A first analysis of the spectrum allows us to determine that Otawara is an S-type asteroid. Based on only the visible spectrophotometric data, Doressoundiram et al. (1999) determined that their spectrum could be consistent with either a S- or V-type asteroid. From our IR data we can exclude any link between Otawara and V class due to the very small 2-micron absorption compared to that of a typical V asteroid. The shape of the spectrum over the wavelength interval 0.42–2.50 μm is consistent with an S-type object.

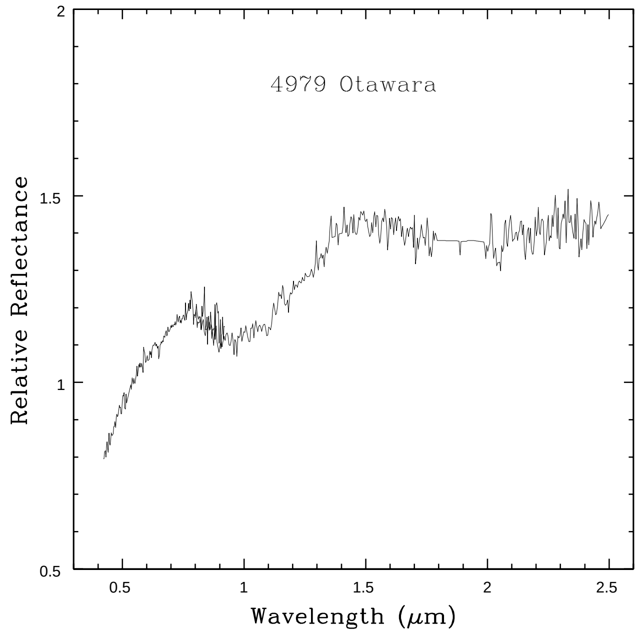

Fig. 2. Visible and infrared spectral reflectance of 4979 Otawara. The noise introduced by water band at 1.8 μm has beed excluded. The spectrum is normalized at 5500 Å.

We also compared our visible data obtained from Palomar with the visible spectrum published by Doressoundiram et al. (1999). Even though the previously published spectrum is noisier than our data, the spectral behaviour is exactly the same, confirming the visible trend previously observed.

In order to investigate possible variations of the surface properties during the rotational period, we examined the IRTF near infrared data time over 3 intervals (named I, II, III), each of them with 24 min of exposure time. The total elapsed time is 86 min, corresponding to 53% of the rotational period of the asteroid. The central universal time of each of these interval is 10:08, 10:36 and 11:06, corresponding to a rotational phase of 0.40, 0.57 and 0.76 respectively. These spectra were filtered with a median filter (box size of 39 points) since they were noisier than the spectrum obtained with the total exposure.

There is no obvious difference between the three composite spectra shown in Fig. 3, meaning that for almost half of the rotational period Otawara's composition is homogeneous within ±5–10% variation, the limit of our precision.

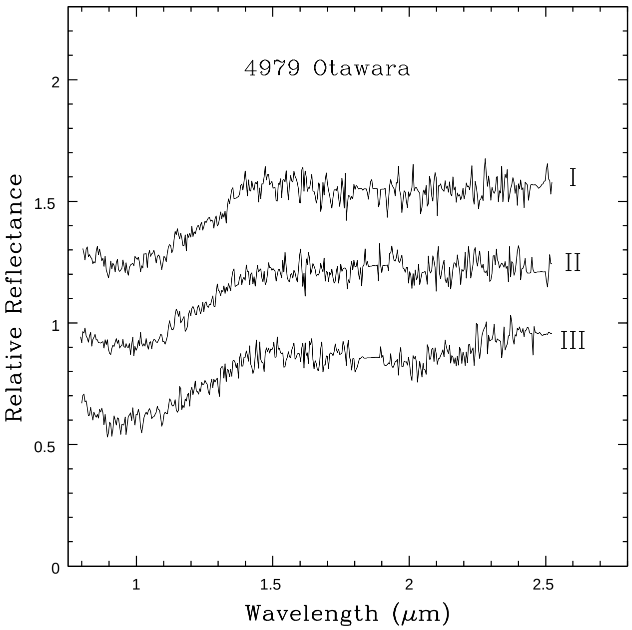

Fig. 3. Infrared spectra of 4979 Otawara: I is the spectrum relative to the first 24 min of integration, II that relative to the following 24 min and III that relative to the last 24 min (the total exposure time was 72 min). Spectral data have been normalized at 1.25 μm; spectra I and III are vertically shifted by 0.3 for clarity.

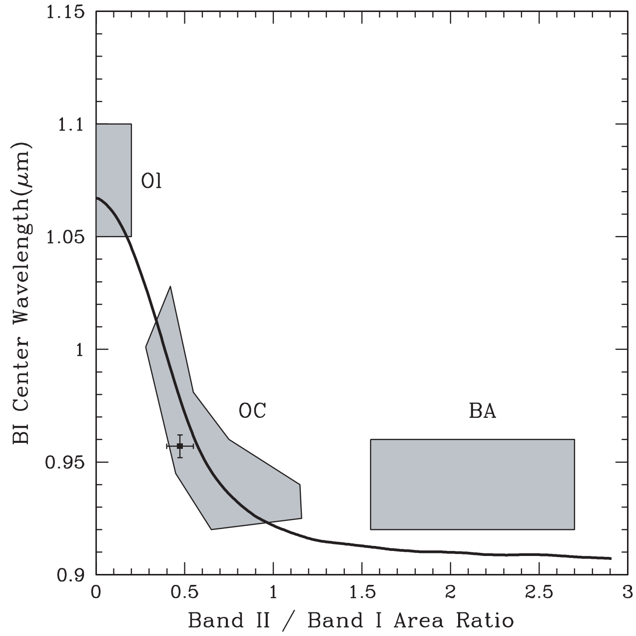

Fig. 4. BI center versus the Band II/Band I area ratio for 4979 Otawara (squared point). The three background regions are defined by meteorite spectra by Gaffey et al. (1993). The Ol rectangular region includes essentially monomineralic olivine assemblages; the OC polygonal region represents the mafic silicate components of ordinary chondrites and corresponds to the location of the S(IV) subtype in the Gaffey et al. classification scheme (1993); the BA rectangular zone includes the pyroxene dominated basaltic achondrites assemblages. The heavy solid line indicates the location of the olivine-orthopyroxene mixing line (Cloutis et al. 1986).

We tried to better analyze the data in order to identify which S subclass of the Gaffey et al. (1993) classification scheme best describes the Otawara spectrum. In this classification, the S class is divided into 7 subclasses on the basis of the area ratio between the 2 μm/1 μm band, the center position of these two bands, the depth and slope of the 1 μm absorption, as these parameters are intrinsically related to the mineralogy of the asteroid surface.

The analysis of the spectrum (see the procedure described by Gaffey et al. 1993) gives the center position of the band BI (that around 1 micron) at $0.9570 \pm 0.0050\,\mu$m, with a band depth of 0.18 ± 0.01 and a spectral slope of 0.0804% per 1000 Å (evaluated from 0.75 μm to 1.45 μm). This band is due to the presence of both olivine and pyroxene. Regarding the band around 2 μm, associated with the presence of pyroxene, it is centered at $1.9780 \pm 0.0050\,\mu$m and has a band depth of 0.07 ± 0.01.

The 2 μm/1 μm band area ratio is 0.47 ± 0.09. On the basis of these values 4979 Otawara is well placed in the space of S(IV) class (see Fig. 4).

4. Comparison to ordinary chondrites

The assignment of Otawara to the S(IV) subclass is particularly interesting as the S(IV) asteroids are characterized by a composition that includes the silicate components of the ordinary chondrites. S(IV) members are the most probable candidates for parent bodies of ordinary chondrites among the S-type asteroid population (Gaffey et al. 1993; Gaffey 2000, 2001). For this reason, we want to investigate the possible links with OC meteorites.

Plotting the BI band center position versus Band II/Band I area ratio places Otawara in the ordinary chondrite (OC) field (Fig. 4), lying near the olivine-pyroxene mixing line. This similarity to OC meteorites implies that Otawara is not a differentiated asteroid.

We analyzed the percentage of orthopyroxene present on Otawara, using the method suggested by Cloutis et al. (1986):

$$\mathrm{OPX}(\%) = \frac{\mathrm{OPX}}{\mathrm{OPX}+\mathrm{OL}} = 0.4187 \times \left(\frac{\mathrm{BII}}{\mathrm{BI}} + 0.125\right) \quad (1)$$

where OPX is the orthopyroxene mass fraction, OL the olivine mass fraction and BI and BII are the band area corresponding to the 1 and 2 micron absorptions, respectively.

This method was recently tested by Gaffey (1999) and Berthoud et al. (2001) on samples of ordinary chondrites, finding good agreement between the orthopyroxene abundance computed and the normative abundances derived from chemical analysis (Jarosewich 1990; McSween et al. 1991). For Otawara we find a percentage of 25 ± 3 of orthopyroxene, consistent with the abundance typical of L and LL ordinary chondrites.

In fact S(IV) objects are composed of olivine-orthopyroxene (Ca-poor) mixtures which could be representative assemblages that are similar to undifferentiated ordinary chondrites but also to unmelted silicate portions of primitive achondrite. As the band depth at 2 μm of measured

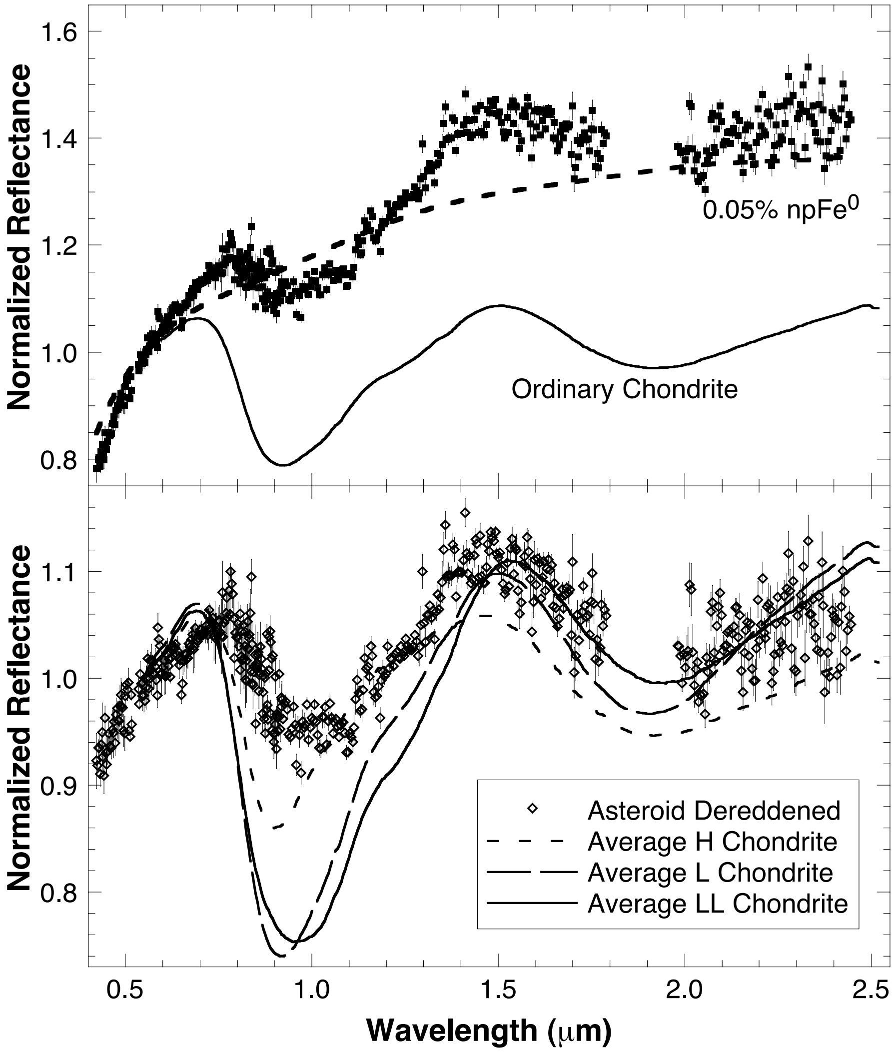

Fig. 5. Top panel: combined near-infrared plus visible spectrum of 4979 Otawara (data points), where the gap at 1.9 μm is due to telluric water. For comparison, the dashed curve shows the reddening model for the presence of 0.05% nanophase iron ($npFe^0$) as determined by Pieters et al. (2001). The neutral slope of an ordinary chondrite meteorite (average LL chondrite) is shown for comparison. Bottom panel (with the vertical scale expanded to twice that of the top panel): Otawara spectrum (data points) de-reddened for 0.05% nanophase iron. Spectral slope and location of the 1 μm and 2 μm bands are consistent within the range of properties for ordinary chondrite meteorites (lines). All spectra are normalized to unity at 0.55 μm. Meteorite spectra are from Gaffey (1976).

primitive achondrites is greater than that for S(IV) asteroids (Burbine et al. 2001; Binzel et al. 2001a), we tried to make a comparison between Otawara and representative ordinary chondrites.

However, as has long been noted (see for example Wetherill & Chapman 1988) and is evident in the upper panel of Fig. 5, spectra of S-class asteroids are significantly reddened compared with this meteorite analog, and this difference could probably be explained by space weathering effects. This process may be the result of dust impacts and solar wind sputtering on the surface of atmosphereless bodies and gives rise to a reddening of the spectral slope, a decrease of spectral absorption intensities and a diminishing of albedo. In fact surfaces of atmosphereless bodies exposed to the space environment for millions to billions of years are inevitably altered in physical, optical and/or chemical properties, as first demonstrated by analysis on the lunar soils (see for example Adams et al. 1971; Hapke et al. 1975).

While the effects of space weathering processes have long been debated, new results are supporting their validity. The Galileo mission for the first time demonstrated that a kind of alteration affects the surfaces of Gaspra, Ida and Dactyl (three S-type asteroids), modifying the reflectance spectra of fresh material to be redder, straighter and with shallower absorption bands, as reported by Chapman (1996). Recently the NEAR mission to 433 Eros (another S-type object) allowed a determination, thanks to X-ray and near-infrared spectrometer measurements, of an ordinary chondrite composition of Eros despite a red sloped, S-type spectrum, suggesting once again that some process such as reddening and/or darkening has altered the optical properties of the surface (Clark et al. 2000; Chapman 2000; McFadden et al. 2001; Bell et al. 2002).

Recent work of Binzel et al. (2001b) shows also that there is a continuous transition in the spectral behaviour between a sample of small S-Q type Near Earth Objects and that of ordinary chondrites, arguing that a continuous natural process such as space weathering could affect these bodies in different ways, depending on their age and collisional history.

Moreover Pieters et al. (2000) demonstrated that the spectral properties of S-type asteroids are well modeled by the space weathering of ordinary chondrite material that is associated with accumulation of reduced nano-phase iron on soil grains. This kind of model was also successfully applied by Binzel et al. (2001a) for the interpretation of spectral differences between asteroid (25143) 1998 SF36, the S(IV) target of MUSES-C mission, and ordinary chondrites.

Following the de-reddening model developed by Binzel et al. (2001a), we divide the spectrum of Otawara by the curve for the minimal (0.05%) component of nanophase iron. The results are shown in the lower panel of Fig. 5. We find an excellent match (within the noise of our spectrum) to the typical slopes for ordinary chondrite meteorites. Speculating on a more specific match, however, remains problematic. We find the 1 μm band depth is shallow relative to the meteorite comparisons, but most consistent with the H chondrites. However, perhaps more diagnostic is the 1 μm band center which is most consistent with LL chondrites, as is the depth of the 2 μm band.

Thus, while we slightly favor an analogy between Otawara and LL chondrites, (based on the preceeding analysis and our OPX analysis), we consider this only a tentative result.

5. Conclusion

In conclusion, our results can be summarized as follows:

1. Our combined visible and infrared spectral data of Otawara put this object in the S taxonomic class composed of olivine and orthopyroxene.
2. Following the Gaffey et al. classification scheme (1993), Otawara belongs to the S(IV) subgroup.
3. A comparison between Otawara and H, L and LL ordinary chondrites shows the typical differences found in the literature between these meteorites and S-asteroids. Otawara could be a potential parent body of OC meteorites as the spectral reddening and shallow absorption features compared to OC spectra are consistent with trends that may be caused by space weathering processes. In fact a spectral analysis using current models for space weathering shows that the presence of only 0.05% nanophase iron may account for the spectral slope difference between Otawara and ordinary chondrite meteorites.
4. Our lightcurve data confirm the fast rotation period of Otawara ($P_{\rm syn}$ = 2.707 ± 0.005 h) previously determined by other authors.
5. A first estimation of the complete spin state is presented with most likely a retrograde sense of rotation. Further observations during upcoming apparitions are needed to verify and improve this result.

All this information will allow the Rosetta scientists and mission planners to optimise the science operation planning during Otawara flyby, but only the analysis of the Rosetta data will permit a much more detailed investigation of the physical and compositional properties of 4979 Otawara.

Acknowledgements. The authors thank L. McFadden and P. Weissman for their detailed reviews and suggestions, and T. Cline who provided data for meteorite fields. Spin vector determination was performed after a suggestion by A. Erikson. T.M. was supported by the Polish KBN Grant 2 P03D 007 18.

References

Adams, J. B., & McCord, T. B. 1971, Proc. 2nd Lunar Sci. Conf., 2183
Bell, J. F., Izenberg, N. I., Lucey, P. G., et al. 2002, Icarus, 155, 119
Berthoud, M. G., Bell, J. F., Clark, B. E., & Gaffey, M. J. 2001, Lunar Planet. Sci., 32, 2080
Binzel, R. P., Rivkin, A. S., Bus, S. J., Sunshine, J. M., & Burbine, T. H. 2001a, Meteorit. Planet. Sci., 36, 116
Binzel, R. P., Harris, A. W., Bus, S. J., & Burbine, T. H. 2001b, Icarus, 151, 139
Bowell, E., Hapke, B., Domingue, D., et al. 1989, in Asteroids II (Univ. of Arizona Press, Tucson), 524
Burbine, T. H., McCoy, T. J., Nittler, L. R., & Bell, J. F. 2001, Lunar Planet. Sci., 32, 1860
Bus, S. J., Ph.D. Thesis, Massachusset Institute of technology, Cambridge, MA, USA
Chapman, C. R. 1996, Meteoritics & Plan. Sci., 31, 699
Chapman, C. R., & Near MSI-Nis Team 2000, Meteoritics & Plan. Sci., 35, 39
Clark, B. E., Bell, J. F., Veverka, J., et al. 2000, Meteoritics & Plan. Sci., 35, 41
Cloutis, E. A., Gaffey, M. J., Jackowski, T. L., & Reed, K. L. 1986, J. Geoph. Res., 91, 11641
Doressoundiram, A., Weissman, P. R., Fulchignoni, M., et al. 1999, A&A, 352, 697
Gaffey, M. J. 1976, J. Geoph. Res., 81, 905
Gaffey, M. J., Burbine, T. H., Piatek, J. L., et al. 1993, Icarus, 106, 573
Gaffey, M. J. 1999, Lunar Planet. Sci., 30, 1375
Gaffey, M. J. 2000, Lunar Planet. Sci., 31, 1092
Gaffey, M. J. 2001, Lunar Planet. Sci., 32, 1587
Hapke, B., Cassidy, W., & Wells, E. 1975, The moon, 13, 339
Harris, A. W., Young, J. W., Bowell, E., et al. 1989, Icarus, 77, 171
Jarosewich, E. 1990, Meteoritics, 25, 323
Le Bras, A., Dotto, E., Fulchignoni, M., et al. 2001, A&A, 379, 660
Michałowski, T. 1993, Icarus, 106, 563
McFadden, L. A., Wellnitz, D. D., Schnaubelt, M., et al. 2001, Meteoritics & Plan. Sci., 36, 1711
McSween, H. Y., Bennett, M. E., & Jarosewich, E. 1991, Icarus, 90, 107
Pieters, C. M., Taylor, L. A., Noble, S. K., et al. 2000, Meteoritics & Plan. Sci., 35, 1101
Rayner, J. T., Toomey, D. W., Onaka, P. M., et al. 1998, Proc. SPIE, 3354, 468-479
Wetherill, G. W., & Chapman, C. R. 1988, Asteroids and meteorites, in Meteorites and the Early Solar System, ed. J. F. Kerridge, & M. S. Matthews (University of Arizona Press, Tucson, Arizona), 35
Xu, S., Binzel, R. P., Burbine, T. M., & Bus, S. J. 1995, Icarus, 115, 1
Zappala, V., Cellino, A., Barucci, M. A., et al. 1990, A&A, 231, 548

2.5 Les astéroïdes ignés : le type E

Les astéroïdes de type E sont rares (environ 30 connus jusqu'à présent) et ils ont le plus grand albédo parmi les différentes classes taxonomiques. Ce sont des objets évolués qui ont subi des températures > 2000 K, situés dans la partie interne de la ceinture principale, avec une composition riche en enstatite, forstérite et feldspaths. Initialement, on croyait que les spectres de ces astéroïdes étaient sans bandes d'absorption, mais les observations récentes ont montré que beaucoup de ces objets ont des bandes d'absorption et une composition de surface assez complexe. Leur étude est importante pour avoir des contraintes sur les températures présentes dans les différentes régions de la ceinture principale pendant sa formation. En particulier, la découverte d'une bande d'absorption à 3 μm sur des astéroïdes de type E et M (Rivkin et al. 2000), typiquement associée aux silicates hydratés, a ouvert un débat dans la communauté scientifique car cela implique que ces objets n'ont pas tous approché des températures très élevées comme supposé auparavant.
Trois minéralogies différentes ont été proposées pour cette petite population, et 3 sous-groupes identifiés (Clark et al. 2004) : le type E[I], caractérisé par des spectres sans bande d'absorption ; le type E[II], dont les spectres montrent une bande à 0,49 μm due à des sulfites comme l'oldhamite ; le type E[III], qui présente des spectres avec une bande d'absorption à 0,9 μm et parfois aussi à 1,8 μm associée à des pyroxènes comme la forstérite.

Pour mieux comprendre cette classe d'astéroïdes, j'ai mené des campagnes observationnelles dans le visible et le proche infrarouge aux télescopes TNG, NTT, et ESO-1.52m. Nos premières observations sur 5 astéroïdes de type E faites en 1999 confirmaient et/ou révélaient la présence de la bande très particulière centrée à 0,49 μm sur 64 Angelina, 2035 Stearn, et le géocroiseur 3103 Eger (Fornasier & Lazzarin 2001). Les campagnes observationnelles de 2004-2007 nous ont permis d'obtenir des nouveaux spectres de 19 astéroïdes du type E, c'est-à-dire environ 2/3 de la population.
Les données confirment la présence de 3 différentes mineralogies dans les astéroïdes de type E et la présence de bandes d'absorption à 0,5, 0,9 et 1,8 μm. Nous avons donc inclus dans l'analyse les spectres observés précédemment et nous avons classifié 5 astéroïdes dans la sub-classe E[I] (les objets 504, 1025, 2449, 6435, et 144898), 8 dans le type E[II] (les objets 64, 434, 2048, 2035, 2867, 3103, 4660, et 6911, qui montrent la bande d'absorption à 0,49 μm), et 8 de type E[III] (les astéroïdes 44, 214, 317, 437, 620, 1103, 1251 et 3050, qui ont la bande d'absorption dans la région 0,9 μm). Trois astéroïdes initialement classifiés comme de type E ont montré des spectres non similaires à ceux de cette classe taxonomique et nous les avons classifiés comme de type A (les objets Litva et 1990 TN, qui ont une composition riche en olivine), ou de type S(IV) (5806 Archieroy).
La distribution des pentes spectrales en fonction des 3 sous-groupes et de la distance héliocentrique a été investiguée. Enfin, les spectres des astéroïdes ont été comparés avec ceux des météorites pour contraindre leur composition de surface (Fornasier et al., 2008). Nous confirmons que les astéroïdes de type E sont les corps parents les plus probables des aubrites. Nous avons trouvé une forte similitude spectrale entre l'astéroïde 317 Roxane (type E[III]) et la météorite Pena Blanca.
Pour les astéroïdes de type E[II], la seule météorite qui montre une bande d'absorption à 0,49 μm est l'aubrite ALH78113. Cependant, il faut enrichir la météorite avec des quantités considérables d'oldhamite (8%) pour pouvoir reproduire la bande observée sur 64 Angelina. Ceci pose des problèmes car l'oldhamite est un constituant des aubrites, mais présent en très petites quantités (< 1%, Burbine et al. 2002). Cependant, l'oldhamite est très instable dans les conditions terrestres. Il est donc possible que la quantité d'oldhamite présente sur les astéroïdes soit

plus grande de celle que nous observons sur les météorites en laboratoire, où elle pourrait avoir précédemment subi des processus d'altération.

2.5.1 Article : Visible and near infrared spectroscopic survey of E-type asteroids, including 2867 Steins, a target of the Rosetta mission

Available online at www.sciencedirect.com

ScienceDirect

Icarus 196 (2008) 119–134

ICARUS

www.elsevier.com/locate/icarus

Visible and near infrared spectroscopic investigation of E-type asteroids, including 2867 Steins, a target of the Rosetta mission ☆

S. Fornasier [a,b,*], A. Migliorini [c], E. Dotto [d], M.A. Barucci [a]

[a] *LESIA, Observatoire de Paris, 5 Place Jules Janssen, F-92195 Meudon Principal Cedex, France*
[b] *Université de Paris 7 Denis Diderot, 4, rue Elsa Morante, 75205 Paris Cedex 13, France*
[c] *IASF-INAF, via del Fosso del Cavaliere 100, 00133 Roma, Italy*
[d] *INAF, Osservatorio Astronomico di Roma, via Frascati 33, I-00040 Monteporzio Catone, Roma, Italy*

Received 10 October 2007; revised 26 February 2008

Available online 16 March 2008

Abstract

We present the results of a visible spectroscopic survey of igneous asteroids belonging to the small and intriguing E-class, including 2867 Steins, a target of the Rosetta mission. The survey was carried out at the 3.5 m Telescopio Nazionale Galileo (TNG), and at the 3.5 m New Technology Telescope (NTT) of the European Southern Observatory. We obtained new visible spectra for eighteen E-type asteroids, and near infrared spectra for eight of them. We confirm the presence of three different mineralogies in the small E-type populations. We classify each object in the E[I], E[II] or E[III] subgroups [Gaffey, M.J., Kelley, M.S., 2004. Lunar Planet. Sci. XXXV. Abstract 1812] on the basis of the spectral behavior and of the eventual presence of absorption features attributed to sulfides (such the 0.49 μm band, on E[II]), or to iron bearing silicates (0.9 μm band, on E[III]). We suggest that some asteroids (i.e. 64 Angelina, 317 Roxane, and 434 Hungaria), which show different spectral behavior comparing our data with those available in literature, have an inhomogeneous surface composition. 2867 Steins, a target of the Rosetta mission, shows a spectral behavior typical of the E[II] subgroup, as already suggested by Barucci et al. [Barucci, M.A., Fulchignoni, M., Fornasier, S., Dotto, E., Vernazza, P., Birlan, M., Binzel, R.P., Carvano, J., Merlin, F., Barbieri, C., Belskaya, I., 2005. Astron. Astrophys. 430, 313–317] and Fornasier et al. [Fornasier, S., Marzari, F., Dotto, E., Barucci, M.A., Migliorini, A., 2007. Astron. Astrophys. 474, 29–32]. Litva and 1990 TN1, initially classified as E-types, show a visible and near infrared behavior consistent with the olivine rich A-class asteroids, while 5806 Archieroy, also supposed to belong to the E-class, has a spectral behavior consistent with the S(V) classification following the Gaffey et al. [Gaffey, M.J., Burbine, T.H., Piatek, J.L., Reed, K.L., Chaky, D.A., Bell, J.F., Brown, R.H., 1993. Icarus 106, 573–602] classification scheme. To fully investigate the E-type population, we enlarged our sample including 6 E-type asteroids spectra available in literature, resulting in a total sample of 21 objects. The analysis of the spectral slope for the 3 different E-type subgroups versus the orbital elements show that E[III] members have the lowest mean spectral slope value inside the whole sample, and that they are located between 2.2–2.7 AU in low inclination orbits. E[II] members has the highest spectral slope inside the sample, half of them are located in the Hungaria region, 2 are NEA and 2 (64 Angelina and 2867 Steins), are in the main belt. A similar distribution is found for the 5 featureless E[I] members, located mainly in the Hungaria region (3 members), one in the middle main belt while one is a NEA (2004 VD17). Finally, for the five E-type asteroids observed both in the visible and near infrared range, plus 2867 Steins, we attempt to model their surface composition using linear geographical mixtures of no more than 3 components, selected from aubrite meteorites and correlated minerals. In particular we suggest that the aubrite Peña Blanca might have the E[III] Asteroid 317 Roxane as parent body, and that the aubrite ALH78113 might be related to the E[II] subgroup asteroids.

Keywords: Asteroids, surface; Spectroscopy

☆ Based on observations carried out at the European Southern Observatory (ESO), La Silla, Chile, ESO proposals 074.C-0049 and 078.C-0115 and at the Telescopio Nazionale Galileo.

* Corresponding author at: LESIA, Observatoire de Paris, Batiment 17, 5 Place Jules Janssen, 92195 Meudon Cedex, France. Fax: +33 145077144.
E-mail address: sonia.fornasier@obspm.fr (S. Fornasier).

0019-1035/$ – see front matter
doi:10.1016/j.icarus.2008.02.015

1. Introduction

The E-type asteroids are a small population which comprises around 25 asteroids to date. These bodies are called igneous as they formed and differentiated under relatively reducing conditions, with parent bodies heated to at least 1580 °C (Keil, 1989). The population is dynamically concentrated into 2 groups, located respectively in the Hungaria region, around 1.9 AU, and in the inner part of the main belt, between 2.1 and 2.7 AU. In addition, some near Earth asteroids were recognized to belong to the E-class (De Luise et al., 2007; Delbó et al., 2003; Harris et al., 2007).

E-type asteroids were grouped, together with M- and P-type, in the X-type complex following Tholen (1989) taxonomic system. They have the highest albedo than any other asteroids class (around 0.4–0.6).

Their surface composition seems to be dominated by iron-free or iron-poor silicates such as enstatite, forsterite or feldspar, and they are thought to be the parent bodies of the aubrite (enstatite achondrites) meteorites (Gaffey et al., 1989, 1992; Zellner et al., 1977). Initially, E-type asteroids were believed to have a quite flat or slightly reddish featureless spectral behavior (Tholen, 1989), but, since 1995, some absorptions bands, both in the visible and near infrared region, were identified on their surface: a very sharp absorption band, until now observed only for these bodies, centered at 0.49–0.50 μm, extended from 0.43 to 0.55 μm (Burbine et al., 1998; Fornasier and Lazzarin, 2001; Bus and Binzel, 2002; Clark et al., 2004), attributed to the presence of sulfides (known constituent of the aubrite meteorites) such as oldhamite; two weaker features centered at around 0.9 and 1.8 μm attributed to iron bearing pyroxene such as orthopyroxene or forsterite (Clark et al., 2004); an absorption feature at 3 μm (Rivkin et al., 1995), typically associated with the first overtone of H_2O and with OH vibrational fundamentals on hydrated silicates, not expected on highly evolved bodies like the E-type asteroids. After the discovery of these absorptions features, 3 different mineralogies have been suggested to be present inside the E-type population (Clark et al., 2004; Gaffey and Kelley, 2004). Following the Gaffey and Kelley (2004) classification scheme, we observe 3 subgroups, named E[I], E[II] and E[III]. E[I] asteroids do not present absorption features, but a slightly reddish slope in the visible spectral range; this spectral behavior is characteristic of aubritic pyroxene plus feldspar assemblage. E[I] asteroids might be the parent bodies of the aubrite meteorites. The parent bodies of the E[I] subgroup attained temperatures in excess of 1400 °C (McCoy et al., 1999).

The subgroup E[II] presents the strong absorption at ∼0.49 μm and occasionally at 0.90–0.96 μm. These features are possibly due to the calcium sulfide mineral oldhamite (present in highly reduced assemblages such as aubrites). The typical example of the E[II] subgroup is 64 Angelina. These bodies are probably composed of basalt equivalents from enstatite chondrite-like parent bodies which underwent at least partial melting (Gaffey and Kelley, 2004).

Finally, E[III] are characterized by a flat or reddish spectral curve with a well defined band centered at 0.89–0.9 μm, due to enstatite pyroxene containing Fe^{2+}. Some of the asteroids having the 0.9 μm band shows an absorption feature also at 1.8 μm (Clark et al., 2004). 44 Nysa is a typical member of this subclass. The asteroids of this subgroup are supposed to be derived from oxidized parent bodies which underwent extensive reduction during their igneous processing (Gaffey and Kelley, 2004).

An exhaustive discussion on the E-type asteroids composition and classification throughout different taxonomic schemes is reported in Clark et al. (2004), and in Gaffey and Kelley (2004).

Since 2004 we have carried out a spectroscopic survey in the visible and near infrared range of E-type asteroids at the 3.5 m Telescopio Nazionale Galileo (TNG), La Palma, Spain, and at the 3.5 m New Technology Telescope (NTT) of the European Southern Observatory, La Silla, Chile. The aim is to extend the spectral analysis to a larger number of E-type asteroids, investigate their surface properties throughout the rotational period and define the mineralogical properties of each sub-group. We obtained new spectra on 18 asteroids previously classify as E-type asteroids, that is more than 2/3 of the known population. These data, together with those already published in literature, draw a representative picture of the spectral properties of this peculiar class of asteroids.

2. Observations and data reduction

The data presented in this work were obtained during 2 runs (February and November 2004) at the TNG telescope, and during 3 runs (May 2004, August 2005 and January 2007) at the NTT telescope. We get a total of 11 observing nights devoted to the investigation of asteroids belonging to the E, M and X taxonomic classes. Here we present the results of our E-type observations.

At the TNG telescope, for visible spectroscopy we used the DOLORES (Device Optimized for the LOw RESolution) instrument equipped with the low resolution red grism (LR-R) covering the 0.51–0.95 μm range with a spectral dispersion of 2.9 Å/pixel. Most part of the objects were observed also with the low resolution blue grism (LR-B, dispersion of 2.8 Å/pixel) on February 2004, covering the 0.38-0.80 μm range, and with the medium resolution blue grism (MR-B, dispersion of 1.7 Å/pixel, 0.38–0.70 μm range), for the November 2004 run. The 'red' and 'blue' spectra in the visible range were separately reduced and finally combined together to obtain a spectral coverage from 0.38 to 0.95 μm. The DOLORES detector is a Loral thinned and back-illuminated CCD with 2048 × 2048 pixels, with a pixel size of 15 μm and a pixel scale of 0.275 arcsec/pixel. Like most of the Loral CCDs, that of DOLORES is affected by moderate-to-strong fringing at red wavelengths. Despite taking as much care as possible in the data reduction, for two asteroids (317 Roxane and 2048 Dwornik) we get a lot of fringing residuals and we were obliged to cut their spectra for wavelengths longer than ∼0.8 μm.

For the infrared spectroscopic investigation at the TNG telescope we used the near infrared camera and spectrometer (NICS) equipped with an Amici prism disperser. This equipment covers the 0.85–2.40 μm range during a single exposure

Table 1
Observational circumstances

Object	Night	UT-start (hh:mm)	T_{exp} (s)	Tel.	Instr.	Grism	Airm.	Solar analog (airm.)
44 Nysa	29 Feb. 04	06:58	40	TNG	DOLORES	LR-R	1.40	la107684 (1.15)
44 Nysa	13 Aug. 05	05:40	30	NTT	EMMI	GR1	1.05	HD1835 (1.07)
44 Nysa	12 Aug. 05	05:59	60	NTT	SOFI	GBF	1.06	hip103572 (1.06)
44 Nysa	12 Aug. 05	06:01	60	NTT	SOFI	GRF	1.06	hip103572 (1.06)
44 Nysa	20 Jan. 07	04:13	5	NTT	EMMI	GR1	1.65	la98-978 (1.35)
64 Angelina	16 Nov. 04	00:49	50	TNG	DOLORES	LR-R	1.02	Hyades64 (1.03)
64 Angelina	16 Nov. 04	00:52	80	TNG	DOLORES	MR-B	1.02	Hyades64 (1.03)
64 Angelina	19 Nov. 04	01:33	120	TNG	NICS	AMICI	1.08	Hyades64 (1.01)
214 Aschera	25 May 04	10:18	150	NTT	EMMI	GR1	1.11	la112-1333 (1.17)
214 Aschera	18 Nov. 04	19:49	240	TNG	NICS	AMICI	1.24	la93-101 (1.34)
317 Roxane	29 Feb. 04	03:04	120	TNG	DOLORES	LR-R	1.14	hd89010 (1.02)
317 Roxane	29 Feb. 04	03:07	180	TNG	DOLORES	LR-B	1.14	hd89010 (1.18)
317 Roxane	13 Aug. 05	02:22	180	NTT	EMMI	GR1	1.07	HD1835 (1.07)
317 Roxane	13 Aug. 05	05:21	180	NTT	EMMI	GR1	1.10	HD1835 (1.07)
317 Roxane	12 Aug. 05	05:16	320	NTT	SOFI	GBF	1.09	hip096165 (1.09)
317 Roxane	12 Aug. 05	05:24	320	NTT	SOFI	GRF	1.10	hip096165 (1.09)
317 Roxane	20 Jan. 07	03:24	180	NTT	EMMI	GR1	1.57	Hyades64 (1.45)
434 Hungaria	16 Nov. 04	00:10	180	TNG	DOLORES	LR-R	1.51	Hyades64 (1.03)
434 Hungaria	16 Nov. 04	00:15	180	TNG	DOLORES	MR-B	1.50	Hyades64 (1.03)
437 Rhodia	29 Feb. 04	02:42	180	TNG	DOLORES	LR-R	1.28	la107684 (1.20)
437 Rhodia	29 Feb. 04	02:48	180	TNG	DOLORES	LR-B	1.28	la107684 (1.20)
437 Rhodia	01 Mar. 04	04:17	480	TNG	NICS	AMICI	1.54	la102-1081 (1.46)
504 Cora	29 Feb. 04	05:55	180	TNG	DOLORES	LR-R	1.28	la107684 (1.20)
504 Cora	29 Feb. 04	05:59	180	TNG	DOLORES	LR-B	1.29	la107684 (1.20)
504 Cora	13 Aug. 05	00:16	300	NTT	EMMI	GR1	1.02	HD144585 (1.05)
620 Drakonia	20 Jan. 07	08:06	1800	NTT	EMMI	GR1	1.19	la98-978 (1.22)
1103 Sequoia	20 Jan. 07	01:01	600	NTT	EMMI	GR1	1.64	Hyades64 (1.45)
1251 Hedera	18 Nov. 04	06:01	600	TNG	DOLORES	LR-R	1.06	Hyades64 (1.40)
1251 Hedera	18 Nov. 04	06:13	720	TNG	DOLORES	MR-B	1.07	Hyades64 (1.40)
2048 Dwornik	16 Nov. 04	05:42	1200	TNG	DOLORES	LR-R	1.26	Hyades64 (1.03)
2048 Dwornik	20 Jan. 07	01:17	2400	NTT	EMMI	GR1	1.54	Hyades64 (1.45)
2449 Kenos	20 Jan. 07	06:06	2400	NTT	EMMI	GR1	1.16	la98-978 (1.22)
2577 Litva	29 Feb. 04	05:26	480	TNG	DOLORES	LR-R	1.29	la107684 (1.20)
2577 Litva	29 Feb. 04	05:35	360	TNG	DOLORES	LR-B	1.30	la107684 (1.20)
2577 Litva	01 Mar. 04	05:44	720	TNG	NICS	AMICI	1.32	la107648 (1.20)
2867 Steins	25 May 04	00:16	1200	NTT	EMMI	GR1	1.45	la102-1081 (1.22))
5806 Archieroy	16 Nov. 04	02:02	480	TNG	DOLORES	LR-R	1.13	HD28099 (1.05)
5806 Archieroy	19 Nov. 04	02:20	1440	TNG	NICS	AMICI	1.13	la98-978 (1.17)
6435 Daveross	16 Nov. 04	03:33	900	TNG	DOLORES	LR-R	1.60	Hyades64 (1.03)
6911 Nancygreen	20 Jan. 07	07:17	1200	NTT	EMMI	GR1	1.06	la102-1081 (1.14)
7579 1990TN1	15 Nov. 04	22:58	600	TNG	DOLORES	LR-R	1.03	Hyades64 (1.03)
7579 1990TN1	19 Nov. 04	00:47	1080	TNG	NICS	AMICI	1.30	la93-101 (1.34)

with a spectral resolution of about 35. The detector is a 1024 × 1024 pixel Rockwell HgCdTe Hawaii array.

The spectra were acquired nodding the objects along the spatial direction of the slit, in order to obtain alternated pairs (named A and B) of near-simultaneous images for the background removal. Both for the visible and near infrared observations we utilized a 1.5 arcsec wide slit, oriented along the parallactic angle to minimize the effect of atmospheric differential refraction.

At the NTT telescope, the visible spectra were acquired using the EMMI instrument, equipped with a 2 × 1 mosaic of 2048 × 4096 MIT/LL CCD with square 15 µm pixels. We used the grism #1 (150 gr/mm) in RILD mode to cover the wavelength range 4100–9600 Å with a dispersion of 3.1 Å/pixel at the first order.

For the near infrared spectroscopy, we utilized the instrument SOFI (Son OF Isaac) in the low resolution mode. The blue and red grisms, covering respectively the 0.95–1.64 µm (dispersion of 6.96 Å/pixel) and the 1.53–2.52 µm range (dispersion of 10.22 Å/pixel) were used. The acquisition technique was identical to that explained for the TNG observations, except the slit was wider (2 arcsec) but always oriented along the parallactic angle. The two parts of the blue and red grisms observations were combined matching the overlapping region in the 1.53–1.64 µm range.

The visible and near infrared spectra were reduced using ordinary procedures of data reduction with the software packages Midas and IDL as described in Fornasier et al. (2004a,2004b). For the visible spectra, the procedure includes the subtraction of the bias from the raw data, flat-field correction, cosmic rays removal, sky subtraction, collapsing the two-dimensional spectra to one dimension, wavelength calibration and atmospheric extinction correction. The reflectivity of each asteroid was obtained by dividing its spectrum by that of the solar analog star

Table 2
Spectral slopes for different wavelength range for the investigated asteroids

Asteroid	a (AU)	e	i (°)	D (km)	Albedo	Rot. (h)	$S1$ (%/10^3 Å)	$S2$ (%/10^3 Å)	$S3$ (%/10^3 Å)	Tx
44 Nysa (Jan07)	2.42	0.148	3.70	70.6	0.55	6.42	5.92 ± 0.89	1.52 ± 0.61	-3.83 ± 0.69	E[III]
44 Nysa (Feb 04)	2.42	0.148	3.70	70.6	0.55	6.42	–	3.18 ± 1.02	-1.47 ± 0.73	
44 Nysa (Aug 05)	2.42	0.148	3.70	70.6	0.55	6.42	5.39 ± 0.80	2.34 ± 0.61	-1.31 ± 0.63	
64 Angelina	2.68	0.124	1.30	59.8	0.43	8.75	16.32 ± 0.84	4.06 ± 0.61	1.62 ± 0.65	E[II]
214 Aschera	2.61	0.029	3.43	23.2	0.52	6.83	6.03 ± 1.16	1.15 ± 0.62	-4.02 ± 0.81	E[III]
317 Roxane (Aug05A)	2.28	0.085	1.76	18.7	0.49	8.16	4.38 ± 1.18	2.65 ± 0.62	-4.18 ± 0.89	E[III]
317 Roxane (Aug05B)	2.28	0.085	1.76	18.7	0.49	8.16	6.16 ± 0.97	2.72 ± 0.61	-1.26 ± 0.69	
317 Roxane (Jan 07)	2.28	0.085	1.76	18.7	0.49	8.16	9.40 ± 0.88	2.92 ± 0.61	-0.61 ± 0.65	
317 Roxane (Feb 04)	2.28	0.085	1.76	18.7	0.49	8.16	10.73 ± 1.10	4.43 ± 0.61	–	
434 Hungaria	1.94	0.073	22.50	10.0	0.46	26.51	14.49 ± 0.85	6.09 ± 0.61	3.65 ± 0.73	E[II]
437 Rhodia	2.38	0.247	7.35	13.2	0.70	–	11.24 ± 1.09	2.90 ± 0.62	-9.48 ± 0.86	E[III]
504 Cora	2.72	0.217	12.89	30.0	0.34	24.06	10.93 ± 0.81	5.43 ± 0.62	2.83 ± 0.84	E[I]
504 Cora	2.72	0.217	12.89	30.0	0.34	24.06	3.92 ± 2.44	4.42 ± 0.65	1.75 ± 1.34	
620 Drakonia	2.43	0.134	7.73	11.6[g]	–	5.485	7.49 ± 0.95	3.66 ± 0.61	-0.44 ± 0.69	E[III] ?
1025 Riema[a]	1.98	0.039	26.8	7.0	–	3.58	20.23 ± 2.59	5.63 ± 0.61	-2.37 ± 0.74	E[I]
1103 Sequoia	1.93	0.094	17.90	6.1	0.48	3.049	7.55 ± 0.92	3.27 ± 0.61	-0.14 ± 0.71	E[III]
1251 Hedera	2.71	0.154	6.03	14.6	0.41	15.01	3.97 ± 0.86	2.86 ± 0.62	-3.23 ± 1.90	E[III]
2035 Stearns[b]	1.88	0.131	27.7	5.5	–	85.0	12.50 ± 0.56	3.98 ± 0.62	-3.81 ± 1.18	E[II]
2048 Dwornik (Nov 04)	1.95	0.042	23.74	5.0[g]	–	3.66	15.54 ± 1.21	4.51 ± 0.63	-1.39 ± 0.84	E[II]
2048 Dwornik (Jan 07)	1.95	0.042	23.74	11.6[g]	–	3.66	–	5.96 ± 1.02	–	
2449 Kenos	1.91	0.168	24.98	3.0[g]	–	4.19	13.73 ± 1.26	5.16 ± 0.63	2.30 ± 0.86	E[I]
2577 Litva	1.90	0.138	22.90	–	–	2.82	18.21 ± 1.31	12.83 ± 0.62	-4.56 ± 0.84	A
2867 Steins	2.36	0.145	9.94	4.6	0.45	6.05	34.03 ± 1.49	8.10 ± 0.65	2.89 ± 1.03	E[II]
2867 Steins (May 04)[c]	2.36	0.145	9.94	4.6	0.45	6.05	32.02 ± 1.59	6.93 ± 0.65	2.24 ± 1.03	
2867 Steins (Aug 05)[c]	2.36	0.145	9.94	4.6	0.45	6.05	33.05 ± 1.35	7.62 ± 0.64	2.45 ± 0.86	
3050 Carrera[d]	2.22	0.188	1.306	3.6	–	–	7.82 ± 1.96	0.50 ± 0.65	-8.30 ± 1.3	E[III]
3103 Eger[c]	1.40	0.354	20.93	1.4	0.63	5.70	24.90 ± 1.28	7.43 ± 0.63	3.99 ± 0.76	E[II]
4660 Nereus[e]	1.49	0.360	1.432	1.0	0.55	15.10	5.68 ± 2.06	4.32 ± 0.55	2.53 ± 1.63	E[II]
5806 Archieroy	1.96	0.36	20.82	–	–	12.16	–	9.50 ± 0.63	-8.13 ± 0.96	S[V]
6435 Daveross	1.91	0.057	23.43	3.0[g]	–	–	–	5.37 ± 0.64	2.40 ± 1.27	E[I]
6911 Nancygreen	1.93	0.090	22.90	4.9[g]	–	5.38	12.30 ± 1.30	4.76 ± 0.65	-0.26 ± 0.95	E[II]
7579 1990 TN1	1.98	0.065	16.98	–	–	–	–	10.71 ± 0.67	-8.11 ± 0.98	A
144898 2004 VD17[f]	1.51	0.588	4.22	0.64	0.45	1.99	7.76 ± 2.74	2.38 ± 0.70	–	E[I]

$S1$, $S2$, and $S3$ are the spectral slopes evaluated respectively in the 4900–5500, 5500–8000, and 8000–9000 Å wavelength range.
[a] Visible spectrum taken from Bus and Binzel (2002).
[b] Visible spectrum and albedo taken from Fornasier and Lazzarin (2001).
[c] Visible spectra taken from Fornasier et al. (2007).
[d] Visible spectrum taken from Barucci et al. (2005).
[e] Visible spectrum taken from Binzel et al. (2004) and the albedo from Delbó et al. (2003).
[f] Visible spectrum and albedo taken from De Luise et al. (2007). Diameter, albedo, and rotational periods are taken from IRAS observations (Tedesco et al., 1989, 2002) and from the asteroid physical parameters data in the Jet Propulsional Laboratory Horizon webpage (http://ssd.jpl.nasa.gov/horizons.cgi#top).
[g] Are evaluated from the asteroid absolute magnitude assuming an albedo value of 0.4. Tx is the suggested taxonomy.

closest in time and airmass to the object. Spectra were finally smoothed with a median filter technique, using a box of 19 pixels in the spectral direction for each point of the spectrum. The threshold was set to 0.1, meaning that the original value was replaced by the median value if the median value differs by more than 10% from the original one.

For the observations in the infrared range, first, spectra were corrected for flat fielding, then bias and sky subtraction was performed by producing A–B and B–A frames. Then, the positive spectrum of B–A frame was shifted and added on the positive spectrum of A–B frame. The final spectrum is the result of the mean of all pairs of frames previously combined. The spectrum was then extracted and wavelength calibrated. For the NTT-SOFI spectra, this last step was performed acquiring the spectrum in the blue and red grisms of a Xenon lamp, and comparing the observed line with those of a reference table, obtaining the dispersion relation. For the TNG-NICS spectra, due to the very low resolution of the Amici prism, the lines of Ar/Xe lamps are blended and cannot be easily used for standard reduction procedures. For this reason, the wavelength calibration was obtained using a look-up table which is based on the theoretical dispersion predicted by ray-tracing and adjusted to best fit the observed spectra of calibration sources. Finally, the extinction correction and solar removal was obtained by division of each asteroid spectrum by that of the solar analog star closest in time and airmass to the object. The stellar and asteroid spectra were cross-correlated and, if necessary, sub-pixel shifts were made before the asteroid-ratio star division was done. This reduction step is needed to reduce the noise and/or the changes in the final asteroid slope due to small changes in the wavelength dispersion between asteroid and star observations, introduced by instrumental flexure.

The infrared and visible range spectra of each asteroid were finally combined overlapping the spectra, merging the two

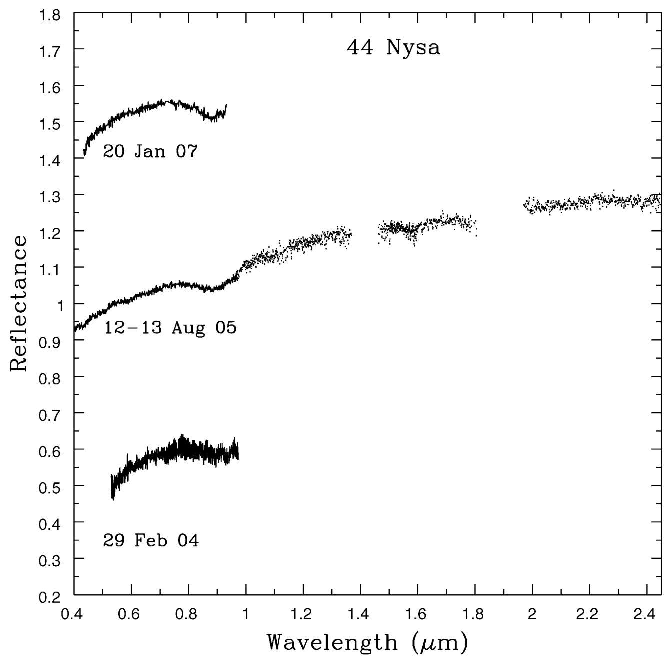

Fig. 1. Visible and near infrared spectra of 44 Nysa.

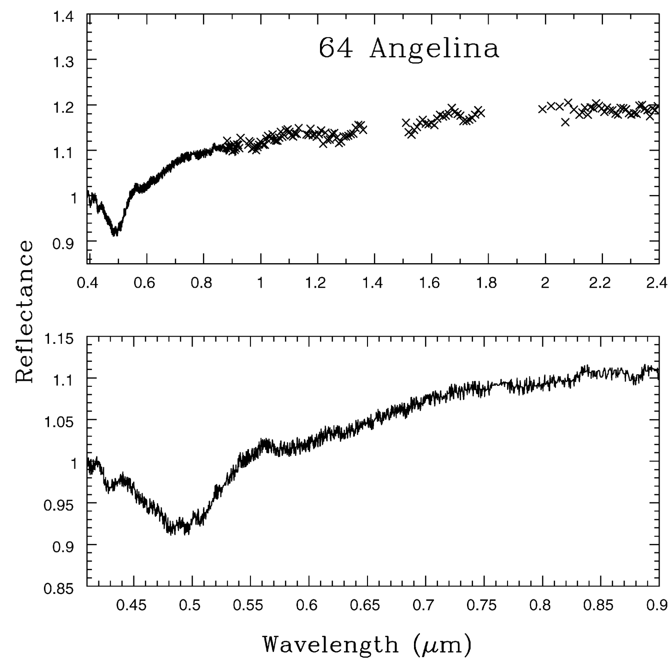

Fig. 2. Visible and near infrared spectrum of 64 Angelina.

wavelength regions at the common wavelengths and utilizing the zone of good atmospheric transmission to find the normalization factor between the two spectral parts. For the TNG data the overlapping region goes from 0.88 to 0.94 μm, and we took the average value over the 0.89–0.91 micron region of the visible spectrum to normalize the infrared one. For the NTT data, considering that the overlapping region is very small (0.95–0.96 μm) we use curve fitting at the ends of each spectral part to extrapolate to the beginning of the next spectral region and to overlap the data. The spectra of the observed asteroids, all normalized at 0.55 μm, are shown in Figs. 1–16. The conditions of the observations are reported in Table 1.

3. Results

We investigated 16 out of the 23 known E-type asteroids listed in Clark et al. (2004, see Table 1) plus 2867 Steins, a target of the Rosetta mission, and 437 Rhodia, that were classified as E-types (Barucci et al., 2005). Eight of them were investigated both in the visible and near infrared range. We obtained the first spectroscopic observations for 8 E-type asteroids listed in Clark et al. (2004), discovering that 3 of them (2577 Litva, 5806 Archieroy, and 7579 1990TN1), never observed before, show a spectral behavior in the visible and near infrared region that is not consistent with the E-type classification.

In the following subsections we discuss the spectral properties of each of the investigated asteroids, and we attempt to classify each of them into the 3 different subgroups proposed for the E-class, using the Gaffey and Kelley (2004) classification scheme, that we described previously. We also evaluate the spectral slope in 3 different wavelength regions (4900–5500 Å ($S1$), 5500–8000 Å ($S2$) and 8000–9000 Å ($S3$)), using a standard least squared technique. The spectral slope values (see Table 2) help us identify of the subgroup memberships. Asteroids belonging to the E[II] subgroup usually have a large value of the $S1$ slope (steep rise of the 0.49 μm band), while asteroids belonging to the E[III] subgroup have negative or very small values of the $S3$ slope (indicative of the presence of the absorption band centered at around 0.9 μm). For a more complete analysis, we include in Table 2 the spectral slope values for 6 E-type asteroids (1025 Riema, 2035 Stearn, 3050 Carrera, 3103 Eger, 4660 Nereus, 144989 2000VD17) not presented here but whose spectra are available in literature (Bus and Binzel, 2002; Fornasier and Lazzarin, 2001; Barucci et al., 2005; De Luise et al., 2007; Fornasier et al., 2007).

3.1. 44 Nysa

44 Nysa is a main belt asteroid located at 2.42 AU. It has an albedo of 0.55 ± 0.07 (Tedesco et al., 2002), a diameter of 71 km and a rotational period of 6.42 h.

We get a full V + NIR spectrum of Nysa at the NTT telescope during Aug. 2005, plus 2 additional visible spectra obtained at the NTT (Jan. 07) and TNG telescopes (Feb. 04). All the spectra show an absorption band (Fig. 1) centered at ∼0.9 μm, that appears to be deepest in the Jan. 07 spectrum, as can be seen comparing the $S3$ slope in Table 2. The NIR spectrum indicates the presence of a broad absorption feature at ∼1.8 μm, confirming the detection already reported by Clark et al. (2004). 44 Nysa is the archetype of the E[III] subgroup, with both the 0.9 and 1.8 μm absorption band indicative of iron bearing pyroxene such as orthopyroxene or forsterite.

The visible spectra shows slight differences in the spectral slopes evaluated in the 5500–8000 Å region, with the Feb. 04 spectrum being the steeper one. We also identify on the Aug.

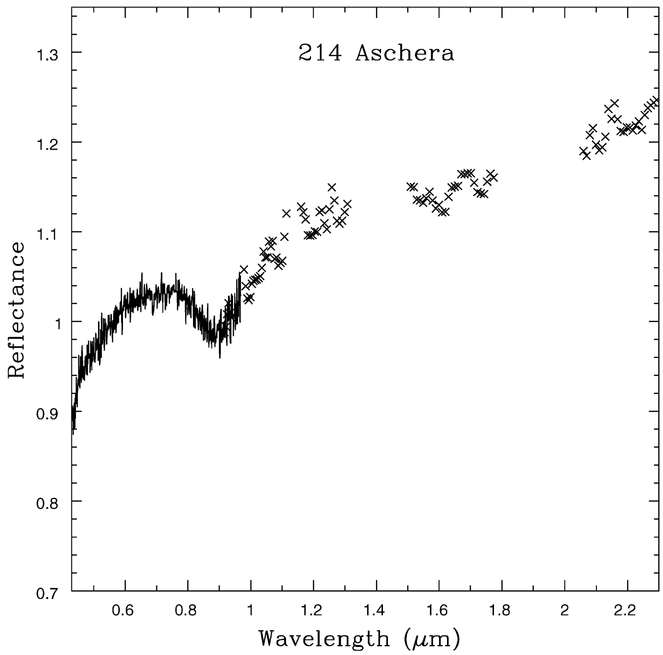

Fig. 3. Visible and near infrared spectrum of 214 Aschera.

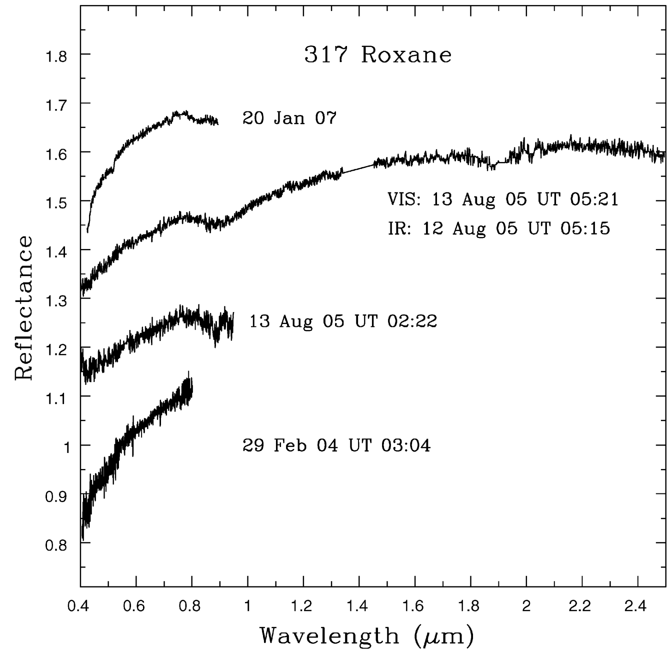

Fig. 4. Visible and near infrared spectra of 317 Roxane.

05 spectrum a very faint band (depth ∼1.2% as compared to the continuum) centered at 0.433 micron, wide around 0.02 μm. Due to its faintness, the detection of this band needs to be confirmed. If real, the band is not easily attributable: it might be associated to chlorites and Mg-rich serpentines, as suggested by King and Clark (1989) on enstatite chondrites; to pyroxenic minerals such us pigeonite or augite as suggested by Busarev (1998) on M-asteroids; or to an Fe^{3+} spin-forbidden transition in the iron sulfate jarosite, as suggested by Vilas et al. (1993) on low-albedo asteroids. Rivkin et al. (1995) detected the 3 micron absorption band on 44 Nysa and they suggested that it can be attributed to the presence of hydrated phases on its surface. Our detection of the 0.43 μm band, if it is really due to the presence of chlorites—Mg rich serpentines and/or to jarosite, might support this interpretation as these minerals are aqueous alteration products.

3.2. 64 Angelina

64 Angelina is located in the main belt, at 2.68 AU. It is the second largest E-type asteroid, after Nysa, with a diameter of about 60 km and an albedo of 0.43 (Tedesco et al., 1989). We obtained new visible and near infrared spectroscopic observations of 64 Angelina (Fig. 2) on November 2004, at the TNG telescope. The visible spectrum clearly shows the presence of the sharp absorption band centered at ∼0.492 μm, with a FWHM of 0.055 μm and a depth of about 8%, probably due to the presence of oldhamite. Similar parameters for this absorption band were reported also by Fornasier and Lazzarin (2001), and the presence of the band confirmed by Burbine et al. (1998) and Clark et al. (2004). In addition, our spectrum clearly shows an absorption feature centered at 0.431 μm, with a width around 0.019 μm and a depth of ∼2% as compared to the continuum. This feature is similar to the aforementioned but fainter one detected on 44 Nysa, and, once again, if it is due to aqueous alteration products such as chlorites, serpentines or jarosite, it might support the hypothesis of the presence of hydrated phased on Angelina, as suggested by Rivkin et al. (1995) who observed the 3 micron band on its spectrum.

We do not have evidence on our spectrum of a shallow absorption feature at 0.92 μm reported by Burbine et al. (1998) and Clark et al. (2004). Our near infrared spectrum has a spectral behavior slightly reddish and different than that published by Clark et al. (2004). The difference could be associated with different rotational phases seen in the two observations (Angelina's rotational period is 8.75 h), and could indicate some inhomogeneities on the surface of 64 Angelina.

Because of the sharp 0.49 μm band absorption, Angelina belongs to the E[II] sub-type.

3.3. 214 Aschera

214 Aschera has a semimajor axis of 2.61 AU, an IRAS albedo of 0.52 ± 0.05 (Tedesco et al., 2002) and a diameter of 23 km. We obtained new data on two different runs at the NTT (May 04, visible spectrum) and TNG (Nov. 04, IR spectrum) telescopes. The spectrum shows the presence of a sharp band centered at 0.9 μm; in addition, there is an indication of a possible feature at ∼1.8 μm (Fig. 3), even though our spectrum has been cut in this region for the telluric bands residuals. These two bands were both detected by Clark et al. (2004) on their spectra. Using literature data from SMASS survey, Gaffey and Kelley (2004) classified Aschera as an E[I] subgroup member, due to the lack of any discrete disagnostic mineral absorption features. Nevertheless, the presence of the 0.9 and 1.8 μm spectral bands, independently detected by Clark et al. (2004) and in

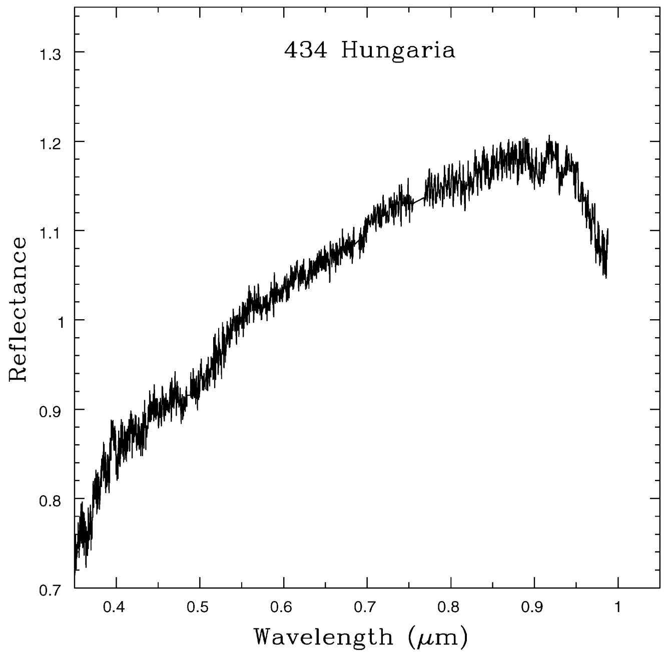

Fig. 5. Visible spectrum of 434 Hungaria.

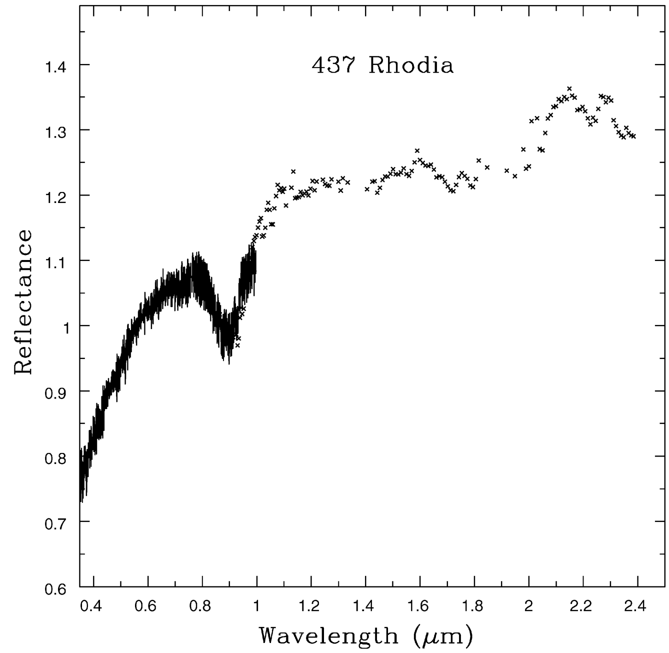

Fig. 6. Visible and near infrared spectra of 437 Rhodia.

this work, confirms that 214 Aschera is a Nysa-like object, and so it can be placed into the E[III] subgroup.

3.4. *317 Roxane*

317 Roxane has a semimajor axis of 2.29 AU, an IRAS albedo of 0.49 ± 0.08 (Tedesco et al., 2002) and an estimated diameter of ∼19 km. We acquired four new visible spectra and one in the infrared region using both the NTT and TNG telescopes (Fig. 4). All the three visible spectra obtained at the NTT telescope show the 0.9 μm band, despite there are some variations in the shape within the different data set. The visible spectrum obtained at the TNG telescope does not give information on this absorption as it was cut at 0.81 μm, because of the fringing problems. The TNG spectrum also has a higher spectral slope value in the 5500–8000 Å region compared to the NTT spectra (Table 2). It also shows a drop off of the reflectance for wavelength <5200 Å that is similar to the behavior of the Jan. 07 spectrum, but different from the 2 spectra acquired on Aug. 05.

The Jan. 07 spectrum shows also a faint absorption centered at 0.51 μm, seen also on some M-type asteroids (Busarev, 1998, 2002) and possibly attributed to Fe^{2+} spin forbidden charge field transitions in pyroxenes.

The IR spectrum shows the 0.9 μm feature together with a faint absorption at 1.8 μm. Clark et al. (2004) present a spectrum which, in the infrared region, is different from the one we present here: it shows the 0.9 μm band and the 1.8 μm band, but there is a steep decrease in the spectral slope in the 1.3–1.9 μm range, while our spectrum has a gently reddish behavior. The variation in the spectral behavior of 317 Roxane in our data and those coming from the literature can be attributed to some inhomogeneities in the surface composition of the asteroid, that has a rotational period of 8.17 h.

Due to the presence of the 0.9 and 1.8 μm bands, 317 Roxane is then classified as a E[III] subgroup member. Additional observations covering the whole rotational period of this object are needed to fully investigate its surface composition.

3.5. *434 Hungaria*

434 Hungaria is located just outside the inner edge of main belt, at a semimajor axis of 1.94 AU. We get a spectrum only in the visible range that shows a faint absorption band centered at ∼0.49 micron, and a feature beyond 0.89 μm (Fig. 5). Burbine et al. (1998) and Bus and Binzel (2002) also reported the presence of two absorption bands at 0.49 and 0.92 μm on their Hungaria spectrum. Nevertheless, in the Bus and Binzel (2002) spectrum, the reflectance has a maximum at ∼0.75 μm and then decreases, while in our spectrum the reflectance has a red linear slope up to 0.89 μm. The visible spectra presented by Sawyer (1991) and Kelley and Gaffey (2002) do not shown the 0.9 μm band, while this absorption is clearly present in the infrared spectrum of Clark et al. (2004). 434 Hungaria, that has a long rotational period of 26.5 h, shows different spectral behaviors that can be associated with some inhomogeneities in the surface composition. Due to the presence of the 0.5 μm band we classify Hungaria as a member of the E[II] subgroup.

3.6. *437 Rhodia*

437 Rhodia is the asteroid with the highest albedo (0.70 ± 0.08) in the IRAS dataset (Tedesco et al., 2002). It has a semimajor axis of 2.38 AU and an estimated diameter of 13 km. The first visible and near infrared spectrum of Rhodia was obtained by Barucci et al. (2005), who suggests a possible E-type

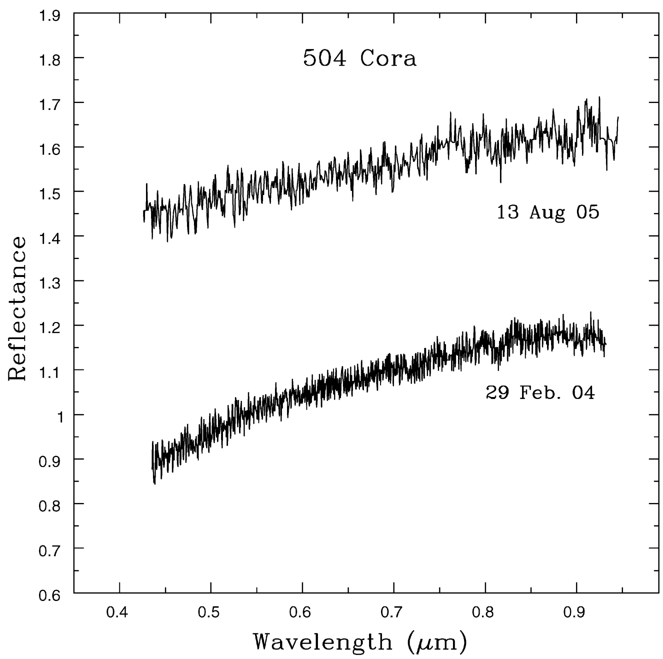

Fig. 7. Visible spectra of 504 Cora.

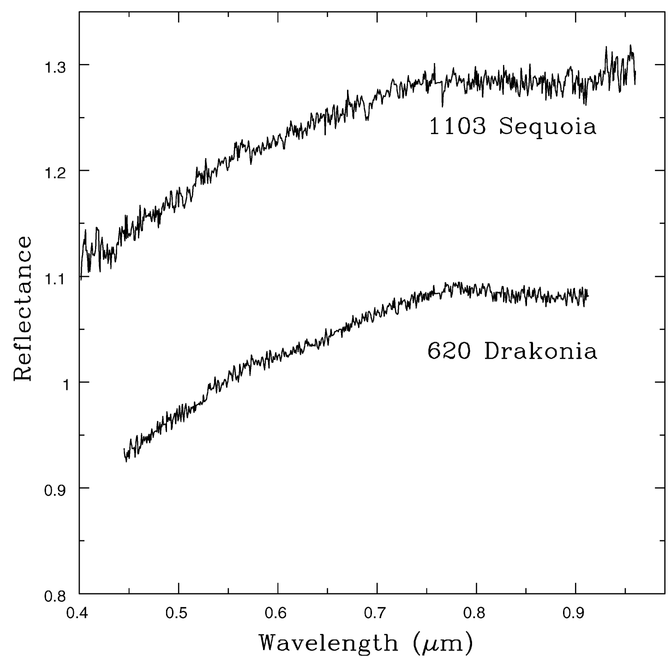

Fig. 8. Visible spectra of 620 Drakonia and 1103 Sequoia.

classification on the basis of its high albedo and of its spectral behavior, which is similar to that of 44 Nysa. We obtained new spectra of Rhodia (Fig. 6) which clearly show both the 0.9 ad 1.8 μm bands, already reported by Barucci et al. (2005). The spectral behavior, together with the high albedo value, allow us to definitively classify Rhodia as an E-type asteroids, and in particular as a member of the E[III] subgroup. As compared to the two infrared spectra reported by Barucci et al. (2005, see their Fig. 2), that are slightly different beyond 1.4 μm, our IR spectrum is similar to first one (named a) they obtained.

3.7. 504 Cora

504 Cora was suggested to be an E-type asteroid by Clark et al. (2004) on the basis of the IRAS albedo (0.34, Tedesco et al., 2002) and of the X classification given by Bus and Binzel (2002). It is located in the middle of the main belt (semimajor axis of 2.72 AU) in an orbit with an eccentricity of 0.217. We observed Cora twice in visible spectroscopy both at the TNG and NTT telescopes, on February 2004 and August 2005, respectively (Fig. 7). The 2 spectra have a very similar featureless linear reddish behavior.

Due to the absence of any absorption feature, 504 Cora might be classified as an E[I] subgroup member.

3.8. 620 Drakonia

We present the first spectroscopic observations, only in the visible range, of 620 Drakonia, a main belt asteroid with a semimajor axis of 2.43 AU and a rotational period of 5.48 h. The spectrum, obtained at the NTT telescope on Jan. 07 (Fig. 8), is featureless and reddish from 0.45 to 0.77 μm, and it has a shallow broad absorption feature (depth of 1.4%) centered at around 0.9 μm. Unfortunately, we do not have any IR data so it is not possible to independently confirm the presence of the 0.9 μm band. The visible spectrum of Drakonia is very similar to that of 1103 Sequoia, an E[III] member discusses later. We suggest that 620 Drakonia might also belong to the E[III] subgroup.

3.9. 1103 Sequoia

We obtained a visible spectrum of 1103 Sequoia, an asteroid located in Hungaria's region with an IRAS albedo of 0.48 (Tedesco et al., 1989). The spectrum (Fig. 8) is analogous to that of 620 Drakonia: flat red sloped spectral shape from 0.45 to 0.77 μm, then a gentle drop-off of the reflectance with the presence of a shallow absorption feature (depth 1.5%) centered at ∼0.89 μm. The spectrum is similar to that presented by Bus and Binzel (2002). The NIR Sequoia' spectrum presented in Clark et al. (2004) shows the 0.9 and 1.8 μm absorption bands. On the basis of these data, 1103 Sequoia can be classified as an E[III] subgroup member.

3.10. 1251 Hedera

1251 Hedera is located in the middle of the main belt. Its IRAS albedo is of 0.41 (Tedesco et al., 1989). We obtained a visible spectrum at the TNG telescope on Nov. 04 (Fig. 9), that clearly shows an absorption band centered at 0.9 μm. Also Clark et al. (2004) reported the presence of the 0.9 μm band, together with an absorption feature at 1.8 μm. The visible spectrum was obtained also by Fornasier and Lazzarin (2001), who reported a spectral slope value in the 5500–8000 Å range ($2.58\%/10^3$ Å) very close to what we determine (see Table 2). 1251 Hedera might then be classify as an E[III] subgroup member.

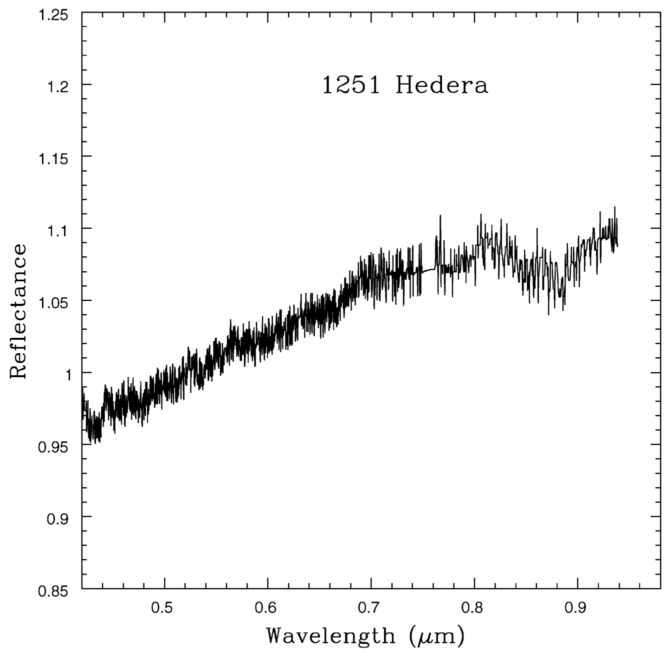

Fig. 9. Visible spectrum of 1251 Hedera.

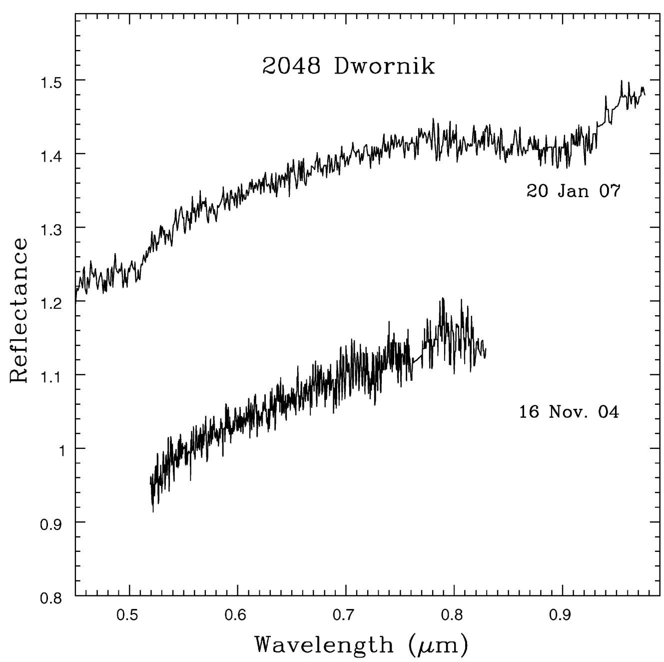

Fig. 10. Visible spectrum of 2048 Dwornik.

3.11. *2048 Dwornik*

2048 Dwornik is located in the Hungaria region. It has a rotational period of 3.66 h. We observed it twice with the TNG and NTT telescope, but only in the visible range (Fig. 10). The spectrum obtained at the TNG telescope on Nov. 2004 has been cut at 0.83 μm because of large residual in the fringing corrections at longer wavelength. Its spectral slope, evaluated in the 5500–8000 Å range, is comparable to the value computed from the NTT spectrum (see Table 2). The NTT spectrum has a higher signal to noise ratio and a wider wavelength coverage. It shows an absorption band centered at 0.9 μm (3.8% depth), and a shallow feature (depth ∼1.5%) at 0.49 μm. The 0.9 μm band was detected also by Clark et al. (2004) in their NIR spectrum. The visible spectrum appears similar to the Hungaria one. We suggest that 2048 Dwornik, having both the 0.49 and 0.9 micron bands, might be an E[II] subgroup member.

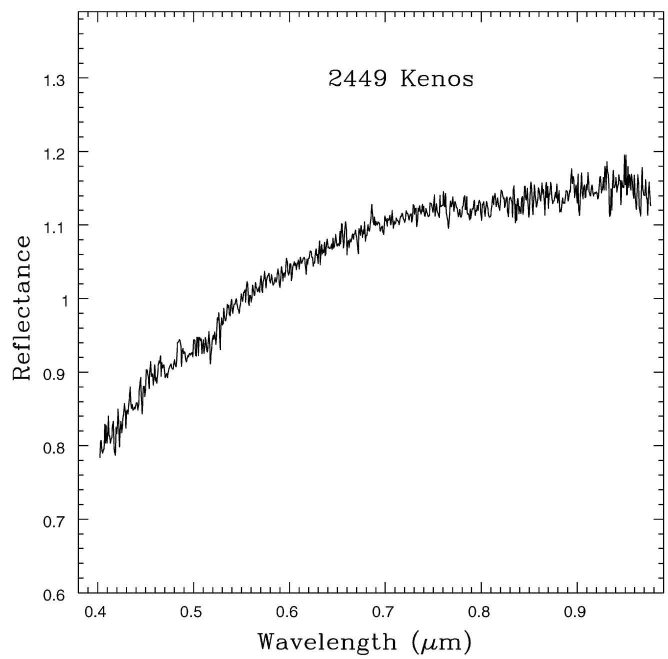

Fig. 11. Visible spectrum of 2449 Kenos.

3.12. *2449 Kenos*

2449 Kenos is located in the Hungaria region. We obtained the first spectroscopic observations, only in the visible range, of this asteroid which has a known rotational period of 4.188 h (Fig. 11). The spectrum is curved with a gently reddish behavior. No infrared data are available in literature for this asteroid. We do not identify any absorption features, so we suggest to classify Kenos as an E[I] subgroup member.

3.13. *2577 Litva*

2577 Litva is a Hungaria family asteroid that was classify as E-type by Tholen (1989), even if its U–B and B–V colors were compatible with a TS classification. We obtain the first visible and near infrared Litva' spectrum which, as shows in Fig. 12, definitively ruled out the E-type classification. 2577 Litva has a strong absorption (band I) centered at 1.08 micron that suggests a high presence of olivine in its surface composition. The band I depth is 36%, the peak just before the olivine absorption is located at 0.78 μm, and the reflectance at 1.65 μm is 2.08. A minor content of pyroxene is present on the asteroid surface as shown by the weaker absorption (Band II) centered at 2 μm. The Band II/Band I area ratio is 0.39 ± 0.07.

From our data, 2577 Litva has to be classified as an A-type asteroid. The diameter estimated from the absolute magnitude

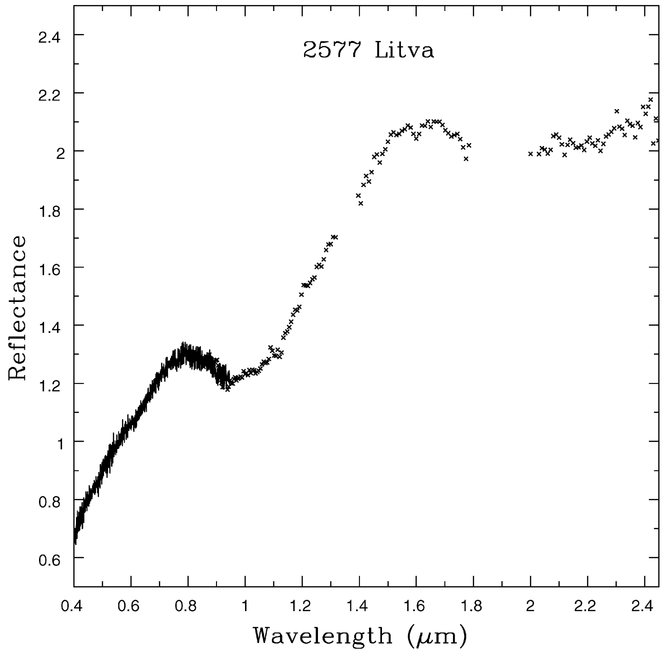

Fig. 12. Visible and near infrared spectra of 2577 Litva.

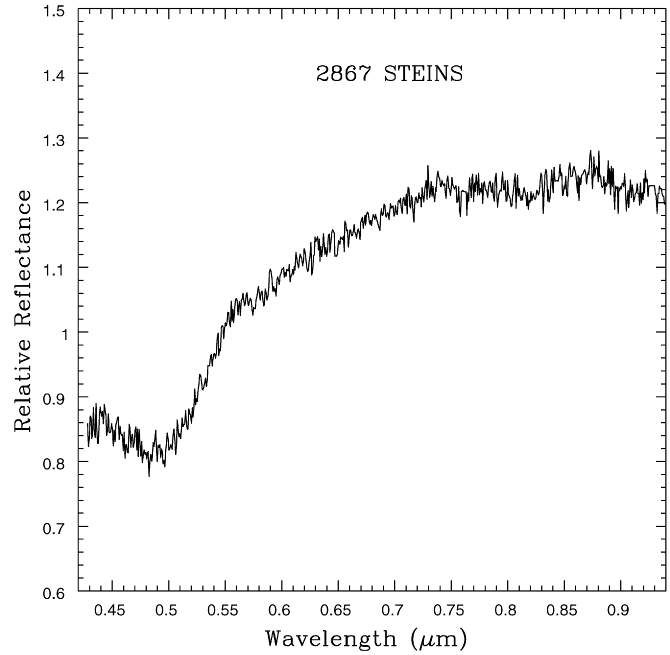

Fig. 13. Visible spectrum of 2867 Steins, a target of the Rosetta mission.

(13.18), assuming an albedo value of 0.2, is between 8–10 km. Comparing the spectral behavior of Litva with that of 9 A-type asteroids reported by Burbine and Binzel (2002), it appears that Litva has a higher abundance of olivine as compared to other small-sized A-type asteroids.

3.14. 2867 Steins

2867 Steins is the first target that will be visited by the Rosetta mission on September 2008. Its classification as an E-type asteroid was suggested based on its spectral behavior (Barucci et al., 2005), that shows a strong 0.49 μm band similar to that seen on the 64 Angelina spectrum, and on the high albedo value (0.45 ± 0.10) determined by polarimetry (Fornasier et al., 2006). Recently Lamy et al. (2008) find a smaller albedo value of 0.34 ± 0.06 by modeling the spectral data in the 5–38 μm wavelength range obtained with the Spitzer space telescope. This value is still consistent with the E-type classification. Moreover, Barucci et al. (2008), analyzing the Steins emissivity spectrum derived from the aforementioned Spitzer data, find that it is similar to the enstatite achondrites (aubrites) and to the enstatite mineral, confirming once again the E-type classification.

The asteroid is located at 2.36 AU, it has a rotational period of 6.052 ± 0.007 h (Kuppers et al., 2007), and an estimated diameter of about 5 km.

We obtained a new spectrum on 25 May 2004 in the visible range (Fig. 13). Unfortunately, our attempt to observe the asteroid in the infrared region failed both at the TNG and NTT telescopes due to bad weather conditions or technical problems. The spectrum clearly shows the presence of the 0.49 μm band. More precisely, the band is centered at 4939 ± 20 Å, extends from around 4300 to 5500 Å and its depth as compared to the continuum is 12%. The spectral behavior confirms that 2867 Steins belongs to the E[II] subgroup.

We do not detect any feature in the 0.9 μm region, that is often associated to the 0.49 μm band. Barucci et al. (2005) reported the presence of a faint feature at about 0.96 μm and a flat and featureless behavior over 1 μm. The new spectrum here presented is very similar to those published by Fornasier et al. (2007) and Barucci et al. (2005), and also the spectral slope values are comparable within the errors bars. This may imply that the asteroid surface is quite homogeneous, or that we always observed the same part of the surface (the two spectra of May 04, one reported in Fornasier et al., 2007, and one here, covered almost the same portion of the surface, being separated by 3.88 rotational periods).

Steins has a deep and well-shaped 0.49 μm band, with the steepest spectral slope in the E-type population both in the 4900–5500 Å and 5500–8000 Å wavelength range (Table 2). Only the near Earth Asteroid 3103 Eger has a similar spectral behavior (Fornasier et al., 2007), having both a high spectral slope value $S2$ and a deep (∼8%) 0.49 μm band. On the basis of this strong spectral similarity, Fornasier et al. (2007) suggest that these two objects might have a possible common origin in spite of their presently different orbits, and that they are both remnants of an old asteroid family, the outcome of the breakup of a parent body at about 2.36 AU.

3.15. 5806 Archieroy

5806 Archieroy is located in the Hungaria region (semimajor axis of 1.96 AU) and was suggested to belong to the E-class by Gil-Hutton and Benavides Gil-Hutton and Benavidez (2001) on the basis of its polarimetric properties. The rotational period is of 12.16 h. We obtain the first visible and near infrared spectrum of 5806 Archieroy at the TNG telescope during the November

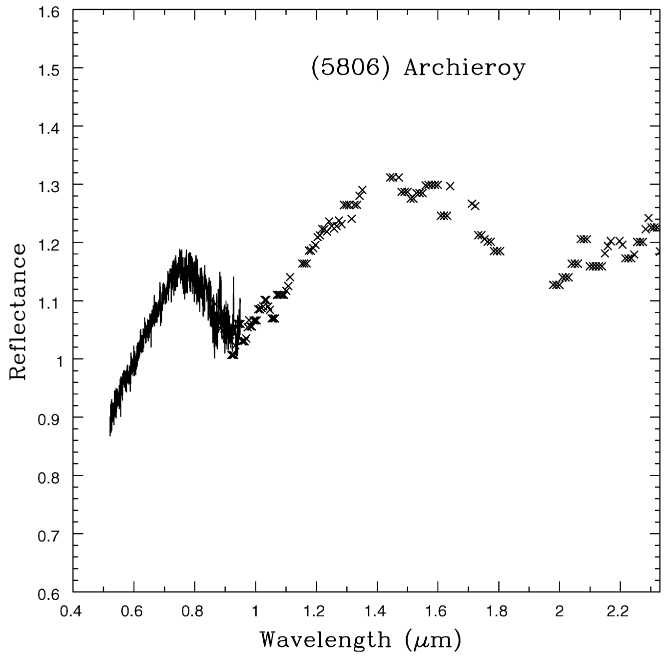

Fig. 14. Visible and near infrared spectrum of 5806 Archieroy.

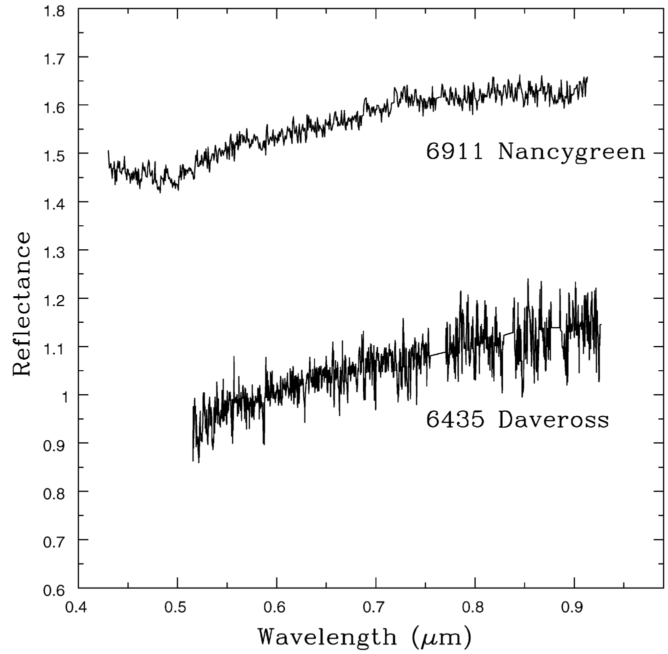

Fig. 15. Visible spectra of 6435 Daveross and 6911 Nancygreen.

2004 observing run (Fig. 14). Our data definitively ruled out the E-type classification for this asteroid. In fact, 5806 Archieroy presents two absorption bands at ~0.9 and 2 μm typically seen on the S-type spectra, and due to olivine and pyroxene. The first absorption band (Band I) is centered at 0.948 μm, and the second one (Band II) at 1.996 μm. The Band II/Band I area ratio is of 1.37, so 5806 Archieroy is placed in the S(V) subtype following the Gaffey et al. (1993) classification scheme.

3.16. 6435 Daveross

6435 Daveross is located in the Hungarias region (semimajor axis of 1.91 AU) and was suggested to belong to the E-class by Gil-Hutton and Benavidez (2001) on the basis of its polarimetric properties. We obtained the first visible spectrum of this asteroid at the TNG telescope on November 04 (Fig. 15). The spectrum is featureless, with a spectral slope $S2$ of 5.4%/10^3 Å. No other data are available in literature. We suggest that 6435 Daveross belongs to the E[I] subtype.

3.17. 6911 Nancygreen

6911 Nancygreen is another asteroid located in the Hungaria region (semimajor axis of 1.93 AU) that was suggested to belong to the E-class by Gil-Hutton and Benavides (2001) on the basis of its polarimetric properties. Its rotational period is of 5.38 h. We observed this asteroid at the NTT telescope on Jan. 07, in the visible range. The spectrum shows a faint band centered at 4966 ± 0.30 Å, about 3% depth as compared to the continuum (Fig. 15). There are no other data in the literature about this asteroid. On the basis of the visible spectrum, we suggest that 6911 Nancygreen belongs to the E[II] subgroup.

3.18. 7579 1990 TN1

1990 TN1 is a Hungaria family asteroid that, on the basis of its polarimetric properties, was suggested to belong to the E-type by Gil-Hutton and Benavidez (2001). We obtained the first visible and near infrared spectrum of 1990 TN1 (Fig. 16) that ruled out the E-type classification. The spectrum shows a sharp absorption band centered at 1.04 micron with a depth of 39% as respect to a continuum line, indicative of the presence of olivine. The relative reflectance value at 1.65 micron is 2.01, and there is no evidence of the pyroxene absorption band at 2 micron. 1990 TN1 is then a typical olivine rich A-type asteroid.

4. Spectral modeling

E-type asteroids are thought to be the parent bodies of the aubrite meteorites (Burbine et al., 2002a). These meteorites are composed primarily of enstatite, a Ca-rich silicate; metal Fe is also present in minor amounts, according to the theory that enstatitic meteorites formed in an O-poor environment. Other minerals, also supposed to be present on the aubrites, are feldspates (1–16%), diopside (0.2–8%), olivine (0.3–10%), Fe–Ni rich minerals (0.1–3.7%), and troilite (0.1–7%) (Reid and Cohen, 1967; Olsen et al., 1977; Watters and Prinz, 1979; Watters et al., 1980; Keil et al., 1989), and, in minor amount, oldhamite, caswellsilverite, daubreelite, alabandite and shreibersite (Keil and Fredriksson, 1963; Okada and Keil, 1982).

In order to investigate the possible surface composition of the E-type asteroids, we attempt to reproduce their spectral behaviors by obtaining synthetic spectra of different geographical mixtures (spatially segregated) of meteorites and minerals (Fornasier et al., 2004b; Dotto et al., 2006). We considered meteorites and minerals that are compositionally related to the

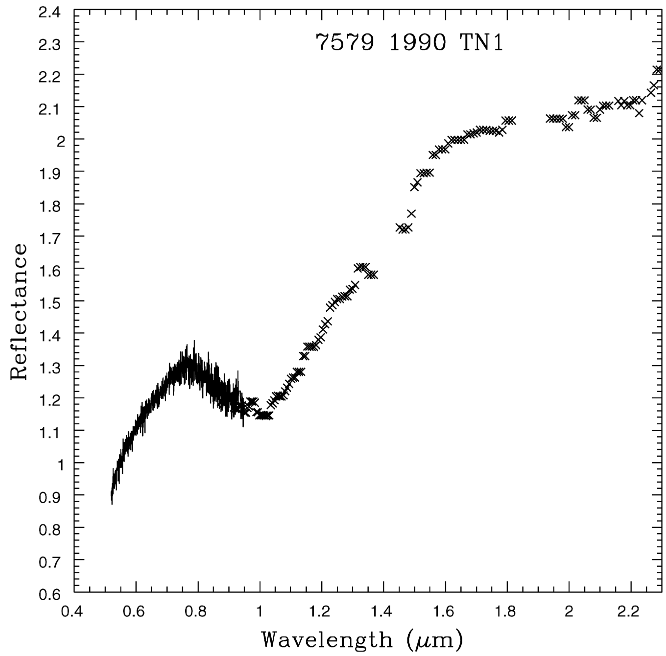

Fig. 16. Visible and near infrared spectrum of 7579 1990 TN1.

igneous asteroids, such as aubrite achondrites, enstatite, orthopyroxene, diopside, troilite and oldhamite. We limited our investigation to the E-type asteroids for which we have both the visible and near infrared data. We made the assumption that our combined visible and near infrared spectra, acquired on two different nights and not simultaneously, are representative of the same reflecting surface. Our first aim was to identify the meteorites samples with a spectral behavior very similar to that of the observed asteroids; should that not be the case, we enriched the meteorites with some minerals, already known to be constituent of the aubrites, in order to reproduce both the asteroid's spectral behavior and its albedo value. We took into account the complete sample of minerals and meteorites included in the RELAB catalog. We developed a Fortran code to calculate the reflectance of the mixtures which better match the observed asteroids spectra, according to a chi-square test. We decided to consider only the mixtures composed of no more than 3 end-members, as, including a greater number of compounds, the fit improves but it becomes very difficult to control the relationship between the asteroids composition and meteorites/minerals abundances. The main meteorites and minerals samples used in our models are listed in Table 3 and represented in Fig. 17.

For Asteroid *44 Nysa* it was not possible to find a compositional model able to reproduce both the visible and near-infrared spectral behavior, and the albedo value. The spectral trend of the near-infrared part of the spectrum is well reproduced by mixing the meteorite Peña Blanca (55%) with a huge amount of troilite (45%). This mixture, nevertheless, has a visible spectrum steeper compared to that of Nysa (Fig. 18, continuous line) and a lower albedo (0.33). In addition, is not easy to justify such huge amount of troilite, as it is present in lower percentages (<10%) inside the aubrites. A second possible model of the surface composition of Nysa is given by a

Table 3
List of the main meteorites and minerals used in our models, selected from RELAB catalogue

Name	RELAB code	Grain size (μm)
Meteorites:		
Abee	c1mt40	<125
Bishopville	c1tb47	<125
Happy Canyon	cbea03	<45
Mayo Belwa	s1tb46	<125
Norton Country	cbea04	<45
Pe na Blanca	c1tb45	<125
ALH 78113	c4lm04	Frag.
Y-793592	BKR1MP105	<125
Minerals:		
Clinopyroxene	c1pp21	<45
Orthopyroxene	c1pe30	<45
Diopside	c2pd01	<45
Forsterite	c1po76	<45
Oldhamide	c1tb38	<125
Troilite	cdmb06	63–125

mixture made of the aubrite meteorite Peña Blanca (77%), enriched with troilite (8%) and diopside (15%); the albedo value of the mixture is 0.49, in good agreement with the asteroid one (Fig. 18, dashed line), although the spectral slope is not well reproduced.

Asteroid *64 Angelina* (IRAS albedo = 0.43) is compatible with the aubrite ALH78113 (albedo = 0.49). To better reproduce the asteroid spectral behavior, we enriched the meteorites with oldhamide (Fig. 18). The model we propose is then constituted of 92% of meteorite ALH78113 and 8% of oldhamite, and has an albedo value of 0.47.

For Asteroid *214 Aschera* we propose a mixture (Fig. 18) constituted of 88% of the aubrite Peña Blanca enriched with a 12% of orthopyroxene. This simple mixture reproduces quite well the visible and near infrared behavior, and in particular the 0.9 μm absorption band. The albedo of the mixture is 0.53, higher than the asteroid value (0.40).

Asteroid *317 Roxane*, as previously discussed, shows both the 0.9 and 1.8 μm absorption features. We find a good spectral match between the asteroid spectrum and that of the aubrite Peña Blanca (Fig. 18). Moreover, also the meteorite albedo value (0.52) is very close to the asteroid one (0.49). This is the first meteorite—E[III] asteroid match found to date (Gaffey and Kelley, 2004).

For *437 Rhodia*, it is again not easy to reproduce the well pronounced 0.9 μm band, the overall spectral behavior and the very high albedo value (0.70 ± 0.08 in Tedesco et al., 2002, but 0.56 ± 0.03 in Tedesco et al., 1989). A mixture of the aubrite meteorite Peña Blanca (90%) with 10% of orthopyroxene gives a high albedo value (0.53) and nicely reproduced the 0.9 μm absorption band and the spectral behavior in the visible range, but does not match the infrared data (Fig. 18, dash line). Another model is proposed, constituted of 85% of the aubrite Y-793592 and 15% orthopyroxene, for an albedo value of 0.47 (Fig. 18, continuous line). This mixture better reproduces the spectral behavior of Rhodia in the infrared range, but does not match the visible data.

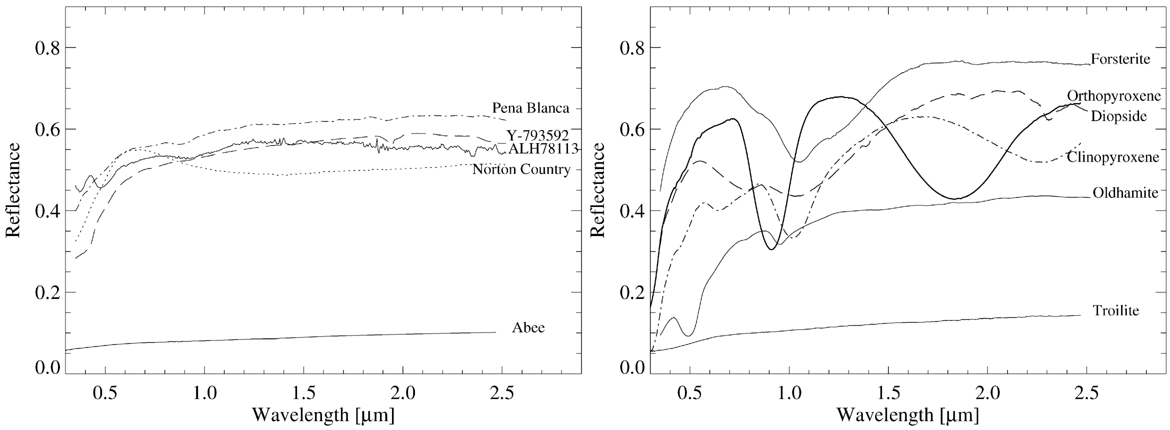

Fig. 17. Spectra of the main endmembers (meteorites and minerals) used in our compositional models of E-type asteroids.

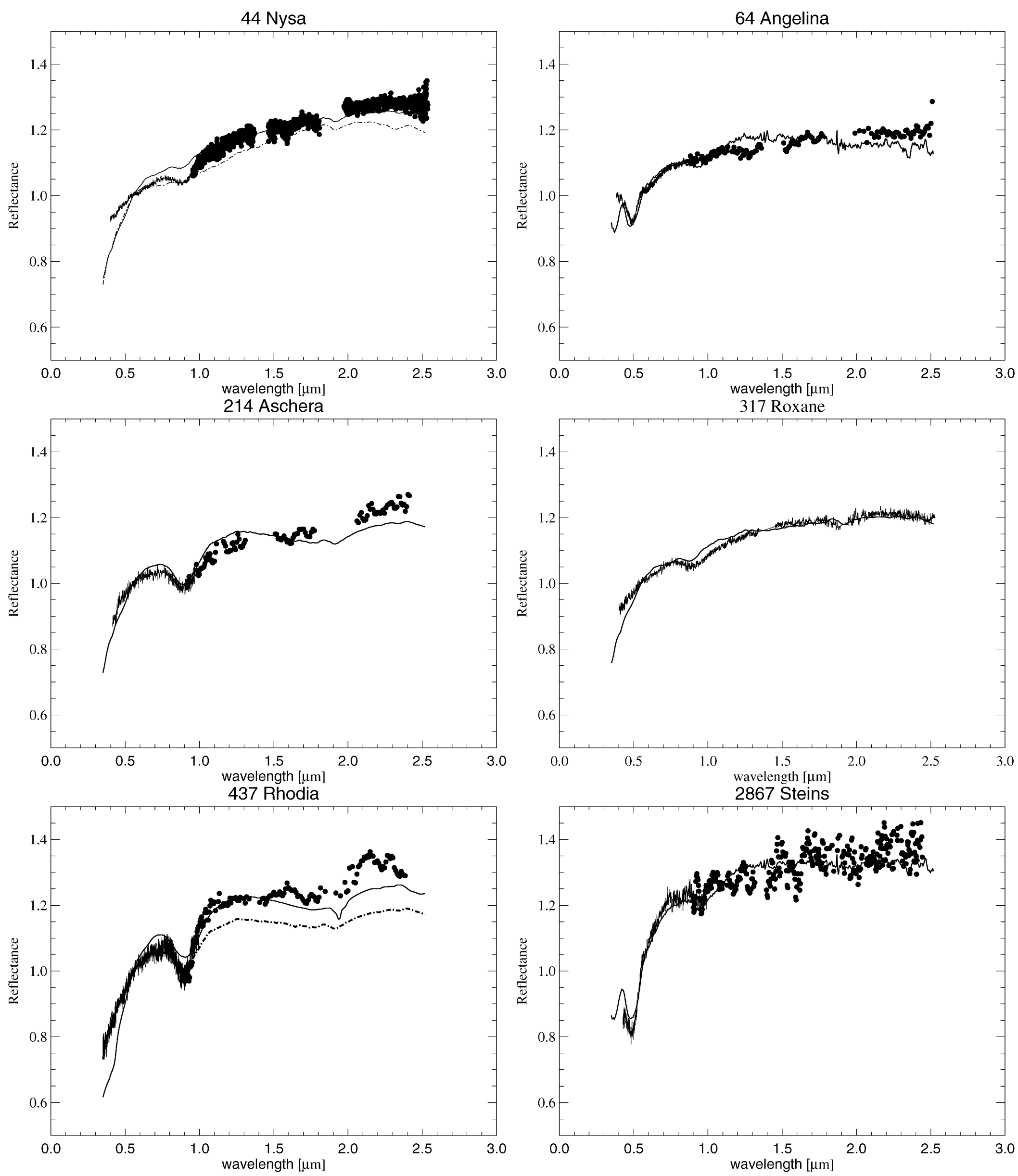

Fig. 18. Compositional mixtures (represented as continuous line) proposed for the asteroids with visible and near infrared spectra. In the case of 317 Roxane, the spectrum of the aubrite Peña Blanca nicely fit the asteroid's spectral behavior.

For *2867 Steins* we considered the visible spectrum presented here together with the near infrared one published by Barucci et al. (2005). The resulting spectrum is quite red and presents a wide band at about 0.5 µm. The best model we find is constituted of 65% of the meteorite ALH78113 and 35% of oldhamite. The model albedo is 0.38, in good agreement with the albedo of Steins (0.34 ± 0.06) derived from radiometric analysis of the IRS–Spitzer data (Barucci et al., 2008), and inside the error bars of the polarimetric albedo (0.45 ± 0.10, (Fornasier et al., 2006)). Our model is in good agreement with one of the models recently published by Nedelcu et al. (2007) given by a geographical mixture of enstatite (57%), oldhamite (42%) and orthopyroxene (1%). At the present time, oldhamite is the only endmember that, added to the ALH78113 meteorite, allow us to fit both the deep 0.5 µm band and the visible red slope of Steins. All the other attempts made with more than 2 endmembers failed to satisfactory fit the Steins spectral behavior, and in any case a relevant percentage (>18%) of oldhamite was needed to reproduce the 0.5 µm feature.

Such a huge amount of oldhamite on the Steins' surface is quite surprising, due to the fact that the percentage of sulfide oldhamite found in aubrite samples is smaller than 1% (Burbine et al., 2002b). Nevertheless, it is well known that oldhamite is extremely unstable in terrestrial conditions, and we cannot exclude that the abundance of oldhamite in aubrite materials and/or on the surface of the aubrite parent bodies might actually be larger than the one detected in terrestrial laboratory (Clark et al., 2004; Burbine et al., 2002b).

5. Discussion

Considering our observations and those available in literature, the known E-type population can be divided as follows:

- 5 E[I] members (504, 1025, 2449, 6435, and 144898);
- 8 E[II] members (64, 434, 2048, 2035, 2867, 3103, 4660 and 6911), but the faint absorption bands on 2048 and 6911 need to be confirmed by independent observations;
- 8 E[III] members (44, 214, 317, 437, 620, 1103, 1251 and 3050), but the faint absorption band at 0.9 µm on 620 Drakonia needs to be confirmed.

Looking into the list of the known or suggested E-type asteroids presented by Clark et al. (2004), 3 of the listed asteroids (2577, 5806 and 7579) have spectral behaviors different from the E-type objects and should not be considered E-class members. On the other side, 437 Rhodia, 2867 Steins and 144898 2004 VD17 have high albedo values and spectra consistent with the E-type classification and should be added to the list (Barucci et al., 2005; Fornasier et al., 2006; De Luise et al., 2007). Also 3050 Carrera, on the basis of its spectral behavior (but the albedo is not known) probably belongs to the E-type (Barucci et al., 2005).

In Fig. 19 we plot the spectral slope value $S2$ evaluated in the 5500–8000 Å wavelength range versus the semimajor axis and inclination for the E-type members investigated in this paper and those whose spectra are available in literature. The three different sub-group members are represented with different symbols: E[I] in triangles, E[II] in circles, and E[III] in squares. The points are expanded with size proportional to the diameter of each target (see Table 2). The E[III] members are situated mostly between 2.2 and 2.7 AU, with only 1 member populating the Hungaria region. They have the lower mean $S2$ spectral slope value (2.43 ± 1.12) and all, except 1103 Sequoia, have inclinations lower than 8 degrees. The E[I] members have a mean S3 slope of 4.59 ± 1.32; 3 are located in the Hungaria family, one is a NEO and the biggest member has the largest semimajor axis (2.72 AU) inside the E-type class. The E[II] members have the largest mean $S2$ slope value (5.44 ± 1.45). Four members populated the Hungaria regions, 2 are NEOs, and 2 are main belt members (2867 Steins, the Rosetta target, and 64 Angelina, the largest member). The spectral similarity of 2867 Steins and the NEO 3103 Eger was reported in Fornasier et al. (2007), who explore the possibility that the two objects are both remnants of an old asteroid family, the outcome of the breakup of a parent body at about 2.36 AU. Despite their presently different orbits, numerical orbital integrations show that there is a dynamical pathway between the present orbit of Steins, possibly the largest remnant of the family, and Earth-crossing orbits like that of Eger. Members of the putative Steins family might be driven by the Yarkovsky force and gravitational influence of the planets into the 3:1 and 7:2 mean motion resonances with Jupiter and finally be injected in the Earth-crossing region.

6. Summary

We present the results of a survey on igneous E-type asteroids started on 2004 at the TNG and NTT telescopes. We got new visible spectra of 18 asteroids, and 8 of them were observed also in the near infrared range. We confirm that the small E-type population shows 3 different mineralogies and we classified the observed objects in the 3 subgroups following the Gaffey and Kelley (2004) classification scheme.

Few objects (i.e. 64 Angelina, 317 Roxane and 434 Hungaria) present different spectral behaviors in our data and those coming from literature, and we suggest that they may have an inhomogeneous surface composition. For these asteroids, additional observation covering the whole rotational period are needed to fully investigate their surface composition.

We investigated the spectral slope distribution for the three E-subgroups members versus the asteroids' semimajor axis and inclination. We also include in our sample the spectra of 6 E-type available in literature and not observed in this work, for a total sample of 21 E-type asteroids.

E[III] subgroup members have the lowest mean spectral slope value inside the whole sample. Within the E-type population, they are the more distant from the Sun, being located mainly between 2.2–2.7 AU in low inclination orbit. E[II] members has the highest spectral slope inside the sample. Both E[II] and E[I] members are mainly located in the Hungaria region, but some members are present both in the NEA population and in the main belt.

Finally, for the five E-type asteroids observed both in the visible and near infrared range, plus 2867 Steins, a target of

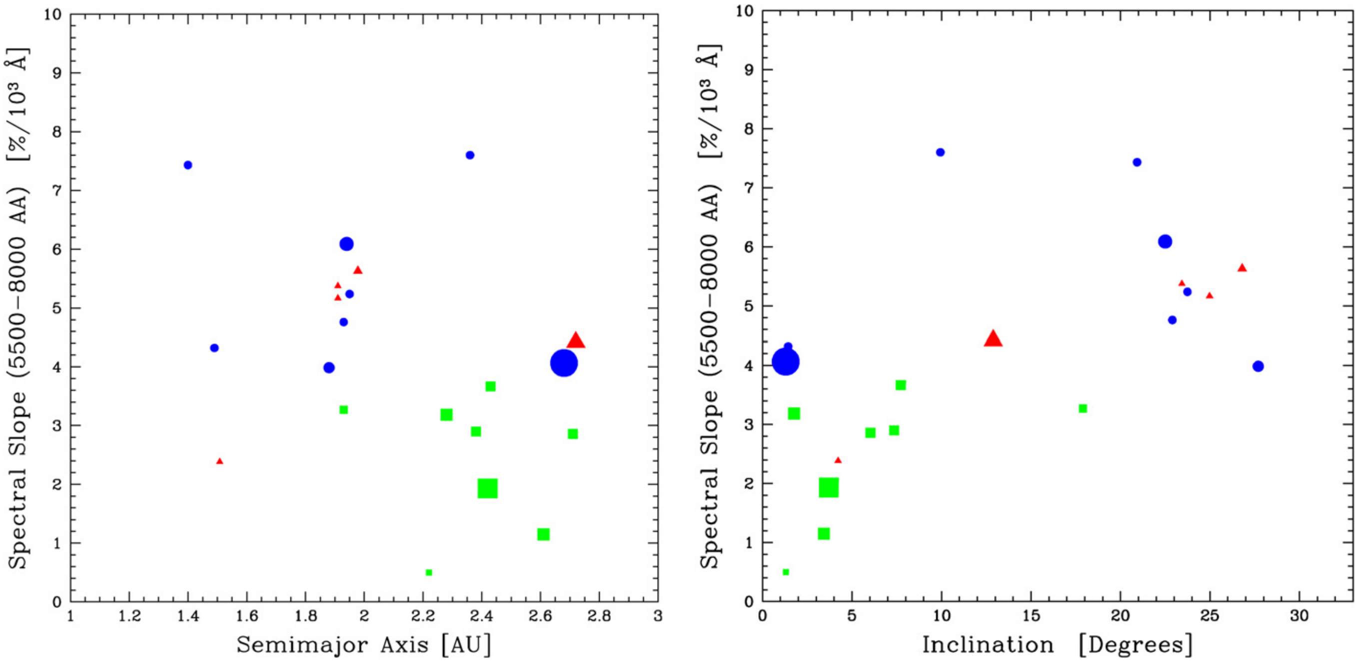

Fig. 19. Spectral slope value ($S3$) versus the semimajor axis (left) and the orbital inclination (right). E[I] subgroup members are displayed with triangles, E[II] with circles, and E[III] with squares. The size is proportional to the asteroids' diameter.

the Rosetta mission, we attempt to model their surface composition using geographical mixtures of aubrite meteorites and minerals. The spectrum of the E[III]-type asteroid 317 Roxane is nicely matched by the aubrite Peña Blanca, that has also a similar high albedo value. We then suggest that this aubrite might have 317 Roxane as a possible parent body. The compositional model that better fit the E[III] type 214 Aschera is mainly composed of aubrite Peña Blanca enriched with orthopyroxene. Also the spectrum and albedo of the E[II]-type 64 Angelina and 2867 Steins might be reproduced by an aubrite, ALH78113, but it must be enriched with a considerably amount of oldhamite. On the other hand, the compositional models proposed for the E[III]-type asteroids 44 Nysa and 437 Rhodia do not match their whole spectral behavior and albedo values.

The results of the spectral modeling show that two different aubrites match the albedo and the V + NIR spectral behavior of two different E-type asteroids. The aubrite Peña Blanca nicely matches the spectrum and albedo of 317 Roxane, that could be its parent body, and, enriched with orthopyroxene, that of 214 Aschera, so it is related to the E[III] subgroup asteroids. The aubrite ALH78113, the only one surveyed to now showing the ~0.5 μm band, is clearly related to the E[II] subgroup, but it must be enriched in oldhamite to give rise to the strong 0.5 μm band seen in the Angelina and Steins spectra.

Acknowledgments

The authors thank F. DeMeo for her help in the language revision. This research utilizes spectra acquired with the NASA RELAB facility at Brown University by: McCoy and Burbine; Cloutis; Hiroi; Hiroi, Zolensky and Lipschults; McFadden; Pieters and Britt; Pieters and Crown; Pieters and Sunshine. This work has been partly supported by an Europlanet personnel exchange grant.

References

Barucci, M.A., Fulchignoni, M., Fornasier, S., Dotto, E., Vernazza, P., Birlan, M., Binzel, R.P., Carvano, J., Merlin, F., Barbieri, C., Belskaya, I., 2005. Asteroid target selection for the new Rosetta mission baseline: 21 Lutetia and 2867 Steins. Astron. Astrophys. 430, 313–317.

Barucci, M.A., Fornasier, S., Dotto, E., Lamy, P., Jorda, L., Groussin, O., Brucato, J.R., Carvano, J., Alvarez-Candal, A., Cruikshank, D., Fulchignoni, M., 2008. Asteroids 2867 Steins and 21 Lutetia: Surface composition from far infrared observations with the Spitzer space telescope. Astron. Astrophys. 477, 665–670.

Binzel, R.P., Birlan, M., Bus, S.J., Harris, A.W., Rivkin, A.S., Fornasier, S., 2004. Spectral observations for near-Earth objects including potential target 4660 Nereus: Results from Meudon remote observations at the NASA Infrared Telescope Facility (IRTF). Planet. Space Sci. 52, 291–296.

Burbine, T.H., Binzel, R.P., 2002. Small Main Belt Asteroid Spectroscopic Survey in the near infrared. Icarus 159, 468–499.

Burbine, T.H., Cloutis, E.A., Bus, S.J., Meibom, A., Binzel, R.P., 1998. The detection of troilite (FeS) on the surfaces of E-class asteroids. Bull. Am. Astron. Soc. 30, 711.

Burbine, T.H., McCoy, T.J., Meibom, A., 2002a. Meteorite parent bodies. In: Bottke, W.F., Cellini, A., Paolicchi, P., Binzel, R.P. (Eds.), Asteroids III. Univ. of Arizona Press, Tucson.

Burbine, T.H., McCoy, T.J., Nittler, L., Benedix, G., Cloutis, E., Dickenson, T., 2002b. Spectra of extremely reduced assemblages: Implications for Mercury. Meteorit. Planet. Sci. 37, 1233–1244.

Bus, S.J., Binzel, R.P., 2002. Phase II of the Small Main-Belt Asteroid Spectroscopic Survey: The observations. Icarus 158, 106–145.

Busarev, V.V., 1998. Spectral features of M-asteroids: 75 Eurydike and 201 Penelope. Icarus 131, 32–40.

Busarev, V.V., 2002. Hydrated silicates on M-, S-, and E-type asteroids as possible traces of collisions with bodies from the Jupiter growth zone. Solar System Res. 36, 35–42.

Clark, B.E., Bus, S.J., Rivkin, A.S., McConnochie, T., Sander, J., Shah, S., Hiroi, T., Shepard, M., 2004. E-type asteroid spectroscopy and compositional modeling. J. Geophys. Res. 109, doi:10.1029/2003JE002200. E02001.

Delbó, M., Harris, A.W., Binzel, R.P., Pravec, P., Davies, J.K., 2003. Keck observations of near-Earth asteroids in the thermal infrared. Icarus 166, 116–130.

De Luise, F., Perna, D., Dotto, E., Fornasier, S., Belskaya, I., Boattini, A., Valsecchi, G.B., Milani, A., Rossi, A., Lazzarin, M., Paolicchi, P., Flchignoni, M., 2007. Physical investigation of the potentially hazardous Asteroid (144898) 2004 VD17. Icarus 191, 628–635.

Dotto, E., Fornasier, S., Barucci, M.A., Licandro, J., Boehnhardt, H., Hainaut, O., Marzari, F., de Bergh, C., de Luise, F., 2006. The surface composition of Jupiter Trojans: Visible and near-infrared survey of dynamical families. Icarus 183, 420–434.

Fornasier, S., Lazzarin, M., 2001. E-type asteroids: Spectroscopic investigation on the 0.5 μm absorption band. Icarus 152, 127–133.

Fornasier, S., Dotto, E., Marzari, F., Barucci, M.A., Boehnhardt, H., Hainaut, O., de Bergh, C., 2004a. Visible spectroscopic and photometric survey of L5 Trojans: Investigation of dynamical families. Icarus 172, 221–232.

Fornasier, S., Dotto, E., Barucci, M.A., Barbieri, C., 2004b. Water ice on the surface of the large TNO 2004 DW. Astron. Astrophys. 422, L43–L46.

Fornasier, S., Belskaya, I., Fulchignoni, M., Barucci, M.A., Barbieri, C., 2006. First albedo determination of 2867 Steins, target of the Rosetta mission. Astron. Astrophys. 449, L9–L12.

Fornasier, S., Marzari, F., Dotto, E., Barucci, M.A., Migliorini, A., 2007. Are the E-type Asteroids (2867) Steins, a target of the Rosetta mission, and NEA (3103) Eger remnants of an old asteroid family? Astron. Astrophys. 474, 29–32.

Gaffey, M.J., Kelley, M.S., 2004. Mineralogical variation among high albedo E-type asteroids: Implications for asteroid igneous processes. Lunar Planet. Sci. XXXV. Abstract 1812.

Gaffey, M.J., Bell, J.F., Cruikshank, D.P., 1989. Reflectance spectroscopy and asteroids surface mineralogy. In: Binzel, R.P., Gehrels, T., Matthews, M.S. (Eds.), Asteroids II. Univ. of Arizona Press, Tucson, pp. 98–127.

Gaffey, M.J., Reed, K.L., Kelley, M.S., 1992. Relationship of E-type Apollo Asteroids 3103 (1982 BB) to the enstatite achondrite meteorites and Hungaria asteroids. Icarus 100, 95–109.

Gaffey, M.J., Burbine, T.H., Piatek, J.L., Reed, K.L., Chaky, D.A., Bell, J.F., Brown, R.H., 1993. Mineralogical variations within the S-type asteroids class. Icarus 106, 573–602.

Gil-Hutton, R., Benavidez, P., 2001. Polarimetric albedo of Hungarian asteroids: Preliminary results. Paper presented at the International Conference Asteroids 2001, Osserv. Astron. di Palermo, Palermo, Italy, 11–16 June.

Harris, A.W., Mueller, M., Delb, M., Bus, S.J., 2007. Physical characterization of the potentially hazardous high-albedo Asteroid (33342) 1998 WT24 from thermal-infrared. Icarus 188, 414–424.

Keil, K., Fredriksson, K., 1963. Electron microprobe analysis of some rare minerals in the Norton County achondrite. Geochim. Cosmochim. 27, 939–942.

Keil, K., Ntaflos, Th., Taylor, G.J., Brearley, A.J., Newsom, H.E., 1989. The Shallowater aubrite—Evidence for origin by planetesimal impacts. Geochim. Cosmochim. 53, 3291–3307.

Kelley, M.S., Gaffey, M.J., 2002. High-albedo Asteroid 434 Hungaria: Spectrum, composition and genetic connections. Meteorit. Planet. Sci. 37, 1815–1827.

King, T.V.V., Clark, R.N., 1989. Spectral characteristics of chlorites and Mg-serpentines using high resolution reflectance spectroscopy. J. Geophys. Res. 94, 13997–14008.

Kuppers, M., Mottola, S., Lowry, S.C., A'Hearn, M.F., Barbieri, C., Barucci, M.A., Fornasier, S., Groussin, O., Gutirrez, P., Hviid, S.F., Keller, H.U., Lamy, P., 2007. Determination of the light curve of the Rosetta target Asteroid (2867) Steins by the OSIRIS cameras onboard Rosetta. Astron. Astrophys. 462, 13–16.

Lamy, P., Jorda, L., Fornasier, S., Groussin, O., Barucci, M.A., Carvano, J., Dotto, E., Fulchignoni, M., Toth, I., 2008. Asteroid Steins. III. Spitzer space telescope observations, size determination and thermal properties. Astron. Astrophys., in press.

McCoy, T.J., Dickinson, T.L., Lofgren, G.E., 1999. Partial melting of the Indarch (EH4) Meteorite: A textural, chemical and phase relations view of melting and melt migration. Meteorit. Planet. Sci. 34, 735–746.

Nedelcu, D.A., Birlan, M., Vernazza, P., Binzel, R.P., Fulchignoni, M., Barucci, M.A., 2007. E-type Asteroid (2867) Steins: Flyby target for Rosetta. Astron. Astrophys. 473, 33–36.

Okada, A., Keil, K., 1982. Caswellsilverite, $NaCrS_2$: A new mineral in the Norton County enstatite achondrite. Am. Mineral. 67, 132–136.

Olsen, E.J., Bunch, T.E., Jarosewich, E., Noonan, A.F., Huss, G.I., 1977. Happy Canyon—A new type of enstatite achondrite. Meteoritics 12, 109–123.

Reid, A.M., Cohen, A.J., 1967. Some characteristics of enstatite from enstatite achondrites. Geochim. Cosmochim. 31, 661–670.

Rivkin, A.S., Howell, E.S., Britt, D.T., Lebofsky, L.A., Nolan, M.C., Branston, D.D., 1995. 3-μm spectrophotometric survey of M and E class asteroids. Icarus 117, 90–100.

Sawyer, S.R., 1991. A high resolution CCD spectroscopic survey of low albedo main belt asteroids. Ph.D. thesis, University of Texas, Austin, TX, USA.

Tedesco, J.G., Williams, D.L., Matson, J.C., Gradie, Lebofsky, L.A., 1989. Three-parameter asteroid taxonomic classifications. In: Binzel, R.P., Gehrels, T., Matthews, M.S. (Eds.), Asteroids II. Univ. of Arizona Press, Tucson, pp. 1151–1161.

Tedesco, J.G., Noah, P.V., Noah, M., Price, S.D., 2002. The Supplemental IRAS Minor Planet Survey. Astron. J. 123, 1056–1085.

Tholen, D.J., 1989. Asteroids taxonomy. In: Binzel, R.P., Gehrels, T., Matthews, M.S. (Eds.), Asteroids II. Univ. of Arizona Press, Tucson, pp. 1139–1153.

Vilas, F., Hatch, E.C., Larson, S.M., Sawyer, S.R., Gaffey, M.J., 1993. Ferric iron in primitive asteroids: a 0.43 μm absorption feature. Icarus 102, 225–231.

Watters, T.P., Prinz, M., 1979. Aubrites: Their origin and relationship to enstatite chondrites. Proc. Lunar Sci. Conf. 10, 1073–1093.

Watters, T.P., Prinz, M., Rambaldi, E.R., Wasson, J.T., 1980. ALHA 78113, Mt. Egerton and the aubrite parent body. Meteoritics 15, 386.

Zellner, B., Leake, M., Williams, J.G., Morrison, D., 1977. The E asteroids and the origin of the enstatite achondrites. Geochim. Cosmochim. Acta 41, 1759–1767.

2.6 Les astéroïdes de type M

Nous avons mené une campagne observationnelle sur 30 astéroïdes de type M. Ces astéroïdes ont un albédo compris entre 0,1 et 0,3 et on croyait que leur composition de surface était purement métallique et semblable aux météorites de fer. Plusieurs résultats récents en spectroscopie, polarimétrie et radar montrent que les astéroïdes de type M n'ont pas tous une composition totalement métallique (Shepard et al. 2008, Rivkin et al. 2000, Lupisko & Belskaya, 1989). Les études spectroscopiques ont montré la présence de bandes dans la région visible (par exemple une bande d'absorption à 0,9 μm due à l'orthopyroxène) ou dans l'infrarouge (à 3 μm typiquement associée aux silicates hydratés). Ceci indique que la composition des astéroïdes de type M n'est pas exclusivement métallique, et aussi que les corps parents d'une partie des astéroïdes de la classe M n'ont pas tous approché des températures très élevées ($>$ 1500 K) comme cela était supposé auparavant. Peu d'astéroïdes de type M ont un albédo radar compatible avec une composition dominée par des métaux (Shepard et al. 2010).
Nos observations montrent une large variété spectrale des objets observés. Des bandes d'absorption ont été détectées, en particulier 13 astéroïdes montrent une faible bande d'absorption (profondeur entre 1-5% par rapport au continuum) centrée à 0,9 μm due à l'orthopyroxène pauvre en fer et en calcium. Nous avons découvert pour la première fois sur les spectres des astéroïdes de type M la présence d'une faible bande à 0,43 μm. Six astéroïdes (16 Psyche, 22 Kalliope, 69 Hesperia, 216 Kleopatra, 338 Budrosa, and 498 Tokio) ont cette bande d'absorption, que nous avons associé à la présence de chlorites et de serpentines riches en magnésium, ou de pigeonite. 132 Aertha montre une bande d'absorption à 0,49 μm similaire à celle observée sur les astéroïdes E [II] et due à l'oldhamite. L'astéroïde 755 Quintilla montre des bandes d'absorption à 0,9 et 1,9 μm, dues aux silicates, mais aussi à 1,37 et 1,61 μm, d'origine encore incertaine.
En comparant les spectres observés avec ceux déjà publiés, nous trouvons qu'au moins 4 astéroïdes (129, 325, 478, 785) peuvent avoir une composition de surface hétérogène.

Les spectres des astéroïdes ont été comparés avec ceux de différentes météorites afin de contraindre leur composition de surface. Nous confirmons que les astéroïdes de type M sont associés aux météorites ferreuses, aux pallasites et aux chondrites à enstatite (Fornasier et al. 2010 ; Ockert-Bell et al. 2010).

2.7 Les astéroïdes de type X

Sont classifiés comme de type X des astéroïdes qui ont des spectres très semblables mais qui peuvent avoir des compositions très différentes. Le groupe X comprend les types E, M et P, c'est-à-dire des astéroïdes ignés à enstatite (E), métalliques (M), et les plus primordiaux riches en composés carbonés/organiques (P), et pour lesquels on ne disposait pas de la valeur d'albédo (nécessaire pour faire la distinction entre type E, M ou P) à l'époque de leur classification (Tholen 1989).
J'ai mené des campagnes d'observations sur 25 astéroïdes de type X. Les données spectroscopiques obtenues, combinées avec des mesures d'albédo récentes, nous ont permis de contraindre leur composition de surface, d'investiguer les liens possibles avec les météorites et de fournir une nouvelle classification pour les objets observés. Dans notre échantillon nous avons 10 astéroïdes avec des spectres semblables à ceux de type M, donc probablement de composition métallique, interprétation renforcée par la similitude spectrale à des météorites de fer ou à des pallasites. Douze des astéroïdes observés montrent par contre une composition beaucoup plus primitive, correspondant aux classes C (6), P (5) ou D (1), et montrant une similitude spectrale avec des météorites carbonées CM, inaltérées ou altérées par irradiation laser ou thermique, ce qui

donne des contraintes sur les conditions de température et d'irradiation de ces objets. Plusieurs astéroïdes montrent de faibles bandes d'absorption, en particulier une bande à 0,9 μm due à l'orthopyroxène, mais aussi des bandes à 0,43, 0,49, 0,51 μm, d'interprétation plus complexe (Fornasier et al. 2011a).

2.8 Observations à partir de la Terre et de l'espace des astéroïdes 2867 Steins et 21 Lutétia, cibles de la mission Rosetta

J'ai dédié une partie de ma recherche à la caractérisation des propriétés physiques des astéroïdes cibles de la missions Rosetta. La connaissance des propriétés physiques comme la forme, l'orientation du pôle, la période de rotation, l'albédo, la composition de surface etc. est très importante pour préparer au mieux les rencontres et les observations des astéroïdes avec Rosetta. Cette activité a été particulièrement frénétique et intense suite au changement de la date de lancement de Rosetta, reportée d'un an, et j'ai participé à plusieurs campagnes observationnelles qui ont permis de caractériser les propriétés de surface de 21 Lutétia et 2867 Steins, cibles de la mission choisies juste après le lancement de Rosetta.

2.8.1 2867 Steins

Steins est un petit astéroïde de la ceinture principale, et son étude n'a commencé que début 2004, quand il a été inclus dans la liste des cibles possibles de Rosetta. Steins a été choisi comme cible seulement après le lancement de la mission, quand on a vérifié la disponibilité d'énergie en terme de Δ_v de la sonde. Le premier spectre dans le visible et proche infrarouge (0,5-2,4 μm) de cet objet montrait une ressemblance avec les spectres des astéroïdes de type E, qui sont très rares dans la ceinture principale (Barucci et al. 2005a). Ces types d'astéroïdes ont une valeur d'albédo très élevée. La connaissance de l'albédo était donc une information nécessaire pour la classification définitive de l'astéroïde, pour la compréhension de sa composition de surface et pour déterminer le diamètre réel de l'objet. La taille et l'albédo étaient donc des informations importantes pour la planification du fly-by de Rosetta, pour la préparation des séquences observationnelles et pour le choix du temps de pose avec les différents instruments à bord de la sonde. On peut déterminer l'albédo d'un astéroïde avec 2 méthodes : la polarimétrie et la radiométrie. J'ai donc mené une campagne observationnelle en polarimétrie au télescope VLT-ESO pour étudier la polarisation de l'astéroïde aux différents angles de phase. Des observations en polarimétrie avec les filtres R et V ont été obtenues pour six angles de phase différents compris entre 28 et 10 degrés. Cette étude a montré une faible polarisation de Steins, des paramètres de polarisation (pente, minimum de polarisation, angle d'inversion de la courbe) similaires à ceux des astéroïdes de type E et une valeur élevée d'albédo (0,45$\pm$0,10, Fornasier et al. 2006a) typique des astéroïdes E, et totalement en accord avec la valeur déterminée par la suite par Rosetta pendant le survol (0,40$\pm$0,01, Keller et al. 2010). A noter, la valeur d'incertitude relativement grande sur l'estimation de l'albédo par la polarimétrie est liée aux incertitudes dans la relation empirique entre la pente de polarisation et l'albédo. Cette relation était calibrée, pour les astéroïdes de type E, utilisant seulement deux astéroïdes (44 Nysa et 64 Angelina).

La deuxième méthode qui permet de déterminer l'albédo est la radiométrie, qui utilise le fait que le flux thermique émis par un astéroïde doit être égal à l'énergie solaire absorbée. Pour un astéroïde à une distance héliocentrique donnée, la quantité d'énergie absorbée dépend de la taille de l'astéroïde et de son albédo. En mesurant le flux réfléchi dans le visible et le flux thermique émis, on peut déduire la taille et l'albédo d'un astéroïde.

J'ai participé à la préparation d'une demande d'observation pour l'étude des propriétés radiométriques de Steins et Lutétia avec le télescope de la NASA SPITZER, et à l'analyse et interprétation des données. Les cibles de Rosetta ont été observées avec l'instrument IRS dans le domaine 5-38 μms, ce qui a permis non seulement de déterminer l'albédo (0,34±0,06 pour Steins, Lamy et al. 2008a), mais également d'en étudier l'émissivité. Les spectres d'émissivité permettent de rechercher les signatures en absorption (Rehstraler) ou en émission (pic de Christiansen) qui peuvent contraindre la composition chimique des astéroïdes en les comparant avec des spectres de minéraux et de météorites obtenus en laboratoire.
Le spectre d'émissivité de Steins entre 5 et 38 μm mesuré par Spitzer est également conforme à celui des aubrites et de l'enstatite (Barucci et al. 2008a), et confirme le classement E.

Les observations spectrales dans le domaine visible et proche infrarouge ont montré que Steins est un astéroïde de type E qui présente une bande très particulière à 0,49 μm caractéristique de l'oldhamite, un minéral de sulfure de calcium qui n'est présent que dans des assemblages résultant d'un processus chimique de réduction très fort, tels que les aubrites. Steins en particulier appartient au type E[II] et la similitude entre les spectres pris à différentes phases rotationnelles montre que l'astéroïde a une composition de surface très homogène (Dotto et al. 2009).
Nous avons aussi remarqué une frappante similitude spectrale entre Steins et le géocroiseur 3103 Eger (Fornasier et al. 2007a). Sur la base de cela, nous avons effectué des simulations dynamiques afin de voir si ces deux objets pouvaient être liés. Nos résultats ont montré qu'en effet Steins et Eger peuvent être des membres d'une même famille dynamique et provenir du même corps parent.

Enfin, j'ai aussi participé à des campagnes pour déterminer les propriétés rotationnelles et la forme de Steins. Les courbes de lumière donnent un modèle de forme de l'astéroïde (Jorda et al. 2008 ; Lamy et al. 2008b, Dotto et al. 2009), la période synodique de rotation Psyn = 6,04681±0,00002, et une limite inférieure au rapport des axes a/b > 1,20±0,02.

2.8.2 Article : First albedo determination of 2867 Steins, target of the Rosetta mission

A&A 449, L9–L12 (2006)
DOI: 10.1051/0004-6361:20064913

Astronomy & Astrophysics

First albedo determination of 2867 Steins, target of the Rosetta mission*

S. Fornasier[1], I. Belskaya[2], M. Fulchignoni[3], M. A. Barucci[3], and C. Barbieri[1]

[1] Astronomy Department and CISAS, Padova University, Italy
e-mail: fornasier@pd.astro.it
[2] Institute of Astronomy of Kharkiv National University, Ukraine
[3] Paris Observatory, France

Received 25 January 2006 / Accepted 9 February 2006

ABSTRACT

Aims. We present the first albedo determination of 2867 Steins, the asteroid target of the Rosetta space mission together with 21 Lutetia.
Methods. The data were obtained in polarimetric mode at the ESO-VLT telescope with the FORS1 instrument in the V and R filters. Observations were carried out from June to August 2005 covering the phase angle range from 10.3° to 28.3°, allowing the determination of the asteroid albedo by the well known experimental relationship between the albedo and the slope of the polarimetric curve at the inversion angle.
Results. The measured polarization values of Steins are small, confirming an E-type classification for this asteroid, as already suggested from its spectral properties. The inversion angle of the polarization curve in the V and R filters is respectively of 17.3 ± 1.5° and 18.4 ± 1.0°, and the corresponding slope parameter is of 0.037 ± 0.003%/deg and 0.032 ± 0.003%/deg. On the basis of its polarimetric slope value, we have derived an albedo of 0.45 ± 0.1, that gives an estimated diameter of 4.6 km, assuming an absolute V magnitude of 13.18 mag.

Key words. minor planets, asteroids – techniques: polarimetric

1. Introduction

Rosetta is the ESA cornerstone mission devoted to the study of minor bodies. Successfully launched on March 2, 2004, Rosetta, in its journey to the comet 67P Churyumov-Gerasimenko, will fly by two main belt asteroids, 2867 Steins on September 2008 and 21 Lutetia on July 2010.

All the targets have been changed with respect to the original mission plans due to the Rosetta launch postponement of about one year. Several observational campaigns have been promoted to increase knowledge of the physical properties of these new targets.

While 21 Lutetia is a large main belt asteroid with a long history of investigation, 2867 Steins has been observed in detail only from 2004, and its physical properties are still not completely known.

The first Steins lightcurve was reported by Hicks & Bauer (2004), who found a rotational period of 6.06 ± 0.05 h and an amplitude of approximately 0.2 mag, values confirmed by Weissman et al. (2005).

The spectroscopic investigation in the visible and near infrared range presented by Barucci et al. (2005) show a strong feature at 0.5 μm, a weaker feature at 0.96 μm and a flat and featureless behavior above 1 μm. This spectral behavior is very similar to that of the E-type objects (Fornasier & Lazzarin 2001; Burbine et al. 1998), and in particular to that of the E subtype II (Angelina like) following Clark et al. (2004) and Gaffey & Kelley (2004) classification scheme. Nevertheless, as E type objects are characterized by the highest albedo values found in the asteroid population, knowledge of Steins' albedo is needed for a definitive taxonomic classification and a proper understanding of its surface properties and size determination.

In this paper, we present the first polarimetric investigation of 2867 Steins and discuss its albedo and size evaluation based on polarimetric properties. This information will aid the Rosetta mission in planning science operations and optimizing the flyby trajectory.

2. Data acquisition and reduction

Observations of 2867 Steins were carried out in service mode at the VLT telescope UT2 KUEYEN with the FORS1 instrument in polarimetric mode (see http://www.eso.org/instruments/fors1) from June to August 2005. Linear polarimetry was obtained in the two broadband filters R and V at 4 angles of the $\lambda/2$ retarder plate (0°, 22.5°, 45° and 67.5° with respect to celestial coordinate system), covering the phase angle range from 10.3° to 28.3°.

* Based on observations carried out at European Southern Observatory (ESO), Paranal, Chile, Prog. 075.C-0201(A).

Table 1. Observational conditions for 2867 Steins. The exposure time (exp) is the same for each of the four images obtained at the four different $\lambda/2$ retarder plate positions, while nset represents the number of repetitions of the full polarimetric sequences. Data on the position angle of the scattering plane (ϕ), on the phase angle (α), on the heliocentric (r) and geocentric (Δ) distances of Steins have been taken from the JPL ephemeris service (`http://ssd.jpl.nasa.gov/cgi-bin/eph`).

DATE	UT	Fil.	exp (s)	nset	m_v	airm	ϕ (°)	α (°)	r (AU)	Δ (AU)	seeing (″)
11 Jun. 05	08:50	R	33	3	16.45	1.05	252.6	28.3	2.0201	1.4315	1.45
11 Jun. 05	09:08	V	35	3	16.45	1.02	252.6	28.3	2.0201	1.4315	1.35
01 Jul. 05	09:23	R	26	3	16.06	1.02	258.2	24.3	2.0197	1.2563	0.55
01 Jul. 05	09:40	V	26	3	16.06	1.03	258.2	24.3	2.0197	1.2563	0.54
14 Jul. 05	05:43	R	15	3	15.78	1.17	265.0	20.6	2.0217	1.1653	0.80
14 Jul. 05	05:58	V	15	4	15.78	1.12	265.0	20.6	2.0217	1.1653	0.99
06 Aug. 05	04:16	R	15	3	15.31	1.13	294.1	12.3	2.0295	1.0654	0.60
06 Aug. 05	04:31	V	15	4	15.31	1.10	294.2	12.3	2.0295	1.0654	0.55
09 Aug. 05	07:56	R	10	4	15.26	1.09	301.7	11.3	2.0310	1.0594	0.74
09 Aug. 05	08:14	V	10	4	15.26	1.12	301.7	11.3	2.0310	1.0594	0.71
13 Aug. 05	07:49	R	10	4	15.22	1.10	313.2	10.3	2.0330	1.0547	2.10
13 Aug. 05	08:16	V	10	4	15.22	1.16	313.2	10.3	2.0330	1.0547	1.94

The procedure during each observing run included the acquisition of several flat field images, taken during twilight time without polarimetric optics in the light path, and of at least one unpolarized standard star to calibrate the instrumental polarization. The zero points of the position angles both for V and R images were taken from the FORS1 user manual (`http://www.eso.org/instruments/fors/doc`).

The asteroid and standard star images have been corrected for bias and master flat, and the cosmic rays removed. The center of the asteroid image in each of the two channels is evaluated by a 2 dimensional centroid algorithm. The flux for each channel is integrated over a radius corresponding to 3−4 times the average seeing, and the sky is subtracted using a 3−5 pixel wide annulus around the object.

The Stokes parameters are derived in the following manner:

$$Q = 0.5\left[\left(\frac{f^{\rm o}-f^{\rm e}}{f^{\rm o}+f^{\rm e}}\right)_{\lambda/2\rm pos.=0^{o}} - \left(\frac{f^{\rm o}-f^{\rm e}}{f^{\rm o}+f^{\rm e}}\right)_{\lambda/2\rm pos.=45^{\circ}}\right] \quad (1)$$

and

$$U = 0.5\left[\left(\frac{f^{\rm o}-f^{\rm e}}{f^{\rm o}+f^{\rm e}}\right)_{\lambda/2\rm pos.=22.5^{\circ}} - \left(\frac{f^{\rm o}-f^{\rm e}}{f^{\rm o}+f^{\rm e}}\right)_{\lambda/2\rm pos.=67.5^{\circ}}\right] \quad (2)$$

where $f^{\rm o}$ and $f^{\rm e}$ are the background subtracted object flux of the ordinary and extra-ordinary beam inside each image and $\lambda/2$ pos. indicates the position of the retarder plate.

The degree of polarization P and the position angle θ of the polarization plane in the instrumental reference system are expressed via the parameters Q and U with the well-known formulae

$$P = \sqrt{U^2+Q^2} \qquad \sigma_P = \frac{|U*{\rm d}U + Q*{\rm d}Q|}{P} \quad (3)$$

$$\theta = \frac{1}{2}\arctan\frac{U}{Q} \qquad \sigma_\theta = \frac{28.65*\sigma_P}{P} \quad (4)$$

where dU and dQ are the errors on the Stokes parameters (Shakhovskoy & Efimov 1972).

The position angle of the polarization plane relative to the plane perpendicular to the scattering plane, θ_r, is expressed as $\theta_r = \theta - (\phi \pm 90°)$, where ϕ is the position angle of the scattering plane and the sign inside the bracket is chosen to assure the condition $0° \leq (\phi \pm 90°) \leq 180°$.

The polarization quantity P_r is computed as $P_r = P * \cos(2\theta_r)$.

During each run, Steins observations at the four retarder positions were repeated at least three times (see nset column in Table 1) and the polarization values derived as the median of these multiple exposures.

3. Results

The polarimetric characteristics of 2867 Steins derived from the above observations are reported in Table 2 and visualized in Fig. 1. Our data permit the determination of the inversion angle and of the slope of the polarization phase curve at the inversion angle in the V and R bands. We used the linear fit to the data weighted according to their errors (see Fig. 1). The use of a linear fit is reasonable because of the small curvature of the ascending branch of the asteroid polarization phase dependence (Zellner & Gradie 1976). The obtained parameters are given in Table 3.

For comparison, in Table 3 we also give the mean values of the corresponding parameters for the main asteroid types according to Goidet-Devel et al. (1995). The polarimetric characteristics of Steins correspond to the mean values of E-type asteroids.

Currently, detailed polarimetric observations are available only for two E-type asteroids, 44 Nysa and 64 Angelina. We report in Fig. 2 observations in the V band obtained with an accuracy better than 0.1% together with our data on Steins, showing that all the three asteroids have very similar polarimetric properties. Fitting the data with the linear-exponential function (Fig. 2) proposed by Kaasalainen et al. (2003) gives almost the same polarimetric slope (0.038 ± 0.006%/deg) derived by a linear fit.

As it is well known, accurate measurements of the polarimetric slope are very important for the determination of the asteroid albedo. The empirical correlation of polarimetric slope

Table 2. Results of 2867 Steins polarimetric observations in the *R* and *V* filters.

DATE	Fil.	*P* (%)	θ (°)	P_r (%)	θ_r (°)
11 Jun.	*R*	0.287 ± 0.062	163.9 ± 6.1	+0.287 ± 0.062	1.3 ± 6.1
11 Jun.	*V*	0.369 ± 0.068	171.7 ± 5.2	+0.351 ± 0.062	9.1 ± 5.2
01 Jul.	*R*	0.204 ± 0.052	170.0 ± 5.2	+0.204 ± 0.054	1.8 ± 5.2
01 Jul.	*V*	0.309 ± 0.047	166.5 ± 4.3	+0.309 ± 0.050	–1.7 ± 4.3
14 Jul.	*R*	0.178 ± 0.057	25.6 ± 9.7	+0.086 ± 0.057	30.6 ± 9.7
14 Jul.	*V*	0.146 ± 0.060	11.1 ± 11.7	+0.124 ± 0.060	16.2 ± 11.7
06 Aug.	*R*	0.209 ± 0.048	113.9 ± 6.5	–0.209 ± 0.050	89.8 ± 6.5
06 Aug.	*V*	0.205 ± 0.053	114.5 ± 6.8	–0.204 ± 0.053	90.4 ± 6.8
09 Aug.	*R*	0.213 ± 0.068	122.3 ± 9.1	–0.213 ± 0.068	90.6 ± 9.1
09 Aug.	*V*	0.284 ± 0.080	155.1 ± 10.9	–0.205 ± 0.080	111.9 ± 10.9
13 Aug.	*R*	0.265 ± 0.071	140.7 ± 7.5	–0.256 ± 0.071	97.5 ± 7.5
13 Aug.	*V*	0.239 ± 0.080	135.0 ± 9.5	–0.238 ± 0.080	91.8 ± 9.5

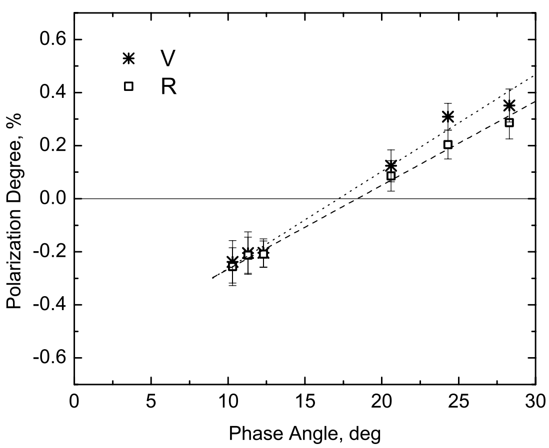

Fig. 1. Polarization degree versus phase angle in the *V* and *R* bands for asteroid 2867 Steins.

Table 3. Polarimetric parameters of 2867 Steins in comparison to mean values for the main asteroid classes (Goidet-Devel et al. 1995).

AST.	slope (%/deg)	inv. angle (°)
2867 Steins	0.037 ± 0.003 (*V*)	17.3 ± 1.5
	0.032 ± 0.003 (*R*)	18.4 ± 1.0
E-type	0.04	17.8
S-type	0.09	20.1
M-type	0.09	23.5
C-type	0.28	20.5

vs. albedo has been successfully used for asteroid albedo determinations e.g. by Zellner & Gradie (1976) and Cellino et al. (1999, 2005). It has the simple form:

$$\log(p_v) = C1 \times \log(h) + C2$$

where p_v is the geometric albedo and $C1$ and $C2$ are empirical constants. The values of these constants are slightly different, depending on the dataset used for their determination. The constants used by Zellner & Gradie (1976) were derived from laboratory data for meteorites and terrestrial samples (Bowell & Zellner 1974). Lupishko & Mohamed (1996) gave new constants based on asteroid data using albedos derived from different sources, including IRAS data, Earth-based radiometric observations and stellar occultation. Cellino et al. (1999) derived

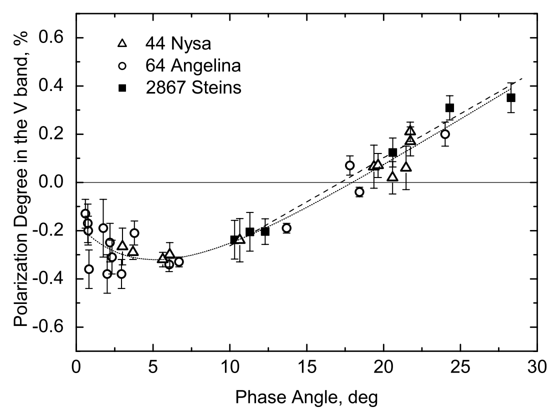

Fig. 2. Polarization–phase dependence of E-type asteroids. Data for 44 Nysa and 64 Angelina are taken from Zellner & Gradie (1976), Cellino et al. (2005), Rosenbush et al. (2005), Fornasier et al. (2006). The continuous line shows the fitting of all data by the linear-exponential function proposed by Kaasalainen et al. (2003); the dashed line shows the linear fit to Steins' data.

the constants from the data set of asteroids with well-measured IRAS albedos.

The differences between the albedos calculated using different constant values are shown in Fig. 3. The main discrepancy arises for high albedo asteroids due to the very few objects for which data are available. The measured polarimetric slope of Steins in the *V* band is very similar to that of 64 Angelina (see Fig. 3).

Unfortunately, Angelina's albedo has not been measured from the IRAS satellite. The usually adopted albedo value of 0.43 was given by Tedesco et al. (1989), with reference to unpublished Earth-based radiometric observations. Later Tedesco et al. (2002) derived a value of 0.40 ± 0.05 from the Midcourse Space Experiment data. At the same time, the IRAS albedo of another E-type asteroid, 44 Nysa, is higher (p_v = 0.55), in spite of the larger polarimetric slope (see Fig. 3). Its polarimetric properties are similar to those of the A-type asteroid 863 Benkoela (Cellino et al. 2005; Fornasier et al. 2006), which has an IRAS albedo of 0.6. However, such high values of IRAS albedos could be an overestimation connected with using non-simultaneous photometric and radiometric data.

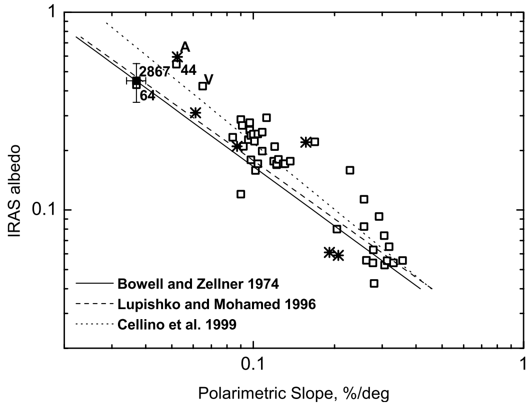

Fig. 3. IRAS albedo versus polarimetric slope. Polarimetric data taken from Lupishko & Mohamed (1996) are marked with open squares and data from Fornasier et al. (2006) with star symbols. Lines represent albedo-slope dependences used by different authors for albedo calculations. High-albedo asteroids are marked by their spectral types (V and A). E-type asteroids are designated by number.

Uncertainty in absolute magnitude is more critical for high albedo asteroids, as shown by Harris & Harris (1997). Thus, to estimate Steins' albedo we prefer using constants derived by Bowell & Zellner (1974) from laboratory data. They give an albedo estimation independent of other techniques.

The albedo of Steins based on its polarimetric slope value is 0.45 ± 0.1 (see Fig. 3), where the error comprises both the uncertainty on the slope and that of constants in the slope-albedo relation. Assuming an absolute visual magnitude V = 13.18 mag (Hicks et al. 2004), its estimated diameter is approximately 4.6 km.

Our observations also show systematic differences in the V and R bands at phase angles larger than the inversion angle (Fig. 1). Both positive polarization degree and polarimetric slope decrease with increasing wavelength, while negative polarization is practically the same in both filters. This behavior reflects the inverse dependence of positive polarization on albedo observed also for S-type asteroids (e.g. Lupishko et al. 1995).

4. Conclusions

Our polarimetric investigation shows that 2867 Steins is a high albedo asteroid ($p_v = 0.45 \pm 0.1$) with an estimated diameter of approximately 4.6 km. The high albedo, together with the peculiar polarimetric properties typical of E-type asteroids, lead to the conclusion that 2867 Steins is an E-type object, as already suggested on the basis of its spectral behavior (Barucci et al. 2005).

Rosetta will be the first space mission to fly by an E-type asteroid, and its results will be very important in the understanding of the physical properties of this peculiar class, whose high albedo members show different spectral behaviors (Clark et al. 2004).

Acknowledgements. This work has been partly supported by the ASI-Rosetta contract to CISAS (University of Padova) and by an Europlanet personnel exchange grant.

References

Barucci, M. A., Fulchignoni, M., Fornasier, S., et al. 2005, A&A, 430, 313
Bowell, E., & Zellner, B. 1974, in Planets, stars, and nebulae studied with photopolarimetry, ed. T. Gehrels (Tuscon: Univ. Arizona Press), 381
Clark, B. E., Bus, S. J., Rivkin, A. S., et al. 2004, J. Geophys. Res., 109, 2001
Cellino, A., Hutton, R. G., Tedesco, E. F., di Martino, M., & Brunini, A. 1999, Icarus, 138, 129
Cellino, A., Hutton, R. G., di Martino, M., et al. 2005, Icarus, 179, 304
Fornasier, S., Belskaya, I., Shkuratov, Yu. G., et al. 2006, A&A, submitted
Fornasier, S., & Lazzarin, M. 2001, Icarus, 152, 127
Gaffey, M. J., & Kelley, M. S. 2004, LPI XXXV, 1812
Goidet-Devel, B., Renard, J. B., & Levasseur-Regourd, A. C. 1995, Planet. Space Sci., 46, 779
Harris, A. W., & Harris, A. W. 1997, Icarus, 126, 450
Hicks, M. D., Bauer, J. M., & Tokunaga, A. T. 2004, IAU Circ., 8315, 3
Kaasalainen, S., Piironen, J., Kaasalainen, M., et al. 2003, Icarus, 161, 34
Lupishko, D. F., & Mohamed, R. A. 1996, Icarus, 119, 209
Lupishko, D. F., Vasilyev, S. V., Efimov, Yu. S., & Shakhovskoj, N. M. 1995, Icarus, 113, 200
Rosenbush, V. K., Kiselev, N. N., Shevchenko, V. G., et al. 2005, Icarus, 178, 222
Shakhovskoy, N. M., & Efimov, Yu. S. 1972, Izv. Krymskoi Astrofiz. Obs., 45, 90
Tedesco, E. F., Williams, J. C., Matson, D. L., et al. 1989, in Asteroids II, ed. R. P. Binzel, T. Gehrels, & M. S. Matthews (Tucson: Univ. of Arizona Press), 1151
Tedesco, E. F., Egan, M. P., & Price, S. D. 2002, AJ, 124, 583
Weissman, P. R., Lowry, S. C., & Choi, Y. J. 2005, Am. Astron. Soc., DPS meeting, 37, 15.28
Zellner, B., & Gradie, J. 1976, AJ, 81, 262

2.8.3 21 Lutétia

Plusieurs campagnes observationnelles (auxquelles j'ai participé) en photométrie, spectroscopie, polarimétrie, ainsi que des images et spectres résolus avec l'optique adaptative pour plusieurs phases rotationnelles, ont été obtenus avec les télescopes VLT, NTT, TNG, Keck afin de mieux comprendre la composition chimique de la surface de 21 Lutétia et de mieux déterminer l'axe des pôles et sa période de rotation avant le survol de Rosetta, qui a eu lieu en juillet 2010.
21 Lutétia est un grand astéroïde qui a été observé pendant longtemps et qui a été choisi comme cible de Rosetta grâce à sa taille, d'environ 100 kilomètres, qui permettait à l'instrument RSI à bord de Rosetta de déterminer sa masse et de déduire sa densité pendant le survol. En raison d'une valeur d'albédo d'environ 20%, Lutétia a été précédemment classifié comme de type M (composition métallique). Les campagnes d'observation auxquelles j'ai participé ont prouvé que cette classification était discutable, car son spectre infrarouge est exceptionnellement plat comparé à celui d'autres astéroïdes de type M (Birlan et al. 2004, Barucci et al. 2005a). Le comportement spectral suggère une similitude avec les spectres des chondrites carbonées et des astéroïdes de classe C. Les observations spectroscopiques menées au télescope TNG ont montré que Lutétia semble avoir des variations spectrales à différentes phases rotationnelles et que sa surface pourrait donc être hétérogène (Perna et al. 2010).
Nous avons déterminé avec précision l'amplitude de la courbe de lumière de Lutétia, sa magnitude absolue, son effet d'opposition, son coefficient de phase et les couleurs BVRI (Belskaya et al. 2010a). Nous avons aussi montré que Lutétia a des propriétés polarimétriques particulières, avec un angle d'inversion de la courbe de polarisation élevé (24,4^o), et semblables à celles des chondrites carbonées CV3-CO3 (Fornasier et al. 2006b, Belskaya et al. 2010a). Sa surface semble être couverte par une fine couche de régolithe avec des grains de dimensions < 20 μm. Enfin, sur la base de notre analyse, nous avons prédit que la surface de Lutétia est non convexe, à cause de la présence d'un gros cratère, prédiction qui a été confirmée par les images de Rosetta (gros cratère d'environ 40 km de diamètre observé au pôle nord de l'astéroïde).
La forme et les propriétés rotationnelles de Lutétia ont été déterminées en utilisant des observations en optique adaptative couplées avec toutes les courbes de lumière (50) de Lutétia disponibles dans la littérature (Carry et al., 2010 ; méthode KOALA). Lutétia a une forme ellipsoïdale avec des axes de dimensions a= 124± 5km, b= 101±4 km et c=93±13. L'orientation du pôle a aussi été déterminée. La qualité de la méthode KOALA est démontrée par la frappante similitude entre les images observées par OSIRIS-Rosetta et celles produites par le modèle de forme.

Lutétia a été aussi observé avec le télescope spatial Spitzer. Le modèle thermique appliqué aux 14 spectres obtenus avec IRS (5–38 μm) donne une valeur petite pour l'inertie thermique (I $< 30\ JK^{-1}m^{-2}s^{-1/2}$), consistante avec les valeurs des astéroïdes de la ceinture principale, un albédo de 0,19±0,02 et une rugosité de surface élevée et non homogène au niveau de la région équatoriale de l'astéroïde où la composition peut être hétérogène (Lamy et al. 2010). Le spectre d'émissivité de Lutétia dans la région 5–38 μm ressemble aux spectres des chondrites carbonées du type CO et CV, confirmant une composition chimique assez primitive de sa surface (Barucci et al. 2008a).

2.8.4 Article : Asteroids 2867 Steins and 21 Lutétia : surface composition from far infrared observations with the Spitzer space telescope

2.8.5 Article : Puzzling asteroid 21 Lutétia : our knowledge prior to the Rosetta fly-by

A&A 477, 665–670 (2008)
DOI: 10.1051/0004-6361:20078085

Astronomy & Astrophysics

Asteroids 2867 Steins and 21 Lutetia: surface composition from far infrared observations with the Spitzer space telescope

M. A. Barucci[1], S. Fornasier[1,2], E. Dotto[3], P. L. Lamy[4], L. Jorda[4], O. Groussin[4], J. R. Brucato[5], J. Carvano[6], A. Alvarez-Candal[1], D. Cruikshank[7], and M. Fulchignoni[1,2]

[1] LESIA, Observatoire de Paris, 92195 Meudon Principal Cedex, France
e-mail: antonella.barucci@obspm.fr
[2] Université Paris Diderot, Paris VII, France
[3] INAF, Osservatorio Astronomico di Roma, via Frascati 33, 00040 Monteporzio Catone, Roma, Italy
[4] Laboratoire d'Astrophysique de Marseille, BP 8, 13376 Marseille Cedex 12, France
[5] INAF, Osservatorio Astronomico di Capodimonte, via Moiariello 16, 80131 Napoli, Italy
[6] Observatorio National (COAA), rua Gal. José Cristino 77, CEP20921–400 Rio de Janeiro, Brazil
[7] NASA Ames Research Center, MS 245-6, Moffett Field, CA 94035-1000, USA

Received 14 June 2007 / Accepted 3 October 2007

ABSTRACT

Aims. The aim of this paper is to investigate the surface composition of the two asteroids 21 Lutetia and 2867 Steins, targets of the Rosetta space mission.

Methods. We observed the two asteroids through their full rotational periods with the Infrared Spectrograph of the Spitzer Space Telescope to investigate the surface properties. The analysis of their thermal emission spectra was carried out to detect emissivity features that diagnose the surface composition.

Results. For both asteroids, the Christiansen peak, the Reststrahlen, and the Transparency features were detected. The thermal emissivity shows a clear analogy to carbonaceous chondrite meteorites, in particular to the CO–CV types for 21 Lutetia, while for 2867 Steins, already suggested as belonging to the E-type asteroids, the similarity to the enstatite achondrite meteorite is confirmed.

Key words. minor planets, asteroids – techniques: spectroscopic – methods: observational

1. Introduction

The Rosetta spacecraft was successfully launched on 2 March 2004 and is now on its way to rendez-vous with comet 67P/Churyumov-Gerasimenko in May 2014 at a heliocentric distance of 4.5 AU. During its journey to the comet, the spacecraft will fly by two main belt asteroids 2867 Steins and 21 Lutetia, selected after detailed studies of the candidates for all possible mission scenarios (Barucci et al. 2005). Nominally the fly-by of asteroid Steins will take place on 5 September 2008, at a velocity of 8.6 $\mathrm{km\,s^{-1}}$ and a closest approach of about 800 km. That of Lutetia will take place on 10 June 2010 at a velocity of 15 $\mathrm{km\,s^{-1}}$ and a closest approach of about 3000 km. As for all targets of space missions, an a priori knowledge of these *terra incognita* is crucial to preparing and optimizing the operations of the spacecraft and its instruments so as to maximize the scientific return.

We briefly summarize the properties of these two asteroids as presently known, based on the recent review article by Barucci et al. (2007). Asteroid 2867 Steins is a small asteroid whose knowledge is still limited. The first spectroscopic observations (Barucci et al. 2005) suggested a similarity between Steins and E-type asteroids, a rare class of objects with properties similar to the enstatite meteorites. Similar results have been obtained recently by Fornasier et al. (2007) and by Nedelcu et al. (2007a). Fornasier et al. (2006), using polarimetric technique, determined for the first time the albedo value of 0.45 ± 0.10, a high value that implies a diameter of approximately 4.6 km and confirms the E-type classification. Asteroid 21 Lutetia, a large object with a diameter of about 100 km, has a V+NIR spectral behaviour similar to the carbonaceous chondrites (Birlan et al. 2004; Barucci et al. 2005; Birlan et al. 2006; Nedelcu et al. 2007b), but an IRAS albedo (0.22 ± 0.02, Tedesco & Veeder 1992) that is not compatible with C-type asteroids, which are associated to this type of meteorite. Instead, the IRAS albedo leads Lutetia to be classified as an M-type asteroid, suggesting a metallic composition. Nevertheless several different albedo values have been published. A lower albedo 0.09–0.10 has been estimated from ground–based polarimetric measurements (Zellner et al. 1977; Lupisko & Mohamed 1996), while a high value of 0.23 ± 0.05 was given by Mueller et al. (2006) with thermal-infrared observations. Other intermediate values of 0.15 ± 0.05 have been obtained by Magri et al. (1999) using a shape modelled by new radar observations, and 0.13 ± 0.03 by Carvano et al. (2007) analysing recent thermal-infrared observations.

We now report on far-infrared observations of these two asteroids carried out with the Infrared Spectrograph (IRS) of the Spitzer space telescope (SST) in a series of companion articles that allow us to discuss and try to solve some controversies before the Rosetta fly-bys. A detailed account of the observations, data processing, and results on the size, the albedo, and the thermal properties are presented in Lamy et al. (2007a,b). The present article analyses the emissivity spectra and discusses

Article published by EDP Sciences and available at http://www.aanda.org or http://dx.doi.org/10.1051/0004-6361:20078085

the mineralogical composition and the classification of the two Rosetta asteroid targets.

2. Observations and data analysis

2867 Steins and 21 Lutetia were observed with the IRS spectrograph which covers the wavelength range 5.2–38.0 μm in four long-slit segments: the short wavelength, 2nd order (SL2, from 5.2 to 8.5 μm); the short wavelength, 1st order (SL1, from 7.4 to 14.2 μm); the long wavelength, 2nd order (LL2, from 14.0 to 21.5 μm); and the long wavelength, 1st order (LL1, from 19.5 to 38.0 μm). The observations of 2867 Steins were carried out on 22 November 2005 from 06:23 to 13:18 UT, catching 14 full range (5–38 μm), low resolution spectra that covered the asteroid' s full rotational period of 6.052 ± 0.007 h (Kuppers et al. 2007). All the spectra were acquired with single ramps of 14.68 s, except for the SL1 segment where we used a 6.29 s ramp. The observations were carried out when the asteroid was at heliocentric distance of 2.13 AU, 1.60 AU far away from SPITZER and seen with a phase angle of 27.2 deg.

Lutetia was observed from 17:32 UT on 10 December 2005 to 02:27 on 11 December 2005, obtaining 14 individual full wavelength range spectra covering the rotational period of 8.17 ± 0.10 h (Zappalà et al. 1984). An exposure time of 6.29 s was used for each of the 4 spectral segments. The observations were carried out when the asteroid was at a heliocentric distance of 2.81 AU, 2.66 AU far away from Spitzer and seen with a phase angle of 21.1 deg.

Data reduction of the Basic Calibrated Data (BCD) was provided by the Spitzer pipeline (`http://ssc.spitzer.caltech.edu/documents/SOM/irs60.pdf` and `http://ssc.spitzer.caltech.edu/irs/dh/ IrsPDDmar30.pdf`); background correction by differencing the 2 nodding positions was performed using SPICE, the Spitzer IRS Custom Extraction software. More details on the acquisition and data reduction steps are reported in Lamy et al. (2007a).

To interpret the infrared spectra, the thermal model (Groussin et al. 2004) was used and all the details are presented in Lamy et al. (2007a,b). The thermal balance on the surface includes the solar flux received by the object, on the one hand, the re-radiated flux and the heat conduction, on the other. The solar flux depends mainly on the albedo, the re-radiated flux on the beaming factor, and the heat conduction on the thermal inertia. We used a visible geometric albedo of 0.34 ± 0.06 for Steins and 0.19 ± 0.02 for Lutetia, a thermal inertia of ~100 J/K/m^2/s$^{0.5}$ for Steins, and 25 J/K/m^2/s$^{0.5}$ for Lutetia, and a beaming factor $\eta = 0.9$ for both asteroids, consistent with Lamy et al. (2007a,b).

Using the above parameters, we calculated the infrared spectral energy distribution (SED) of Steins and Lutetia. The SED is normalized to the SST data using a multiplicative coefficient, which corresponds to the change in cross-section as a function of time (light curve). Each spectrum observed by SST is then divided by the normalized SED to obtain the emissivity as a function of wavelength. The 14 individual emissivity spectra of 21 Lutetia and 2867 Steins are presented in Figs. 1 and 2.

We investigated the differences between the individual spectra for each asteroid by a χ-squared value defined as:

$$\chi^2 = \sum_{i=1}^{N} \left(\frac{e_{\text{mean}}(i) - e(i)}{N} \right)^2 \tag{1}$$

where N is the number of data points in the wavelength range 11–32 μm ($N = 196$) for Steins, and 6–36 μm ($N = 331$) for Lutetia, e_{mean} the mean flux of the 14 different data sets and e the emissivity of each individual data set. We report in Table 1 the computed residuals of each individual data set compared to the spectrum derived from the mean. The higher computed residual values for Steins are attributable to the lower signal to noise ratio for its spectral data. Considering the flux errors and the defects of the detector, we did not find any difference in the emissivity spectra of Lutetia and Steins during their rotational periods. Therefore, we take the mean of all the 14 spectra available for each object in order to increase the S/N ratio, which, particularly in the case of 2867 Steins, was quite low in the SL2 range and for $\lambda > 30$ μm.

3. Data interpretation

To interpret the resulting emissivity of both targets in terms of their composition, we compared the mean emissivity (the average of the 14 observed spectra) with a wide sample of laboratory spectra of minerals and meteorites (Dotto et al. 2000, 2004; Barucci et al. 2002; Salisbury et al. 1991a,b; ASTER spectral library on `http://speclib.jpl.nasa.gov`; Relab database `http://lf314-rlds.geo.brown.edu`).

As thoroughly discussed by Salisbury (1993), the most diagnostic spectral characteristics in the analysed wavelength range are the Christiansen peak, the Reststrahlen, and Transparency features. The Christiansen peak is related to the mineralogy and grain size, and for silicates it occurs between 8 and 9.5 μm, just before the Si-O stretching vibration bands. Reststrahlen bands are due to vibrational modes of molecular complexes, and for silicates they occur in the 8–25 μm region. The Transparency features are volume scattering features of fine particulates, and they form troughs between the main Reststrahlen bands. At a small grain size, volume scattering occurs and Transparency features are observable due to a loss of photons crossing many grains.

The spectral behaviour of Lutetia, shown at the top of Fig. 3, appears to be consistent with that of carbonaceous chondrites, which exhibit the Christiansen peak at distinctively long wavelengths (Salisbury et al. 1991b). After analysing a large sample of meteorites taken from the RELAB and ASTER databases, we report in Fig. 3 a comparison with the carbonaceous chondrite Allende (CV type), which shows a very good spectroscopic match. The emissivity spectrum of the meteorite Odessa is also reported as an example. Odessa is an iron meteorite that contains some silicate inclusions. The spectral behaviour is completely different from that of Lutetia, so the possible metallic nature for this asteroid is rejected. A 10 μm emission feature, together with a broad emissivity structure between about 16 and 28 μm, has been found in the emissivity spectra of Trojan asteroids observed with the Spitzer Space Telescope (Emery et al. 2006). They propose that the Trojan emission spectra may best be explained by a very underdense surface structure consisting of particles of just a few microns in size or by very small mineral and carbonaceous particles suspended in a matrix material that is relatively transparent in the mid-infrared. However, the detailed shape of the spectra and the C, R, and T features are different in the Trojans than in the data presented here.

To better investigate the primitive nature of 21 Lutetia and its similarity with carbonaceous chondrite meteorites, we compared the Spitzer spectrum with laboratory spectra of different samples at different grain sizes published by Barucci et al. (2002). The Lutetia emissivity spectrum matches very well the emissivity spectrum of Ornans meteorites, a CO3 type carbonaceous chondritic (Barucci et al. 2002), with grains in a size range smaller than 20 μm. In fact, the peak at about 9.3 μm in the emissivity spectrum of Lutetia is consistent with the Christiansen

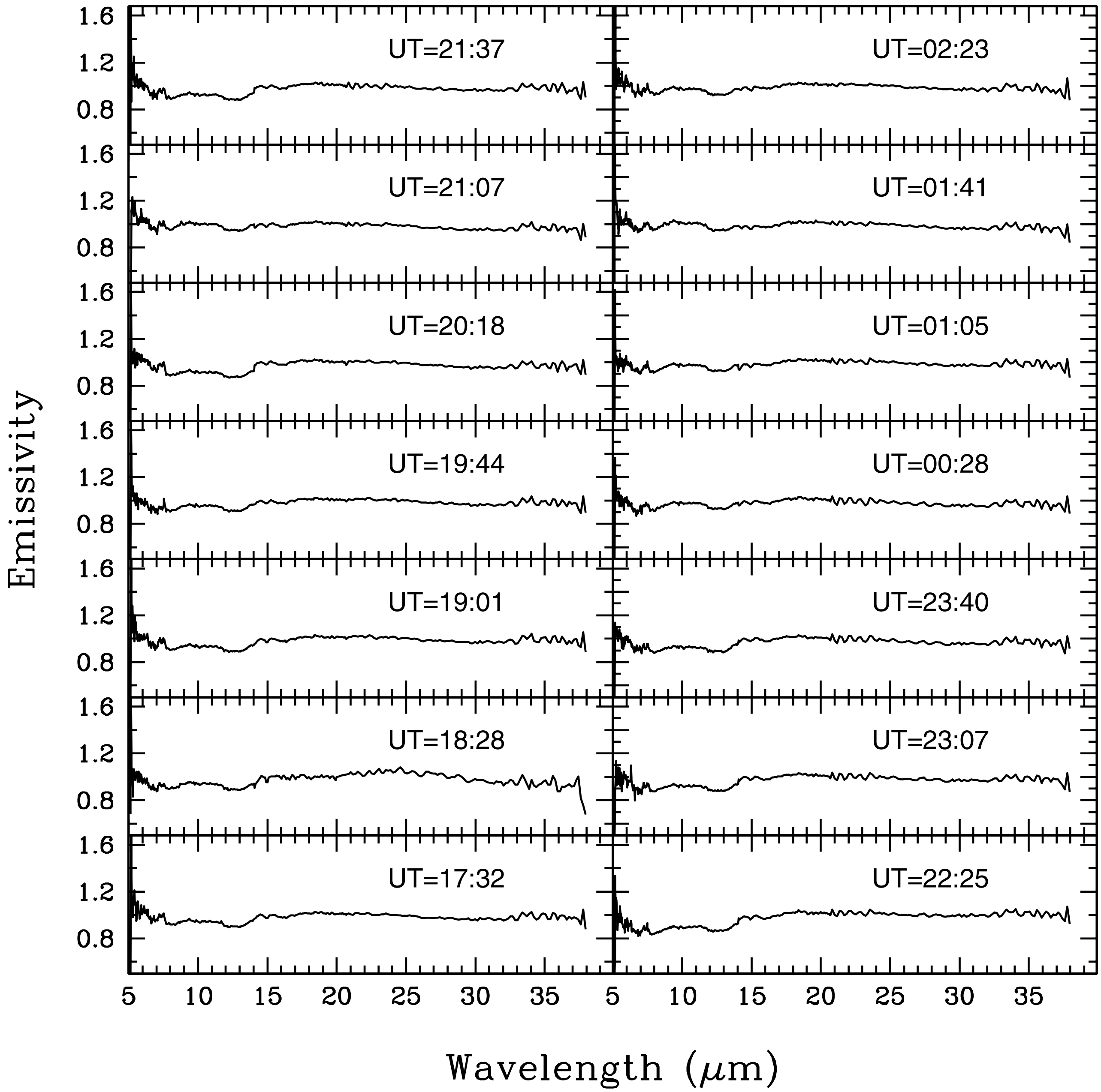

Fig. 1. Individual emissivity spectra of 21 Lutetia acquired on 10 December 2005 from 17:32 UT to 11 December 2006 02:27 UT (the UT time corresponds to the start of the exposure).

peak of the Ornans meteorite, and the plateau between 9 and 12 μm is consistent with the Reststrahlen features, as well as the Transparency band around 13 μm. The match of the mid-infrared spectrum of Lutetia with that of Ornans, which suffered aqueous alteration processes (Zolensky & McSween 1988), confirms the primitive chondritic character of this asteroid already proposed by Barucci et al. (2005) and Birlan et al. (2004, 2006) on the basis of ground-based observations. In fact, the visible and near-infrared spectra are very similar to those of CO3 or CV3 type meteorites, with a stronger similarity to the Vigarano (CV3 type) meteorite.

Since few data in far-infrared region on asteroid analogue materials with different grain sizes exist in the literature, we performed new laboratory experiments for Vigarano using the Bruker IFS66v interferometer at the INAF Astronomical Capodimonte Observatory (Italy). We used the same equipment and the same conditions as was previously used to obtain the Ornans data (Barucci et al. 2002), and the results are reported in Fig. 4. Also, Vigarano with small grain size (0–20 μm) fits the Lutetia spectrum well as shown by the correspondence of the Christiansen, Reststrahlen, and Transparency features. The Vigarano sample is characterised by the presence of aqueous alterations in its matrix. The close similarity to CO3 and CV3 meteorites containing hydrous mineral, suggests that Lutetia underwent some aqueous alteration. This result confirms what has already been inferred by Rivkin et al. (2000) by the detection

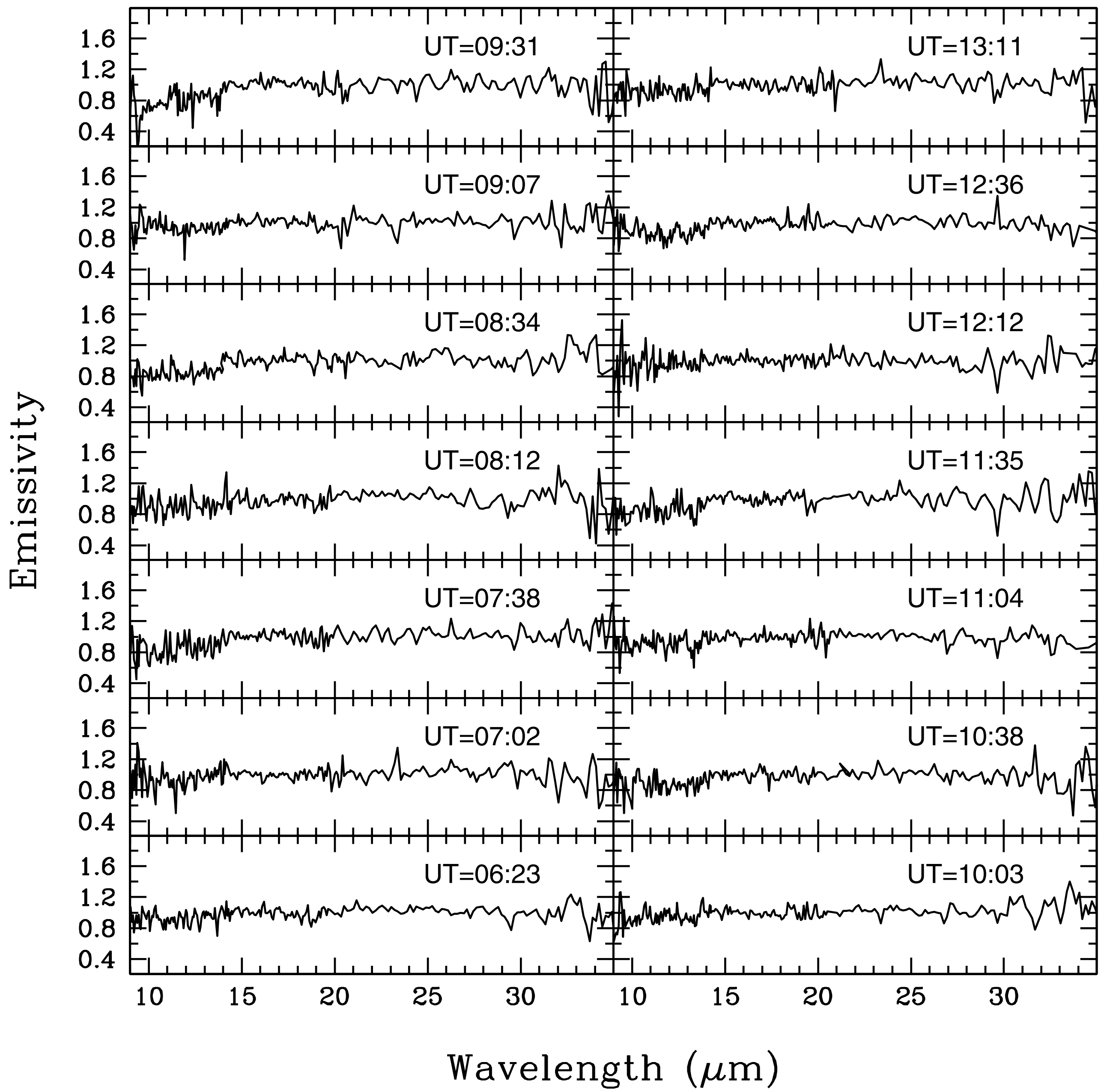

Fig. 2. Individual emissivity spectra of 2867 Steins acquired on 22 November 2005 from 06:23 to 13:11, UT time (the UT time corresponds to the start of the exposure).

of the 3 μm absorption feature, a diagnostic for hydrated minerals. Birlan et al. (2006) also observed the 3 μm band in the Lutetia spectrum, and they found a 2.9 vs. 3.2 μm ratio value close to that of the CV-CO meteorites. Furthermore, Lazzarin et al. (2004) and Prokof'eva et al. (2005) obtained several visible specta and detected the possible presence of features at 0.44 and 0.67 μm, attributed to hydrated silicates.

Figure 5 shows the emissivity spectrum of Steins obtained with Spitzer as mean of all the 14 individual spectra. Although its signal is not precise enough to clearly distinguish the exact position of the different bands, the general behaviour of the spectrum and, in particular, the wavelength position of the Christiansen, Reststrahlen, and Transparency features, suggests a similarity to the aubrite (enstatite achondrite) meteorite and the enstatite mineral, a single-chain pyroxene of which the aubrite meteorites are primarily composed. In fact, as noted by Salisbury et al. (1991a), the aubrite spectrum exhibits the Christiansen peak at short wavelengths, around 8.3 μm, and strong Reststrahlen bands between 8.5 and 9.5 μm. Transparency features are evident around 12–13 μm. As a comparison, Fig. 5 also shows the emissivity spectrum of a sample of enstatite analysed and published by Barucci et al. (2002) and of the aubrite meteorite ALH84007 as taken from the ASTER library. The behaviour of our Spitzer mid-infrared spectrum and the match with laboratory spectra of the enstatite mineral and the aubrite meteorite support the classification of Steins given by

Table 1. Residuals of each individual emissivity spectrum compared to the mean flux of the 14 spectra.

Set	Steins residuals	Lutetia residuals
1	2.40e−05	8.22e−07
2	3.71e−05	1.91e−06
3	3.30e−05	5.71e−07
4	3.80e−05	2.69e−07
5	2.71e−05	1.38e−06
6	2.62e−05	3.32e−06
7	4.51e−05	6.40e−07
8	2.61e−05	5.76e−06
9	2.54e−05	1.58e−06
10	2.81e−05	8.71e−07
11	4.24e−05	9.29e−07
12	3.81e−05	6.76e−07
13	2.74e−05	3.21e−06
14	2.81e−05	8.61e−07

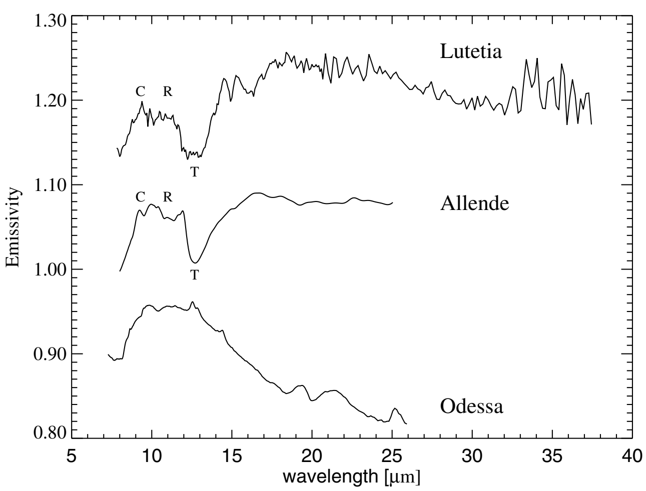

Fig. 3. The emissivity of Lutetia (average of the 14 individual spectra) compared with the emissivity of the Allende meteorite (from the ASTER database, with particle size 0–75 μm) and of the Odessa meteorite (from the RELAB database, with particle size 45–90 μm). The error bars of the emissivity spectrum of Lutetia are ∼5% considering errors due both to the thermal data and to the model incertitude. The Christiansen, Reststrahlen and Transparency features are indicated as C, R, and T.

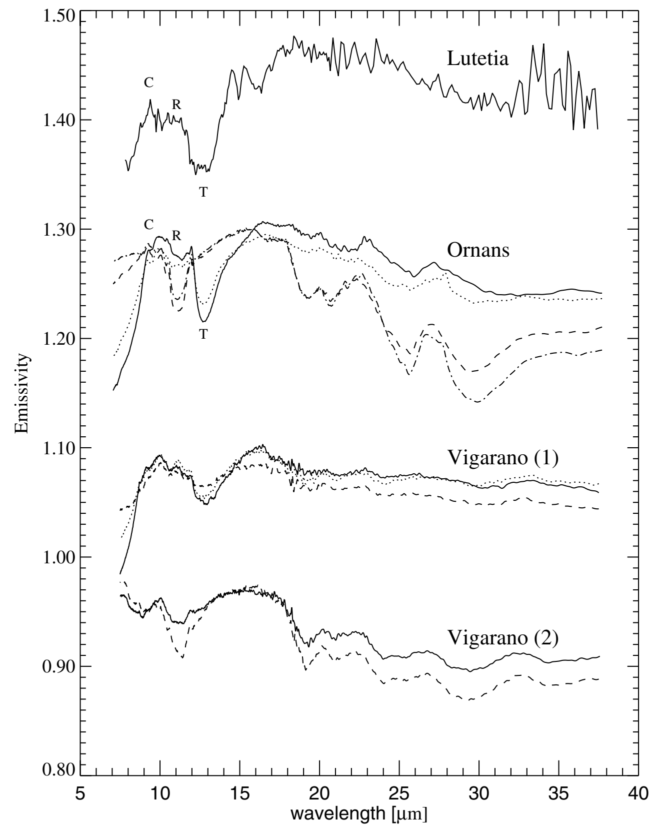

Fig. 4. The emissivity of Lutetia (average of the 14 individual spectra) compared with the emissivity of the Ornans meteorite by Barucci et al. (2005) at different grain dimensions (0–20 μm, continuous line; 20–50 μm, dotted line; 50–100 μm, dashed line; and >100 μm , dashed-dotted line), and the emissivity of the Vigarano meteorite obtained with new laboratory experiments at different grain dimensions. Vigarano (1): continuous line for 0–20 μm; dotted line for 20–50 μm, and dashed line for 50–100 μm; Vigarano (2): continuous line for 100–150 μm, and dashed line for grain size >150 μm. All the spectra are shifted for clarity. The Christiansen, Reststrahlen, and Transparency features are indicated as C, R, and T.

Barucci et al. (2005) as an E-type asteroid with an enstatite composition. This classification is also strengthened by the polarimetric properties (Fornasier et al. 2006).

4. Conclusions

21 Lutetia and 2867 Steins were observed with the Infrared Spectrograph (IRS) of the Spitzer Space Telescope. The emissivity spectra for each asteroid were derived after the division of the spectral energy distribution with a thermal model. To interpret the emissivity spectral features above the thermal emission continuum, we compared the Spitzer emissivity both with laboratory spectra available in the literature and with new laboratory experiments on the Vigarano meteorite at various grain sizes.

The Steins emissivity spectrum, even though it has low signal precision, is similar to the enstatite achondrite meteorites and to the enstatite mineral, confirming the rare E-type classification already suggested on the basis of ground-based spectral and polarimetric observations.

For 21 Lutetia, the emissivity spectrum departs significantly from the typical metallic meteorites, so that the first M classification derived from its high IRAS albedo is not confirmed. On the other hand, its emissivity in the 6–38 μm range is similar to that of the CO3 and CV3 carbonaceous chondrites with a small grain size. Even though it is difficult to distinguish between the CO and CV spectra, the emissivity of the Lutetia spectrum seems more similar to that of Ornans with a smaller grain size (0–20 μm), shown by the better correspondence of the Christiansen peak and the Restrahlen and Transparency features. The CO carbonaceous chondrites consist of small chondrules and aggregates set in a fine-grained matrix consisting of a heterogeneous mixture of fine-grained, iron-rich olivine and hydrated silicates (Sandford 1984). This similarity with the carbonaceous chondrites implies that Lutetia is a primordial body. Its surface has to be composed of particles of small size, with the possible presence of aqueous altered material that underwent slight thermal alteration.

The behaviour of the obtained emissivity data, in particular the broad analysed features are independent of albedo determination.

A&A 515, A29 (2010)
DOI: 10.1051/0004-6361/201013994

Astronomy & Astrophysics

Puzzling asteroid 21 Lutetia: our knowledge prior to the Rosetta fly-by★

I. N. Belskaya[1,2], S. Fornasier[1,3], Yu. N. Krugly[2], V. G. Shevchenko[2], N. M. Gaftonyuk[4], M. A. Barucci[1], M. Fulchignoni[1,3], and R. Gil-Hutton[5]

[1] LESIA, Observatoire de Paris, France
e-mail: irina.belskaya@obspm.fr
[2] Institute of Astronomy of Kharkiv Karazin National University, Kharkiv, Ukraine
[3] Université de Paris 7 Denis Diderot, France
[4] Crimean Astrophysical Observatory, Crimea, Simeiz, Ukraine
[5] Complejo Astronómico El Leoncito (Casleo) and Universidad Nacional de San Juan, San Juan, Argentina

Received 5 January 2010 / Accepted 2 March 2010

ABSTRACT

Aims. A wide observational campaign was carried out in 2004–2009 that aimed to complete the ground-based investigation of Lutetia prior to the Rosetta fly-by in July 2010.

Methods. We obtained *BVRI* photometric and *V*-band polarimetric measurements over a wide range of phase angles, and visible and infrared spectra in the 0.4–2.4 μm range. We analyze them with previously published data to retrieve information about Lutetia's surface properties.

Results. Values of lightcurve amplitudes, absolute magnitude, opposition effect, phase coefficient, and *BVRI* colors of Lutetia surface seen at near pole-on aspect are determined. We define more precisely parameters of polarization phase curve and show their distinct deviation from any other moderate-albedo asteroid. An indication of possible variations in both polarization and spectral data across the asteroid surface are found. To explain features found by different techniques, we propose that (i) Lutetia has a non-convex shape, probably due to a large crater, and heterogeneous surface properties probably related to surface morphology; (ii) at least part of the surface is covered by a fine-grained regolith of particle size smaller than 20 μm; (iii) the closest meteorite analogues of Lutetia's surface composition are particular types of carbonaceous chondrites, or Lutetia has specific surface composition that is not representative among studied meteorites.

Key words. minor planets, asteroids: individual: 21 Lutetia – techniques: photometric – techniques: spectroscopic – techniques: polarimetric

1. Introduction

Asteroid 21 Lutetia has been extensively observed using different techniques for more than 30 years. The interest in this object was initially related to its classification as an M-type asteroid with a possible metallic composition (see Bowell et al. 1978). Since 2004 when Lutetia was selected as a target of the Rosetta mission, the volume of observational data for this asteroid has rapidly grown (see Barucci & Fulchignoni 2009, for a review).

On the basis of photometric data obtained in 1962–1998, Torppa et al. (2003) determined the pole coordinates $\lambda_{\rm p}$ = 39° (220°), $\beta_{\rm p}$ = 3° and the sidereal rotation period $P_{\rm sid}$ = 8.165455 h. The shape was found to have some irregular features with rough global dimensions a/b = 1.2 and b/c = 1.2. Drummond et al. (2009) provided new estimates of these parameters using adaptive optics images of Lutetia at the Keck telescope, of $\lambda_{\rm p} = 49°$, $\beta_{\rm p} = -8°$ and a shape of $132 \times 101 \times 76$ km with formal uncertainties of 1 km in the equatorial dimensions, and 31 km for the shortest axis.

On the basis of spectral and polarimetric observations, three types of meteorites are generally taken into consideration as possible analogues: iron meteorites (Bowell et al. 1978; Dollfus et al. 1979), enstatite chondrites (Chapman et al. 1975; Vernazza et al. 2009), and some types of carbonaceous chondrites, mainly CO3 or CV3 (Belskaya & Lagerkvist 1996; Birlan et al. 2004; Barucci et al. 2008; Lazzarin et al. 2009). The main problem in spectral data interpretation is the featureless spectrum of Lutetia. A few minor features in the visible range were reported and interpreted as being indicative of aqueous alteration material consistent with carbonaceous chondrites composition (see Lazzarin et al. 2009, and references therein). A 3 μm feature associated with hydrated minerals was found by Rivkin et al. (2000). In the emissivity spectra, a narrow 10 μm emission feature was found (Feierberg et al. 1983; Barucci et al. 2008). It was interpreted as being indicative of fine silicate dust (Feierberg et al. 1983). According to Barucci et al. (2008), the emissivity spectrum is similar to that of the CO3 and CV3 carbonaceous chondrites with a grain size smaller than 20 μm.

To constrain the surface composition it is important to know Lutetia's albedo. However, the diversity in albedo estimates

★ Based on observations carried out at the ESO-NTT (La Silla, Chile), the Telescopio Nazionale Galileo (La Palma, Spain), the Crimean Astrophysical Observatory (Ukraine), the Asiago Astrophysical Observatory (Italy) and Complejo Astronómico El Leoncito (Casleo, Argentine).

Table 1. Aspect data of photometric observations and magnitudes.

Date (UT)	r (AU)	Δ (AU)	λ (deg)	β (deg)	α (deg)	$V_0(1, \alpha)$ (mag)	Filter
2004 09 16.07	2.163	1.416	47.72	–3.86	22.17	8.32 ± 0.03	*BVRI*
2004 09 17.06	2.164	1.408	47.74	–3.86	21.87	8.35 ± 0.04	*BVRI*
2004 10 07.06	2.195	1.285	46.31	–3.93	14.12	8.06 ± 0.03	*BVRI*
2004 10 08.09	2.197	1.281	46.15	–3.93	13.65	8.04 ± 0.02	*BVRI*
2004 11 10.81	2.254	1.274	38.40	–3.34	4.75	7.63 ± 0.02	*V*
2008 11 28.96	2.420	1.434	69.00	–1.15	0.91	–	*V*
2008 11 29.76	2.421	1.435	68.79	–1.12	0.58	7.28 ± 0.02	*V*
2008 11 30.91	2.423	1.437	68.50	–1.10	0.51	7.24 ± 0.02	*V*
2008 12 01.96	2.425	1.440	68.22	–1.08	0.89	7.30 ± 0.02	*V*
2008 12 02.99	2.427	1.442	67.95	–1.05	1.39	7.36 ± 0.02	*V*
2008 12 03.86	2.429	1.445	67.74	–1.03	1.81	7.40 ± 0.02	*V*
2008 12 15.71	2.450	1.499	64.80	–0.74	7.59	7.78 ± 0.02	*V*
2009 03 10.80	2.593	2.569	70.60	0.63	22.18	8.28 ± 0.03	*VR*
2009 03 11.75	2.594	2.583	70.87	0.64	22.12	8.25 ± 0.03	*VR*

by different techniques has been quite large, from 0.1 (Zellner et al. 1976) to 0.22 (Tedesco et al. 2002). Polarimetric means of albedo determination have provided contradictory results (Zellner et al. 1976; Gil-Hutton 2007). The accuracy of radiometric albedo measured strongly depends on the adopted absolute magnitude, which is not well-determined for Lutetia due to a lack of observations at small phase angles.

In this paper, we present new photometric, polarimetric and spectral observations of Lutetia carried out in 2004–2009. These observations were performed to determine absolute magnitude and albedo, and to place additional constraints on surface properties. We present an analysis of these data performed together with previously published data. This should be important not only for deriving physical characteristics of this particular asteroid but first of all for checking the efficiency of remote techniques in the study of atmosphereless bodies.

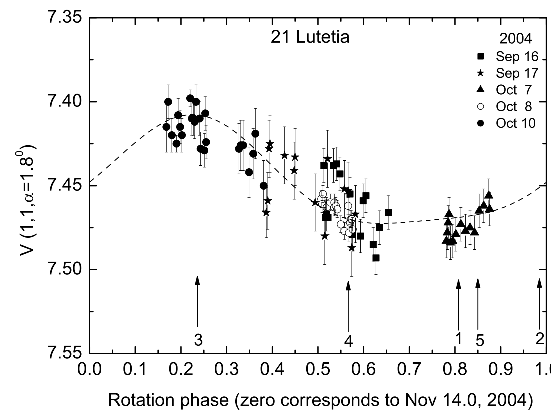

Fig. 1. Composite lightcurves of 21 Lutetia in 2004 apparition fitted with the Fourier fit. The arrows indicate rotation phases of our spectral observations (see Table 3 and Fig. 8).

2. Observations and results

2.1. Photometry

The observations were carried out in 2004 using the 0.7-m telescope of Chuguev Observational Station situated 70 km from Kharkiv, and in 2008–2009 using the 1-m telescope of the Crimean Astrophysical Observatory in Simeiz, Crimea. The 0.7-m telescope was equipped with a SBIG ST-6 UV camera mounted at the Newtonian focus ($f/4$). In Simeiz, we used a SBIG ST-6 camera placed on the 1-m Ritchey-Chretien telescope equipped with a focal reducer ($f/5$ system). The photometric reduction of the CCD frames was performed using the ASTPHOT package developed at DLR by Mottola (Mottola et al. 1994). The absolute calibration was performed using standard stars of colors close to those of the Sun taken from Landolt (1983, 1992) and Lasker et al. (1988). The measurements were obtained in the standard Johnson-Cousins photometric system. The method of CCD observations and data processing included all standard procedures and was described in detail by Krugly et al. (2002). The mean time of observations in UT, the heliocentric (r) and geocentric (Δ) distances, the solar phase angle (α), the ecliptic longitude (λ) and latitude (β) in epoch J2000.0, the magnitude $V_0(1, \alpha)$ reduced to the lightcurve primary maximum and its estimated error, and finally photometric bands of observations are given in Table 1. The estimated error in the absolute photometry includes both the uncertainty in photometric reduction, typically 0.01–0.02^{m}, and the uncertainty in the lightcurve amplitude correction.

During our observations in 2004 we were unable to cover small phase angles due to bad weather conditions, and the observational program was continued in 2008. According to the latest estimates of Lutetia's pole coordinates $\lambda_p = 51°$ (220°), $\beta_p = -4°$ (B. Carry, personal communication), all of our observations were made close to the pole-on direction with an aspect angle ≈10° in 2004 and ≈20° in 2008–2009. The composite lightcurves of each apparation are shown in Figs. 1 and 2. The lightcurve amplitude increased from 0.06^{m} in 2004, to 0.09^{m} in 2008, and 0.12^{m} in 2009 at a phase angle as large as 22°. The lightcurves exibit an irregular behaviour with one pair of extrema. The measured lightcurve amplitudes and features are consistent with the observations of 1981 (Lupishko et al. 1983; Zappala et al. 1984) and 1985 (Lupishko et al. 1987; Dotto et al. 1992), which were also near pole-on aspect.

To obtain the phase function, we normalized all the data to the lightcurve primary maximum. Errors due to amplitude corrections were taken into account in the magnitude's uncertainties. We also used the V-magnitudes measured in 2004 at the phase angle of 27.4° by Mueller et al. (2006) and normalized it to the lightcurve maximum using our lightcurve for the 2004 opposition. We applied the same procedure to the available observations of Lutetia from the 1981, 1983, and 1985

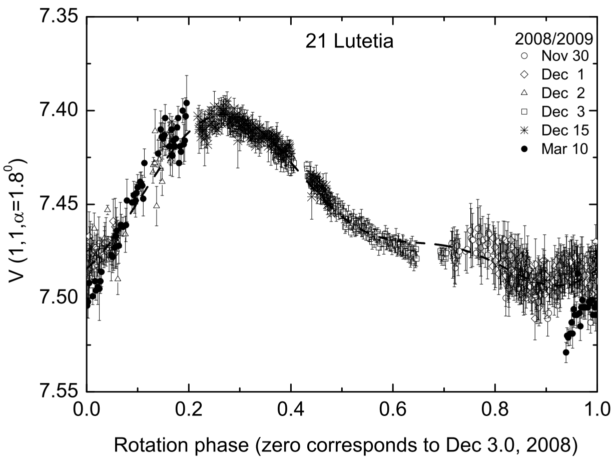

Fig. 2. Composite lightcurves of 21 Lutetia in 2008/2009 apparition fitted with the Fourier fit.

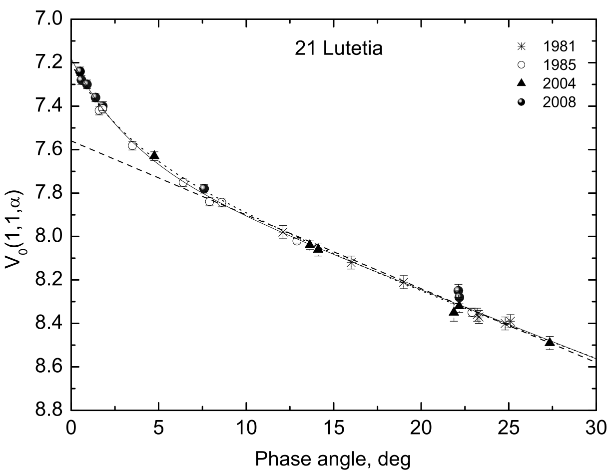

Fig. 3. Magnitude phase dependence for Lutetia based on observations at different apparitions at near polar aspects fitted by the HG function (the dotted line) and the linear-exponential function (the solid line). The dashed line shows liner fit to the data at $\alpha \geq 7°$.

oppositions, separately for each opposition. These data were obtained by different authors (Lupishko et al. 1983, 1987; Dotto et al. 1992; Lagerkvist et al. 1995; Zappala et al. 1984) at a variety of phase angles and were not analyzed jointly. In our analysis, we used an updated value of Lutetia's sidereal rotation period $P_{\rm sid}$ = 8.168268 h and normalized all the data to the same maximum.

We found that observations in the four oppositions corresponding to pole-on aspect are mutually in good agreement within the error bars. The phase function obtained is shown in Fig. 3. Fitting the data with both a HG fit (Bowell et al. 1989) and with a linear-exponential fit (Kaasalainen et al. 2003), we obtained practically identical curves. The HG-fit to the phase curve normalized to the lightcurve primary maximum inferred $H = 7.20 \pm 0.01$ and $G = 0.12 \pm 0.01$. We note that, for the phase function normalized to the mean lightcurve, $H = 7.25 \pm 0.01$. The phase coefficient obtained by the linear fit to the data at phase angles $\alpha \geq 7°$ is equal to $\beta = 0.034 \pm 0.001^{\rm m}$/deg and the magnitude at zero phase angle corresponding to the extrapolation of the linear fit is $V(1, 0) = 7.56 \pm 0.01$. The amplitude of the opposition effect, defined as an increase in magnitude above the linear fit at zero phase angle, was estimated to be $0.36^{\rm m}$. Both the opposition effect amplitude and the value of the phase slope are consistent with a moderate-albedo surface. Based on the empirical correlation between phase coefficient and albedo (Belskaya & Shevchenko 2000), an average albedo in the range of 0.12–0.20 is expected for Lutetia's surface.

The phase function obtained for the observations in 1983 at near-equatorial aspects is characterized by systematically lower magnitudes that are described well by the *HG*-function with $H = 7.29 \pm 0.02$ and $G = 0.13 \pm 0.03$. Thus, the difference between the absolute magnitudes at near polar and near equatorial aspects is found to be as small as $0.1^{\rm m}$. It implies that an upper limit to Lutetia's shape elongation is given by $b/c \leq 1.1$ in the case of a homogeneous surface albedo.

We also measured the *BVRI* colors of Lutetia at different phase angles and found a slight increasing trend toward larger phase angles, not exceeding a level of $0.001^{\rm m}$/deg. The mean measured colors are $B - V = 0.65 \pm 0.01$, $V - R = 0.42 \pm 0.01$, and $V - I = 0.76 \pm 0.01$.

2.2. Polarimetry

The first polarimetric observations of Lutetia were performed in 1973 by Zellner & Gradie (1976). They derived a polarimetric slope $h = 0.169$%/deg in the green filter with an effective wavelength of 0.52 μm and an albedo of 0.10 based on the empirical relationship "*h*-albedo". They also measured the inversion angle $\alpha_{\rm inv} = 24.2°$, which appeared to be the largest of all asteroids in their data-set. Polarimetric observations of Lutetia were successively carried out in 1985 in *UBVRI* filters at a phase angle of 7.5 deg close to the polarization minimum (Belskaya et al. 1987). These data revealed that the depth of polarimetric minimum reached 1.3% in the *V* band and slightly increased with wavelength. Other observations of Lutetia were carried out in the framework of a coordinate program at three observatories: the Crimean Astrophysical Observatory (Ukraine), the Asiago Observatory (Italy) and Complejo Astronómico El Leoncito (Casleo, Argentine), to cover phase angles that had not been previously observed. A part of these data was published among results of observations at each telescope (Fornasier et al. 2006; Gil-Hutton 2007; Belskaya et al. 2009). Here we report complementary observations of Lutetia that have not yet been published. Table 2 presents the mean time of observations in UT, the phase angle α, the polarization degree P and position angle Θ in the equatorial coordinate system, together with the root-mean-square errors σ_P and σ_Θ, the calculated values of the corresponding P_r and position angle Θ_r in the coordinate system referring to the scattering plane as defined by Zellner & Gradie (1976), and the telescope. Methods of observations and data processing were identical to those described by Fornasier et al. (2006) for Asiago, Belskaya et al. (2009) for Crimea, and Gil-Hutton (2007) for Casleo. The polarization-phase function of Lutetia obtained using both new and published data is shown in Fig. 4. The data were fitted with a linear-exponential function as described by Kaasalainen et al. (2003). Similar curves were obtained by fitting the data with either a trigonometric fit (Lumme & Muinonen 1993) or parabolic fit. The scatter of the data, which is rather large and exceeds the estimated errors in each measurement, may be indicative of a variation in polarization degree across the asteroid surface.

We analyzed the deviations of the polarization degree from the fitted phase curve and found that they are of a systematic rather than a random nature. Figure 5 plots these deviations versus rotation phase for observations in 1973 corresponding to the

Table 2. Results of polarimetric V-band observations of 21 Lutetia.

Date UT	α (deg)	P (%)	σ_P (%)	Θ (deg)	σ_Θ (deg)	P_r (%)	Θ_r (deg)	Tel.
2004 10 17.96	8.75	1.37	0.09	80.8	1.9	–1.36	87.0	1
2006 04 06.79	17.38	0.81	0.07	97.0	2.0	–0.72	78.1	2
2008 10 31.30	14.80	1.28	0.02	93.0	0.5	–1.25	97.0	3
2008 11 04.25	13.10	1.31	0.02	90.9	0.4	–1.29	94.8	3

Notes. 1. 1.25 m, Crimea. 2. 1.82 m, Asiago. 3. 2.15 m, Casleo.

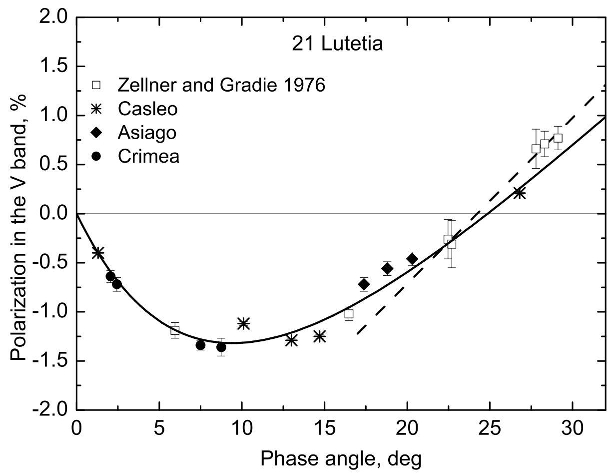

Fig. 4. Polarization phase dependence for Lutetia based on observations in 1973–2008 at different observational sites fitted by the linear-exponential function (solid line). The dashed line indicates the polarimetric slope h as defined by Zellner & Gradie (1976).

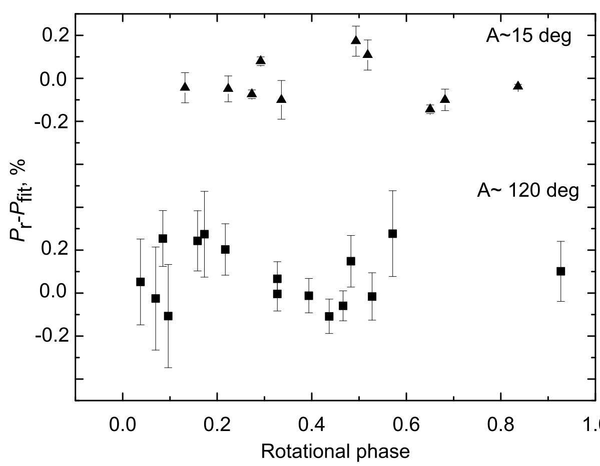

Fig. 5. The deviations of the polarization degree (P_r) from the linear-exponential fit to polarization phase curve ($P_{\rm fit}$) versus rotation phase at different aspect angle A.

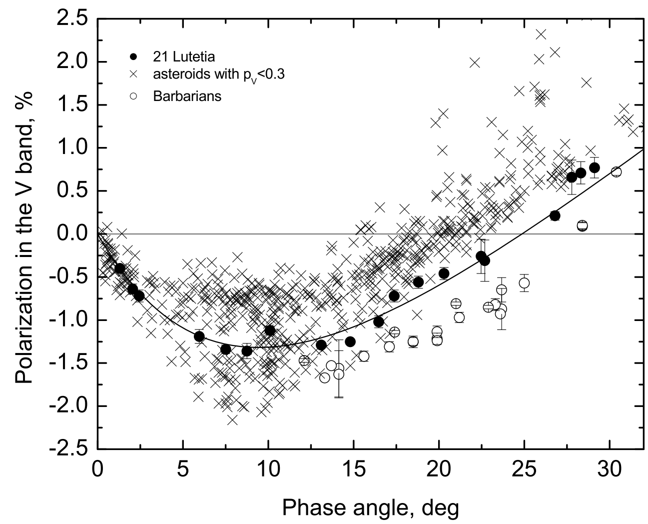

Fig. 6. The polarization-phase dependence of Lutetia (solid line) compared with available observations of moderate and low albedo asteroids (crosses) taken from the Asteroid Polarimetric Database (Lupishko & Vasilyev 2008) and data for Barbara-like asteroids (circles) from Cellino et al. (2006), Gil-Hutton et al. (2008), and Masiero & Cellino (2009).

aspect angle of about 120°, and in 2004 and 2008 oppositions when the aspect was close to pole-on (6–24°). One can see that variations in the polarization degree tend to increase toward equatorial aspect and can reach up to 0.2%.

The amplitude of variations in polarization degree across the Lutetia's surface resembles that measured on asteroid 4 Vesta (e.g., Lupishko et al. 1988) and could have the same cause, i.e. macroscale surface heterogeneity. The mean polarization phase dependence of Lutetia is characterized by the parameters $P_{\rm min} = -1.30 \pm 0.07\%$, $\alpha_{\rm min} = 9.1 \pm 0.8$ deg, $\alpha_{\rm inv} = 25.0 \pm 0.4$ deg, and $h = 0.131 \pm 0.009\%$/deg.

The polarimetric slope h has a smaller value than that defined by Zellner & Gradie (1976). It corresponds to the geometric albedo $p_V = 0.13 \pm 0.02$ when using the empirical relationship "h-albedo" based on meteorite data (Zellner & Gradie 1976), and $p_V = 0.16 \pm 0.02$ using the calibration based on IRAS albedos (Cellino et al. 1999). The difference between these two values is caused by the different calibration scales of albedos. Albedos of meteorites were measured in the laboratory at phase angle $\alpha = 5°$ while IRAS albedos were determined at zero phase angle using asteroid absolute magnitude H.

The most interesting polarimetric characteristic of Lutetia is its wide branch of negative polarization. Figure 6 compares Lutetia's data with available polarimetric measurements of low and moderate albedo asteroids. In this comparison, we used the Asteroid Polarimetric Database (Lupishko & Vasilyev 2008) selecting data of an accuracy superior to 0.2% for asteroids of albedo less than 0.3. Lutetia's observations characterized by an inversion angle as large as 25° represent a marginal case compared to a variety of asteroids observed so far. Only asteroid 234 Barbara and four other asteroids called "Barbarians" exhibited a polarization branch wider than that of Lutetia (see Fig. 6). This group of moderate-albedo asteroids of spectral type L, K or Ld have anomalous polarization properties which may be related to their specific surface composition (Cellino et al. 2006; Gil-Hutton et al. 2008; Masiero & Cellino 2009). We note, that the polarization minimum value of these asteroids deviates considerably from the well-known correlation "$P_{\rm min}$-albedo" and cannot be used for albedo estimation. In the case of Lutetia, this correlation also fails.

A negative polarization can be explained by several physical mechanisms, the most appropriate of which appear to be the coherent backscattering mechanism (see Shkuratov et al. 1994, for a review) and the single particle scattering (e.g., Muñoz et al. 2000). The coherent backscattering mechanism contributes to both the brightness opposition effect and the negative polarization branch and is particularly efficient for high albedo surfaces producing narrow backscattering peaks (Mishchenko et al. 2006). The measured phase curves of Lutetia (Figs. 3 and 4) do not exibit any sharp features toward zero phase angle. Both phase curves are characterized by wide opposition effects that assume relatively small contribution from the coherent backscattering. The contribution of the mechanism of the single particle scattering remains poorly understood but its efficiency in producing wide negative polarization branch has been demonstrated by laboratory and numerical modeling (e.g. Muñoz et al. 2000; Shkuratov et al. 2002). The negative branch was found to become more prominent and the inversion angle to increase in the cases of a) an increase in the refractive index; b) a decrease in the particle sizes to sizes comparable wavelength; c) complex internal structure of particles; and d) the mixture of particles with high contrast in albedo (Muñoz et al. 2000; Shkuratov et al. 1994, 2002; Zubko et al. 2005). One or several of the above-mentioned properties can be responsible for the particular polarization characteristics of Lutetia.

On the basis of the relationship between $P_{\rm min}$ and $\alpha_{\rm inv}$, Dollfus et al. (1975) noted that 21 Lutetia belongs to a group with a regolith of fines. This group was separated on the basis of the measurements of lunar fines with average grain sizes of the order of 10 μm across a range from smaller than 1 μm to several tens of microns (e.g., Geake & Dollfus 1986). Lutetia's data were later interpreted as being indicative of a metallic surface with a grain size of 20–40 μm (Dollfus et al. 1979). This conclusion was based on measurements of specific powders, such as titanium, dural, limonite, carbonyl iron globules, while the properties of neither pulverized iron meteorites nor pulverized enstatite chondrites were consistent with the polarimetric curves of M-type asteroids. Laboratory measurements of iron meteorites and enstatite chondrites with particle sizes smaller than 50 μm infer smaller inversion angles than measured for Lutetia's surface (Lupishko & Belskaya 1989). A CV3 type of carbonaceous chondrites was mentioned as the closest polarimetric analogue of Lutetia (Belskaya & Lagerkvist 1996).

Figure 7 shows an updated relationship between $P_{\rm min}$ and $\alpha_{\rm inv}$ for asteroids and meteorites. Among meteorites, the widest negative polarization branches are found for CV3 and CO3 types of carbonaceous chondrites. These types of chondrites are distinguished by their relative abundances of refractory inclusions, in particular calcium-aluminum rich inclusions (CAI) (e.g. Scott & Krot 2005). Sunshine et al. (2008) assumed that the presence in some CAIs of spinel, which has one of the highest indices of refraction among meteorite minerals, may explain the large inversion angles. Another possible explanation is related to the fine structure of CV3 and CO3 meteorite samples measured with the polarimetric technique. The measurements of cleavage faces of solid pieces and pulverized samples for CV3 Allende and CO3 Kanzas chondrites (Shkuratov et al. 1984) showed that the depth

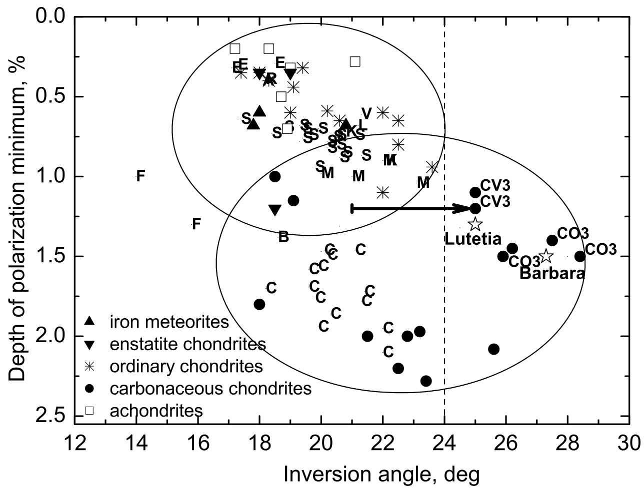

Fig. 7. Minimum polarization $P_{\rm min}$ (in absolute term) versus inversion angle for asteroids and meteorites. The two ellipses outline the location of carbonaceous chondrites and all other types of meteorites. The arrow shows the changes in the inversion angle for the CV3 chondrite Allende when these angles are measured for either a solid piece or a crushed sample. Data for meteorites are taken from Zellner et al. (1977), Geake & Dollfus (1986), Shkuratov et al. (1984), Lupishko & Belskaya (1989). Asteroid polarimetric parameters were calculated by fitting a linear-exponentional function to the data for individual asteroids in the Asteroid Polarimetric Database. Letters designate taxonomic class of asteroids according to the classification scheme of Tholen (1989).

of the negative branch was practically identical for powder and solid samples while the inversion angle noticeably increased for a powder sample (see Fig. 7). However it is difficult to explain why pulverized samples of other types of carbonaceous chondrites have smaller inversion angles.

Laboratory measurements are presently available for a rather limited sample of meteorites that do not cover all known meteorite classes. None of the measured iron meteorites nor enstatite and ordinary chondrites exhibited an inversion angle as large as found for Lutetia. Only particular types of carbonaceous chondrites are found to have a wide negative polarization branch. It is possible that a fine-grained mixture of components with highly different optical properties (carbon, silicates, irons) is required to produce the large inversion angle seen for Lutetia.

2.3. Spectral observations

The observations were performed during two runs in November 2004 at the TNG telescope at la Palma, Spain and in January 2007 at the NTT telescope of the European Southern Observatory in Chile.

At the TNG telescope, we used the DOLORES spectrometer with two grisms: the low resolution red grism (LR-R) covering the 0.51–0.95 μm range with a spectral dispersion of 2.9 Å/px and the medium resolution blue grism MR-B covering the 0.4–0.7 μm range with a dispersion of 1.7 Å/px . The spectra obtained were separately reduced and then combined together to obtain a spectral coverage from 0.4 to 0.95 μm. For the infrared range, we used the near infrared camera and spectrometer (NICS) equipped with an Amici prism disperser covering the 0.85–2.4 μm range.

At the NTT telescope, visible spectra were acquired using the EMMI instrument with the grism covering the wavelength range of 0.41–0.96 μm with a dispersion of 3.1 Å/px. The data acquisition and reduction techniques are described by

Table 3. Description of spectral observations of 21 Lutetia.

Date	UT-start (hh:mm)	T_{exp} (s)	Tel.	Instr.	Grism	Airm.	Solar analog
2004 11 04	23:35	40	TNG	DOLORES	LR-R	1.05	1
2004 11 15	23:37	40	TNG	DOLORES	MR-B	1.05	1
2004 11 16	01:10	40	TNG	DOLORES	LR-R	1.11	1
2004 11 16	01:12	40	TNG	DOLORES	MR-B	1.11	1
2004 11 16	03:06	40	TNG	DOLORES	LR-R	1.50	1
2004 11 16	03:08	40	TNG	DOLORES	MR-B	1.51	1
2004 11 18	23:11	60	TNG	NICS	AMICI	1.05	1
2007 01 20	08:47	120	NTT	EMMI	GR1	1.55	2
2007 01 20	08:42	240	NTT	EMMI	GR5	1.58	2

Notes. 1. Hyades64 (airmass 1.03). 2. La102-1081 (airmass 1.22).

Fornasier et al. (2008). The observational details are summarized in Table 3, which contains the date and UT-time at the start of observations, the exposure time, telescope, instrument, airmass of the object, the name and the airmass of solar analog star, and the number corresponding to the rotation phase at the time of the observation, as shown in Fig. 1.

The spectral data are presented in Fig. 8. Three visible spectra measured on Nov. 15/16 ($\alpha = 7.3°$) at different rotation phases (see arrows in Fig. 1) show noticeably different shapes. In two spectra (1 and 2), a broad band at 0.45–0.55 μm is clearly visible, while in the spectrum close to the lightcurve maximum (3) it is less evident. For comparison, we also presented the spectrum taken on May 26, 2004 by Barucci et al. (2005) at close to the same pole-on aspect but at a larger phase angle ($\alpha = 24°$), which does not contain a broad band at 0.45–0.55 μm. This band is also not seen in the spectrum taken in 2007. The spectrum corresponds to the opposite side of Lutetia from that covered by the spectra taken in 2004. The faint absorption around 0.83 μm seen in the spectrum is probably caused by the incomplete removal of telluric bands. On the other hand, the faint absorption feature around 0.43 μm appears in all our spectra and appears to be real.

The near-infrared spectrum measured on Nov. 18, 2004 at the phase angle of $\alpha = 8.8°$ is flat with a small negative slope. It does not show any features detectable within the noise of the data. We compared it with the spectrum obtained by Birlan et al. (2006) at the same opposition but at a larger phase angle $\alpha = 28.3°$ and did not detect any phase angle effect. Both spectra acquired at almost the same rotational phase are flat. The reddening at relatively high phase angle is not seen for Lutetia's surface in the spectral range of 0.8–2.5 μm.

Our visible spectra are in a good agreement with previous observations of Lutetia. In some of our spectra, we confirmed the presence of a broad feature at 0.45–0.55 μm previously reported by Lazzarin et al. (2009) for observations of the same 2004 apparition. Lazzarin et al. (2009) attributed this feature to a superposition of several absorption bands caused by a charge transfer involving various metal ions in pyroxenes. The faint absorption feature around 0.43 μm was not detected in the 2004 spectra by Lazzarin et al. (2009) but was identified in some Lutetia spectra obtained in both 2000 (Busarev et al. 2004; Prokof'eva et al. 2005) and in 2003 (Lazzarin et al. 2004). The feature was interpreted to be indicative of aqueous alteration activity (Lazzarin et al. 2004, 2009; Prokof'eva et al. 2005).

Both the features and the overall shape of spectrum appear tend to change with Lutetia's rotation. Variations in spectral slope over the surface were found previously by Nedelcu et al. (2007) in the near-infrared wavelength range and by Busarev (2008) in the visible range. These data are related to

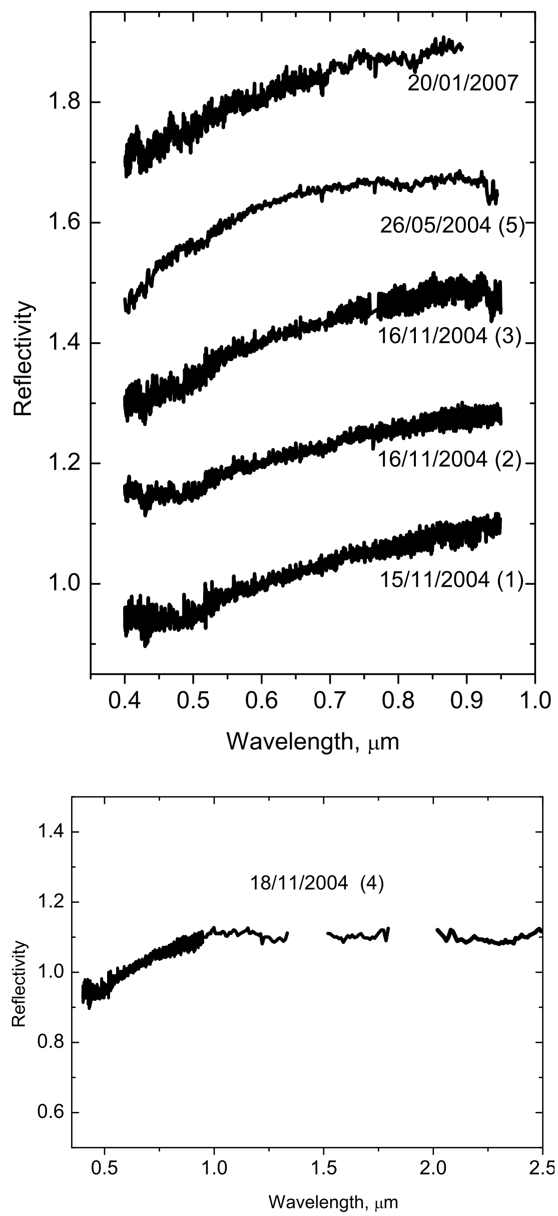

Fig. 8. Visual and near-infrared spectra of Lutetia. The spectra have been shifted by 0.2 for clarity. The numbers in parentheses correspond to the numbers in Fig. 1. The spectrum on May 26, 2004 was taken from Barucci et al. (2005).

the equatorial aspect and were interpreted as being indicative of variations in the surface mineralogy (Nedelcu et al. 2007). Our data corresponding to the aspect angle of 14 deg appear to confirm surface heterogeneity for Lutetia.

3. Discussion

We have described the results of photometric, polarimetric and spectral observations of Lutetia that indicate the use of different techniques provides a rather consistent picture of the main physical and optical properties of the asteroid which appears to have a highly heterogeneous surface. The conclusion follows from: 1) the non-zero lightcurve amplitude measured at the polar aspect; 2) spectral slope variations found at both the near polar and equatorial aspects; and 3) observed variations in polarization degree over the surface. These features could be explained by assuming a global non-convex shape (e.g. caused by a large crater) and a heterogeneous surface texture and/or mineralogy. The hypothesis of a large crater in the northern hemisphere was also proposed by Carvano et al. (2008) to explain the value of Lutetia's albedo $p_V = 0.13$ derived from their thermophysical model, which was smaller than the previous value of radiometric albedo $p_V = 0.22$ obtained by Mueller et al. (2006).

We have no strong evidence in favor of large albedo variegations over Lutetia's surface. Available radiometric measurements performed for different aspects infer rather consistent values of Lutetia's albedo in the range of 0.19–0.22 with an estimated uncertainty of 0.02 (Tedesco et al. 2002; Mueller et al. 2006; Lamy et al. 2008). Our new estimation of the polarization albedo of 0.16 ± 0.02 remains lower than radiometric albedo. However, it was shown in Sect. 2.2 that the determination of Lutetia's albedo from polarimetric data can be difficult because of the particular polarization properties of this asteroid. The measured values of opposition effect and phase slope are consistent with a moderate-albedo surface.

Using our precise determination of the absolute magnitude of Lutetia $H = 7.25$ mag for the near polar aspect (corresponding to observations in 2004 and 2008), we calculated its albedo from available size estimates for these apparitions. The albedo ranges from 0.18 for an assumed effective diameter of 110 km (Drummond et al. 2009) to 0.22 for an effective diameter of 100 km (Mueller et al. 2006). The above values of albedo correspond to zero phase angle and cannot be directly compared to the albedos of meteorites, which are usually measured at $\alpha \approx 3{-}5°$. We calculated the so-called four-degree albedo proposed by Shevchenko & Tedesco (2006) using $V(1,\ \alpha = 4°) = 7.63^{\mathrm{m}}$. This value roughly corresponds to the absolute magnitude of the asteroid without taking into account the opposition surge. The four-degree albedo of Lutetia is in the range of 0.13–0.16 for an effective diameter in the range of 100–110 km. These values of albedo are consistent with particular types of carbonaceous chondrites and enstatite chondrites and are smaller than typical values for iron meteorites (e.g. Gaffey 1976).

To compare the albedo and spectral properties of Lutetia with laboratory measurements, we need to take into account that these properties are sensitive to particle size. On the basis of the available data, we expect Lutetia's surface to be covered with fine-grained regolith. This conclusion follows from 1) the polarimetric properties of Lutetia characterizing by large inversion angle, and 2) the behaviour of the emissivity spectra of Lutetia with a narrow 10 μm emission feature (Feierberg et al. 1983; Barucci et al. 2008). According to estimations, at least a portion of Lutetia's surface should be covered by fine regolith with a grain size $\leq$20 μm.

Fine-grained mixtures of components with different optical properties (irons, silicates, carbon) can drastically alter the spectral reflectivity and suppress silicate bands (e.g. Feierberg et al. 1982). The particle size is not well-controlled in laboratory measurements of crushed meteorites because of the different fragility of the meteorite components. Moreover, the processes that can affect the optical properties of regolith exposed to space are not enough understandable to confidently interpret asteroid spectra (see Chapman 2004, for review). It is possible that the observed variations in spectral properties of Lutetia are related to the different exposure history of its regolith due to a large impact.

Both spectral and polarimetric observations indicate that Lutetia's surface properties are quite different from those of most asteroids studied so far. In a new asteroid taxonomy, Lutetia was classified in the Xc subclass (DeMeo et al. 2009), to which very few members belong, among them 97 Klotho, which has spectral properties similar to those of Lutetia (Vernazza et al. 2009). The polarization properties of Klotho (Belskaya et al. 2009) also resemble those of Lutetia and deviate distinctly from those of other moderate-albedo asteroids. We expect that these two bodies have a very similar surface composition. According to Vernazza et al. (2009), they are most probable candidates to be the parent bodies of enstatite chondrites. This conclusion has difficulties in explaining 1) the observed features in the Lutetia's visible spectra which are interpreted as being indicative of aqueous alteration material (Lazzarin et al. 2004, 2009; Busarev 2004); 2) the presence of a 3 μm feature associated with hydrated minerals (Rivkin et al. 2000); 3) the features of 5.2–38 μm emissivity spectrum (Barucci et al. 2008); and 4) the particular polarization properties of Lutetia. The above-mentioned features can be more naturally explained by assuming similarity of Lutetia's surface to particular types of carbonaceous chondrites. In turn, this assumption requires an explanation of relatively flat spectral slope of Lutetia toward ultraviolet wavelengths. Lazzarin et al. (2009) suggested several possible explanations but not exclude that available meteorite assemblages might not be representative of the Lutetia surface composition.

All of the above mentioned data are related to the surface properties of Lutetia. To constrain the interior composition, we need to estimate the mass and density of the asteroid. Although Prokof'eva-Mikhailovskaya et al. (2007) concluded about a complex satellite system of Lutetia, no satellites have yet been detected around the asteroid (Busch et al. 2009). The only available mass estimations of Lutetia come from the astrometric method and infer a density comparable to those of iron meteorites (Baer et al. 2009). However, available radar observations raise doubts about the reliability of the estimated mass. The radar albedo of Lutetia span from 0.17 ± 0.07 (Magri et al. 1999) to 0.24 ± 0.07 (Shepard et al. 2008) and both exclude a metallic surface composition. Radar data are consistent with the composition being similar to either enstantite chondrites or particular metal-rich CH type of carbonaceous chondrites (Shepard et al. 2010). A possible similarity with a CO/CV composition is also not excluded within the available uncertainties.

Observed variations in spectral and polarimetric properties across Lutetia's surface can be attributed not only to the heterogeneity of the surface texture but also of the surface composition, e.g. due to contamination during a large impact, which might also explain particular properties of Lutetia. However, neither satellites nor family members have yet been found for this asteroid. Previously classified as a member of Nysa family (Williams 1989), Lutetia does not belong to any family in later classifications (e.g., Zappala et al. 1995). Further study of these questions is needed. We note that the existence of satellites smaller than 6 km in diameter is not excluded by available observations (Busch et al. 2009).

4. Conclusions

On the basis of a detailed analysis of new photometric, polarimetric, and spectral data of the asteroid 21 Lutetia, together with observational data from the literature, we can draw some conclusions, which should be checked during the Rosetta fly-by:

– Lutetia has a non-convex shape, probably due to a large crater, and a heterogeneous surface properties, probably due to variations in the texture and/or mineralogy related to the surface morphology.
– At least part of Lutetia's surface is covered by regolith composed of particles with a mean grain size smaller than 20 μm.
– The closest meteorite analogues of Lutetia's surface composition are particular types of carbonaceous chondrites (CO, CV, CH). It is also possible that Lutetia has a specific surface composition that is not representative among studied meteorites or has a mixed mineralogy, e.g. due to surface contamination.

Flyby observations of Lutetia by the Rosetta spacecraft in July 2010 will provide a cross-check and verification of Earth-based remote sensing.

Acknowledgements. The research of INB has been supported by a Marie Curie Fellowship of the European Community. R.G.-H. acknowledges the support from CONICET through grant PIP114-200801-00205, and the partial financial support by CICITCA, Universidad Nacional de San Juan, through a research grant. We thanks to B. Carry for providing results on Lutetia's rotation properties prior to publication.

References

Baer, J., Chesley, S., & Britt, D. 2009, Asteroid Masses V1.0. EAR-A-COMPIL-5-ASTMASS-V1.0. NASA PDS
Barucci, M. A., & Fulchignoni, M. 2009, in Rosetta: ESA's Mission to the Origin of the Solar System (Springer Science), 55
Barucci, M. A., Fulchignoni, M., Fornasier, S., et al. 2005, A&A, 430, 313
Barucci, M. A., Fornasier, S., Dotto, E. et al. 2008, A&A, 477, 665
Belskaya, I. N., & Lagerkvist, C.-I. 1996, Planet. Space Sci., 44, 783
Belskaya, I. N., & Shevchenko, V. G. 2000, Icarus, 147, 94
Belskaya, I. N., Lupishko, D. F., & Shakhovskoj, N. M. 1987, Pis'ma Astron. Zh., 13, 530
Belskaya, I. N., Levasseur-Regourd, A.-C., Cellino, A., et al. 2009, Icarus, 199, 97
Birlan, M., Barucci, M. A., Vernazza, P., et al. 2004, New Astron., 9, 343
Birlan, M., Vernazza, P., Fulchignoni, M., et al. 2006, A&A, 454, 677
Bowell, E., Chapman, C. R., Gradie, J. C., Morrison, D., & Zellner, B. 1978, Icarus, 35, 313
Bowell, E., Hapke, B., Domingue, D., et al. 1989, in Asteroids II (Univ. of Arizona Press), 524
Busarev, V. V. 2008, In Asteroids, Comets, Meteors 2008, July 14–18, LPI Contr., 1405
Busarev, V. V., Bochkov, V. V., Prokof'eva, V. V., & Taran, M. N. 2004, in The New Rosetta Targets (ASSL Kluwer), 79
Busch, M. W., Kulkarni, S. R., & Conrad, A. 2009, Icarus, 203, 681
Carvano, J. M., Barucci, M. A., Delbo, M., et al. 2008, A&A 479, 241
Cellino, A., Gil-Hutton, R., Tedesco, E. F., Di Martino, M., & Brunini, A. 1999, Icarus, 138, 129
Cellino, A., Belskaya, I. N., Bendjoya, Ph., et al. 2006, Icarus, 180, 565
Chapman C. R. 2004, Ann. Rev. Earth & Planetary Sci., 32, 539
Chapman C. R., Morrison, D., & Zellner, B. 1975, Icarus, 25, 104
DeMeo, F. E., Binzel, R. P., Slivan, S. M., & Bus, S. J. 2009, Icarus, 202, 160
Dollfus, A., & Geake, J. E. 1975, In Lunar Sci Conf. Proc., 6th, Houston, 3, 2749
Dollfus, A., Mandeville, J. C., & Duseaux, M. 1979, Icarus, 37, 124
Dotto, E., Barucci, M. A., Fulchignoni, M., et al. 1992, A&AS, 95, 195
Drummond, J. D., Conrad, A., Merline, W., & Carry, B. 2009, DPS abstract, 41, 59.07
Feierberg, M. A., Larson, H. P., & Chapman, C. R. 1982, ApJ, 257, 361
Feierberg, M. A., Witteborn, F. C., & Lebofsky, L. A. 1983, Icarus, 56, 393
Fornasier, S., Belskaya, I., Shkuratov, Y. G., et al. 2006, A&A, 455, 371
Fornasier, S., Migliorini, A., Dotto, E., & Barucci, M. A. 2008, Icarus, 196, 119
Gaffey, M. J. 1976, JGR, 81, 905
Geake, J. E., & Dollfus, A. 1986, MNRAS, 218, 75
Jonson, T. V., & Fanale, F. P. 1973, JGR, 78, 8507
Gil-Hutton, R. 2007, A&A, 464, 1127
Gil-Hutton, R., Mesa, V., Cellino, A., et al. 2008, A&A, 482, 309
Kaasalainen, S., Piironen, J., Kaasalainen, M., et al. 2003, Icarus, 161, 24
Krugly, Yu. N., Belskaya, I. N., Shevchenko, V. G., et al. 2002, Icarus, 158, 294
Lagerkvist, C.-I., Erikson, A., Debehogne, H., et al. 1995, A&AS, 113, 115
Landolt, A. U. 1983, AJ, 88, 439
Landolt, A. U. 1992, AJ, 104, 436
Lamy, P. L., Barucci, A., Fornasier, S., et al. 2008, In Asteroids, Comets, Meteors, LPI Contr., 1405
Lasker, B. M., Sturch, C. R., Lopez, C., et al. 1988, ApJS, 68, 1
Lazzarin, M., Marchi, S., Magrin, S., & Barbieri, C. 2004, A&A, 425, L25
Lazzarin, M., Marchi, S., Moroz, L. V., & Magrin, S. 2009, A&A, 498, 307
Lumme, K., & Muinonen, K., 1993, Abstr. for the IAU Symp. 160, Asteroids, Comets, Meteors, 194
Lupishko, D. F., & Belskaya, I. N. 1989, Icarus, 78, 395
Lupishko, D. F., & Vasilyev, S. V. 2008, Asteroid Polarimetric Database V6.0, NASA PDS
Lupishko, D. F., Belskaya, I. N., & Tupieva, F. A. 1983, Pis'ma Astron. Zh., 9, 691
Lupishko, D. F., Velichko, F. P., Belskaya, I. N., & Shevchenko, V. G. 1987, Kinem. Fiz. Nebesn. Tel, 3, 36
Lupishko, D. F., Belskaya, I. N., Kvaratskheliia, O. I., Kiselev, N. N., & Morozhenko, A. V. 1988, Astron. Vestnik, 22, 142
Magri, C., Ostro, S. J., Rosema, K. D., et al. 1999, Icarus, 140, 379
Masiero, J., & Cellino, A. 2009, Icarus, 199, 333
Mishchenko, M. I., Rosenbush, V. K., & Kiselev, N. N. 2006, Appl. Opt. IP, 45, 4459
Mottola, S., Gonano-Beurer, M., Green, S. F., et al. 1994, Planet. Space Sci., 42, 21
Mueller, M., Harris, A. W., Bus, S. J., et al. 2006, A&A, 447, 1153
Muñoz, O., Volten, H., de Haan, J. F., Vassen, W., & Hovenier, J. W. 2000, A&A, 360, 777
Nedelcu, D. A., Birlan, M., Vernazza, P., et al. 2007, A&A, 470, 1157
Prokof'eva, V. V., Bochkov, V. V., & Busarev, V. V. 2005, Solar System Res., 39, 410
Prokof'eva-Mikhailovskaya, V. V., Batrakov, Yu.V., Bochkov, V. V., Busarev, V. V., & Karachkina, L. G. 2007, Solar System Res., 41, 307
Rivkin, A. S., Howell, E. S., Lebofsky, L. A., Clark, B. E., & Britt, D. T. 2000, Icarus, 145, 351
Scott, E. R. D., & Krot, A. N. 2005, ASP Conf. Ser., 341
Shepard, M. K., Clark, B. E., Nolan, M. C., et al. 2008, Icarus, 195, 184
Shepard, M. K., Clark, B. E., Oskert-Bell, M., et al. 2010, Icarus, in press
Shevchenko, V. G., & Tedesco, E. F. 2006, Icarus, 184, 211
Shkuratov, Yu. G., Akimov, L. A., & Tishkovets, V. P. 1984, SvA Lett., 10, 331
Shkuratov, Yu. G., Muinonen, K., Bowell, E., et al. 1994, EMP, 65, 201
Shkuratov, Yu. G., Ovcharenko, A., Zubko, E., et al. 2002, Icarus, 159, 396
Sunshine, J., Kolokolova, L., Connolly, H. C., et al. 2008, BAAS, 40, 509
Tedesco, E. F., Noah, P. V., Noah, M., & Price, S. D. 2002, AJ, 123, 1056
Tholen, D. J. 1989, in Asteroids II, ed. R. P. Binzel, T. Gehrels, & M. S. Matthews (Tucson: Univ. of Arizona Press), 1139
Torppa, J., Kaasalainen, M., Michalowski, T., et al. 2003, Icarus, 164, 346
Vernazza, P., Brunetto, R., Binzel, R. P., et al. 2009, Icarus, 202, 477
Williams, J. G. 1989, in Asteroids II (Univ. of Arizona Press), 1034
Zappala, V., di Martino, M., Knezevic, Z., & Djurasevic, G. 1984, A&A, 130, 208
Zappala, V., Bendjoya, Ph., Cellino, A., Farinella, P., & Froeschle, C. 1995, Icarus, 116, 291
Zellner, B., & Gradie, J. 1976, AJ, 81, 262
Zellner, B., Leake, M., Lebertre, T., Duseaux, M., & Dollfus, A. 1977, Proc. Lunar Sci. Conf., 8th, 1, Houston, Tex., 1091
Zubko, E., Petrov, D., Shkuratov, Yu., & Videen, G. 2005, Appl. Opt. IP, 44, 6479

Chapitre 3

La mission Rosetta

3.1 Introduction

Rosetta est la mission phare de l'agence spatiale européenne (ESA) dédiée à l'étude des petits corps du Système Solaire. Succédant à Giotto, qui a survolé successivement la comète de Halley et la comète Grigg-Skjellerup, la sonde Rosetta aura une mission beaucoup plus ambitieuse, consistant à se placer en orbite autour d'un noyau cométaire et à en analyser la surface *in situ*. Emportant 12 équipements scientifiques, Rosetta effectuera de nombreuses mesures, procédera à une cartographie complète du noyau et observera les modifications d'activité de la comète au fur et à mesure que celle-ci s'approchera du Soleil. Elle larguera aussi un atterrisseur de 100 kg et fournira des informations inédites sur la nature et la composition du noyau. Rosetta étudiera la matière primordiale constituant les comètes et les astéroïdes, et permettra donc une bien meilleure compréhension de la formation du Système Solaire et des processus qui ont marqués son évolution, d'où le nom donné à la mission, par analogie avec la "pierre de Rosette", qui a permis à Champollion de déchiffrer les hiéroglyphes égyptiens.

La cible principale de la mission est la comète 67P/Churyumov-Gerasimenko, qui sera rejointe par Rosetta en mai 2014 à une distance d'environ 4 UA. Lors de son périple vers la comète, Rosetta a effectué 3 assistances gravitationnelles avec la Terre et 1 avec Mars, et a survolé deux astéroïdes de la ceinture principale, 2867 Steins et 21 Lutétia. En effet, les cibles de la mission ont été totalement redéfinies suite à des problèmes avec le lanceur Arianne 5 G+ en 2003. Á l'origine, la comète Wirtanen et les astéroïdes 140 Siwa et 4979 Otawara étaient les cibles de la mission. Le lancement a été reporté d'un an et la mission a été lancée avec succès le 2 mars 2004, mais ceci a entrainé la modification du plan de vol et des cibles de la mission.
En 2003-2004 j'ai participé activement aux observations des astéroïdes cibles potentielles de la mission. En effet les 2 astéroïdes, cibles secondaires de la mission, ont été sélectionnés par l'ESA après le lancement de la sonde et la vérification de ressources disponibles pour effectuer deux survols avec deux astéroïdes de la ceinture principale. Sur la base du Δv disponible, l'ESA a décidé les survols de 2 objets appartenant à des types spectraux jamais observés auparavant par des sondes : 2867 Steins, objet igné avec un albédo élevé et une composition dominée par l'enstatite, de type E, et 21 Lutétia, un astéroïde assez grand (diamètre de 100 km) de la ceinture principale, dont la composition de surface et la classe taxonomie étaient (et sont encore) débattues (classe C ou M).

Dès 1998 j'ai commencé à m'investir sur la mission Rosetta avec des activités scientifiques et instrumentales : observations au sol de ses cibles, afin d'améliorer leur connaissance et donc optimiser l'orbite de la sonde et les séquences observationnelles pendant les rencontres, participation active à la réalisation de la caméra à grand champ de vue WAC du système d'imagerie OSIRIS

(travail de caractérisation de propriétés optiques des matériaux employés dans la caméra WAC et simulations de type *ray-tracing* de son complexe système de suppression de la lumière diffuse), et participation à toutes les activités de calibration scientifique faites au MPS (Max-Planck-Institut für Sonnensystemforschung), en Allemagne, dans le calme et bucolique village de Lindau.
Suite à ces efforts, je suis entrée officiellement dans l'équipe OSIRIS, d'abord comme scientifique associée, et, dès 2006, comme co-investigatrice. J'ai participé ensuite à la définition des séquences observationnelles pour les observations scientifiques (les OIOR, Orbiter Instrument Operation Request), à l'analyse des images et à l'activité de calibration en vol, devenant responsable des calibrations photométriques d'OSIRIS. Je suis membre de 3 groupes de travail qui gèrent les différentes phases de la mission (survol des astéroïdes, calibration et noyau cométaire). J'ai participé à la rédaction de plusieurs rapports techniques et effectué de nombreuses présentations dans les réunions de l'équipe et dans des congrès scientifiques. C'est seulement après 7 ans de travail (de ma part, mais encore plus pour les collègues qui ont entamé ce projet) sur Osiris-Rosetta que tous ces efforts ont été récompensés avec la première publication dans une revue à comité de lecture (dédiée aux observations de la comète Tempel 1), suivie, heureusement, des merveilleuses images et des exceptionnels résultats des 2 survols des astéroïdes Steins et Lutétia.

Avoir participé à la réalisation de la WAC, avoir passé beaucoup de nuits sans sommeil pour les calibrations scientifiques au MPS (le jour étant réservé au travail des ingénieurs), avoir vécu les innombrables problèmes et imprévus (fort heureusement résolus !) qui accompagnent la réalisation d'un instrument spatial, cela ajouté aux craintes concernant la fiabilité du lanceur Arianne 5G+, au renvoi du lancement de Rosetta et à la redéfinition de son orbite et de ses cibles..., tout ceci a rendu la mission Rosetta unique à mes yeux et dans mon cœur, et je dois avouer que la toute première image du ciel acquise par la WAC le 25 avril 2004, avec ses 144 degrés carrés pleins d'étoiles, m'a remplie d'émotion jusqu'aux larmes.

3.2 Partie instrumentale : le système d'imagerie OSIRIS

Je suis co-investigatrice du système d'imagerie OSIRIS et très fortement impliquée dans les calibrations de l'instrument. Dès 1998 j'ai commencé à travailler sur la caméra à grand champ de vue ($12 \mathrm{x} 12^o$) WAC (Wide Angle Camera) d'OSIRIS, qui comprend aussi une caméra à haute résolution NAC (Narrow Angle Camera, 2.3×2.3^o), réalisée au LAM de Marseille. La WAC a été réalisée au Centre des sciences et des activités spatiales 'G. Colombo' (CISAS) de l'Université de Padoue, où j'ai fait mon doctorat en cotutelle avec l'Université Paris Diderot. Cette caméra a comme objectif principal l'étude du noyau cométaire, du gaz et de la poussière de la coma avec des filtres étroits centrés sur des longueurs d'onde typiques de certaines émissions cométaires. En particulier, avec son grand champ, la WAC doit analyser les faibles émissions de gaz et de poussière de la coma cométaire, ce qui demande une forte capacité de contraste.
Pour atteindre ces objectifs la WAC a été créée avec un dessin optique innovateur, avec deux miroirs asphériques hors d'axe et un système complexe de suppression de la lumière diffuse afin d'améliorer la capacité de contraste et de pouvoir détecter des sources faibles.

3.2.1 La caméra WAC : le système de suppression de la lumière diffuse

La WAC doit donner des images de la comète avec le meilleur contraste possible. Le contraste se dégrade généralement à cause de la lumière diffuse (*stray-light*) présente dans la caméra : ceci correspond à la lumière qui entre dans le système en dehors du champ de vue, ou celle qui passe par le champ de vue mais en dehors de la pupille d'entrée et va se réfléchir sur la structure intérieure de la caméra ou sur les montages des optiques. Afin de réduire la lumière diffuse, on a mis à l'intérieur de la caméra des cloisons rectangulaires, placées de façon à ne pas intercepter les rayons utiles et recouverts par un vernis très absorbant. L'ensemble des éléments destinés au contrôle de la lumière diffuse s'appelle système de 'baffling'. Pour la WAC, ce système a un dessin très compliqué car il doit satisfaire à 2 contraintes : 1) on demande que la réduction de la lumière diffuse produite par des sources situées à l'extérieur du champ de vue (à 45^o d'incidence) soit meilleure que 10^{-9} 2) on demande que la réduction de la lumière diffuse produite par des sources situées dans le champ de vue de la caméra soit meilleure que 10^{-4} afin de réussir à étudier les émissions de la poussière et du gaz proche du noyau cométaire.

J'ai commencé mes activités sur OSIRIS en travaillant justement sur le système de 'baffling' de la caméra. Une première partie du travail a été consacrée à l'activité de simulation des performances de ce système grâce au logiciel de *ray-tracing* OPTICAD. Tous les éléments optiques de la WAC et les cloisons, considérés comme des surfaces très absorbantes (absorption de 95%) avec des propriétés lambertiennes, ont été insérés dans le logiciel de simulation. On a donc simulé des sources situées à l'infini à l'extérieur comme à l'intérieur du champ de vue en utilisant un nombre élevé de rayons (400000-1000000, chose qui a requis à l'époque un grand temps de calcul pour chaque position) en faisceaux inclinés pour différents angles d'incidence. Grâce aux simulations nous avons ainsi pu vérifier la qualité du système et ses performances, qui satisfaisaient aux contraintes exigées.

Par la suite j'ai travaillé sur une caractérisation spectrale et goniophotométrique complète des matériaux utilisés dans la caméra, afin d'en vérifier leurs propriétés optiques. Cette activité a été importante pour vérifier que l'absorption des matériaux reste dans les limites requises et qu'elle ne compromettrait pas les performances de la caméra. On demande en effet que les matériaux utilisés dans le système de 'baffling' aient des valeurs d'absorption de la lumière très hautes (supérieures à 95%) et des propriétés optiques diffusantes avec une petite composante spéculaire. Les mesures spectrophotométriques, de réflectivité avec une sphère intégrante, de brillance avec un glossimètre et enfin de réflectivité bidirectionnelle avec un gonioréflectomètre sur différents échantillons vernis ont été faites à la Stazione Sperimentale del Vetro (SSV), à Murano, Venise, et à l'Istituto Elettrotecnico Nazionale Galileo Ferraris (IENGF), à Turin.

Les mesures ont permis de choisir le vernis Electrodag 501 pour les cloisons internes du système de *baffling* de la caméra. Ce vernis a montré la meilleure performance en terme d'absorption de la lumière dans le domaine de longueur d'onde de la WAC. Quand à la partie extérieure du baffling, elle a été réalisée avec de la fibre de verre vernie en utilisant 3 couches de Electrodag 501, combinaison qui a montré une très faible réflectivité. J'ai montré avec ces mesures que la fibre de verre a une petite réflectivité, légèrement supérieure à 5% lorsqu'il n'y a pas de vernis, donc ce matériel donne des bonnes performances même en cas de forte dégradation.
Enfin, j'ai effectué des mesures sur des échantillons anodisés et allodinés pour la partie intérieure du couvercle de la caméra. Celle-ci doit avoir une réflectivité élevée et des propriétés diffusantes, car elle doit réfléchir la lumière provenant de lampes de calibration interne de la WAC (ceci est nécessaire pour des mesures de référence de la caméra, afin d'évaluer la dégradation de l'optique et des matériaux pendant le long voyage). Suite aux mesures, nous avons choisi l'échantillon anodisé, qui a montré une réflectivité à peu près constante sur l'intervalle de longueur d'onde d'intérêt.

3.2.2 OSIRIS : les calibrations scientifiques faites au sol

Après la réalisation de la caméra, j'ai participé à l'activité de calibration scientifique qui a eu lieu au Max Planck Institut fur Sonnensystemforschung (MPS), Lindau, Allemagne pendant l'été 2001. Ce travail a été fait soit sur le modèle de qualification (QM) de la caméra, soit (et surtout) sur le modèle de vol (FM). Pendant cette activité on a mis en évidence des problèmes qui auraient compromis les performances de l'instrument, et qui heureusement ont été résolus en temps utile :

1. problèmes avec les performances de l'obturateur. L'analyse des formes d'onde envoyées à l'obturateur et les améliorations ultérieures ont permis le bon fonctionnement de ce mécanisme délicat.
2. Détection des nombreux défauts (dits défaut *pinhole*) sur le vernissage des filtres ultraviolets de la WAC, responsables de la détérioration de l'image sur le détecteur. Il n'a pas été possible de résoudre ces défauts, mais leurs positions ont été bien localisées pour chaque filtre et une procédure mathématique de correction de ces effets sur les images scientifiques a été développée.
3. Détection de lumière diffuse dans la WAC, due soit à la lumière passant entre l'arrière du miroir M1 et la structure de la caméra, soit enfin à une petite fente entre les filtres et leur structure de logement.

Une analyse précise a permis d'identifier les problèmes qui ont été résolus en apportant des modifications structurelles et en demandant à l'ESA un délai sur la livraison de la WAC. Nous avons procédé aux vérifications sur le caractère fonctionnel de la caméra et aux calibrations scientifiques. Nous avons effectué les calibrations concernant le détecteur (courant d'obscurité, biais, *flat field*, carte des mauvais pixels), les calibrations radiométriques (mesures radiométriques absolues, lampes de calibration, mesures de lumière diffuse et de polarisation), les calibrations géométriques et optiques (performances optiques du télescope, calibrations des filtres, vérification du foyer et de sa dépendance avec la température, distorsion géométrique, résolution de la caméra, *Point Spread Function (PSF), vignetting*), et enfin les calibrations spectrales (fonction de réponse du CCD et réponse spectrale absolue).

3.3 Les observations en vol

Dès la première lumière en avril 2004, l'instrument OSIRIS a fonctionné très bien et a déjà acquis plus de 4000 images avant de rejoindre sa cible principale, la comète 67P. Une bonne partie de ces images sont issues des rencontres planifiées avec les astéroïdes Steins et Lutétia, dont je résumerai quelques résultats dans les sections qui suivent, mais également des calibrations et des événements non prévus initialement, comme la campagne d'observations de la comète Tempel 1 en 2005. OSIRIS a donc déjà observé :

– 4 comètes : Tempel 1, LINEAR 2002 T7, Machholz 2004 Q2 et 67P. La comète Tempel 1 a été observée par OSIRIS pendant 18 jours, 8 avant et 10 après l'impact du projectile envoyé par la sonde Deep Impact le 4 juillet 2005, et les résultats ont été publiés par Küppers et al. (2005) et Keller et al. (2007). Les autres comètes ont fait l'objet d'observations ponctuelles et, en particulier, la comète 67P, cible de la mission, a été détectée le 25/26 mars 2011 par OSIRIS-NAC, juste avant l'hibernation de la sonde, sur des images combinées sur 13 heures d'observations (magnitude de la comète 19.9 !).
– 3 astéroïdes : 2867 Steins et 21 Lutétia pendant les rencontres respectivement en 2008 et 2010, et 4 Vesta en mai 2010, pour tester la calibration absolue de l'instrument. Steins et Lutétia ont été aussi observés par OSIRIS avant leur rencontre pour en obtenir des courbes de lumière à grand angle de phase et contraindre leurs propriétés rotationnelles (Küppers et al. 2007, Lamy et al. 2008a).
– L'objet P/2010 A2, découvert en janvier 2010 et classifié comme comète suite à la présence de matière dispersé autour de lui. Les images d'OSIRIS ont montré que la matière autour

de l'objet ne vient pas d'une activité cométaire mais est issue d'une collision ayant eu lieu en février 2009 qui a dispersé de larges particules (Snodgrass et al. 2010).
- La Terre et la Lune en novembre 2007 et 2009 lors de la deuxième et troisième assistance gravitationnelle avec la Terre (OSIRIS n'était pas active pendant le premier survol de la Terre en février 2005).
- Mars et ses satellites Phobos et Deimos pendant l'assistance gravitationnelle avec Mars en février 2007.
- Plusieurs étoiles pour les calibrations en flux absolues (Vega et 16 Cygne A&B en particulier) et des champs d'étoiles pour les calibrations géométriques des caméras.

3.3.1 Calibration radiométrique et vérification sur l'astéroïde Vesta

Je suis responsable des calibrations radiométriques absolues du système d'imagerie OSIRIS. Je participe donc à l'activité d'observation et à l'analyse des étoiles standard qui nous permettent de transformer le flux de chaque pixel de DU/s en W/(m^2 nm sr). En effet, après le lancement, nous nous sommes aperçus des différences considérable entre les coefficients de calibrations obtenus au sol avec des lampes calibrées et ceux obtenus en vol. Nous avons donc essayé de comprendre quelle était la raison de ces différences et quels coefficients il fallait utiliser. J'ai analysé les données de plusieurs étoiles pour en dériver les coefficients de calibration radiométrique. Pour vérifier leur fiabilité, l'équipe OSIRIS a demandé et obtenu des observations de 4 Vesta dont le spectre est bien connu. Vesta a donc été observé le 1er mai 2010 avec plusieurs filtres des caméras WAC et NAC, pour une durée de 10.8 heures et à un angle de phase très grand (52.5^o), non observable depuis la Terre. Vesta était à une distance de 0.28 UA de Rosetta, ce qui donne une résolution de 800 km/px avec la NAC. Les résultats de la spectrophotométrie montrent un parfait accord avec les spectres de Vesta obtenus au sol, ce qui nous permet de valider les coefficients de calibration radiométrique.
Les observations ont aussi donné des résultats scientifiques importants (voir Fornasier et al. 2011b), car ces données prises à grand angle de phase ont permis de contraindre la fonction de phase de Vesta, de dériver les paramètres G (0,27$\pm$0,01) et la magnitude absolue H (2,80$\pm$0,01 en R), d'obtenir une courbe de lumière à phase élevée, donnant une amplitude de 0,19 et une période de 5,355$\pm$0,025 heures, et d'estimer l'albédo à plusieurs longueurs d'onde (0,34 à 535 nm). Toutes ces informations ont été très appréciées par l'équipe de la mission Dawn, qui est en train d'observer Vesta, car cela leur a permis une meilleure estimation du temps de pose.
La spectrophotométrie de Vesta obtenue par OSIRIS est en parfait accord avec les résultats obtenus avec les télescopes Swift et HST (Li et al. 2011). La comparaison avec les météorites confirme une forte similitude entre Vesta et les spectres des grains d'howardites de tailles relativement petites ($<$25 μm).

3.3.2 Article : Photometric observations of asteroid 4 Vesta by the OSIRIS cameras onboard the Rosetta spacecraft

A&A 533, L9 (2011)
DOI: 10.1051/0004-6361/201117600

Astronomy & Astrophysics

Letter to the Editor

Photometric observations of asteroid 4 Vesta by the OSIRIS cameras onboard the Rosetta spacecraft⋆

S. Fornasier[1,2], S. Mottola[3], M. A. Barucci[1], H. Sierks[4], and S. Hviid[4]

[1] LESIA-Observatoire de Paris, CNRS, UPMC Univ. Paris 06, Univ. Paris-Diderot, 5 place J. Janssen, 92195 Meudon Pricipal Cedex, France
e-mail: sonia.fornasier@obspm.fr
[2] Univ. Paris Diderot, Sorbonne Paris Cité, 4 rue Elsa Morante, 75205 Paris, France
[3] Institute of Planetary Research, DLR, Rutherfordstrasse 2, 12489 Berlin, Germany
[4] Max-Planck-Institut für Sonnensystemforschung, Max-Planck-Strasse 2, 37191 Katlenburg-Lindau, Germany

Received 30 June 2011 / Accepted 13 August 2011

ABSTRACT

Aims. We report on new observations of asteroid 4 Vesta obtained on 1 May 2010 with the optical system OSIRIS onboard the ESA Rosetta mission. One lightcurve was taken at a phase angle (52°) larger than achievable from ground-based observations together with a spectrophotometric sequence covering the 260 to 990 nm wavelength range.

Methods. Aperture photometry was used to derive the Vesta flux at several wavelengths. A Fourier analysis and the HG system formalism were applied to derive the Vesta rotational period and characterize its phase function.

Results. We find a G parameter value of 0.27 ± 0.01 and an absolute magnitude $H(R) = 2.80 \pm 0.01$. The lightcurve has the largest amplitude ever reported for Vesta (0.19 ± 0.01 mag), and we derive a synodic rotational period of 5.355 ± 0.025 h. The Rosetta spectrophotometry, covering the Vesta western hemisphere, is in perfect agreement with visible spectra from the literature and close to the IUE observations related to the same hemisphere. The new spectrophotometric data reveal that there is no global ultraviolet/visible reversal on Vesta. The Vesta spectrophotometry is well reproduced by spectra of howardite meteorite powders (grain size <25 μm). From the Rosetta absolute spectrophotometry and from the phase function behaviour, we estimate a geometric albedo of 0.36 ± 0.02 at 649 nm and 0.34 ± 0.02 at 535 nm.

Key words. minor planets, asteroids: individual: 4 Vesta – techniques: photometric

1. Introduction

Vesta is the most massive asteroid in the main belt (considering that Ceres has been classified as a dwarf planet) orbiting the Sun at a distance of about 2.36 AU. From HST images, Thomas et al. (1997a) derived a Vesta shape fit by an ellipsoid with semi-axes of 289, 280, 229 (±5) km, and J2000 pole coordinates RA = 308 ± 10°, Dec = 48 ± 10°, which was more recently updated to RA = 305.8 ± 3.1°, Dec = 41.4 ± 1.5° (Li et al. 2011a). These HST data were also analysed to uncover a large (460 km wide) basin near the south pole with a pronounced central peak of 13 km, together with other depressions and large craters (Thomas et al. 1997b). The discovery of substantial impact excavation on Vesta is consistent with the idea that this asteroid is the source of HED meteorites. Several "Vestoids", i.e. asteroids with spectral properties and orbital parameters similar to Vesta, have also been discovered. They have therefore probably been caused by impact events on Vesta.

Vesta is large enough to have experienced a differentiation phase during its accretion and is the only large asteroid known to have a basaltic surface that retains a record of ancient volcanic activity (McCord et al. 1970; Gaffey et al. 1997). Geological diversity revealing longitudinal variations in albedo and mineralogy was detected from polarimetric and spectroscopic measurements obtained at different rotational phases (Gaffey 1997; Binzel et al. 1997; Li et al. 2010).

Vesta is the first target of the NASA Dawn mission, that just entered orbit around the asteroid in July 2011 and will remain in orbit for one complete year, undertaking a detailed study of its geophysics, mineralogy, and geochemistry (Russell et al. 2007; Sierks et al. 2011).

In this paper we report on observations of Vesta obtained with the scientific optical camera system OSIRIS onboard Rosetta. One new lightcurve taken at an unprecedented large phase angle (52°) has been obtained together with spectrophotometry from 260 to 990 nm. These data, taken at a nearly equatorial aspect, allow us to more tightly constrain the Vesta phase function, to provide the absolute reflectance from the UV to the NIR range at large phase angle, and to estimate the geometric albedo.

2. Observations and data reduction

OSIRIS is the imaging system onboard Rosetta mission. It consists of a narrow-angle camera (NAC, field of view of 2 × 2°) and a wide-angle camera (WAC, field of view of 12 × 12°). They are unobstructed mirror systems with focal lengths of 72 cm and 14 cm, respectively. Both cameras are equipped with 2048 × 2048 pixel CCD detectors with a pixel size of 13.5 μm. The image scale is 3.9 arcsec/pixel for the NAC and 20.5 arcsec/pixel for the WAC. The cameras have a set of broadband and narrowband filters covering the wavelength range 240–990 nm. We refer to Keller et al. (2007) for a detailed description of the instrument.

⋆ Table 2 is available in electronic form at http://www.aanda.org

During its approach to asteroid 21 Lutetia, which was successfully flown by on 10 July 2010, Rosetta observed the asteroid 4 Vesta on 1 May 2010 for a total duration of 10.8 h. These observations included lightcurve coverage with the two "red" filters of the cameras (the NAC filter F22 centred at 649.2 nm, and the WAC filter F12, centred at 629.8 nm), and a spectrophotometric sequence including 12 NAC filters and 9 WAC filters, covering the wavelength range 269−989 nm (Table 1). The observations were made at a spacecraft-target distance $0.285879 < \Delta < 0.283682$ AU, at a Vesta heliocentric distance of 2.324 AU, and at a phase angle $52.1 < \alpha < 52.8°$, the largest one covered up to date, before the DAWN encounter. Vesta was observed at equatorial aspect, at a sub-spacecraft latitude of 3.0−2.7°, and was not resolved (resolution of 800 km/px and 4000 km/px with the NAC and WAC cameras, respectively).

The data were reduced using the OSIRIS standard pipeline, but the flux calibration was done using revised values of the conversion factors that had been recently computed. The data reduction steps are the same as those described in Küppers et al. (2007). The data are converted from digital units to W m^{-2} nm^{-1} sr^{-1}, using conversion factors derived from observations of Vega taken on 1 May 2010 and 12 July 2010. These factors were reduced to a solar input spectrum. The absolute calibration factors were computed using the Vega (*alpha_lyr_stis_*005.*ascii*) and sun flux (*sun_reference_stis_*001.*ascii*) standard spectra from the HST CALSPEC catalogue[1].

The Vesta flux was calculated from the images using aperture photometry with an aperture radius of five (WAC) and six (NAC) pixels. These radii allow us to acquire more than 99% of the target flux and to minimize the background contribution and cosmic ray hits. Aperture correction factors were derived from the high signal-to-noise ratio observations of Vega and the fluxes were divided by 0.992446 for the WAC and 0.992918 for the NAC observations to get the total flux (estimated from Vega growth curves for an aperture of 15 px). The background was evaluated in four rectangular regions around the target and then subtracted from the total flux.

3. Lightcurve and phase function

We used the 44 WAC and NAC images in the red filters to build the Vesta lightcurve. To derive the absolute magnitude at the observed phase angle, we follow the method described by Küppers et al. (2007). We first corrected the Vesta flux by considering its spectrum, which is redder than that of the sun, using:

$$F_c = F_o \times \frac{\int_\lambda F_\odot(\lambda)T(\lambda)\mathrm{d}\lambda}{\int_\lambda F_{\mathrm{Vesta}}(\lambda)T(\lambda)\mathrm{d}\lambda}, \quad (1)$$

where F_c and F_o are the corrected and uncorrected Vesta fluxes at a given central filter wavelength λ_c, $T(\lambda)$ is the system throughput (telescope optics and CCD quantum efficiency), $F_\odot(\lambda)$ and $F_{\mathrm{Vesta}}(\lambda)$ are solar (from HST catalogue) and Vesta spectra (from Xu et al. 1995), respectively, both normalized to unity at the λ_c of the considered filter.

The absolute magnitude $R(1, 1, \alpha)$ reduced to the R-Bessel filter was finally computed, and we derived a mean value of 4.485 ± 0.003. The data were phase corrected to $\alpha = 52.26°$ using the HG phase function with $g = 0.27$, as described later in the paper. The results are shown in Fig. 1 and reported in Table 2. The lightcurve is single peaked, consistent with an albedo driven behaviour. Its amplitude is 0.19 ± 0.01, the largest one observed so far for Vesta as a consequence of the well-known amplitude-phase effect (Zappalá et al. 1995).

[1] www.caha.es/pedraz/SSS/HST_CALSPEC

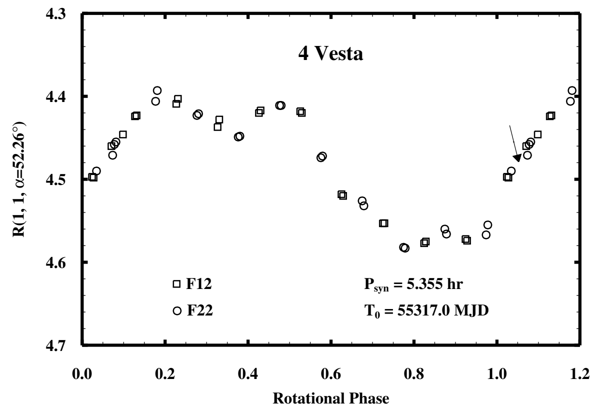

Fig. 1. The lightcurve of asteroid 4 Vesta from OSIRIS observations. The arrow show the rotational phase corresponding to the spectrophotometric data set acquisition. Points beyond rotational phase 1.0 are repeated for clarity. F12 and F22 are the red filters of the WAC and NAC cameras, respectively.

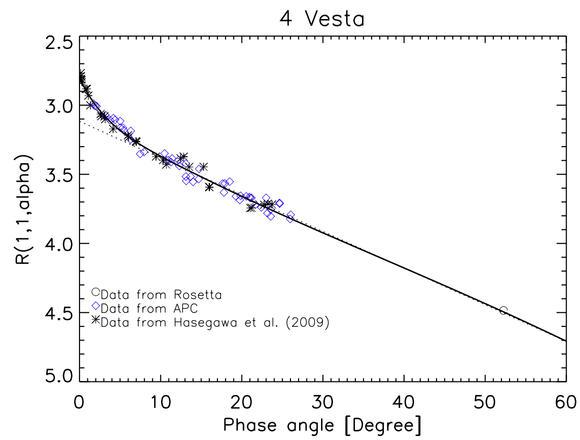

Fig. 2. Phase curve of asteroid 4 Vesta. Beside the Rosetta point, data come from the Asteroid Photometric Catalogue (Lagerkvist et al. 1995) and from Hasegawa et al. (2009). The dashed-line represents the linear fit to the data.

The Vesta time-series were modelled with a ninth order Fourier polynomial (Harris et al. 1989), whose best-fit relation corresponded to a synodic rotation period (P_{syn}) of 5.355 ± 0.025 h. The relatively large error is related to the limited time-span of the Rosetta observations. The data folded with the best-fit period are shown in Fig. 1. The Rosetta P_{syn} is slightly longer, but still compatible within the error bars, than the very precise value of the sidereal period ($5.34212971 \pm 0.00000096$ h) derived by Drummond et al. (1998).

The Rosetta observations, taken at a large phase angle, are important to constrain the Vesta phase function. We compiled the asteroid phase curve in R band (Fig. 2) combining the Rosetta data with those coming from the Asteroid Photometry Catalogue (APC, V filter) dataset (Lagerkvist et al. 1995), and from Hasegawa et al. (2009, R filter). We used a $V - R$ colour index of 0.385, derived from a Vesta visual spectrum (Xu et al. 1995) to combine the visual magnitude from the APC with the other data. We take the mean value from each individual data

Table 1. Vesta spectrophotometry from Osiris.

UT_{start}	Inst.	F	λ_c	exp. (s)	$F_{Abs}(\alpha)$	p
10:56:26	NAC	15	269.30	48.52	0.021 ± 0.002	0.10
10:57:26	NAC	16	360.00	1.67	0.042 ± 0.002	0.20
10:57:39	NAC	28	743.70	0.26	0.080 ± 0.001	0.38
10:57:50	NAC	27	701.20	0.74	0.078 ± 0.002	0.37
10:58:03	NAC	24	480.70	0.23	0.066 ± 0.002	0.32
10:58:14	NAC	23	535.70	0.24	0.071 ± 0.001	0.34
10:58:25	NAC	22	649.20	0.15	0.076 ± 0.001	0.36
10:58:37	NAC	41	882.10	0.70	0.057 ± 0.001	0.27
10:58:49	NAC	51	805.30	0.79	0.072 ± 0.001	0.34
10:59:01	NAC	61	931.90	1.96	0.055 ± 0.001	0.26
10:59:14	NAC	71	989.30	4.34	0.061 ± 0.002	0.29
10:59:30	NAC	58	790.50	10.00	0.075 ± 0.001	0.36
11:00:29	WAC	18	612.60	14.70	0.073 ± 0.002	0.35
11:00:52	WAC	17	631.60	57.77	0.075 ± 0.003	0.36
11:01:57	WAC	16	590.70	43.57	0.073 ± 0.003	0.35
11:02:48	WAC	15	572.10	16.76	0.072 ± 0.002	0.35
11:03:13	WAC	14	388.40	270.88	0.054 ± 0.006	0.26
11:07:51	WAC	13	375.60	119.46	0.048 ± 0.004	0.23
11:09:58	WAC	12	629.80	1.00	0.076 ± 0.001	0.36
11:10:07	WAC	21	537.20	2.74	0.072 ± 0.001	0.34
11:10:18	WAC	71	325.80	441.86	0.029 ± 0.006	0.14

Notes. The observations were acquired on 1 May 2010, at a phase angle of 52.45−52.47° and at a Rosetta-Vesta distance of 0.284857285−0.284809694 AU. F is the filter combination, λ_c the filter central wavelength, exp. the exposure time, F_{Abs} the absolute reflectance at $\alpha = 52.4°$, and p the geometric albedo estimated assuming the same phase function for all the wavelengths.

set of observations from Hasegawa et al. (2009). The data correspond to very different Vesta aspects, which causes considerable scatter in the data (Fig. 2). The $H - G$ function (Bowell et al. 1989) that most closely fits the data gives an $H_R = 2.80 \pm 0.01$ and $G = 0.27 \pm 0.01$. Our G value, well-constrained by the Rosetta point at $\alpha = 52°$, is in-between the previous estimates of Lagerkvisk et al. (1990, $G = 0.33$ in V filter) and Hasegawa et al. (2009, $G = 0.21$ in R filter). Vesta displays a high opposition effect: its linear slope (calculated for $\alpha > 7°$) is 0.02654 mag/° and the magnitude from the linear slope (thereby excluding the opposition effect) is $R_{lin} = 3.12$. The Vesta linear slope and opposition surge values are comparable with those of S-type asteroids (Belskaya & Shevchenko 1999). The new H and G values can be used to estimate the Vesta albedo (see following section) and its flux at large phase angles.

4. Spectrophotometry

A spectrophotometric sequence including 12 NAC filters and 9 WAC filters, covering the wavelength range 269−989 nm, was acquired at a sub-spacecraft latitude of 2.8° and a sub-spacecraft longitude of 205−221° (the longitude and latitude were calculated from the Rosetta spice kernels following the IAU convention, that is longitude increasing in the East direction). Rosetta looked then mostly at the western hemisphere. The details of these observations together with the absolute reflectance value at a phase angle of 52.4° are reported in Table 1. The absolute reflectance (F_{Abs}) was computed for each filter as follows

$$F_{Abs}(\alpha = 52.4°) = \frac{F_V \times R_\odot^2 \times \Delta^2}{r_V^2 * F_\odot}, \tag{2}$$

where F_V is the Vesta flux expressed in W/m^2/nm, $R_\odot$ is the heliocentric distance of Vesta at the time of observation (2.3241538 AU), Δ the distance between Rosetta and the target (in AU), r_V the Vesta radius (260 km, estimated from the Vesta cross-section area at the Rosetta observing conditions using the Thomas et al. (1997a) shape model), and $F_\odot$ is the solar flux (in W/m^2/nm) through a given filter.

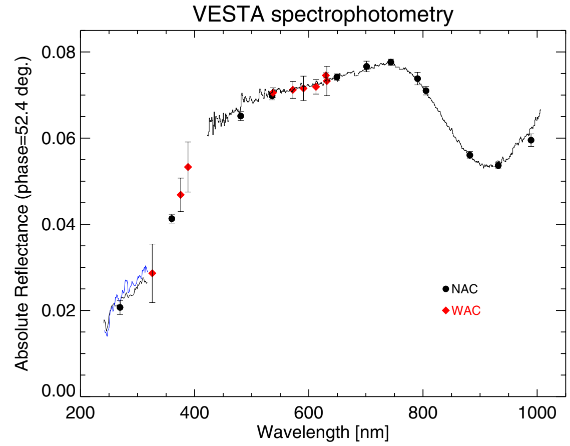

Fig. 3. Spectrophotometry of 4 Vesta from the WAC and NAC cameras of the OSIRIS imaging system. For comparison, a ground-based spectrum taken from the SMASS survey is shown (Xu et al. 1995). In the UV, data come from the IUE telescope: in blue the LWP 18955 observation, in black the LWP 18952 one (Hendrix et al. 2003).

We can estimate the geometric albedo multiplying the absolute reflectance by a phase correction factor derived from the phase function ($G = 0.27$). With this method, we find a geometric albedo of 0.36 ± 0.02 at 649 nm. In Table 1, we report the geometric albedo estimated for all the Rosetta observations, assuming the same phase function for the different wavelengths. These values must be interpreted with caution for the UV and NIR regions, as we do not know the wavelength dependence of the phase curve.

Tedesco et al. (2002) reported a geometric albedo of 0.42 ± 0.05 at visible wavelength from IRAS data. However, they used a diameter value of 468 km, which is smaller than that estimated from HST images (Thomas et al. 1997a). Using Thomas' et al. size, their geometric albedo would be 0.34 (Li et al. 2011b), in perfect agreement with the Rosetta one.

The Osiris spectrophotometry of Vesta is shown in Fig. 3. For comparison, we present a visual spectrum from the SMASS survey (Xu et al. 1995, spectrum resulting from the mean of three separate observations taken at sub-Earth lat. 24−38°), scaled to the Rosetta absolute reflectance at 535 nm, and two UV spectra from IUE observations (Hendrix et al. 2003), scaled to the same phase angle of the Rosetta observations with our phase function parameters. The IUE observations correspond to the sets LWP 18952 and LWP 18955 that Hendrix et al. related to the eastern and western hemispheres, respectively. Hendrix et al. (2003) claim to have detected evidence of Vesta's spectral reversal, that is regions that are brighter in the visible range (Vesta eastern hem.) seem to be darker in the UV range. We recalculated the sub-Earth longitude (λ_{subE}) of the IUE observations with the IMCCE ephemeris server[2] finding $\lambda_{subE} = 277°$ for the LWP 18952 set, corresponding to the western hemisphere, and $\lambda_{subE} = 133°$ for the LWP 18955, corresponding to the eastern hemisphere, opposite to the Hendrix et al. (2003) results. As shown in Fig. 3, the Rosetta data,

[2] http://www.imcce.fr

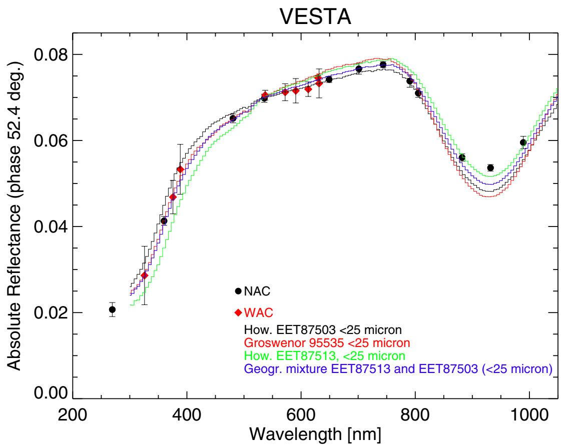

Fig. 4. Spectrophotometry of 4 Vesta from OSIRIS imaging system with the best meteorite analogues found.

taken in the western hemisphere, are in good agreement with the SMASS spectrum and close to the IUE LWP 18952 observation, which also seems to fall in the western hemisphere according to the revisited λ_{subE}. The Rosetta data, taken from UV to NIR almost simultaneously, are inconsistent with the UV spectral reversal. Analysing UV data from HST and Swift telescopes and combining them with V+NIR data, also Li et al. (2011) conclude that there is no global ultraviolet/visible reversal on Vesta, implying lack of global space weathering.

The band-pass of the NIR filters is too broad to determine a meaningful mineralogical characterisation from the absorption-band position and depth in the 0.9 micron region. We refer the reader to the works, for example, of Gaffey et al. (1997), Binzel et al. (1997), Burbine et al. (2001), and Reddy et al. (2010) for the mineralogical interpretation of Vesta. We attempt to characterize the observed Vesta spectrum by looking for meteorite analogues from the RELAB database. It is well-known that Vesta is associated with the basaltic achondrites howardite, eucrite, and diogenite (HED) (Clayton & Mayeda 1983; McSween et al. 2011). These meteorites are the equivalent of terrestrial magmatic rocks, and their igneous appearance proves the existence of magmatic activity on their parent body very early in the evolution of the Solar System (McSween 1989). The spectra of individual HED meteorites are quite diverse in both terms of spectral slope and 0.9−1 μm and 2 μm absorption bands centre and depth, even for similar grain sizes (Burbine et al. 2001; Hiroi et al. 1994). This is directly linked to meteorite mineralogy as reported by Pieters et al. (2006).

We find that the Rosetta spectrophotometric data are close to the spectral behavior of fine-grained powder samples (grain size <25 μm) of howardite meteorites (Fig. 4). A geographical mixture obtained with 50% of EET87503 and 50% of EET87513 howardites, both from Elephant Moraine (Antarctica), shows a very good match to the Rosetta data in the 260−850 nm region, but has a slightly larger 0.93 μm depth. This mixture has an albedo of 0.36 at 535 nm, compatible with the estimated Vesta geometric albedo. Additional components, which must also be constrained using Vesta data in the NIR range, are needed to improve the spectral match. Our meteorite match confirms the results previously found by Hiroi et al. (1994), suggesting that Vesta's surface must be covered by relatively fine-grained basaltic materials.

5. Conclusions

We have analysed Rosetta data of asteroid Vesta taken at a phase angle of ~52° to extend and more tightly constrain its phase function. Using the $H-G$ formalism, we have found a G parameter value of 0.27 ± 0.01 and an absolute magnitude $H(R)$ = 2.80 ± 0.01. The new lightcurve has the largest amplitude ever seen for this object. The Rosetta absolute reflectance obtained in 19 filters covering the near UV up to the near IR region does not support the previously reported spectral reversal suggested by Hendrix et al. (2003). The Rosetta data are well-matched from the UV region up to about 850 nm by a mixture of two howardite fine-grained powder samples. This mixture has an albedo similar to that of Vesta but a deeper 0.93 μm band.

We have estimated from our absolute reflectance at $\alpha = 52°$ and the phase function a Vesta geometric albedo of 0.36 ± 0.02 at 649 nm and 0.34 ± 0.02 at 535 nm. This information will be very useful to the Dawn team in preparing their observations. These results attest to the excellent capabilities of the OSIRIS camera in terms of both scientific usefulness and technical performance.

Acknowledgements. S.F. thanks Dr. Li for helpful discussion and information exchange, and Dr. Hasegawa for proving his phase function data. OSIRIS was built by a consortium of the Max-Planck-Institut für Sonnensystemforschung, Katlenburg-Lindau, Germany, CISAS–University of Padova, Italy, the Laboratoire d'Astrophysique de Marseille, France, the Instituto de Astrofísica de Andalucia, CSIC, Granada, Spain, the Research and Scientific Support Department of the European Space Agency, Noordwijk, The Netherlands, the Instituto Nacional de Técnica Aeroespacial, Madrid, Spain, the Universidad Politéchnica de Madrid, Spain, the Department of Physics and Astronomy of Uppsala University, Sweden, and the Institut für Datentechnik und Kommunikationsnetze der Technischen Universität Braunschweig, Germany. The support of the national funding agencies of Germany (DLR), France (CNES), Italy (ASI), Spain (MEC), Sweden (SNSB), and the ESA Technical Directorate is gratefully acknowledged. This research utilizes spectra acquired with the NASA RELAB facility at Brown University.

References

Belskaya, I. N., & Shevchenko, V. G. 1999, Icarus, 147, 94
Binzel, R. P., Gaffey, M. J., Thomas, P. C., et al. 1997, Icarus, 128, 95
Burbine, T. H., Buchanan, P. C., Binzel, R. P., et al. 2001, Meteor. Planet. Sci., 36, 761
Clayton, R. N., & Mayeda, T. K. 1983, Earth Plan. Sci. Lett., 62, 1
Drummond, J. D., Fugate, R. Q., & Christou, J. C. 1998, Icarus, 132, 80
Gaffey, M. J. 1997, Icarus, 127, 130
Hasegawa, S., Miyasaka, S., & Tokimasa, N. 2009, Lunar Plan. Sci. Conf. 40th, 1503
Harris, A. W., Young, J. W., Bowell, E., et al. 1989, Icarus, 77, 171
Hendrix, A. R., Vilas, F., & Festou, M. C. 2003, Icarus, 162, 1
Hiroi, T., Pieters, C. M., & Takeda, H. 1994, Meteoritics, 29, 394
Keller, H. U., Barbieri, C., Lamy, P. L., et al. 2007, Space Sci. Rev., 128, 26
Küppers, M., Mottola, S., Lowry, S., et al. 2007, A&A, 462, 13
Lagerkvist, C. I., & Magnusson, P. 1990, A&AS, 86, 199
Lagerkvist, C. I., Magnusson, P., Belskaya, I., et al. 1995, EAR-A-3-DDR-APC-LIGHTCURVE-V1.0 NASA Planetary Data System
Li, J. Y., McFadden, L. A., Thomas, P. C., et al. 2010, Icarus, 208, 238
Li, J. Y., Thomas, P. C., Carcich, B., et al. 2011a, Icarus, 211, 528
Li, J. Y., Bodewits, D., Feaga, L. M., et al. 2011b, Icarus, submitted
McCord, T. B., Adams, J. B., & Johnson, T. V. 1970, Science, 178, 745
McSween, H. Y. 1989, Ann. Rev. Earth Planet. Sci., 17, 119
McSween, H. Y., Mittlefehldt, D. W., Beck, A. W., Maine, R. G., & McCoy, T. J. 2011, Space Sci. Rev., in press
Pieters, C. M., Binzel, R. P., Bogard, D., et al. 2006, Proc. IAU Symp., 229, 273
Reddy, V., Gaffey, M. J., Kelley, M. S., et al. 2010, Icarus, 210, 693
Russell, C. T., Capaccioni, F., Coradini, A., et al. 2007, Earth Moon Planets, 101, 65
Sierks, H., Keller, H. U., Jaumann, R., et al. 2011, Space Sci. Rev., in press
Thomas, P. C., Binzel, R. P., Gaffey, M. J., et al. 1997a, Icarus, 128, 88
Thomas, P. C., Binzel, R. P., Gaffey, M. J., et al. 1997b, Science, 277, 1492
Zappalá, V., Cellino, A., Barucci, A. M., Fulchignoni, M., & Lupishko, D. F. 1990, A&A, 231, 548

Page 5 is available in the electronic edition of the journal at http://www.aanda.org

3.3.3 2867 Steins

La rencontre de Rosetta avec 2867 Steins a eu lieu le 5 septembre 2008, à une distance minimale de 803 km. J'ai assisté à la rencontre au MPS avec l'équipe OSIRIS. Malheureusement, avant de recevoir les images, nous avons reçu des messages d'erreurs de la NAC suite à des disfonctionnement de l'obturateur, et la caméra s'est mise en *safe mode* et a cessé les opérations d'observation 10 minutes avant la rencontre la plus proche. La déception a été grande, mais l'équipe s'est tout suite reprise avec les premières images reçues et la bonne nouvelle à savoir que la caméra WAC marchait parfaitement.
Les images montrent un objet fascinant, en forme en diamant, avec un gros cratère de 2.3 km de diamètre près du pôle Sud et un bourrelet équatorial, suggérant une rotation rapide autour de son axe dans le passé, et une forme façonnée par l'effet YORP (Keller et al. 2010). On observe aussi un chapelet de 7 cratères parfaitement alignés. Ce type de formation est connu mais habituellement observé sur des gros corps tels que les satellites de Jupiter, Mercure, la Lune ou encore Mars. C'est la première fois qu'une telle structure est observée sur un objet de si petite taille. Cette formation est due au passage rapproché d'un impacteur qui a explosé par effet de marée gravitationnelle puis ses fragments ont percuté la cible les uns après les autres, créant ainsi un chapelet de cratères.

La spectrophotométrie met en évidence une bande d'absorption à 0,49 micron due aux sulfites comme l'oldhamite, une chute de la réflectance dans l'ultraviolet qui indique des minéraux pauvres en fer, une composition à enstatite confirmant sa classification dans la classe E, comme vue à partir des observations au sol. Osiris a, entre autres, déterminé la forme, la dimension, la période de rotation, l'orientation du pôle (l'astéroïde tourne de manière rétrograde), la courbe de phase et la valeur de l'albédo, qui est très élevée (0,40) et consistante avec la valeur typique des astéroïdes appartenant à la classe E.
L'analyse de la composition de différentes régions montre que la surface de Steins est très homogène (Leyrat et al. 2010). L'âge estimé est très faible, entre 150 et 400 millions d'années, la surface est donc relativement fraîche, peu altérée et récente. Cette étude *in-situ* de Steins semble montrer que le *space weathering* n'a que peu d'effets sur les astéroïdes de type E, pour des durées inférieures à 150 millions d'années (l'âge minimum du gros cratère).

Steins semble avoir été totalement re-surfacé par le gros impact qui a produit le gros cratère près du pôle sud et qui a rajeuni sa surface en déposant des débris/éjecta issus de l'impact. En effet, nous observons aussi des cratères partiellement comblés qui ont été remplis par les éjectas d'un impact plus récent.
En considérant la présence d'un gros cratère, qui aurait détruit un objet monolithique, et la forme façonnée par l'effet YORP (qui ne peut agir que sur un tas de gravats), nous concluons que la structure interne de Steins est de type tas de gravats (*rubble pile*).

3.3.4 Article : E-Type Asteroid (2867) Steins as Imaged by OSIRIS on Board Rosetta

3.3.5 Article : Search for Steins' surface inhomogeneities from OSIRIS Rosetta images

We explored spectral models of SDSS 1102+2054 with the abundances kept fixed as in Table 3, but adopting surface gravities of $\log(g) = 8.5$ and 9.0, which correspond to masses of 0.9 $M_\odot$ and 1.2 $M_\odot$ (SOM text, section 2). Broadly similar fits to the absorption lines can be achieved for higher surface gravities, if the temperature is increased by 1000 to 2000 K as well. For $\log(g) = 9.0$, the strongest O I lines become somewhat too broad as compared with the observations, and we conclude that the currently available data are consistent with masses of up to ~1 $M_\odot$.

Initial models of the evolution of intermediate-mass stars predict that ONe cores should also contain substantial amounts of Mg. Updated nuclear reaction rates have lead to a marked downward revision of the Mg abundances (*30*). For SDSS 1102+2054, which has the better-quality spectrum of the two white dwarfs presented here, we can place an upper limit on the Mg abundance of $\log[\mathrm{Mg/He}] < -6.1$ from the absence of the Mg II 448-nm line.

References and Notes

1. K. Nomoto, *Astrophys. J.* **277**, 791 (1984).
2. A. Heger, C. L. Fryer, S. E. Woosley, N. Langer, D. H. Hartmann, *Astrophys. J.* **591**, 288 (2003).
3. O. Straniero, I. Domínguez, G. Imbriani, L. Piersanti, *Astrophys. J.* **583**, 878 (2003).
4. S. J. Smartt, J. J. Eldridge, R. M. Crockett, J. R. Maund, *Mon. Not. R. Astron. Soc.* **395**, 1409 (2009).
5. K. A. Williams, M. Bolte, D. Koester, *Astrophys. J.* **693**, 355 (2009).
6. A. H. Córsico, E. García-Berro, L. G. Althaus, J. Isern, *Astron. Astrophys.* **427**, 923 (2004).
7. T. S. Metcalfe, D. E. Winget, P. Charbonneau, *Astrophys. J.* **557**, 1021 (2001).
8. G. Fontaine, P. Brassard, *Astrophys. J.* **581**, L33 (2002).
9. K. Werner, F. Herwig, *Publ. Astron. Soc. Pac.* **118**, 183 (2006).
10. F. Herwig, T. Blöcker, N. Langer, T. Driebe, *Astron. Astrophys.* **349**, L5 (1999).
11. K. Werner, T. Rauch, M. A. Barstow, J. W. Kruk, *Astron. Astrophys.* **421**, 1169 (2004).
12. J. Liebert *et al.*, *Astrophys. J.* **126**, 2521 (2003).
13. P. Dufour, J. Liebert, G. Fontaine, N. Behara, *Nature* **450**, 522 (2007).
14. P. Dufour, G. Fontaine, J. Liebert, G. D. Schmidt, N. Behara, *Astrophys. J.* **683**, 978 (2008).
15. L. G. Althaus, E. García-Berro, A. H. Córsico, M. M. Miller Bertolami, A. D. Romero, *Astrophys. J.* **693**, L23 (2009).
16. I. J. Iben, C. Ritossa, E. Garcia-Berro, *Astrophys. J.* **489**, 772 (1997).
17. K. N. Abazajian *et al.*, *Astrophys. J. Suppl.* **182**, 543 (2009).
18. D. J. Eisenstein *et al.*, *Astrophys. J. Suppl.* **167**, 40 (2006).
19. B. T. Gänsicke, T. R. Marsh, J. Southworth, *Mon. Not. R. Astron. Soc.* **380**, L35 (2007).
20. We inspected a representative subset of all the DR7 spectra in our sample and estimate that our analysis comprised ≅ 6000 genuine white dwarfs. Applying the same color constraints used in our query on DR7 to the DR4 white dwarf catalog (*18*) left ≅ 2400 objects, which implies that using DR7 more than doubles the available candidate sample.
21. S. Lépine, M. M. Shara, *Astrophys. J.* **129**, 1483 (2005).
22. We specifically did not restrict our search to objects classified as "stars" by the SDSS processing pipeline, because very unusual objects may be misidentified by the SDSS spectroscopic classification algorithm. Within DR7, the algorithm correctly identified SDSS 0922+2928 as a star but left SDSS 1102+2054 as an object of unknown type.
23. P. Dufour, P. Bergeron, G. Fontaine, *Astrophys. J.* **627**, 404 (2005).
24. M. A. Wood, *White Dwarfs*, D. Koester, K. Werner, Eds., no. 443 in *Lecture Notes in Physics* (Springer, Heidelberg, Germany, 1995), pp. 41–45.
25. D. Koester, V. Weidemann, E.-M. Zeidler, *Astron. Astrophys.* **116**, 147 (1982).
26. C. Pelletier, G. Fontaine, F. Wesemael, G. Michaud, G. Wegner, *Astrophys. J.* **307**, 242 (1986).
27. E. Garcia-Berro, I. Iben, *Astrophys. J.* **434**, 306 (1994).
28. E. Garcia-Berro, C. Ritossa, I. J. Iben, *Astrophys. J.* **485**, 765 (1997).
29. D. Koester, S. Knist, *Astron. Astrophys.* **454**, 951 (2006).
30. J. Gutiérrez, R. Canal, E. García-Berro, *Astron. Astrophys.* **435**, 231 (2005).

31. J.G. is supported by a Science and Technology Facilities Council (STFC) studentship. B.T.G., T.R.M., and D.S. are supported by an STFC rolling grant. We thank D. Townsley for useful discussions.

Supporting Online Material

www.sciencemag.org/cgi/content/full/1180228/DC1
SOM Text
Figs. S1 and S2
References

5 August 2009; accepted 30 October 2009
Published online 12 November 2009;
10.1126/science.1180228
Include this information when citing this paper.

E-Type Asteroid (2867) Steins as Imaged by OSIRIS on Board Rosetta

H. U. Keller,[1]* C. Barbieri,[2] D. Koschny,[3] P. Lamy,[4] H. Rickman,[5,20] R. Rodrigo,[6] H. Sierks,[1] M. F. A'Hearn,[7] F. Angrilli,[2] M. A. Barucci,[8] J.-L. Bertaux,[9] G. Cremonese,[2] V. Da Deppo,[21] B. Davidsson,[10] M. De Cecco,[2] S. Debei,[2] S. Fornasier,[8] M. Fulle,[11] O. Groussin,[4] P. J. Gutierrez,[6] S. F. Hviid,[1] W.-H. Ip,[12] L. Jorda,[4] J. Knollenberg,[13] J. R. Kramm,[1] E. Kührt,[13] M. Küppers,[14] L.-M. Lara,[6] M. Lazzarin,[2] J. Lopez Moreno,[6] F. Marzari,[2] H. Michalik,[15] G. Naletto,[2] L. Sabau,[16] N. Thomas,[17] K.-P. Wenzel,[3] I. Bertini,[6] S. Besse,[4] F. Ferri,[2] M. Kaasalainen,[18] S. Lowry,[19] S. Marchi,[2] S. Mottola,[13] W. Sabolo,[6] S. E. Schröder,[1] S. Spjuth,[1] P. Vernazza[3]

The European Space Agency's Rosetta mission encountered the main-belt asteroid (2867) Steins while on its way to rendezvous with comet 67P/Churyumov-Gerasimenko. Images taken with the OSIRIS (optical, spectroscopic, and infrared remote imaging system) cameras on board Rosetta show that Steins is an oblate body with an effective spherical diameter of 5.3 kilometers. Its surface does not show color variations. The morphology of Steins is dominated by linear faults and a large 2.1-kilometer-diameter crater near its south pole. Crater counts reveal a distinct lack of small craters. Steins is not solid rock but a rubble pile and has a conical appearance that is probably the result of reshaping due to Yarkovsky-O'Keefe-Radzievskii-Paddack (YORP) spin-up. The OSIRIS images constitute direct evidence for the YORP effect on a main-belt asteroid.

The European Space Agency's (ESA) Rosetta mission was launched in 2004 to rendezvous with comet 67P/Churyumov-Gerasimenko in 2014. It passed the asteroid (2867) Steins with a relative velocity of 8.6 km s^{-1} on 5 September 2008. Closest approach (CA) took place at 18:38:20 UTC at a distance of 803 km, chosen such that the spacecraft could keep the instruments continuously pointed toward the asteroid. Early in the approach, the solar phase angle (Sun–object–observer) was 38°. It decreased to a minimum of 0.27° (opposition) 2 min before CA. It increased again to 51° at CA, and finally to 141° at the end of observations. The scientific camera system OSIRIS consists of a narrow-angle camera (NAC) and a wide-angle camera (WAC) (*1*). The NAC (with five times higher resolving power) unfortunately stopped its automatic operation at a distance of 5200 km, 10 min before CA. Thus the highest-resolution images of the surface of Steins were taken by the WAC.

The shape of Steins resembles that of a brilliant cut diamond. The last NAC image, taken at 31° before reaching minimum phase angle, and the best WAC image, near CA at 61.5° phase angle, show a very similar outline (Fig. 1). The surface of Steins is mostly covered by shallow craters, often with subdued, ambiguous rims. Some of the larger craters are pitted with smaller ones. The overall crater shape and depth-to-diameter ratio (~0.12) are consistent with degradation

[1]Max Planck Institute for Solar System Research, Katlenburg-Lindau, Germany. [2]University of Padova, Padova, Italy. [3]European Space and Technology Centre, Noordwijk, Netherlands. [4]Laboratoire d'Astrophysique de Marseille, Université de Provence, Marseille, France. [5]Institute för Astronomi och Rymdfysik, Uppsala, Sweden. [6]Instituto de Astrofísica de Andalucía–Consejo Superior de Investigaciones Científicas, Granada, Spain. [7]University of Maryland, College Park, MD 20742, USA. [8]Observatoire de Paris, Meudon, France. [9]Services d'Aéronomie de CNRS, Verrières le Buisson, France. [10]Department of Physics and Astronomy, Uppsala University, Uppsala, Sweden. [11]International School for Advanced Studies, Trieste, Italy. [12]National Central University, Jhongli City, Taiwan. [13]German Aerospace Center, Berlin, Germany. [14]European Space Astronomy Centre (ESAC), Madrid, Spain. [15]Institute of Computer and Network Engineering, Braunschweig, Germany. [16]Instituto Nacional de Técnica Aérospacial, Torrejon de Ardoz, Spain. [17]Physikalisches Institut der Universität Bern, Switzerland. [18]Tampere University of Technology, Tampere, Finland. [19]University of Kent, Canterbury, UK. [20]Polish Academy of Sciences Space Research Center, Warsaw, Poland. [21]Consiglio Nazionale delle Ricerche-Istituto Nazionale per la Fisica della Materia, Luxor, Padova, Italy.

*To whom correspondence should be addressed. E-mail: keller@linmpi.mpg.de

caused by ejecta blanketing and regolith disturbance by impact seismic shaking (2). A large, 2.1-km-diameter crater is located near the south pole. A series of circular indentations and irregular ridges in an almost linear arrangement extending northward from this crater features prominently on the side that was visible during CA (Fig. 1). Chains of pits (or crater-like indentations) were also observed on other asteroids visited by spacecraft (3, 4), but not to the global extent seen on Steins. Chance formation of a chain (catena) of seven craters of roughly similar size is highly improbable. Instead, this feature may be linked to the impact that caused the large crater. It indicates partial drainage of loose surface material into a fracture within stronger, deeper material, possibly marking pre-existing physical inhomogeneities (5). Therefore, we do not consider the seven pits of the catena to be impact craters. Another elongated feature (groove), surrounded by small pits and craters, is visible in NAC images (Fig. 1). This groove is located along a meridian approximately opposite to the catena.

We identified and counted impact craters in near-CA WAC images using different methods, from visual inspection to contrast-enhancing filtering, and we obtained consistent counts for craters as small as 3 pixels across (corresponding to 240 m). From the resulting cumulative distribution of crater sizes (Fig. 2), we estimated the cratering age (6) based on the impactor population derived for asteroids in the main belt (7). Corresponding crater sizes were derived from scaling laws based on hydrocode simulations [(NSL) (8)] or laboratory experiments [(HSL) (9)]. The crater-erasing rate was obtained by scaling a model for the asteroid Gaspra (6). An age of 154 ± 35 million years (My) old, based on NSL, fits the distribution for craters larger than 0.5 km in diameter. Cratering ages based on HSL are typically up to a factor of 10 older (10), and depend on the asteroid tensile strength. We found ages of 0.4 ± 0.2 and 1.6 ± 0.5 billion years (Gy) for 10^5 and 10^6 dyne cm^{-2}, respectively. The surface of Steins is not saturated with craters like the surfaces of Ida and Mathilde (6). The fall-off in the distribution for crater sizes below 0.5-km diameter shows that smaller craters are underrepresented, similarly to what was found for the asteroid Eros. The NSL age that is most representative for the small craters is only 32 ± 4 My (72 ± 10 and 240 ± 30 My for HSL), possibly because the small craters were erased recently, compared with the age of the large craters. According to Asphaugh (11), the diameter of the largest undegraded crater on an asteroid is close to the critical diameter that is associated with an impact that "resets" the surface, that is, erases all traces of earlier craters. We then attribute the deficiency in small craters to surface reshaping (through landslides) due to spin-up by the YORP effect. YORP can modify the rotation rate and spin-axis orientation of small asteroids and has been identified as an important process driving their physical and dynamical evolution (12). The derived ages are younger than the collisional lifetime of 2.2 Gy that is expected for a main-belt asteroid of Steins's size (13).

Approximately 60% of the surface of Steins was resolved during the fly-by. We modeled the asteroid's shape (Fig. 3), based on limb positions from 1 NAC and 61 WAC images and the simultaneous inversion of a set of 28 light curves taken from Earth and during approach (14). Steins's overall dimensions are 6.67 × 5.81 × 4.47 km^3 and its spherical equivalent radius is 2.65 km. Its shape is best approximated by an oblate spheroid rotating about its short axis with a mean equatorial radius of 3.1 km and mean polar radius of 2.2 km. The pole direction is defined by right ascension = 91.6° and declination = –68.2°, resulting in an obliquity of 169.5°, that is, close to perpendicular to the ecliptic plane and retrograde rotation with a sidereal period of 6.04679 ± 0.00002 hours (15).

The disk-integrated geometric albedo of Steins at a wavelength of 632 nm, which was directly calculated from the radiance of the image obtained at the lowest phase angle (0.36°), is 0.40 ± 0.01. This value is consistent with Earth-based determinations (14, 16) and the high albedos of other E-type asteroids. The slope of the phase curve for phase angles between 5° and 30° is 0.024 magnitude/degree. The parameters in the International Astronomical Union (IAU) H-G photometric system (17) are H = 12.90 and G = 0.45. We used more than 100 WAC images covering the range of wavelengths from 296 to 632 nm and phase angles between 0° and 132° to characterize the disk-resolved photometry following Hapke's model (18). A relatively large mean slope angle θ indicates a surface roughness higher than that typical for C- or S-type asteroids, but similar to that estimated for the asteroid 951 Gaspra (19). Radar observations of E-type asteroids also reveal an enhanced surface roughness (20). Steins's integrated geometric albedo is 0.41 ± 0.016 and its Bond

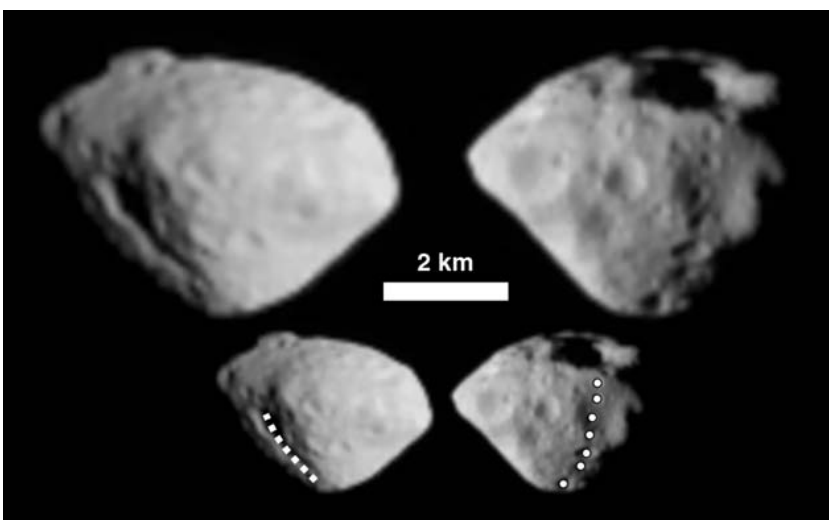

Fig. 1. The WAC image (top right) taken around CA at a phase angle of 61.5° shows the surface of Steins at a resolution of 80 m/pixel. The NAC image (top left) taken 10 min before CA has a slightly lower resolution of 100 m/pixel. The scale is given by the 2-km bar. The difference in viewing angle between the images is 91°, so they show opposite sides of the body. Celestial north is up. A large crater is visible near the south pole; Steins's rotation is retrograde and therefore its north pole points toward the celestial south according to IAU rules. The positions of the catena with the seven pits (bottom right image) and of the large fault on the opposite side (bottom left image) are indicated on the small annotated image copies. [Source: ESA copyright 2008 MPS for OSIRIS Team MPS/UPD/LAM/IAA/RSSD/INTA/UPM/DASP/IDA]

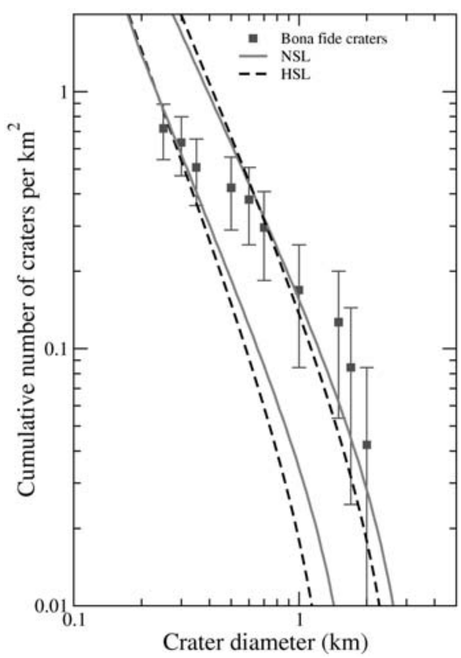

Fig. 2. The cumulative distribution of craters with diameter larger than 3 pixels (~240 m) visible in the WAC images around CA. The seven pits of the catena are excluded. Error bars are estimated on the basis of Poisson statistics. The pair of solid and dashed lines on the right represent best-fit models based on NSL and HSL, respectively, for craters >0.5 km. The pair on the left represents fits for craters <0.4 km.

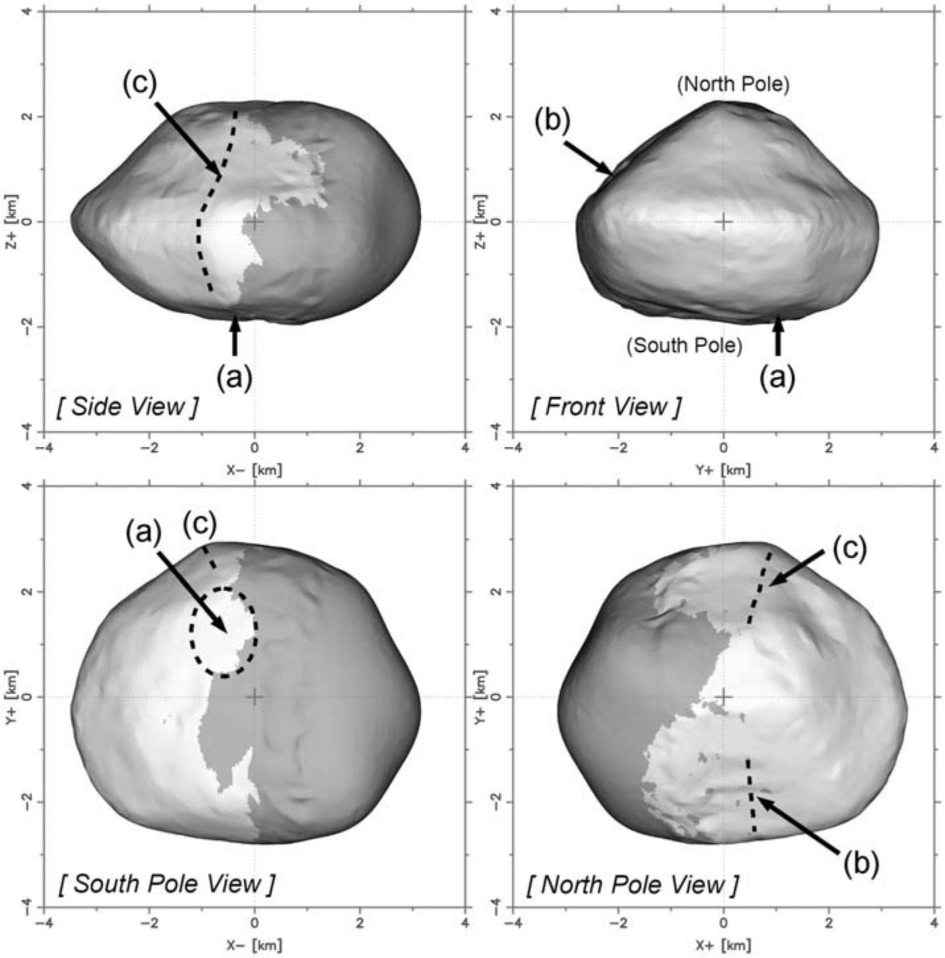

Fig. 3. The shape of asteroid (2867) Steins, reconstructed from limb positions, is illustrated by two equatorial views (top panels) and two polar views (bottom panels). Craters are not modeled. The north pole is up. The polar views show the shape looking down on the south (left) and north pole (right). Bright terrain represents surface visible in at least one image used to construct the shape model. The shape of the dark terrain is constrained by light curve analysis. The features indicated are labeled as follows: (a) large crater, (b) meridianal fault visible in the NAC image, and (c) catena with seven pits. Details visible on the dark terrain are artifacts from the model merging process.

Fig. 4. Spectrum of Steins derived from images with 11 filters of the OSIRIS WAC (triangles) and with 9 filters of the NAC (circles). A ground-based spectrum (*24*) scaled to match at 632 nm is shown for comparison.

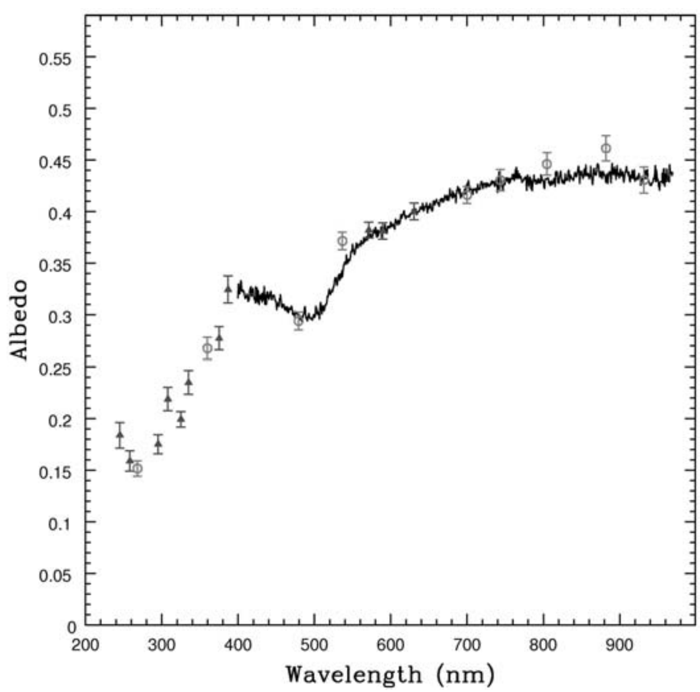

albedo is 0.22 ± 0.01, both calculated at 632 nm from the Hapke parameters.

The spectrum of Steins derived from OSIRIS multicolor photometry (Fig. 4) is in agreement with ground-based observations. It is slightly reddish, and phase reddening is observed over the wavelength range from 296 to 632 nm (for filter wavelengths, see Fig. 4). The spectrum shows a steep drop in the previously unexplored wavelength range below 400 nm, which is typical for low–iron content minerals (*21*). The surface composition of E-type asteroids is dominated by iron-free or iron-poor silicates such as enstatite, forsterite, or feldspar (*22*). Three different subgroups of E-type asteroids are identified by their spectral properties (*23*, *24*). The OSIRIS data confirm that Steins is a member of subtype E[II] (*24*, *25*) with a characteristic strong absorption feature at 490 nm of uncertain origin, tentatively attributed to sulfides (*23*, *26*, *27*). E-type asteroids are commonly thought to be parent bodies of enstatite meteorites, in particular of aubrites. Aubrites are highly reduced achondrites, composed of large white crystals of Fe-poor, Mg-rich orthopyroxene, or enstatite ($Mg_2Si_2O_6$), and they contain variable amounts of metallic Fe, Ni, sulfides such as troilite and oldhamite, and rare minerals. Aubrites are breccias of igneous cumulates that are not derived from shock melts but formed in an environment with temperatures higher than 1000°C (*28*).

No surface color variegation larger than 1% was detected in a principal component analysis based on six NAC images through different filters. This contrasts with previous asteroid encounters, all of which found color variegation (*4*). This uniformity suggests that Steins is compositionally homogenous and that its regolith does not display signs of space weathering (*29*) over time scales shorter than 150 My, which is the minimum age of the large craters.

Other eye-catching features on Steins are the equatorial bulge and the relatively smooth, roughly rotationally symmetric northern hemisphere, which are clearly visible in the images (Fig. 1) and in the derived shape model (Fig. 3). The shape of the northern hemisphere is reminiscent of that of the near-Earth asteroid 1999 KW4 (*30*, *31*), which has been attributed to spin-up by the YORP effect. The typical time scale associated with YORP is 250 My for a 5-km main-belt asteroid (*32*). Whereas the current rotation period of 6 hours is too long to induce shape changes, Steins's evolution may have been dominated by YORP torques in the past. A plausible scenario is that Steins was spun up by YORP, leading to material sliding toward the equator to form the typical cone shape (*33*). Such reshaping requires that Steins has a rubble pile structure, consistent with the presence of the large impact crater on the south pole. Small craters have accumulated after YORP reshaping.

The presence of the large crater at the south pole provides information about the physical properties of the interior of Steins. The specific energy of the impactor, inferred by assuming a solid impactor and appropriate scaling (*9*), is about 6×10^6 erg g^{-1}. This is considerably larger than the energy required for shattering a solid rock Steins [10^4 to 10^6 erg g^{-1} (*34*)]. The ratio of the crater diameter (2.1 km) to the effective asteroid diameter (5.3 km) is 0.4, which is not particularly high. This ratio is lower than those recorded on Ida (0.44), Mathilde (0.62), and Vesta (0.87); however, it is high for an asteroid of Steins's size. The implication for Steins is that the attenuation of seismic waves is relatively strong, placing it in the same range as Mathilde. The interior of Mathilde, a low-density C-type asteroid, is inferred to be porous (*34*). Steins, on the other hand, is not expected to be composed of porous, primitive aggregate material because of its taxonomic type and the existence of meteorite analogs of rocky composition. Thus, before the big impact occurred, Steins was not a monolith but strongly fractured; it may even have been a rubble pile. The big impact must have converted Steins into a rubble pile, consistent with the requirement for YORP reshaping. The relative scarceness of small craters also points in this direction. Its igneous composition argues for an origin from the interior of a much larger differentiated parent body.

References and Notes

1. H. U. Keller *et al.*, *Space Sci. Rev.* **128**, 433 (2007).
2. J. E. Richardson Jr., H. Melosh, R. Greenberg, D. O'Brien, *Icarus* **179**, 325 (2005).
3. M. J. S. Belton *et al.*, *Science* **265**, 1543 (1994).
4. C. R Chapman, in *Asteroids III*, W. F. Bottke, P. Paolicchi, R. P. Binzel, A. Cellino, Eds. (Univ. of Arizona Press, Tucson, AZ, 2002), pp. 315–329.
5. D. C. Richardson *et al.*, in *Asteroids III*, W. F. Bottke, P. Paolicchi, R. P. Binzel, A. Cellino, Eds. (Univ. of Arizona Press, Tucson, AZ, 2002), pp. 501–515.
6. D. P. O'Brien, R. Greenberg, J. Richardson, *Icarus* **183**, 79 (2006).
7. W. F. Bottke Jr. *et al.*, *Icarus* **179**, 63 (2005).
8. M. C. Nolan, E. Asphaug, H. J. Melosh, R. Greenberg, *Icarus* **124**, 359 (1996).
9. K. A. Holsapple, K. R. Housen, *Icarus* **191**, 586 (2007).
10. P. Michel, D. P. O'Brien, S. Abe, N. Hirata, *Icarus* **200**, 503 (2009).
11. E. Asphaug, *Meteorit. Planet. Sci.* **43**, 1075 (2008).
12. D. Vokrouhlický, D. Nesvorný, W. F. Bottke, *Nature* **425**, 147 (2003).
13. S. Marchi, P. Paolicchi, M. Lazzarin, S. Magrin, *Astron. J.* **131**, 1138 (2006).
14. P. Lamy *et al.*, *Astron. Astrophys.* **487**, 1179 (2008).
15. P. Lamy *et al.*, *Astron. Astrophys.* **487**, 1187 (2008).
16. S. Fornasier, I. Belskaya, M. Fulchignoni, M. A. Barucci, C. Barbieri, *Astron. Astrophys.* **449**, L9 (2006).
17. E. Bowell, *Asteroids* **II**, 524 (1989).
18. B. Hapke, *Icarus* **157**, 523 (2002).
19. B. Clark *et al.*, *Icarus* **155**, 189 (2002).
20. L. A. M. Benner *et al.*, *Icarus* **198**, 294 (2008).
21. A. R. Hendrix, F. Vilas, *Astron. J.* **132**, 1396 (2006).
22. M. J. Gaffey *et al.*, *Icarus* **100**, 95 (1992).
23. B. E. Clark *et al.*, *J. Geophys. Res.* **109**, E12S03 (2004).
24. S. Fornasier, A. Migliorini, E. Dotto, M. Barucci, *Icarus* **196**, 119 (2008).
25. M. A. Barucci *et al.*, *Astron. Astrophys.* **430**, 313 (2005).
26. S. Fornasier, M. Lazzarin, *Icarus* **152**, 127 (2001).
27. T. H. Burbine *et al.*, *Meteorit. Planet. Sci.* **37**, 1233 (2002).
28. T. J. McCoy *et al.*, *Meteorit. Planet. Sci.* **34**, 735 (1999).
29. M. Lazzarin *et al.*, *Astrophys. J.* **647**, L179 (2006).
30. D. J. Scheeres *et al.*, *Science* **314**, 1280 (2006).
31. S. J. Ostro *et al.*, *Science* **314**, 1276 (2006).
32. D. P. Rubincam, *Icarus* **148**, 2 (2000).
33. K. J. Walsh, D. C. Richardson, P. Michel, *Nature* **454**, 188 (2008).
34. K. A. Holsapple, *Planet. Space Sci.* **57**, 127 (2009).

35. OSIRIS was built by a European consortium and is part of the Rosetta spacecraft, provided by the European Space Agency (ESA). We thank the Rosetta Science Operations Centre and the Rosetta Mission Operations Centre for their support. We acknowledge the funding of the national space agencies Agenzie Spaziale Italiana, Centre National d'Etudes Spatiales, Deutsches Zentrum für Luft- und Raumfahrt (contract number 50 QP 9703/8), Swedish National Space Board, the Spanish Space Program (Ministerio de Educación y Ciencia), and the ESA.

23 July 2009; accepted 9 November 2009
10.1126/science.1179559

Iron Partitioning and Density Changes of Pyrolite in Earth's Lower Mantle

Tetsuo Irifune,[1]* Toru Shinmei,[1] Catherine A. McCammon,[2] Nobuyoshi Miyajima,[2] David C. Rubie,[2] Daniel J. Frost[2]

Phase transitions and the chemical composition of minerals in Earth's interior influence geophysical interpretations of its deep structure and dynamics. A pressure-induced spin transition in olivine has been suggested to influence iron partitioning and depletion, resulting in a distinct layered structure in Earth's lower mantle. For a more realistic mantle composition (pyrolite), we observed a considerable change in the iron-magnesium partition coefficient at about 40 gigapascals that is explained by a spin transition at much lower pressures. However, only a small depletion of iron is observed in the major high-pressure phase (magnesium silicate perovskite), which may be explained by preferential retention of the iron ion Fe^{3+}. Changes in mineral proportions or density are not associated with the change in partition coefficient. The observed density profile agrees well with seismological models, which suggests that pyrolite is a good model composition for the upper to middle parts of the lower mantle.

The evolution of the structure and dynamics of Earth's interior is influenced primarily by its composition. Based on geophysical interpretations, the lower mantle is typically considered relatively homogenous; however, recent seismological studies have demonstrated that there are some minor discontinuous changes in seismic velocities in the upper to middle parts of the lower mantle (*1*–*3*). Some of these changes are attributed to the presence of subducted slabs (*1*, *2*) or to unresolved phase transitions in mantle materials, including electron spin transitions in Fe-bearing minerals (*1*, *4*). To resolve the origin of these seismic discontinuities, precise observations of phase transitions and associated changes in chemical compositions, densities, and elastic wave velocities of mantle materials are needed.

Pyrolite is a hypothetical representative bulk composition for the mantle. Experimental studies of phase transitions and composition changes in this material have been made at high pressures and temperatures using both the multianvil apparatus (*5*–*8*) and the laser-heated diamond anvil cell (LHDAC) (*9*, *10*). The major phases in the pyrolite model for the lower mantle are orthorhombic Mg-silicate perovskite (Mg-Pv), magnesiowüstite (Mw, also known as ferropericlase), and cubic Ca-silicate perovskite (Ca-Pv). Majorite garnet (*5*) and post-perovskite (*11*) are known to be present as major high-pressure phases in the uppermost and lowermost portions of the lower mantle, respectively.

Understanding the nature of Fe partitioning between the two major phases, Mg-Pv and Mw, under lower mantle conditions may provide important clues for interpreting seismic discontinuities. Fe^{2+} has been known to preferentially partition into Mw relative to Mg-Pv in the simple MgO-FeO-SiO_2 system (*12*). Recent multianvil experiments on more complex mixtures of pyrolite and peridotite—the dominant rock type of the upper mantle—demonstrated that the Fe-Mg partition coefficient between Mg-Pv and Mw [$K_D = (Fe/Mg)_{Mg\text{-}Pv}/(Fe/Mg)_{Mw}$] increases considerably with pressure and approaches unity as a result of Fe enrichment in Mg-Pv (*5*, *6*, *8*, *13*). This is attributed to a coupled substitution of Mg^{2+} and Si^{4+} by Fe^{3+} and Al^{3+} in Mg-Pv (*6*, *13*, *14*) due to the progressive transformation of majorite garnet to the perovskite structure under the pressures and temperatures of the uppermost lower mantle (*5*, *6*). In contrast, LHDAC studies showed substantially smaller values of K_D = ~0.4 to 0.5 under the pressure and temperature conditions of the entire lower mantle (*9*, *10*).

To determine the phase and density changes in pyrolite, we conducted in situ synchrotron-based x-ray diffraction measurements at pressures up to 47 GPa and at temperatures of 1873 to 2073 K along a typical adiabatic geotherm (*15*) using a multianvil apparatus with sintered diamond anvils (*16*). The chemical compositions of the coexisting

[1]Geodynamics Research Center, Ehime University, Matsuyama 790-8577, Japan. [2]Bayerisches Geoinstitut, Universitaet Bayreuth, D-95440 Bayreuth, Germany.

*To whom correspondence should be addressed. E-mail: irifune@dpc.ehime-u.ac.jp

Planetary and Space Science 58 (2010) 1097–1106

Contents lists available at ScienceDirect

Planetary and Space Science

journal homepage: www.elsevier.com/locate/pss

Search for Steins' surface inhomogeneities from OSIRIS Rosetta images

C. Leyrat [a,*], S. Fornasier [a], A. Barucci [a], S. Magrin [d], M. Lazzarin [d], M. Fulchignoni [a], L. Jorda [b], I. Belskaya [c,a], S. Marchi [d], C. Barbieri [d], U. Keller [e], H. Sierks [e], S. Hviid [e]

[a] Observatoire de Paris-Meudon, LESIA, 5 place Jules Janseen, 92190 Meudon, France
[b] LAM Laboratoire d'Astrophysique de Marseille, 38 rue Frédéric Joliot-Curie, 13388 Marseille, France
[c] Astronomical Observatory of Kharkiv National University, Ukraine
[d] Dipartimento di Astronomia, Universita di Padova, Vicolo dell'Osservatorio 2, 35122 Padova, Italy
[e] Max Planck Institut für Sonnensystemforschung, Max-Planck-Str. 2, 37191 Katlenburg-Lindau, Germany

A R T I C L E I N F O

Article history:
Received 5 November 2009
Received in revised form
1 April 2010
Accepted 6 April 2010
Available online 14 April 2010

Keywords:
Steins
Asteroids surface
Asteroid composition
2867 Steins

A B S T R A C T

We investigate the possible presence of heterogeneous surface features on asteroid (2867) Steins, using the G-mode multivariate statistical method (Coradini et al., 1977) applied to Rosetta/OSIRIS images. We analyze both NAC and WAC images obtained near around the closest approach that occurred on September 5th, 2008, through different filters centered on wavelengths ranging from 295 to 986 nm. The shape of Steins is modeled as a polyhedron of almost 58 000 facets. Photometric corrections were performed using Hapke's (2002) model to compensate for the variable illuminations conditions at the surface. The G-mode classification method was performed on all visible and illuminated facets, i.e. in a region limited to $[-50^\circ,+60^\circ]$ in latitude and $[-40^\circ,+90^\circ]$ in longitude, that represents almost 30% of the total surface. The analyzed set of facets does not show any significant difference in the reflected light content, suggesting no surface inhomogeneities larger than 4% at the 95% confidence level.

1. Introduction

On its way to comet 67/P Churymov-Gerasimenko, the ESA Rosetta spacecraft flew by the tiny and very rare E-type asteroid (2867) Steins during its first passage into the asteroid belt. The closest approach occurred on September 5th, 2008, at 18:38:20 (UTC on Earth) at a relative velocity of 8.6 km s^{-1} and a distance of 802 km. The optical spectroscopic and infrared remote imaging system (OSIRIS) cameras onboard the Rosetta spacecraft obtained several images at different geometries of this rare type of asteroid.

Barucci et al. (2007) present a full overview of our knowledge on both Steins and Lutetia, the two target asteroids of Rosetta. Steins is a small E-type asteroid, but few properties were known about this object when it was chosen as a target. Its synodic rotation period, first estimated by Hicks et al. (2004) and revised by Weissman et al. (2007), Dotto et al. (2009) and Jorda et al. (2008), is now known to be $P=6.04684\pm0.00002h$ (Lamy et al., 2008) with a retrograde rotation. Steins is oriented almost perpendicularly to the ecliptic plane (Lamy et al., 2008). The albedo was estimated to be $p_v=0.45\ \pm0.10$ by Fornasier et al. (2006), which corresponds to a spherical equivalent diameter of 4.6 km. A non-spherical shape was first suggested by Lamy et al. (2008), indicating polar flattening. Using disk resolved images obtained during the Rosetta flyby, the three dimensional shape was retrieved (Besse et al., 2009) suggesting that this body is to first order rotationally symmetric, with measured overall dimensions $6.67\times5.81\times4.47$ km (corresponding to a spherical equivalent radius of 2.65 km) (Keller et al., 2010). Steins' surface is covered by a number of impact craters and linear depressions indicating a complex evolution (Besse et al., PSS this issue, Marchi et al., PSS, this issue). Among the most prominent features is the 2 km impact crater near the south pole.

Barucci et al. (2005) presented the first spectroscopic observations of (2867) Steins, finding a spectral behavior similar to the E-type asteroid (64) Angelina. This spectrum was characterized by a strong 0.49 μm absorption band of uncertain origin, which was tentatively attributed to the presence of sulfides at the surface of the asteroid (Gaffey and Kelley, 2004; Clark et al., 2004). There are only two dozen known E-type in the Solar System (Clark et al., 2004). They are generally considered to be the parent bodies of the aubrite meteorites. They must have experienced considerable thermal evolution (temperatures higher than 1400 °C) which could be the outcome of a disruptive collision of a larger body (Fornasier et al., 2007).

The surface composition of E-type asteroids seems to be dominated by iron-free to iron-poor silicates such as enstatite, forsterite or feldspar (Gaffey et al., 1992). Fornasier et al. (2008) have shown that the taxonomic E class can be divided into three sub-classes (E(I), E(II), E(III)) as defined by Gaffey and Kelley (2004) and Clark et al. (2004). Many spectral observations of Steins show the 0.49 μm feature meaning that this asteroid belongs to the E(II) class (Barucci et al., 2008; Fornasier et al.,

* Corresponding author. Tel.: +33 1 4507 7606; fax: +33 1 4507 7144.
E-mail address: cedric.leyrat@obspm.fr (C. Leyrat).

0032-0633/$ - see front matter © 2010 Elsevier Ltd. All rights reserved.
doi:10.1016/j.pss.2010.04.003

2008, 2007; Dotto et al., 2009; Weissman et al., 2007). However, its visible spectrum seems to be slightly redder than other E type bodies (Jorda et al., 2008; Weissman et al., 2008). Weissman et al. (2008) emphasize potential evidence for heterogeneity on hemispheric scales, with one side of Steins appearing redder than the other. This result was contradicted by Dotto et al. (2009) who found no spectral variation for different rotational phases, suggesting an homogeneous surface.

The main results on Steins obtained during by the OSIRIS imaging system during the Rosetta flyby have been reported in Keller et al. (2010). In this paper, we investigate the possible presence of heterogeneous areas on the surface of Steins, especially near the rim of craters and around the equatorial ridge. We apply the statistical G-mode method on disk-resolved images obtained in different filters by the Wide Angle Camera (WAC) and the Narrow Angle Camera (NAC) of the OSIRIS instrument on board Rosetta. In Section 2, we describe observations performed during the asteroid encounter on September 5, 2008. Section 3 is dedicated to a preliminary color–color analysis on calibrated images. In Section 4, we describe step by step the procedures that we use to generate map surfaces by using a three dimensional shape. In Section 5, results of the analysis using the G-mode method is presented. Section 6 is dedicated to the conclusion.

2. Steins observations with OSIRIS

During the Rosetta-Steins encounter on September 5th, 2008, the closest approach (CA) occurred at 18:38:20 UT and the minimum phase angle ($\alpha = 0.3^\circ$) was reached 2 min earlier when the spacecraft was at a distance of 1295 km from the asteroid. The phase angle ranged from 40° to 141°, through 0.3°, during the observations taken before, and after closest approach.

The OSIRIS instrument is equipped with the Narrow-Angle Camera (NAC) and the Wide-Angle Camera (WAC). We refer the reader to Keller et al. (2007) for a detailed instrument description. The NAC would have performed high resolution observations but the automatic sequence acquisition stopped 10 min before the CA at a distance of 5200 km from Steins, due to a shutter problem. Therefore the highest spatial resolution obtained with the NAC is limited to 110 m/pixel, while it reaches 80 m/pixel in the WAC images during the CA. Both NAC and WAC images allow us to explore about 50% of the surface at varying spatial resolutions.

The total data set comprises 405 WAC images and 146 NAC images. In this paper, we only consider four NAC and 12 WAC images obtained with the best spatial resolution available and with a variety of filters. Steins did not rotate much compared to the fast flyby and additional images obtained at lower spatial resolution will not contribute more information on the hypothetical variations of the surface composition.

The last four NAC images were obtained 10 min before the CA, while the 12 WAC images were acquired around the CA (Fig. 1). The complete geometry of the encounter is described in Tables 1 and 2. The two sets of data provide images obtained with different filters, in the wavelength range 250–1000 nm.

In this paper, we use level 3 images of the OSIRIS pipeline calibration. These images have been corrected for coherent noise, dark current and bias. Flat field corrections were applied to take into account the pixel to pixel sensitivity variations. Then the images were calibrated in absolute flux ($\mathrm{W\,m^{-2}\,nm^{-1}\,sr^{-1}}$) and corrected for geometric distortion.

For each image, we compute the reflectance I/F for each pixel. I is the observed scattered radiance in units ($\mathrm{W\,m^{-2}\,nm^{-1}\,sr^{-1}}$), $F = i_o/R_h^2$ is the incoming solar irradiance divided by π ($\mathrm{W\,m^{-2}\,nm^{-1}}$) at the Steins heliocentric distance ($R_h = 2.13563$ AU during observations), and i_o the spectral density ($\mathrm{W\,m^{-2}\,nm^{-1}}$) of the solar irradiance at 1 AU. i_o is wavelength dependent and calculated at the central wavelength of each filter.

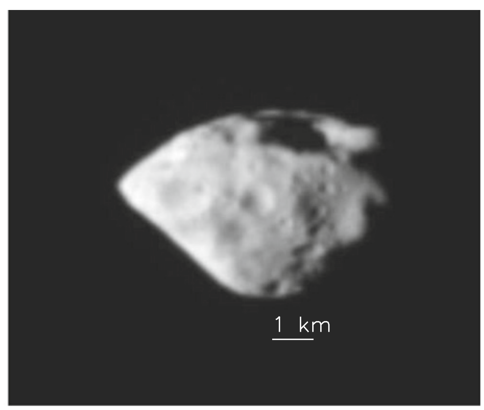

Fig. 1. *Left*: NAC image of Steins obtained 10 min before the CA on September 5, 2008 at 18:27:34.5 UTC. The North pole is down—*Right*: image of Steins obtained near the CA by the WAC camera on September 5, 2008 at 18:38:02.5 UTC.

Table 1
List of the OSIRIS-NAC images we used. *N* is the number of observation and refers to the numbers of triplets we used for the preliminary color–color analysis. *Wavelength* is the central wavelength of the used filter, *Distance* is the Steins–Rosetta distance during the observation, *Phase angle* is the solar phase angle, *Resolution* is the spatial resolution on each image at the nadir point on the asteroid, *SobsLon* and *SobsLat* are, respectively, the sub observer Longitude and Latitude in the Steins frame.

Observation name	*N*	Wavelength (Å)	Distance (km)	Phase angle (deg)	Resolution (m/pixel)	SobsLon (deg)	SobsLat (deg)
NAC_2008-09-05T18.27.34.555Z_F82	1	6475	5486.8	30.11	109.7	45.58	0.71
NAC_2008-09-05T18.27.38.435Z_F84	2	4793	5453.8	30.06	109.1	45.65	0.71
NAC_2008-09-05T18.27.42.331Z_F83	3	5366	5420.6	30.01	108.4	45.72	0.71
NAC_2008-09-05T18.27.46.259Z_F71	4	9873	5387.1	29.96	107.1	45.78	0.71

Table 2
List of OSIRIS-WAC images used in this paper. See Table 1 for more details.

Observation name	N	Wavelength (Å)	Distance (km)	Phase angle (deg)	Resolution (m/pixel)	SobsLon (deg)	SobsLat (deg)
WAC_2008-09-05T18.38.02.520Z_F17	1	6306	802.8	50.25	80.27	10.94	−4.18
WAC_2008-09-05T18.38.04.306Z_F14	2	3869	802.58	51.34	80.25	10.09	−4.26
WAC_2008-09-05T18.38.05.803Z_F15	3	5711	802.65	52.26	80.26	9.38	−4.32
WAC_2008-09-05T18.38.07.357Z_F17	4	6306	802.95	53.22	80.30	8.65	−4.39
WAC_2008-09-05T18.38.09.436Z_F51	5	2949	803.70	54.50	80.36	7.67	−4.48
WAC_2008-09-05T18.38.11.653Z_F61	6	3086	804.92	55.85	80.49	6.63	−4.57
WAC_2008-09-05T18.38.15.334Z_F17	7	6306	807.97	58.10	80.79	4.91	−4.72
WAC_2008-09-05T18.38.16.924Z_F71	8	3245	809.66	59.06	80.96	4.18	−4.78
WAC_2008-09-05T18.38.19.052Z_F14	9	3869	812.29	60.34	81.22	3.21	−4.87
WAC_2008-09-05T18.38.21.012Z_F17	10	6306	815.07	61.52	81.51	2.30	−4.93
WAC_2008-09-05T18.38.23.097Z_F13	11	3752	818.39	62.76	81.8	1.36	−5.01
WAC_2008-09-05T18.38.25.238Z_F51	12	2949	822.20	64.02	82.22	0.40	−5.10

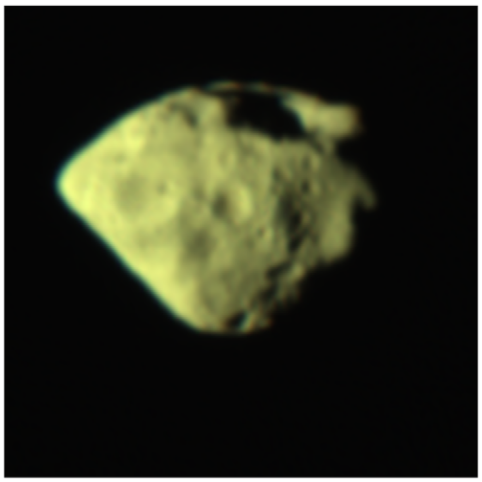

Fig. 2. False-color rendering of the asteroid Steins obtained by overlapping the three images 4, 3 and 2, as defined in Table 2, acquired during the closest approach: WAC filters OI, NH2 and OH are the R, G and B channel, respectively.

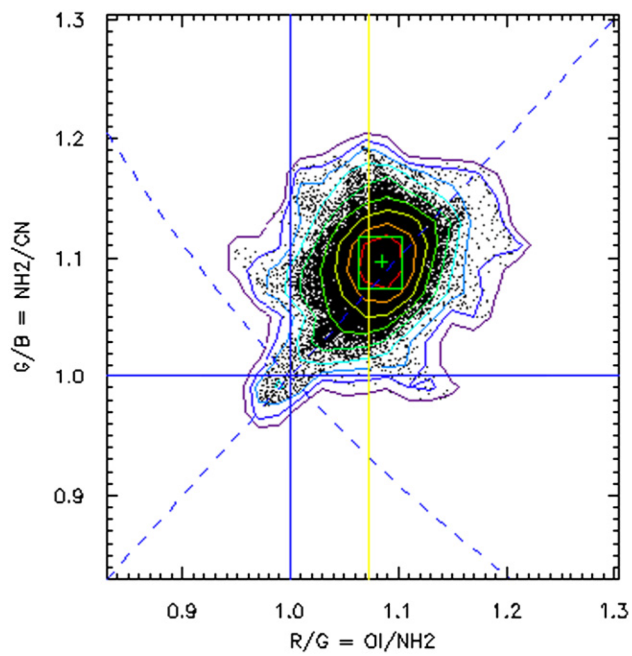

Fig. 3. Color–color plot from the triplet 4, 3, 2 defined in Table 2: we considered OI, NH2 and CN WAC filters as R, G and B5, respectively. Contours are in logarithmic scale. The green "+" corresponds to the median value while the green box refers to the 10th–90th percentile. The yellow line refers to the ratio deduced from ground based observed spectra (Fornasier et al., 2008). (For interpretation of the references to color in this figure legend, the reader is referred to the web version of this article.)

3. Preliminary color–color analysis

In this section, we first explore and analyze the possible color variegation of the surface of Steins, using a direct reflectance comparison on a pixel by pixel basis, in three different filters. In what follows, the term *color* is intended to refer to the ratio of spectral albedos (or reflectances) obtained at different wavelengths. The accuracy of this direct pixel to pixel analysis is spatially limited to the pixel field of view (i.e. at least 80–110 m/pixel at the surface of Steins) and requires comparing images obtained at very similar geometries to limit the effects of Steins' spin and of the variations of the illumination conditions at its surface.

Tables 1 and 2 indicate that the geometry varies significantly during the closest approach. Thus, we consider only triplets of data (acquired with different filters) consisting of consecutive images as listed in Table 2, in order to minimize geometry variations. In particular, we have considered three triplets numbered, respectively, by N=(4,3,2), (7,6,5), (7,8,6), where N is the number of the image as defined in Table 2.

We focus on the triplet N=(4,3,2) in Table 2 (composed of the images WAC_2008-09-05T18.38.07.357Z_F17, WAC_2008-09-05T18.38.05.803Z_F15, and WAC_2008-09-05T18.38.04.306Z_F14), which were obtained, respectively, with the OI, NH2 and CN filters of the WAC instrument. For simplicity, in what follows, we will refer to them as the R, G, B images, respectively.

Each image has been shifted in order to overlap the others, with an accuracy of a fraction (1/10) of a pixel. The rebinning was performed by applying a smooth interpolation using Akima's (1978) quintic polynomials, by using the IDL TRIGRID function. The color RGB image of Steins is shown in Fig. 2. The overlap is not perfect, particularly at the limb of the asteroid because the spacecraft was moving during the observations.

We have produced a color–color diagram (Fig. 3) of a region of interest (ROI) from this triplet. This ROI was chosen in order to avoid shadow regions and limb areas.

Each single point on the color–color diagram corresponds to a pixel on the frame. These points belong to a unique cluster located in a specific region defined by $R/G = 1.085^{+0.019}_{-0.021}$;

$G/B = 1.097^{+0.021}_{-0.023}$ (median value, 90th and 10th percentile). This suggests the absence of variegation $>4\%$ across the surface analyzed. All the distributions produced by the different triplets considered are located on the upper right side above the hyperbolic line, meaning that the overall spectrum of the analyzed area is generally reddish, as also seen from ground based data (Fornasier et al., 2008).

However, small discrepancies in the distributions correlate with the asteroid border regions, where the overlap of the images in the three different filters is not accurate due to changes in scale and geometry during observations. In order to reduce these effects, we have used a different method, dealing with the asteroid's surface itself and not with the pixels.

4. Images reduction and analysis

4.1. Method

Each image was obtained with a unique observational geometry (i.e. spacecraft relative distance, phase angle, spatial resolution, sub-observer latitude and longitude, etc.). Therefore, a direct pixel to pixel comparison between images obtained at very different times is not adequate, not even with a basic re-centering algorithm as described above. Moreover, as the asteroid rotates around its own axis over the sequence of observations, the illumination conditions (defined by the incidence, emission and solar phase angles), vary at the surface of Steins over time. Thus, accurate disk-resolved photometric analysis requires photometric and geometric corrections that must be applied on each image.

Instead of using the camera pixel for photometric measurements, which depends on the scale and geometry of each observation, we prefer to consider here the elementary facets of the asteroid, that describe the asteroid surface itself. Facet orientations that describe the shape of the asteroid depend on the three dimensional shape model. Their photometry is then independent on the image scale and can be easily treated for separate analysis.

The following sections explain how we retrieve I/F for each facet from the calibrated images.

4.2. Retrieving the geometry

The geometric parameters (instrument pointing, Rosetta-Steins distance, phase angle, orientation of the axes of inertia in the field of view, ...) have been retrieved using the SPICE kernels 79, providing the best accuracy available to date on the pointing.

For each observed image, we have produced a simulated image by using the OASIS simulator, developed by Jorda at the Max Planck Institute and later at the Laboratoire d'Astrophysique de Marseille. Given (i) the expected orientation of the asteroid in the OSIRIS frame, (ii) the 58 144 facets shape model obtained from light curve and limb fitting methods by Besse et al. (2009), and (iii) a photometric law (Hapke, 2002), a simulated image of the asteroid is produced and the geometric angles (i, e, ϕ) can be computed for each facet (i is the incidence angle, e the emission angle, ϕ the angle between incidence and emission planes.

Two additional maps are stored when computing the simulated image:

- A geometrical map that contains i, e and ϕ of all facets in each image.
- A map that contains information of the intersection of each facet (k) on pixels (l) (i.e. the fraction of the solid angle subtended by the facet (k) in the pixel (l)).

Had the SPICE Kernels been sufficiently accurate, the simulated and observed images would perfectly overlap, allowing us to make a direct link between the observed reflectance I/F of each pixel and the triplets (i,e, ϕ) of each facet contained in each pixel. Unfortunately, pointing kernels are not accurate to the sub-pixel level so image matching is necessary in order to refine the direction of the line of sight.

We use here an algorithm based on an auto-correlation method to find the best alignment and transformation of each observed image to the corresponding simulated one. We first define and store the position of at least four similar reference points of interest (limb, craters, bright features, ...) on each set of simulated/observed images. The observed image is then geometrically transformed using a spatial polynomial warping algorithm (we use the IDL POLY_2D function) following the polynomial coefficients defined in the first step. The algorithm is able to shift, rotate, scale and warp the image, but we have restricted the transformation to only shifting, rotating and scaling images (linear transformation), in order to guarantee flux conservation in each pixel (Fig. 4). We then compute the auto-correlation using the initial transformation estimate. The I/F value of each pixel is taken into account. The adjustment is tweaked until a maximum in the cross correlation is found using a powell minimization procedure. The iteration stops when the correlation coefficient converges to a constant value. The correlation coefficient reached 99.9% for all images.

Thereafter, the pixel coordinates of the vertices of each facet are known in the new aligned image. The reflectance $I/F(k)$ associated with each facet (k) can then be extracted from the observed flux $I/F(l)$ in pixels (l) it intersects, weighted by its projected area therein.

Fig. 5 represents a cylindrical map of the observed regions obtained by using the images we considered. About 45% of the surface was observed with a spatial resolution equal to 80 m/pixel for the WAC images, and 110 m/pixel for NAC images.

4.3. Photometric correction

A detailed analysis of disk-resolved reflectance and color variations requires photometric corrections for the effects of varying i, e, and α during the observations. The phase angle α can be expressed by

$$\cos(\alpha) = \arccos(\cos(\phi)\sin(e)\sin(i) + \cos(e)\cos(i)) \tag{1}$$

The equation used for the photometric correction is given by

$$r_{corrected}(i_o,e_o,\alpha_o) = r_{obs}(i,e,\alpha) \times \frac{r_{model}(i_o,e_o,\alpha_o)}{r_{model}(i,e,\alpha)} \tag{2}$$

where $r_{corrected}$, r_{obs}, and r_{model} correspond, respectively, to the photometrically corrected, raw observed and modeled reflectance of facets in the shape model. The photometric correction has been computed for the reference geometry (i_o, e_o, α_o) $\equiv$ (0°,30°,30°) in order to avoid the opposition surge effect.

Our final reliable measurements are the facets with incidence i and emission e angles $<70^\circ$. This constraint excludes extreme geometries near the limb (high emission angle) where spatial resolution decreases and where the uncertainties on the shape model becomes important; or near the terminator (high incidence angle) where the S/N ratio may not be good enough.

We used the bidirectional reflectance *BDR* model described by Hapke (2008), that has also been used by Spjuth (2009) on Steins disk-resolved OSIRIS images during the Rosetta flyby to derive model's parameters at each filter wavelength. The *BDR* of each facet can be expressed as follows:

$$r(i,e,\alpha) = \frac{\omega}{4\pi}\frac{\mu_i}{\mu_i\mu_e}([1+B_{SH}(\alpha)]p(\alpha)+M(\mu_i,\mu_e))(1+B_{CB}(\alpha))S(i,e,\alpha) \tag{3}$$

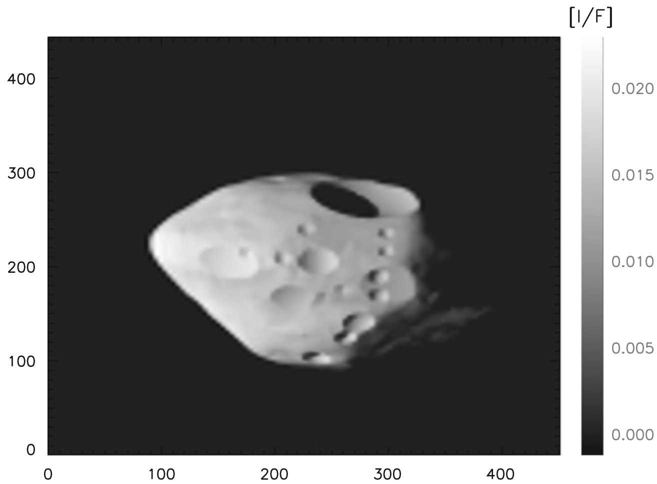

Fig. 4. *Left*: simulated image created with the OASIS simulator using Hapke (2002) photometric model with Spjuth (2009) parameters and Besse et al. (2009) shape model, which corresponds to the WAC image obtained with the filter OI at 18:38:02 UTC. *Right*: corresponding calibrated observed and registered image. This image has been aligned to the simulated one (see text). Black lines represent the contours of the simulated image.

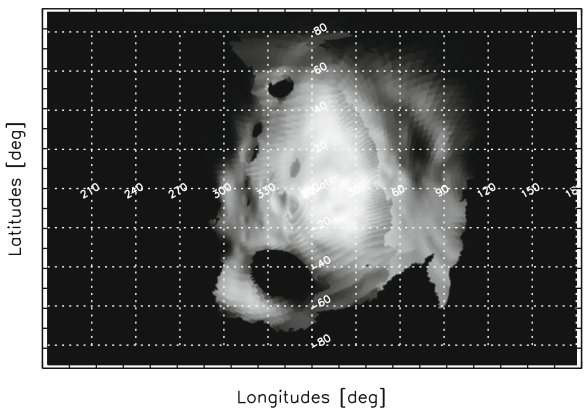

Fig. 5. Cartographic map of the observed surface of Steins constructed from the WAC image at CA and the highest resolution image from the NAC before the flyby. Axis are the latitude and longitude in degrees. Steins' rotation axis points ecliptic South. The WAC image cover 29%, the NAC image cover 37% and they both cover 45% of the surface together.

where ω is the single scattering albedo, μ_i and μ_e are the effective cosines of the incidence angle and emission angle, respectively, i.e. the actual angles accounting for the tilt of facets. All functions are fully described by Hapke (1993, 2002, 2008). $p(\alpha)$ is the single particle phase function. $M(\mu_i,\mu_e)$ accounts for the anisotropic multiple scattering light (Hapke, 2002). $B_{SH}(\alpha)$ represents the shadow hiding opposition effect (SHOE) (Hapke, 1993) and depends on B_{SO} and h_S which are, respectively, the amplitude and the width of the SHOE. B_{CB} accounts for the coherent back-scatter opposition effect (CBOE) (Hapke, 2002) and depends also on B_{CO} and h_C that represent the amplitude and the width of the CBOE, respectively. Because of the high albedo of E type asteroids, the CBOE is important due to a major contribution from the multiple scattering component. The $S(i,e,\alpha)$ function is the shadowing function representing the non-smooth shape of the surface, and it is written as a photometric correction needed to account for the roughness of the regolith. The roughness parameter is described by a characteristic mean slope angle $\overline{\theta}$ (Hapke, 1984). The physical meaning of the Hapke parameters ω, B_{CO}, h_C, B_{SO}, h_S and θ is more fully discussed in Hapke (1981, 1984, 1986, 1993, 2002, 2008), Helfenstein and Veverka (1989), and Helfenstein et al. (1994, 1996).

Table 3
Hapke's parameters used for different wavelengths from Spjuth (2009). h_S, B_{SO}, h_C and B_{CO} are the same for all filters. The Model rms error (as a percentage of average data) is also given. It has been obtained by comparing the observed and modeled I/F at several geometries of observation during the spacecraft flyby (i.e. with a large range of phase angles).

λ (nm)	ω	$\overline{\theta}$ (deg)	h_S	B_{SO}	h_C	B_{CO}	g	rms (%)
630.0	0.64	28	0.074	0.63	0.0056	0.26	−0.28	3.62
295.2	0.33	26	0.074	0.63	0.0056	0.26	−0.30	5.99
308.8	0.45	27	0.074	0.63	0.0056	0.26	−0.30	5.33
325.5	0.38	25	0.074	0.63	0.0056	0.26	−0.30	7.64
335.5	0.41	26	0.074	0.63	0.0056	0.26	−0.33	4.44
375.4	0.50	26	0.074	0.63	0.0056	0.26	−0.30	5.32
387.5	0.57	26	0.074	0.63	0.0056	0.26	−0.29	6.20
571.6	0.59	26	0.074	0.63	0.0056	0.26	−0.28	4.88
589.1	0.58	28	0.074	0.63	0.0056	0.26	−0.28	5.75

The result, r, is the bidirectional radiance factor, defined as the ratio of the bidirectional reflectance of a surface to that of a perfectly diffuse surface illuminated at incidence angle $i=0$. When $r(i,e,\alpha)$ is evaluated at zero incidence, emission and phase angles, it is called "normal reflectance".

Spjuth (2009) have fitted Hapke model on Steins disk resolved I/F measurements. The best fit was obtained by modeling the single particle phase function $p(\alpha)$ by a single term empirical Henyey-Greenstein phase function:

$$p_{HG}(\alpha,g)=\frac{(1-g^2)}{(1+2g\cos(\alpha)+g^2)^{3/2}} \tag{4}$$

where g is the asymmetry factor ($g=0$ for isotropic scattering, $g>0$ for forward scattering, and $g<0$ for backward scattering). The best-fit parameters including CBOE and SHOE effect were determined for the 630 nm case (Filter 17 of the WAC) as most images taken around the opposition were obtained at this wavelength. The remaining parameters for eight other wavelengths corresponding to the WAC filters were found by fixing the SHOE and CBOE parameters. All Hapke parameters and the rms errors are given in Table 3.

4.4. *I/F extraction and sources of uncertainties*

On each facet k where the reflectance $(I/F)_k$ and the angles (i_k, e_k, α_k) have been calculated (see above), we apply Eq. (2) in

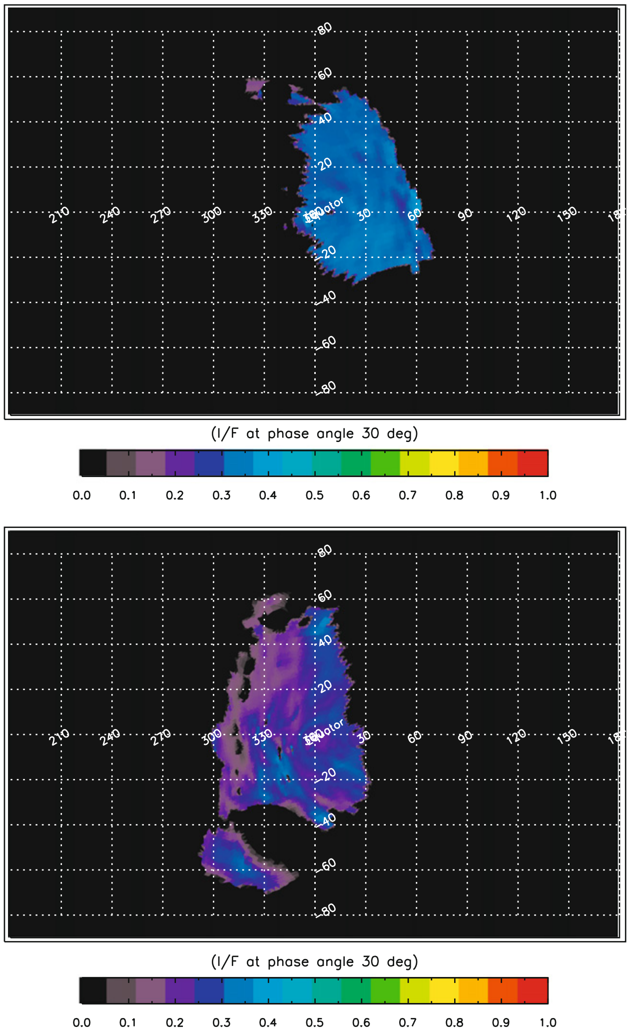

Fig. 6. *Top*: Cartographic projection I/F Steins' surface photometrically corrected by using a NAC image. I/F is computed for a phase angle $\alpha = 30^\circ$ (see text). Limb and terminator area where i or e are higher than 70° are not taken into account. The surface covered here is almost 16%.—*Bottom*: same projection for a WAC image near the CA. The large crater appears near the South pole. This maps represents 20% of the asteroid surface. Both data set represent almost 30% of the surface.

order to correct the measured reflectance for the illumination conditions. For each wavelength, we use the corresponding Hapke parameters found by Spjuth (2009) listed in Table 3. The correction is photometrically homogeneous, i.e. at a given wavelength we use the same Hapke parameters for all facets. For wavelengths >630 nm (i.e. for NAC data), no Hapke fit has been obtained because of a lack of observation geometries due to a shutter problem that occurred during the approach. Thus, for these wavelengths, we use the 630 nm parameters. Fig. 6 represents the map of photometrically corrected reflectances.

Quantifying the errors on the $I/F_{Corrected}$ is important to estimate the accuracy of our results. During the process discussed above, uncertainties in the calculated reflectances may arise mainly from (i) noise and misregistration of the data, (ii) inaccuracies in the global photometric model, and (iii) inaccuracies in the shape model used to derive photometric angles. All data we used have a high signal-to-noise ratio ($S/N \sim 10^3$) and are sub-pixel registered, so photon noise and misregistration effects are assumed to be negligible. Uncertainties in the theoretical BDR obtained with Hapke's model vary slightly with the wavelength and are estimated to be only a few percents of the reflectance (see

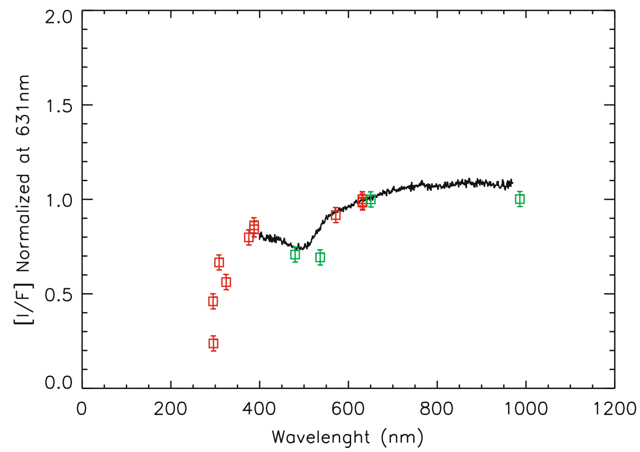

Fig. 7. Comparison between ground based spectrum obtained by Fornasier et al. (2008) (in black) and NAC and WAC broad band spectra (respectively in green and red). The OSIRIS spectrum has been obtained on photometrically corrected images in the two area shown by the white hatched areas in Fig. 6. Both spectra have been normalized to 1 at 630 nm. (For interpretation of the references to color in this figure legend, the reader is referred to the web version of this article.)

rms in Table 3). The remaining shape model errors are likely to result in a dependance of the albedo and color on the illumination geometry. We thus estimate the errors to be about 4% of the I/F measurement, due to photometric corrections uncertainties.

To test the effectiveness of our photometric correction procedure, we have produced several broad band spectra of different regions on the observed surface of Steins (each region covers typically a range of 5° in latitude and longitude). No spectral variations greater than the error bars due to the photometric corrections uncertainties have been detected. Fig. 7 shows an example of the spectro-photometric data derived from OSIRIS, which are in agreement with ground based data obtained by Fornasier et al. (2008).

5. G-mode analysis

5.1. Summary of the method

We provide here a brief summary of the G-mode method we use in this paper. We refer the reader to the papers by Coradini et al. (1977), Barucci et al. (1987), Gavrishin et al. (1992) for more detailed discussions about the G-mode statistics and its applications. The G-mode statistic has been extensively used to define taxonomic classes of asteroids (Zellner et al., 1985; Fulchignoni et al., 2000; Birlan et al., 1996; Barucci et al., 1987) and to retrieve their compositional properties. Here, we rather apply this method to search for ''taxonomic'' classes at the surface of Steins, defined by its facets.

The G-mode classification technique separates a sample of N_{tot} object into J homogeneous classes, each of them containing N_l objects such that $N_{tot} = \sum_{l=1}^{J} N_l$. Each object is described by M variables i $(i = 1, \ldots, M)$. In this paper, the term *objects* refers to the facets of the 3D shape model of Steins, while the term *variables* accounts for the I/F measurements obtained for each filters (wavelengths). The classification is performed with no *a priori* grouping criteria, taking into account the instrumental errors in measuring each variable, and looking for the true number of degrees of freedom characterizing the grouping.

First, the initial multivariate sample is arranged in a $N_{tot} \times M$ matrix, and the mean value $(\overline{X}_i)$ and variance (σ_i) for each variable, as well as the correlation matrix, are computed.

Each sample is represented by a new variable z_j^2 such that

$$z_j^2 = \sum_{i=1}^{M} z_{ij}^2 = \sum_{i=1}^{M} \frac{(X_{ij} - \overline{X}_i)^2}{\sigma_i^2} \tag{5}$$

where X_{ij} is the ith variable of the jth sample. If X_{ij} are independent and normally distributed, the new variables follow a χ^2 distribution with M degrees of freedom. If the X_{ij} are not independent from each others, the dependence of the variables is represented by

$$R = \frac{M}{\sum_{k,m=1}^{M} r_{km}} \tag{6}$$

where r_{km} are the elements of the correlation matrix. The distribution becomes

$$z_j^2 = R_l \times \sum_{i=1}^{M} z_{ij}^2 \tag{7}$$

that is a χ^2 distribution with $f = N \times M \times R$ degrees of freedom (*dof*). When the number of *dof* becomes high, this latest distribution can be replaced by the g-parameters defined as

$$g_j = \sqrt{2z_j^2} - \sqrt{2f-1} \tag{8}$$

where g_j follows a standard normal distribution $N(0,1)$.

The identification of homogeneous classes inside the new defined G distribution consists of an iterative procedure based on a test of the hypothesis of membership of the jth sample to the first class. The center of the first class is obtained on the basis of the three closest samples, i.e. of the samples with the minimum value of z as

$$z_{p,q,t}^2 = \sum_{i=1}^{3} [(z_{pi} - z_{qi})^2 + (z_{pi} - z_{ti})^2 + (z_{qi} - z_{ti})^2] \tag{9}$$

where z_{pi}, z_{qi}, z_{ti} are the normalized values of the ith variable of the pth, qth, and tth samples, respectively, according to Eq. (7). When the three samples satisfying Eq. (9) are found, their mean value and variance are computed as follows:

$$X_* = \frac{\sum_{j=1}^{3} x_{ij}}{3} \quad \text{and} \quad \sigma_* = \sqrt{\frac{\sum_{j=1}^{3} (x_{ij} - x_*)^2}{2}} \tag{10}$$

The values of z^2, f ,and g are recomputed using X_* and σ_* into relations (5)–(7), and the value given by Eq. (8) is compared with a critical value q_1 selected by the user. q_1 allows the user to infer the membership of the sample into a class, and it defines the classification confidence level. The larger q_1, the less detailed the classification is. We thus test the membership of a given sample described by its g_j value to the class defined by x_* and σ_*.

The N_a samples with $g < q_1$ are considered to belong to the first class a. New values of the mean and the variance for all these samples are computed and substituted into the expressions (5)–(8). The procedure is considered to converge when N_a and R_a are unchanged in two successive cycles.

The same procedure is then applied to the remaining $N - N_a$ samples. The grouping part of the method is concluded when the number of samples left is <3. Thus, the G-mode method defines for each class s the mean value x_{is} and the standard deviation σ_{is} (for each variable i in the class s), and a statistical indicator of the variable independence, R_s, which is related both to the variance–covariance matrix of the variable on the s-class and to the number of *dof* of the s-class.

Once all classes have been found, we can check the role that each variable had in the classification. If N_c classes have been found, with $N_C > 2$, the following quantities are computed:

$$z_i^2(a,b) = \sum_{j=1}^{N_b} z_{ijb}^2 = \sum_{j=1}^{N_b} \frac{(x_{ijb} - \mu_a)}{\sigma_a^2} \tag{11}$$

where $z(a,b)$ is the statistical distance between the samples forming the class b and the mean value of the class a (μ_a). Comparing the classes to each others, M square matrices $N_c \times N_c$ are obtained. As the matrices defined by the relation (11) are not symmetrical, a generalized distance can be introduced as the following symmetric matrices:

$$d_i^2 = \frac{[z_i^2(a,b) + z_i^2(b,a)]}{N_a + N_b - 2} \tag{12}$$

The M matrices $N_c \times N_c$ defined above can then be collapsed into a unique matrix D^2 whose elements are

$$D^2(a,b) = \frac{[z^2(a,b) + z^2(b,a)]}{R_a(N_b - 1) + R_b(N_a - 1)} \tag{13}$$

where

$$z^2(a,b) = R_a \sum_{i=1}^{M} z_i^2(a,b) \tag{14}$$

If some elements in relation (12) of the ith matrix relative to the variable i have values greater than a critical value so-called q_2, then the classes a and b are distinguished by the ith variable. If all these elements are less than q_2, then the ith variable does not play any role in the discrimination of the a and b classes, and is therefore not relevant for the classification.

In conclusion, the differences between two classes considering only one variable are given by the matrices (12), while the differences between two classes with respect to the entire set of variables can be read in the D^2 matrix in Eq. (13). The statistical weight of each variable can be obtained by means of the parameters defined as

$$W_i = \left[\frac{d_i^2}{\sum_{i=1}^{M} d_i^2} \right] \times 100\% \tag{15}$$

The following section is dedicated to the results we obtained with the G-mode central method applied to the N variables (facets) described by the M parameters (wavelengths).

5.2. Results and discussion

We have used the G-mode statistical method to retrieve possible classes defined by the albedo at the surface of Steins. We treat NAC and WAC data separately as the latitudes and longitudes simultaneously covered by both data sets overlap by only few tens of percents.

5.2.1. G-mode with NAC data

We have used four maps of reflectance $I/F_{corrected}$ obtained with the NAC camera, corresponding to four different wavelengths. The G-mode central method was applied to classify the sample composed of $N = 9282$ facets of the surface of Steins described by the $M = 4$ variables (wavelengths). Those facets have been selected where the number of facet per pixel is <30 to avoid wrong estimations of the reflectance inside pixels where the number of facets is too high. They also correspond to facets where the reflectance $I/F \neq 0$ has been retrieved for all four wavelengths. Based on the previous analysis, we assume the uncertainties to be around 4% (attributed to errors on the photometric corrections) in what follows. The estimation of errors is later checked in the process and the dispersion of the data never exceeds the assumed errors.

Table 4
Mean and variance of the reflectance for each NAC image used with respect to each class.

Classes	N		F82	F84	F83	F71
1	8668	$\overline{x_i}$	0.298	0.212	0.207	0.299
		σ_i	0.040	0.040	0.040	0.040
2	20	$\overline{x_i}$	0.379	0.254	0.270	0.374
		σ_i	0.040	0.0421	0.040	0.040
3	155	$\overline{x_i}$	0.279	0.192	0.181	0.0803
		σ_i	0.040	0.0400	0.0404	0.0588
W			24.8	18.0	26.7	30.4

Table 5
Mean and variance of the reflectance for each WAC image used with respect to each class.

Classes	N		F17	F14	F15	F51	F61	F71	F13
1	8221	$\overline{x_i}$	0.219	0.189	0.201	0.102	0.147	0.125	0.175
		σ_i	0.040	0.040	0.040	0.040	0.040	0.040	0.040
2	712	$\overline{x_i}$	0.103	0.085	0.089	0.475	0.066	0.059	0.074
		σ_i	0.041	0.0421	0.040	0.040	0.040	0.040	0.040
3	46	$\overline{x_i}$	0.312	0.274	0.294	0.142	0.210	0.178	0.266
		σ_i	0.040	0.0400	0.040	0.040	0.040	0.040	0.040
4	61	$\overline{x_i}$	0.251	0.213	0.223	0.103	0.124	0.078	0.019
		σ_i	0.040	0.0400	0.040	0.040	0.069	0.064	0.040
W			13.0	12.6	18.6	9.1	12.1	13.9	20.6

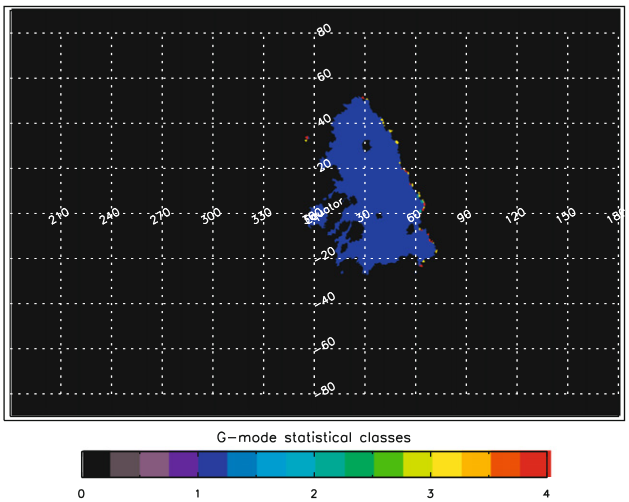

Fig. 8. Cartographic projection of G-mode classes obtained with the NAC data, with 4 variables. Each color represents a statistical class.

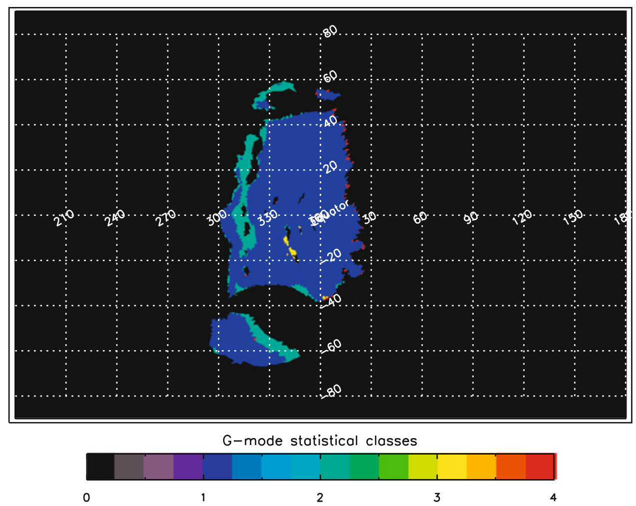

Fig. 9. Cartographic projection of G-mode classes obtained with the WAC data, with 7 variables. Each color represents a statistical class.

We fix $q_1=2$ for a confidence level of 95% in the selection of the classification units, and $q_2=3$. We found three main possible classes, where their mean and sigma values are reported in Table 4. Almost 95% of the area analyzed here defined the first class, indicating a strong homogeneity of the observed surface within the observed wavelengths. The second and third classes are marginal and appears to be located at the edge of the region observed. This suggests that these two last classes are artificial and are probably due to the uncertainties in the shape model, that has a greater effect for high emission angles. Therefore, we confirm the absence of color variegation larger than 4% (1σ) with 95% of confidence level in the region located in the latitude range $[-40^\circ,+60^\circ]$ and longitude range $[0^\circ,65^\circ]$ East. The location of groups is displayed in Fig. 8.

5.2.2. *G-mode with WAC data*

The same process was repeated with WAC data. We used seven reflectance maps corresponding to the filters listed in Table 2 covering the wavelength range [295–630] nm. Our sample is composed of 9135 facets, i.e. 15.7% of the total surface of Steins. We keep $q_1=2$ for a confidence level of 95% in the selection of the classification units, and $q_2=3$ We found four main possible classes, where their mean and sigma values are listed in Table 5. Fig. 9 is a cylindrical projection of the four classes found. The first class can be assigned to most of the area studied here, confirming that this observed surface (defined by a latitude range $[-40,60]$ and longitude range $[-40\text{W},75\text{E}]$) is characterized by no inhomogeneities larger than 4% with 95% of confidence level in the spectral range 295–630 nm, meaning that no statistical variation of colors is detected.

However, the second group that comes from the G-mode process which contain 712 facets (8% of the observed surface), is interestingly located near the rim of the large 3 km size crater close to the South pole, and around the region where small craters, located from latitude -30° to $+40^\circ$, are aligned in the North–South direction. This region is characterized by an albedo which is half that of the first region in the range 295–630 nm. A more detailed analysis of the d^2 matrices suggests that images obtained with filters F15 and F13 (i.e. $\lambda=571.5$ and 375.3 nm) play a major role in the discrimination of this class.

While a high albedo is expected around craters because of the presence of fresh material due to quite recent impacts, we observe a low albedo (two times lower than the average value), which is not consistent with the expected result of the formation of craters. The detection of a low albedo inside the rim of the large crater could not be real and could be due to the poor spatial resolution on our images where the estimation of the local topography is not accurate. Around the small craters, such kind of conclusion is not obvious. Either this variations of albedo is real, or this region being observed near the limb during Rosetta observations, it is still possible that the local topography of the 3D shape model may have introduced some errors, that could have been propagated on the photometric correction. We cannot confirm the presence of a regolith with such low albedo, as the others larger craters, located near the equator, do not exhibit the same albedo behavior. A more accurate three dimensional shape model could be useful to check if we underestimate the shadowing in this cratered region.

Keller et al. (2010) had already pointed out the absence of color variegation on Steins. We have shown that most of the observed surface appears homogeneous with $<4\%$ of spectral variations at 95% of confidence level. While such homogeneity is not unlikely for such small sized asteroid, this is somewhat in contrast with other asteroids visited by a spacecraft (Chapman, 2004).

The dynamical implications of such high level of homogeneity are not obvious. Numerical simulations of impacts have been performed by Jutzi et al. (2010) to reproduce the large crater near the South pole. They have shown that before the impact, Steins must have been either a rubble pile with microporosity, or a monolithic body with or without microporosity. In all cases, the impact would have transformed Steins into a rubble pile structure. Its surface may then have been considerably refreshed by seismic erasing (Marchi et al., 2010), especially when assuming an initial monolithic structure. The relative deficiency in small craters on Steins is attributed to the surface reshaping due to the YORP spin-up thermal effect (Keller et al., 2010) that occurred in the rubble-pile asteroid newly formed after the collision which created a big crater. Thus, the lack of spectral variations over Steins could then be explained either by the relatively insensitive response of the E type Steins surface to space weathering, or by a complete alteration of the surface. The degrees of alteration on E-type surfaces has not yet been investigated in details, but the fresh unaltered surface scenario seems more likely as no obvious spectral variations have been found around young small craters. Thus, space weathering seems to have few effects on Steins' surface over time scales shorter than 150 My which is the minimum age of the large craters (Keller et al., 2010).

6. Conclusion

The recent Rosetta flyby of Steins, a rare E-type asteroid, has provided the opportunity to observe almost 45% of its surface. We have analyzed approximately 30% of the total surface using the G-mode statistical method. Despite a non-spherical shape and the presence of large craters (one of them being comparable to the size of the body itself), most of the observed surface is homogeneous in the visible wavelengths. The G-mode statistical method applied to the OSIRIS disk resolved images reveals no spectral variations larger than 4% threshold (1σ) with 95% of confidence level, confirming the great homogeneity of the surface. This homogeneity could to be consistent with the possible outcome of an impact that may have ejected the first layer of the regolith on the whole surface (Jutzi et al., 2010). It may also be explained by a fresh surface, insensitive to the space weathering. Note that the albedo variations observed on a few percent of the total surface around the linear depression and close to the rim of the 2 km crater are likely due to an inaccurate estimation of the local topography provided by the shape model, and the low spatial resolution of the images instead of being a real variation in the albedo.

The Rosetta spacecraft will flyby the large asteroid (21) Lutetia in July 2010. This will be the largest asteroid observed "in situ" by a spacecraft, before the orbit insertion of the Dawn spacecraft around (2) Vesta. The Lutetia flyby will certainly provide high resolution images as the body will cover the whole field of view of the NAC instrument, and such analysis will be helpful to better estimate local variations of the surface composition of this body.

Acknowledgments

We thank Stefano Mottola and an anonymous reviewer for their helpful comments.

References

Akima, H., 1978. A method of bivariate interpolation and smooth surface fitting for irregularly distributed data points. ACM Transactions on Mathematical Software 4, 148–159.
Barucci, M.A., Capria, M.T., Coradini, A., Fulchignoni, M., 1987. Classification of asteroids using G-mode analysis. Icarus 72, 304–324.
Barucci, M.A., Fornasier, S., Dotto, E., Lamy, P.L., Jorda, L., Groussin, O., Brucato, J.R., Carvano, J., Alvarez-Candal, A., Cruikshank, D., Fulchignoni, M., 2008. Asteroids 2867 Steins and 21 Lutetia: surface composition from far infrared observations with the Spitzer space telescope. Astronomy & Astrophysics 477, 665–670.
Barucci, M.A., Fulchignoni, M., Fornasier, S., Dotto, E., Vernazza, P., Birlan, M., Binzel, R.P., Carvano, J., Merlin, F., Barbieri, C., Belskaya, I., 2005. Asteroid target selection for the new Rosetta mission baseline. 21 Lutetia and 2867 Steins. Astronomy & Astrophysics 430, 313–317.
Barucci, M.A., Fulchignoni, M., Rossi, A., 2007. Rosetta asteroid targets: 2867 Steins and 21 Lutetia. Space Science Reviews 128, 67–78.
Besse, S., Groussin, O., Jorda, L., Lamy, P., Kaasalainen, M., Gesquiere, G., Remy, E., Osiris Team, 2009. 3-Dimensional reconstruction of asteroid 2867 Steins. In: Lunar and Planetary Institute Science Conference Abstracts, vol. 40, pp. 1545–+.
Birlan, M., Barucci, M.A., Fulchignoni, M., 1996. G-mode analysis of the reflection spectra of 84 asteroids. Astronomy & Astrophysics 305 984–+..
Chapman, C.R., 2004. Space weathering of asteroid surfaces. Annual Review of Earth and Planetary Sciences 32, 539–567.
Clark, B.E., Bus, S.J., Rivkin, A.S., McConnochie, T., Sanders, J., Shah, S., Hiroi, T., Shepard, M., 2004. E-type asteroid spectroscopy and compositional modeling. Journal of Geophysical Research (Planets) 109 (18), 2001.
Coradini, A., Fulchignoni, M., Fanucci, O.I.G.A., 1977. A FORTRAN V program for a new classification technique: the g-mode central method. Computers & Geosciences 3, 85–105.
Dotto, E., Perna, D., Fornasier, S., Belskaya, I.N., Barucci, M.A., Shevchenko, V.G., Krugly, Y.N., Gaftonyuk, N.M., Tereschenko, I.A., Scipioni, F., de Luise, F., 2009. Photometric and spectroscopic investigation of 2867 Steins, target of the Rosetta mission. Ground-based results prior to the Rosetta fly-by. Astronomy & Astrophysics 494, L29–L32.
Fornasier, S., Belskaya, I., Fulchignoni, M., Barucci, M.A., Barbieri, C., 2006. First albedo determination of 2867 Steins, target of the Rosetta mission. Astronomy & Astrophysics 449, L9–L12.
Fornasier, S., Marzari, F., Dotto, E., Barucci, M.A., Migliorini, A., 2007. Are the E-type asteroids (2867) Steins, a target of the Rosetta mission, and NEA (3103) Eger remnants of an old asteroid family? Astronomy & Astrophysics 474 L29–L32.
Fornasier, S., Migliorini, A., Dotto, E., Barucci, M.A., 2008. Visible and near infrared spectroscopic investigation of E-type asteroids, including 2867 Steins, a target of the Rosetta mission. Icarus 196, 119–134.
Fulchignoni, M., Birlan, M., Antonietta Barucci, M., 2000. The extension of the G-mode asteroid taxonomy. Icarus 146, 204–212.
Gaffey, M.J., Kelley, M.S., 2004. Mineralogical variations among high Albedo E-type asteroids: implications for asteroid igneous processes. In: Mackwell, S., Stansbery, E. (Eds.), Lunar and Planetary Institute Science Conference Abstracts, vol. 35, pp. 1812–+.
Gaffey, M.J., Reed, K.L., Kelley, M.S., 1992. Relationship of E-type Apollo asteroid 3103 (1982 BB) to the enstatite achondrite meteorites and the Hungaria asteroids. Icarus 100, 95–109.
Gavrishin, A.I., Coradini, A., Cerroni, P., 1992. Multivariate classification methods in planetary sciences. Earth Moon and Planets 59, 141–152.
Hapke, B., 1981. Bidirectional reflectance spectroscopy. I—Theory. Journal of Geophysical Research 86, 3039–3054.
Hapke, B., 1984. Bidirectional reflectance spectroscopy. III—Correction for macroscopic roughness. Icarus 59, 41–59.
Hapke, B., 1986. Bidirectional reflectance spectroscopy. IV—The extinction coefficient and the opposition effect. Icarus 67, 264–280.
Hapke, B., 1993. Theory of reflectance and emittance spectroscopy.
Hapke, B., 2002. Bidirectional reflectance spectroscopy 5. The coherent backscatter opposition effect and anisotropic scattering. Icarus 157, 523–534.
Hapke, B., 2008. Bidirectional reflectance spectroscopy 6. Effects of porosity. Icarus 195, 918–926.
Helfenstein, P., Veverka, J., 1989. Physical characterization of asteroid surfaces from photometric analysis. In: Binzel, R.P., Gehrels, T., Matthews, M.S. (Eds.), Asteroids II, pp. 557–593.
Helfenstein, P., Veverka, J., Thomas, P.C., Simonelli, D.P., Klaasen, K., Johnson, T.V., Fanale, F., Granahan, J., McEwen, A.S., Belton, M., Chapman, C., 1996. Galileo photometry of asteroid 243 Ida. Icarus 120, 48–65.
Helfenstein, P., Veverka, J., Thomas, P.C., Simonelli, D.P., Lee, P., Klaasen, K., Johnson, T.V., Breneman, H., Head, J.W., Murchie, S., 1994. Galileo photometry of asteroid 951 Gaspra. Icarus 107 37–+.
Hicks, M.D., Bauer, J.M., Tokunaga, A.T., 2004. 2867 Steins. IAU Circulars 8315 3–+.
Jorda, L., Lamy, P.L., Faury, G., Weissman, P., Barucci, M.A., Fornasier, S., Lowry, S., Toth, I., Küppers, M., 2008. Asteroid 2867 Steins I. Photometric properties from OSIRIS/Rosetta and ground-based visible observations. Astronomy & Astrophysics 487, 1171–1178.
Jutzi, M., Michel, P., Benz, W., 2010. A large crater as a probe of the internal structure of the E-type asteroid Steins. Astronomy & Astrophysics 509 L2+.

Keller, H.U., Barbieri, C., Koschny, D., Lamy, P., Rickman, H., Rodrigo, R., Sierks, H., AHearn, M.F., Angrilli, F., Barucci, M.A., Bertaux, J., Cremonese, G., Da Deppo, V., Davidsson, B., De Cecco, M., Debei, S., Fornasier, S., Fulle, M., Groussin, O., Gutierrez, P.J., Hviid, S.F., Ip, W., Jorda, L., Knollenberg, J., Kramm, J.R., Kührt, E., Küppers, M., Lara, L., Lazzarin, M., Moreno, J.L., Marzari, F., Michalik, H., Naletto, G., Sabau, L., Thomas, N., Wenzel, K., Bertini, I., Besse, S., Ferri, F., Kaasalainen, M., Lowry, S., Marchi, S., Mottola, S., Sabolo, W., Schröder, S.E., Spjuth, S., Vernazza, P., 2010. E-Type asteroid (2867) Steins as imaged by OSIRIS on Board Rosetta. Science 327 190–.

Keller, H.U., Barbieri, C., Lamy, P., Rickman, H., Rodrigo, R., Wenzel, K., Sierks, H., A'Hearn, M.F., Angrilli, F., Angulo, M., Bailey, M.E., Barthol, P., Barucci, M.A., Bertaux, J., Bianchini, G., Boit, J., Brown, V., Burns, J.A., Büttner, I., Castro, J.M., Cremonese, G., Curdt, W., da Deppo, V., Debei, S., de Cecco, M., Dohlen, K., Fornasier, S., Fulle, M., Germerott, D., Gliem, F., Guizzo, G.P., Hviid, S.F., Ip, W., Jorda, L., Koschny, D., Kramm, J.R., Kührt, E., Küppers, M., Lara, L.M., Llebaria, A., López, A., López-Jimenez, A., López-Moreno, J., Meller, R., Michalik, H., Michelena, M.D., Müller, R., Naletto, G., Origné, A., Parzianello, G., Pertile, M., Quintana, C., Ragazzoni, R., Ramous, P., Reiche, K., Reina, M., Rodríguez, J., Rousset, G., Sabau, L., Sanz, A., Sivan, J., Stöckner, K., Tabero, J., Telljohann, U., Thomas, N., Timon, V., Tomasch, G., Wittrock, T., Zaccariotto, M., 2007. OSIRIS The Scientific Camera System Onboard Rosetta. Space Science Reviews 128, 433–506.

Lamy, P.L., Kaasalainen, M., Lowry, S., Weissman, P., Barucci, M.A., Carvano, J., Choi, Y.-J., Colas, F., Faury, G., Fornasier, S., Groussin, O., Hicks, M.D., Jorda, L., Kryszczynska, A., Larson, S., Toth, I., Warner, B., 2008. Asteroid 2867 Steins. II. Multi-telescope visible observations, shape reconstruction, and rotational state. Astronomy & Astrophysics 487, 1179–1185.

Marchi, S., Barbieri, C., Küppers, M., Marzari, F., Davidsson, B., Keller, H., Besse, S., Mottola, S., Massironi, M., Cremonese, G., 2010. The cratering history of asteroid (2867) Steins. PSS, this issue.

Spjuth, S., 2009. Disk-resolved photometry of small bodies. Ph.D. Thesis, Technische Universität Braunschweig.

Weissman, P.R., Hicks, M.D., Abell, P.A., Choi, Y.-J., Lowry, S.C., 2008. Rosetta target asteroid 2867 Steins: an unusual E-type asteroid. Meteoritics and Planetary Science 43, 905–914.

Weissman, P.R., Lowry, S.C., Choi, Y.-J., 2007. Photometric observations of Rosetta target asteroid 2867 Steins. Astronomy & Astrophysics 466, 737–742.

Zellner, B., Tholen, D.J., Tedesco, E.F., 1985. The eight-color asteroid survey—results for 589 minor planets. Icarus 61, 355–416.

3.3.6 21 Lutétia

Rosetta a survolé l'astéroïde 21 Lutétia le 10 juillet 2010 avec une vitesse relative de 15,4 km/s. La distance minimale de la rencontre a été de 3160 km, permettant d'obtenir des images de la surface avec une résolution de 59 m/pixel avec la caméra haute résolution NAC du système d'imagerie OSIRIS. Osiris a obtenu 462 images de l'astéroïde avec 21 filtres différents, couvrant des longueurs d'onde de 245 à 980 nm et pour des angles de phase très différents, compris entre 0.15 dégrés (pratiquement à l'opposition) et 156 dégrés.
J'ai participé à la rencontre au MPS avec l'équipe OSIRIS, et cette fois-là nous n'avons eu que de belles surprises, car les 2 caméras ont parfaitement fonctionné et nous ont donné des images merveilleuses de l'astéroïde.
Lutétia est un objet de forme irrégulière qui résulte d'une longue histoire collisionnelle : le bombardement par des astéroïdes plus petits a produit de nombreux cratères de plusieurs dizaines de kilomètres, jusqu'à 55 km. L'âge estimé est de 3,6 milliard d'année, donc Lutétia est un objet ancien, vestige des planétésimaux primordiaux dont sont formées toutes les planètes du Système Solaire. Cependant la surface de l'astéroïde montre aussi beaucoup d'éboulements qui semblent être jeunes et de formation récente, avec un âge estimé de seulement 100 millions d'années. La région du pôle Nord est ainsi couverte par une épaisse couche de régolithe où se développent des glissements de terrain importants, sous l'effet de l'activité sismique liée aux impacts. Plus de 237 gros rochers de taille $>$ 100 m ont été identifiés à l'intérieur des cratères, et ceci indique un mécanisme d'impact complexe. Les images montrent des variations d'albédo notables et une grande variété de structures géologiques : puits, chaînes de cratères, crêtes, failles, escarpements, glissements de terrain et larges plaines récentes.
OSIRIS a, entre autres, déterminé l'orientation du pôle de l'astéroïde, la période de rotation, les dimensions, a produit le modèle de forme de l'objet et aussi le volume global. Cette information, couplée avec la masse déterminée par l'instrument radio (RSI), a permis de déterminer la valeur de la densité de Lutétia, qui est très élevée (3,4$\pm$0,3 kg/m^3).
Sa géologie complexe, l'âge de la surface et la densité élevée suggèrent que Lutétia n'est pas un tas de gravats mais un corps monolithique, vestige des planétésimaux qui ont formé les planètes du Système Solaire il y a 4,5 milliards d'années (Sierks et al. 2011).
La spectrophotométrie dans le visible obtenue avec OSIRIS et la spectroscopie dans le visible et le proche infrarouge obtenue par le spectromètre VIRTIS ne montrent pas de bandes d'absorption particulières, chose qui rend difficile l'interprétation de la composition de surface. On peut exclure la présence d'olivine et pyroxène riche en fer, de matériaux organiques et de silicates hydratés sur les régions observées. En effet, la valeur intermédiaire de l'albédo et les propriétés spectrales observées depuis la Terre ou à partir des télescopes spatiaux (Herschel et Spitzer) ont conduit à des discussions animées entre experts ces dernières années, qui penchent vers une composition primordiale similaire aux chondrites carbonées ou à enstatite, bien qu'aucune météorite ne ressemble à Lutétia dans le domaine allant de ultraviolet à l'infrarouge.

3.3.7 Article : Images of Asteroid 21 Lutétia : A Remnant Planetesimal from the Early Solar System

Images of Asteroid 21 Lutetia: A Remnant Planetesimal from the Early Solar System

H. Sierks,[1]* P. Lamy,[2] C. Barbieri,[3,32] D. Koschny,[4] H. Rickman,[5,31] R. Rodrigo,[6] M. F. A'Hearn,[7] F. Angrilli,[8,32] M. A. Barucci,[9] J.-L. Bertaux,[10] I. Bertini,[32] S. Besse,[7] B. Carry,[11] G. Cremonese,[12,32] V. Da Deppo,[13,32] B. Davidsson,[5] S. Debei,[8,32] M. De Cecco,[14] J. De Leon,[6] F. Ferri,[32] S. Fornasier,[9,33] M. Fulle,[15] S. F. Hviid,[1] R. W. Gaskell,[16] O. Groussin,[2] P. Gutierrez,[6] W. Ip,[17] L. Jorda,[2] M. Kaasalainen,[18] H. U. Keller,[19] J. Knollenberg,[20] R. Kramm,[1] E. Kührt,[20] M. Küppers,[11] L. Lara,[6] M. Lazzarin,[3] C. Leyrat,[9] J. J. Lopez Moreno,[6] S. Magrin,[3] S. Marchi,[21,32] F. Marzari,[22,32] M. Massironi,[23,32] H. Michalik,[24] R. Moissl,[1,11] G. Naletto,[25,32] F. Preusker,[20] L. Sabau,[26] W. Sabolo,[6] F. Scholten,[20] C. Snodgrass,[1] N. Thomas,[27] C. Tubiana,[1] P. Vernazza,[2] J.-B. Vincent,[1] K.-P. Wenzel,[4] T. Andert,[28] M. Pätzold,[29] B. P. Weiss[30]

Images obtained by the Optical, Spectroscopic, and Infrared Remote Imaging System (OSIRIS) cameras onboard the Rosetta spacecraft reveal that asteroid 21 Lutetia has a complex geology and one of the highest asteroid densities measured so far, 3.4 ± 0.3 grams per cubic centimeter. The north pole region is covered by a thick layer of regolith, which is seen to flow in major landslides associated with albedo variation. Its geologically complex surface, ancient surface age, and high density suggest that Lutetia is most likely a primordial planetesimal. This contrasts with smaller asteroids visited by previous spacecraft, which are probably shattered bodies, fragments of larger parents, or reaccumulated rubble piles.

The European Space Agency's Rosetta mission flew by asteroid Lutetia on 10 July 2010, with a closest approach distance of 3170 km. Lutetia was chosen because of its size and puzzling surface spectrum (*1*, *2*). The Optical, Spectroscopic, and Infrared Remote Imaging System (OSIRIS) on board Rosetta (*3*) took 462 images, in 21 broad- and narrowband filters extending from 240 to 1000 nm, through both its narrow-angle camera (NAC) and wide-angle camera (WAC). These images covered more than 50% of the asteroid surface, mostly of the northern hemisphere (figs. S1 and S2). The resolved observations started 9 hours 30 min before the closest approach (CA) and finished 18 min after CA. At CA, the asteroid filled the field of view of the NAC with a spatial scale of ~60 m per pixel. The observations reveal a morphologically diverse surface, indicating a long and complex history.

We modeled the global shape of Lutetia, combining two techniques: stereophotoclinometry (*4*) using 60 NAC and WAC images, and inversion of a set of 50 photometric light curves and of contours of adaptive optics images (*5*, *6*). The asteroid's overall dimensions are (121 ± 1) × (101 ± 1) × (75 ± 13) km^3 along the principal axes of inertia. The north pole direction is defined by a right ascension of 51.8° ± 0.4° and a declination of +10.8° ± 0.4°, resulting in an obliquity of 96°. From the global shape model, we derived a volume of $(5.0 \pm 0.4) \times 10^5$ km^3. The volume error is well constrained by (i) the dynamical requirement of principal-axis rotation, (ii) the existence of ground-based adaptive optics images from viewing directions other than that of the flyby, and (iii) the pre-flyby Knitted Occultation, Adaptive-optics and Light-curves Approach (KOALA) model (*5*), which matched the shape model of the imaged part within 5%, giving us confidence that this model is accurate at this level for the southern hemisphere of Lutetia not seen during the flyby. The volume-equivalent diameter of Lutetia is 98 ± 2 km. Combining our volume estimate with the mass of $(1.700 \pm 0.017) \times 10^{18}$ kg measured by the Radio Science Investigation (*7*), we obtained a density of 3.4 ± 0.3 g/cm^3. This value is higher than that found for most nonmetallic asteroids, whose bulk densities are in the range from 1.2 to 2.7 g/cm^3, well below the average grain density of their likely meteoritic analogs. Such low densities imply large macroporosities (*8*) that are associated with "rubble pile" asteroids (*9*).

Using crater density, cross-cutting and overlapping relationships, and the presence of deformational features such as faults, fractures, and grooves, we have identified five major regions on the surface observed during CA. Two regions (Pannonia and Raetia) imaged at lower resolution were defined on the basis of sharp morphological boundaries as crater walls and ridges [Fig. 1 and see the supporting online material (SOM) for details]. The surface is covered in regolith, with slopes below the angle of repose for talus almost everywhere, but large features reveal the underlying structure. A cluster of craters close to the pole in the Baetica region is one of the most prominent features of the northern hemisphere. The most heavily cratered, and therefore oldest, regions (Noricum and Achaia) are separated by the Narbonensis region, which is defined by a crater ~55 km in diameter (Fig. 2). This crater (Massilia) contains several smaller units and is deformed by grooves and pit chains, indicating modifications that took place after its initial formation. Another large impact crater is seen close to the limb (Raetia region). A subparallel ridge formation is seen close to the terminator. A number of scarps and linear features (grooves, fractures, and faults) transecting several small craters (Fig. 2 and fig. S3) are organized along systems characterized by specific orientations for each region and with no obvious relationships with the major craters. However, in the Noricum region, a prominent scarp bounds a local topographic

[1]Max-Planck-Institut für Sonnensystemforschung, Max-Planck-Strasse 2, 37191 Katlenburg-Lindau, Germany. [2]Laboratoire d'Astrophysique de Marseille, CNRS and Université de Provence, 38 Rue Frédéric Joliot-Curie, 13388 Marseille, France. [3]University of Padova, Department of Astronomy, Vicolo dell'Osservatorio 3, 35122 Padova, Italy. [4]Research and Scientific Support Department, European Space Agency (ESA), 2201 Noordwijk, Netherlands. [5]Department of Physics and Astronomy, Uppsala University, 75120 Uppsala, Sweden. [6]Instituto de Astrofísica de Andalucía, Consejo Superior de Investigaciones Cientificas (CSIC), 18080 Granada, Spain. [7]Department of Astronomy, University of Maryland, College Park, MD 20742–2421, USA. [8]Department of Mechanical Engineering, University of Padova, Via Venezia 1, 35131 Padova, Italy. [9]Laboratoire d'Etudes Spatiales et d'Instrumentation en Astrophysique, Observatoire de Paris, 5 Place Jules Janssen, 92195 Meudon, France. [10]LATMOS, CNRS/UVSQ/IPSL, 11 Boulevard d'Alembert, 78280 Guyancourt, France. [11]European Space Astronomy Centre, ESA, Villanueva de la Cañada, Madrid, Spain. [12]Istituto Nazionale di Astrofisica, Osservatorio Astronomico di Padova, Vicolo dell'Osservatorio 5, 35122 Padova, Italy. [13]CNR-IFN UOS Padova LUXOR, Via Trasea 7, 35131 Padova, Italy. [14]UNITN, Università di Trento, Via Mesiano, 77, 38100 Trento, Italy. [15]Osservatorio Astronomico de Trieste, 34014 Trieste, Italy. [16]Planetary Science Institute, 1700 East Fort Lowell, Suite 106, Tucson, AZ 85719, USA. [17]Institute for Space Science, National Central University, 32054 Chung-Li, Taiwan. [18]Department of Mathematics, Tampere University of Technology, 33101 Tampere, Finland. [19]Institute for Geophysics and Extraterrestrial Physics, Technische Universität Braunschweig, 38106 Braunschweig, Germany. [20]Institut für Planetenforschung, Deutsches Zentrum fuer Luft- und Raumfahrt, Rutherfordstrasse 2, 12489 Berlin, Germany. [21]Universite de Nice–Sophia Antipolis, Observatoire de la Cote d'Azur, CNRS, 06304 Nice, France. [22]Department of Physics, University of Padova, Via Marzolo 8, 35131 Padova, Italy. [23]Dipartimento di Geoscienze, Università di Padova, Via Gradenigo 6, 35131 Padova, Italy. [24]Institut für Datentechnik und Kommunikationsnetze, 38106 Braunschweig, Germany. [25]Department of Information Engineering, University of Padova, Via Gradenigo 6, 35131 Padova, Italy. [26]Instituto Nacional de Técnica Aeroespacial, 28850 Torrejon de Ardoz, Spain. [27]Physikalisches Institut der Universität Bern, Sidlerstrasse 5, 3012 Bern, Switzerland. [28]Institut für Raumfahrttechnik, Universität der Bundeswehr München, Neubiberg, Germany. [29]Rheinisches Institut für Umweltforschung, Abteilung Planetenforschung, Universität zu Köln, Cologne, Germany. [30]Department of Earth, Atmospheric, and Planetary Sciences, Massachusetts Institute of Technology, Cambridge, MA, USA. [31]Polish Academy of Sciences Space Research Center, Bartycka 18A, 00-716 Warsaw, Poland. [32]Centro Interdipartimentale di Studi e Attività Spaziali (CISAS)–G. Colombo, Università di Padova, Via Venezia 15, 35131 Padova, Italy. [33]Universite Paris Diderot, Sorbonne Paris Cité, 4 Rue Elsa Morante, 75205 Paris, France.

*To whom correspondence should be addressed. E-mail: sierks@mps.mpg.de

high where lineaments run almost parallel to the scarp itself and to the rims of the crater cluster in Baetica. High-resolution topography models produced by stereo image processing (*10*) show that one long (>10 km) groove in the Noricum region (Fig. 2C and fig. S4) is roughly 100 m deep and on a local topographic high. The linear features are similar in appearance to those on the martian moon Phobos, which are commonly interpreted as resulting from a large impact (*11*). On 433 Eros, the existence of similar grooves has been interpreted as evidence of competent rock below the regolith, although this asteroid is thought to be heavily fractured (*12–14*). Recent work suggests that cracks can be supported in very low-strength material on a body as small as Eros (*15*). The pattern of grooves on Lutetia suggests strain structures or fractures within a body of considerable strength.

Lutetia is heavily cratered, although the crater spatial density varies considerably across the imaged hemisphere. We have identified more than 350 craters with diameters between 600 m and 55 km, which allowed us to determine Lutetia's crater retention age by measuring the crater size-frequency distribution (SFD). We chose to perform the crater count on the Achaia region because it is a remarkably flat area imaged with uniform illumination conditions. In this region, we counted 153 craters over an area of 2800 km^2. We compared Achaia's SFD with those for asteroids 253 Mathilde and 243 Ida (Fig. 3). At large crater sizes (>10 km), the crater SFD of Achaia is quite similar to that of Ida, whereas Mathilde is only slightly less cratered. There are about two or three times fewer craters at a diameter of 1 km than on Ida or Mathilde, respectively. At very small sizes (<1 km), there is a strong depletion of craters. Asteroids as large as Lutetia can be globally affected by seismic shaking; this argument has been used to explain the depletion of <200-m-diameter craters on Eros (*13*, *16*) but cannot explain the observed paucity of craters with diameters up to 5 to 8 km (*17*). The apparent break in the SFD at this size range is statistically significant: According to the Kolmogorov-Smirnov test, the probability that the observed crater SFD (for diameter > 0.8 km) is consistent with a simple hard rock scaling law model (for an approximately linear crater SFD, see Fig. 3C) is only ~3%.

Small crater obliteration by Massilia crater ejecta seems unlikely given that the Achaia region does not show a systematic decrease in crater density with increasing distance to Massilia. A possible explanation for the break is a transition in the physical properties of the target. Small craters, which affect only the upper layers, form in shattered material. Larger craters, able to excavate to greater depth, form in competent rock.

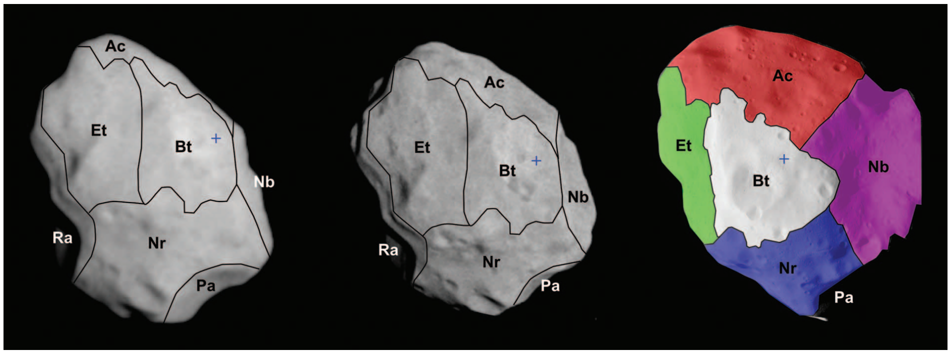

Fig. 1. Regions on Lutetia. Three images taken at −60, −30, and −3 min before CA (left to right) showing the different regions: Bt, Baetica; Ac, Achaia; Et, Etruria; Nb, Narbonensis; Nr, Noricum; Pa, Pannonia; and Ra, Raetia. The images were taken at distances of 53, 27, and 3.5 × 10^6 m and phase angles of 8°, 4°, and 52°. The resolutions of each image are approximately 1000, 500, and 60 m per pixel; Lutetia has been scaled to appear approximately the same size in each panel. The north pole is indicated by the blue cross.

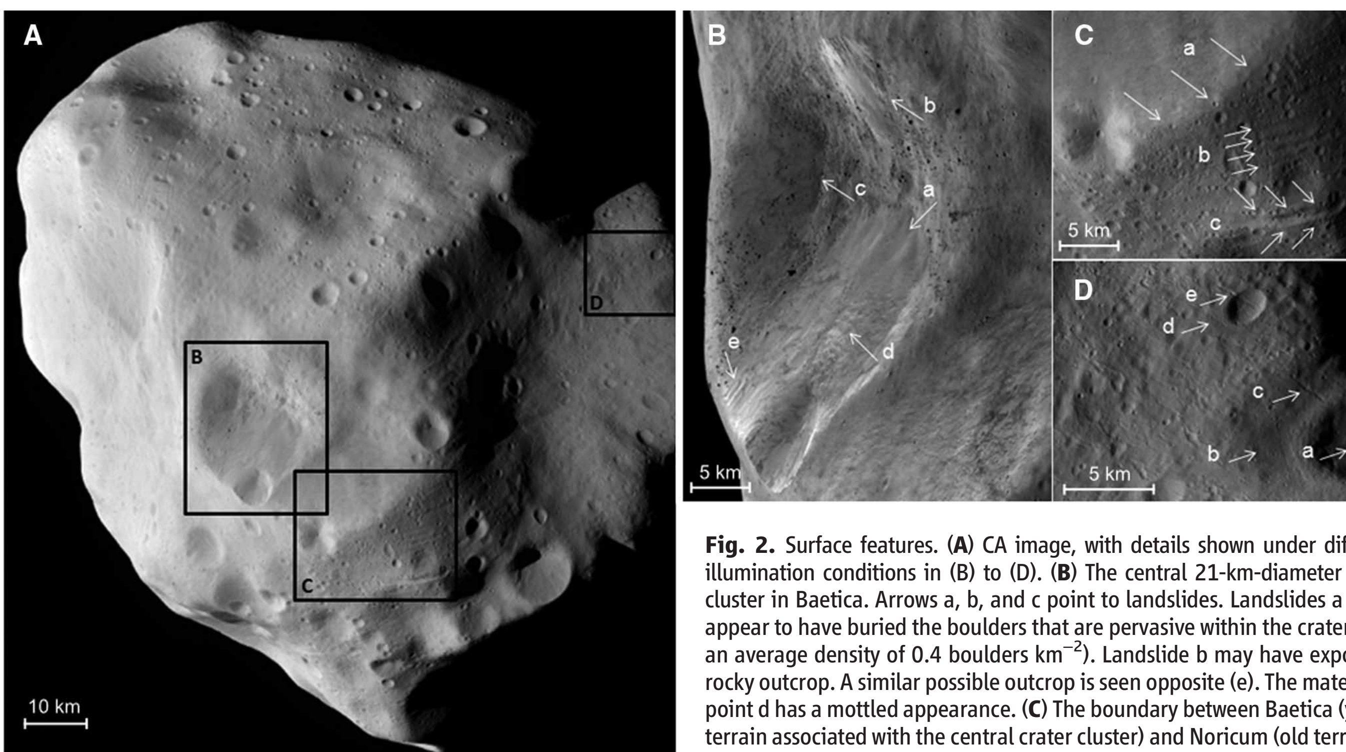

Fig. 2. Surface features. (**A**) CA image, with details shown under different illumination conditions in (B) to (D). (**B**) The central 21-km-diameter crater cluster in Baetica. Arrows a, b, and c point to landslides. Landslides a and b appear to have buried the boulders that are pervasive within the crater (with an average density of 0.4 boulders km^{-2}). Landslide b may have exposed a rocky outcrop. A similar possible outcrop is seen opposite (e). The material at point d has a mottled appearance. (**C**) The boundary between Baetica (young terrain associated with the central crater cluster) and Noricum (old terrain) is extremely well defined in some places, as indicated by the arrow a. Arrows b and c highlight curvilinear features. (**D**) Arrows c, d, and e point to further curvilinear features on the surface of Lutetia. In the Narbonensis region, most curvilinear features show this orientation. The curvilinear features cut the crater and its rim. Feature c cuts through the debris apron (b) of the crater (a). This implies that these linear features are younger than the craters or impact into an area with existing large-scale cracks and subsequent regolith movement.

We therefore modeled a gradual transition in the crater scaling law as strength and density increase with depth in a fractured layer (*18*). We determined the depth of this layer by fitting the model to the observed crater SFD (*19*, *20*) (Fig. 3C). For typical rock properties (SOM text), the depth of the fractured layer is ~3 km. Based on this model, and using the lunar chronology as calibration (*20*), we find a crater retention age of 3.6 ± 0.1 billion years for Achaia.

Scaling laws (*21*) and hydrocode simulations performed with the iSALE (impact Simplified Arbitrary Lagrangian Eulerian code) (*22*) show that the impactor that produced Massilia had a diameter ~ 8 km. According to the simulation, this impact heavily fractured but did not completely shatter Lutetia. The current main-belt impact rate suggests that such an impact occurs every ~9 billion years; therefore, the impact may have occurred relatively early in Solar System history, when the collisional environment in the asteroid belt was more intense. The early occurrence of such an impact is in agreement with the crater retention age for Lutetia.

The Baetica region is partially covered by smooth material that is interpreted as ejecta from the 21-km-diameter crater cluster. The images show evidence that older, smaller craters were partially buried by the ejecta. The depth of the ejecta blanket is estimated to be up to ~600 m, based on the depth-to-diameter ratios of these buried craters. The asymmetric shape of the 21-km crater cluster may be the result of internal inhomogeneity. Preexisting planes of weakness in bedrocks may control final crater shapes and facilitate the detachment of blocks and their emplacement within ejecta deposits (*23*). The crater interior (Fig. 2B) shows a great variety of deposits: smooth and fine deposits with boulders, gravitational taluses, and landslide accumulations. Ejecta blocks have been recorded on other asteroids (*13*) and Phobos (*24*). On Lutetia, approximately 200 blocks of up to 300 m in dimension were found around the central crater region alone. Their steep size distribution (a power law equation with an exponent of –5) is comparable to that seen on Eros (*13*). The presence of boulders adjacent to another impact site in the Pannonia region suggests that boulder generation is a common feature of large impacts on Lutetia, and points to excavation of shattered bedrock. The landslides appear to have been emplaced after the boulders and may have been triggered by further impacts.

To investigate the reflectance properties of the surface, OSIRIS obtained images (including several color sequences) at different asteroid rotational phases and over a range of phase angles from 0.15° to 156°. The slope of the phase curve (fig. S5) for phase angles between 5° and 30° is 0.030 mag/° for the 631-nm filter. The Lutetia disk-integrated geometric albedo was measured to be 0.194 ± 0.006 at 631 nm and 0.169 ± 0.009 at 375 nm, giving an average value in the V band (550 nm) of 0.19 ± 0.01 and a Bond albedo of 0.073 ± 0.002.

We computed disk-resolved reflectivity maps at 10° solar phase angle using the three-dimensional shape model and light-scattering theory (*25*) in order to remove the effect of variation in illumination conditions due to the topography (Fig. 4). We detected variations of the surface reflectivity at 647 nm wavelength. The most important variegations are located inside the crater cluster in the Baetica region (Fig. 4A), where reflectivity varies up to 30% between the darkest and brightest areas. Small spatial variations in reflectivity are also present on surrounding terrain (Fig. 4B) but with a much lower contrast. In Baetica, a clear correlation is found with the local surface slope. Landslide flows or possible rock outcrops appear much brighter than the accumulation areas or surrounding cratered terrains. This suggests either a different texture of regolith or that space weathering modified the surface of the oldest areas, whereas young surfaces have been less exposed to solar radiation. Similar variations of reflectivity have been already observed on Eros, where a strong correlation between the spectral slope and the downslope movement of regolith was found (*13*). Disk-integrated spectrophotometry obtained 1 hour before CA reveals a flat and featureless spectrum, with a moderate spectral slope in the visible range (3%/10^3 Å between 536 and 804 nm), in agreement with spectra obtained from the Rosetta Visible InfraRed Thermal Imaging Spectrometer (VIRTIS) (*26*) and ground-based spectra taken at a similar phase angle (fig. S6). These data are consistent with both particular types of carbonaceous chondrite meteorites, namely CO3 and CV3 (*1*, *27*), and enstatite chondrites (ECs) (*28*). Average bulk densities (*8*, *29*) range from 2.96 to 3.03 g/cm^3 for CO and CV meteorites and 3.55 g/cm^3 for ECs. If Lutetia were composed purely of EC material, this would imply a bulk asteroid macroporosity of ~0 to 13% (given the uncertainty range on Lutetia's density). The low densities of COs and CVs preclude the possibility of

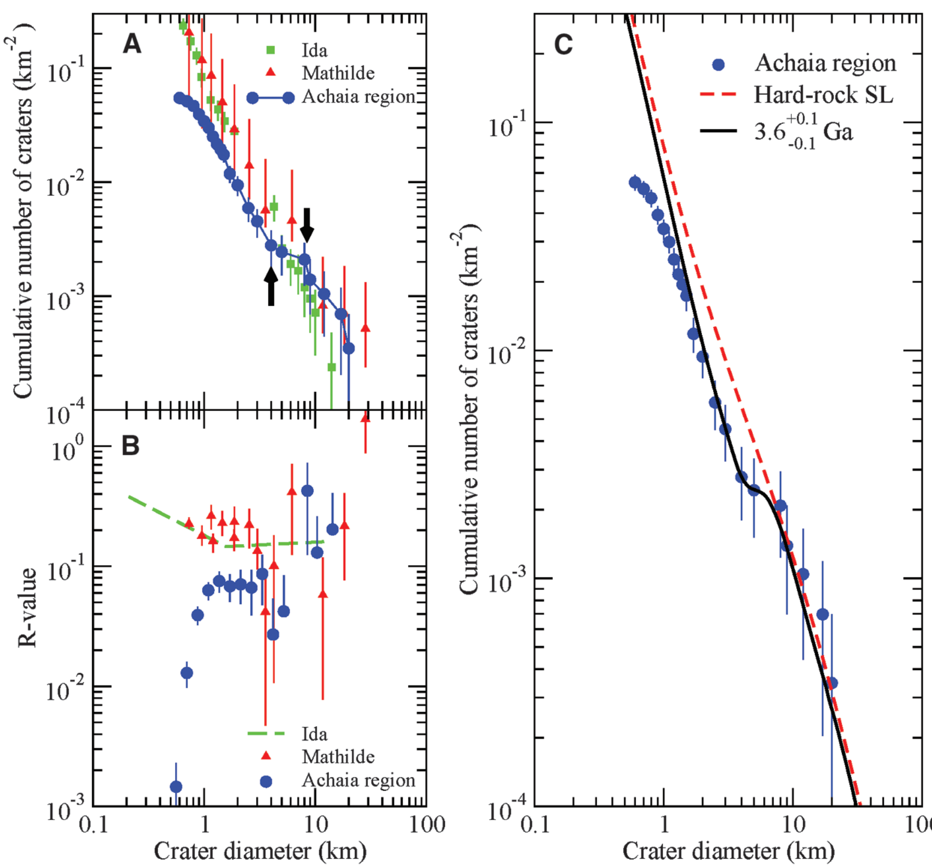

Fig. 3. Crater SFD. (**A**) Cumulative crater SFD of the Achaia region compared with those for Ida and Mathilde, the second- and third-largest asteroids imaged by spacecraft so far, respectively [data from (*17*)]. The arrows indicate the suggested break at 5 to 8 km in the Achaia crater SFD. (**B**) SFD shown in (A) expressed in terms of relative (*R*) values (cumulative crater SFD normalized to a power law with exponent –2). *R* values for Ida are not published, but the overall trend (dashed line) was computed from the published cumulative distribution. (**C**) Achaia crater SFD model fit. The dashed red curve represents a fit of the largest craters of the distribution (diameter > 10 km) obtained using current models for the main-belt asteroid size distribution (*35*) and the crater scaling law (SL) for hard rock (*21*). The black curve is the best fit achieved by a two-layer (fractured material over competent rock) model, which gives a crater retention age of 3.6 ± 0.1 billion years.

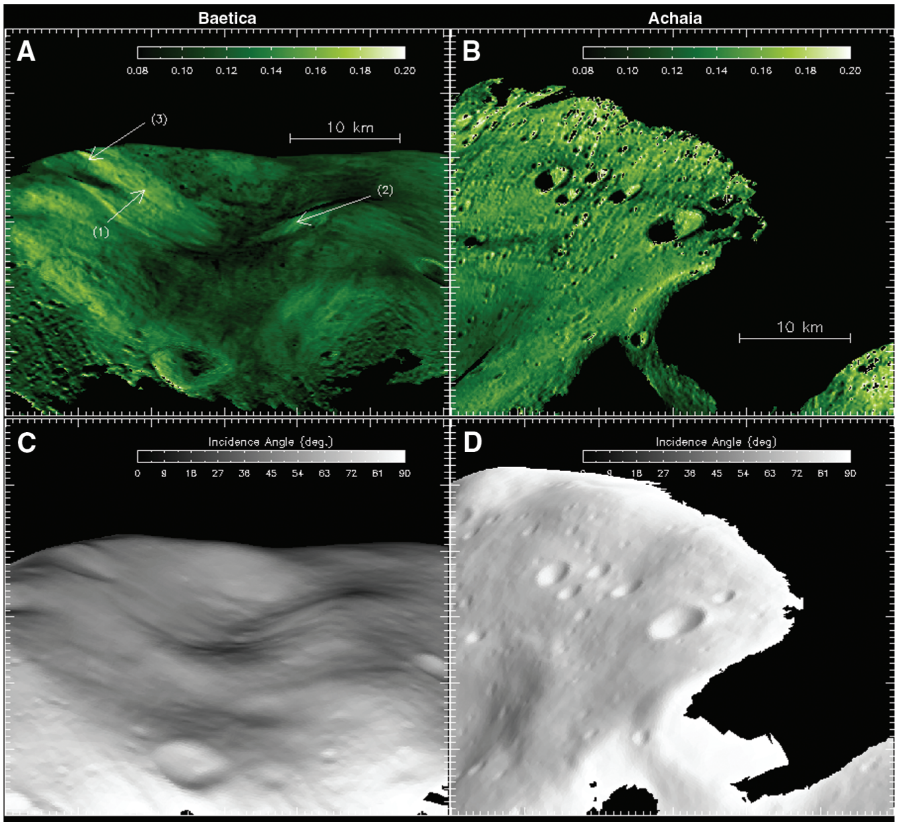

Fig. 4. Slope-corrected reflectivity maps (**A** and **B**) and incidence angle maps (**C** and **D**). These are images at 647 nm of parts of the Baetica [(A) and (C)] and Achaia [(B) and (D)] regions that have been photometrically corrected with Hapke bidirectional reflectance theory (*25*) to remove the effect of different angles of incidence and emission for different local slopes, leaving variations in brightness due only to local albedo variations (resolution, 60 m per pixel). During the photometric correction, the Hapke model parameters describing the single scattering albedo, the coherent backscattering, the shadow hiding, the surface roughness, and the asymmetric factor were all fixed to the value that best reproduced the overall surface reflectivity. The images are corrected to a solar phase angle of 10° for both Baetica and Achaia (the original phase angles for these regions were ~70° to 95°). This phase angle was arbitrarily chosen to avoid the opposition effect that may affect the reflectivity near 0° phase angle. Large variations are visible in the younger Baetica region, whereas the older Achaia region is more uniform (aside from a dark streak associated with a crater in the left of the image). The landslide indicated by 1 and possible outcrops 2 and 3 in Baetica have a reflectivity up to 30% brighter than the accumulation area.

a pure composition of either meteorite group. If Lutetia's surface were made of these materials, this would suggest that the interior may be differentiated (*30*).

These macroporosities for Lutetia clearly exclude a rubble-pile structure, which typically have macroporosities >25 to 30% (*9*). Such a high porosity structure is also inconsistent with the extensive ejecta blankets observed around the large craters (*31*). If Lutetia is undifferentiated, these porosities would also exclude a completely shattered but coherent structure (total porosity in the range of 15 to 25%) (*32*). Partial differentiation (*30*) could permit much higher grain densities in the interior and therefore higher porosity and a heavily fractured body. It is therefore likely that Lutetia has survived the age of the Solar System with its primordial structure intact; i.e., it has not been disrupted by impacts. This interpretation is consistent with the current view that the collisional lifetime against catastrophic destruction of bodies with diameters ≥100 km exceeds the age of the Solar System (*33*). The network of curvilinear features, the crater morphology, and the crater SFD discussed above both indicate that Lutetia's interior has considerable strength and relatively low porosity as compared to that expected for primordial aggregates of fine dust. One possibility is that Lutetia is partially differentiated, with a fractured but unmelted chondritic surface overlaying a higher-density sintered or melted interior (*30*). In any case, Lutetia is closer to a small planetesimal than to the smaller asteroids seen by previous missions, which are thought to be shattered or rubble-pile minor bodies.

References and Notes

1. M. A. Barucci, M. Fulchignoni, in *Rosetta: ESA's Mission to the Origin of the Solar System*, R. Schulz, C. Alexander, H. Boehnhardt, K.-H. Glassmeier, Eds. (Springer, New York, 2009), pp. 55–68.
2. M. Lazzarin *et al.*, *Mon. Not. R. Astron. Soc.* **408**, 1433 (2010).
3. H. U. Keller *et al.*, *Space Sci. Rev.* **128**, 433 (2007).
4. R. W. Gaskell *et al.*, *Meteorit. Planet. Sci.* **43**, 1049 (2008).
5. B. Carry *et al.*, *Astron. Astrophys.* **523**, A94 (2010).
6. M. Kaasalainen, *Inverse Problem and Imaging* **5**, 37 (2011).
7. M. Pätzold *et al.*, *Science* **334**, 491 (2011).
8. G. Consolmagno, D. Britt, R. Macke, *Chemie der Erde Geochemistry* **68**, 1 (2008).
9. We use rubble pile to mean a "strengthless aggregate held together by gravity only," following the definition of (*34*)
10. J. Oberst *et al.*, *Icarus* **209**, 230 (2010).
11. P. Thomas, J. Veverka, A. Bloom, T. Duxbury, *J. Geophys. Res.* **84**, 8457 (1979).
12. J. Veverka *et al.*, *Science* **289**, 2088 (2000).
13. R. J. Sullivan, P. C. Thomas, S. L. Murchie, M. S. Robinson, in *Asteroid III*, W. F. Bottke Jr., A. Cellino, P. Paolicchi, R. P. Binzel, Eds. (Univ. of Arizona Press, Tucson, AZ, 2002), pp. 331–350.
14. A. F. Cheng, in *Asteroid III*, W. F. Bottke Jr., A. Cellino, P. Paolicchi, R. P. Binzel, Eds. (Univ. of Arizona Press, Tucson, AZ, 2002), pp. 351–366.
15. E. Asphaug, *Annu. Rev. Earth Planet. Sci.* **37**, 413 (2009).
16. J. E. Richardson Jr., H. J. Melosh, R. J. Greenberg, D. P. O'Brien, *Icarus* **179**, 325 (2005).
17. D. P. O'Brien, R. Greenberg, J. E. Richardson, *Icarus* **183**, 79 (2006).
18. S. Marchi, M. Massironi, E. Martellato, L. Giacomini, L. M. Prockter, *Planet. Space Sci.*, available at http://arxiv.org/abs/1105.5272.
19. S. Marchi *et al.*, *Planet. Space Sci.* **58**, 1116 (2010).
20. S. Marchi, S. Mottola, G. Cremonese, M. Massironi, E. Martellato, *Astron. J.* **137**, 4936 (2009).
21. K. A. Holsapple, K. R. Housen, *Icarus* **187**, 345 (2007).
22. K. Wünnemann, G. S. Collins, H. J. Melosh, *Icarus* **180**, 514 (2006).
23. H. J. Melosh, in *Impact Cratering—A Geological Process* (Oxford Univ. Press, New York, 1989), p. 84.
24. P. C. Thomas *et al.*, *J. Geophys. Res.* **105**, 15091 (2000).
25. B. Hapke, *Icarus* **157**, 523 (2002).
26. A. Coradini *et al.*, *Science* **334**, 492 (2011).
27. M. A. Barucci *et al.*, *Astron. Astrophys.* **477**, 665 (2008).
28. P. Vernazza *et al.*, *Icarus* **202**, 477 (2009).
29. R. J. Macke, G. J. Consolmagno, D. T. Britt, M. L. Hutson, *Meteorit. Planet. Sci.* **45**, 1513 (2010).
30. L. T. Elkins-Tanton, B. P. Weiss, M. T. Zuber, *Earth Planet. Sci. Lett.* **305**, 1 (2011).
31. K. R. Housen, K. A. Holsapple, *Icarus* **163**, 102 (2003).
32. D. T. Britt, D. Yeomans, K. Housen, G. Consolmagno, in *Asteroid III*, W. F. Bottke Jr., A. Cellino, P. Paolicchi, R. P. Binzel, Eds. (Univ. of Arizona Press, Tucson, AZ, 2002), pp. 485–500.
33. A. Morbidelli, W. F. Bottke, D. Nesvorný, H. F. Levison, *Icarus* **204**, 558 (2009).
34. S. L. Wilkison *et al.*, *Icarus* **155**, 94 (2002).
35. W. F. Bottke Jr. *et al.*, *Icarus* **175**, 111 (2005).

Acknowledgments: OSIRIS was built by a consortium of the Max-Planck-Institut für Sonnensystemforschung, Katlenburg-Lindau, Germany; CISAS–University of Padova, Italy; the Laboratoire d'Astrophysique de Marseille, France; the Instituto de Astrofísica de Andalucia, CSIC, Granada, Spain; the Research and Scientific Support Department of the ESA, Noordwijk, Netherlands; the Instituto Nacional de Técnica Aeroespacial, Madrid, Spain; the Universidad Politéchnica de Madrid, Spain; the Department of Physics and Astronomy of Uppsala University, Sweden; and the Institut für Datentechnik und Kommunikationsnetze der Technischen Universität Braunschweig, Germany. The support of the national funding agencies of Germany (DLR), France (CNES), Italy (ASI), Spain (MEC), Sweden (SNSB), and the ESA Technical Directorate is gratefully acknowledged. We thank the Rosetta Science Operations Centre and the Rosetta Mission Operations Centre for the successful flyby of 21 Lutetia.

Supporting Online Material

www.sciencemag.org/cgi/content/full/334/6055/487/DC1
SOM Text
References (*36*, *37*)

21 April 2011; accepted 21 September 2011
10.1126/science.1207325

Chapitre 4

Troyens de Jupiter

4.1 Introduction

La région de transition entre les corps rocheux (astéroïdes) et les corps constitués principalement de glaces (comètes, Centaures et objets de Kuiper) se situe au niveau de l'orbite de Jupiter. Les groupes des astéroïdes Troyens et Grecs, qui occupent les points de Lagrange L4 et L5 de Jupiter, peuvent contenir des membres qui marquent cette transition, comme semble le suggérer la frappante similitude spectrale entre les Troyens et une partie des Centaures et transneptuniens. Les Troyens semblent avoir une densité inférieure aux astéroïdes de la ceinture principale (le couple binaire Patrocle-Ménoétius a une densité de 0.8 gr/cm^3, Marchis et al. (2006)) mais similaire à celle des objets de Kuiper.
Deux théories principales ont émergé pour expliquer la formation et l'évolution des Troyens de Jupiter. La première suggère que les Troyens se sont formés dans la même partie du Système Solaire que Jupiter, qui les a capturés sur des orbites stables pendant sa phase de formation (Marzari et al. 2002). La deuxième théorie propose que les Troyens aient été capturés pendant la migration planétaire (modèle de Nice), qui s'est produite environ 500-600 millions d'années après la formation du Système Solaire (Morbidelli et al., 2005). La migration a été déclenchée par le passage de Jupiter et de Saturne dans la résonance 1 : 2. Au cours de cette période Uranus et Neptune ont migré vers la partie extérieure du Système Solaire, alors que Jupiter se déplaçait vers l'intérieur. Cette migration aurait déstabilisé la ceinture de Kuiper, éjectant des millions d'objets vers les régions internes du Système Solaire, avant qu'ils ne soient capturés par Jupiter, et confinés dans des zones dynamiquement stables.
Plusieurs auteurs (Shoemaker et al. 1989, Marzari et al. 1997) suggèrent que les Troyens de Jupiter ont subi de nombreux processus de collisions, comparables à ceux qui ont intéressé les astéroïdes de la ceinture principale. Dans ce scénario, une partie des Troyens aurait été éjectés de leurs orbites suite aux collisions, devenant une source possible de comètes à courte période et de Centaures (Marzari et al., 1995, 1997 ; Levison et al., 1997). Vu leur région de formation au–delà de la ligne de glace (environ 3 AU), on imagine que les Troyens ont une composition riche en matériaux organiques, en substances volatiles et en glace d'eau, bien que, jusqu'à présent, aucune bande d'absorption due à la glace d'eau n'ait été détectée sur leurs surfaces (Jewitt & Luu 1990, Dotto et al. 2006, Emery et al. 2006, Emery & Brown 2003, 2004).

4.2 Etude des Troyens membres de familles dynamiques

Pour mieux comprendre les propriétés physique et la composition de ces objets j'ai participé à une campagne observationnelle aux télescopes NTT et VLT de l'ESO et TNG de l'ENO en collaboration avec E. Dotto. Nous avons fait des observations en spectroscopie et photométrie dans la région visible et dans le proche infrarouge dédiées aux Troyens de Jupiter de dimensions relativement petites (20 km < diamètre < 50 km), qui n'avaient jamais été étudiés en spectroscopie auparavant. En particulier, le projet a été dédié à l'étude des Troyens qui sont membres de familles dynamiques identifiées par Beaugé et Roig (2001). En effet, comme les familles d'astéroïdes se sont formées par rupture collisionnelle d'un corps parent, l'étude de leurs membres permet de comprendre la nature de ces familles et peut donner un aperçu sur la structure interne du corps parent, probablement riche en glace d'eau.

Nous avons obtenu des spectres dans le visible pour un échantillon de 80 Troyens membres de familles dynamiques (Fornasier et al. 2004a ; 2007b), dont 31 ont été aussi observés dans la région du proche infrarouge (Dotto et al. 2006, de Luise et al. 2010). Les familles observées sont les suivantes : Astyanax, Aneas, Anchises, Misenus, Phereclos, Sarpedon, Panthoos pour le nuage L5, et Eurybates, Menelaus, 1986 WD et 1986 TS6 en L4. Ces familles ont été définies avec un algorithme de *Hierarchical Clustering*, en comparant les distances mutuelles des objets avec une métrique des éléments propres. Les familles sont identifiées en utilisant une valeur seuil (cut-off) qui donne la signification statistique de la famille (plus la valeur du cut-off est petite, et plus la famille est robuste d'un point de vue statistique). Pour sélectionner les membres des familles nous avons choisi une valeur de cut-off de 100 m/s pour les familles du nuage L4 (familles plus 'robustes' comparé au nuage L5), et de 150 m/s pour les familles du nuage L5. Pour la famille d'Eurybates (L4), qui est très robuste, nous avons décidé d'utiliser une valeur du cut-off encore plus petite (70 m/s).

La plus grande partie des Troyens ont des spectres rouges (réflectance qui augmente avec la longueur d'onde) semblables à ceux des astéroïdes de la ceinture principale externe, et appartiennent principalement aux classes primitives D et P. Nous n'avons pas détecté de bandes d'absorption, ni dans la région visible, sauf exception pour quelques objets de la famille d'Eurybates (Fornasier et al. 2004a, 2007b), ni dans la région infrarouge (en particulier il n'y a pas de bande d'absorption due à la glace d'eau).

En analysant les données, la famille de Sarpedon se montre très robuste, pas seulement d'un point de vue dynamique, mais aussi d'un point de vue compositionnel, car les spectres de ses membres sont tous très similaires (type D). Une autre famille très robuste est celle d'Eurybates. Cette famille est atypique car ses membres ont des spectres moins rouges que ceux des autres Troyens et appartiennent aux classes C et P.
Certains astéroïdes ont des caractéristiques différentes par rapport aux autres membres d'une même famille et sont de possibles *interlopers*. C'est le cas par exemple de l'astéroïde 18493 dans la famille d'Aneas (L5) ou des objets 15094 et 13463 pour la famille de Makhaon (L4)

Pour les objets observés dans le visible et le proche infrarouge, nous avons essayé de contraindre leur composition de surface grâce à des modèles de transfert radiatif. L'allure spectrale des Troyens et leur faible valeur d'albédo est reproduite par des mélanges de carbone amorphe, de composés organiques et de faibles quantités des silicates (< 4%).

4.2.1 Article : The surface composition of Jupiter Trojans : Visible and near-infrared survey of dynamical families

Available online at www.sciencedirect.com
SCIENCE DIRECT®
Icarus 183 (2006) 420–434
ICARUS
www.elsevier.com/locate/icarus

The surface composition of Jupiter Trojans: Visible and near-infrared survey of dynamical families ☆

E. Dotto [a,*], S. Fornasier [b], M.A. Barucci [c], J. Licandro [d,e], H. Boehnhardt [f], O. Hainaut [g], F. Marzari [h], C. de Bergh [c], F. De Luise [a]

[a] *INAF, Osservatorio Astronomico di Roma, Via Frascati 33, I-00040 Monteporzio Catone (Roma), Italy*
[b] *Department of Astronomy, University of Padova, Vicolo dell'Osservatorio 2, I-35122 Padova, Italy*
[c] *LESIA, Observatoire de Paris-Meudon, 5 Place Jules Janssen, 92195 Meudon, France*
[d] *Isaac Newton Group of Telescopes, P.O. Box 321, E-38700 Santa Cruz de la Palma, Tenerife, Spain*
[e] *Instituto de Astrofisica de Canarias, c/Via Lactea s/n, E-38200 La Laguna, Tenerife, Spain*
[f] *Max Planck Institute for Solar System Research, Max-Planck-Strasse 2, D-37191 Katlenburg-Lindau, Germany*
[g] *European Southern Observatory, Casilla 19001, Santiago, Chile*
[h] *Department of Physics, University of Padova, Via Marzolo 8, I-35131 Padova, Italy*

Received 27 June 2005; revised 14 February 2006

Available online 24 April 2006

Abstract

Asteroid dynamical families are supposed to be formed from the collisional disruption of parent bodies. As a consequence, the investigation of the surface properties of small and large family members may give some hints on the nature of the dynamical group, the internal composition of the parent body, and the role played by space weathering processes in modifying the spectral behavior of the members' surfaces. In this work we present visible–near-infrared observations of 24 Jupiter Trojans belonging to seven dynamical families of both the L4 and L5 swarms. The most important characteristics we found is the uniformity of the Trojans population. All the investigated Trojans have featureless spectra and a spectral behavior typical of the primitive P and D taxonomic classes. In particular, no signatures of water ice have been found on the spectra of these primordial bodies. From our investigation, the L4 and L5 clouds appear to be compositionally indistinguishable. Tentative models of the surface composition, based on the Hapke theory, are presented and discussed.

Keywords: Asteroids; Photometry; Spectroscopy

1. Introduction

Beyond the asteroid main belt, in the Jupiter Lagrangian points L4 and L5, there are two clouds of small bodies of the Solar System, called Jupiter Trojans. The origin of these bodies is still far from being completely understood and several hypothesis have been so far proposed (Marzari et al., 2003; Morbidelli et al., 2005). Morbidelli et al. (2005) suggested that Jupiter Trojans, like Kuiper belt objects and the scattered disk, originated in the planetesimal disk which drove the planetary migration. Before being captured in the region where they are still observable, Jupiter Trojans had temporarily large eccentricity that brought them relatively close to the Sun, where cometary activity should have been intense. Although the scenario of their formation has not been definitively assessed, it is widely accepted that Jupiter Trojans formed at large heliocentric distances, in a region rich in frozen volatiles. Moreover, they are widely believed to have now stable orbits and to have suffered an intense collisional evolution. The recent discovery of dynamical families among Jupiter Trojans seems to support this idea.

☆ Based on observations carried out at the European Southern Observatory (ESO), La Silla, Chile, ESO proposals 69.C-0524 and 71.C-0650, and at the Telescopio Nazionale Galileo, La Palma, Canary Island, proposals TAC06 (AOT7) and TAC705 (AOT6).

* Corresponding author. Fax: +39 06 9447243.
E-mail address: dotto@mporzio.astro.it (E. Dotto).

0019-1035/$ – see front matter
doi:10.1016/j.icarus.2006.02.012

So far we know more than 1900 Jupiter Trojans. Their physical properties and their surface composition are at present not yet fully understood. Visible and near-infrared spectra are available for a limited sample of these objects (Jones et al., 1990; Jewitt and Luu, 1990; Luu et al., 1994; Fitzsimmons et al., 1994; Lazzarin et al., 1995; Dumas et al., 1998; Emery and Brown, 2001, 2003; Bendjoya et al., 2004; Fornasier et al., 2004a). The main characteristics are featureless spectra, low albedo and red colors: the large majority of them belongs to the D taxonomic class but P- and C-types are also present among them.

Although Jupiter Trojans are believed to have formed in a region rich in frozen volatiles, water ice is still undetected in their spectra. A large part of the infrared spectra of Jupiter Trojans available in the literature has been recently published by Emery and Brown (2004) who obtained 0.3–4.0 μm spectra of 17 bodies and presented also models of the surface composition. They did not detect water ice and hydrated silicate features in their V–NIR spectra and they estimated upper limits of a few percents and up to 30%, respectively, for these materials at the surface. To explain this lack of water ice on the surface of the observed objects, space weathering mechanisms can be invoked. Laboratory experiments have shown that solar wind, high-energy particles and microimpacts can alter icy surfaces of atmosphereless bodies, producing an irradiation mantle spectrally red and with low albedo (Moore et al., 1983; Thompson et al., 1987; Strazzulla, 1998; Hudson and Moore, 1999). However, if Jupiter Trojans experienced a phase of cometary activity water ice on their surface could have been devolatized early in their history, when they went through the high eccentricity phase. Alternatively, they could have formed a dust mantle as shown by Tancredi et al. (2006) for large comets (a few km-size comet nuclei). As a consequence, water ice, originally present on the surface of Jupiter Trojans, would be now completely covered and still present only in their interiors. In this scenario ice signatures could be detectable only if recent collisions would expose inner fresh material.

In order to increase the available sample of visible and near-infrared spectra of Jupiter Trojans and to investigate the surface composition of these objects, we started in 2002 an observational program at the European Southern Observatory (ESO, Chile), using both the New Technology Telescope (NTT) and the Very Large Telescope (VLT), and at the 3.6-m Telescopio Nazionale Galileo (TNG, La Palma, Spain). The sample selection done by the other teams which studied the physical properties of Jupiter Trojans was not based on dynamical constraints. On the contrary, we concentrated on members of dynamical families, as defined by Beaugé and Roig (2001), with the aim to look for the presence of water ice on their surfaces. In fact, the collisional disruptions which are supposed to have produced dynamical families might have exposed on the surface of the fragments some of the ices originally present in the interior of the parent body. Therefore, water ice likely present in the interior of larger Trojans, might be observable on the surfaces of the family members if the family formation is somewhat recent.

2. Observations

We carried out visible and near-infrared spectroscopy and photometry of Jupiter Trojans belonging to different dynamical families. We selected our targets from a list kindly provided by Beaugé and Roig (personal communication) as an update of the list by Beaugé and Roig (2001) and P.E.Tr.A. Project at www.daf.on.br/froig/petra/. In particular our selection was based on a cutoff threshold $Q = 0.014$ (Q is the upper limit of a metric so that a cluster be significant), corresponding to relative velocities of about 180 m/s.

Simultaneous visible and near-infrared spectroscopic and photometric observations of the L5 cloud have been carried out during 3 nights on November 2002 from ESO-NTT and ESO-VLT telescopes. Additional near-infrared spectroscopic observations have been performed at the TNG telescope during 3 nights on November–December 2002. From ESO-NTT and ESO-VLT we observed six objects belonging to the dynamical families of Aneas (1172 Aneas, 15502 1999 NV27, and 18493 1996 HV9) and Astyanax (1871 Astyanax, 23694 1997 KZ3, and 30698 Hippokoon). From the TNG we obtained near-infrared spectra of five objects belonging to the dynamical families of Sarpedon (2223 Sarpedon and 5130 Ilioneus) and Phereclos (2357 Phereclos, 6998 Tithonus and 18940 2000 QV49).

The L4 cloud has been observed on April–May 2003. Simultaneous visible and near-infrared spectroscopic and photometric observations have been carried out during 3 nights on April 2003 from ESO-NTT and ESO-VLT, acquiring data on six members of the Makhaon family (12917 1998 TG16, 13463 Antiphos, 15094 1999 WB2, 15535 2000 AT177, 20738 1999 XG191, 24390 2000 AD177). Further non-simultaneous visible and near-infrared spectroscopic observations have been carried out from TNG during 3 nights on May 2003, observing eight objects, members of the dynamical families Makhaon (12921 1998 WZ5, 20738 1999 XG191), 1986 WD (4035 1986 WD, 6545 1986 TR6, 11351 1997 TS25), and Menelaus (1647 Menelaus, 5244 Amphilochos, 5258 1989 AU1).

All the observations have been carried out in visitor mode.

The circumstances of the photometric and spectroscopic observations are reported in Appendix A, Tables A.1–A.7.

2.1. *Visible spectroscopy and photometry*

2.1.1. *ESO-NTT visible observations*

In November 2002 and April 2003 visible observations carried out at the ESO-NTT telescope were performed simultaneously to the ESO-VLT near-infrared observations. During these observing runs we performed both photometric and spectroscopic observations. Visible data of L5 Trojans obtained on November 2002 have been already published by Fornasier et al. (2004a).

The broadband B, V, R, and I photometric data of each target observed on April 2003 were obtained just before the spectral observations (Table 1). We used the RILD mode of EMMI for wide field imaging with the broadband B, V, R, and I filters, centered respectively at 4139, 5426, 6410, and 7985 Å. The

Table 1
Visible photometric observations of L4 Trojans (ESO-NTT EMMI): for each object, date, computed V magnitude, B–V, V–R, and V–I colors are reported

Object	Date	UT	V	B–V	V–R	V–I
12917	10 Apr. 03	00:30	18.835 ± 0.031	0.724 ± 0.042	0.537 ± 0.042	0.947 ± 0.055
13463	11 Apr. 03	00:38	18.239 ± 0.032	0.692 ± 0.045	0.449 ± 0.034	0.861 ± 0.057
15094	11 Apr. 03	06:08	19.123 ± 0.053	0.652 ± 0.065	0.477 ± 0.065	0.799 ± 0.068
15535	10 Apr. 03	07:51	17.843 ± 0.031	0.727 ± 0.041	0.495 ± 0.042	0.913 ± 0.055
15535	10 Apr. 03	08:26	17.831 ± 0.031	0.751 ± 0.042	0.446 ± 0.042	0.950 ± 0.055
20738	10 Apr. 03	04:56	18.749 ± 0.031	0.776 ± 0.041	0.472 ± 0.042	0.939 ± 0.055
24390	11 Apr. 03	03:23	18.815 ± 0.032	0.700 ± 0.042	0.513 ± 0.034	0.975 ± 0.057

The given UT is relative to the V filter acquisition. The observing photometric sequence (V–R–B–I) took a few minutes.

observations were carried out in 2×2 binning mode, yielding a pixel scale of 0.33 arcsec/pixel. Several standard stars (Landolt, 1992) have been observed over a wide range of airmasses and stellar types. The CCD images were reduced and calibrated with a standard method. First, bias and flat-field corrections were performed: a master flat field was obtained as a median of several flat fields obtained during twilight. Then the instrumental magnitudes have been computed, together with zero point, extinction and color terms necessary to convert instrumental magnitudes to apparent magnitudes. The final colors are reported in Table 1. The error bars take into account both the instrumental errors, given by photon statistics alone, and the calibration errors. By visual inspection no coma was detected for any of the observed objects.

Visible spectroscopy has been performed at ESO-NTT on April 2003 using the grism #7 (150 g/mm) in the RILD arm of EMMI, covering the spectral range 5200–9600 Å, with a dispersion of 3.6 Å/pixel at the first order. Spectra were taken through a 1 arcsec wide slit oriented along the parallactic angle in order to avoid flux loosing due to the atmospheric diffraction. Appendix A, Table A.1 reports the circumstances of these observations. Bias, flat-field, calibration lamp (He–Ar) and several (6–7) solar analog stars spectra have been recorded during each night. Spectra were reduced with the software packages Midas and IDL using standard procedures (see Fornasier et al., 2004a) which include: subtraction of the bias from the raw data, flat field correction, cosmic rays removal, background subtraction, collapsing the two-dimension spectra to one-dimension, wavelength calibration and atmospheric extinction correction (using La Silla atmospheric extinction coefficients). Wavelength calibration was made using a lamp with He and Ar emission lines. The reflectivity of the asteroids was then obtained by dividing their spectra by the spectrum of the solar analog star the closest in time and airmass to the object, as reported in Appendix A, Table A.1. Finally, spectra have been smoothed with a median filter technique, using a box of 19 pixels.

2.1.2. *TNG visible observations*

Visible spectroscopy has been acquired at the TNG telescope on May 2003. We used the DOLORES (Device Optimized for the LOw RESolution) instrument equipped with the low resolution red grism (LR-R) covering the 0.51–0.98 μm range with a spectral dispersion of 2.9 Å/pixel (http://www.tng.iac.es). During the observing run we also acquired bias, flat-field, calibration lamp (Ne–Ar lines) and several solar analog spectra. For all the targets, with the exception of 11351, the total exposure time was divided into 2 acquisitions of respectively 10 min. This allowed us also to check the asteroid position inside the slit before each acquisition and to reduce the cosmic rays hits on each spectrum. For data reduction we followed the same procedure applied for the NTT spectra. Appendix A, Table A.2 reports the observational circumstances of these observations.

2.2. *Near-infrared spectroscopy and photometry*

2.2.1. *ESO-VLT near-infrared observations*

To perform near-infrared photometry and spectroscopy at ESO-VLT we used the first Unit Telescope (UT1, Antu) equipped with the infrared-cooled grating spectrometer ISAAC (Infrared Spectrometer And Array Camera) (www.eso.org/instruments/isaac) and with a Rockwell Hawaii 1024×1024 pixel Hg:Cd:Te array. Photometric J, H, and Ks measurements (centered at 1.25, 1.65, and 2.2 μm) have been performed before and after the spectra. The details of the near-infrared photometric observations are reported in Appendix A, Tables A.3 and A.4. Near-infrared photometry has been carried out using the jitter imaging technique: a combined image is generated with the jitter routine from the ECLIPSE package. The used data processing routines are described in Dotto et al. (2003a) and Romon et al. (2001). The calibration was performed by the observation of several faint infrared standard stars from Hunt et al. (1998) and Persson et al. (1998). Final colors are reported in Table 2.

Spectroscopic observations were performed in the SW mode (1–2.5 μm wavelength range). We used the ISAAC low resolution spectroscopic mode with a 1 or 1.5 arcsec wide slit and the grating at three different central wavelengths corresponding to J, H, and K bands (Appendix A, Table A.5). The pixel scale is 0.147 arcsec/pixel. We observed separately the three spectral ranges (J, H, and K) corresponding to 1.10–1.39, 1.42–1.83, and 1.84–2.56 μm. The final spectral resolution for the 1 arcsec slit is 500 for the J and H bands and 450 for the K band. The observations were done by nodding the object along the slit by 10 arcsec between two positions A and B. The two averaged A and B images in each spectral range (J, H, and K) were subtracted from each other. The A–B and B–A images were flat-fielded, corrected for spatial and spectral distortion and finally combined with a 10-arcsec offset. The spectra were extracted from the resulting combined images, and wavelength calibration was performed using xenon–argon lamp spectra. The telluric ab-

Table 2
V magnitude and color indices of family Trojans

Object	V	J	H	K	V–J	J–K	H–K
L5							
1172	16.174 ± 0.020	14.597 ± 0.030	14.167 ± 0.030	14.032 ± 0.020	1.577 ± 0.030	0.565 ± 0.040	0.135 ± 0.030
1871	18.379 ± 0.034	16.848 ± 0.036	16.510 ± 0.036	16.391 ± 0.020	1.531 ± 0.050	0.457 ± 0.030	0.119 ± 0.030
1871	18.379 ± 0.034	16.888 ± 0.036	16.540 ± 0.036	16.388 ± 0.020	1.491 ± 0.050	0.500 ± 0.030	0.153 ± 0.030
1871	18.293 ± 0.027	16.949 ± 0.027	16.532 ± 0.027	16.429 ± 0.016	1.344 ± 0.040	0.520 ± 0.022	0.103 ± 0.022
15502	17.061 ± 0.023	15.523 ± 0.032	15.031 ± 0.032	14.876 ± 0.020	1.538 ± 0.040	0.647 ± 0.025	0.155 ± 0.025
15502	17.061 ± 0.023	15.457 ± 0.023	14.964 ± 0.024	14.817 ± 0.015	1.604 ± 0.030	0.640 ± 0.018	0.147 ± 0.019
18493	18.298 ± 0.023	16.898 ± 0.036	16.520 ± 0.036	16.445 ± 0.020	1.400 ± 0.040	0.453 ± 0.030	0.075 ± 0.030
18493	18.393 ± 0.022	17.022 ± 0.029	16.633 ± 0.029	16.528 ± 0.017	1.371 ± 0.040	0.494 ± 0.023	0.105 ± 0.023
23694	18.593 ± 0.024	16.936 ± 0.023	16.443 ± 0.024	16.232 ± 0.015	1.657 ± 0.030	0.704 ± 0.018	0.211 ± 0.019
30698	19.244 ± 0.035	17.757 ± 0.053	17.322 ± 0.053	17.140 ± 0.035	1.487 ± 0.060	0.617 ± 0.040	0.182 ± 0.040
30698	19.244 ± 0.035	17.680 ± 0.050	17.319 ± 0.044	17.135 ± 0.060	1.465 ± 0.060	0.545 ± 0.078	0.184 ± 0.074
L4							
12917	18.835 ± 0.031	17.128 ± 0.058	16.653 ± 0.064	16.448 ± 0.050	1.707 ± 0.066	0.680 ± 0.076	0.205 ± 0.081
13463	18.239 ± 0.032	16.822 ± 0.036	16.479 ± 0.042	16.376 ± 0.030	1.417 ± 0.048	0.446 ± 0.046	0.103 ± 0.051
15094	19.123 ± 0.033	17.764 ± 0.036	17.422 ± 0.050	17.327 ± 0.030	1.359 ± 0.051	0.437 ± 0.046	0.095 ± 0.058
15535	17.843 ± 0.031	16.156 ± 0.032	15.656 ± 0.036	15.533 ± 0.030	1.687 ± 0.045	0.623 ± 0.044	0.123 ± 0.047
15535	17.831 ± 0.031	16.156 ± 0.032	15.656 ± 0.036	15.533 ± 0.030	1.675 ± 0.045	0.623 ± 0.044	0.123 ± 0.047
20738	18.749 ± 0.031	17.156 ± 0.054	16.636 ± 0.064	16.523 ± 0.050	1.593 ± 0.062	0.633 ± 0.073	0.113 ± 0.081
24390	18.815 ± 0.032	17.131 ± 0.036	16.670 ± 0.042	16.530 ± 0.030	1.684 ± 0.048	0.601 ± 0.047	0.140 ± 0.051

sorption correction and the removal of the solar contribution were obtained dividing the spectra of the asteroids by those of different solar analog stars, observed at similar airmasses. The resulting spectra were smoothed with a median filtering technique. The edges of each spectral region have been cut to avoid low S/N spectral regions.

2.2.2. *TNG near-infrared observations*

Near-infrared spectroscopic data, non-simultaneous to the visible observations, have been carried out on November 2002 and May 2003 with the 3.6-m TNG telescope at La Palma (Appendix A, Tables A.6 and A.7). We used the Near-Infrared Camera and Spectrometer (NICS), a FOSC-type cryogenic focal reducer, equipped with two interchangeable cameras feeding a Rockwell HgCdTe Hawaii 1024 × 1024 pixel array. NICS was used in its low-resolution spectroscopic mode and equipped with an Amici prism disperser, which allowed us to obtain a continuous spectrum in the wavelength range 0.8–2.4 μm. A slit of 1.5 arcsec was used, providing a final spectral resolution of 34. The pixel scale is 0.25 arcsec/pixel. Also in this case, the observations were carried out by offsetting the telescope by 30 arcsec in the direction of the slit between two different positions A and B. Several A and B images of 60-, 90-, and 120-s individual exposure time were obtained to avoid saturation. Reduction of the spectra was done by subtracting consecutive A and B images and applying the procedure already used by Licandro et al. (2002). Both 2002 and 2003 observing runs were carried out in non-photometric conditions, and the composite visible and near infrared spectra have been obtained by overlapping the spectral interval between 0.8 and 0.9 μm which is common to NICS and DOLORES. The wavelength calibration has been performed following the NICS manual, using a look-up table which is based on the theoretical dispersion predicted by ray-tracing and adjusted to best fit the deep telluric absorption features. The resolution given by the instrument is in fact so low, that all the Ar–Xe lines are blended and cannot be easily used for standard reduction procedures.

Each asteroid spectrum has been reduced vs each solar analog and normalized at 1.6 μm. Considering that the spectra of the solar analogs divided by each other were very similar with differences in slope smaller that 0.4%/1000 Å, the final asteroid spectra have been computed averaging the spectra of each object divided by different solar analogs (see Appendix A, Tables A.6 and A.7). Finally, the composite visible and near infrared spectrum for each asteroid has been obtained scaling the infrared spectra in order to be attached to the visual part (normalized to 5500 Å).

3. Spectral analysis and surface modeling

Figs. 1 and 2 show the whole sample of visible spectra obtained at the TNG telescope and at the ESO-NTT telescope.

Figs. 3–6 show the visible and near-infrared spectra obtained for each dynamical family. For observations carried out at ESO, where the photometric calibration has been performed, the different spectral ranges have been adjusted using the computed color indices. For TNG observations the photometric calibration was not possible. In any case they are not needed as visible and near-infrared spectra have an overlapping region between 0.80–0.95 μm. The values and slopes of visible and near-infrared spectra in this spectral region have been used to adjust them. For the L5 family members our near-infrared spectra are shown along with the visible spectra published by Fornasier et al. (2004a).

We estimated the diameter of 19 of our targets, with the exception of 1172, 2223, 2357, 1647, 4035 whose diameters have

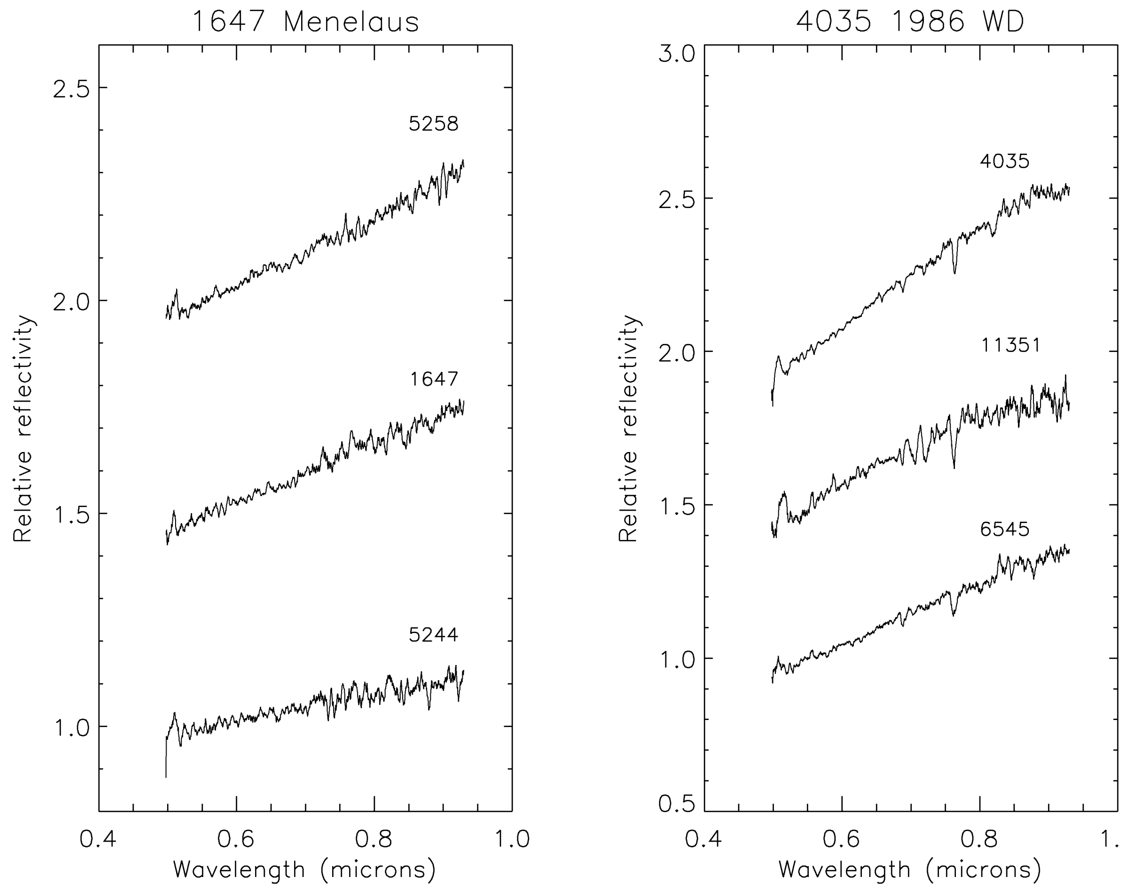

Fig. 1. Visible spectra of the L4 Trojans belonging to the Menelaus and 1986 WD families, obtained at TNG on May 2003. All the spectra are normalized to 1 at 0.55 μm and shifted by 1 in reflectance for clarity.

been taken from the IRAS data. We used the V magnitudes here presented (Table 1) and those already published by Fornasier et al. (2004a) to compute the absolute magnitudes H applying the (G, H) model by Bowell et al. (1989)

$$H = \mathrm{V} - 5\log(r\Delta) + 2.5\log\Big\{(1-G)\exp\big[-3.33\tan^{0.63}(\alpha/2)\big] + G\big[-1.87\tan^{1.22}(\alpha/2)\big]\Big\},$$

where V is the observed magnitude, r and Δ are the heliocentric and geocentric distances (in AU), respectively, α is the phase angle, and G is the slope parameter assumed of 0.05 in agreement with Fernandez et al. (2003). For the 7 objects observed at TNG (1647, 4035, 5244, 5258, 6545, 11351, 12921), for which we do not have visible photometric data, we rely upon the Lowell Observatory absolute magnitudes, derived from the astorb.dat file. Diameters D have been computed from the absolute magnitudes H and the albedos p as

$$D = \frac{1329 \times 10^{-H/5}}{\sqrt{p}}$$

assuming an albedo range of 0.03–0.07, with a mean value of 0.04 (Fernandez et al., 2003; Jewitt et al., 2000). The obtained H and D values are reported in Table 3.

To interpret the spectra of the observed Jupiter Trojans in terms of the surface composition we ran a radiative transfer model, based on the Hapke theory and already applied to centaurs and trans-neptunian objects (Barucci et al., 2002; Dotto et al., 2003a, 2003b, 2003c; de Bergh et al., 2004; Fornasier et al., 2004b). We considered several compounds that are expected to be present on the surface of Trojans, taking into account that they likely formed at large heliocentric distances. In particular we considered the following materials at different grain sizes: organics solids (e.g., kerogens by Clark et al., 1993 and Khare et al., 1991; Titan tholins from Khare et al., 1984; and Triton tholins from McDonald et al., 1994), amorphous carbon (by Zubko et al., 1996), and different minerals (silicates [e.g., olivines, pyroxenes], phyllosilicates [e.g., montmorillonite, serpentine], oxides [e.g., hematite], sulfates [e.g., jarosite] and all the minerals included in the US Geological Digital Spectral Library http://speclab.cr.usgs.gov/spectral-lib.html), bitumen (by Moroz et al., 1998), and ices (H_2O, CH_4, CH_3OH, NH_3, and ice tholins by McDonald et al., 1996, and Khare et al., 1993). Several geographical (spatially segregated) mixtures of all these compounds have been modeled and for each combination synthetic spectra were compared with the observed ones. The constraints to be satisfied were: low albedo, visible spectral slope, spectral behavior in the near-infrared wavelengths. Table 3 reports for each object the combination of compounds and their percentages which best reproduces the observed spectral behav-

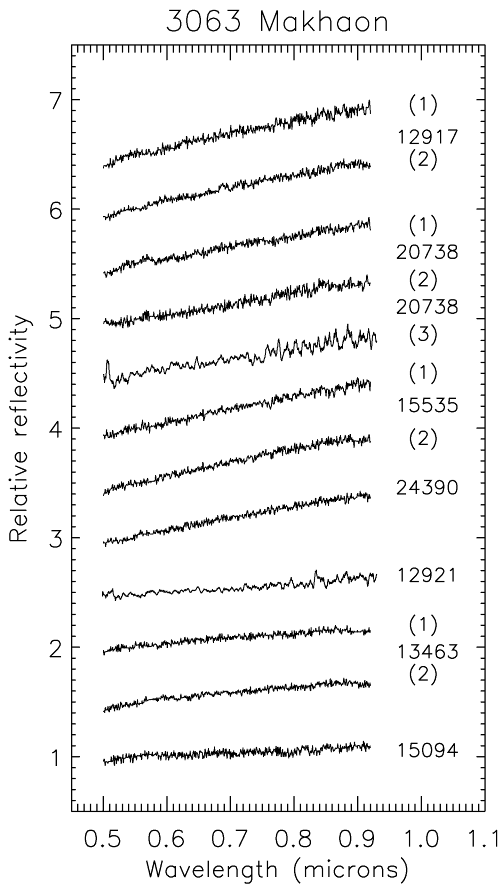

Fig. 2. Visible spectra of the L4 Trojans belonging to the Makhaon family, obtained at ESO-NTT on April 2003. Spectrum (3) of 20738 and the spectrum of 12921 have been obtained at TNG on May 2003. All the spectra are normalized to 1 at 0.55 μm and shifted by 1 in reflectance for clarity.

iors, together with the albedo values at 0.55 μm resulting from our modeling (all ranging between 0.03 and 0.06). In Table 3 we show also the IRAS albedo available for five objects (1172, 1647, 2223, 2357, and 4035). For four of these asteroids (1172, 1647, 2223, 2357) the albedos we have computed on the basis of the synthetic spectra are in agreement with the IRAS values. For 4035 we did not find a mixture of minerals able to reproduce the observed spectrum, maintaining the albedo at 0.08, a quite high value for a Jupiter Trojan. Further observations of this object are recommended in order to check the albedo and diameter computation as well as the thermal properties and the spectral behavior.

The synthetic spectra corresponding to the model of the surface composition of each target are represented in Figs. 3–6 as superimposed solid lines.

Of course the used spectral inversion method does not produce unique solution: different combinations of other minerals in different percentages and grain sizes can lead to synthetic spectra compatible with the observed ones. The spectra we obtained are featureless, no signature related to minerals or icy component has been detected. To reproduce the uniformly red spectral behavior, observed between 0.3 and 1.2 μm, we considered tholins and kerogens. Cruikshank et al. (2001) demonstrated that organic solids are not necessary to reproduce the spectral behavior of red spectra and modeled the spectrum of 624 Hektor with Mg-rich pyroxenes and serpentine. Also Emery and Brown (2004) limited the inclusion of tholins in their models of the surface composition of Trojans as they did not find in their spectra any absorption at about 3 μm. Our spectra, limited to 2.4 μm, do not allow to check the feature at 3 μm and to verify the presence of tholins on the surface of our targets. As a consequence, tholins and kerogens included in our models have to be considered only as reddening agents.

3.1. The L5 families

3.1.1. Aneas family

Five out of six members of this family were observed in the visible range by Fornasier et al. (2004a). Four of them were classified as D-types and their visible spectral slopes showed an increasing trend at decreasing sizes. One object (18493 1996 HV9) classified as P-type was out of this trend. We observed in the near-infrared region three of these objects: the two largest members of the family (1172 has a diameter of about 143 km, and 15502 has a diameter of about 68 km) and the possible interloper 18493. Fig. 3 shows the complete visible and near infrared spectra. 1172 and 15502 have very similar spectral behavior: their colors are comparable (see Tables 1 and 2) and their spectra are both reddish, suggesting that they might have common origin and composition. Their surface composition has been modeled with the same mixture of kerogens, amorphous carbon, silicates and Titan tholins (see Table 3). On the contrary, the spectrum of 18493 is flatter than the others and the color indices are very different. Its surface composition has been modeled with a different mixture composed of a higher amount of amorphous carbon and a small percentage of organic compounds (kerogens and tholins).

Even considering that the available sample is very small, the analysis of the obtained visible and near-infrared spectra confirms that 18493 is different from the other members of Aneas. Its spectral diversity compared to 1172 and 15502 could indicate either that 18493 is an interloper or that it comes from the interior of the parent body. This last hypothesis would imply that this object has experienced during its life-time a low degree of space weathering alteration, or, alternatively, that it has a peculiar surface composition if the parent body was differentiated.

3.1.2. Astyanax family

Fornasier et al. (2004a) presented the visible spectra of 4 out of 5 members of this family and classified all of them as belonging to the D-type. We obtained simultaneous near-infrared observations of three of these members (1871, 23694, and 30698) which have similar estimated diameters (around 25–35 km). If the analysis of the visible colors and spectra suggested a quite homogeneous composition, the near-infrared spectra show very different behaviors. 1871 and 30698 have similar colors and moderately red spectra, while 23694 exhibit a slope in the infrared range steeper than the other two family members. To reproduce the observed spectral behaviors we considered sev-

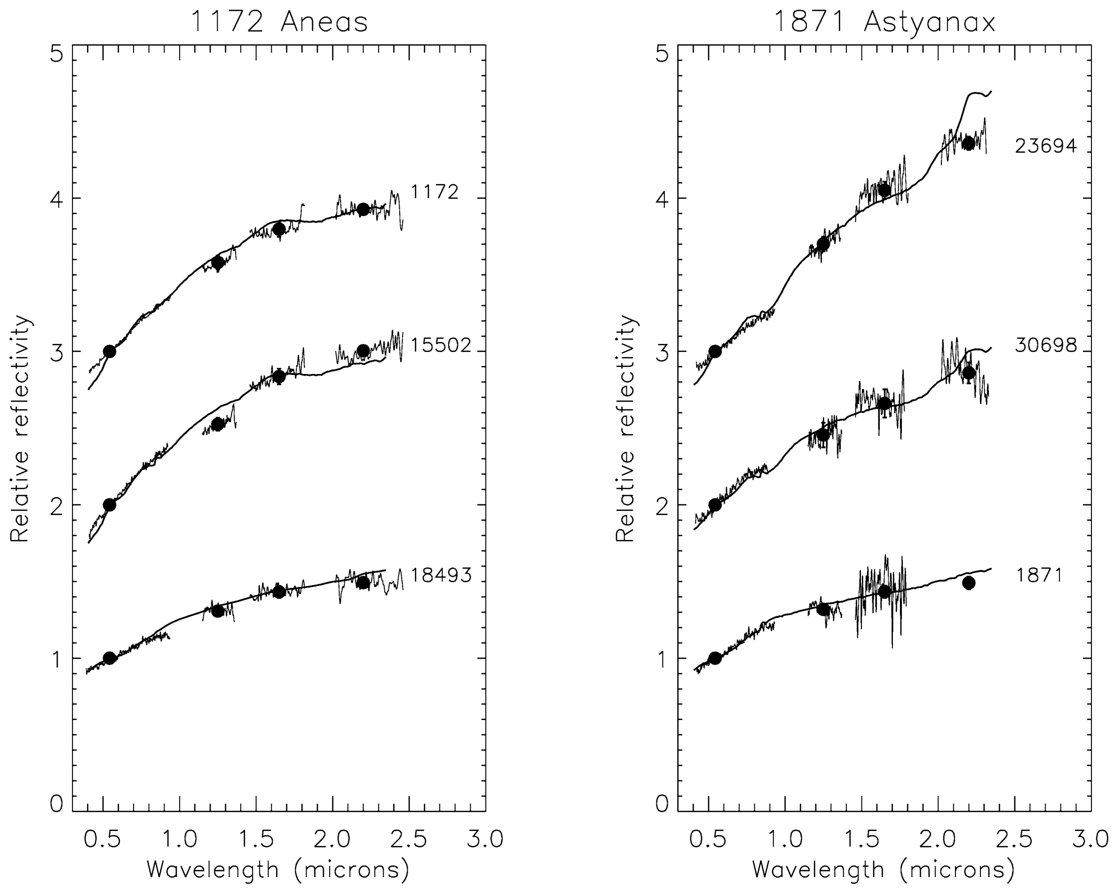

Fig. 3. Near-infrared spectra of L5 Trojans belonging to the Aneas and Astyanax families obtained at ESO-VLT on November 2002, together with the visible part already published by Fornasier et al. (2004a). All the spectra are normalized to 1 at 0.55 µm and shifted by 1 in reflectance for clarity. The superimposed continuous lines represent the synthetic spectra obtained modeling the surface composition.

eral combinations of minerals. The synthetic spectra reported in Fig. 3 have been obtained considering different combinations of amorphous carbon, small amounts of silicates and organic compounds (see Table 3). From the spectrally flattest to the spectrally reddest object the percentage of amorphous carbon decreases while the percentage of organics increases, giving a higher albedo value. Further observations of all the family members would be necessary to investigate the reliability of Astyanax family and the composition and structure of the parent body.

3.1.3. *Sarpedon family*

All 4 members of this family were observed in the visible range by Fornasier et al. (2004a). This is a strong cluster from the dynamical point of view and all the objects were classified as belonging to the D-type. We observed the two larger members (2223 and 5130) also in the near-infrared range, obtaining the 0.4–2.4 µm spectra reported in Fig. 4. The visible part in this case was not simultaneously acquired to the near-infrared one. Visible spectra of 2223 and 5130 are very similar each other, while the near-infrared behavior is quite different. The suggested surface compositions are constituted by different mixtures of amorphous carbon, tholins and kerogens. From our proposed compositional models 2223 seems to contain some percentage of silicates and a larger amount of tholins, while 5130 was modeled with kerogens, amorphous carbon, and a few percentages of Triton tholins (see Table 3). Observations of more members are absolutely needed to constrain the homogeneity of the family and, as a consequence, the nature of the parent body.

3.1.4. *Phereclos family*

The Phereclos cluster contains 6 members at a cutoff level of $Q = 0.014$. We observed 3 of them in the near-infrared range (Fig. 4). These spectra are quite different from each other, confirming the diversity already reported by Fornasier et al. (2004a) from visible spectroscopy. The models of the surface composition of 6998 and 18940 contain different percentages of amorphous carbon, kerogens, and tholins. The spectrum of 2357, the largest member of the family, is redder up to 1.6 µm, suggesting a surface rich in tholins and containing a few percents of silicates.

3.2. *The L4 families*

3.2.1. *Menelaus*

Menelaus is a very huge cluster, surviving up to a cutoff of 100 m/s, of which we observed only three members (Fig. 5).

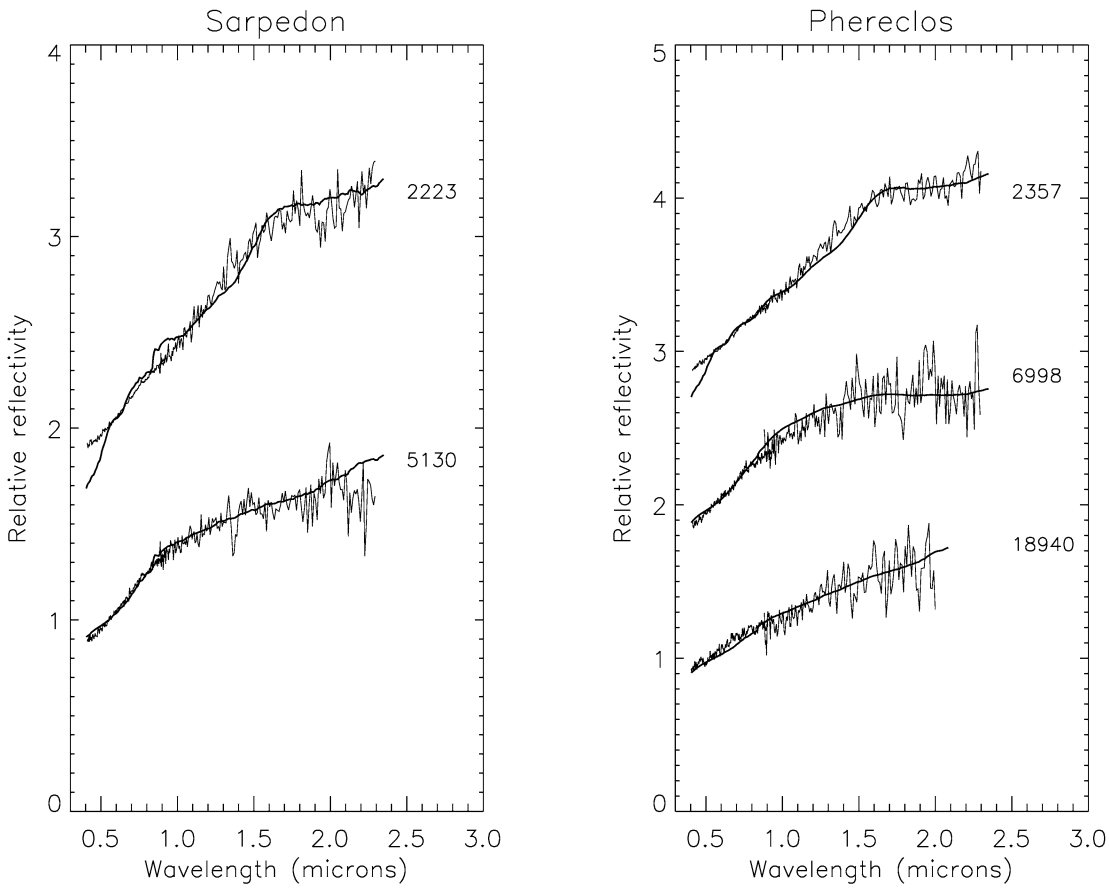

Fig. 4. Near-infrared spectra of L5 Trojans belonging to the Sarpedon and Phereclos families obtained at TNG on November–December 2002, together with the visible part already published by Fornasier et al. (2004a). All the spectra are normalized to 1 at 0.55 µm and shifted by 1 in reflectance for clarity. The superimposed continuous lines represent the synthetic spectra obtained modeling the surface composition.

The obtained spectra show a continuous trend with increasing spectral slope from 5244 and 5258. Since the spectral behaviors are very similar, this spread can be interpreted as due to different levels of space weathering processing. The compositional models that reproduces the spectral behavior of these members (see Table 3) are very similar to each other, being composed by a mixture of a high percentage of amorphous carbon and few percent of tholins: from 2% in the case of 5244 to 6% in the case of 5258.

3.2.2. 1986 WD

This cluster includes 6 members at a cutoff of 0.010, corresponding to a relative velocity of the order of 130 m/s. We carried out non-simultaneous visible and near-infrared observations of 3 of them and the obtained 0.4–2.4 µm spectra are shown in Fig. 5. All the objects have similar spectral behaviors: the visible spectrum of 4035, the biggest member of the family, is slightly redder than the visible spectra of the other two observed objects, and this difference is evident also in the whole 0.4–2.4 µm spectra. As a consequence the compositional models are quite different: the surfaces of 6545 and 11351 are modeled with the same combination of kerogens, amorphous carbon and tholins, while the percentages of tholins increases in the model of 4035 to better reproduce its redder spectral slope. In any case the cluster seems to be quite homogeneous, even if the observational sample need to be extended to the whole family to give an insight of its nature and of the possible structure of the parent body.

3.2.3. Makhaon family

Makhaon is a very strong dynamical family which survives up to a cutoff of 100 m/s. We observed all the 7 members present at a cutoff of $Q = 0.10$ corresponding to a relative velocity of the order of 130 m/s. Among these objects 12917, 12921, 20738, and 15535 represent a strong core of the family, surviving up to values of the relative velocities around 100 m/s. The obtained visible and near-infrared spectra are shown in Fig. 6. They present a continuous range of variation, starting from 15094 which could be classified as a C-type, up to 12917, 15535, 20738, and 24390 which show very similar red spectra. These four objects have similar dimensions (between 29 and 48 km) and show very similar spectral behaviors. Small differences in spectral slope can be, also in this case, attributed to different level of space weathering processing of their surfaces. In the new version of the member lists of Jupiter dynamical families (www.daf.on.br/froig/petra/families.htm) 15094 is no more included in this family and 13463 appears only at a cutoff of 130 m/s. On the basis of this consideration we can assume

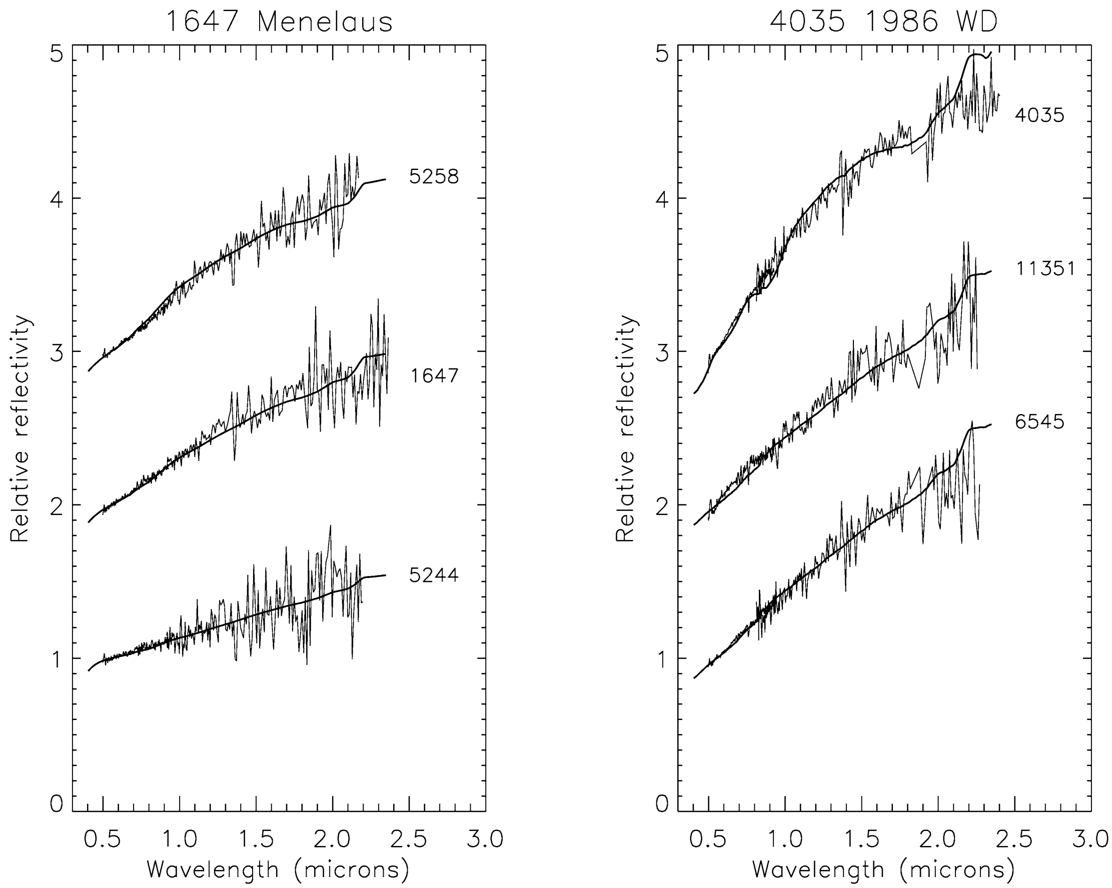

Fig. 5. Visible and near-infrared spectra of L4 Trojans belonging to the Menelaus and 1986 WD families obtained at TNG on May 2003 All the spectra are normalized to 1 at 0.55 µm and shifted by 1 in reflectance for clarity. The superimposed continuous lines represent the synthetic spectra obtained modeling the surface composition.

that these two objects, which have the flattest spectra shown in Fig. 6, could be interlopers in our sample. The obtained models (see Table 3) are very similar to each other, being composed by a mixture of a high percentage of amorphous carbon and kerogens with few percents of tholins, with the amount of this latter slightly increasing with the increasing of the spectral slope.

4. Discussion

A strong homogeneity of the Trojan population is the main characteristic we derived from our survey. Most of the observed Trojans family members appear to belong to the P–D taxonomic type. No diagnostic spectral signatures have been found to distinguish a family with respect to the others. All the observed spectra have been modeled with a surface composition given by mixtures of amorphous carbon and organic compounds with small percentages of silicates. Different slopes in the region 0.5–1.2 µm, probably due to different degrees of space weathering, have been reproduced with mixtures of different percentages of organic compounds which redden the spectra, without changing neither the albedo value, nor the nature of the surface composition. As discussed by Cruikshank et al. (2001) and Cruikshank and Dalle Ore (2003), organic compounds are only one possibility to model low-albedo surfaces having spectra as red as the Jupiter Trojans, but they are not essential for this kind of models. Other mineral mixtures, e.g., Mg-rich pyroxene and serpentine as used in the case of Hektor, can produce spectra similar to those of Jupiter Trojans. Since in our spectra we cannot check the presence of the tholin spectral feature at about 3 µm, we cannot affirm the presence of tholins on the surface of the observed targets, but we can consider them as possible reddening agents allowing us to reproduce the slope observed between 0.5 and 1.2 µm.

We investigated also the possible relations between spectral slopes, color indices and dynamical characteristics. We computed the difference between the reflectance at 0.85 µm (corresponding approximately to the center of the x filter in the ECAS survey) and at 2.2 µm (corresponding to the K color) for all the 24 investigated Trojans to obtain the x–K color index. The choice of this wavelength range allows us to include in the data set also the results on the 0.85–2.2 µm color index of 16 Trojans presented by Emery and Brown (2004, Table 4). Considering that Asteroid 1172 Aneas was observed both by us and Emery and Brown (2004), with results quite in agreement (x–K values respectively of 1.14 ± 0.04 and 1.25 ± 0.03) we can investigate the (x–K) color index for a total sample of 39 Trojans. We analyzed the x–K color index distribution versus different proper elements (eccentricity, inclination and frequency of libration), but no relationships have been found

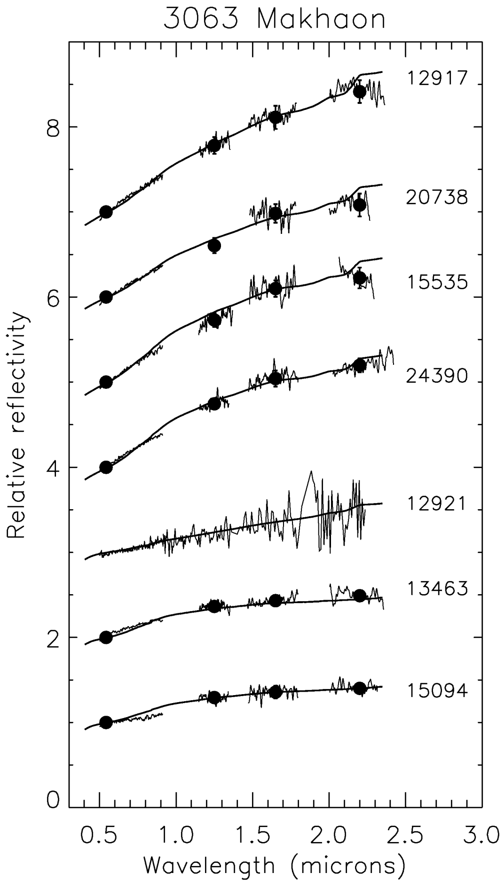

Fig. 6. Visible and near-infrared spectra of L4 Trojans belonging to the Makhaon family (ESO-NTT& VLT, TNG telescopes data). All the spectra are normalized to 1 at 0.55 μm and shifted by 1 in reflectance for clarity. The superimposed continuous lines represent the synthetic spectra obtained modeling the surface composition.

with these dynamical elements. The distribution of the x–K vs B–V and V–R color indices is shown in Fig. 7 and does not exhibit a clear trend. Trojans with low B–V color index have also a small value of the x–K color, but for higher B–V color values we see a high dispersion in the infrared colors. Objects with a high V–R color index also have high x–K value, but Trojans with lower V–R color index show a high variety in the x–K color index.

As shown in Fig. 7, the whole sample of objects has quite similar spectral characteristics and as a consequence appears to be quite homogeneous in surface composition. No differences have been found in the spectral slopes between Trojans belonging to the L4 and L5 clouds. In fact the 26 L4 Trojans analyzed have a mean x–K color $= 1.16 \pm 0.16$, while the 13 L5 Trojans have a mean x–K color 1.12 ± 0.12, therefore there are no differences within the uncertainties.

Analyzing the x–K color as a function of the diameter (see Fig. 8), we find that both small objects (diameter <80 km) and large ones have similar mean x–K values (1.12 ± 0.16 and 1.18 ± 0.11, respectively). Larger bodies have a lower dispersion in the x–K color index as compared to smaller ones. This characteristics can be interpreted as possibly due to different degrees of space weathering alteration: larger family members probably show an ageing coming in part from the parent body, while smaller fragments can came indifferently from the interior or the surface of the parent body and exhibit different degrees of space weathering alteration.

The most important result of our modeling is that none of the observed objects show the presence of spectral features at 1.5 and 2 μm, related to the presence of water ice. This is surprising, since Trojans formed beyond the snow line and the early temperatures in the protoplanetary disk were probably low enough to allow water ice condensation during their formation. The lack of detection of water ice, which is expected to be constituent of Trojans, might be due to the formation of a thick irradiation mantle on their surfaces by solar ultraviolet radiation and cosmic ray bombardment. These space weathering processes could have altered the surface properties of the reddest family members causing a reddening of the spectral slope (and a consequent darkening of the surface) as a consequence of chemical modification and the formation of complex organic materials. Alternatively, the water ice originally present on the surface of Jupiter Trojans could have been covered or removed after the cometary activity suggested by Morbidelli et al. (2005). The observations of short-periodic comets available in the literature evidence that they do not show water ice absorption features either. Only very few spectra of comets—also from spacecraft—exist, but no water ice is found on these objects down to the level of a few percent, although there is not doubt that water should exist in comets, actually as a major constituent. As a consequence, one could argue that water ice is just evaporated from the surface when they become active, or that the cometary surface is now covered by a dust mantle as shown by Tancredi et al. (2006) in the case of large comets (a few km-size comet nuclei).

In conclusion, the Trojans' surface could be covered by a dust or irradiation mantle which could inhibit the detection of water ice. Nevertheless, on the basis of the available data sample, we cannot check if water ice is present but covered by darker materials which reduce its spectral features. Further observations are needed to investigate the mechanisms which alter water ice or inhibit the detection of its signatures.

5. Conclusion

In this paper we present visible and near-infrared data of 24 Jupiter Trojans belonging to seven different families. Absolute magnitudes have been computed for 17 objects and an estimation of the diameter has been presented for 19 bodies. Tentative models of the surface composition of the whole sample of observed targets have been obtained by applying a radiative transfer model based on the Hapke theory. We considered several mixtures of minerals, and organic and icy compounds which are supposed to be present on the surface of objects at large heliocentric distances. The presented models, although not unique, can help us to investigate the nature of the observed targets, giving an insight of the surface composition of the members of each family and on the structure (homogeneity/heterogeneity) of the parent bodies.

Table 3
Absolute magnitudes (H), estimated diameters (D), models of the surface composition and albedo values at 0.55 μm resulting from modeling

Object	H	D (km)	Model	Albedo
Aneas:				
1172	8.54	143^{+5}_{-5}*	36% KE, 55% AC, 5% Tit. th., 2% Ol, 2% Ens	0.04[a]
15502	9.94	68^{+10}_{-16}	36% KE, 55% AC, 5% Tit. th., 2% Ol, 2% Ens	0.04
18493	10.78	46^{+7}_{-11}	4% KE, 94% AC, 2% Ol, 2% Ens	0.03
Astyanax:				
1871	11.29	37^{+6}_{-9}	23% KE, 76% AC, 1% Tr. th.	0.03
23694	11.59	32^{+5}_{-8}	30% KE, 55% AC, 12% Tit. th., 3% Ens	0.04
30698	12.23	24^{+4}_{-6}	29% KE, 64% AC, 5% Tit. th., 2% Ens	0.04
Sarpedon:				
2223	9.25	95^{+4}_{-4}*	70% KE, 21% AC, 4% Ol, 5% Tit. th.	0.04[b]
5130	9.85	71^{+11}_{-18}	33% KE, 65% AC, 2% Tr. th.	0.03
Phereclos:				
2357	8.86	95^{+4}_{-4}*	13% KE, 75% AC, 4% Ol, 8% Tit. th.	0.05[c]
6998	11.43	34^{+5}_{-8}	8% KE, 89% AC, 3% Tit. th.	0.03
18940	11.81	29^{+4}_{-7}	17% KE, 80% AC, 3% Tr. th.	0.03
Menelaus:				
1647	10.3**	72^{+5}_{-5}*	95% AC, 1% Tit. th., 4% Tr. th.	0.03[d]
5244	10.1**	63^{+10}_{-15}	98% AC, 2% Tr. th.	0.03
5258	10.0**	66^{+10}_{-16}	94% AC, 2% Tit. th., 4% Tr. th.	0.03
1986 WD:				
4035	9.3**	68^{+5}_{-5}*	36% KE, 41% AC, 4% Tit. th., 14% Tr. th., 5% Ens	0.05[e]
6545	10.0**	66^{+10}_{-16}	20% KE, 73% AC, 7% Tr. th.	0.03
11351	10.5**	53^{+8}_{-13}	20% KE, 73% AC, 7% Tr. th.	0.03
Makhaon:				
12917	11.61	32^{+5}_{-8}	8% KE, 83% AC, 2% Tit. th., 7% Tr. th.	0.03
12921	10.7**	48^{+7}_{-12}	4% KE, 94% AC, 2% Tr. th.	0.03
13463	11.27	37^{+6}_{-9}	10% KE, 89% AC, 1% Tit. th.	0.03
15094	11.76	30^{+5}_{-7}	4% KE, 95% AC, 1% Tit. th.	0.03
15535	10.70	48^{+7}_{-12}	5% KE, 87% AC, 3% Tit. th., 5% Tr. th.	0.03
20738	11.67	31^{+5}_{-8}	5% KE, 88% AC, 2% Tit. th., 5% Tr. th.	0.03
24390	11.80	29^{+5}_{-7}	5% KE, 88% AC, 3% Tit. th., 4% Tr. th.	0.04

The used acronyms are: KE = kerogen, AC = amorphous carbon, Tit. th. = Titan tholins, Tr. th. = Triton tholin, Ol = olivine, Ens = enstatite. Diameters marked by $*$ are taken from IRAS data. Absolute magnitudes marked by $**$ are taken from the astorb.dat file of the Lowell Observatory.

[a] Albedo IRAS = 0.04 ± 0.003.
[b] Albedo IRAS = 0.034 ± 0.003.
[c] Albedo IRAS = 0.052 ± 0.003.
[d] Albedo IRAS = 0.028 ± 0.004.
[e] Albedo IRAS = 0.086 ± 0.015.

The obtained results can be summarized as follows:

- None of the observed spectra exhibit spectral features at 1.5 and 2 μm related to the presence of water ice on the surface of the observed bodies.
- All the spectra belong to the primitive taxonomic classes (P and D type) and can be reproduced by modeling the surface composition with mixtures of amorphous carbon, silicates and a reddening compound (tholins and/or kerogens). We did not detect any diagnostic feature that allows us to distinguish the family members from the background objects of the Trojan population. Some small differences in the spectral behaviors can probably be explained by different degrees of space weathering alteration.
- L4 and L5 clouds are spectrally very similar and there is no evidence of compositional difference between the Jupiter preceding and following clouds.
- All the investigated dynamical families appear quite similar in surface composition, without any peculiar difference. The Jupiter Trojan population exhibit a great uniformity.

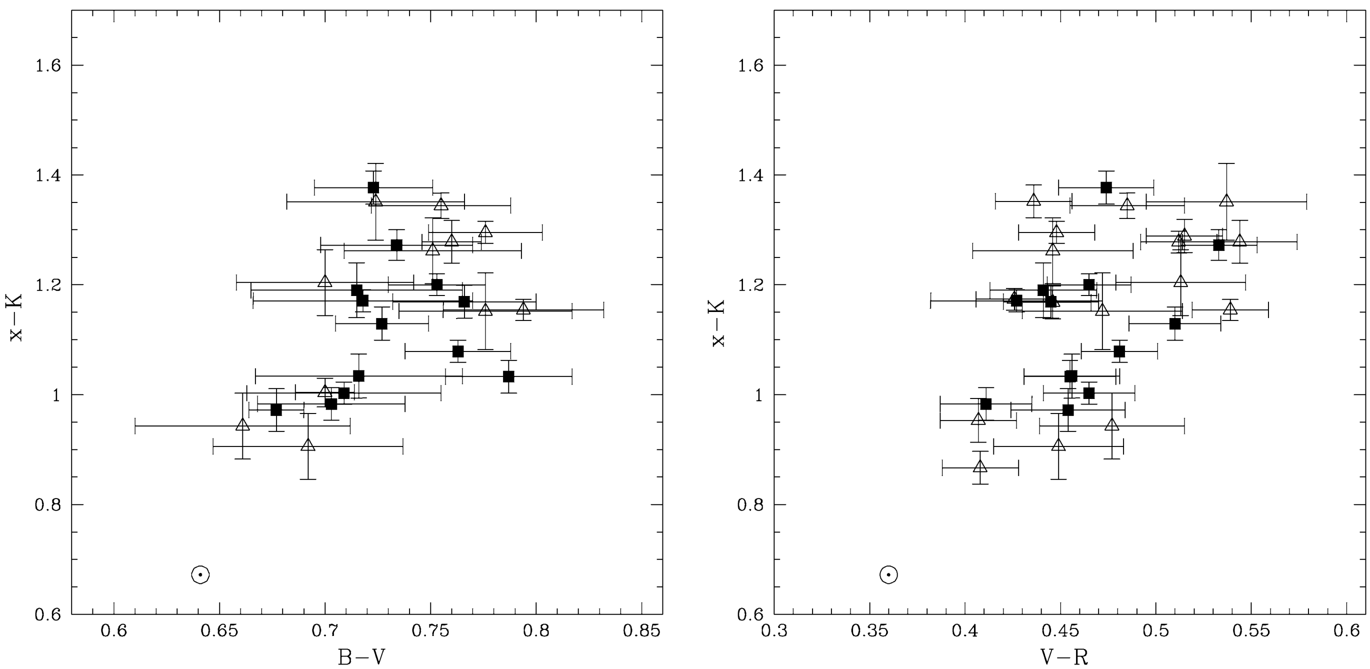

Fig. 7. The x–K color index (derived from the difference between the reflectance at 0.85 and at 2.2 µm), vs the B–V and V–R color indices for a Trojans data set composed by our data and those of Emery and Brown (2004). Open triangles correspond to data on Trojans belonging to L4 cloud, while black square are those for Trojans belonging to the L5 cloud. B–V and V–R colors have been derived directly from photometry for our NTT data, while for the TNG only data, the V–R color index has been derived from reflectance spectroscopy. B–V and V–R color indices for Emery and Brown (2004). Trojans targets have been derived from photometry or spectroscopy available in the literature, when existing (Planetary Data System—Small Bodies Data Base at http://pdssbn.astro.umd.edu/nodehtml/sbdb.html). The (x–K) color index includes the solar color both for our and Emery and Brown (2004) data. The Sun colors are represented with the ⊙ symbol.

Also for the families that show some variation among members the detected differences seem to be just random deviation within the entire population.

- The analysis of the visible and near-infrared spectra confirm that 18493 is different from other Aneas family members. This spectral diversity might indicate that 18493 is an interloper or that it comes from the interior of the parent body.
- 15094 and 13463 in Makhaon family have a spectral behavior flatter than the other family members. Considering also that they do not dynamically belong to the Makhaon family for a cutoff value of 100 m/s, they can be considered as interlopers.
- No relation has been found between color indices and dynamical characteristics. All the spectra have similar behaviors independently from proper elements. Considering the size, small objects have a slightly larger dispersion in the spectral slope than the large ones. This feature could be possibly due to different degrees of space weathering ageing.

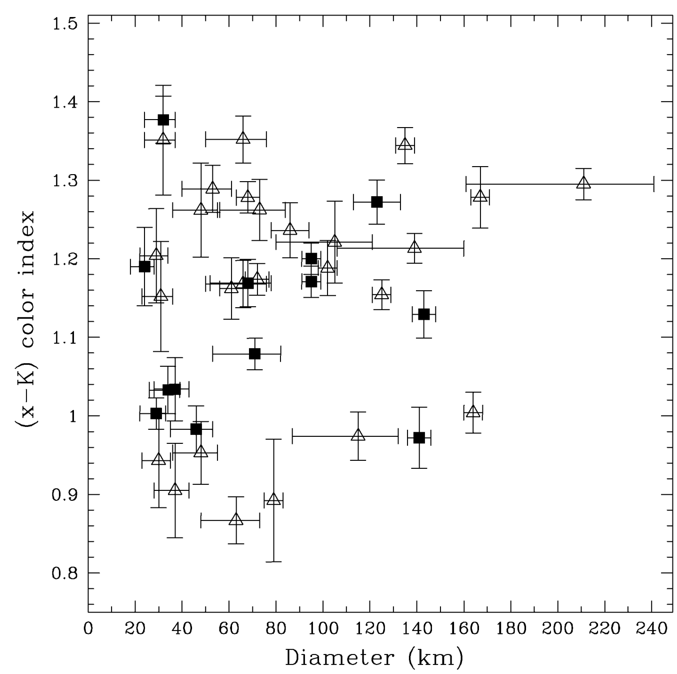

Fig. 8. The x–K color index (derived from the difference between the reflectance at 0.85 and at 2.2 µm), vs the estimated diameter. The (x–K) color index includes the solar color both for our and Emery and Brown (2004) data. Open triangles correspond to data on the L4 cloud, while black squares are for the L5 cloud.

On the basis of these results we can suppose that the parent bodies of all the analyzed families had a quite homogeneous structure. Also the whole population of Jupiter Trojans is quite homogeneous, even considering the two L4 and L5 clouds. Small members show a wide range of variation of their spectral slopes probably as a consequence of the different level of ageing due to space weathering of fragments coming from the interior or the surface of the parent bodies. Larger members show a smaller range of variation of their spectral slope. Their spectra have redder behavior which is probably a consequence of the ageing effect produced by space weathering processes on the surface of the parent body. Icy component, if present, is not detected. Laboratory experiments are still needed to investigate the mechanism able to hide the ices which should be present of the surface of objects formed at large heliocentric distances.

Acknowledgments

We thank C. Beaugé and F. Roig for kindly providing us with updated Trojan family list. We thank D. Lazzaro and R.P. Binzel for having revised this paper, providing useful comments. E. Dotto, invited scientist at the European Southern Observatory on February–March 2003, thanks all the ESO staff for the hospitality.

Appendix A

Table A.1
Observational circumstances for visible spectroscopy of L4 family Trojans—ESO-NTT EMMI

Object	Night	UT start (hh:mm)	Slit ($''$)	Airm.	T_{exp} (s)	Solar analog (airmass)
12917	10 Apr. 03	01:27	1	1.29	1200	SA102-1081 (1.40)
12917	10 Apr. 03	04:36	1	1.11	900	SA107-684 (1.15)
13463	11 Apr. 03	00:59	1	1.55	1200	SA107-684 (1.49)
13463	11 Apr. 03	02:28	1	1.14	1200	SA107-684 (1.16)
15094	11 Apr. 03	07:19	1	1.18	900	SA107-684 (1.16)
15535	10 Apr. 03	08:08	1	1.45	900	SA102-1081 (1.40)
15535	10 Apr. 03	08:44	1	1.69	900	SA107-684 (1.54)
20738	10 Apr. 03	05:35	1	1.34	1200	SA102-1081 (1.40)
20738	10 Apr. 03	06:09	1	1.48	1200	SA102-1081 (1.40)
24390	11 Apr. 03	04:05	1	1.24	1200	SA107-684 (1.16)

Table A.2
Observational circumstances for visible spectroscopy of L4 family Trojans—TNG DOLORES

Object	Night	UT start (hh:mm)	Slit ($''$)	Airm.	T_{exp} (s)	Solar analog (airmass)
1647	06 May 03	22:49	2	1.2	600	SA P330E (1.2)
1647	06 May 03	22:59	2	1.2	600	SA P330E (1.2)
4035	07 May 03	01:16	2	1.6	600	SA P330E (1.2)
4035	07 May 03	01:27	2	1.6	600	SA P330E (1.2)
5244	07 May 03	00:03	2	1.3	600	SA P330E (1.2)
5244	07 May 03	00:13	2	1.3	600	SA P330E (1.2)
5258	06 May 03	22:09	2	1.2	600	SA P330E (1.2)
5258	06 May 03	22:19	2	1.2	600	SA P330E (1.2)
6545	07 May 03	00:38	2	1.7	600	SA P330E (1.2)
6545	07 May 03	00:48	2	1.7	600	SA P330E (1.2)
11351	07 May 03	02:53	2	1.8	600	SA P330E (1.2)
12921	07 May 03	01:59	2	1.3	600	SA P330E (1.2)
12921	07 May 03	02:09	2	1.3	600	SA P330E (1.2)
20738	06 May 03	23:26	2	1.1	600	SA P330E (1.2)
20738	06 May 03	23:36	2	1.1	600	SA P330E (1.2)

Table A.3
Observational circumstances for photometric data of L5 family Trojans—ESO-VLT ISAAC

Object	Night	UT start (hh:mm)	Filter	Airm.	T_{exp} ($s \times n_{acq}$)
1172	11 Nov. 02	07:57	J	1.475	1.7×2
1172	11 Nov. 02	08:02	H	1.488	1.7×2
1172	11 Nov. 02	08:07	K	1.501	1.7×2
1871	09 Nov. 02	01:01	J	1.757	30×4
1871	09 Nov. 02	02:44	J	1.247	60×4
1871	10 Nov. 02	01:17	J	1.594	60×5
1871	09 Nov. 02	01:06	H	1.710	15×4
1871	09 Nov. 02	02:44	H	1.236	60×4
1871	10 Nov. 02	01:03	H	1.694	15×4
1871	09 Nov. 02	01:12	K	1.664	15×4
1871	09 Nov. 02	02:44	K	1.213	30×2
1871	10 Nov. 02	01:09	K	1.650	15×4
15502	10 Nov. 02	02:20	J	1.963	30×4
15502	10 Nov. 02	04:15	J	1.986	30×4
15502	10 Nov. 02	02:25	H	1.948	15×4
15502	10 Nov. 02	04:03	H	1.949	10×4
15502	10 Nov. 02	02:31	K	1.934	15×4
15502	10 Nov. 02	04:09	K	1.967	10×4
18493	09 Nov. 02	07:33	J	1.287	60×4
18493	10 Nov. 02	07:27	J	1.283	60×4
18493	09 Nov. 02	07:38	H	1.297	20×4
18493	10 Nov. 02	07:32	H	1.292	10×4
18493	09 Nov. 02	07:44	K	1.308	20×4
18493	10 Nov. 02	07:38	K	1.305	10×4
23694	10 Nov. 02	04:37	J	1.217	30×4
23694	10 Nov. 02	04:43	H	1.219	10×4
23694	10 Nov. 02	04:49	K	1.221	10×4
30698	09 Nov. 02	03:40	J	1.443	60×4
30698	11 Nov. 02	03:28	J	1.451	15×4
30698	09 Nov. 02	03:46	H	1.426	30×4
30698	11 Nov. 02	03:34	H	1.434	5×4
30698	09 Nov. 02	03:53	K	1.409	20×4
30698	11 Nov. 02	03:40	K	1.416	3×6

Table A.4
Observational circumstances for photometric data of L4 family Trojans—ESO-VLT ISAAC

Object	Night	UT start (hh:mm)	Filter	Airm.	T_{exp} ($s \times n_{acq}$)
12917	10 Apr. 03	00:20	J	1.68	15×4
12917	10 Apr. 03	00:27	H	1.63	5×4
12917	10 Apr. 03	00:34	K	1.58	3×4
13463	11 Apr. 03	00:20	J	1.93	15×4
13463	11 Apr. 03	00:20	H	1.93	5×4
13463	11 Apr. 03	00:33	K	1.78	3×4
15094	11 Apr. 03	06:00	J	1.04	15×4
15094	11 Apr. 03	06:06	H	1.05	5×4
15094	11 Apr. 03	06:13	K	1.05	3×4
15535	10 Apr. 03	07:50	J	1.30	15×4
15535	10 Apr. 03	07:56	H	1.32	5×4
15535	10 Apr. 03	08:03	K	1.35	3×4
20738	10 Apr. 03	04:43	J	1.16	15×4
20738	10 Apr. 03	04:49	H	1.17	5×4
20738	10 Apr. 03	04:56	K	1.18	3×4
24390	11 Apr. 03	03:05	J	1.35	15×4
24390	11 Apr. 03	03:11	H	1.33	5×4
24390	11 Apr. 03	03:18	K	1.30	3×4

Table A.5
Observational circumstances for near-infrared spectroscopy of L5 and L4 family Trojans—ESO-VLT ISAAC

Object	Night	UT start (hh:mm)	Filter	Airm.	T_{exp} (s × n_{acq})	Slit ($''$)	Solar analog (airmass)
L5							
1172	11 Nov. 02	08:18	J	1.53	30 × 14	1.0	La93-101 (1.16)
1172	11 Nov. 02	08:39	H	1.61	30 × 4	1.0	La93-101 (1.17)
1172	11 Nov. 02	08:45	K	1.64	30 × 8	1.0	HD209847 (1.77)
1871	09 Nov. 02	01:30	J	1.53	60 × 8	1.0	La93-101 (1.50)
1871	10 Nov. 02	01:31	J	1.50	120 × 12	1.0	La93-101 (1.55)
1871	09 Nov. 02	01:48	H	1.44	120 × 8	1.0	HD209847 (1.03)
1871	09 Nov. 02	02:15	K	1.32	180 × 8	1.0	La93-101 (1.44)
15502	10 Nov. 02	02:45	J	1.90	60 × 10	1.0	HD209847 (2.10)
15502	10 Nov. 02	03:10	H	1.88	60 × 12	1.0	HD209847 (2.10)
15502	10 Nov. 02	03:27	K	1.88	60 × 14	1.0	HD209847 (2.12)
18493	10 Nov. 02	08:31	J	1.48	120 × 12	1.0	HD209847 (1.26)
18493	10 Nov. 02	07:52	H	1.34	180 × 10	1.0	La98-978 (1.13)
18493	09 Nov. 02	07:56	K	1.34	120 × 30	1.0	La98-978 (1.15)
23694	10 Nov. 02	05:00	J	1.23	60 × 10	1.0	HD209847 (1.26)
23694	10 Nov. 02	05:22	H	1.25	180 × 8	1.0	HD209847 (1.28)
23694	10 Nov. 02	05:55	K	1.32	180 × 12	1.0	HD209847 (1.29)
30698	09 Nov. 02	04:11	J	1.37	60 × 18	1.0	La93-101 (1.50)
30698	09 Nov. 02	04:50	H	1.33	120 × 16	1.0	La93-101 (1.47)
30698	09 Nov. 02	05:33	H	1.34	120 × 32	1.0	La93-101 (1.15)
L4							
12917	10 Apr. 03	00:53	J	1.44	180 × 4	1.0	La102-1081 (1.40)
12917	10 Apr. 03	01:17	H	1.32	180 × 16	1.0	La102-1081 (1.39)
12917	10 Apr. 03	02:27	K	1.12	180 × 28	1.5	La102-1081 (1.24)
13463	11 Apr. 03	00:49	J	1.63	120 × 4	1.0	La102-1081 (1.77)
13463	11 Apr. 03	02:05	H	1.22	180 × 6	1.0	La98-978 (1.17)
13463	11 Apr. 03	01:16	K	1.43	180 × 12	1.0	La102-1081 (1.35)
15094	11 Apr. 03	09:11	J	1.64	180 × 6	1.0	La102-1081 (1.77)
15094	11 Apr. 03	08:09	H	1.28	180 × 16	1.0	La102-1081 (1.36)
15094	11 Apr. 03	06:28	K	1.06	180 × 28	1.0	La102-1081 (1.10)
15535	10 Apr. 03	08:20	J	1.43	60 × 6	1.5	La107-998 (1.46)
15535	10 Apr. 03	08:30	H	1.48	60 × 8	1.5	La107-998 (1.48)
15535	10 Apr. 03	08:43	K	1.57	60 × 12	1.5	La107-998 (1.57)
20738	10 Apr. 03	05:14	H	1.21	180 × 8	1.5	La102-1081 (1.23)
20738	10 Apr. 03	05:58	K	1.33	180 × 18	1.5	La102-1081 (1.24)
24390	11 Apr. 03	05:15	J	1.13	120 × 4	1.0	La102-1081 (1.10)
24390	11 Apr. 03	03:34	H	1.25	180 × 8	1.0	La102-1081 (1.10)
24390	11 Apr. 03	04:08	K	1.18	180 × 18	1.0	La102-1081 (1.10)

Table A.6
Observational circumstances for near-infrared spectroscopy of L5 family Trojans—TNG NICS + Amici

Object	Night	UT start (hh:mm)	Airm.	T_{exp} (s × n_{acq})	Slit ($''$)	Solar analog (airmass)
L5						
2223	30 Nov. 02	04:36	1.4–1.6	120 × 8	1.5	1,2,4,5
2223	01 Dec. 02	04:47	1.5–1.7	60 × 24	1.5	1,2,5
2357	01 Dec. 02	04:47	1.5–1.7	60 × 4	1.5	1,2,4,5
2357	02 Dec. 02	05:10	1.9–2.4	60 × 28	1.5	1,2,3,4
5130	30 Nov. 02	20:09	1.2	60 × 16	1.5	1,2,5
6998	30 Nov. 02	20:09	1.2	60 × 72	1.5	1,2,5
18940	30 Nov. 02	00:46	1.0–1.1	120 × 12	1.5	1,2,4,5
18940	30 Nov. 02	21:28	1.2	120 × 4	1.5	1,2,5

Solar analog and airmasses (30 Nov.; 1 Dec.; 2 Dec.): 1—HD209847 (2.15; 1.42; 1.43); 2—Hy 142 (1.13; 1.04 and 2.11; 1.07 and 2.38); 3—Landolt 112-1133 (–; –; 1.43); 4—Landolt 98-978 (1.38; –; 1.23 and 1.43); 5—Landolt 93-101 (1.14 and 1.23; 1.76; –).

Table A.7
Observational circumstances for near-infrared spectroscopy of L4 family Trojans—TNG NICS + Amici

Object	Night	UT start (hh:mm)	Airm.	T_{exp} (s × n_{acq})	Slit ($''$)	Solar analog (airmass)
L4						
1647	05 May 03	22:44	1.2	90 × 6	1.5	1,2,3
5258	05 May 03	23:11	1.3	90 × 6	1.5	1,2,3
5244	06 May 03	00:39	1.4	90 × 6	1.5	1,2,3
6545	03 May 03	23:30	1.6	90 × 6	1.5	1,2,3
4035	03 May 03	23:05	1.4	90 × 6	1.5	1,2,3
11351	04 May 03	01:33	1.6	90 × 12	1.5	1,2,3
12921	04 May 03	00:16	1.1	90 × 24	1.5	1,2,3

Solar analog and airmasses (03 May; 05 May): 1—Land102-10 (1.19; 1.16); 2—Land107-68 (1.2–1.7; 1.16); 3—Land110-36 (1.14; 1.14).

References

Barucci, M.A., Boehnhardt, H., Dotto, E., Doressoundiram, A., Romon, J., Lazzarin, M., Fornasier, S., de Bergh, C., Tozzi, G.P., Delsanti, A., Hainaut, O., Barrera, L., Birkle, K., Meech, K., Ortiz, J.L., Sekiguchi, T., Thomas, N., Watanabe, J., West, R.M., Davies, J.K., 2002. Visible and near-infrared spectroscopy of the Centaur 32532 (2001 PT13). ESO large program on TNOs and centaurs: First spectroscopy results. Astron. Astrophys. 392, 335–339.

Beaugé, C., Roig, F., 2001. A semianalytical model for the motion of the Trojan asteroids: Proper elements and families. Icarus 53, 391–415.

Bendjoya, P., Cellino, A., Di Martino, M., Saba, L., 2004. Spectroscopic observations of Jupiter Trojans. Icarus 168, 374–384.

Bowell, E., Hapke, B., Domingue, D., Lumme, K., Peltoniemi, J., Harris, A.W., 1989. Application of photometric models to asteroids. In: Binzel, R.P., Gehrels, T., Matthews, M.S. (Eds.), Asteroids II. Univ. of Arizona Press, Tucson, pp. 524–556.

Clark, R.N., Swayze, G.A., Gallagher, A.J., King, T.V.V., Calvin, W.M., 1993. U.S. Geological Survey Open File Report 93-592, http://speclab.cr.usgs.gov.

Cruikshank, D.P., Dalle Ore, C.M., Roush, T.L., Geballe, T.R., Owen, T.C., de Bergh, C., Cash, M.D., Hartmann, W.K., 2001. Constraints on the composition of Trojan Asteroid 624 Hektor. Icarus 153, 348–360.

Cruikshank, D.P., Dalle Ore, C.M., 2003. Spectral models of Kuiper belt objects and centaurs. Earth Moon Planets 92, 315–330.

de Bergh, C., Boehnhardt, H., Barucci, M.A., Lazzarin, M., Fornasier, S., Romon-Martin, J., Tozzi, G.P., Doressoundiram, A., Dotto, E., 2004. Aqueous altered silicates at the surface of two Plutinos? Astron. Astrophys. 416, 791–798.

Dotto, E., Barucci, M.A., Leyrat, C., Romon, J., de Bergh, C., Licandro, J., 2003a. Unveiling the nature of 10199 Chariklo: Near-infrared observations and modeling. Icarus 164, 122–126.

Dotto, E., Barucci, M.A., de Bergh, C., 2003b. Colors and composition of the centaurs. Earth Moon Planets 92, 157–167.

Dotto, E., Barucci, M.A., Boehnhardt, H., Romon, J., Doressoundiram, A., Peixinho, N., de Bergh, C., Lazzarin, M., 2003c. Searching for water ice on 47171 1999 TC36, 1998 SG35, and 2000 QC243: ESO large program on TNOs and centaurs. Icarus 162, 408–414.

Dumas, C., Owen, T., Barucci, M.A., 1998. Near-infrared spectroscopy of low-albedo surfaces of the Solar System: Search for the spectral signature of dark material. Icarus 133, 221–232.

Emery, J.P., Brown, R.H., 2001. Near-infrared spectroscopy of Trojan asteroids: Implications for the evolution of the Solar System. Lunar Planet. Sci. 32. Abstract 1385.

Emery, J.P., Brown, R.H., 2003. Constraints on the surface composition of Trojan asteroids from near-infrared (0.8–4.0 μm) spectroscopy. Icarus 164, 104–121.

Emery, J.P., Brown, R.H., 2004. The surface composition of Trojan asteroids: Constraints set by scattering theory. Icarus 170, 131–152.

Fernandez, Y.R., Sheppard, S.S., Jewitt, D.C., 2003. The albedo distribution of jovian Trojan asteroids. Astron. J. 126, 1563–1574.

Fitzsimmons, A., Dahlgren, M., Lagerkvist, C.I., Magnusson, P., Williams, I.P., 1994. A spectroscopic survey of D-type asteroids. Astron. Astrophys. 282, 634–642.

Fornasier, S., Dotto, E., Marzari, F., Barucci, M.A., Boehnhardt, H., Hainaut, O., de Bergh, C., 2004a. Visible spectroscopic and photometric survey of L5 Trojans: Investigation of dynamical families. Icarus 172, 221–232.

Fornasier, S., Dotto, E., Barucci, M.A., Barbieri, C., 2004b. Water ice on the surface of the large TNO 2004 DW. Astron. Astrophys. 422, L43–L46.

Hudson, R.L., Moore, M.H., 1999. Laboratory studies of the formation of methanol and other organic molecules by water + carbon monoxide radiolysis: Relevance to comets, icy satellites, and interstellar ices. Icarus 140, 451–461.

Hunt, L.K., Mannucci, F., Testi, L., Migliorini, S., Stanga, R.M., Baffa, C., Lisi, F., Vanzi, L., 1998. Northern JHK standard stars for array detectors. Astron. J. 115, 2594–2603.

Jewitt, D.C., Luu, J.X., 1990. CCD spectra of asteroids. II. The Trojans as spectral analogs of cometary nuclei. Astron. J. 100, 933–944.

Jewitt, D.C., Trujillo, C.A., Luu, J.X., 2000. Population and size distribution of small jovian Trojan asteroids. Astron. J. 120, 1140–1147.

Jones, T.D., Lebofsky, L.A., Lewis, J.S., Marley, M.S., 1990. The composition and origin of the C, P, and D asteroids—Water as a tracer of thermal evolution in the outer belt. Icarus 88, 172–192.

Khare, B.N., Sagan, C., Arakawa, E.T., Suits, F., Callcott, T.A., Williams, M.W., 1984. Optical constants of organic tholins produced in a simulated titanian atmosphere—From soft X-ray to microwave frequencies. Icarus 60, 127–137.

Khare, B.N., Thompson, W.R., Sagan, C., Arakawa, E.T., Meisse, C., Gilmour, I., 1991. Optical constants of kerogen from 0.15 to 40 micron: Comparison with meteoritic organics. In: Levasseur-Regours, A.C., Hasegawa, H. (Eds.), Origin and Evolution of Interplanetary Dust, IAU Colloq. 126. Kluwer Academic, Dordrecht. ASSL 173, 99.

Khare, B.N., Thompson, W.R., Cheng, L., Chyba, C., Sagan, C., Arakawa, E.T., Meisse, C., Tuminello, P.S., 1993. Production and optical constraints of ice tholin from charged particle irradiation of (1:6) C_2H_6/H_2O at 77 K. Icarus 103, 290–300.

Landolt, A.U., 1992. UBVRI photometric standard stars in the magnitude range 11.5–16.0 around the celestial equator. Astron. J. 104, 340–371, 436–491.

Lazzarin, M., Barbieri, C., Barucci, M.A., 1995. Visible spectroscopy of dark, primitive asteroids. Astron. J. 110, 3058–3072.

Licandro, J., Ghinassi, F., Testi, L., 2002. Infrared spectroscopy of the largest known trans-neptunian object 2001 KX75. Astron. Astrophys. 388, L9–L12.

Luu, J.X., Jewitt, D., Cloutis, E., 1994. Near-infrared spectroscopy of primitive Solar System objects. Icarus 109, 133–144.

Marzari, F., Scholl, H., Murray, C., Lagerkvist, C., 2003. Origin and evolution of Trojan asteroids. In: Bottke, W., Cellino, A., Paolicchi, P., Binzel, R.P. (Eds.), Asteroids III. Univ. of Arizona Press, Tucson, pp. 725–738.

McDonald, G.D., Thompson, W.R., Heinrich, M., Khare, B.N., Sagan, C., 1994. Chemical investigation of Titan and Triton tholins. Icarus 108, 137–145.

McDonald, G.D., Whited, L.J., Deruiter, C., Khare, B.N., Patnaik, A., Sagan, C., 1996. Production and chemical analysis of cometary ice tholins. Icarus 122, 107–117.

Moore, M.H., Donn, B., Khanna, R., A'Hearn, M.F., 1983. Studies of proton-irradiated cometary-type ice mixtures. Icarus 54, 388–405.

Morbidelli, A., Levinson, H.F., Tsiganis, K., Gomes, R., 2005. Chaotic capture of Jupiter's Trojan asteroids in the early Solar System. Nature 435, 462–464.

Moroz, L.V., Arnold, G., Korochantsev, A.V., Wasch, R., 1998. Natural solid bitumens as possible analogs for cometary and asteroid organics. Icarus 134, 253–268.

Persson, S.E., Murphy, D.C., Krzeminski, W., Roth, M., Rieke, M.J., 1998. A new system of faint near-infrared standard stars. Astron. J. 116, 2475–2488.

Romon, J., de Bergh, C., Barucci, M.A., Doressoundiram, A., Cuby, J.-G., Le Bras, A., Douté, S., Schmitt, B., 2001. Photometric and spectroscopic observations of Sycorax, satellite of Uranus. Astron. Astrophys. 376, 310–315.

Strazzulla, G., 1998. Chemistry of ice induced by bombardment with energetic charged particles. In: Schmitt, B., de Bergh, C., Festou, M. (Eds.), Solar System Ices. Kluwer Academic, Dordrecht. ASSL 281.

Tancredi, G., Fernandez, J.A., Rickman, H., Licandro, J., 2006. Nuclear magnitudes and size distribution of Jupiter family comets. Icarus. In press.

Thompson, W.R., Murray, B.G.J.P.T., Khare, B.N., Sagan, C., 1987. Coloration and darkening of methane clathrate and other ices by charged particle irradiation—Applications to the outer Solar System. J. Geophys. Res. 92, 14933–14947.

Zubko, V.G., Mennella, V., Colangeli, L., Bussoletti, E., 1996. Optical constants of cosmic carbon analogue grains. I. Simulation of clustering by a modified continuous distribution of ellipsoids. Mon. Not. R. Astron. Soc. 282, 1321–1329.

4.3 La famille d'Eurybates

La famille d'Eurybates comprend 28 membres pour une valeur de cut-off de 70m/s. Nous avons observé 17 membres de cette famille en spectroscopie visible au télescope NTT en mai 2004. La famille est très particulière car elle montre une dominance d'astéroïdes du type C (10) et P (7), mais pas d'astéroïdes de type D, contrairement aux autres familles de Troyens. Les objets ont des pentes spectrales comprises entre -0,5 et 4,6 %/10^3Å, et certains astéroïdes de type C (18060, 24380, 24420, 39285 et peut-être 1996 RD29 et 28958) ont une chute de réflectivité en-dessous de 5000 Å qui est vue sur les spectres d'astéroïdes de la ceinture principale soumis aux processus d'altération aqueuse (Vilas 1994, Fornasier et al. 1999). Cette chute de réflectivité est due aux transitions de transfert de charge dans les oxydes de fer et, dans les astéroïdes qui ont subi le processus d'altération aqueuse, elle est accompagnée par d'autres bandes d'absorption dans la région visible (comme la bande à 0,7 micron), qui n'ont pas été identifiées dans les spectres des membres d'Eurybates.
Nous avons donc demandé des observations dans l'infrarouge au TNG pour des membres de cette famille atypique, qui pourraient avoir retenu de la glace d'eau à la surface. Malheureusement, aucune signature due à la glace d'eau n'a été détectée sur les spectres des 7 astéroïdes étudiés de la famille d'Eurybates (deLuise et al., 2010). Les modèles de composition appliqués à ces objets montrent une composition de surface dominée par le carbone amorphe, en particulier pour les objets 13862, 18060 et 163135. Des silicates comme l'olivine peuvent être présents en très petites quantités (1%) sur la surface de 3548 Eurybates, 24380 et 24420, mélangés au carbone amorphe. Bien que la glace d'eau n'ait pas été clairement identifiée à la surface de ces astéroïdes, nous ne pouvons pas exclure qu'elle soit présente et qu'elle soit cachée par des matériaux sombres produits par des processus d'altération de surface. En effet, des mesures de laboratoire ont montré que des fines couches de matériaux riches en substances organiques (de quelques dizaines de microns de dimension), produites par l'altération de surface, masquent les bandes d'absorption de la glace d'eau ou d'autres éléments volatils présents juste en dessous de ce manteau d'irradiation (Brunetto & Roush 2008).
Sur l'origine de la famille d'Eurybates deux scénarios sont envisagés : 1) la famille a été produite par rupture collisionnelle d'un objet provenant du Système Solaire externe et capturé par Jupiter ; 2) la famille vient de la disruption d'un objet formé dans la région de Jupiter et les différences spectrales par rapport aux autres membres des familles dynamiques sont le résultat de processus d'irradiation et d'altération de surface. Dans le deuxième scénario, si les surfaces des Troyens de Jupiter sont riches en glace d'eau et/ou silicates, ceci signifie que la famille d'Eurybates est relativement jeune, car les effets de l'irradiation sur ces matériaux produisent un rougissement des spectres, phénomène non observé sur ces astéroïdes. Par contre, si la surface est riche en matériaux organiques, les effets d'irradiation aplatissent les spectres (Moroz et al. 1998, 2004), et, dans ce cas, la famille d'Eurybates serait ancienne. De futures études dynamiques pouvant établir l'âge de cette famille sont donc nécessaires pour comprendre la nature et l'origine du corps parent d'Eurybates.

4.3.1 Article : A peculiar family of Jupiter Trojans : The Eurybates

Icarus 209 (2010) 586–590

Contents lists available at ScienceDirect

Icarus

journal homepage: www.elsevier.com/locate/icarus

A peculiar family of Jupiter Trojans: The Eurybates ☆

F. De Luise [a,b,*], E. Dotto [a], S. Fornasier [c,d], M.A. Barucci [c], N. Pinilla-Alonso [e,f], D. Perna [a,c,g], F. Marzari [h]

[a] INAF – Osservatorio Astronomico di Roma, Via Frascati 33, 00040 Monteporzio Catone (Roma), Italy
[b] INAF – Osservatorio Astronomico di Collurania-Teramo, Via Mentore Maggini, s.n.c., 64100 Teramo (TE), Italy
[c] LESIA, Paris Observatory, 5 Place Jules Janssen, 92195 Meudon Cedex, France
[d] University of Paris VII "Denis Diderot", 4 rue Elsa Morante, 75013 Paris, France
[e] Fundación Galileo Galilei & Telescopio Nazionale Galileo, PO Box 565, 38700 S/C de La Palma, Tenerife, Spain
[f] Oak Ridge Associated Universities (ORAU) – NASA Ames Research Center, MS 245-3, Moffett Field, CA 94035-1000, USA
[g] University of Rome "Tor Vergata", Via della Ricerca Scientifica 1, 00133 Roma, Italy
[h] Dipartimento di Fisica – University of Padova, Via Marzolo 8, 35131 Padova, Italy

ARTICLE INFO

Article history:
Received 30 January 2009
Revised 23 April 2010
Accepted 28 April 2010
Available online 11 May 2010

Keyword:
Trojan asteroids
Asteroids, surface
Asteroids, composition
Spectroscopy

ABSTRACT

The Eurybates family is a compact core inside the Menelaus clan, located in the L_4 swarm of Jupiter Trojans. Fornasier et al. (Fornasier, S., Dotto, E., Hainaut, O., Marzari, F., Boehnhardt, H., De Luise, F., Barucci, M.A. [2007]. Icarus 190, 622–642) found that this family exhibits a peculiar abundance of spectrally flat objects, similar to Chiron-like Centaurs and C-type main belt asteroids. On the basis of the visible spectra available in literature, Eurybates family's members seemed to be good candidates for having on their surfaces water/water ice or aqueous altered materials.

To improve our knowledge of the surface composition of this peculiar family, we carried out an observational campaign at the Telescopio Nazionale Galileo (TNG), obtaining near-infrared spectra of 7 members. Our data show a surprisingly absence of any spectral feature referable to the presence of water, ices or aqueous altered materials on the surface of the observed objects. Models of the surface composition are attempted, evidencing that amorphous carbon seems to dominate the surface composition of the observed bodies and some amount of silicates (olivine) could be present.

1. Introduction

Jupiter Trojans (JTs) are small bodies of the Solar System located in the Jupiter's Lagrangian points L_4 and L_5. Their origin is not yet well understood and it is still matter of debate. Several mechanisms were proposed to model their origin (Marzari and Scholl, 1998a,b, 2000, 2007; Marzari et al., 2002; Morbidelli et al., 2005), and it is widely accepted that they formed in the outer Solar System, in regions rich in frozen volatiles. The JT population is supposed to have undergone a significant collisional evolution, and to be at least as collisionally evolved as main belt asteroids. The discovery of dynamical families in both L_4 and L_5 clouds supports this hypothesis (e.g. Milani, 1993; Milani and Knezević, 1994; Beaugé and Roig, 2001; Dell'Oro et al., 1998).

Physical properties of JTs are poorly known. The presently available spectroscopic data set is largely unsatisfactory, covering only about 10% of the entire JT population. To improve our knowledge of the nature of these bodies, in the last years several surveys have been carried out, both in visible and infrared wavelengths (Dotto et al., 2008, and reference therein). Although JTs formed at large heliocentric distances, the data so far acquired have shown a lack of any evidence of ices on their surfaces. Emery and Brown (2003, 2004) analysed the content of water ice and hydrated materials on the surface of 17 JTs, obtaining upper limits of a few % for water ice and of 30% for hydrated materials. More recently, Yang and Jewitt (2007) suggested that water ice can occupy no more than 10% of the total surface of (4709) Ennomos. JTs belonging to dynamical families do not exhibit any spectral feature related to the presence of ices on their surface (Dotto et al., 2006).

The data so far available in the literature put in evidence a great homogeneity in the whole population: all of the known JTs are low albedo bodies belonging to the primitive *C*, *P* or *D* classes. The same uniformity is also found in JTs belonging to dynamical families (Fornasier et al., 2004, 2007; Dotto et al., 2006). However, some dif-

☆ Based on observations made with the Italian Telescopio Nazionale Galileo (TNG) operated on the island of La Palma by the Fundacion Galileo Galilei of the INAF (Istituto Nazionale di Astrofisica) at the Spanish Observatorio del Roque de los Muchachos of the Instituto de Astrofisica de Canarias, programmes: TAC41(AOT14) and TAC69(AOT15).

* Corresponding author at: INAF – Osservatorio Astronomico di Collurania-Teramo, Via Mentore Maggini, s.n.c., I-64100 Teramo (TE), Italy. Fax: +39 0861 439740.

E-mail address: deluise@oa-teramo.inaf.it (F. De Luise).

0019-1035/$ - see front matter © 2010 Elsevier Inc. All rights reserved.
doi:10.1016/j.icarus.2010.04.024

Table 1
Observational circumstances. For each object, we report observing date, exposure time, airmass and solar analog used (with correspondent airmass).

Object	Date	T_{exp} ($s \times n_{acq}$)	Airmass	Solar analog (airmass)
3548 Eurybates	18 August 2006	120×8	1.8	Hip102491 (1.9)
13862	15 July 2007	120×16	1.6	HD210078 (1.4)
18060	16 July 2007	120×16	1.3	HD210078 (1.3)
9818 Eurymachos	17 July 2007	120×24	1.7	HD210078 (1.4)
24380	17 July 2007	120×16	1.4	HD210078 (1.3)
24420	04 August 2007	120×16	1.5	HD210078 (1.3)
163135	04 August 2007	120×32	1.5–1.8	HD210078 (1.3)

ferences between the L_4 and L_5 swarms are evident: as discussed by Fornasier et al. (2007), the majority of L_5 JTs are D-types, while an higher presence of C- and P-types is observed among the L_4 objects.

A peculiar case is given by the Eurybates dynamical family, in the L_4 swarm. This family is a strong cluster inside the Menelaus clan (Roig et al., 2008), which survives also at a very low relative velocity cut-off, as defined by Beaugé and Roig (2001). The family population, up to date, is composed by 28 members at a cut-off of 70 m/s, 22 of them surviving also at 40 m/s. On the basis of the dynamical properties, it is still not possible to understand if the Eurybates members constitute a distinct family that lies in the same space of proper elements of Menelaus or, as suggested by Roig et al. (2008), they formed by a secondary break-up of a former Menelaus member.

Although the Eurybates family is clustered, in the space of proper elements, in a small portion of the region occupied by the Menelaus clan, its members show spectral properties quite different from those of Menelaus: as shown by Roig et al. (2008) the Menelaus clan evidences a larger diversity of taxonomic classes including C-, P-, and D-type objects in agreement with the whole JT population, while the Eurybates members are characterized by almost flat visible spectra (see e.g. Fig. 12 in Roig et al., 2008), with spectral slopes strongly clustered around $2\%/10^3$ Å, and spectral behaviors similar to those of C-type main belt asteroids and/or Chiron-like Centaurs (Fornasier et al., 2007).

The Eurybates family assumes a great importance in the study of JTs because such a peculiar clustering of spectrally flat objects strongly affects the color-size-orbital parameter distributions of the whole JT population investigated up to now. Fornasier et al. (2007) noted how this family fills the distribution of spectrally neutral JTs at low inclination and appears to be the major responsible of a color-inclination trend (bluer bodies concentrated at lower inclination) of the whole JT population. In the same paper, the Eurybates family appears also to be the major cause of the abundance of C- and P-types among the L_4 objects, which would imply a more heterogeneous composition of this swarm than the L_5 one. Moreover, the Eurybates family strongly contributes to the population of L_4 small JTs (with a $D < 40$ km) having low spectral slopes.

The observations made by Fornasier et al. (2007) showed the presence of a drop-off of reflectance shortward of 0.52 μm in the visible spectra of four Eurybates members (18060, 24380, 24420 and 39285). This behavior is detected on the spectra of many main belt C-type asteroids (Vilas, 1994, 1995), and it is often associated to other spectral features due to aqueous alteration products. Since no other absorption features were found on the visible spectra of Eurybates members, we still do not have a final proof that aqueous alteration processes occurred on the surface of these bodies. Nevertheless, the presence of the ultraviolet drop-off could suggest that subsurface water or water ice could have been present on Eurybates members at a certain moment of their life, in order to cause aqueous alteration on their surfaces. They are therefore good candidates to preserve still detectable spectral signatures of water/water ice or aqueous altered materials.

2. Observations and data analysis

To constrain the surface composition of Eurybates family's members, we performed an observational spectroscopic campaign in the near infrared (NIR) wavelength range.

The observations were carried out at the 3.6 m Telescopio Nazionale Galileo (TNG) at Roque de Los Muchachos in La Palma (Canary Islands, Spain) in 2006 and 2007 (AOT14-TAC41 and AOT15-TAC69, respectively). The targets were selected using the list defined by Beaugé and Roig (2001) and the P.E.Tr.A. project.[1] We observed 7 objects already investigated in visible range by Fornasier et al. (2007). With the exception of 163135, all of our targets survive at a velocity cut-off of 40 m/s. The observational circumstances are summarized in Table 1.

We used the Near-Infrared Camera Spectrometer (NICS), a multimode instrument based on a HgCdTe Hawaii 1024×1024 array, with a field of view of 4.2×4.2 arcmin, coupled with the AMICI prism. Our observations were carried out in low resolution spectroscopic mode, covering the 0.9–2.4 μm spectral range, using a 5 arcsec wide slit, oriented in the object moving direction. The total exposure time was divided into several sub-spectra of 120 s each, to reduce the noise contribution typical of sky at NIR wavelengths. The observations were done by nodding the object along the slit by 30 arcsec between two positions *A* and *B*. Flat-fields were also acquired at the beginning of each night.

Data were reduced using the standard procedure (e.g. Dotto et al., 2006) with MIDAS and the IDL software packages. The two averaged *A* and *B* images were subtracted from each other. The $A - B$ and $B - A$ images were flat-fielded, corrected for spatial and spectral distortion and finally combined with a 30-arcsec offset. The spectra were hence extracted from the resulting combined images. Wavelength calibration was obtained using a look-up table, available on the TNG website, which is based on the theoretical dispersion predicted by ray-tracing and adjusted to best fit the observed spectra of calibration sources. The telluric absorption correction and the removal of the solar contribution were obtained by dividing the spectrum of each object by the spectrum of the solar analog star closest in time and airmass to the target (see Table 1). The resulting spectra were smoothed with a median filtering technique, to reach a spectral resolution of about 20. The edges of each spectral region were cut to avoid low S/N regions at wavelength lower than about 0.90 μm and greater than about 2.2 μm. Only for 163135 we cut the spectrum at 1.65 μm, as due to sky variability, it was not possible to properly remove the sky contribution. The obtained NIR spectra are shown in Fig. 1.

Our NIR spectra were finally combined with the visible spectra published by Fornasier et al. (2007), overlapping the common region between 0.9 and 0.95 μm. The resulting V + NIR spectra, normalized at 0.55 μm, are shown in Fig. 2. We computed the spectral slopes of all the observed objects between 1.0 and 1.6 μm (see Table 2). The obtained values span a small range of values,

[1] http://www.daf.on.br/froig/petra/.

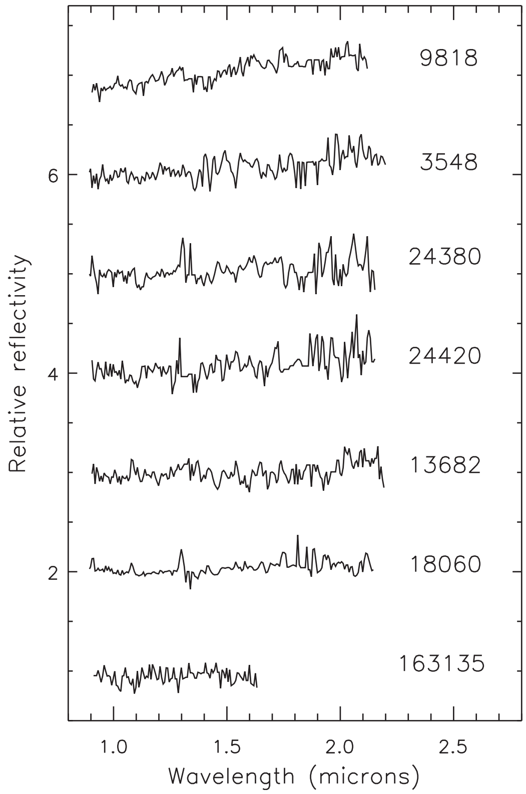

Fig. 1. Near-infrared spectra of Jupiter Trojans belonging to Eurybates family. All the spectra are normalized at 1.25 μm and shifted by 1.0 in reflectance for clarity. Their mean S/N ratio value, measured at about 1.25 μm, is around 15.

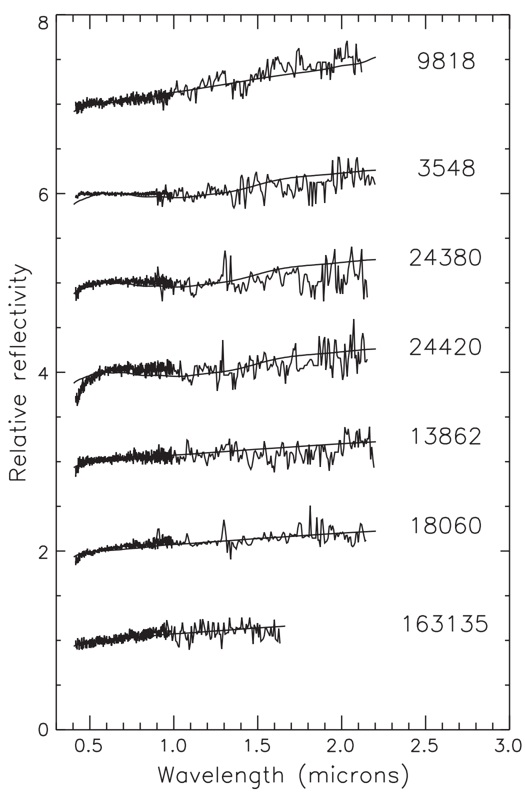

Fig. 2. Near-infrared spectra of Eurybates family members obtained by our observations, together with the visible part already published by Fornasier et al. (2007). All the spectra are normalized at 0.55 μm and shifted by 1 in. reflectance for clarity. The superimposed continuous lines represent the synthetic spectra obtained modeling the surface composition.

Table 2
For each object, the spectral slope S_{NIR} (computed between 1.0 and 1.6 μm), taxonomic classification given by Fornasier et al. (2007), the model of the surface composition and computed albedo value at 0.55 μm are reported. The used acronyms are: AC = amorphous carbon, Tr. th. = Triton tholin, Ol = olivine.

Object	S_{NIR} (%/10^3 Å)	Tax. class	Model	Albedo
3548 Eurybates	1.82 ± 0.41	C	99% AC – 1% Ol	0.03
13862	0.11 ± 0.31	C	100% AC	0.03
18060	1.11 ± 0.27	P	100% AC	0.03
9818 Eurymachos	3.60 ± 0.38	P	98% AC – 2% Tr. th.	0.03
24380	0.98 ± 0.55	C	99% AC – 1% Ol	0.03
24420	2.12 ± 0.50	C	99% AC – 1% Ol	0.03
163135	0.25 ± 0.55	P	100% AC	0.03

from 0.11% to 3.60%/10^3 Å, with a mean value of 1.43 ± 0.41%/10^3 Å.

The obtained spectral behaviors allow us to confirm the taxonomic classification published by Fornasier et al. (2007) (see Table 2). Our investigation in NIR wavelengths has surprisingly shown featureless spectra: we did not detect any spectral feature between 0.9 and 2.2 μm referable to the presence, on the surface of the observed bodies, of water, ices or hydrated minerals.

To model the surface composition of the observed Eurybates members we used the radiative transfer model, based on the Hapke theory, already applied to JTs by Dotto et al. (2006). We took into consideration the following materials: amorphous carbon (by Zubko et al., 1996), organic solids (e.g. kerogens by Clark et al., 1993; and Khare et al., 1991), Triton tholins (by McDonald et al., 1994), titan tholins (by Khare et al., 1984) all the minerals present in the RELAB database,[2] bitumen (by Moroz et al., 1998), and ices (H_2O, CH_4, CH_3OH, NH_3, and ice tholin by McDonald et al., 1996; and Khare et al., 1993). To model the surface composition of each observed object, we considered several geographical mixtures of all these compounds. For each mixture, the modeling procedure produced a synthetic spectrum, to be compared with the observed one, and calculated the geometric albedo value at 0.55 μm. A χ^2-test was applied to compare the different models tentatively considered for each target, and to select the model which better reproduces the observed spectrum. In this analysis we did not take into account the critical regions of the spectrum, around 1.4 and 1.9 μm, where telluric bands occur. We considered as best model the geographical mixture best fitting the asteroid spectrum, and having an albedo value compatible with the typical value of C- or P-type dark asteroids and the mean value for JTs (0.041 ± 0.002, as computed by Fernández et al., 2003). In Fig. 2 the synthetic spectra of final models (continuous lines) are superimposed on the observed spectra. Table 2 reports, for each object, the model of surface composition, as well as the computed albedo.

The obtained spectra suggest the predominance of amorphous carbon on the surface of the observed members of the Eurybates family. In particular, the spectra of 13862, 18060 and 163135 are similar to the one of pure amorphous carbon. The spectral behaviors of (3548) Eurybates, 24380 and 24420 suggest the presence on their surface of a few amount of olivine. The slightly spectral reddening of (9818) Eurymachos has been modeled using a small percentage of a reddening agent (e.g. Triton tholin).

3. Discussion and conclusions

All the spectra of Eurybates members presented in this work appear flat and featureless and confirm the taxonomic classification

[2] http://www.planetary.brown.edu/relabdocs/relab_disclaimer.htm.

published by Fornasier et al. (2007). Our surface modeling has shown that the amorphous carbon seems to dominate the surface composition of the observed bodies and some amount of silicates (olivine) could be present. The proposed models are not unique, since they depend on many parameters (e.g. physical properties of the surface, optical constants and particle size), but a complete lack of diagnostic features typical of water, ices and hydrated minerals is evident in our spectra. This result does not allow us to definitively exclude that some percentage of water ice is still present on the observed bodies, hidden by dark materials. Brunetto and Roush (2008) showed that few tens of microns of an organic-rich layer (e.g. irradiated methane ice), produced by space weathering, are enough to mask spectroscopically, in the near-infrared wavelength range, the presence of water and other volatiles below the surface.

The spectral evidences presented in this paper leave open several possibilities about the origin of the Eurybates family.

A first scenario implies the formation of the Eurybates family by the disruption of an exogenous body, i.e. coming from other Solar System regions, probably captured by Jupiter gravitational field and trapped in L_4 Lagrangian point. In this case, the origin of the parent body is a crucial point that must yet be assessed, as well as the nature and the efficiency of the capture mechanism. Of course, it is plausible that this captured parent body is not the only one in the Trojan clouds, but the population of these objects must be still assessed.

Other scenarios take into account the action of space weathering processes, still efficient at 5.2 AU from the Sun where JTs are presently orbiting (see e.g. Strazzulla et al., 2005; Melita et al., 2009). We know, from laboratory experiments, that the effect of aging mechanisms strongly depends on the composition and nature of the surfaces exposed to space weathering. Since we still do not know the origin and primordial composition of JTs, and therefore we do not know how space weathering processes acted on JT surfaces, several scenarios have to be considered:

(a) if JTs had icy surfaces, the space weathering processes would have produced an irradiation mantle spectrally red and with low albedo (Moore et al., 1983; Thompson et al., 1987; Strazzulla, 1998; Hudson and Moore, 1999; Brunetto et al., 2006; Brunetto and Roush, 2008);
(b) a similar result would have been produced on silicatic composition, where space weathering produces a gradual spectral reddening, as already observed in several dynamical families in the asteroid main belt (e.g. the Eunomia family by Lazzaro et al., 1999; the Flora clan by Florczak et al., 1998; and the Eos family by Doressoundiram et al., 1998) and shown by laboratory experiments (e.g. Strazzulla et al., 2005; Lazzarin et al., 2006);
(c) an opposite result would have been produced on a surface covered of natural complex hydrocarbons, where ion irradiation would have produced gradually neutralized spectra (Moroz et al., 2004).

The first two cases bring to the possibility that the Eurybates is a young family, produced either by a fragmentation of an object coming from outside the present Trojan population and trapped around L_4, or by a secondary collision involving one of Menelaus' family members.

Under the scenario (*c*), Eurybates should be an old family, with an initial hydrocarbon composition, on which space weathering flattened the members' spectra, wiping out the primordial differences.

Whether JTs experienced a phase of cometary activity, water ice on their surface could have been devolatized, or they could have formed a thin dust mantle as shown by Rickman et al. (1990) and Tancredi et al. (2006). This mechanism is quite probable for large JTs not belonging to dynamical families, and it is still plausible for members of dynamical families, since we cannot exclude that they suffered some episodic cometary activity during their life after the fragmentation of the parent body. In a recent work Melita et al. (2009) estimated the timescales of the sublimation of amorphous water ice, the collisional resurfacing, and the flattening of the spectral slopes by solar irradiation in the region of JTs. According to these authors, a dust layer, probably with a red spectroscopic slope, does exist on the surface of JTs as a result of the rapid sublimation of water ice after resurfacing impact events. If this dust layer remains unaltered for more than 10^3 years, its spectroscopic slope is flattened by the action of solar protons. According to the estimated timescales, impacts are so frequent that the irradiation mantle is usually disrupted for JTs, but in the case of the Eurybates family the flat spectra would suggest that we are seeing aged surfaces.

The knowledge of the age of the Eurybates family is hence fundamental for understanding the parent body origin and nature. More observations are also absolutely needed to see whether this peculiar family is unique or if more Eurybates-like families are present in both L_4 and L_5 swarms.

At the same time more observations of Menelaus objects are needed to compare Eurybates and Menelaus members with the whole population of JTs, to have more hints on the relation between Eurybates family and Menelaus clan, and to cast some light on their (common or not) origin.

Acknowledgments

FDL want to thank the TNG support astronomers and telescope operators, in particular W. Boschin and G. Tessicini, for their support and for the kind help to optimize the observations. The authors thank G.A. Baratta for the helpful discussions. The authors thank as well both the anonymous reviewers for providing comments and suggestions helpful to improve the manuscript.

References

Beaugé, C., Roig, F., 2001. A semianalytical model for the motion of the Trojan asteroids: Proper elements and families. Icarus 153, 391–415.
Brunetto, R., Roush, T.L., 2008. Impact of irradiated methane ice crusts on compositional interpretations of TNOs (research note). Astron. Astrophys. 481, 879–882.
Brunetto, R., Barucci, M.A., Dotto, E., Strazzulla, G., 2006. Ion irradiation of frozen methanol, methane, and benzene: Linking to the colors of centaurs and trans-neptunian objects. Astrophys. J. 644, 646–650.
Clark, R.N., Swayze, G.A., Gallagher, A.J., King, T.V.V., Calvin, W.M., 1993. US Geological Survey Open File Report 93-592. <http://speclab.cr.usgs.gov>.
Dell'Oro, A., Marzari, P., Paolicchi, F., Dotto, E., Vanzani, V., 1998. Trojan collision probability: A statistical approach. Astron. Astrophys. 339, 272–277.
Dotto, E., Fornasier, S., Barucci, M.A., Licandro, J., Boehnhardt, H., Hainaut, O., Marzari, F., de Bergh, C., De Luise, F., 2006. The surface composition of Jupiter Trojans: Visible and near-infrared survey of dynamical families. Icarus 183, 420–434.
Dotto, E., Emery, J.P., Barucci, M.A., Morbidelli, A., Cruikshank, D.P., 2008. De Troianis: The Trojans in the planetary system. In: Barucci, M.A., Boehnhardt, H., Cruikshank, D.P., Morbidelli, A. (Eds.), The Solar System Beyond Neptune, vol. 592. Univ. of Arizona Press, Tucson, pp. 383–395.
Doressoundiram, A., Barucci, M.A., Fulchignoni, M., Florczak, M., 1998. EOS family: A spectroscopic study. Icarus 131, 15–31.
Emery, J.P., Brown, R.H., 2003. Constraints on the surface composition of Trojan asteroids from near-infrared (0.8–4.0 μm) spectroscopy. Icarus 164, 104–121.
Emery, J.P., Brown, R.H., 2004. The surface composition of Trojan asteroids: Constraints set by scattering theory. Icarus 170, 131–152.
Fernández, Y.R., Sheppard, S.S., Jewitt, D.C., 2003. The albedo distribution of jovian Trojan asteroids. Astron. J. 126, 1563–1574.
Florczak, M., Barucci, M.A., Doressoundiram, A., Lazzaro, D., Angeli, C.A., Dotto, E., 1998. A visible spectroscopic survey of the flora clan. Icarus 133, 233–246.
Fornasier, S., Dotto, E., Marzari, F., Barucci, M.A., Boehnhardt, H., Hainaut, O., de Bergh, C., 2004. Visible and near-infrared spectroscopic survey of Jupiter Trojan asteroids: Investigation of dynamical families. Icarus 172, 221–232.

Fornasier, S., Dotto, E., Hainaut, O., Marzari, F., Boehnhardt, H., De Luise, F., Barucci, M.A., 2007. Visible spectroscopic and photometric survey of Jupiter Trojans: Final results on dynamical families. Icarus 190, 622–642.

Khare, B.N., Sagan, C., Arakawa, E.T., Suits, F., Callcott, T.A., Williams, M.W., 1984. Optical constants of organic tholins produced in a simulated titanian atmosphere – From soft X-ray to microwave frequencies. Icarus 60, 127–137.

Khare, B.N., Thompson, W.R., Sagan, C., Arakawa, E.T., Meisse, C., Gilmour, I., 1991. Optical constants of kerogen from 0.15 to 40 μm: Comparison with meteoritic organics. In: Levasseur-Regours, A.C., Hasegawa, H. (Eds.), Origin and Evolution of Interplanetary Dust, IAU Colloq. 126, ASSL vol. 173. Kluwer Academic, Dordrecht, pp. 99–101.

Khare, B.N., Thompson, W.R., Cheng, L., Chyba, C., Sagan, C., Arakawa, E.T., Meisse, C., Tuminello, P.S., 1993. Production and optical constraints of ice tholin from charged particle irradiation of (1:6) C_2H_6/H_2O at 77 K. Icarus 103, 290–300.

Hudson, R.L., Moore, M.H., 1999. Laboratory studies of the formation of methanol and other organic molecules by water + carbon monoxide radiolysis: Relevance to comets, icy satellites, and interstellar ices. Icarus 140, 451–461.

Lazzarin, M., Marchi, S., Moroz, L.V., Brunetto, R., Magrin, S., Paolicchi, P., Strazzulla, G., 2006. Space weathering in the main asteroid belt: The big picture. Astrophys. J. 647, 179–182.

Lazzaro, D., and 11 colleagues, 1999. The eunomia family: A visible spectroscopic survey. Icarus 142, 445–453.

Marzari, F., Scholl, H., 1998a. Capture of Trojans by a growing proto-Jupiter. Icarus 131, 41–51.

Marzari, F., Scholl, H., 1998b. The growth of Jupiter and Saturn and the capture of Trojans. Astron. Astrophys. 339, 278–285.

Marzari, F., Scholl, H., 2000. The role of secular resonances in the history of Trojans. Icarus 146, 232–239.

Marzari, F., Scholl, H., 2007. Dynamics of Jupiter Trojans during the 2:1 mean motion resonance crossing of Jupiter and Saturn. Mon. Not. R. Astron. Soc. 380, 479–488.

Marzari, F., Scholl, H., Murray, C., Lagerkvist, C., 2002. Origin and evolution of Trojan asteroids. In: Bottke, W.F., Jr., Cellino, A., Paolicchi, P., Binzel, R.P. (Eds.), Asteroids III. Univ. of Arizona Press, Tucson, pp. 725–738.

McDonald, G.D., Thompson, W.R., Heinrich, M., Khare, B.N., Sagan, C., 1994. Chemical investigation of Titan and Triton tholins. Icarus 108, 137–145.

McDonald, G.D., Whited, L.J., Deruiter, C., Khare, B.N., Patnaik, A., Sagan, C., 1996. Production and chemical analysis of cometary ice tholins. Icarus 122, 107–117.

Melita, M.D., Strazzulla, G., Bar-Nun, A., 2009. Collisions, cosmic radiation and the colors of the Trojan asteroids. Icarus 203, 134–139.

Milani, A., 1993. The Trojan asteroid belt: Proper elements, stability, chaos and families. Celest. Mech. Dynam. Astron. 57, 59–94.

Milani, A., Knezević, Z., 1994. Asteroid proper elements and the dynamical structure of the asteroid main belt. Icarus 107, 219–254.

Moore, M.H., Donn, B., Khanna, R., A'Hearn, M.F., 1983. Studies of proton irradiated cometary-type ice mixtures. Icarus 54, 388–405.

Morbidelli, A., Levison, H.F., Tsiganis, K., Gomes, R., 2005. Chaotic capture of Jupiter's Trojan asteroids in the early Solar System. Nature 435, 462–465.

Moroz, L.V., Arnold, G., Korochantsev, A.V., Wasch, R., 1998. Natural solid bitumens as possible analogs for cometary and asteroid organics. Icarus 134, 253–268.

Moroz, L., Baratta, G., Strazzulla, G., Starukhina, L., Dotto, E., Barucci, M.A., Arnold, G., Distefano, E., 2004. Optical alteration of complex organics induced by ion irradiation. 1. Laboratory experiments suggest unusual space weathering trend. Icarus 170, 214–228.

Rickman, H., Fernández, J.A., Gustafson, B.A.S., 1990. Formation of stable dust mantles on short-period comet nuclei. Astron. Astrophys. 237, 524–535.

Roig, F., Ribeiro, A.O., Gil-Hutton, R., 2008. Taxonomy of asteroid families among the Jupiter Trojans: Comparison between spectroscopic data and the sloan digital sky survey colors. Astron. Astrophys. 483, 911–931.

Strazzulla, G., 1998. Chemistry of ice induced by bombardment with energetic charged particles. In: Schmitt, B., de Bergh, C., Festou, M. (Eds.), Solar System Ices International Symposium, ASSL vol. 227. Kluwer Academic, Dordrecht, pp. 281–301.

Strazzulla, G., Dotto, E., Binzel, R., Brunetto, R., Barucci, M.A., Blanco, A., Orofino, V., 2005. Spectral alteration of the Meteorite Epinal (H5) induced by heavy ion irradiation: A simulation of space weathering effects on near-Earth asteroids. Icarus 174, 31–35.

Tancredi, G., Fernández, J.A., Rickman, H., Licandro, J., 2006. Nuclear magnitudes and the size distribution of Jupiter family comets. Icarus 182, 527–549.

Thompson, W.R., Murray, B.G.J.P.T., Khare, B.N., Sagan, C., 1987. Coloration and darkening of methane clathrate and other ices by charged particle irradiation – Applications to the outer Solar System. J. Geophys. Res. 92, 14933–14947.

Vilas, F., 1994. A quick look method of detecting water of hydration in small Solar System bodies. Lunar Planet. Sci. 25, 1439–1440.

Vilas, F., 1995. Is the U-B color sufficient for identifying water of hydration on Solar System bodies? Icarus 115, 217–218.

Yang, B., Jewitt, D., 2007. Spectroscopic search for water ice on jovian Trojan asteroids. Astron. J. 134, 223–228.

Zubko, V.G., Mennella, V., Colangeli, L., Bussoletti, E., 1996. Optical constants of cosmic carbon analogue grains. I. Simulation of clustering by a modified continuous distribution of ellipsoids. Mon. Not. R. Astrophys. Soc. 282, 1321–1329.

4.4 Analyse des nuages L4 et L5

Les nuages L4 et L5 présentent une dominance d'astéroïdes primitifs du type D, et le nuage L4 montre une variété importante de types spectraux. Pour étudier les deux nuages, nous avons créé et analysé une base de données incluant les Troyens membres de familles observées par notre équipe et ceux dont les spectres étaient publiés et disponibles dans la littérature, pour un échantillon global de 142 Troyens, 68 du nuage L5 et 74 de L4. Nous avons calculé les pentes spectrales de manière homogène pour tous les astéroïdes (entre 5000 et 8000 Å).
La plus grande partie (73,5%) des astéroïdes du nuage L5 appartient à la classe D (pente > 7 %/10^3 Å), 11,8% sont de type DP/PD (pente 5 –7 %/10^3 Å), 10,3% de type P–type, et seulement 4,4% sont de type C. Dans le nuage L4 les astéroïdes de type D dominent encore mais en pourcentage plus petit (48,6%), et on y trouve aussi beaucoup d'objets avec des pentes spectrales petites : 20,3% de type P, 8,1% de type DP/PD, 12,2% de type C, et même 10,8% d'astéroïdes avec des pentes négatives.
Dans le nuage L4, les résultats sur la pente spectrale sont fortement influencés par la famille d'Eurybates, où les astéroïdes de type C et P dominent. Si on exclut les membres de cette famille particulière, il reste 57 astéroïdes dans le nuage L4 et la distribution des différentes classes taxonomiques se rapproche de celle du nuage L5.

Aucune relation pente-diamètre n'a été établie pour les Troyens observés. En étudiant les paramètres orbitaux, nous avons trouvé que les astéroïdes avec une petite inclinaison ont des couleurs/spectres plus bleues par rapport à ceux avec une grande inclinaison. Cette corrélation est opposée à celle que nous observons pour les autres petits corps du Système Solaire externe, où les objets dynamiquement plus excités et avec de grandes inclinaisons ont des spectres plus neutres/bleus, par effets de collisions qui rajeunissent leurs surfaces. Ce résultat est associé principalement à la famille d'Eurybates, car la corrélation disparaît si on ne considère pas les membres de cette famille.

4.5 Corrélations entres les Troyens et les petits corps du Système Solaire externe

Nous avons comparé les couleurs/spectres de Troyens avec celles/ceux d'autres objets du Système Solaire externe, trouvant que leurs couleurs moyennes sont identiques à celles des comètes et de la partie bleue de la population des Centaures et OTNs. Par contre, la distribution de couleurs de Troyens n'est pas compatible avec celle des autres classes d'objets, et elle montre que les Troyens forment une population assez particulière (Dotto et al., 2006, Fornasier et al., 2007b).
Les Troyens ont des couleurs plus neutres/bleues (similaires à celles du Soleil) par rapport aux autres petits corps du Système Solaire externe, et leur distribution de couleurs est la plus étroite. La différence avec les autres objets est une fois encore principalement due à la famille d'Eurybates.

4.5.1 Article : Visible spectroscopic and photometric survey of Jupiter Trojans : final results on dynamical families

Available online at www.sciencedirect.com
ScienceDirect
ELSEVIER
Icarus 190 (2007) 622–642
ICARUS
www.elsevier.com/locate/icarus

Visible spectroscopic and photometric survey of Jupiter Trojans: Final results on dynamical families ☆

S. Fornasier [a,b,*], E. Dotto [c], O. Hainaut [d], F. Marzari [e], H. Boehnhardt [f], F. De Luise [c], M.A. Barucci [b]

[a] *University of Paris 7 "Denis Diderot," 10 rue Alice Domon et Leonie Duquet, 75013 Paris, France*
[b] *LESIA, Paris Observatory, Batiment 17, 5 Place Jules Janssen, 92195 Meudon Cedex, France*
[c] *INAF–Osservatorio Astronomico di Roma, Via Frascati 33, 00040 Monteporzio Catone (Roma), Italy*
[d] *European Southern Observatory, Casilla 19001, Santiago, Chile*
[e] *Dipartimento di Fisica, Università di Padova, Via Marzolo 8, 35131 Padova, Italy*
[f] *Max-Planck Institute for Solar System Research, Max-Planck-Str. 2, 37191 Katlenburg-Lindau, Germany*

Received 2 December 2006; revised 20 March 2007
Available online 29 April 2007

Abstract

We present the results of a visible spectroscopic and photometric survey of Jupiter Trojans belonging to different dynamical families. The survey was carried out at the 3.5 m New Technology Telescope (NTT) of the European Southern Observatory (La Silla, Chile) in April 2003, May 2004 and January 2005. We obtained data on 47 objects, 23 belonging to the L5 swarm and 24 to the L4 one. These data together with those already published by Fornasier et al. [Fornasier, S., Dotto, E., Marzari, F., Barucci, M.A., Boehnhardt, H., Hainaut, O., de Bergh, C., 2004a. Icarus 172, 221–232] and Dotto et al. [Dotto, E., Fornasier, S., Barucci, M.A., Licandro, J., Boehnhardt, H., Hainaut, O., Marzari, F., de Bergh, C., De Luise, F., 2006. Icarus 183, 420–434], acquired since November 2002, constitute a total sample of visible spectra for 80 objects. The survey allows us to investigate six families (Aneas, Anchises, Misenus, Phereclos, Sarpedon, Panthoos) in the L5 cloud and four L4 families (Eurybates, Menelaus, 1986 WD and 1986 TS6). The sample that we measured is dominated by D-type asteroids, with the exception of the Eurybates family in the L4 swarm, where there is a dominance of C- and P-type asteroids. All the spectra that we obtained are featureless with the exception of some Eurybates members, where a drop-off of the reflectance is detected shortward of 5200 Å. Similar features are seen in main belt C-type asteroids and commonly attributed to the intervalence charge transfer transition in oxidized iron. Our sample comprises fainter and smaller Trojans as compared to the literature's data and allows us to investigate the properties of objects with estimated diameter smaller than 40–50 km. The analysis of the spectral slopes and colors versus the estimated diameters shows that the blue and red objects have indistinguishable size distribution, so any relationship between size and spectral slopes has been found. To fully investigate the Trojans population, we include in our analysis 62 spectra of Trojans available in literature, resulting in a total sample of 142 objects. Although the mean spectral behavior of L4 and L5 Trojans is indistinguishable within the uncertainties, we find that the L4 population is more heterogeneous and that it has a higher abundance of bluish objects as compared to the L5 swarm. Finally, we perform a statistical investigation of the Trojans's spectra property distributions as a function of their orbital and physical parameters, and in comparison with other classes of minor bodies in the outer Solar System. Trojans at lower inclination appear significantly bluer than those at higher inclination, but this effect is strongly driven by the Eurybates family. The mean colors of the Trojans are similar to those of short period comets and neutral Centaurs, but their color distributions are different.

Keywords: Trojan asteroids; Asteroids, composition; Photometry; Spectroscopy

1. Introduction

Jupiter Trojans are small bodies of the Solar System located in the Jupiter Lagrangian points L4 and L5. Up to now more than 2000 Trojans have been discovered, ∼1150 belonging to the L4 cloud and ∼950 to the L5 one. The number of L4 Trojans

☆ Based on observations carried out at the European Southern Observatory (ESO), La Silla, Chile, ESO proposals 71.C-0650, 73.C-0622, 74.C-0577.

* Corresponding author. Fax: +33 145077144.
E-mail address: sonia.fornasier@obspm.fr (S. Fornasier).

0019-1035/$ – see front matter
doi:10.1016/j.icarus.2007.03.033

with radius greater than 1 km is estimated to be around 1.6×10^5 (Jewitt et al., 2000), comparable with the estimated main belt population of similar size.

The debate about the origin of Jupiter Trojans and how they were trapped in librating orbits around the Lagrangian points is still open to several possibilities. Considering that Trojans have orbits stable over the age of the Solar System (Levison et al., 1997; Marzari et al., 2003) their origin must date back to the early phase of the Solar System formation. Some authors (Marzari and Scholl, 1998a, 1998b; Marzari et al., 2002) suggested that they formed very close to their present location and were trapped during the growth of Jupiter. Morbidelli et al. (2005) suggested that Trojans formed in the Kuiper belt and were subsequently captured in the Jupiter L4 and L5 Lagrangian points during planetary migration, just after Jupiter and Saturn crossed their mutual 1:2 resonances. In this scenario, Jupiter Trojans would give important clues on the composition and accretion of bodies in the outer regions of the solar nebula.

Several theoretical studies conclude that Jupiter Trojan clouds are at least as collisionally evolved as main belt asteroids (Shoemaker et al., 1989; Binzel and Sauter, 1992; Marzari et al., 1997; Dell'Oro et al., 1998). This result is supported by the identification of several dynamical families, both in the L4 and L5 swarm (Shoemaker et al., 1989; Milani, 1993; Beaugé and Roig, 2001).

Whatever the Trojan origin is, it is plausible to assume that they formed beyond the frost line and that they are primitive bodies, are possibly composed of anhydrous silicates and organic compounds, and possibly still contain ices in their interior. Several observations of Trojans in the near infrared region (0.8–2.5 μm) have failed to clearly detect any absorption features indicative of water ice (Barucci et al., 1994; Dumas et al., 1998; Emery and Brown, 2003, 2004; Dotto et al., 2006). Also in the visible range Trojan spectra appear featureless (Jewitt and Luu, 1990; Fornasier et al., 2004a; Bendjoya et al., 2004; Dotto et al., 2006). Up to now only 2 objects (1988 BY1 and 1870 Glaukos) show the possible presence of faint bands (Jewitt and Luu, 1990). However, these bands are comparable to the peak to peak noise and are not yet confirmed.

Recently, mineralogical features have been detected in emissivity spectra of three Trojan asteroids measured by the Spitzer Space Telescope. These features are interpreted as indicating the presence of fine-grained silicates on the surfaces (Emery et al., 2006).

Several questions about Jupiter Trojans' dynamical origin, physical properties, composition and link with other groups of minor bodies such as outer main belt asteroids, cometary nuclei, Centaurs and KBOs are still open.

In order to shed some light on these questions, we have carried out a spectroscopic and photometric survey of Jupiter Trojans at the 3.5 m New Technology Telescope (NTT) of the European Southern Observatory (La Silla, Chile) and at the 3.5 m Telescopio Nazionale Galileo (TNG), La Palma, Spain. In this paper we present new visible spectroscopic and photometric data, obtained during 7 observing nights, carried out at ESO-NTT on April 2003, May 2004, and January 2005, for a total of 47 objects belonging to the L5 (23 objects) and L4 (24 objects) swarms. Considering also the results already published in Fornasier et al. (2004a) and Dotto et al. (2006), obtained in the framework of the same project, we collected a total sample of 80 Jupiter Trojan visible spectra, 47 belonging to the L5 clouds and 33 to the L4. This is the largest homogeneous data set available up to now on these primitive asteroids.

The principal aim of our survey was the investigation of Jupiter Trojans belonging to different dynamical families. In fact, since dynamical families are supposed to be formed from the collisional disruption of parent bodies, the investigation of the surface properties of small and large family members can help in understanding the nature of these dynamical groups and might provide a glimpse of the interior structure of the larger primordial parent bodies.

We also present an analysis of the visible spectral slopes for all the data in our survey along with those available in the literature, for a total sample of 142 Trojans.

This enlarged sample allowed us to carry out a significant statistical investigation of the Trojans' spectral property distributions, as a function of their orbital and physical parameters, and in comparison with other classes of minor bodies in the outer Solar System. We also discuss the spectral slope distribution within the Trojan families.

2. Observations and data reduction

The data were obtained in the visible range during 3 different observing runs at ESO-NTT: 10 and 11 April 2003 for the spectroscopic and photometric investigation of 6 members of the 4035 1986 WD and 1 member of 1986 TS6 families; 25 and 26 May 2004 for a spectroscopic survey of L4 Eurybates family; 17, 18, and 19 January 2005 for the spectroscopic and photometric investigation of 5 Anchises, 6 Misenus, 5 Panthoos, 2 Cloanthus, 2 Sarpedon and 3 Phereclos family members (L5 swarm).

We selected our targets from the list of Jupiter Trojan families provided by Beaugé and Roig (2001) and P.E.Tr.A. Project at http://www.daf.on.br/froig/petra/.

The authors have used a cluster-detection algorithm called Hierarchical Clustering Method (HCM, e.g. Zappalà et al., 1990) to find asteroid families among Jupiter Trojans starting from a data-base of semi-analytical proper elements (Beaugé and Roig, 2001). The identification of families is performed by comparing the mutual distances with a suitable metric in the proper elements' space. The clustering chain is halted when the mutual distance, measuring the incremental velocity needed for orbital change after the putative parent body breakup, is larger than a fixed cut-off value. A lower cutoff implies a higher statistical significance of the family. Since families in L4 are on average more robust than those around L5 (Beaugé and Roig, 2001), we prefer to adopt a cutoff of 100 m/s for the L4 cloud and of 150 m/s for L5. For the very robust Eurybates family we decided to limit our survey to those family members defined with a cutoff of 70 m/s.

All the data were acquired using the EMMI instrument, equipped with a 2×1 mosaic of 2048×4096 MIT/LL CCD with square 15 μm pixels. For the spectroscopic investigation during May 2004 and January 2005 runs we used the grism #1 (150 g/mm) in RILD mode to cover the wavelength range 4100–9400 Å with a dispersion of 3.1 Å/pixel (200 Å/mm) at the first order, while on April 2003 we used a different grism, the #7 (150 g/mm), covering the spectral range 5200–9500 Å, with a dispersion of 3.6 Å/pixel at the first order. April 2003 and January 2005 spectra were taken through a 1 arcsec wide slit, while during May 2004 we used a larger slit (1.5 arcsec). The slit was oriented along the parallactic angle during all the observing runs in order to avoid flux loss due to the atmospheric differential refraction.

For most objects, the total exposure time was divided into several (usually 2–4) shorter acquisitions. This allowed us to check the asteroid position in the slit before each acquisition, and correct the telescope pointing and/or tracking rates if necessary. During each night we also recorded bias, flat-field, calibration lamp (He–Ar) and several (6–7) spectra of solar analog stars measured at different airmasses, covering the airmass range of the science targets. During 17 January 2005, part of the night was lost due to some technical problems and only 2 solar analog stars were acquired. The ratio of these 2 stars show minimal variations (less than 1%) in the 5000–8400 Å range, but higher differences at the edges of this range. For this reason we omit the spectral region below 4800 Å for most of the asteroids acquired that night.

The spectra were reduced using ordinary procedures of data reduction as described in Fornasier et al. (2004a). The reflectivity of each asteroid was obtained by dividing its spectrum by that of the solar analog star closest in time and airmass to the object. Spectra were finally smoothed with a median filter technique, using a box of 19 pixels in the spectral direction for each point of the spectrum. The threshold was set to 0.1, meaning that the original value was replaced by the median value if the median value differs by more than 10% from the original one. The obtained spectra are shown in Figs. 1–5. In Tables 1 and 2 we report the circumstances of the observations and the solar analog stars used respectively for the L5 and L4 family members.

The broadband color data were obtained during the April 2003 and January 2005 runs just before the Trojans' spectral observation. We used the RILD mode of EMMI for wide field imaging with the Bessell-type B, V, R, and I filters (centered respectively at 4139, 5426, 6410, and 7985 Å). The observations were carried out in a 2×2 binning mode, yielding a pixel scale of 0.33 arcsec/pixel. The exposure time varied with the object magnitude: typically it was about 12–90 s in V, 30–180 s in B, 12–70 s in R and I filters.

The CCD images were reduced and calibrated with a standard method (Fornasier et al., 2004a), and absolute calibration was obtained through the observations of several Landolt fields (Landolt, 1992). The instrumental magnitudes were measured using aperture photometry with an integrating radius typically about three times the average seeing, and sky subtraction was performed using a 5–10 pixels wide annulus around each object.

Table 1
Observing conditions of the investigated L5 asteroids

Object	Date	UT	T_{exp} (s)	n_{exp}	Air.	Solar an. (air.)
Anchises						
1173	17 Jan 05	06:06	60	1×60 s	1.42	HD76151 (1.48)
23549	17 Jan 05	07:20	480	2×240 s	1.60	HD76151 (1.48)
24452	17 Jan 05	07:54	960	4×240 s	1.44	HD76151 (1.48)
47967	17 Jan 05	05:34	800	2×400 s	1.38	HD76151 (1.48)
2001 SB173	17 Jan 05	06:28	1200	2×600 s	1.35	HD76151 (1.48)
Cloanthus						
5511	19 Jan 05	06:04	960	4×240 s	1.26	HD76151 (1.12)
51359	19 Jan 05	04:13	660	1×660 s	1.36	HD76151 (1.12)
Misenus						
11663	17 Jan 05	05:13	400	1×400 s	1.21	HD44594 (1.12)
32794	18 Jan 05	03:13	1800	2×900 s	1.39	HD28099 (1.44)
56968	17 Jan 05	04:31	400	2×400 s	1.21	HD44594 (1.12)
1988 RE12	18 Jan 05	04:12	2000	2×1000 s	1.31	HD28099 (1.44)
2000 SC51	18 Jan 05	06:09	1320	2×660 s	1.16	HD44594 (1.17)
2001 UY123	18 Jan 05	06:46	1320	2×660 s	1.32	HD44594 (1.17)
Phereclos						
9030	18 Jan 05	08:19	1000	1×1000 s	1.37	HD44594 (1.17)
11488	19 Jan 05	03:31	1320	2×660 s	1.99	HD76151 (1.12)
31820	19 Jan 05	07:02	1320	2×660 s	1.35	HD76151 (1.11)
Sarpedon						
48252	18 Jan 05	02:32	1320	2×660 s	1.30	HD28099 (1.44)
84709	19 Jan 05	05:35	1320	2×660 s	1.34	HD76151 (1.12)
Panthoos						
4829	17 Jan 05	08:37	720	3×240 s	1.45	HD76151 (1.48)
30698	18 Jan 05	01:54	1320	2×660 s	1.73	HD28099 (1.44)
31821	18 Jan 05	05:27	1320	2×660 s	1.35	HD28099 (1.44)
76804	17 Jan 05	03:35	1800	3×600 s	1.38	HD44594 (1.12)
2001 VK85	18 Jan 05	07:31	2000	2×1000 s	1.23	HD44594 (1.17)

For each object we report the observational date and universal time, total exposure time, number of acquisitions with exposure time of each acquisition, airmass, and the observed solar analogs with their airmass.

The results are reported in Table 3. From the visual inspection and the radial profiles analysis of the images, no coma was detected for any of the observed Trojans.

On May 2004, as the sky conditions were clear but not photometric, we did not perform photometry of the Eurybates family targets.

3. Results

For each Trojan we computed the slope S of the spectral continuum using a standard least squared technique for a linear fit in the wavelength range between 5500 and 8000 Å. The choice of these wavelength limits has been driven by the spectral coverage of our data. We choose 5500 Å as the lower limit because of the different instrumental setup used during different observing runs (with some spectra starting at wavelength $\geqslant$5200 Å), while beyond 8000 Å our spectra are generally noisier due to a combination of the CCD drop-off in sensitivity and the presence of the strong atmospheric water bands.

The computed slopes and errors are listed in Tables 4 and 5. The reported error bars take into account the 1σ uncertainty of the linear fit plus $0.5\%/10^3$ Å attributable to the use of different instruments and solar analog stars (estimated from the

Table 2
Observing conditions of the investigated L4 asteroids

Object	Date	UT	T_{exp} (s)	n_{exp}	Air.	Solar an. (air.)
Eurybates						
3548	25 May 04	05:14	600	2 × 300 s	1.02	SA107-684 (1.19)
9818	26 May 04	00:13	780	1 × 780 s	1.19	SA102-1081(1.15)
13862	25 May 04	03:35	1200	2 × 600 s	1.09	SA107-998 (1.15)
18060	25 May 04	02:47	1500	2 × 750 s	1.07	SA107-998 (1.15)
24380	25 May 04	06:53	780	1 × 780 s	1.18	SA107-684 (1.19)
24420	25 May 04	08:49	900	1 × 900 s	1.59	SA112-1333 (1.17)
24426	26 May 04	00:13	1440	2 × 720 s	1.13	SA107-684 (1.17)
28958	26 May 04	07:14	1800	2 × 900 s	1.35	SA107-684 (1.17)
39285	25 May 04	05:40	2700	3 × 900 s	1.09	SA107-684 (1.19)
43212	25 May 04	07:39	2340	3 × 780 s	1.39	SA110-361 (1.15)
53469	25 May 04	02:05	1800	2 × 900 s	1.04	SA107-998 (1.15)
65150	26 May 04	01:59	3600	4 × 900 s	1.07	SA102-1081 (1.20)
65225	26 May 04	03:40	3600	4 × 900 s	1.04	SA107-684 (1.17)
1996RD29	26 May 04	05:12	2700	3 × 900 s	1.10	SA107-684 (1.17)
2000AT44	25 May 04	04:14	1800	2 × 900 s	1.04	SA107-684 (1.19)
2002CT22	26 May 04	00:49	2400	4 × 600 s	1.08	SA102-1081 (1.15)
2002EN68	26 May 04	08:10	1800	2 × 900 s	1.62	SA107-684 (1.17)
1986 WD						
4035	10 Apr 03	03:28	600	1 × 600 s	1.09	SA107-684 (1.15)
6545	10 Apr 03	02:39	900	1 × 900 s	1.16	SA107-684 (1.15)
11351	10 Apr 03	09:21	900	1 × 900 s	1.28	SA107-684 (1.15)
14707	11 Apr 03	08:11	1200	1 × 1200 s	1.15	SA107-684 (1.15)
24233	11 Apr 03	02:29	1200	1 × 1200 s	1.39	SA107-684 (1.37)
24341	11 Apr 03	05:47	900	1 × 900 s	1.16	SA107-684 (1.17)
1986 TS6						
12921	10 Apr 03	07:33	900	1 × 900 s	1.39	SA107-684 (1.40)

For each object we report the observational date and universal time, total exposure time, number of acquisitions with exposure time of each acquisition, airmass, and the observed solar analogs with their airmass.

different efficiency of the grism used, and from flux losses due to different slit apertures). In Tables 4 and 5 we also report the taxonomic class derived following the Dahlgren and Lagerkvist (1995) classification scheme.

In the L5 cloud we find 27 D-, 3 DP-, 2 PD-, and 1 P-type objects. In the L4 cloud we find 10 C-type and 7 P-type objects inside the Eurybates family, while for the Menelaus, 1986 TS6 and 1986 WD families, including the data published in Dotto et al. (2006), we get 9 D-, 3 P-, 3 C-, and 1 DP-type asteroids.

The majority of the spectra are featureless, although some of the observed Eurybates' members show weak spectral absorption features (Fig. 5). These features are discussed in the following section.

We derived an estimated absolute magnitude H by scaling the measured V magnitude to $r = \Delta = 1$ AU and to zero phase assuming $G = 0.15$ (Bowell et al., 1989). The estimated H magnitude of each Trojan might be skewed uncertain rotational phase, as the lightcurve amplitudes of Trojans might vary up to 1 magnitude. In order to investigate possible size dependence inside each family, and considering that IRAS diameters are available for very few objects, we estimate the size using the following relationship:

$$D = \frac{1329 \times 10^{-H/5}}{\sqrt{p}},$$

where D is the asteroid diameter, p is the geometric albedo, and H is the absolute magnitude. We use H derived from our observations when available, and from the ASTORB.DAT file (Lowell Observatory) for the Eurybates members, for which we did not carry out visible photometry. We evaluated the diameter for an albedo range of 0.03–0.07, assuming a mean albedo of 0.04 for these dark asteroids (Fernandez et al., 2003). The resulting D values are reported in Tables 4 and 5.

3.1. *Dynamical families: L5 swarm*

3.1.1. *Anchises*

We investigated 5 of the 15 members of the Anchises family (Fig. 1): 1173 Anchises, 23549 1994 ES6, 24452 2000 QU167, 47967 2000 SL298 and 124729 2001 SB173 on 17 January 2005. For 4 out of 5 observed objects we omit the spectral range below 4800 Å due to low S/N ratio and problems with the solar analog stars. The spectral behavior is confirmed by photometric data (see Table 3). All the obtained spectra are featureless.

The Anchises family survives at a cutoff corresponding to relative velocities of 150 m/s. The biggest member, 1173 Anchises, has a diameter of 126 km (IRAS data) and has the lowest spectral slope ($3.9\%/10^3$ Å) among the investigated family members. It is classified as P-type, while the other 4 members are all D-types. Anchises was previously observed in the 4000–7400 Å region by Jewitt and Luu (1990), who reported a spectral slope of $3.8\%/10^3$ Å, in perfect agreement with the value we found. The three 19–29 km sized objects have a steeper spectral slope (7.4–$9.2\%/10^3$ Å), while the smallest

Table 3
Visible photometric observations of L4 and L5 Trojans (ESO-NTT EMMI)

Object	Date	UT	V	B–V	V–R	V–I
L4						
1986 WD						
4035	10 Apr 03	03:11	16.892 ± 0.031	0.752 ± 0.040	0.473 ± 0.042	0.926 ± 0.055
4035	10 Apr 03	04:22	16.981 ± 0.031	0.752 ± 0.040	0.495 ± 0.042	0.945 ± 0.055
6545	10 Apr 03	02:22	17.558 ± 0.031	0.734 ± 0.041	0.499 ± 0.042	0.935 ± 0.055
11351	10 Apr 03	09:03	18.407 ± 0.032	0.739 ± 0.044	0.498 ± 0.044	0.900 ± 0.057
14707	11 Apr 03	06:46	18.666 ± 0.031	0.751 ± 0.041	0.401 ± 0.033	0.804 ± 0.055
14707	11 Apr 03	08:37	18.873 ± 0.031	0.754 ± 0.041	0.424 ± 0.033	0.790 ± 0.056
24233	11 Apr 03	01:33	18.894 ± 0.034	0.704 ± 0.051	0.481 ± 0.037	0.899 ± 0.058
24341	11 Apr 03	05:05	19.376 ± 0.032	0.713 ± 0.043	0.369 ± 0.035	0.759 ± 0.057
1986 TS6						
12921	10 Apr 03	07:12	18.393 ± 0.031	0.673 ± 0.040	0.421 ± 0.042	0.786 ± 0.055
L5	Cut off	150 m/s				
Anchises						
1173	17 Jan 05	05:54	16.595 ± 0.024	0.811 ± 0.034	0.402 ± 0.035	0.805 ± 0.038
23549	17 Jan 05	07:09	18.969 ± 0.050	0.800 ± 0.071	0.485 ± 0.068	0.872 ± 0.075
24452	17 Jan 05	07:48	18.757 ± 0.043	0.872 ± 0.056	0.441 ± 0.056	0.847 ± 0.066
47967	17 Jan 05	05:27	19.382 ± 0.044	0.899 ± 0.058	0.489 ± 0.069	0.965 ± 0.075
2001 SB173	17 Jan 05	06:20	19.882 ± 0.043	0.992 ± 0.060	0.503 ± 0.064	0.927 ± 0.078
Cloanthus						
5511	19 Jan 05	05:52	17.968 ± 0.020	0.906 ± 0.027	0.442 ± 0.027	0.968 ± 0.032
51359	19 Jan 05	03:54	19.631 ± 0.102	0.864 ± 0.201	0.447 ± 0.131	0.885 ± 0.164
Misenus						
11663	17 Jan 05	05:05	18.473 ± 0.022	0.837 ± 0.030	0.409 ± 0.030	0.872 ± 0.039
32794	18 Jan 05	03:07	19.685 ± 0.038	0.923 ± 0.065	0.393 ± 0.056	0.879 ± 0.057
56968	17 Jan 05	04:18	18.596 ± 0.026	0.986 ± 0.040	0.494 ± 0.033	1.003 ± 0.036
1988 RE12	18 Jan 05	04:00	20.892 ± 0.081	0.826 ± 0.132	0.388 ± 0.108	0.871 ± 0.106
2000 SC51	18 Jan 05	06:03	19.876 ± 0.038	1.016 ± 0.055	0.444 ± 0.059	0.896 ± 0.056
2001 UY123	18 Jan 05	06:41	19.869 ± 0.047	0.890 ± 0.058	0.537 ± 0.056	0.971 ± 0.063
Phereclos						
9030	18 Jan 05	08:14	18.397 ± 0.020	0.887 ± 0.024	0.493 ± 0.027	0.973 ± 0.028
11488	19 Jan 05	02:57	18.931 ± 0.066	0.868 ± 0.101	0.430 ± 0.079	0.848 ± 0.084
31820	19 Jan 05	06:39	20.041 ± 0.077	0.889 ± 0.093	0.520 ± 0.091	0.916 ± 0.123
Sarpedon						
48252	18 Jan 05	02:25	19.878 ± 0.060	0.949 ± 0.100	0.467 ± 0.093	0.903 ± 0.090
84709	19 Jan 05	05:10	19.862 ± 0.068	0.855 ± 0.087	0.462 ± 0.090	1.010 ± 0.094
Panthoos						
4829	17 Jan 05	08:18	18.430 ± 0.029	0.851 ± 0.050	0.420 ± 0.039	0.792 ± 0.052
30698	18 Jan 05	01:45	19.353 ± 0.036	–	0.472 ± 0.042	0.865 ± 0.047
31821	18 Jan 05	05:21	19.328 ± 0.076	0.980 ± 0.111	0.440 ± 0.097	0.901 ± 0.108
76804	17 Jan 05	03:21	19.471 ± 0.065	0.803 ± 0.082	0.446 ± 0.070	0.889 ± 0.080
2001 VK85	18 Jan 05	07:23	20.179 ± 0.038	0.822 ± 0.063	0.462 ± 0.048	1.020 ± 0.050

For each object, date, computed V magnitude, B–V, V–R and V–I colors are reported. The given UT is for the V filter acquisition. The observing photometric sequence (V–R–B–I) took a few minutes.

object, 2001 SB173 (spectral slope $= 14.78 \pm 0.99\%/10^3$ Å) is the reddest one (Table 4).

Even with the uncertainties in the albedo and diameter, a slope–size relationship is evident among the observed objects, with smaller-fainter members redder than larger ones (Fig. 7).

3.1.2. Misenus

For this family we investigated 6 members (11663 1997 GO24, 32794 1989 UE5, 56968 2000 SA92, 99328 2001 UY123, 105685 2000 SC51 and 120453 1988 RE12) out of the 12 grouped at a relative velocity of 150 m/s. The family survives with the same members also at a stringent cut-off velocity of 120 m/s. The spectra, together with magnitude color indices transformed into linear reflectance, are shown in Fig. 2, while the color indices are reported in Table 3. All the spectra are featureless with different spectral slope values covering the 4.6–15.9%/10^3 Å range (Table 4): 1988 RE12 has the lowest spectral slope and is classified as P-type, 3 objects (11663, 32794 and 2000 SC51) are in the transition region between P- and D-type, with very similar spectral behavior, while the two other observed members are D-types. Of these last, 56968 has the highest spectral slope not only inside the family (15.86%/10^3 Å) but also inside the whole L5 sample analyzed in this paper.

Table 4
L5 families

Object	H	D (km)	S (%/10^3 Å)	T
Anchises				
1173	8.99	126^{+11b}_{-11}	3.87 ± 0.70	P
23549	12.04	26^{+4}_{-6}	8.49 ± 0.88	D
24452	11.85	29^{+5}_{-7}	7.42 ± 0.70	D
47967	12.15	25^{+4}_{-6}	9.21 ± 0.78	D
2001 SB173	12.77	19^{+3}_{-5}	14.78 ± 0.99	D
Cloanthus				
5511	10.43	55^{+8}_{-13}	10.84 ± 0.65	D
51359	12.25	24^{+6}_{-4}	12.63 ± 1.30	D
Misenus				
11663	10.95	44^{+7}_{-10}	6.91 ± 0.70	DP
32794	12.77	19^{+3}_{-5}	6.59 ± 0.88	DP
56968	11.72	30^{+5}_{-7}	15.86 ± 0.71	D
1988 RE12	13.20	16^{+2}_{-4}	4.68 ± 1.20	P
2000 SC51	12.69	20^{+3}_{-5}	6.54 ± 0.98	DP
2001 UY123	12.75	19^{+3}_{-5}	8.28 ± 0.88	D
Phereclos				
2357[a]	8.86	95^{+4b}_{-4}	9.91 ± 0.68	D
6998[a]	11.43	34^{+5}_{-8}	11.30 ± 0.75	D
9030	11.14	40^{+6}_{-10}	10.35 ± 0.76	D
9430[a]	11.47	35^{+5}_{-8}	10.02 ± 0.90	D
11488	11.82	29^{+5}_{-7}	5.37 ± 0.92	PD
18940[a]	11.81	29^{+4}_{-7}	7.13 ± 0.75	D
31820	12.63	20^{+3}_{-5}	7.53 ± 0.80	D
Sarpedon				
2223[a]	9.25	95^{+4b}_{-4}	10.20 ± 0.65	D
5130[a]	9.85	71^{+11}_{-18}	10.45 ± 0.65	D
17416[a]	12.83	18^{+3}_{-5}	10.80 ± 0.90	D
25347[a]	11.59	33^{+5}_{-8}	10.11 ± 0.83	D
48252	12.84	18^{+3}_{-5}	9.62 ± 0.82	D
84709	12.70	19^{+3}_{-5}	11.64 ± 0.84	D
Panthoos				
4829	11.16	39^{+6}_{-10}	5.03 ± 0.70	PD
23694[a]	11.61	32^{+5}_{-8}	8.20 ± 0.72	D
30698	12.14	25^{+4}_{-6}	8.23 ± 1.00	D
30698[a]	12.27	25^{+4}_{-6}	9.08 ± 0.82	D
32430[a]	12.23	25^{+4}_{-6}	8.12 ± 1.00	D
31821	11.99	27^{+4}_{-6}	10.58 ± 0.82	D
76804	12.16	25^{+4}_{-6}	7.29 ± 0.71	D
2001 VK85	12.79	19^{+3}_{-5}	14.39 ± 0.81	D

We report for each target the absolute magnitude H and the estimated diameter (diameters marked by [b] are taken from IRAS data), the spectral slope S computed between 5500 and 8000 Å, and the taxonomic class (T) derived following Dahlgren and Lagerkvist (1995) classification scheme. The asteroids marked with [a] were observed by Fornasier et al. (2004a), and their spectral slope values have been recomputed in the 5500–8000 Å wavelength range; asteroids 23694, 30698 and 32430, previously Astyanax members, have been reassigned to the Panthoos family due to refined proper elements.

All the investigated Misenus members are quite faint and have diameters of a few tens of kilometers. No clear size-slope relationship has been found inside this family (Fig. 7).

Table 5
L4 families

Object	H	D (km)	S (%/10^3 Å)	T
Eurybates				
3548	9.50[c]	72^{+4b}_{-4}	-0.18 ± 0.57	C
9818	11.00[c]	42^{+6}_{-10}	2.12 ± 0.72	P
13862	11.10[c]	40^{+6}_{-10}	1.59 ± 0.70	C
18060	11.10[c]	40^{+6}_{-10}	2.86 ± 0.60	P
24380	11.20[c]	38^{+6}_{-9}	0.34 ± 0.65	C
24420	11.50[c]	33^{+5}_{-8}	1.65 ± 0.70	C
24426	12.50[c]	21^{+3}_{-5}	4.64 ± 0.80	P
28958	12.10[c]	25^{+4}_{-6}	-0.04 ± 0.80	C
39285	12.90[c]	17^{+3}_{-4}	0.25 ± 0.69	C
43212	12.30[c]	23^{+4}_{-6}	1.19 ± 0.78	C
53469	11.80[c]	29^{+4}_{-7}	0.17 ± 0.80	C
65150	12.90[c]	17^{+3}_{-4}	4.14 ± 0.70	P
65225	12.80[c]	18^{+3}_{-4}	0.97 ± 0.85	C
1996 RD29	13.06[c]	16^{+3}_{-4}	2.76 ± 0.89	P
2000 AT44	12.16[c]	24^{+3}_{-6}	-0.53 ± 0.83	C
2002 CT22	12.04[c]	26^{+4}_{-6}	2.76 ± 0.73	P
2002 EN68	12.30[c]	23^{+3}_{-6}	3.60 ± 0.98	P
1986 WD				
4035	9.72	68^{+5b}_{-5}	9.78 ± 0.61	D
4035[a]	9.30[c]	68^{+5b}_{-5}	15.19 ± 0.61	D
6545	10.42	55^{+8}_{-13}	11.32 ± 0.63	D
6545[a]	10.00[c]	66^{+10}_{-16}	9.88 ± 0.56	D
11351	10.88	44^{+7}_{-11}	10.26 ± 0.67	D
11351[a]	10.50[c]	53^{+8}_{-13}	10.44 ± 0.61	D
14707	11.25	$38^{+6}_{-9.4}$	-1.06 ± 1.00	C
24233	11.58	$33^{+5}_{-8.0}$	6.37 ± 0.67	DP
24341	11.99	27^{+4}_{-6}	-0.26 ± 0.71	C
1986 TS6				
12917	11.61	32^{+5}_{-8}	10.98 ± 0.68	D
12921	11.12	40^{+6}_{-10}	4.63 ± 0.75	P
12921[a]	10.70[c]	48^{+7}_{-12}	3.74 ± 1.00	P
13463	11.27	37^{+6}_{-9}	4.37 ± 0.65	P
15535	10.70	48^{+7}_{-12}	10.67 ± 0.65	D
20738	11.67	31^{+5}_{-8}	8.84 ± 0.70	D
24390	11.80	29^{+5}_{-7}	9.53 ± 0.62	D

We report for each target the absolute magnitude H and the estimated diameter (diameters marked by [b] are taken from IRAS data, while absolute magnitudes marked by [c] are taken from the astorb.dat file of the Lowell Observatory), the spectral slope S computed between 5500 and 8000 Å, and the taxonomic class (T) derived following Dahlgren and Lagerkvist (1995) classification scheme. The asteroids marked with [a] were observed by Dotto et al. (2006), and their spectral slope values have been recomputed in the 5500–8000 Å wavelength range.

No other data on the Misenus family members are available in the literature, so we do not know if the large gap between the spectral slope of 56968 and those of the other 5 investigated objects is real or it could be filled by other members not yet observed. If real, 56968 can be an interloper inside the family.

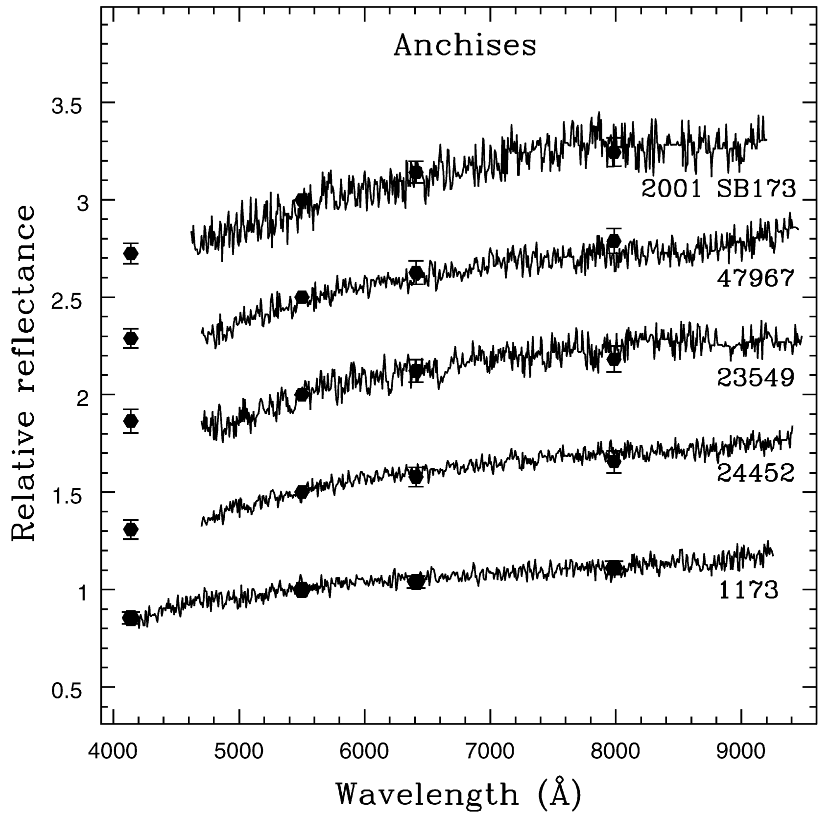

Fig. 1. Reflectance spectra of 5 Anchises family members (L5 swarm). The photometric color indices are also converted to relative reflectance and overplotted on each spectrum. Spectra and photometry are shifted by 0.5 in reflectance for clarity.

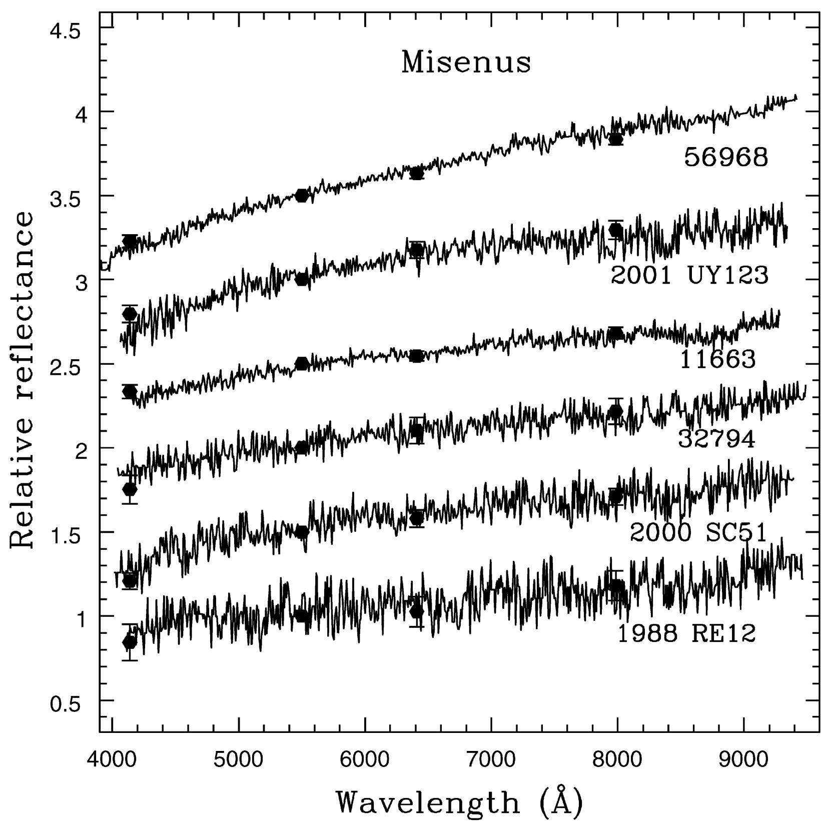

Fig. 2. Reflectance spectra of 6 Misenus family members (L5 swarm). The photometric color indices are also converted to relative reflectance and overplotted on each spectrum. Spectra and photometry are shifted by 0.5 in reflectance for clarity.

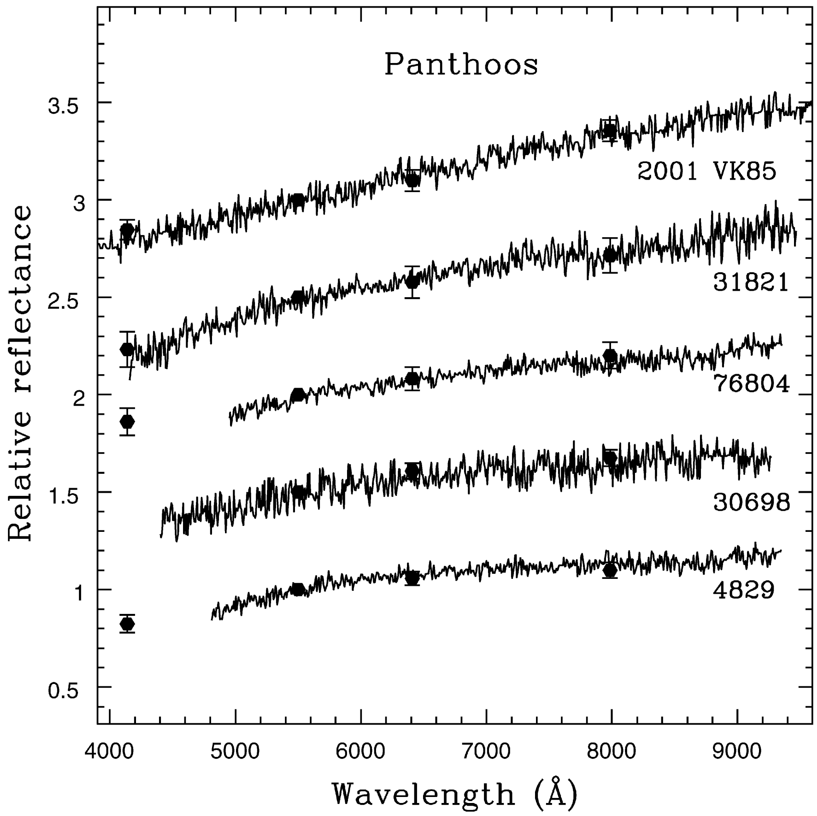

Fig. 3. Reflectance spectra of 5 Panthoos family members (L5 swarm). The photometric color indices are also converted to relative reflectance and overplotted on each spectrum. Spectra and photometry are shifted by 0.5 in reflectance for clarity. For Asteroid 30698, the B–V color is missing as a B filter measurement was not available.

3.1.3. Panthoos

The Panthoos family has 59 members for a relative velocity cutoff of 150 m/s. We obtained new spectroscopic and photometric data of 5 members: 4829 Sergestus, 30698 Hippokoon, 31821 1999 RK225, 76804 2000 QE and 111113 2001 VK85 (Fig. 3). Three objects presented by Fornasier et al. (2004a) as belonging to the Astyanax family (23694 1997 KZ3, 32430 2000 RQ83, 30698 Hippokoon) and one to the background population (24444 2000 OP32) are now included among the members of the Panthoos family. Periodic updates of the proper elements can change the family membership. In particular the Astyanax group disappeared in the latest revision of dynamical families, and its members are now in the Panthoos family within a cutoff of 150 m/s. The Panthos family survives also a cutoff of 120 m/s, with 7 members, and 90 m/s, with 6 members.

We observed 30698 Hippokoon during two different runs (on 9 Nov. 2002 and on 18 Jan. 2005), and both spectral slopes and colors are in agreement inside the error bars (see Tables 3, 4, and Fornasier et al., 2004a). No other data on the Panthoos family are available in the literature.

The analysis of the 8 members (for 24444 only photometry is available) show featureless spectra with slopes that seem to slightly increase as the asteroid size decreases (Table 4 and Fig. 7). However, all the members have dimensions very similar within the uncertainties, making it difficult for any slope–size relationship to be studied. The largest member, 4829 Sergestus, is a PD-type with a slope of about $5\%/10^3$ Å, while all the other investigated members are D-types.

3.1.4. Cloantus

We observed only 2 out of 8 members of the Cloantus family (5511 Cloanthus and 51359 2000 SC17, see Fig. 4) as grouped at a cutoff corresponding to relative velocities of 150 m/s. This family survives at a stringent cutoff and 3 members (including the two that we observed) also survive for relative velocities of 60 m/s. Both of the observed objects are D-types with very similar, featureless, reddish spectra (Table 4 and Fig. 7). 5511 Cloanthus was observed also by Bendjoya et al. (2004), who found a slope of $13.0 \pm 0.1\%/10^3$ Å in the 5000–7500 Å wavelength range, while we measure a value of $10.84 \pm 0.15\%/10^3$ Å. Our spectrum has a higher S/N ratio than the spectrum by Bendjoya et al. (2004), and it is perfectly matched by our measured color indices that confirm the spectral slope. This difference cannot be caused by the slightly different spectral ranges used to measure the slope, but could possibly be due to heterogeneous surface composition.

3.1.5. Phereclos

The Phereclos family comprises 15 members at a cutoff of 150 m/s. The family survives with 8 members also at a cutoff of 120 m/s. We obtained spectroscopic and photometric data of 3 members (9030 1989 UX5, 11488 1988 RM11 and

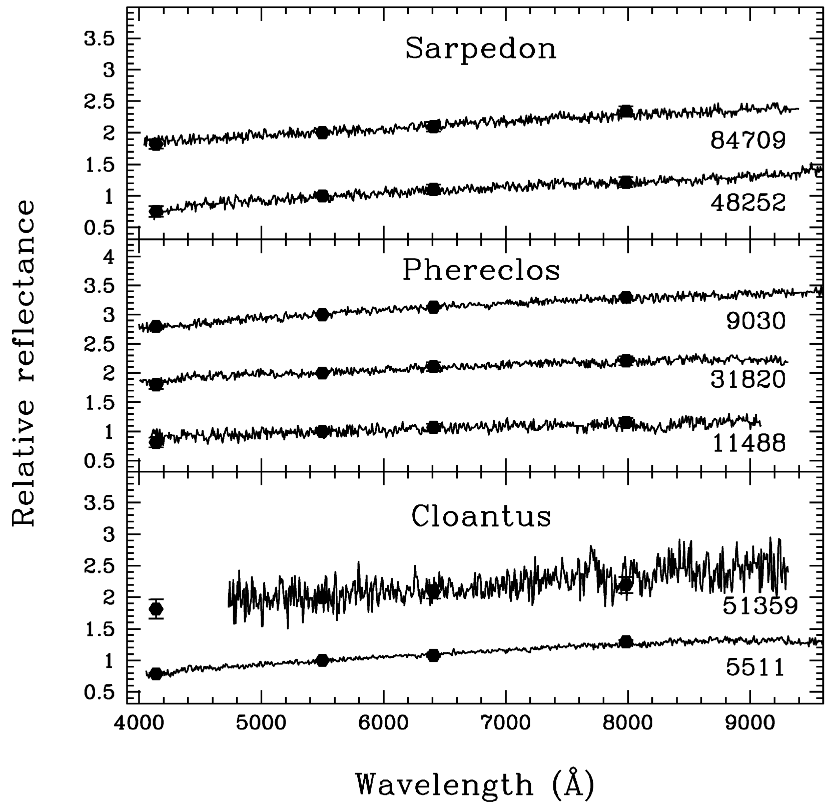

Fig. 4. Reflectance spectra of 2 Cloantus, 3 Phereclos and 2 Sarpedon family members (L5 swarm). The photometric color indices are also converted to relative reflectance and overplotted on each spectrum. Spectra and photometry are shifted by 1.0 in reflectance for clarity.

31820 1999 RT186, see Fig. 4), that, together with the 4 spectra (2357 Phereclos, 6998 Tithonus, 9430 1996 HU10, 18940 2000QV49) already presented by Fornasier et al. (2004a), allow us to investigate about half of the Phereclos family population defined at a cutoff of 150 m/s. The spectral slope of these objects, all classified as D-type except one PD-type (11488), varies from 5.3 to 11.3%/10^3 Å (Table 4). The size of the family members ranges from about 20 km in diameter for 31820 to 95 km for 2357, but we do not observe any clear slope–diameter relationship (Fig. 7 and Table 4).

3.1.6. Sarpedon

We obtained new spectroscopic and photometric data of 2 members of the Sarpedon family (48252 2001 TL212 and 84709 2002 VW120), whose spectra and magnitude color indices are reported in Fig. 4 and Table 4. Including the previous observations (Fornasier et al., 2004a) of 4 other members (2223 Sarpedon, 5130 Ilioneus, 17416 1988 RR10, and 25347 1999 RQ116), we have measurements of 6 of the 21 members of this family dynamically defined at a cutoff of 150 m/s. All the 6 aforementioned objects, except 25347, constitute a robust clustering which survives up to 90 m/s with 9 members. The cluster which contains (2223) Sarpedon was also recognized as a family by Milani (1993).

All the 6 investigated members have very similar colors (see Table 3) and spectral behavior. The spectral slope (Fig. 7) varies over a very restricted range, from 9.6 to 11.6%/10^3 Å (Table 4), despite a significant variation of the estimated size (from the 18 km of 17416 to the 105 km of 2223). Consequently, the surface composition of the Sarpedon family members appears to be very homogeneous.

3.2. Dynamical families: L4 swarm

3.2.1. Eurybates

Eurybates family members were observed in May 2004. The selection of the targets was made on the basis of a very stringent cutoff, corresponding to relative velocities of 70 m/s, that gives a family population of 28 objects. We observed 17 of these members (see Table 2) that constitute a very robust clustering in the space of the proper elements: all the members we studied, except 2002 CT22, survive at a cutoff of 40 m/s.

The spectral behavior of these objects (Fig. 5) is quite homogeneous with 10 asteroids classified as C-type and 7 as P-type. The spectral slopes (Table 5) range from neutral to moderately red (from −0.5 to 4.6%/10^3 Å). The slopes of six members are close to zero (3 slightly negative) with solar-like colors. The Asteroids 18060, 24380, 24420, and 39285, all classified as C-types, clearly show a drop off of reflectance for wavelength shorter than 5000–5200 Å. The presence of the same feature in the spectra of 2 other members (1996 RD29 and 28958) is less certain due to the lower S/N ratio. This absorption is commonly seen on main belt C-type asteroids (Vilas, 1994; Fornasier et al., 1999), where is due to the intervalence charge transfer transitions (IVCT) in oxidized iron, and is often coupled with other visible absorption features related to the pres-

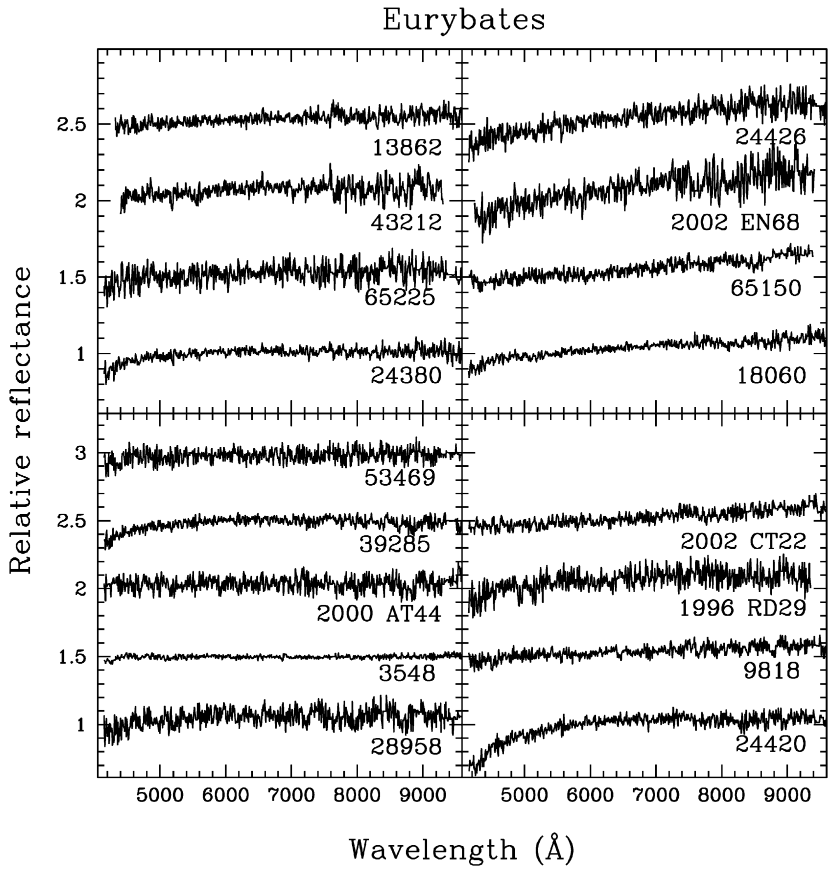

Fig. 5. Reflectance spectra of the 17 Eurybates family members (L4 swarm). Spectra are shifted by 0.5 in reflectance for clarity.

ence of aqueous alteration products (e.g. phyllosilicates, oxides, etc.). These IVCTs comprise multiple absorptions that are not uniquely indicative of phyllosilicates, but are present in the spectrum of any object containing Fe^{2+} and Fe^{3+} in its surface material (Vilas, 1994). Since no other phyllosilicate absorption features are present in the C-type spectra of the Eurybates family, there is no evidence that aqueous alteration processes occurred on the surface of these bodies.

In Fig. 8 we show the spectral slopes versus the estimated diameters for the Eurybates family members. All the observed objects, except the largest member (3548) that has a diameter of about 70 km and exhibit a neutral (∼solar-like) spectral slope, are smaller than ∼40 km and present both neutral and moderately red colors. The spectral slopes are strongly clustered around $S = 2\%/10^3$ Å, with higher S values restricted to smaller objects ($D < 25$ km).

3.2.2. *1986 WD*

We investigated 6 out of 17 members of the 4035 1986 WD family that is dynamically defined at a cutoff of 130 m/s (Fig. 6 and Table 2). Three of our targets (4035, 6545, and 11351) were already observed by Dotto et al. (2006): for 6545 and 11351 there is a good consistency between our spectra and those already published. 4035 was observed also by Bendjoya et al. (2004): all the spectra are featureless, but Bendjoya et al. (2004) obtain a slope of $8.8\%/10^3$ Å, comparable to the one here presented, while Dotto et al. (2006) found a higher value (see Table 5). This could be interpreted as due to the different rotational phases seen in the three observations, and could indicate some inhomogeneities on the surface of 4035.

The observed family members show heterogeneous behaviors (Fig. 8), with spectral slopes ranging from neutral values for the smaller members (24341 and 14707) to reddish ones for the 3 members with size bigger than 50 km (4035, 6545, and 11351). For this family, it seems that a size-slope relationship exists, with smaller members having solar colors and spectral slopes increasing with the object' sizes.

3.2.3. *1986 TS6*

The 1986 TS6 family includes 20 objects at a cut-off of 100 m/s. We present new spectroscopy and photometry of a single member, 12921 1998 WZ5 (Fig. 6). The spectrum we present here is flat and featureless, with a spectral slope of $4.6 \pm 0.8\%/10^3$ Å. Dotto et al. (2006) presented a spectrum obtained a month after our data (in May 2003) that has a very similar spectral slope $3.7 \pm 0.8\%/10^3$ Å. Previously, 12917 1998 TG16, 13463 Antiphos, 12921 1998 WZ5, 15535 2000 AT177, 20738 1999 XG191, and 24390 2000 AD177 were included in the Makhoan family. Refined proper elements now place all of these bodies in the 1986 TS6 family.

In Fig. 8 we report the spectral slopes vs estimated diameters of the 6 observed members. The family shows different spectral slopes with the presence of both P-type (12921 and 13463) and

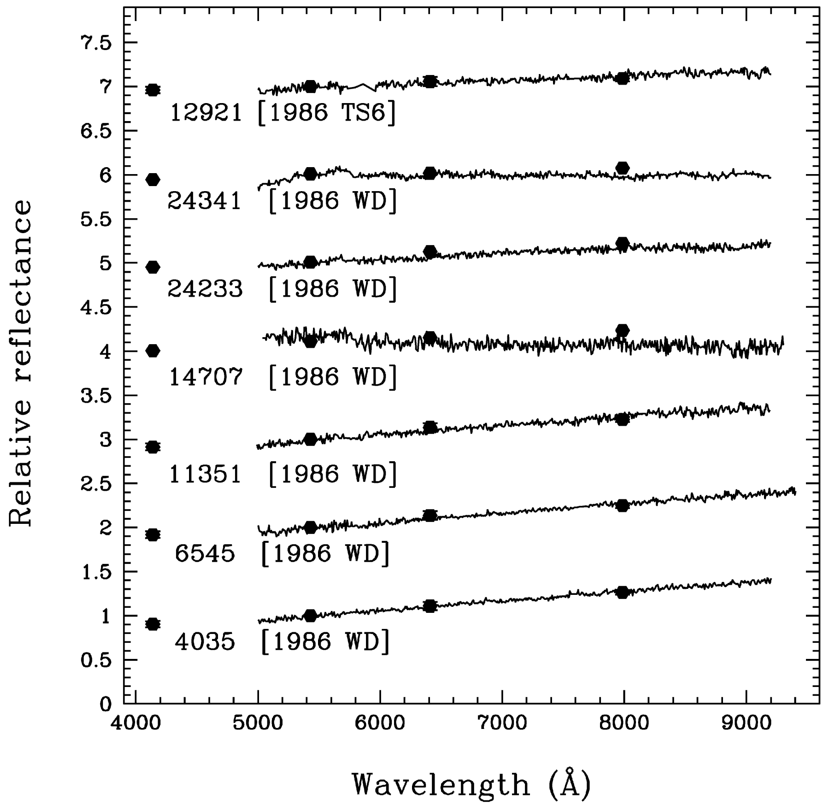

Fig. 6. Reflectance spectra of the 6 1986 WD family members and 12921, which is a member of the 1986 TS6 family (all belonging to the L4 swarm). Spectra are shifted by 1.0 in reflectance for clarity.

D-type asteroids (12917, 15535, 20738, and 24390). Due to the very similar diameters, a slope–size relationship is not found.

4. Discussion

The spectra of Jupiter Trojan members of dynamical families show a range of spectral variation from C- to D-type asteroids. With the exception of the L4 Eurybates family, all the observed objects have featureless spectra, and we cannot find any spectral bands which could help in the identification of minerals present on their surfaces. The lack of detection of any mineralogy diagnostic feature might indicate the formation of a thick mantle on the Trojan surfaces. Such a mantle could be formed by a phase of cometary activity and/or by space weathering processes as demonstrated by laboratory experiments on originally icy surfaces (Moore et al., 1983; Thompson et al., 1987; Strazzulla, 1998; Hudson and Moore, 1999).

A peculiar case is constituted by the Eurybates family, which shows a preponderance of C-type objects and a total absence of D-types. Moreover, this is the only family in which some members exhibit spectral features at wavelengths shorter than 5000–5200 Å, most likely due to the intervalence charge transitions in materials containing oxidized iron (Vilas, 1994).

4.1. Size vs spectral slope distribution: Individual families

The plots of spectral slopes vs diameters are shown in Figs. 7 and 8. A relationship between spectral slopes and diameters seems to exist for only three of the nine families we studied. In the Anchises and Panthoos families, smaller objects have redder spectra, while for the 1986 WD family larger objects have the redder spectra.

Moroz et al. (2004) have shown that ion irradiation on natural complex hydrocarbons gradually neutralizes the spectral slopes of these red organic solids. If the process studied by Moroz et al. (2004) occurred on the surface of Jupiter Trojans, the objects having redder spectra have to be younger than those characterized by bluish-neutral spectra. In this scenario the largest and spectrally reddest objects of the 1986 WD family could come from the interior of the parent body and expose fresh material. In the case of the Anchises and Panthoos families the spectrally reddest members, being the smallest, could come from the interior of the parent body, or alternatively could be produced by more recent secondary fragmentations. In particular, small family members may be more easily resurfaced, as significant collisions (an impactor having a size greater than a few percent of the target), as well as seismic shaking and recoating by fresh dust, may occur frequently at small sizes.

4.2. Size vs slope distribution: The Trojan population as a whole

As compared to the data available in literature, our sample strongly contributed to the analysis of fainter and smaller Trojans, with estimated diameters smaller than 50 km. Jewitt and Luu (1990), analyzing a sample of 32 Trojans, found that the

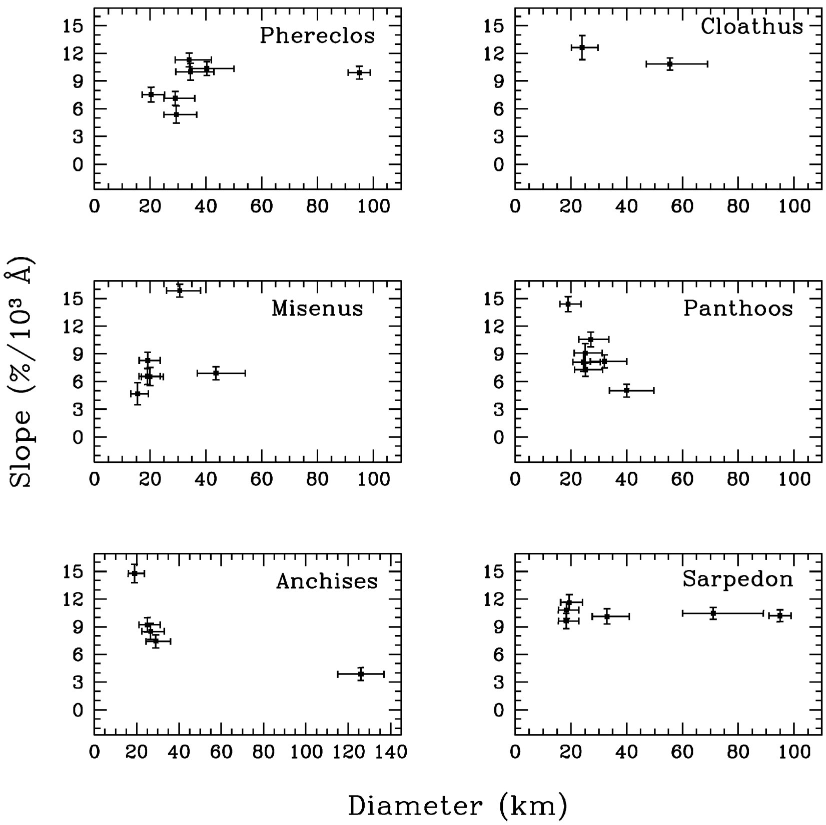

Fig. 7. Plot of the spectral slope versus the estimated diameter for the families observed in the L5 swarm.

smaller objects were redder than the bigger ones. However, our data play against the existence of a possible color-dimension trend. In fact, the spectral slope's range of the objects smaller than 50 km is similar to that of the larger Trojans, as shown in Fig. 9.

The Eurybates family strongly contributes to the population of small spectrally *neutral* objects, filling the region of bodies with mean diameter $D < 40$ km and with spectral slopes smaller than $3\%/10^3$ Å.

In order to carry out a complete analysis of the spectroscopic and photometric characteristics of the whole available data set on Jupiter Trojans, we considered all the visible spectra published in the literature: Jewitt and Luu (1990, 32 objects), Fitzimmons et al. (1994, 3 objects), Bendjoya et al. (2004, 34 objects), Fornasier et al. (2004a, 26 L5 objects), and Dotto et al. (2006, 24 L4 Trojans). We also add several Trojans spectra (11 L4 and 3 L5 Trojans) from the files available on line (Planetary Data System archive, pdssbn.astro.umd.edu, and http://www.daf.on.br/~lazzaro/S3OS2-Pub/s3os2.htm) from the SMASS I, SMASS II and S3OS2 surveys (Xu et al., 1995; Bus and Binzel, 2003; Lazzaro et al., 2004). Including all these data, we compile a sample of 142 different Trojans, 68 belonging to the L5 cloud and 74 belonging to the L4. We performed the taxonomic classification of this enlarged sample, on the basis of the Dahlgren and Lagerkvist (1995) scheme, by analyzing spectral slopes computed in the range 5500–8000 Å. Different authors, of course, considered different spectral ranges for their own slope gradient evaluations: Jewitt and Luu (1990) and Fitzimmons et al. (1994) use the 4000–7400 Å and Bendjoya et al. (2004, Table 2) used a slightly different ranges around 5200–7500 Å. Since all the cited papers show spectra with linear featureless trends, the different wavelength ranges used for the spectral gradient computation by Bendjoya et al. (2004) and Jewitt and Luu (1990) are not expected to influence the obtained slopes.

In order to search for a dependency of the spectral slope distribution with the size of the objects, all observations (from this paper as well as from the literature) were combined. The objects were isolated in 5 size bins (smaller than 25, 25–50, 50–75, 75–100 km and larger than 100 km). Each bin contains between 20 and 50 objects. These subsamples are large enough to be compared using classical statistical tests: the t-test, which estimates if the mean values are compatible, the f-test, which checks if the widths of the distributions are compatible (even if they have different means), and the KS-test, which compares directly the full distributions. A probability is computed for each test; a small probability indicates that the tested distributions are *not* compatible, i.e. the objects are not randomly extracted from the same population, while a large probability value has no meaning (i.e. it is not possible to assure that both samples come from the same population, we can just say in that case that they are not incompatible). In order to quantify the probability levels that we consider as significant, the same tests were run on randomized distributions (see Hainaut and Delsanti, 2002, for the method). Since probability lower than 0.04–0.05 does not ap-

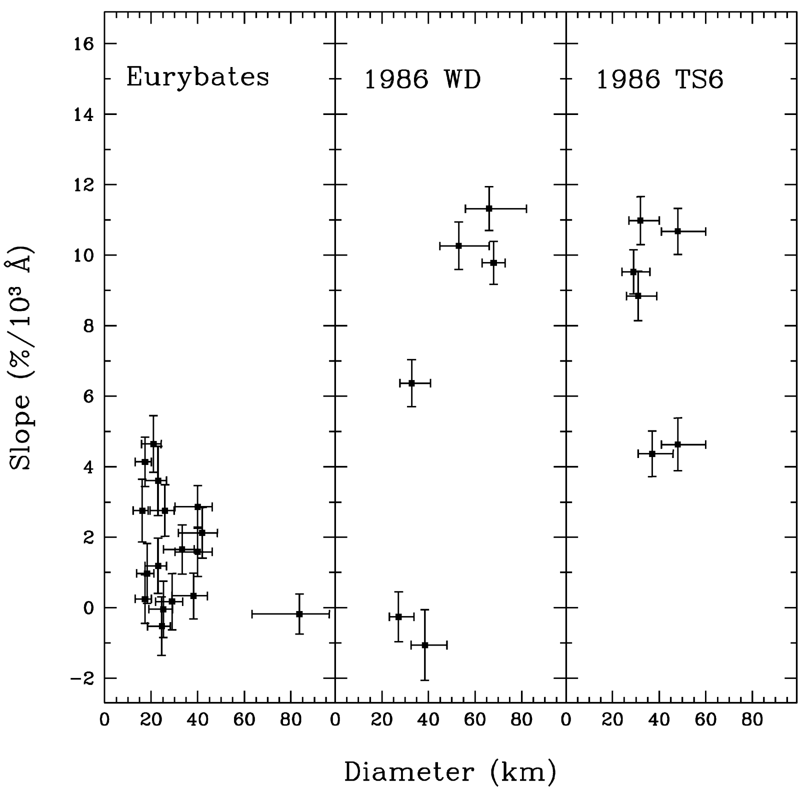

Fig. 8. Plot of the spectral slope versus the estimated diameter for the families observed in the L4 swarm.

pear in these randomized distributions, we consider that values smaller than 0.05 indicate a significant incompatibility.

Each sub-sample was compared with the four others—the results are summarized in Table 6. The average slope of the 5 bins are all compatible among each other. The only marginally significant result is that the width of the slope distribution among the larger objects (diam. > 100 km) is narrower than that of all the smaller objects.

This narrower color distribution could be due to the aging processes affecting the surface of bigger objects, which are supposed to be older. The wider color distribution of small members is possibly related to the different ages of their surfaces: some of them could be quite old, while some other could have been recently refreshed.

4.3. Spectral slopes and L4/L5 clouds

Considering only the Trojan observations reported in this paper, the average slope is $8.84 \pm 3.03\%/10^3$ Å for the L5 population, and $4.57 \pm 4.01\%/10^3$ Å for the L4.

Considering now all the spectra available in the literature, the 68 L5 Trojans have an average slope of $9.15 \pm 4.19\%/10^3$ Å, and the 78 L4 objects, $6.10 \pm 4.48\%/10^3$ Å. Performing the same statistical tests as above, it appears that these two populations are significantly different. In particular, the average slopes are incompatible at the 10^{-5} level.

Nevertheless, as described in Section 3.2.1, the Eurybates family members have quite different spectral characteristics than the other objects and constitute a large subset of the whole sample. Indeed, comparing their distribution with the whole populations, they are found significantly different at the 10^{-10} level. In other words, the Eurybates family members do not constitute a random subset of the other Trojans.

Once excluded the Eurybates family, the remaining 61 Trojans from the L4 swarm have an average slope of $7.33 \pm 4.24\%/10^3$ Å. The very slight difference of average slope between the L5 and remaining L4 objects is very marginally significant (probability of 1.6%), and the shape and width of the slope distributions are compatible with each other.

The taxonomic classification we have performed shows that the majority (73.5%) of the observed L5 Trojans (Fig. 10) are D-type (slope $> 7\%/10^3$ Å) with featureless reddish spectra, 11.8% are DP/PD-type (slope between 5 and $7\%/10^3$ Å), 10.3% are P-type, and only 3 objects are classified as C-type (4.4%).

In the L4 swarm (Fig. 11), even though the D-type still dominate the population (48.6%), the spectral types are more heterogeneous as compared to the L5 cloud, with a higher percentage of neutral-bluish objects: 20.3% are P-type, 8.1% are DP/PD-type, 12.2% are C-type, and 10.8% of the bodies have negative spectral slope. The higher percentage of C- and P-type as compared to the L5 swarm is strongly associated with the presence of the very peculiar Eurybates family. Among 17 observed members 10 are classified as C-types (among which 3 have negative spectral slopes) and 7 are P-types. Considering the 57 asteroids that compose the L4 cloud without the Eurybates family, we find percentages of P, and PD/DP-types very similar to those of the L5 cloud (14.0% and 10.5%, respectively), a smaller percentage of D-types (63.2%) and of the

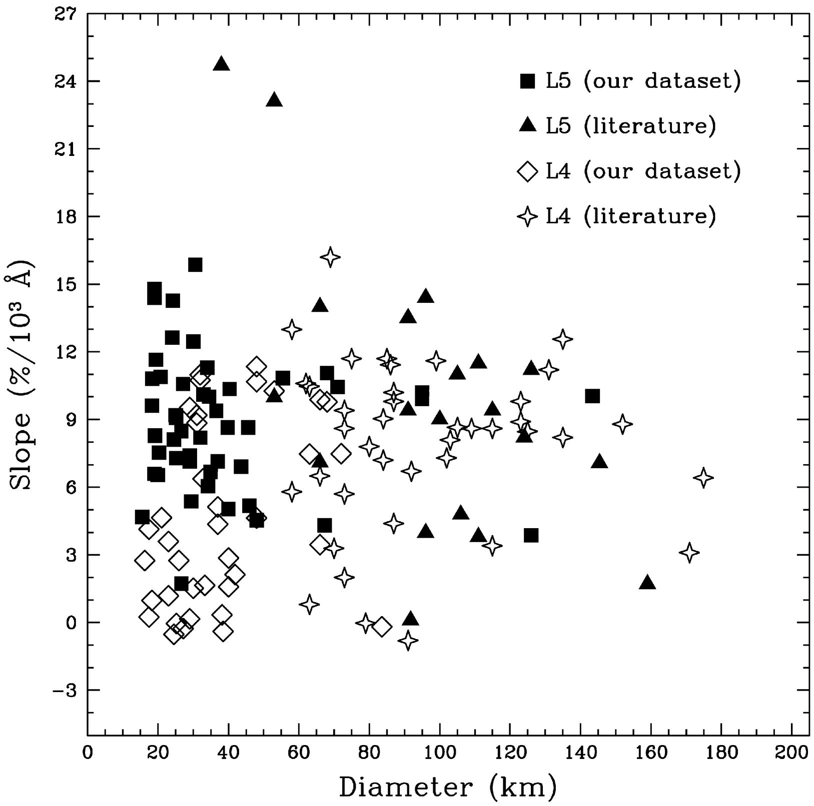

Fig. 9. Plot of the observed spectral slopes versus the estimated diameter for the whole population of Jupiter Trojans investigated by us and available from the literature. The errors on slopes and diameters are not plotted to avoid confusion.

Table 6
Results of the statistical analysis on the spectral slope distribution as a function of the diameters

Diameter range	0–25 km	25–50 km	50–75 km	75–100 km	>100 km
S average $\pm\,\sigma$ (%/10^3 Å)	7.17 ± 4.79 (22)	6.92 ± 4.69 (48)	8.91 ± 4.68 (26)	6.74 ± 5.85 (21)	7.87 ± 2.88 (21)
0–25		0.842, 0.876, 0.579	0.213, 0.903, 0.575	0.792, 0.370, 0.775	0.551, 0.017, 0.494
25–50			0.088, 0.985, 0.150	0.897, 0.216, 0.519	0.286, 0.011, 0.275
50–75				0.176, 0.289, 0.469	0.344, 0.019, 0.440
75–100					0.442, 0.001, 0.469

For each test bin, the average slope and the dispersion are listed; the size of the sample is reported in parenthesis. For each pair of subsamples, the probability that both are randomly extracted from the same global sample is listed, as estimated by the t-, f- and KS-test, respectively. Low probability indicates significant differences between the subsamples.

C-types (3.5%), and the presence of a 8.8% Trojans with negative spectral slopes.

The visible spectra of the Eurybates members are very similar to those of C-type main belt asteroids, Chiron-like Centaurs, and cometary nuclei. This similarity is compatible with three different scenarios: the family could have been produced by the fragmentation of a parent body very different from all the other Jupiter Trojans (in which case the origin of such a peculiar parent must still be assessed); this could be a very old family where space weathering processes have covered any differences in composition among the family members and flattened all the spectra; this could be a young family where space weathering processes occurred within time scales smaller than the age of the family. In the last two cases the Eurybates family would give the first observational evidence of spectra flattened owing to space weathering processes. This would then imply, according to the results of Moroz et al. (2004), that its primordial composition was rich in complex hydrocarbons.

The knowledge of the age of the Eurybates family is therefore a fundamental step to investigate the nature and the origin of the parent body, and to assess the effect of space weathering processes on the surfaces of its members.

The present sample of Jupiter Trojans suggests a more heterogeneous composition of the L4 swarm as compared to the L5 one. As previously noted by Bendjoya et al. (2004), the L4 swarm contains a higher percentage of C- and P-type objects. This result is enhanced by members of the Eurybates family, but remains even when these family members are excluded. Moreover, the dynamical families belonging to the L4 cloud are more robust than those of the L5 one, surviving with densely

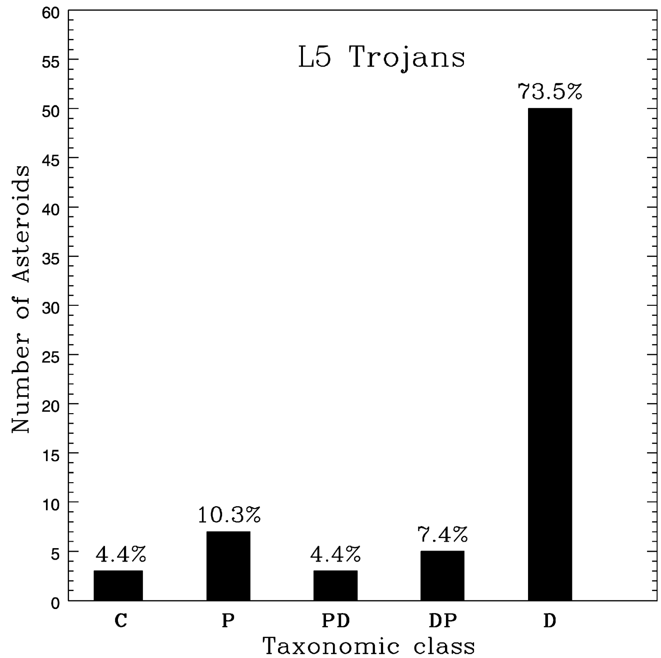

Fig. 10. Histogram of L5 Trojans taxonomic classes.

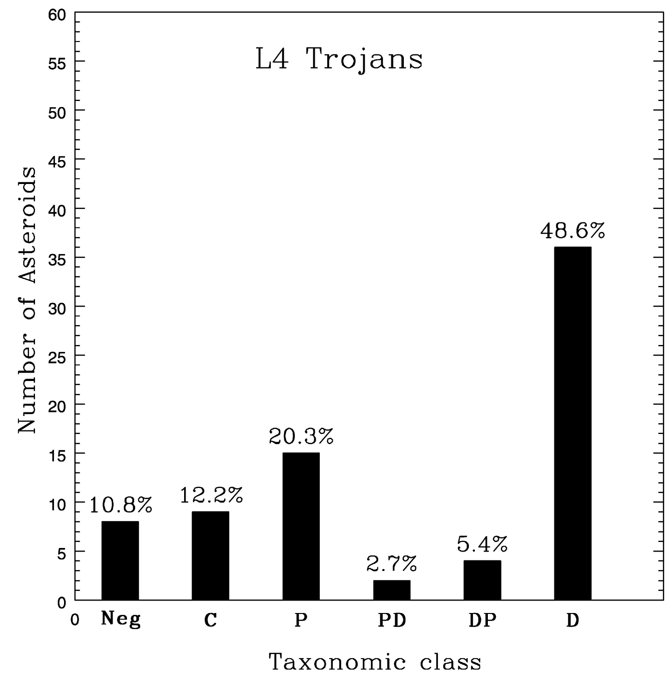

Fig. 11. Histogram of L4 Trojans taxonomic classes (*Neg* indicates objects with negative spectral slope).

populated clustering even at low relative velocity cut-off. We therefore could argue that the L4 cloud is more collisionally active than the L5 swarm. Nevertheless, we still cannot intepret this in terms of the composition of the two populations, since we cannot exclude that as yet unobserved C- and P-type families are present in the L5 cloud.

4.4. Orbital elements

We analyzed the spectral slope as a function of the Trojans' orbital elements. As an illustration, Fig. 12 shows the $B-R$ color distribution as a function of the orbital elements. In order to investigate variations with orbital parameters, the Trojan population is divided in 2 subsamples: those with the considered orbital element lower than the median value, and those with the orbital element higher than the median (by construction, the two subsamples have the same size). Taking a as an example, half the Trojans have $a < 5.21$ AU, and half have a larger than this value.

The mean color, the color dispersion, and the color distribution of the 2 subsamples are compared using the three statistical tests mentioned in Section 4.2. The method is discussed in details in Hainaut and Delsanti (2002). The tests are repeated for all color and spectral slope distributions. The results are the following.

- q, perihelion distance: the color distribution of the Trojans with small q is marginally broader than that of Trojans with larger q. This result is not very strong (5%), and is dominated by the red-end of the visible wavelength. Removing the Eurybates from the sample maintains the result, at the same weak level.
- e, eccentricity: the distribution shows a similar result, also at the weak 5% significance. The objects with larger e have broader color distribution than those with lower e. This result is entirely dominated by the Eurybates' contribution.
- i, inclination: objects with smaller inclination are significantly bluer than those with larger i. This result is observed at all wavelengths. It is worth noting that this is contrary to what is usually observed on other Minor Bodies in the Outer Solar System survey (MBOSSes), where objects with high i, or more generally, high excitation $E = \sqrt{e^2 + \sin^2 i}$, are bluer (Hainaut and Delsanti, 2002; Doressoundiram et al., 2005). This can also be visually appreciated in Fig. 12. This result is also completely dominated by the Eurybates' contribution. The non-Eurybates Trojans do not display this trend.
- $E = \sqrt{e^2 + \sin^2 i}$, orbital excitation: the objects with small E are also significantly bluer than those with high E. This result is also completely dominated by the Eurybates' contribution. The non-Eurybates Trojans do not display this trend.

In summary this analysis shows that the Eurybates subsample of the Trojans is well separated in orbital elements and in colors.

For the other Minor Bodies in the outer Solar System, the relation between color and inclination–orbital excitation (objects with a higher orbital excitation tend to be bluer) is interpreted as a relation between excitation and surface aging/rejuvenating processes (Doressoudiram et al., 2005). The Eurybates family has low excitation and neutral-blue colors, suggesting that the aging/rejuvenating processes affecting them are different from the other objects. This could be due to different surface compositions, different irradiation processes, or different collisional properties—which would be natural for a collisional family.

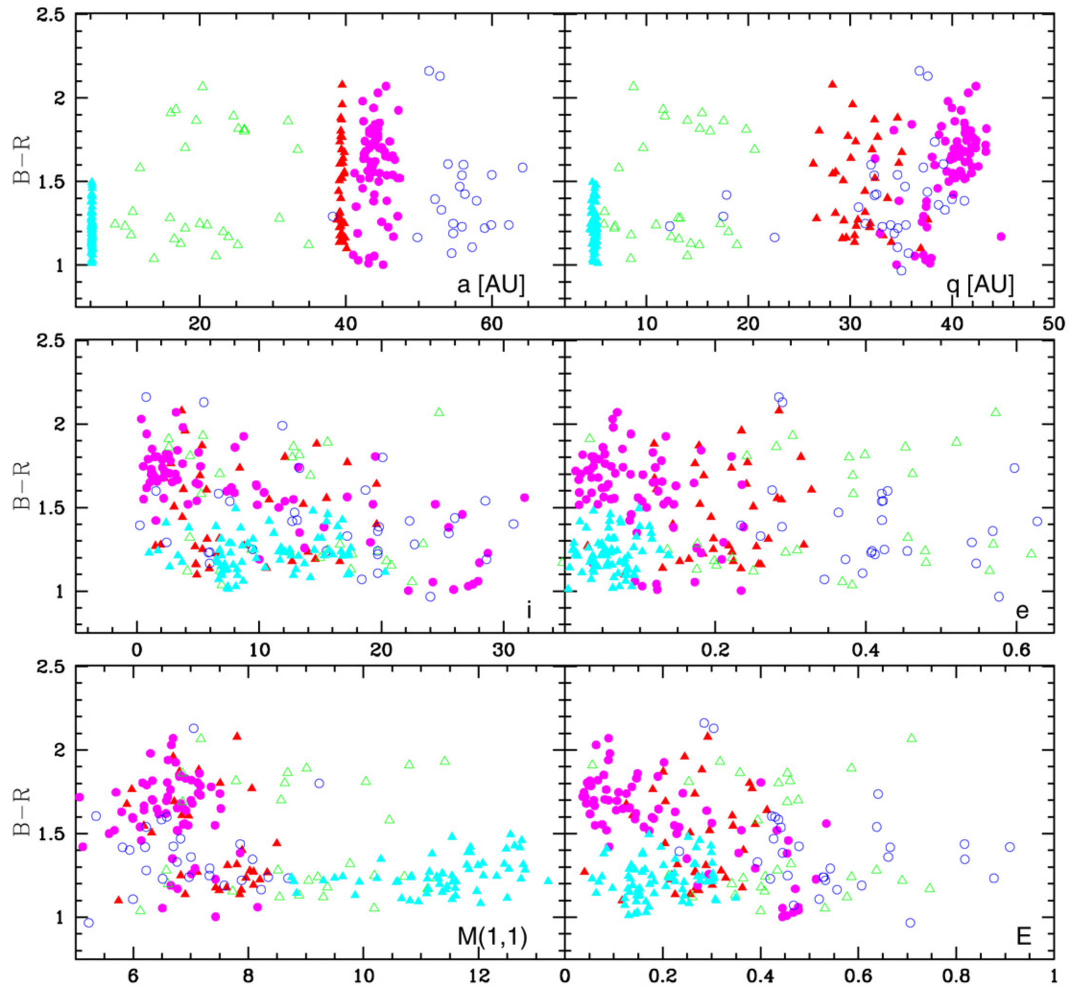

Fig. 12. Color distributions as functions of the absolute magnitude $M(1, 1)$, the inclination i [degrees], the orbital semi-major axis a [AU], the perihelion distance q [AU], the eccentricity e, and the orbital energy E (see text for definition). We include all the available colors for distant minor bodies (TNOs, Centaurs, and cometary nuclei, see Hainaut and Delsanti, 2002). The Plutinos (resonant TNOs) are red filled triangles, Cubiwanos (classical TNOs) are pink filled circles, Centaurs are green open triangles, scattered TNOs are blue open circles, and Trojans are cyan filled triangles.

5. Comparison with other outer Solar System minor bodied

5.1. Introduction and methods

The statistical tests set described in Section 4.2 has also been applied to compare the colors and the spectral slopes distribution of the Trojans with those of the other minor bodies in the outer Solar System taken from the updated, on-line version of the Hainaut and Delsanti (2002) database. Fig. 13, as an example, displays the (R–I) vs (V–R) diagrams, while Fig. 14 shows the (B–V) and (V–R) color distributions, as well as the spectral slope distribution of the different classes of objects. The tests were performed on all the color indices derived from filters in the visible (UBVRI) and near infrared range (JHK) but in Tables 7 and 8 we summarize the most significant results.

In order to "calibrate" the significant probabilities, additional artificial classes are also compared: first, the objects which have an even internal number in the database with the odd ones. As this internal number is purely arbitrary, both classes are statistically indistinguishable. The other tested pair is the objects with a "1999" designation versus the others. Again, this selection criterion is arbitrary, so the pseudo-classes it generates are subsample of the total population, and should be indistinguishable. However, as many more objects have been discovered in all the other years than during that specific year, the size of these subsamples are very different. This permits us to estimate the sensitivity of the tests on sample of very different sizes. Some of the tests found the arbitrary populations incompatible at the 5% level, so we use 0.5% as a conservative threshold for statistical significance of the distribution incompatibility

5.2. Results

Table 7 and Fig. 14 clearly show that the Trojans' colors distribution is different as compare to that of Centaurs, TNOs and comets. Trojans are at the same time bluer, and their distribution is narrower than all the other populations. Using the statistical tests (see Table 8), we can confirm the significance of these results.

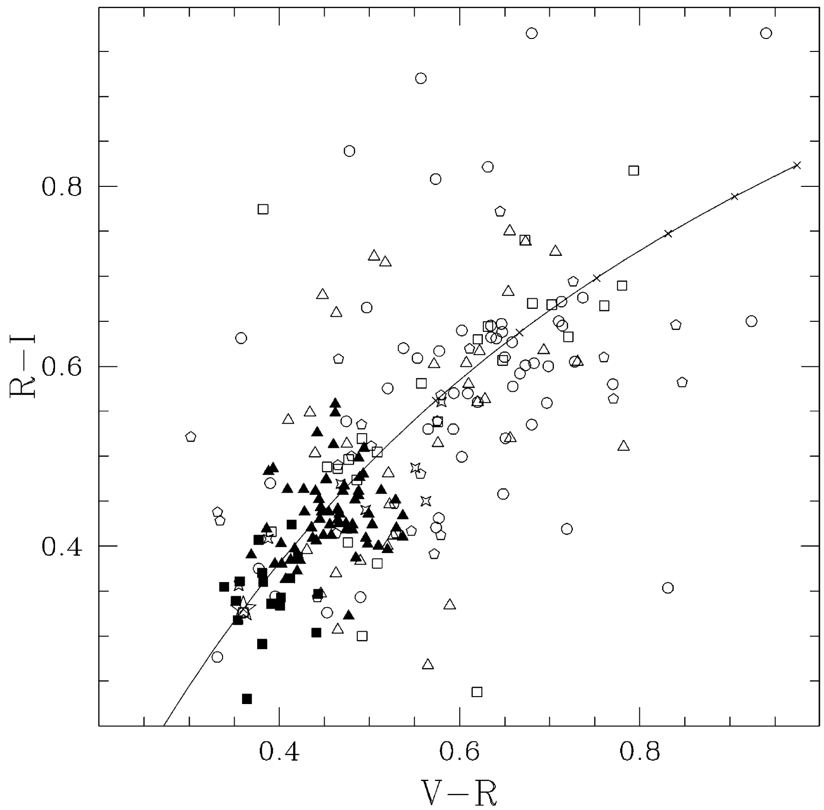

Fig. 13. V–R versus R–I color–color diagram for the observed Trojans and all distant minor bodies available in the updated Hainaut and Delsanti (2002) database. The solid symbols are for the Trojans (square for Eurbybates, triangles for others). The open symbols are used as following: triangles for Plutinos, circles for Cubiwanos, squares for Centaurs, pentagons for scattered, and starry square for Comets. The continuous line represents the "reddening line," that is the locus of objects with a linear reflectivity spectrum. The star symbol represents the Sun.

Table 7
Mean color indices and spectral slope of different classes of minor bodies of the outer Solar System

Color	Plutinos	Cubewanos	Centaurs	Scattered	Comets	Trojans
B–V	36	87	29	33	2	74
	0.895 ± 0.190	0.973 ± 0.174	0.886 ± 0.213	0.875 ± 0.159	0.795 ± 0.035	0.777 ± 0.091
V–R	38	96	30	34	19	80
	0.568 ± 0.106	0.622 ± 0.126	0.573 ± 0.127	0.553 ± 0.132	0.441 ± 0.122	0.445 ± 0.048
V–I	34	64	25	25	7	80
	1.095 ± 0.201	1.181 ± 0.237	1.104 ± 0.245	1.070 ± 0.220	0.935 ± 0.141	0.861 ± 0.090
V–J	10	14	11	8	1	12
	2.151 ± 0.302	1.750 ± 0.456	1.904 ± 0.480	2.041 ± 0.391	1.630 ± 0.000	1.551 ± 0.120
V–H	3	7	11	4	1	12
	2.698 ± 0.083	2.173 ± 0.796	2.388 ± 0.439	2.605 ± 0.335	1.990 ± 0.000	1.986 ± 0.177
V–K	2	5	9	2	1	12
	2.763 ± 0.000	2.204 ± 1.020	2.412 ± 0.396	2.730 ± 0.099	2.130 ± 0.000	2.125 ± 0.206
R–I	34	64	25	26	8	80
	0.536 ± 0.135	0.586 ± 0.148	0.548 ± 0.150	0.517 ± 0.102	0.451 ± 0.059	0.416 ± 0.057
J–H	11	17	21	11	1	12
	0.403 ± 0.292	0.370 ± 0.297	0.396 ± 0.112	0.348 ± 0.127	0.360 ± 0.000	0.434 ± 0.064
H–K	10	16	20	10	1	12
	-0.034 ± 0.171	0.084 ± 0.231	0.090 ± 0.142	0.091 ± 0.136	0.140 ± 0.000	0.139 ± 0.041
Slope	38	91	30	34	8	80
($\%/10^3$ Å)	19.852 ± 10.944	25.603 ± 13.234	20.601 ± 13.323	18.365 ± 12.141	10.722 ± 6.634	7.241 ± 3.909

For each class the number of objects considered is also listed.

- The average colors of the Trojans are significantly different from those of all the other classes of objects (t-test), with the notable exception of the short period comet nuclei. Refining the test to the Eurybates/non-Eurybates, it appears

Table 8
Statistical tests performed to compare the color and slope distributions of different classes of minor bodies (Plt = Plutinos, resonant TNOs; QB1 = Cubiwanos, classical TNOs; Cent = Centaurs; Scat = scattered TNOs; Com = short period comet nuclei) with those of Trojans

Color	All Trojans					Only Eurybates					Only non-Eurybates				
	Plt	QB1	Cent	Scat	Com	Plt	QB1	Cent	Scat	Com	Plt	QB1	Cent	Scat	Com
f-test															
B–V	36.74	83.74	29.74	33.74	2.74	36.14	83.14	29.14	33.14	2.14	36.60	83.60	29.60	33.60	2.60
	0.000	**0.000**	**0.000**	**0.000**	0.600	**0.001**	**0.001**	**0.000**	**0.005**	0.722	**0.000**	**0.000**	**0.000**	**0.000**	0.598
V–R	38.80	92.80	30.80	34.80	19.80	38.17	92.17	30.17	34.17	19.17	38.63	92.63	30.63	34.63	19.63
	0.000	**0.000**	**0.000**	**0.000**	**0.000**	**0.000**	**0.000**	**0.000**	**0.000**	**0.000**	**0.000**	**0.000**	**0.000**	**0.000**	**0.000**
R–I	34.80	62.80	25.80	26.80	8.80	34.17	62.17	25.17	26.17	8.17	34.63	62.63	25.63	26.63	8.63
	0.000	**0.000**	**0.000**	**0.000**	**0.773**	**0.000**	**0.000**	**0.000**	**0.001**	**0.335**	**0.000**	**0.000**	**0.000**	**0.000**	**0.185**
Slope	38.80	87.80	30.80	34.80	8.80	38.17	87.17	30.17	34.17	8.17	38.63	87.63	30.63	34.63	8.63
	0.000	**0.000**	**0.000**	**0.000**	**0.020**	**0.000**	**0.000**	**0.000**	**0.000**	**0.000**	**0.000**	**0.000**	**0.000**	**0.000**	**0.000**
t-test															
B–V	36.74	83.74	29.74	33.74	2.74	36.14	83.14	29.14	33.14	2.14	36.60	83.60	29.60	33.60	2.60
	0.001	**0.000**	**0.012**	**0.002**	0.608	**0.000**	**0.000**	**0.001**	**0.000**	0.139	**0.003**	**0.000**	**0.025**	**0.006**	0.858
V–R	38.80	92.80	30.80	34.80	19.80	38.17	92.17	30.17	34.17	19.17	38.63	92.63	30.63	34.63	19.63
	0.000	**0.000**	**0.000**	**0.000**	**0.916**	**0.000**	**0.000**	**0.000**	**0.000**	**0.083**	**0.000**	**0.000**	**0.000**	**0.000**	**0.532**
R–I	34.80	62.80	25.80	26.80	8.80	34.17	62.17	25.17	26.17	8.17	34.63	62.63	25.63	26.63	8.63
	0.000	**0.000**	**0.000**	**0.000**	**0.154**	**0.000**	**0.000**	**0.000**	**0.000**	**0.001**	**0.000**	**0.000**	**0.001**	**0.000**	**0.502**
Slope	38.80	87.80	30.80	34.80	8.80	38.17	87.17	30.17	34.17	8.17	38.63	87.63	30.63	34.63	8.63
	0.000	**0.000**	**0.000**	**0.000**	**0.185**	**0.000**	**0.000**	**0.000**	**0.000**	**0.008**	**0.000**	**0.000**	**0.000**	**0.000**	**0.404**
KS-test															
B–V	36.74	83.74	29.74	33.74	2.74	36.14	83.14	29.14	33.14	2.14	36.60	83.60	29.60	33.60	2.60
	0.001	**0.000**	**0.001**	**0.004**	0.330	**0.002**	**0.000**	**0.035**	**0.000**	0.065	**0.003**	**0.000**	**0.002**	**0.047**	0.468
V–R	38.80	92.80	30.80	34.80	19.80	38.17	92.17	30.17	34.17	19.17	38.63	92.63	30.63	34.63	19.63
	0.000	**0.000**	**0.000**	**0.000**	**0.040**	**0.000**	**0.000**	**0.000**	**0.000**	**0.008**	**0.000**	**0.000**	**0.000**	**0.000**	**0.056**
R–I	34.80	62.80	25.80	26.80	8.80	34.17	62.17	25.17	26.17	8.17	34.63	62.63	25.63	26.63	8.63
	0.000	**0.000**	**0.000**	**0.000**	**0.201**	**0.000**	**0.000**	**0.000**	**0.000**	**0.000**	**0.000**	**0.000**	**0.000**	**0.000**	**0.587**
Slope	38.80	87.80	30.80	34.80	8.80	38.17	87.17	30.17	34.17	8.17	38.63	87.63	30.63	34.63	8.63
	0.000	**0.000**	**0.000**	**0.000**	**0.088**	**0.000**	**0.000**	**0.000**	**0.000**	**0.002**	**0.000**	**0.000**	**0.000**	**0.000**	**0.211**

The first five columns consider all the Trojans, the second five only the Eurybates family, the third five only the non-Eurybates family Trojans. For each color, the first line shows the number of objects used for the comparison (2nd is the number of Trojans), and the second line reports the probability resulting from the test. A very low value indicates that the two compared distributions are *not* statistically compatible. Probabilities are in boldface when the size of the samples is large enough for the value to be meaningful.

that the Eurybates have marginally different mean colors, while the non-Eurybates average colors are indistinguishable from those of the comets.

- Considering the full shape of the distribution (KS-test), we obtain the same results: the Trojans colors distributions are significantly different from those of all the other classes, with the exception of the SP comets, which are compatible. Again, this result becomes stronger separating the Eurybates: their distributions are different from those of the comets, while the non-Eurybates ones are indistinguishable.
- The results when considering the widths of the color distributions (f-test) are slightly different. Classes of objects with different mean colors could still have the same distribution width. This could suggest that a similar process (causing the width of the distribution) is in action, but reached a different equilibrium point (resulting in different mean values). This time, all classes are incompatible with the Trojans, including the comets, with strong statistical significance.

In order to further explore possible similarities between Trojans and other classes, the comparisons were also performed with the neutral Centaurs. These were selected with $S < 20\%/10^3$ Å; this cut-off line falls in the gap between the "neutral" and "red" Centaurs (Peixinho et al., 2003; Fornasier et al., 2004b).

The t-test (mean color) only reveals a very moderate incompatibility between the Trojans and neutral Centaurs, at the 5% level, i.e. only marginally significant. On the other hand, the f-test gives some strong incompatibilities in various colors (moderate in B–V and H–K, very strong in R–I), but the two populations are compatible for most of the other colors. Similarly, only the R–I KS-test reveals a strong incompatibility. It should also be noted that only 18 neutral Centaurs are known in the database. In summary, while the Trojans and neutral Centaurs have fairly similar mean colors, their color distributions are also different.

6. Conclusions

From 2002, we carried out a spectroscopic and photometric survey of Jupiter Trojans, with the aim of investigating the members of dynamical families. In this paper we present new data on 47 objects belonging to several dynamical families: Anchises (5 members), Cloanthus (2 members), Misenus

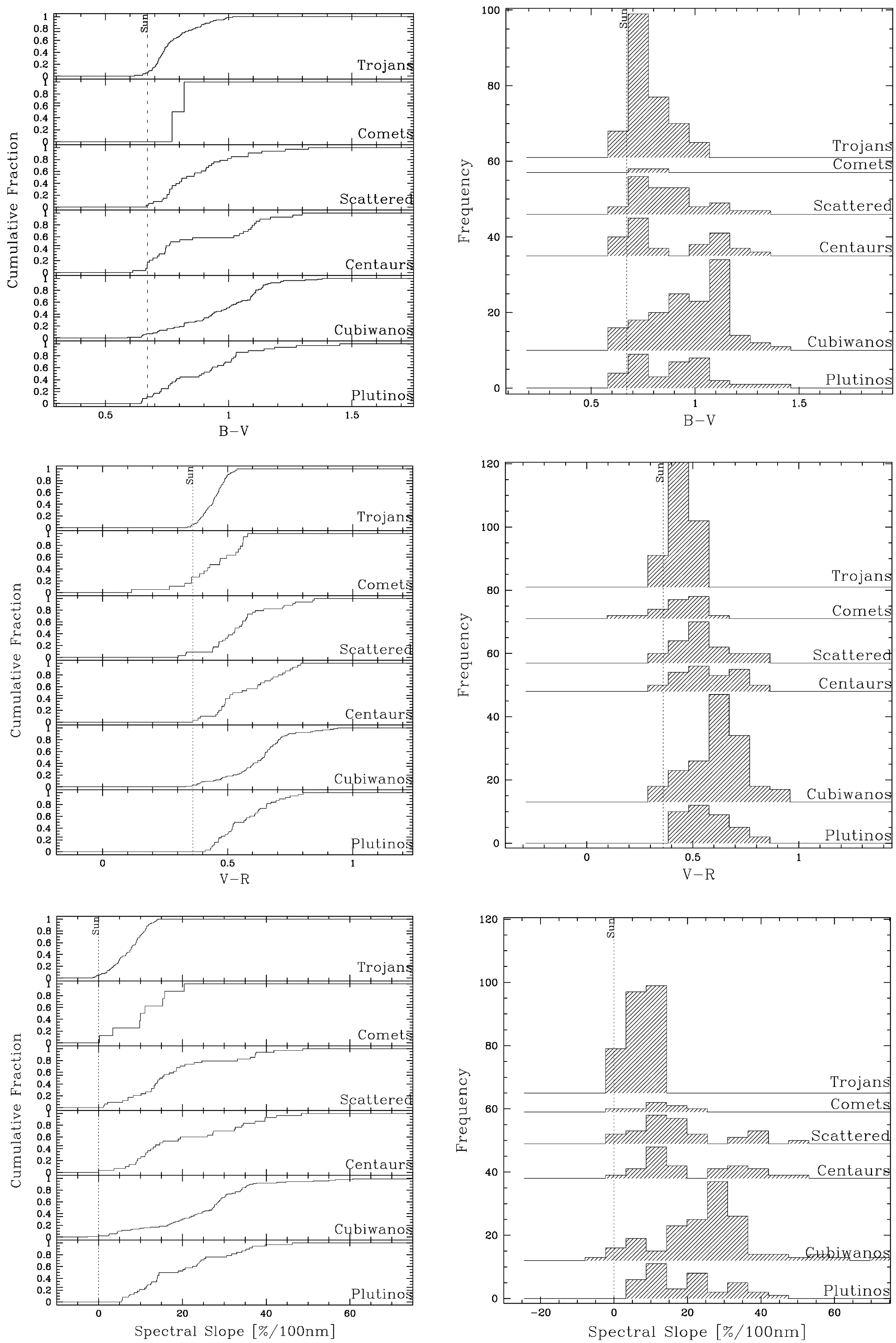

Fig. 14. Cumulative function and histograms of the B−V and V−R color distributions and of the spectral slope for all the considered classes of objects. The dotted line marks the solar colors.

(6 members), Phereclos (3 members), Sarpedon (2 members) and Panthoos (5 members) from the L5 swarm; Eurybates (17 members), 1986 WD (6 members), and Menelaus (1 member) for the L4 swarm. Together with the data already published by Fornasier et al. (2004a) and Dotto et al. (2006), taken within the same observing program, we have a total sample of 80 Trojans, the largest homogeneous data set available to date on these primitive asteroids. The main results coming from the observations presented here, and from the analysis including previously published visible spectra of Trojans, are the following:

- Trojans' visible spectra are mostly featureless. However, some members of the Eurybates family show a UV drop-off in reflectivity for wavelength shorter than 5000–5200 Å that is possibly due to intervalence charge transfer transitions (IVCT) in oxidized iron.
- The L4 Eurybates family strongly differs from all the other families in that it is dominated by C- and P-type asteroids. Also its spectral slope distribution is significantly different when compared to that of the other Trojans (at the 10^{-10} level).
  This family is very peculiar and is dynamically very strong, as it survives also at a very stringent cutoff (40 m/s). Further observations in the near-infrared region are strongly encouraged to look for possible absorption features due to water ice or to material that experienced aqueous alteration.
- The average spectral slope for the L5 Trojans is $9.15 \pm 4.19\%/10^3$ Å, and $6.10 \pm 4.48\%/10^3$ Å for the L4 objects. Excluding the Eurybates, the L4 average slope values becomes $7.33 \pm 4.24\%/10^3$ Å. The slope distributions of the L5 and of the non-Eurybates L4 are indistinguishable.
- Both L4 and L5 clouds are dominated by D-type asteroids, but the L4 swarm has an higher presence of C- and P-type asteroids, even when the Eurybates family is excluded, and appears more heterogeneous in composition as compared to the L5 one.
- We do not find any size versus spectral slope relationship inside the whole Trojans population.
- The Trojans with higher orbital inclination are significantly redder than those with lower i. While this trend is the opposite of that observed for other distant minor bodies, this effect is entirely dominated by the Eurybates family.
- Comparing the Trojans colors with those of other distant minor bodies, they are the bluest of all classes, and their colors distribution is the narrowest. This difference is mostly due to the Eurybates family. In fact, if we consider only the Trojan population without the Eurybates members, their average colors and overall distributions are not distinguishable from that of the short period comets. However, the widths of their color distributions are not compatible. The similarity in the overall color distributions might be caused by the small size of the short period comet sample rather than by a physical analogy. The Trojans average colors are also fairly similar to those of the neutral Centaurs, but the overall distributions are not compatible.

After this study, we have to conclude that Trojans have peculiar characteristics very different from those of all the other populations of the outer Solar System.

Unfortunately, we still cannot assess if this is due to differences in the physical nature, or in the aging/rejuvenating processes which modified the surface materials in different way at different solar distances. Further observations, mainly in V + NIR spectroscopy and polarimetry, are absolutely needed to better investigate the nature of Jupiter Trojans and to definitively assess if a genetical link might exist with Trans-Neptunian Objects, Centaurs and short period comets.

Acknowledgments

We thank Beaugé and Roig for kindly providing us with updated Trojan family list, and R.P. Binzel and J.P. Emery for their useful comments in the reviewing process.

References

Barucci, M.A., Lazzarin, M., Owen, T., Barbieri, C., Fulchignoni, M., 1994. Near-infrared spectroscopy of dark asteroids. Icarus 110, 287–291.

Beaugé, C., Roig, F., 2001. A semi-analytical model for the motion of the Trojan asteroids: Proper elements and families. Icarus 53, 391–415.

Bendjoya, P., Cellino, A., Di Martino, M., Saba, L., 2004. Spectroscopic observations of Jupiter Trojans. Icarus 168, 374–384.

Binzel, R.P., Sauter, L.M., 1992. Trojan, Hilda, and Cybele asteroids—New lightcurve observations and analysis. Icarus 95, 222–238.

Bowell, E., Hapke, B., Domingue, D., Lumme, K., Peltoniemi, J., Harris, A.W., 1989. Application of photometric models to asteroids. In: Binzel, R.P., Gehrels, T., Matthews, M.S. (Eds.), Asteroids II. Univ. of Arizona Press, Tucson, pp. 524–556.

Bus, S.J., Binzel, R.P., 2003. Phase II of the small Main-Belt Asteroid Spectroscopic Survey: The observations. Icarus 158, 106–145.

Dahlgren, M., Lagerkvist, C.I., 1995. A study of Hilda asteroids. I. CCD spectroscopy of Hilda asteroids. Astron. Astrophys. 302, 907–914.

Dell'Oro, A., Marzari, P., Paolicchi, F., Dotto, E., Vanzani, V., 1998. Trojan collision probability: A statistical approach. Astron. Astrophys. 339, 272–277.

Doressoundiram, A., Peixinho, N., Doucet, C., Mousis, O., Barucci, M.A., Petit, J.M., Veillet, C., 2005. The Meudon Multicolor Survey (2MS) of Centaurs and trans-neptunian objects: Extended dataset and status on the correlations reported. Icarus 174, 90–104.

Dotto, E., Fornasier, S., Barucci, M.A., Licandro, J., Boehnhardt, H., Hainaut, O., Marzari, F., de Bergh, C., De Luise, F., 2006. The surface composition of Jupiter Trojans: Visible and Near-Infrared Survey of dynamical families. Icarus 183, 420–434.

Dumas, C., Owen, T., Barucci, M.A., 1998. Near-infrared spectroscopy of low-albedo surfaces of the Solar System: Search for the spectral signature of dark material. Icarus 133, 221–232.

Emery, J.P., Brown, R.H., 2003. Constraints on the surface composition of Trojan asteroids from near-infrared (0.8–4.0 μm) spectroscopy. Icarus 164, 104–121.

Emery, J.P., Brown, R.H., 2004. The surface composition of Trojan asteroids: Constraints set by scattering theory. Icarus 170, 131–152.

Emery, J.P., Cruikshank, D.P., Van Cleve, J., 2006. Thermal emission spectroscopy (5.2–38 μm of three Trojan asteroids with the Spitzer Space Telescope: Detection of fine-grained silicates. Icarus 182, 496–512.

Fernandez, Y.R., Sheppard, S.S., Jewitt, D.C., 2003. The albedo distribution of jovian Trojan asteroids. Astron. J. 126, 1563–1574.

Fitzsimmons, A., Dahlgren, M., Lagerkvist, C.I., Magnusson, P., Williams, I.P., 1994. A spectroscopic survey of D-type asteroids. Astron. Astrophys. 282, 634–642.

Fornasier, S., Lazzarin, M., Barbieri, C., Barucci, M.A., 1999. Spectroscopic comparison of aqueous altered asteroids with CM2 carbonaceous chondrite meteorites. Astron. Astrophys. 135, 65–73.

Fornasier, S., Dotto, E., Marzari, F., Barucci, M.A., Boehnhardt, H., Hainaut, O., de Bergh, C., 2004a. Visible Spectroscopic and Photometric Survey of L5 Trojans: Investigation of dynamical families. Icarus 172, 221–232.

Fornasier, S., Doressoundiram, A., Tozzi, G.P., Barucci, M.A., Boehnhardt, H., de Bergh, C., Delsanti, A., Davies, J., Dotto, E., 2004b. ESO large program on physical studies of trans-neptunian objects and Centaurs: Final results of the visible spectroscopic observations. Astron. Astrophys. 421, 353–363.

Hainaut, O.R., Delsanti, A.C., 2002. Colors of minor bodies in the outer Solar System: A statistical analysis. Astron. Astrophys. 389, 641–664.

Hudson, R.L., Moore, M.H., 1999. Laboratory studies of the formation of methanol and other organic molecules by water + carbon monoxide radiolysis: Relevance to comets, icy satellites, and interstellar ices. Icarus 140, 451–461.

Jewitt, D.C., Luu, J.X., 1990. CCD spectra of asteroids. II. The Trojans as spectral analogs of cometary nuclei. Astron. J. 100, 933–944.

Jewitt, D.C., Trujillo, C.A., Luu, J.X., 2000. Population and size distribution of small jovian Trojan asteroids. Astron. J. 120, 1140–1147.

Landolt, A.U., 1992. UBVRI photometric standard stars in the magnitude range 11.5–16.0 around the celestial equator. Astron. J. 104, 340–371, 436–491.

Lazzaro, D., Angeli, C.A., Carvano, J.M., Mothé-Diniz, T., Duffard, R., Florczak, M., 2004. S^3OS^2: The Visible Spectroscopic Survey of 820 asteroids. Icarus 172, 179–220.

Levison, H., Shoemaker, E.M., Shoemaker, C.S., 1997. The dispersal of the Trojan asteroid swarm. Nature 385, 42–44.

Marzari, F., Farinella, P., Davis, D.R., Scholl, H., Campo Bagatin, A., 1997. Collisional evolution of Trojan asteroids. Icarus 125, 39–49.

Marzari, F., Scholl, H., 1998a. Capture of Trojans by a growing proto-Jupiter. Icarus 131, 41–51.

Marzari, F., Scholl, H., 1998b. The growth of Jupiter and Saturn and the capture of Trojans. Astron. Astrophys. 339, 278–285.

Marzari, F., Scholl, H., Murray, C., Lagerkvist, C., 2002. Origin and evolution of Trojan asteroids. In: Bottke Jr., W.F., Cellino, A., Paolicchi, P., Binzel, R.P. (Eds.), Asteroids III. Univ. of Arizona Press, Tucson, pp. 725–738.

Marzari, F., Tricarico, P., Scholl, H., 2003. Stability of Jupiter Trojans investigated using frequency map analysis: The MATROS project. Mon. Not. R. Astron. Soc. 345, 1091–1100.

Milani, A., 1993. The Trojan asteroid belt: Proper elements, stability, chaos and families. Celest. Mech. Dynam. Astron. 57, 59–94.

Morbidelli, A., Levison, H.F., Tsiganis, K., Gomes, R., 2005. Chaotic capture of Jupiter's Trojan asteroids in the early Solar System. Nature 435, 462–465.

Moore, M.H., Donn, B., Khanna, R., A'Hearn, M.F., 1983. Studies of proton-irradiated cometary-type ice mixtures. Icarus 54, 388–405.

Moroz, L., Baratta, G., Strazzulla, G., Starukhina, L., Dotto, E., Barucci, M.A., Arnold, G., Distefano, E., 2004. Optical alteration of complex organics induced by ion irradiation. 1. Laboratory experiments suggest unusual space weathering trend. Icarus 170, 214–228.

Peixinho, N., Doressoundiram, A., Delsanti, A., Boehnhardt, H., Barucci, M.A., Belskaya, I., 2003. Reopening the TNOs color controversy: Centaurs bimodality and TNOs unimodality. Astron. Astrophys. 410, 29–32.

Shoemaker, E.M., Shoemaker, C.S., Wolfe, R.F., 1989. Trojan asteroids: Populations, dynamical structure and origin of the L4 and L5 swarms. In: Binzel, R.P., Gehrels, T., Matthews, M.S. (Eds.), Asteroids II. Univ. of Arizona Press, Tucson, pp. 487–523.

Strazzulla, G., 1998. Chemistry of ice induced by bombardment with energetic charged particles. In: Schmitt, B., de Bergh, C., Festou, M. (Eds.), Solar System Ices. In: Astrophys. Space Sci. Lib., vol. 281. Kluwer Academic, Dordrecht.

Thompson, W.R., Murray, B.G.J.P.T., Khare, B.N., Sagan, C., 1987. Coloration and darkening of methane clathrate and other ices by charged particle irradiation—Applications to the outer Solar System. J. Geophys. Res. 92, 14933–14947.

Xu, S., Binzel, R.P., Burbine, T.H., Bus, S.J., 1995. Small Main-Belt Asteroid Spectroscopic Survey: Initial results. Icarus 115, 1–35.

Vilas, F., 1994. A quick look method of detecting water of hydration in small Solar System bodies. Lunar Planet. Sci. 25, 1439–1440.

Zappala, V., Cellino, A., Farinella, P., Knežević, Z., 1990. Asteroid families. I. Identification by hierarchical clustering and reliability assessment. Astron. J. 100, 2030–2046.

Chapitre 5

Centaures et Transneptuniens

5.1 Les nouvelles frontières du Système Solaire

Au milieu du XXe siècle, K. E. Edgeworth et G. Kuiper évoquent pour la première fois l'existence d'objets situés au-delà de Pluton. Ils pensent que ces corps, formant une ceinture aplatie, seraient la source des comètes à courte période. Kuiper suggère notamment qu'il s'agirait de résidus de la formation du Système Solaire, qui n'auraient pas pu former des planètes à cause de la faible densité de matière. Mais c'est seulement en 1992 que le premier objet (1992 QB1) de la ceinture de Kuiper est découvert par Jane Luu et David Jewitt. Aujourd'hui, plus de 1500 objets (dits objets trans-neptuniens ou OTNs) ont été découverts dans cette région. Le début des années 2000 a marqué l'âge d'or des observations des OTNs, avec la découverte de nombreux objets dans la ceinture de Kuiper dont certains de dimensions considérables et même similaires à celles de Pluton (Éris notamment). Ceci a posé le problème de la définition de planète et a mené l'IAU au déclassement de Pluton de planète à planète naine en 2006, chose qui a eu un fort écho dans le monde, bouleversant la vision communément admise du Système Solaire avec 9 planètes. Beaucoup de ressources et de temps d'observation ont été investis pour l'étude de ces objets qui constituent la nouvelle frontière de notre Système Solaire. Autant d'intérêt s'explique en considérant que les OTNs sont les corps primitifs qui ont les moins évolués depuis leur formation. Leur étude permet donc d'avoir accès aux premières phases de la formation du Système Solaire ainsi qu'aux processus physiques qui ont été à l'œuvre dans ces zones froides de la nébuleuse depuis que ces objets ont été formés (différents types d'irradiation, collisions, etc...).

5.1.1 Classification dynamique

D'un point de vue dynamique, les OTNs se répartissent en quatre catégories principales (voir Morbidelli et al. 2008 et Gladman et al. 2008 pour plus de détails) :

- les objets classiques : les deux-tiers des objets trans-neptuniens connus ont une faible excentricité et une faible inclinaison. Le demi-grand axe de ces objets est compris entre 42 et 47 UA. Leur faible excentricité leur permet de rester suffisamment loin de Neptune (distance > 10 UA) même lorsqu'ils sont au périhélie.
- Les objets résonnants (à peu prés un tiers de la population des OTNs) dont l'orbite est en résonance avec Neptune : la majorité se trouve en résonance 3 : 2 avec Neptune (ils effectuent deux révolutions autour du Soleil lorsque Neptune en fait trois), comme Pluton, et pour cette raison ils sont appelés Plutinos. Leur excentricité est comprise entre 0,1 et 0,34 et leur inclinaison entre 0 et 20^o. Les résonances protègent probablement ces objets des instabilités gravitationnelles dues aux perturbations de Neptune. Quelques Plutinos

ont un périhélie intérieur à l'orbite de Neptune et seraient immédiatement éjectés sans la protection de la résonance. L'une des hypothèses avancées pour expliquer la capture de tant d'objets sur une orbite résonnante est la migration radiale de Neptune dans les premières phases de la formation du Système Solaire

– les objets diffusés : la troisième classe comprend des objets particuliers (1996 TL66 est le premier OTN découvert de ce type) qui ont des orbites avec une forte excentricité et inclinaison. Leur périhélie (q $\sim$ 35 UA) est proche de celui de Neptune, indiquant une forte interaction dynamique avec la planète géante. Il s'agit probablement d'une population d'objets perturbés gravitationnellement par Neptune (Duncan & Levison 1997). La durée de vie de ces corps sur de telles orbites est de l'ordre de 10^9 ans. Cette population est considérée comme une source possible de comètes à courte période.
– les objets détachés (ou Extended Scattered) : ils ont des orbites très excentriques et un grand aphélie (comme Sedna, 2000 CR105, ou 2006 SQ372), et ne subissent pas l'influence gravitationnelle des planètes, en particulier de Neptune.

Une autre population d'objets liées aux OTNs est celle des Centaures, qui circulent entre les orbites de Jupiter et Neptune (ils ont un demi-grand axe compris entre 5 et 30 UA). Ils occupent des orbites très instables (durée de vie de l'ordre de 10^6 ans), ce qui indique qu'ils ne se sont pas formés sur place. On ne connaît pas avec certitude leur origine, mais la ceinture de Kuiper semble être le réservoir le plus proche et le plus probable. On pense aujourd'hui que les Centaures seraient une population intermédiaire entre les objets trans-neptuniens et les comètes proprement dites. Cette hypothèse semble confirmée par l'activité que l'on a détectée sur Chiron, le plus gros d'entre eux (diamètre de l'ordre de 200 km). Ces corps présentent le grand intérêt d'être plus proches et donc beaucoup plus faciles à étudier que les trans-neptuniens.

5.2 Campagnes d'observation

Pendant ma carrière j'ai eu la possibilité de participer aux observations, réduction, analyse et interprétation de données issues de deux *Large Programme (LP)* dédiés à la caractérisation des propriétés physiques des OTNs et Centaures. Ces campagnes observationnelles de grande envergure (environ 500 heures d'observation chacune) ont été menées à l'ESO en 2000-2002 (PI H. Boehnhardt) et en 2006-2008 (PI M.A. Barucci) en utilisant les grands télescopes du VLT à Paranal (UT1, UT2 et UT4), avec pour la plupart du temps deux télescopes en mode parallèle pour étudier simultanément les domaines visible et proche infrarouge, et le télescope NTT à La Silla. Les résultats obtenus fournissent un aperçu unique des propriétés physiques et compositionnelles de ces objets distants.
J'ai aussi effectué des observations ciblées sur certains objets au télescope TNG (comme pour Orcus) et j'ai participé à des campagnes observationnelles multi-couleur en photométrie menées aux télescopes CFHT et TNG.
Les objectifs de tous ces programmes d'observation sont de caractériser la composition et l'évolution de surface des objets Trans-Neptuniens et des Centaures et de mettre en évidence les relations entre ces objets, afin de fournir des contraintes fortes sur la formation du Système Solaire externe. Pour cela, des études ont été menées avec différentes techniques et méthodes d'analyse :

– spectroscopie dans le visible et le proche infrarouge (principalement avec le VLT+FORS, SINFONI, ISAAC, NACO, également avec le TNG) afin de contraindre la composition de surface des objets. Pour cela, des modèles de diffusion de la lumière basés sur la théorie d'Hapke et aussi des mélanges intimes et géographiques des composés chimiques ont été appliqués aux spectres obtenus

- photométrie dans le visible et le proche infrarouge (VLT+FORS et ISAAC, NTT, TNG, CHFT) pour étudier les propriétés globales de couleurs des différentes populations. Les résultats sur un grand échantillon d'objets nous ont permis d'effectuer des études statistiques des couleurs pour rechercher les corrélations éventuelles entre propriétés physiques (couleur, taille..) et caractéristiques orbitales (inclinaison, excentricité...), et étudier les interrelations entre les différentes populations
- polarimétrie dans la région visible afin de caractériser les propriétés de surface (albédo, dimension des grains, porosité de la surface...)

Des nombreuses publications, auxquelles j'ai contribué et dont je résumerai les résultats les plus marquants dans les sections qui suivent, sont issues de ces campagnes observationnelles.

5.3 Etudes photométriques et statistiques

La photométrie permet d'atteindre un grand nombre d'objets afin d'étudier la population des OTNs et Centaures dans sa globalité, permettant d'avoir des caractéristiques physiques statistiquement relevantes. Les couleurs nous permettent d'avoir une première indication sur la réflectance et donc sur la possible composition de la surface. Voici quelques résultats issus des nombreuses observations en photométrie :

- campagne d'observations multi-couleur de Meudon : nous avons obtenu des données en photométrie BVRI pour 127 objets, et en JHK pour 50 objets (publiées dans Doressoundiram et al. 2002 et 2007). Les différentes classes des objets du Système Solaire externe ne montrent pas de différence particulière entre elles, alors que les objets de chaque classe dynamique ont une grande variété de couleurs, du gris (couleur solaire) au très rouge, qui reflète des effets de rougissement et d'altération du matériau de surface dus à des impacts et à d'éventuelles activités intrinsèques. Une analyse statistique utilisant la méthode de corrélation de Spearman a montré une forte corrélation entre les couleurs (B-R et B-V) des OTNs de type classique et l'inclinaison, l'excentricité et la distance du périhélie. En particulier les objets dynamiquement plus excités, ceux avec une grande inclinaison et excentricité, ont des surfaces moins rouges, ce qui semble indiquer qu'il y a un processus de rajeunissement des surfaces plus efficace dans la région des OTNs classiques. Les objets observés avec un périhélie > 40 UA sont pour la plupart très rouges, comme déjà signalé par Tegler & Romanishing (2000). Les Centaures montrent une distribution bimodale des couleurs, c'est à dire une forte dichotomie entre les objets neutres et les objets très rouges. La comparaison entre les données des OTNs et des Centaures avec ceux des comètes a montré que les couleurs des comètes ne sont pas compatibles avec celles des OTNs et des Centaures, ce qui suggère ainsi qu'un mécanisme modifie la surface des comètes à leur entrée dans le Système Solaire. Les satellites irréguliers ont des couleurs compatibles avec les OTNs dispersés (mais pas avec les Centaures, Plutinos, ou Classiques), plaçant ainsi leur probable origine dans cette population de la ceinture de Kuiper
- *Large Programme* 2006-2008 : taxonomie et études statistiques : Nous avons observé en photométrie V, R, I, J, H et K (avec FORS et ISAAC) plus de 40 objets. Sur la base des indices de couleur obtenus, nous avons classifié 38 objets en appliquant la méthode statistique du G-mode (Fulchignoni et al. 2000). Les quatre classes identifiées (BB, BR, IR, RR, Barucci et al. 2005b) vont d'une couleur neutre (ou solaire, classe BB) à très rouge dans la partie visible (classe RR), en passant par des classes intermédiaires. Les observations effectuées dans le cadre de notre programme ont été combinées avec toutes les données disponibles dans la littérature. Nous avons ainsi analysé un total de 151 objets et effectué une analyse statistique pour étudier toutes les relations entre les différentes classes

et les propriétés dynamiques. Les principaux résultats obtenus sont : i) confirmation de la bimodalité de couleur dans la population des Centaures ; ii) les objets appartenant à la classe IR semblent être concentrés dans les populations classiques et résonnantes ; iii) les objets plus rouges (RR) dominent la population à faible inclinaison orbitale des objets classiques, tandis que les objets bleus (BB) sont plus abondants dans les orbites à haute inclinaison (Perna et al. 2010, Barucci et al. 2011).

- période de rotation (données du *Large Programme* 2006-2008) : l'étude de la rotation des petits corps du Système Solaire permet de contraindre leur forme, leur vitesse de rotation et donne des indications sur leur structure interne. Dans le cadre du *Large Programme*, nous avons obtenu avec le télescope NTT des courbes de rotation pour 12 objets : (12929) 1999 TZ1, (95626) 2002 GZ32, (42355) Typhon, (47932) 2000 GN171, (65489) Ceto, (90568) 2004 GV9, (120132) 2003 FY128, (144987) 2004 UX10, (145451) 2005 RM43, (145453) 2005 RR43, 2003 UZ117, 2003UZ413 (Dotto et al. 2008, Perna et al. 2010). Une analyse de Fourier des courbes de lumière a été réalisée en utilisant la méthode développée par Harris et al. (1989). Pour 9 des 12 OTNs observés, la période de rotation synodique a été obtenue, alors que la qualité des données des 3 objets restant (Typhon, 2003 FY128, et 2003 UZ117) n'était pas suffisante pour trouver une solution unique. De cette étude ressort la rotation rapide de 2003 UZ413 (4,13$\pm$0,05), qui apparait être le deuxième OTN le plus rapide après (136108) Haumea. En supposant que les formes de ces objets sont des ellipsoïdes triaxiaux, nous avons déduit une limite inférieure du rapport a/b à partir de l'amplitude de leur courbe de lumière, sous l'hypothèse que ces dernières ne sont affectées que par la forme. La densité minimale a aussi été estimée sur la base de la variation en magnitude de la courbe de lumière (Perna et al. 2010).

5.3.1 Article : Colors and taxonomy of Centaurs and trans-Neptunian objects

A&A 510, A53 (2010)
DOI: 10.1051/0004-6361/200913654

Astronomy & Astrophysics

Colors and taxonomy of Centaurs and trans-Neptunian objects*

D. Perna[1,2,3], M. A. Barucci[1], S. Fornasier[1,4], F. E. DeMeo[1], A. Alvarez-Candal[1,5], F. Merlin[1,6], E. Dotto[3], A. Doressoundiram[1], and C. de Bergh[1]

[1] LESIA, Observatoire de Paris, 5 Place Jules Janssen, 92195 Meudon Principal Cedex, France
e-mail: davide.perna@obspm.fr
[2] Università di Roma Tor Vergata, Italy
[3] INAF-Osservatorio Astronomico di Roma, Italy
[4] Université Paris Diderot – Paris 7, France
[5] European Southern Observatory, Chile
[6] Department of Astronomy, University of Maryland, USA

Received 12 November 2009 / Accepted 30 November 2009

ABSTRACT

Context. The study of the surface properties of Centaurs and trans-Neptunian objects (TNOs) provides essential information about the early conditions and evolution of the outer Solar System. Due to the faintness of most of these distant and icy bodies, photometry currently constitutes the best technique to survey a statistically significant number of them.

Aims. Our aim is to investigate color properties of a large sample of minor bodies of the outer Solar System, and set their taxonomic classification.

Methods. We carried out visible and near-infrared photometry of Centaurs and TNOs, making use, respectively, of the FORS2 and ISAAC instruments at the Very Large Telescope (European Southern Observatory). Using G-mode analysis, we derived taxonomic classifications according to the Barucci et al. (2005a, AJ, 130, 1291) system.

Results. We report photometric observations of 31 objects, 10 of them have their colors reported for the first time ever. 28 Centaurs and TNOs have been assigned to a taxon.

Conclusions. We combined the entire sample of 38 objects taxonomically classified in the framework of our programme (28 objects from this work; 10 objects from DeMeo et al. 2009a, A&A, 493, 283) with previously classified TNOs and Centaurs, looking for correlations between taxonomy and dynamics. We compared our photometric results to literature data, finding hints of heterogeneity for the surfaces of 4 objects.

Key words. Kuiper Belt: general – techniques: photometric – infrared: planetary systems

1. Introduction

The investigation of the surface properties of the minor bodies in the outer Solar System constitutes a major topic in modern planetary science, since they represent the "vestiges" of the left-over planetesimals from the early accretional phases of the outer proto-planetary disk. Even though they are affected by space weathering and collisional evolution (see, e.g., Hudson et al. 2008; and Leinhardt et al. 2008), they present the most pristine material in present times available for our studies, from which we can learn about the origin and early evolution of the Solar System at large distances from the Sun.

Because of the faintness of trans-Neptunian objects (TNOs) and Centaurs, spectroscopic observations (which could provide the most detailed information about their surface compositions) are feasible only for a small number of them, even when using the largest ground-based telescopes (see Barucci et al. 2008, for a recent review). Hence photometry is still the best tool to investigate the surface properties of a significant sample of these objects, allowing a global view of the whole known population.

To date photometric surveys have observed more than 200 objects. Statistical analyses were performed to search for possible correlations between colors and physical and orbital parameters (see Doressoundiram et al. 2008 and Tegler et al. 2008 for recent reviews). As the major result, a clustering of "cold" (low eccentricity, low inclination) classical TNOs (see Gladman et al. 2008, for a dynamical classification of objects in the outer Solar System) with very red colors was found.

Even if photometric colors cannot provide firm constraints on the surface composition, since they depend also on scattering effects in particulate regoliths and viewing geometry, they can be used to classify the objects in different groups that reasonably indicate different composition and/or evolutional history. A new TNO taxonomy (Barucci et al. 2005a; Fulchignoni et al. 2008) based on color indices ($B-V$, $V-R$, $V-I$, $V-J$, $V-H$, and $V-K$) identifies four classes with increasingly red colors: BB (neutral color), BR, IR, and RR (very red).

An ESO (European Southern Observatory) large programme devoted to the study of TNOs and Centaurs, by means of different techniques, was lead by Barucci in 2006–2008. In this framework, visible and near-infrared (NIR) photometry of a total of 45 objects was performed. The results from data acquired between October 2006 and September 2007 were published in DeMeo et al. (2009a). In this paper we present all the photometric observations executed during the second year of the large programme (November 2007–November 2008), regarding 31 objects. For 28 of these targets we were able to determine the Barucci et al. (2005a) taxonomic classification, via the G-mode

* Based on observations carried out at the European Southern Observatory (ESO), Chile (Programmes 178.C-0036 and 178.C-0867).

statistical method presented in Fulchignoni et al. (2000), and to compare our results with literature data whenever available.

An analysis of the entire sample (151 objects) of taxonomically classified TNOs and Centaurs has been performed, searching for correlations between dynamical properties and taxonomy.

2. Observations and data reduction

All of the data presented in this work were obtained with the ESO Unit Telescope 1 (Antu) of the Very Large Telescope (VLT), located in Cerro Paranal, Chile.

The observational circumstances are reported in Table 1.

2.1. Visible

Visible photometry was performed with the FORS2 instrument (Appenzeller et al. 1998), equipped with a mosaic of two 2000×4000 MIT CCD with square 15 μm pixels. The observations were carried out with the standard resolution (SR) collimator and a 2×2 binning, yielding a resolution of 0.25 arcsec/pixel. We used the broadband V, R, I filters, centered at 0.554, 0.655 and 0.768 μm, respectively, adjusting the exposure time according to the object magnitude.

The images were reduced using standard procedures with the MIDAS software package: after subtraction of the bias from the raw data and flat-field correction, the instrumental magnitudes were measured via aperture photometry, with an integrating radius typically about three times the average seeing and sky subtraction performed using a 5–10 pixel wide annulus around each object. The aperture correction method (see, e.g., Barucci et al. 2000) was used for only a few cases (faint target and/or nearby field stars) to determine the object flux. The absolute calibration of the magnitudes was obtained by means of the observation of several Landolt (1992) standard fields.

2.2. Near-infrared

NIR photometry was performed with the ISAAC instrument (Moorwood et al. 1998), in SWI1 (short wavelength imaging) mode, using the 1024×1024 Hawaii Rockwell array with a pixel size of 18.5 μm and a scale of 0.148 arcsec/pixel. We observed with the J, H, Ks filters, with central wavelength of 1.25, 1.65 and 2.16 μm, respectively. As is typical for NIR observations, the expositions were split in several images with short exposure times, in order to minimize the sky background noise.

The data were pre-reduced (dark subtraction, flat-field correction, bad pixel cleaning, sky subtraction, recombination of the images) by using the ESO ISAAC pipeline. Then, as for the visible images, target fluxes were mostly measured (with MIDAS) using classical photometry methods with apertures determined by the seeing and growth curves of the objects, reserving the aperture correction method to a few cases. To calibrate the instrumental magnitudes, standard stars from different catalogues (Persson et al. 1998; Hawarden et al. 2001) were observed.

3. Results

During the second year of our ESO large programme we obtained visible and NIR photometric measurements for 31 objects, 10 of them have their colors reported for the first time ever.

Table 1. Observational circumstances.

Object	Date	Δ (AU)	r (AU)	α (deg)
(5145) Pholus	12 Apr. 2008	21.212	21.864	2.0
(10199) Chariklo	3 Feb. 2008	13.311	13.395	4.2
	4 Feb. 2008	13.296	13.395	4.2
(20000) Varuna	4 Dec. 2007	42.605	43.391	0.8
(42301) 2001 UR_{163}	5 Dec. 2007	49.625	50.308	0.8
(42355) Typhon	12 Apr. 2008	16.892	17.650	2.2
(44594) 1999 OX_3	21 Sep. 2008	22.025	22.889	1.3
	22 Sep. 2008	22.033	22.888	1.3
(52872) Okyrhoe	3 Feb. 2008	4.883	5.800	3.9
	4 Feb. 2008	4.877	5.800	3.7
(55576) Amycus	12 Apr. 2008	15.205	16.056	1.9
(55637) 2002 UX_{25}	6 Dec. 2007	41.263	41.975	0.9
(55638) 2002 VE_{95}	5 Dec. 2007	27.297	28.248	0.5
	6 Dec. 2007	27.301	28.249	0.6
	22 Nov. 2008	27.379	28.341	0.5
	23 Nov. 2008	27.378	28.341	0.4
(73480) 2002 PN_{34}	10 Nov. 2007	14.894	15.344	3.3
(90377) Sedna	21 Sep. 2008	87.416	88.015	0.5
	22 Sep. 2008	87.402	88.014	0.5
(90482) Orcus	3 Feb. 2008	46.904	47.807	0.5
	4 Feb. 2008	46.900	47.807	0.5
(120061) 2003 CO_1	4 Feb. 2008	10.937	11.080	5.1
	12 Apr. 2008	10.179	11.123	1.8
	13 Apr. 2008	10.175	11.123	1.8
(120132) 2003 FY_{128}	12 Apr. 2008	37.477	38.454	0.3
(120178) 2003 OP_{32}	21 Sep. 2008	40.546	41.365	0.8
(120348) 2004 TY_{364}	22 Nov. 2008	38.840	39.591	0.9
	23 Nov. 2008	38.849	39.591	1.0
(136199) Eris	7 Dec. 2007	49.652	50.310	0.8
(144897) 2004 UX_{10}	4 Dec. 2007	38.145	38.837	1.0
	5 Dec. 2007	38.158	38.837	1.1
	6 Dec. 2007	38.170	38.837	1.1
	23 Nov. 2008	38.059	38.879	0.8
(145451) 2005 RM_{43}	4 Dec. 2007	34.298	35.195	0.7
	7 Dec. 2007	34.316	35.196	0.7
(145453) 2005 RR_{43}	4 Dec. 2007	37.623	38.511	0.6
	7 Dec. 2007	37.642	38.512	0.7
(174567) 2003 MW_{12}	12 Apr. 2008	47.314	47.968	0.9
	13 Apr. 2008	47.302	47.968	0.9
(208996) 2003 AZ_{84}	22 Nov. 2008	44.879	45.458	1.0
	23 Nov. 2008	44.865	45.457	1.0
2002 KY_{14}	21 Sep. 2008	7.802	8.649	3.8
	22 Sep. 2008	7.810	8.649	3.8
2003 UZ_{117}	22 Nov. 2008	38.420	39.368	0.4
	23 Nov. 2008	38.423	39.367	0.4
2003 UZ_{413}	4 Dec. 2007	41.171	42.004	0.7
	21 Sep. 2008	41.466	42.163	1.0
	22 Nov. 2008	41.276	42.197	0.5
	23 Nov. 2008	41.282	42.198	0.5
2007 UK_{126}	21 Sep. 2008	45.131	45.618	1.1
	22 Sep. 2008	45.117	45.617	1.1
2007 UM_{126}	21 Sep. 2008	10.202	11.163	1.5
	22 Sep. 2008	10.199	11.165	1.5
2007 VH_{305}	22 Nov. 2008	7.854	8.638	4.2
	23 Nov. 2008	7.863	8.636	4.3
2008 FC_{76}	20 Sep. 2008	10.968	11.690	3.5
	21 Sep. 2008	10.976	11.688	3.6
2008 SJ_{236}	22 Nov. 2008	5.522	6.364	5.0
	23 Nov. 2008	5.530	6.363	5.1

Notes. Δ, r and α are the topocentric distance, the heliocentric distance, and the phase angle, respectively.

Table 2 lists the resulting magnitude values, as well as the computed absolute magnitudes H of the targets, calculated as

$$H = V - 5\log(r\Delta) - \alpha\beta, \tag{1}$$

Table 2. Observed magnitudes.

Object	Date	UT_{START}	V	R	I	J	H	K_s	H_V
(5145) Pholus	12 Apr. 2008	05:48	21.33 ± 0.09	20.64 ± 0.09	19.95 ± 0.15	...	...	...	7.78 ± 0.09
(10199) Chariklo[a]	3 Feb. 2008	07:41	...	...	...	17.11 ± 0.06	16.61 ± 0.05	16.38 ± 0.06	...
	4 Feb. 2008	07:41	18.79 ± 0.02	18.34 ± 0.02	17.88 ± 0.03	...	...	...	7.07 ± 0.04
(20000) Varuna	4 Dec. 2007	06:09	20.49 ± 0.03	19.88 ± 0.03	...	...	...	...	4.04 ± 0.04
	4 Dec. 2007	06:12	20.46 ± 0.04	19.88 ± 0.03	...	...	...	...	4.01 ± 0.05
(42301) 2001 UR_{163}	5 Dec. 2007	00:52	21.82 ± 0.06	20.98 ± 0.07	...	...	...	...	4.72 ± 0.06
	5 Dec. 2007	00:55	21.81 ± 0.05	20.98 ± 0.07	...	...	...	...	4.71 ± 0.06
(42355) Typhon[b]	12 Apr. 2008	00:59	20.50 ± 0.08	20.00 ± 0.08	19.70 ± 0.08	...	...	...	7.77 ± 0.11
(44594) 1999 OX_3	21 Sep. 2008	04:07	21.26 ± 0.05	20.54 ± 0.06	19.96 ± 0.07	...	...	...	7.57 ± 0.06
	22 Sep. 2008	04:49	...	...	...	19.08 ± 0.12	18.75 ± 0.08	18.69 ± 0.08	...
(52872) Okyrhoe[c]	3 Feb. 2008	06:41	...	...	...	16.84 ± 0.06	16.39 ± 0.07	16.28 ± 0.05	...
	4 Feb. 2008	06:18	18.63 ± 0.02	18.14 ± 0.02	17.64 ± 0.02	...	...	...	10.97 ± 0.04
(55576) Amycus	12 Apr. 2008	03:33	20.42 ± 0.08	19.78 ± 0.08	19.20 ± 0.15	...	...	...	8.27 ± 0.08
(55637) 2002 UX_{25}	6 Dec. 2007	01:19	...	...	...	18.55 ± 0.03	18.25 ± 0.04	18.21 ± 0.06	...
(55638) 2002 VE_{95}	5 Dec. 2007	03:35	20.31 ± 0.03	19.59 ± 0.04	...	...	...	...	5.80 ± 0.03
	5 Dec. 2007	03:38	20.31 ± 0.03	19.59 ± 0.04	...	...	...	...	5.80 ± 0.03
	6 Dec. 2007	02:09	...	...	...	18.11 ± 0.04	17.78 ± 0.04	17.74 ± 0.04	...
	22 Nov. 2008	05:36	20.28 ± 0.06	19.53 ± 0.08	18.77 ± 0.09	...	...	...	5.76 ± 0.06
	23 Nov. 2008	05:57	...	...	...	18.04 ± 0.07	17.68 ± 0.07	17.63 ± 0.09	...
(73480) 2002 PN_{34}[c]	10 Nov. 2007	00:36	20.68 ± 0.03	20.25 ± 0.05	...	19.00 ± 0.05	18.49 ± 0.06	18.29 ± 0.05	8.42 ± 0.10
(90377) Sedna	21 Sep. 2008	06:33	21.34 ± 0.04	20.57 ± 0.05	19.93 ± 0.05	...	...	...	1.84 ± 0.04
	22 Sep. 2008	06:57	...	...	...	19.20 ± 0.04	18.78 ± 0.06	...	...
(90482) Orcus[c]	3 Feb. 2008	04:46	...	...	...	17.91 ± 0.05	17.72 ± 0.07	17.89 ± 0.05	...
	4 Feb. 2008	05:04	19.12 ± 0.02	18.73 ± 0.02	18.37 ± 0.02	...	...	...	2.30 ± 0.03
(120061) 2003 CO_1	4 Feb. 2008	08:17	19.93 ± 0.02	19.45 ± 0.03	19.01 ± 0.03	...	...	...	8.95 ± 0.05
	12 Apr. 2008	04:40	19.63 ± 0.08	19.20 ± 0.09	18.82 ± 0.15	...	...	...	9.16 ± 0.08
(120132) 2003 FY_{128}	12 Apr. 2008	02:22	20.93 ± 0.09	20.34 ± 0.09	19.86 ± 0.15	...	...	...	5.09 ± 0.09
(120178) 2003 OP_{32}	21 Sep. 2008	02:10	20.25 ± 0.03	19.86 ± 0.05	19.50 ± 0.05	...	...	...	4.02 ± 0.04
(120348) 2004 TY_{364}	22 Nov. 2008	04:32	20.64 ± 0.03	20.04 ± 0.04	19.52 ± 0.04	...	...	...	4.58 ± 0.04
	23 Nov. 2008	03:22	...	...	...	18.87 ± 0.03	18.42 ± 0.05	18.39 ± 0.08	...
(136199) Eris[d]	7 Dec. 2007	00:20	...	...	...	17.90 ± 0.06	17.85 ± 0.05	18.15 ± 0.06	...
(144897) 2004 UX_{10}	4 Dec. 2007	00:53	20.61 ± 0.04	20.04 ± 0.04	...	...	...	...	4.62 ± 0.05
	4 Dec. 2007	00:56	20.63 ± 0.04	20.05 ± 0.04	...	...	...	...	4.64 ± 0.05
	5 Dec. 2007	02:24	20.63 ± 0.03	20.06 ± 0.04	...	...	...	...	4.62 ± 0.04
	6 Dec. 2007	00:39	...	...	...	18.97 ± 0.06	18.55 ± 0.08	18.55 ± 0.09	...
	23 Nov. 2008	02:26	...	...	...	19.02 ± 0.03	18.60 ± 0.04	18.64 ± 0.06	...
(145451) 2005 RM_{43}	4 Dec. 2007	03:22	20.04 ± 0.04	19.66 ± 0.03	...	...	...	...	4.53 ± 0.05
	4 Dec. 2007	03:25	20.07 ± 0.04	19.66 ± 0.03	...	...	...	...	4.56 ± 0.05
	7 Dec. 2007	03:14	...	...	...	18.95 ± 0.04	18.76 ± 0.05	18.71 ± 0.06	...
(145453) 2005 RR_{43}	4 Dec. 2007	02:26	20.05 ± 0.03	19.66 ± 0.04	...	...	...	...	4.16 ± 0.03
	4 Dec. 2007	02:29	20.08 ± 0.03	19.66 ± 0.04	...	...	...	...	4.19 ± 0.03
	7 Dec. 2007	02:24	...	...	...	19.28 ± 0.04	19.47 ± 0.07	19.67 ± 0.15	...
(174567) 2003 MW_{12}	12 Apr. 2008	07:07	20.57 ± 0.08	19.99 ± 0.08	19.57 ± 0.15	...	...	...	3.66 ± 0.08
(208996) 2003 AZ_{84}	22 Nov. 2008	06:07	20.46 ± 0.03	20.08 ± 0.04	19.71 ± 0.03	...	...	...	3.77 ± 0.04
	23 Nov. 2008	07:10	...	...	...	19.26 ± 0.04	18.92 ± 0.07	...	...
2002 KY_{14}	21 Sep. 2008	00:56	19.93 ± 0.02	19.23 ± 0.03	18.58 ± 0.04	...	...	...	10.37 ± 0.04
	22 Sep. 2008	02:27	...	...	...	17.85 ± 0.06	17.56 ± 0.07	17.54 ± 0.08	...
2003 UZ_{117}	22 Nov. 2008	03:21	21.13 ± 0.03	20.77 ± 0.04	20.43 ± 0.04	...	...	...	5.18 ± 0.03
	23 Nov. 2008	05:08	...	...	...	20.41 ± 0.09	20.63 ± 0.17	...	...
2003 UZ_{413}	4 Dec. 2007	04:28	20.70 ± 0.04	20.22 ± 0.04	...	...	...	...	4.41 ± 0.05
	4 Dec. 2007	04:31	20.67 ± 0.04	20.22 ± 0.04	...	...	...	...	4.38 ± 0.05
	21 Sep. 2008	05:31	20.71 ± 0.04	20.25 ± 0.05	19.88 ± 0.06	...	...	...	4.36 ± 0.05
	22 Nov. 2008	03:33	20.63 ± 0.03	20.22 ± 0.04	19.82 ± 0.04	...	...	...	4.36 ± 0.03
	23 Nov. 2008	04:03	...	...	...	19.29 ± 0.05	18.92 ± 0.09	18.77 ± 0.09	...
2007 UK_{126}	21 Sep. 2008	08:05	20.41 ± 0.03	19.79 ± 0.04	19.32 ± 0.04	...	...	...	3.69 ± 0.04
	22 Sep. 2008	07:43	...	...	...	18.88 ± 0.07	18.52 ± 0.08	...	...
2007 UM_{126}	21 Sep. 2008	04:26	20.88 ± 0.03	20.44 ± 0.03	20.00 ± 0.03	...	...	...	10.43 ± 0.03
	22 Sep. 2008	05:57	...	...	...	...	18.84 ± 0.13	18.50 ± 0.08	...
2007 VH_{305}	22 Nov. 2008	02:14	21.44 ± 0.04	20.96 ± 0.04	20.48 ± 0.05	...	...	...	11.82 ± 0.06
	23 Nov. 2008	00:38	...	...	...	19.70 ± 0.10	19.06 ± 0.12	19.43 ± 0.15	...
2008 FC_{76}	20 Sep. 2008	23:55	20.38 ± 0.03	19.67 ± 0.05	19.04 ± 0.06	...	...	...	9.46 ± 0.05
	21 Sep. 2008	23:53	...	...	...	18.40 ± 0.08	18.00 ± 0.08	17.88 ± 0.09	...
2008 SJ_{236}	22 Nov. 2008	00:24	20.75 ± 0.03	20.13 ± 0.03	19.63 ± 0.04	...	...	...	12.47 ± 0.06
	23 Nov. 2008	01:28	...	...	...	19.01 ± 0.07	18.60 ± 0.11	18.83 ± 0.12	...

Notes. Objects in bold have their colors reported for the first time ever.
[(a)] Computed magnitudes from Guilbert et al. (2009). [(b)] Computed magnitudes from Alvarez-Candal et al. (2009). [(c)] Computed magnitudes from DeMeo et al. (2009b). [(d)] Computed magnitudes from Merlin et al. (2009).

Table 3. Taxonomic classification.

Object	Dyn. Class	Taxonomy			N
		Fulchignoni et al. 2008	DeMeo et al. 2009a	This work	
(5145) Pholus	Centaur	RR	...	RR	2
(10199) Chariklo	Centaur	BR	BR,BB	BR	5
(42355) Typhon	Scattered	BR	BR	BR,BB	5[a]
(44594) 1999 OX_3	Scattered	RR	...	RR	5
(52872) Okyrhoe	Jupiter-coupled	BR	...	BR,IR	5
(55576) Amycus	Centaur	RR	...	RR,IR	2
(55637) 2002 UX_{25}	Classical	IR	RR,IR	RR	5[b]
(55638) 2002 VE_{95}	Resonant (3:2)	RR	...	RR	5
(73480) 2002 PN_{34}	Scattered	...	...	BR,BB	4
(90377) Sedna	Detached	RR	...	RR	4
(90482) Orcus	Resonant (3:2)	BB	...	BB	5
(120061) 2003 CO_1	Centaur	...	...	BR	2
(120132) 2003 FY_{128}	Detached	...	BR	BR	5[a]
(120178) 2003 OP_{32}	Classical	...	...	BB,BR	2
(120348) 2004 TY_{364}	Classical	...	...	IR,RR,BR	5
(136199) Eris	Detached	BB	BB	BB	5[b]
(144897) 2004 UX_{10}	Classical	...	...	BR	4
(145451) 2005 RM_{43}	Detached	...	BB	BB	4
(145453) 2005 RR_{43}	Classical	...	BB	BB	4
(174567) 2003 MW_{12}	Classical	...	...	IR,BR,RR	2
(208996) 2003 AZ_{84}	Resonant (3:2)	BB	BB	BB	4
2002 KY_{14}	Centaur	...	...	RR	5
2003 UZ_{117}	Classical	...	...	BB	4
2003 UZ_{413}	Resonant (3:2)	...	...	BB	5
2007 UK_{126}	Scattered	...	...	*	4
2007 UM_{126}	Centaur	...	...	BR,BB	4
2007 VH_{305}	Centaur	...	...	BR	5
2008 FC_{76}	Centaur	...	...	RR	5
2008 SJ_{236}	Centaur	...	...	RR	5
(28978) Ixion	Resonant (3:2)	IR	BB		
(32532) Thereus	Centaur	BR	BB		
(47171) 1999 TC_{36}	Resonant (3:2)	RR	RR		
(47932) 2000 GN_{171}	Resonant (3:2)	IR	BR,IR		
(50000) Quaoar	Classical	...	RR		
(54598) Bienor	Centaur	BR	BR		
(55565) 2002 AW_{197}	Classical	IR	IR,RR		
(60558) Echeclus	Jupiter-coupled	BR	BR,BB		
(90568) 2004 GV_9	Classical	...	BR		
2003 QW_{90}	Classical	...	IR,RR,BR		

Notes. Objects from the ESO large programme taken into account for the statistical analysis of taxa. Dynamical classes are according to Gladman et al. (2008). First 29 bodies are classified in this work, last 10 objects come from DeMeo et al. (2009a). Whenever multiple taxonomic types are possible, classes are listed by ascending deviation of the object colors from the class' averages. The symbol * indicates that the object did not fall within any of the four taxonomic classes. N is the number of colors we used in classifying each object.
[(a)] Using near-infrared data from DeMeo et al. (2009a). [(b)] Using visible data from DeMeo et al. (2009a).

where V represents the visible magnitude reported in Col. 4 of Table 2, Δ, r and α are the topocentric and heliocentric distances and the phase angle given in Table 1, respectively, and β is the phase curve slope (mag/deg). For TNOs, we assumed $\beta = 0.14 \pm 0.03$ mag/deg, the modal value of the measurements published by Sheppard & Jewitt (2002). For Centaurs and Jupiter-coupled objects, we assumed $\beta = 0.11 \pm 0.01$ mag/deg, the result of a least squares fit by Doressoundiram et al. (2005) of the linear phase function $\phi(\alpha) = 10^{-\alpha\beta}$ of data from Bauer et al. (2003).

On the basis of the obtained color indices, the taxonomic classification of the targets was derived via the G-mode statistical method presented in Fulchignoni et al. (2000), using the taxonomy for TNOs and Centaurs introduced by Barucci et al. (2005a). This taxonomy identifies four classes, that reasonably indicate different composition and/or evolutionary history, with increasingly red colors: BB (neutral colors with respect to the Sun), BR, IR, RR (very red colors). We applied the above-mentioned algorithm to objects for which two or more color indices were available (i.e., to 29 out of the 31 observed TNOs and Centaurs). We classified each object whenever its colors were within 3σ of the class' average values. Obviously, a higher number of available colors implies a better reliability of the class determination. In cases where more than one class is within 3σ, we assigned a multiple designation to the object, with taxonomic classes ordered by ascending deviation of its colors from the class' averages. The taxonomic designations are reported in Table 3, along with the dynamical classification of the objects (according to Gladman et al. 2008).

We classified 28 objects: seven of them turned out to belong to the BB class, five were BR, eight were RR. The remaining eight targets got a multiple designation. Whenever a previous classification was available in the literature, a consistent result was obtained, even for objects with only 2 colors.

Only 2007 UK_{126}, even with four color measurements, did not fall within any class of the existing taxonomy. Indeed, according to its visible colors an IR, RR classification could be derived, while its infrared colors match those of a BB, BR object. Interestingly, the same result was obtained by DeMeo et al. (2009a) for two other TNOs, (26375) 1999 DE_9 and (145452) 2005 RN_{43}. This fact, as well as the presence of several multiple classifications, could support the idea that further groups could be found as the number of analysed objects increases, leading to a refinement of the current taxonomy.

Below, we discuss selected objects in further detail.

(10199) Chariklo: Using five color indices, we classified this Centaur as a BR object, as did Fulchignoni et al. (2008) on the basis of the mean colors published in literature. Our results, obtained in February 2008 (and already published in Guilbert et al. 2009), agree with these average measurements except for the $V-K$ color which is about 0.2 mag redder in our dataset. Interestingly, Chariklo was already observed in the framework of our programme in March 2007 (DeMeo et al. 2009a, who assigned to Chariklo a BR, BB classification), but we find no match with these previous results. Since the acquisition and the reduction of the data were carried out in the same way in both observing runs, this is a probable indication of heterogeneity on the surface of this Centaur, as already proposed in previous works (see Guilbert et al. 2009, and references therein).

(90377) Sedna: The photometric colors and taxonomic classification (RR) we derived for Sedna are in agreement with those published by Barucci et al. (2005b), except for the $V-J$ color which is approximately 0.2 mag bluer in our case. Since images in different filters have not been acquired simultaneously, the observation of different rotational phases of the object could affect color determinations. Nevertheless the light curve of Sedna has an amplitude of only 0.02 mag (Gaudi et al. 2005), hence different observed silhouettes of the body cannot explain the found discrepancy, which could instead be attributed to surface heterogeneity.

(120348) 2004 TY_{364}: Even if a triple designation (IR, RR, BR) has been assigned to this object, we note that the IR classification is strongly favored.

(145451) 2005 RM_{43}: The new data presented here confirm the BB classification already obtained in the framework of our large programme, even if we found both $V-J$ and $V-H$ colors ~0.2 mag redder than in DeMeo et al. (2009a), while the $V-K$ color is consistent. Observations with different filters have not been carried out simultaneously, but, as for Sedna, the amplitude of the light curve is smaller than the observed discrepancies ($\Delta m = 0.12 \pm 0.05$ mag; Perna et al. 2009), suggesting possible surface heterogeneity.

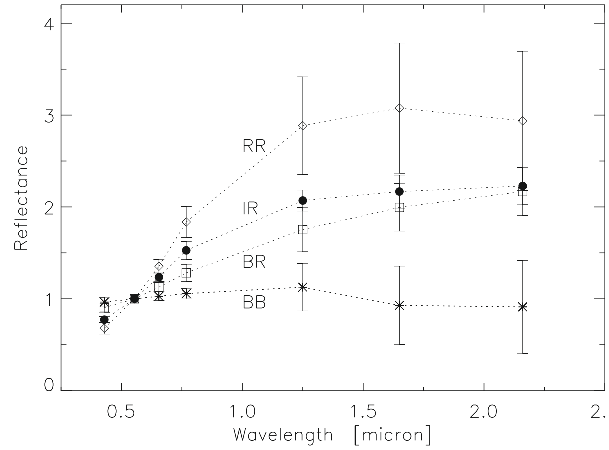

Fig. 1. Average reflectance values for each taxon, normalized to the Sun and to the V colors.

(145453) 2005 RR_{43}: We confirm that 2005 RR_{43} is a BB object, as classified by DeMeo et al. (2009a), but our $V-H$ color is 0.4 mag bluer than published by the same authors. Again, images with different filters have not been acquired at the same moment but the amplitude of the light curve is only $\Delta m = 0.12 \pm 0.03$ mag (Perna et al. 2009), so the observation of different compositions on the surface is a likely explanation for the reported discrepancy.

(174567) 2003 MW_{12}: Although this object was classified as IR, BR, RR by our analysis, as for 2004 TY_{364} the IR designation is strongly favored.

4. Statistical analysis

In the framework of our ESO large programme we derived the taxonomy of 38 objects (28 objects from this work plus 10 objects from DeMeo et al. 2009a; see Table 3). Nineteen of them have been classified for the first time, while 4 targets were assigned different classes with respect to the results by Fulchignoni et al. (2008), who classified all of the 133 TNOs and Centaurs for which data from the literature were available before our observations.

Considering a total sample of 151 objects (because 1998 WU_{24} has an unusual orbit, it is not a Centaur, and therefore is not considered in this analysis), we obtained the average colors of each taxon, reported in Table 4 and represented in Fig. 1 as reflectance values normalized to the Sun and to the V colors. In the cases where multiple taxonomic classes were assigned to an object, we took into account only the first designation. Then, we analysed the distribution of the four taxonomic groups with respect to the dynamical properties of the objects.

First of all, we verified the sampling of the taxa within each dynamical class (Fig. 2). The well-known color bimodality of Centaurs (see, e.g., Peixinho et al. 2003) clearly emerges, since 13 out of 25 objects belong to the BR group, while 10 of them fall in the RR class. All of the four new IR-classified objects are classical TNOs, confirming the finding that IR objects seem to be concentrated in the resonant and classical dynamical classes, as stated by Fulchignoni et al. (2008). As reported by the same

Table 4. Average colors of the four taxa.

Class	$B-V$	$V-R$	$V-I$	$V-J$	$V-H$	$V-K$
BB	0.68 ± 0.06	0.39 ± 0.05	0.75 ± 0.06	1.20 ± 0.25	1.28 ± 0.50	1.32 ± 0.60
BR	0.75 ± 0.06	0.49 ± 0.05	0.96 ± 0.08	1.68 ± 0.15	2.11 ± 0.14	2.26 ± 0.13
IR	0.92 ± 0.05	0.59 ± 0.04	1.15 ± 0.07	1.86 ± 0.06	2.20 ± 0.09	2.29 ± 0.10
RR	1.06 ± 0.10	0.69 ± 0.06	1.35 ± 0.10	2.22 ± 0.20	2.58 ± 0.25	2.59 ± 0.28

Notes. All of the 151 Centaurs and TNOs that have been classified thus far are taken into account. In the cases where multiple taxonomic classes were assigned to an object, we considered the first designation.

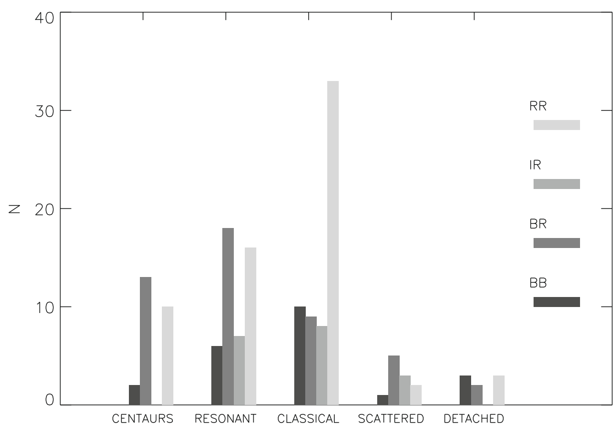

Fig. 2. Distribution of the taxa within each dynamical class, as defined by Gladman et al. (2008).

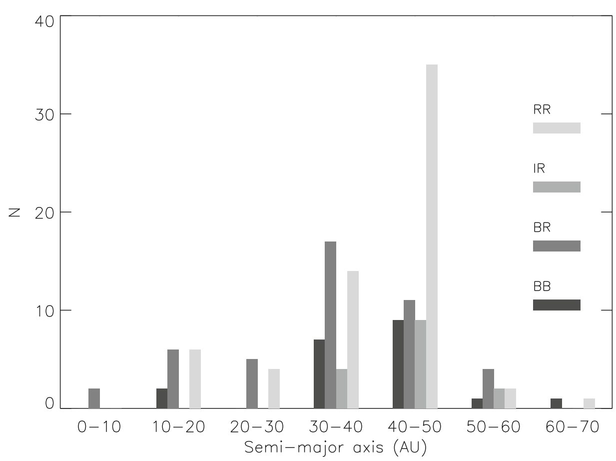

Fig. 3. Distribution of the taxa with respect to the semimajor axis of the objects. A 10 AU binning is adopted.

authors, RR objects dominate the classical TNOs. Our new results, however, do not conform to this behavior, as a quite equal division of the four taxa appears among the classical TNOs in the objects constituting the large programme sample.

In Fig. 3 we present the distribution of taxonomical classes with respect to the semimajor axes a of the objects. A 10 AU binning is adopted (nine objects are out of the scale). As already noted by Fulchignoni et al. (2008), the more distant TNOs belong to all the four taxa in a quite uniform way, while for $a \lesssim 30°$ the BR and RR classes dominate the population.

Finally, Fig. 4 reports the distribution of the taxa with respect to the orbital inclination i. A 5° binning is adopted (two objects are out of the scale). Inclinations of RR-types are quite low, in agreement with the previously mentioned finding of a red

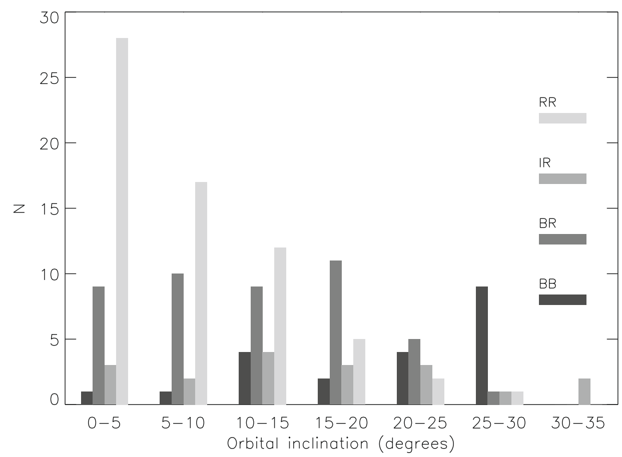

Fig. 4. Distribution of the taxa with respect to the orbital inclination of the objects. A 5° binning is adopted.

dynamically "cold" population. On the contrary, BB-types seem to be concentrated at high inclinations, confirming the suggested association of these objects with the "hot" population (Levison & Stern 2001; Brown 2001; Doressoundiram et al. 2002).

5. Conclusions

During the second year of an ESO large programme on TNOs and Centaurs, photometric observations of 31 objects have been carried out. From the comparison with previous works, hints of heterogeneous surfaces have been found for 4 objects (Chariklo, Sedna, 2005 RM_{43}, and 2005 RR_{43}).

For 28 out of the 31 observed objects we derived the taxomomic classification (within the system by Barucci et al. 2005a), using G-mode analysis. Taxonomy for ten additional objects was obtained in the framework of our programme (DeMeo et al. 2009a), for a total of 38 TNOs and Centaurs. This sample includes 19 objects which are classified for the first time ever, which constitutes about a 14% increase of the sample of 132 objects analysed by Fulchignoni et al. (2008) using the available literature.

We took into account the 151 objects that have been classified thus far to compute the average colors of the four taxonomic groups and to analyse their distribution with respect to the dynamical properties of the objects.

Looking at the distribution of the taxa within dynamical classes, the already known color bimodality (BR, RR) of Centaurs clearly emerges. Also, all of the four objects we classified as IR belong to the classical TNOs, in agreement with the finding that IR-types are concentrated in the resonant and classical dynamical classes (Fulchignoni et al. 2008). RR-types dominate the classical TNOs, but a similar division in the four taxa appears among the classical TNOs classified in the framework of our programme.

BR and RR classes dominate among the population at small ($a \lesssim 30°$) values of semimajor axis, while all the four taxa are well represented at greater distances from the Sun.

RR and BB classes are more abundant at low and high orbital inclinations, respectively, which associates these objects with the dynamically "cold" and "hot" populations.

References

Alvarez-Candal, A., Barucci, M. A., Merlin, F., et al. 2010, A&A, in press
Appenzeller, I., Fricke, K., Frtig, W., et al. 1998, The Messenger, 94, 1
Barucci, M. A., Romon, J., Doressoundiram, A., & Tholen, D. J. 2000, AJ, 120, 496
Barucci, M. A., Belskaya, I. N., Fulchignoni, M., & Birlan, M. 2005a, AJ, 130, 1291
Barucci, M. A., Cruikshank, D. P., Dotto, E., et al. 2005b, A&A, 439, L1
Barucci, M. A., Brown, M. E., Emery, J. P., & Merlin, F. 2008, in The Solar System Beyond Neptune, ed. M. A. Barucci, H. Boehnhardt, D. P. Cruikshank, & A. Morbidelli (Tucson: Univ. of Arizona Press), 143
Bauer, J. M., Meech, K. J., Fernández, Y. R., et al. 2003, Icarus, 166, 195
Brown, M. E. 2001, AJ, 121, 2804
DeMeo, F. E., Fornasier, S., Barucci, M. A., et al. 2009a, A&A, 493, 283
DeMeo, F. E., Barucci, M. A., Fornasier, S., et al. 2009b, A&A, submitted
Doressoundiram, A., Peixinho, N., de Bergh, C., et al. 2002, AJ, 124, 2279
Doressoundiram, A., Peixinho, N., Doucet, C., et al. 2005, Icarus, 174, 90
Doressoundiram, A., Boehnhardt, H., Tegler, S. C., & Trujillo, C. 2008, in The Solar System Beyond Neptune, ed. M. A. Barucci, H. Boehnhardt, D. P. Cruikshank, & A. Morbidelli (Tucson: Univ. of Arizona Press), 91
Fulchignoni, M., Birlan, M., & Barucci, M. A. 2000, Icarus, 146, 204
Fulchignoni, M., Belskaya, I., Barucci, M. A., de Sanctis, M. C., & Doressoundiram, A. 2008, in The Solar System Beyond Neptune, ed. M. A. Barucci, H. Boehnhardt, D. P. Cruikshank, & A. Morbidelli (Tucson: Univ. of Arizona Press), 181
Gaudi, B. S., Stanek, K. Z., Hartman, J. D., Holman, M. J., & McLeod, B. A. 2005, ApJ, 629, L49
Gladman, B., Marsden, B. G., & VanLaerhoven, C. 2008, in The Solar System Beyond Neptune, ed. M. A. Barucci, H. Boehnhardt, D. P. Cruikshank, & A. Morbidelli (Tucson: Univ. of Arizona Press), 43
Guilbert, A., Barucci, M. A., Brunetto, R., et al. 2009, A&A, 501, 777
Hawarden, T. G., Leggett, S. K., Letawsky, M. B., Ballantyne, D. R., & Casali, M. M. 2001, MNRAS, 325, 563
Hudson, R. L., Palumbo, M. E., Strazzulla, G., et al. 2008, in The Solar System Beyond Neptune, ed. M. A. Barucci, H. Boehnhardt, D. P. Cruikshank, & A. Morbidelli (Tucson: Univ. of Arizona Press), 507
Landolt, A. U. 1992, AJ, 104, 340
Leinhardt, Z. M., Stewar, S. T., & Schultz, P. H. 2008, in The Solar System Beyond Neptune, ed. M. A. Barucci, H. Boehnhardt, D. P. Cruikshank, & A. Morbidelli (Tucson: Univ. of Arizona Press), 195
Levison, H. S., & Stern S. A. 2001, AJ, 121, 1730
Merlin, F., Alvarez-Candal, A., Delsanti, A., et al. 2009, AJ, 137, 315
Moorwood, A., Cuby, J.-G., Biereichel, P., et al. 1998, The Messenger, 94, 7
Peixinho, N., Doressoundiram, A., Delsanti, A., et al. 2003, A&A, 410, L29
Perna, D., Dotto, E., Barucci, M. A., et al. 2009, A&A, 508, 451
Persson, S. E., Murphy, D. C., Krzeminski, W., Roth, M., & Rieke, M. J. 1998, AJ, 116, 2475
Sheppard, S. S., & Jewitt D. C. 2002, AJ, 124, 1757
Tegler, S. C., Bauer, J. M., Romanishin, W., & Peixinho, N. 2008, in The Solar System Beyond Neptune, ed. M. A. Barucci, H. Boehnhardt, D. P. Cruikshank, & A. Morbidelli (Tucson: Univ. of Arizona Press), 105

5.4 Polarimétrie

Huit OTNs ont été observés en polarimétrie avec l'instrument FORS1 au VLT. Tous les objets montrent une polarisation négative, comme observée pour les surfaces des petits corps et planètes, mais avec des caractéristiques particulières. Les objets avec un diamètre < 1000 km montrent une polarisation négative qui a une valeur allant jusqu'à -1% pour un angle de phase de 1^o. Les gros OTNs et les planètes naines montrent une polarisation négative plus petite et qui reste presque constante pour les angles de phase $< 2^o$ (à noter que pour les OTNs, les conditions géométriques des observations au sol ne nous permettent pas d'explorer des angles de phase $> 2^o$). Les observations d'Éris montrent un faible degré de polarisation négative dans l'intervalle d'angle de phase observé (0,15-0,5°). Les données photométriques permettent de situer le pic d'opposition de rétrodiffusion cohérente vers 0,2-0,3^o. Ces données présentent des similarités possibles avec les courbes de phase polarimétriques et photométriques de Pluton. La modélisation de ces données indique que le régolithe d'Éris (et par conséquent de Pluton) est très probablement constitué de grandes particules de taille comparable à la longueur d'onde. Ces mesures constituent les premières contraintes polarimétriques sur une planète naine de fort albédo à de très petits angles de phase (Belskaya et al. 2008). Les modèles du comportement polarimétrique des autres gros OTNs observés montrent aussi que leurs surfaces consistent en des particules transparentes, larges par rapport au domaine de longueur d'onde observé, et sont hétérogènes. Les OTNs et Centaures plus petits semblent par contre être couverts par une couche de glace cristalline de dimension <micron déposée sur une surface sombre (Belskaya et al. 2010b).

5.5 Spectroscopie et composition de surface

Une information plus détaillée sur la composition est acquise à partir des observations en spectroscopie, notamment celles couvrant la gamme de longueur d'onde entre 0,4 et 2,4 μm, mais l'échantillon d'objets observables (environ 50) est réduit par rapport à celui de la photométrie. Les résultats les plus marquants viennent du dernier *Large Programme* où des observations simultanées en spectroscopie visible avec FORS et dans le proche infrarouge avec ISAAC (bande J) et avec SINFONI (H et K) ont été effectuées pour 40 objets sélectionnés parmi les différents groupes dynamiques.
Dans la région visible, la grande majorité des spectres des OTNs et Centaures n'ont pas de bandes d'absorption et montrent des pentes spectrales variables. De faibles bandes d'absorption à 0,7 μm similaires à celles produites par le processus d'altération aqueuse sur les astéroïdes primitifs de la ceinture principale ont été détectées sur 2003 AZ84, 10199 Chariklo et 42355 Typhon (Fornasier et al. 2004b ; Alvarez-Candal et al. 2008, 2010 ; Guilbert et al. 2009), et précédemment sur 2000 EB173 et 2000 GN171 (Lazzarin et al. 2003). Cependant, pour ces deux derniers objets, les bandes d'absorption n'ont pas été confirmées (de Bergh et al. 2004, Alvarez-Candal et al. 2008, Fornasier et al. 2004b).

L'étude statistique sur les pentes spectrales obtenues dans la région visible pendant le *Large Programme* et aussi étendue aux pentes spectrales déjà publiées (échantillon de 73 objets : 20 Centaures et 53 OTNs) montre qu' il y a un déficit d'objets très rouges (c'est-à-dire avec une pente spectrale élevée) dans la population des OTNs classiques. Des corrélations possibles ont été recherchées entre les valeurs de la pente spectrale et les éléments orbitaux (inclinaison, excentricité, demi-grand-axe, et aphélie) ou la magnitude absolue H pour les différentes classes dynamiques. Nous confirmons l'anticorrélation entre pente spectrale et inclinaison pour les OTNs classiques, mais nous ne trouvons pas une séparation claire entre les groupes dynamiquement 'froids' et ‘chauds’ (Fornasier et al. 2009).

Certains objets, comme par exemple 2001 PT13, Chariklo, Thereus 1999 OX3 et 2003 FY123 (Guilbert et al. 2009, Fornasier et al. 2009), peuvent avoir des surfaces hétérogènes car ils montrent des variations spectrales dans le visible et le proche infrarouge.

Dans la région infrarouge, les observations effectuées avec SINFONI nous ont permis de détecter des signatures spectrales qui révèlent la présence de dépôts de glaces comme H_2O, CH_4, CH_3OH, C_2H_6, NH_3 et N_2 à la surface de ces corps (voir Dalle Ore et al. 2009, Merlin et al. 2009, 2010, Barucci et al. 2011). Les spectres ont un comportement qui va du bleu/plat au rouge/très rouge. Une grande partie des OTNs ont aussi des spectres sans signatures et des albédos très faibles. Les objets avec des couleurs neutres (spectre plat) semblent être couverts par de la glace d’eau. La diversité de composition de surface et de couleur des populations d’OTNs peut être connectée à différentes compositions initiales ou à divers processus subis, ou enfin à leur taille.

Les objets de plus grandes tailles se montrent les plus intéressants, puisque, grâce à la présence de bandes d’absorption, il nous est possible de mieux contraindre leur composition de surface. On distingue des OTNs/Centaures qui montrent des bandes d’absorption due à la glace d’eau à l’état amorphe et même cristallin, similaires à Charon (comme Quaoar, Orcus, Haumea), et d’autres qui montrent des signatures de glaces d’espèces plus volatiles, en particulier du méthane, qui ressemblent à Pluton (comme Éris, Makemake).
La présence de glace d’eau cristalline à la surface de certains OTNs donne des contraintes très fortes sur les mécanismes d’évolution (altération et/ou renouvellement) de leur surface. En effet, l’eau cristalline indique des températures supérieures à 110/120 K, nécessaires pour cristalliser la glace d’eau amorphe, alors que les températures attendues à la surface des OTNs sont certainement plus froides (20-60 K). De plus, à ces températures, la glace d’eau initialement cristalline est facilement convertie en glace amorphe par irradiation. Les processus de cryovolcanisme ou radiogéniques ont été invoqués pour expliquer la présence de la glace à l’état cristallin (Jewitt and Luu, 2004), aussi bien que les micro-impacts (Gil-Hutton et al. 2009), qui pourraient en effet se révéler efficaces dans le cas des objets de diamètre <800km.

Un exemple typique d’objet ayant de la glace d’eau est Orcus (2004 DW). J’ai acquis le tout premier spectre de ce transneptunien en février-mars 2004, peu de temps après sa découverte, au télescope TNG. Bien qu’il s’agisse d’un télescope de classe moyenne (diamètre de 3.5m), le TNG est équipé du spectrographe NICS avec le prisme d’Amici à basse résolution mais avec une haute efficacité (capture de 80-90% de la lumière incidente), permettant ainsi d’observer des objets jusqu’à une magnitude V = 19,5 dans les régions visible et proche infrarouge. Les spectres obtenus avaient une réflectance neutre dans le visible (couleur similaire au soleil), et montraient deux bandes d’absorption centrées à 1,5 et 2 micron dues à la glace d’eau amorphe. Les modèles de composition de surface donnaient une abondance de la glace d’eau jusqu’à 11% (Fornasier et al. 2004c). De nombreux spectres d’Orcus ont été acquis par la suite avec les grands télescopes de classe 8 m (VLT, KECK), aussi au sein de *Large Programme*. Grâce au meilleur rapport signal sur bruit et à la bien meilleure résolution spectrale comparé au TNG, nous avons aussi détecté sur les spectres d’Orcus l’absorption à 1,65 micron due à la glace d’eau cristalline, et à 2,2 micron, peut-être due à la glace d’ammoniac (Barucci et al. 2008b, Demeo et al. 2010, Delsanti et al. 2010).

Un autre OTNs montrant des bandes d’absorption dues à la glace d’eau est Quaoar. Sa composition a été contrainte avec un mélange intime comprenant les glaces d’eau cristalline et amorphe, de méthane, d’azote, d’éthane et des composés organiques (tholines) (Dalle Ore et al. 2009).
Éris, la plus grande des planètes naines, a été observée à plusieurs reprises et semble être composée essentiellement de méthane dilué dans l’azote, que nous avons détecté indirectement à partir de

la position en longueur d'onde de certaines bandes du méthane (Merlin et al. 2009). Les données indiquent une probable stratification du méthane pur et dilué en surface (couche de méthane pur sur méthane dilué), avec de l'azote qui, à grande distance, serait le seul constituant à se volatiliser et laisserait une couche de méthane appauvrie en azote.

Pour conclure, nous avons mené une étude statistique sur les propriétés de surface des 40 objets observés durant le *Large Programme*, en fonction de leur classe dynamique mais également en fonction de leur classe taxonomique. Ainsi l'ensemble des objets de la classe BB, qui représentent les objets les plus bleus dans le visible, semblent posséder de la glace en surface. Les objets intermédiaires de classe IR, associés uniquement aux trans-neptuniens résonnants et classiques, ne semblent pas présenter de surfaces riches en glace. Enfin, les objets les plus rouges (RR) et les modérément rouges (BR) sont indistinctement recouverts ou non de glace. Une partie des objets les plus rouges ont la particularité de posséder dans certains cas de la glace de méthanol (Barucci et al. 2011).
Ces observations confirment la grande diversité des objets au sein des mêmes populations dynamiques et aussi parfois taxonomiques. Elles montrent également que la couleur d'un objet n'est pas en soit un traceur de la glace d'eau en surface mais pourrait l'être concernant les glaces de méthanol ou de méthane. Subissant les effets de l'irradiation, ces espèces peuvent donner naissance à des espèces organiques plus ou moins rougeâtres. Par contre, les objets très bleus ou neutres dans le visible ont presque tous de la glace d'eau en surface.

5.5.1 Article : Water ice on the surface of the large TNO 2004 DW

5.5.2 Article : Visible spectroscopy of the new ESO *Large Programme* on trans-Neptunian objects and Centaurs : final results

A&A 422, L43–L46 (2004)
DOI: 10.1051/0004-6361:20048004

Astronomy & Astrophysics

Water ice on the surface of the large TNO 2004 DW*

S. Fornasier[1], E. Dotto[2], M. A. Barucci[3], and C. Barbieri[1]

[1] Astronomical Department of Padova, Vicolo dell'Osservatorio 2, 35122 Padova, Italy
e-mail: [fornasier;barbieri]@pd.astro.it
[2] INAF - Osservatorio Astronomico di Roma, via Frascati 33, 00040 Monte Porzio Catone (Roma), Italy
e-mail: dotto@mporzio.astro.it
[3] LESIA, Observatoire de Paris, 92195 Meudon Pricipal Cedex, France
e-mail: antonella.barucci@obspm.fr

Received 14 May 2004 / Accepted 15 June 2004

Abstract. We have obtained visible and near infrared spectra of the Trans Neptunian object 2004 DW, a few days after its discovery, at the Telescopio Nazionale Galileo (TNG). 2004 DW belongs to the plutino dynamical class and has an estimated diameter of about 1600 km, that makes it the largest known object, except Pluto, in the plutino and classical TNO populations. Our data clearly show the 1.5 and 2 μm bands associated to water ice, while the visible spectrum is nearly neutral and featureless. To interpret the available data we modelled the surface composition of 2004 DW with two different mixtures of organics (Titan tholin and kerogen), amorphous carbon and water ice.

Key words. Kuiper Belt – techniques: spectroscopic

1. Introduction

The Trans Neptunian Objects (TNOs), called also Edgeworth-Kuiper Objects, are presumed to be remnant planetesimals of the solar system nebula. Together with the comet nuclei, they represent the most pristine and thermally unprocessed bodies in the Solar System. Their study can provide important information about the conditions present in the early Solar System.

The knowledge of the physical properties and the surface composition of these objects is still limited (Barucci et al. 2004). After the discovery of 1992 QB1, the known TNO population is rapidly growing thanks to powerful discovery programs: to date more than 800 bodies have been discovered. Nowadays we know five TNOs (in addition to Pluto and Charon) with size bigger or around 1000 km: 20000 Varuna (900 ± 140 km, Jewitt et al. 2001), 55565 2002 AW197 (890 ± 120 km, Margot et al. 2002), 50000 Quaoar (1260 ± 190 km, Brown & Trujillo 2004a) and the recently discovered 2004 DW and 2003 VB12 Sedna, whose diameters are estimated to be around 1600 km. 2004 DW is a slow-moving body discovered on February 17, 2004 by Brown et al. (2004a). It is the brightest known object in the plutino and classical TNO populations after Pluto and Charon, with an absolute magnitude $H = 2.2$ (assuming a slope parameter $G = 0.15$). It belongs to the plutino dynamical class, as it is in the 3:2 resonance with Neptune, with orbital characteristics shown in Table 1.

Table 1. Orbital characteristics of the plutino 2004 DW.

perihelion distance (AU)	30.871
aphelion (AU)	48.075
semimajor axis (AU)	39.473
eccentricity	0.218
inclination (degrees)	20.6
orbital period (years)	248.01

No measurement of the 2004 DW albedo is yet available. The known TNO albedos range from 0.04 to 0.12 and, assuming a mean value of 0.09, the derived diameter of 2004 DW is around 1600^{+800}_{-230} km, larger than those of Charon and 50000 Quaoar. Only 2003 VB12 Sedna, discovered on March 15, 2004 seems to have a similar size, but, with a perihelion of 76 AU, it is an atypical TNO, not a classical nor a scattered object. Sedna is probably a member of a substantial population of bodies trapped between the Kuiper Belt and the Oort Cloud (Brown et al. 2004b).

In this paper we present the results of the visible and near infrared spectroscopic investigation of 2004 DW together with two possible compositional models that match its spectral behaviour.

* Bases on observations obtained at the Telescopio Nazionale Galileo, La Palma, Spain.

Table 2. Observational circumstances: the starting and final time of observations (date and universal time), the total exposure time, the instrument used, the airmass value at the beginning and at the end of the acquisitions, and the observed solar analog stars with their airmass used to remove the solar contribution.

Object	UT_{start}	UT_{end}	Exp (min.)	INSTR.	Airm.	Solar analog (airm.)
2004 DW	29 Feb. 04, 23:42	1 Mar. 04, 00:39	50	DOLORES	1.18–1.19	La102-1081 (1.17)
2004 DW	1 Mar. 04, 02:15	1 Mar. 04, 03:54	56	NICS	1.40–2.10	La102-1081 (1.46)
2004 DW	1 Mar. 04, 23:56	2 Mar. 04, 01:31	64	NICS	1.18–1.28	mean of La98-978 (1.21) and La102-1081 (1.14)

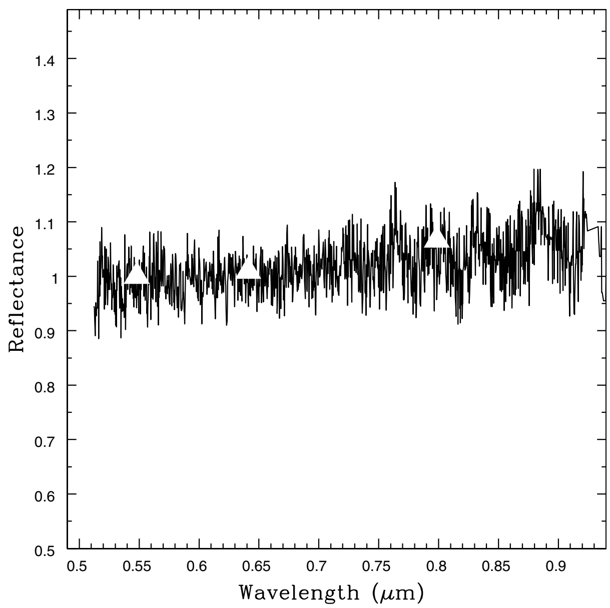

Fig. 1. Visible spectrum of 2004 DW, normalized at 0.55 μm. The $V-R$ and $V-I$ colors derived by Rabinowitz et al. (2004), transformed in spectral reflectance, are also shown on each spectrum as white triangles. The spectrum is in perfect agreement with these color indices.

2. Observations and data reduction

Observations have been made at the 3.56 m Telescopio Nazionale Galileo (TNG) in La Palma, Canary Islands, between February 29 and March 2, 2004. The TNO had an estimated visual magnitude of 19.2 during the observations, as given by the Minor Planet Center ephemeris service. A 1.5 arcsec wide slit, oriented along the parallactic angle to minimize the effect of atmospheric differential refraction, has been used both for the visible and near infrared observations.

For visible spectroscopy we used the DOLORES (Device Optimized for the LOw RESolution) instrument equipped with the low resolution red grism (LR-R) covering the 0.51–0.98 μm range with a spectral dispersion of 2.9 Å/px (`http://www.tng.iac.es`). During the observing run we also acquired bias, flat–field, calibration lamp (Ne-Ar lines) and several solar analog spectra.

The observational circumstances are summarized in Table 2.

The TNO has been identified by taking two images in the V filter separated by about 90 min. In order to make sure we always kept the object in the middle of the slit, the total exposure time was divided into 3 acquisitions of respectively 20, 15 and 15 min. This allowed us to check the asteroid position inside the slit before each acquisition and to reduce the cosmic rays hits on each spectrum. Spectra were reduced using standard data reduction procedures (Fornasier et al. 1999) with the software package Midas. The reflectivity of the TNO was obtained by dividing its total spectrum (mean of the 3 acquisitions) by that of the solar analog star Landolt 102-1081, observed just before the TNO and at very similar airmass.

The reflectance spectrum has been normalized at 0.55 μm and finally smoothed with a median filter technique (Fig. 1).

For the infrared spectroscopic investigation we used the near infrared camera and spectrometer (NICS) equipped with an Amici prism disperser (Oliva 2000). This equipment allows to cover the 0.85−2.40 μm range during a single exposure with a spectral resolution of about 35. The detector is a 1024 × 1024 pixel Rockwell HgCdTe Hawaii array.

The acquisition procedure consisted of a series of 8 cycles of 4 images each (ABBA cycle), for a total exposure time of 64 min. The spectral acquisitions have an exposure time of 120 s each, and were taken in two different positions along the slit, named A and B, offsetting the telescope by 30 arcsec. This technique allows to produce near-simultaneous images for sky subtraction.

A first attempt to get an infrared spectrum was made on March 1st, 2004 just after the visible observations, but this first spectrum, although still useful, has a low signal to noise ratio, because during the exposure time the object reached high airmasses values. Furthermore the solar analog star Landolt 102-1081 was observed just after 2004 DW, but at a different airmass, so the TNO spectrum could be affected by errors in the extinction correction process due to the large variation of the airmass.

We repeated the infrared observations of 2004 DW on the following night, investigating the TNO for about 64 min near its meridian passage. The observing conditions are shown in Table 2. We observed the solar analog stars Landolt 98-978 and Landolt 102-1081 just before and after the TNO investigation.

Data reduction was performed in the standard way for IR observations (Fornasier et al. 2003), except for wavelength calibration where we used a look-up table which is based on the theoretical dispersion predicted by ray-tracing and adjusted to best fit the observed spectra of calibration sources. Finally, the extinction correction and solar removal was obtained by division of the TNO spectrum with that one of the solar analog star.

For the March 1st night we used the Landolt 102-1081 star acquired just after the TNO observations, while for the March 2nd night we used the mean spectrum of the Landolt stars 98-978 and 102-1081 acquired before and after the TNO. To improve the signal to noise ratio, the March 1st spectrum has been smoothed with a gaussian filtering of $\sigma = 3.8$ pixel, providing a final spectral resolution of about 24.

The final infrared spectra are shown in Fig. 2, while in Fig. 3 we represent the full visible and near infrared spectra (infrared spectrum from the March 2nd data), scaled in order to be both normalized at 0.55 μm.

3. Discussion and conclusion

The 2004 DW visible spectrum is represented in Fig. 1: it is practically flat and it does not show any absorption feature, with a behaviour very similar to the typical spectrum of an anhydrous C-type asteroid. We computed the slope of the continuum of the visible spectrum using a standard least square technique for a linear fit of the spectrum in the wavelength range between 0.52 and 0.82 μm. The obtained slope is $1.79 \pm 0.2\%/10^3$ Å. Comparing this value with all the published TNO visible spectral slopes (Fornasier et al. 2004), 2004 DW has one of the smallest values in the TNO population. The spectrum is in good agreement with the $V-R$ (0.37 ± 0.04) and $V-I$ colors (0.76 ± 0.05), transformed into spectral reflectance (Fig. 1), derived by Rabinowitz et al. (2004) on Feb. 26, 2004.

The near-infrared spectra are shown in Fig. 2. The absorption bands around 1.5 and 2.0 μm associated to water ice are evident in the March 2nd spectrum, and seem to be present also on the March 1st spectrum, despite its poor signal to noise ratio and possible errors in the extinction correction procedure.

In order to investigate the possible surface composition of 2004 DW we attempt to reproduce the spectral behaviour by obtaining synthetic spectra of different geographical mixtures (spatially segregated) of minerals, ices and organic compounds at different grain dimensions. In doing this we made the assumption that the TNO has a homogeneous surface composition and/or that our combined visible and near infrared spectra, acquired in two different nights and not simultaneously, are representative of the same reflecting surface. We obtained two models (Fig. 3), with different values of albedo, which well reproduce the V and NIR observed spectra and the signatures at 1.5 and 2 μm. The first one (dashed line) is composed by a geographical mixture of 38% of kerogen (10 μm size), 60% of amorphous carbon (10 μm size), and 2% of water ice (20 μm size), corresponding to an albedo of 0.044 at 0.55 μm. The second one (continuous line) is composed of 4% of Titan tholin (7 μm size), 85% of amorphous carbon (10 μm size), and 11% of water ice (10 μm size), corresponding to an albedo of 0.102 at 0.55 μm. This is only an attempt to analyse the surface composition of this body and the knowledge of the albedo value is necessary to better constrain the obtained compositional models.

Although ices are expected to be a major constituent of TNOs and Centaurs, few spectra of these bodies reveal features attributable to water ice. First evidence of the presence of water ice was detected on the TNO 1996 TO66 infrared spectrum by Brown et al. (1999). The same signatures were found also on the TNOs 20000 Varuna (Licandro et al. 2001), 50000 Quaoar (Brown & Trujillo 2004b) and on the Centaurs 10199 Chariklo (Brown & Koresko 1998; Brown et al. 1998; Dotto et al. 2003a), 2060 Chiron (Luu et al. 2000), 5145 Pholus (Brown 2000), and possibly on one spectrum of 32532 Thereus (Barucci et al. 2002). Features attributable to hydrocarbons have been identified only on 5145 Pholus and 50000 Quaoar: Pholus shows absorption bands possibly attributable to frozen methanol and/or some products of methanol (Cruikshank et al. 1998; Brown 2000), while Quaoar shows distinct absorption features of crystalline water ice, CH_4 and possibly CO_2 (Brown & Trujillo 2004b).

Although 2004 DW is one of the biggest TNOs observed up to now, its spectral behaviour is not peculiar, but it is very similar to that of several other TNOs and Centaurs (Dotto et al. 2003b, and reference therein). Some other components could be present on the surface of this TNO, including both unaltered materials and/or more complex irradiation products as obtained by laboratory experiments by Strazzulla et al. (2003). Further investigations of 2004 DW with an higher resolution and the knowledge of its albedo will help in the fuller comprehension of its spectral properties.

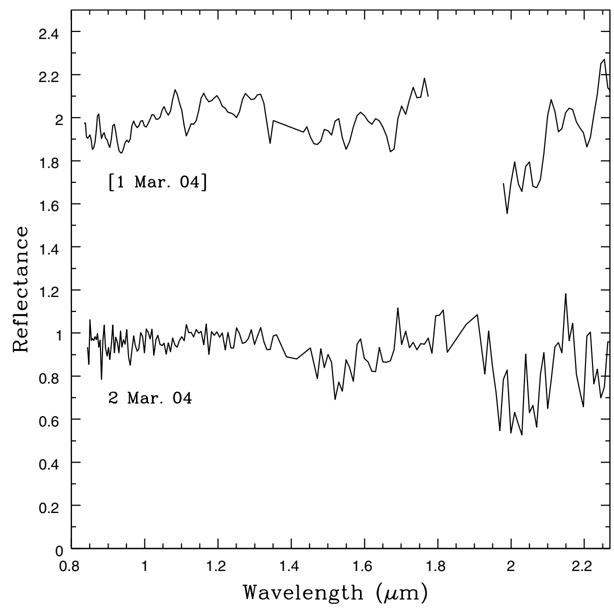

Fig. 2. Infrared spectra of 2004 DW. We show both the spectrum obtained during the 1−2 March night (lower spectrum), and that acquired the 29 February–1 March night (upper spectrum). This last one has been gaussian filtered to improve the signal to noise ratio and could be affected by errors in the extinction correction process, as explained in the text (we also cut the data in the 1.8–2 μm region due to an incomplete removal of the strong telluric water band). The spectra have been normalized at 1.25 μm and the upper one is shifted of 1 for clarity. The water ice absorption bands around 1.5 and 2 μm are clearly visible on the March 2nd spectrum, and seem to be present also on the March 1st one.

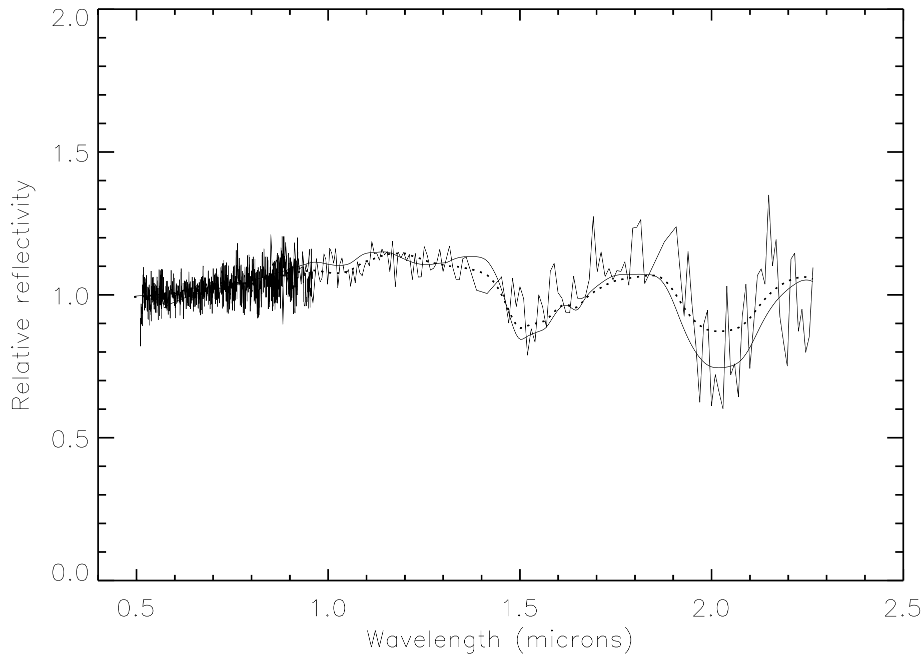

Fig. 3. Visible and near infrared (March 2nd data) spectra of 2004 DW (normalized at 0.55 μm) with superimposed two different compositional models. The dashed line shows the model composed by 38% of kerogen (10 μm size), 60% of amorphous carbon (10 μm size), and 2% of water ice (20 μm size), corresponding to an albedo of 0.044 at 0.55 μm. The continuous line shows the model composed of 4% Titan tholin (7 μm size), 85% of amorphous carbon (10 μm size), and 11% of water ice (10 μm size), corresponding to an albedo of 0.102 at 0.55 μm.

Acknowledgements. S.F. thanks the support astronomer F. Ghinassi for her help during the observations and J. Licandro for interesting discussions and useful suggestions for the observing set-up and procedures.
This paper is based on observations made with the Italian Telescopio Nazionale Galileo (TNG) operated on the island of La Palma by the *Centro Galileo Galilei* of the *INAF (Istituto Nazionale di Astrofisica)* at the Spanish *Observatorio del Roque de los Muchachos* of the *Instituto de Astrofisica de Canarias*.

References

Barucci, M. A., Doressoundiram, A., & Cruikshank, D. P. 2004, in Comets II, ed. M. Festou et al., University of Arizona Press., in press
Barucci, M. A., Boenhardt, H., Dotto, E., et al. 2002, A&A, 392, 33
Brown, R. H., Cruikshank, D. P., Pendleton, Y., & Veeder, G. J. 1998, Science, 280, 1430
Brown, M. E., & Koresko, C. D. 1998, AJ, 505, L65
Brown, R. H., Cruikshank, D. P., & Pendleton, Y. 1999, ApJ, 519, L101
Brown, M. E. 2000, AJ, 199, 977
Brown, M. E., & Trujillo, C. A. 2004a, AJ, 127, 2413
Brown, M. E., & Trujillo, C. A. 2004b, ApJL, submitted
Brown, M. E., Rabinowitz, D. L., Trujillo, C. A., Muller, J. J., & Marsden, B. G. 2004a, Minor Planet Elect. Circ., 2004-D13
Brown, M. E., Trujillo, C. A., & Rabinowitz, D. L. 2004b, ApJL, in press
Cruikshank, D. P., Roush, T. L., Bartholomew, M. J., et al. 1998, Icarus, 135, 389
Dotto, E., Barucci, M. A., Leyrat, C., et al. 2003a, Icarus, 164, 122
Dotto, E., Barucci, M. A., & de Bergh, C. 2003b, in New frontiers in the Solar System: trans-neptunian objects, Comptes Rendus Physique, 4, ed. M. A. Barucci, Académie des Sciences Paris (Elsevier), 775
Fornasier, S., Lazzarin, M., Barbieri, C., & Barucci, M. A. 1999, A&AS, 135, 65
Fornasier, S., Barucci, M. A., Binzel, R. P., et al. 2003, A&A, 398, 327
Fornasier, S., Doressoundiram, A., Tozzi, G. P., et al. 2004, A&A, 421, 353
Jewitt, D., Aussel, H., & Evans, A. 2001, Nature, 411, 446
Licandro, J., Oliva, E., & Di Martino, M. 2001, A&A, 373, L29
Luu, J. X., Jewitt, D. C., & Trujillo, C. 2000, ApJ, 531, L151
Margot, J. L., Trujillo, C., Brown, M. E., & Bertoldi, F. 2002, BAAS, 34, 871
Oliva, E. 2000, Mem. Soc. Astron. Ital., 71, 861
Rabinowitz, D., Tourtellotte, S., Brown, M., & Trujillo, C. 2004, IAU Circ., 8295, 2
Strazzulla, G., Cooper, J. F., Christian, E. R., & Johnson, R. E. 2003, in New frontiers in the Solar System: trans-neptunian objects, Comptes Rendus Physique, 4, ed. M. A. Barucci, Académie des Sciences Paris (Elsevier), 809

A&A 508, 457–465 (2009)
DOI: 10.1051/0004-6361/200912582

Astronomy & Astrophysics

Visible spectroscopy of the new ESO large programme on trans-Neptunian objects and Centaurs: final results[⋆,⋆⋆]

S. Fornasier[1,2], M. A. Barucci[1], C. de Bergh[1], A. Alvarez-Candal[1,3], F. DeMeo[1], F. Merlin[1,4], D. Perna[1,5,6], A. Guilbert[1], A. Delsanti[1], E. Dotto[6], and A. Doressoundiram[1]

[1] LESIA, Observatoire de Paris, 5 Place J. Janssen, 92195 Meudon Pricipal Cedex, France
e-mail: sonia.fornasier@obspm.fr
[2] Université de Paris 7 *Denis Diderot*, 4 rue Elsa Morante, 75013 Paris, France
[3] European Southern Observatory, Casilla 19001, Santiago, Chile
[4] Department of Astronomy, University of Maryland, College Park, MD 20742, USA
[5] Università di Roma Tor Vergata, Italy
[6] INAF-Osservatorio Astronomico di Roma, via Frascati 33, 00040 Monteporzio Catone Roma, Italy

Received 27 May 2009 / Accepted 26 August 2009

ABSTRACT

Context. A second large programme (LP) for the physical studies of TNOs and Centaurs, started at ESO Cerro Paranal on October 2006 to obtain high-quality data, has recently been concluded. In this paper we present the spectra of these pristine bodies obtained in the visible range during the last two semesters (November 2007–November 2008) of the LP.

Aims. We investigate the spectral behaviour of the TNOs and Centaurs observed, and we analyse the spectral slopes distribution of the full data set coming from this LP and from the literature.

Methods. Spectroscopic observations in the visible range were carried out at the UT1 (Antu) telescope using the instrument FORS2. We computed the spectral slope for each observed object, and searched for possible weak absorption features. A statistical analysis was performed on a total sample of 73 TNOs and Centaurs to look for possible correlations between dynamical classes, orbital parameters, and spectral gradient.

Results. We obtained new spectra for 28 bodies (10 Centaurs, 6 classical, 5 resonant, 5 scattered disk, and 2 detached objects), 15 of which were observed for the first time. All the new presented spectra are featureless, including 2003 AZ84, for which a faint and broad absorption band possibly attributed to hydrated silicates on its surface has been reported. The data confirm a wide variety of spectral behaviours, with neutral-grey to very red gradients. An analysis of the spectral slopes available from this LP and in the literature for a total sample of 73 Centaurs and TNOs shows that there is a lack of very red objects in the classical population. We present the results of the statistical analysis of the spectral slope distribution versus orbital parameters. In particular, we confirm a strong anticorrelation between spectral slope and orbital inclination for the classical population. Nevertheless, we do not observe a change in the slope distribution at $i \sim 5°$, the boundary between the dynamically hot and cold populations, but we find that objects with $i < 12°$ show no correlation between spectral slope and inclination, as has already been noticed on the colour-inclination relation for classical TNOs. A strong correlation is also found between the spectral slope and orbital eccentricity for resonant TNOs, with objects having higher spectral slope values with increasing eccentricity.

Key words. methods: observational – methods: statistical – techniques: spectroscopic – Kuiper Belt

1. Introduction

The icy bodies in orbit beyond Neptune (trans-Neptunians or TNOs) and Centaurs represent the most primitive population of all the Solar System objects. They are fossil remnants of the formation of our planetary system and the investigation of their surface properties is essential for understanding the formation and the evolution of the Solar System. Since 1992, more than 1300 TNOs and Centaurs have been detected. The TNO population is dynamically classified into several categories (Gladman et al. 2008): classical objects have orbits with low eccentricities and semi-major axes between about 42 and 48 AU; resonant objects are trapped in resonances with Neptune, the majority of them located in or near the 3:2 mean motion resonance; scattered objects have high-eccentricity, high-inclination orbits and a perihelion distance near $q = 35$ AU; extended scattered disk (or detached) objects (SDOs) are located at distances so great that they cannot have been emplaced by gravitational interactions with Neptune. In addition, the Centaurs are closest to the Sun and have unstable orbits between those of Jupiter and Neptune. They seem to originate from the Kuiper Belt and should have been injected into their present orbits by perturbations from giant planets or mutual collisions.

The investigation of the surface composition of these icy bodies can provide essential information about the conditions in the early Solar System environment at large distances from the Sun.

Aiming at obtaining high-quality data of these populations, a large programme (LP) for the observation of Centaurs and TNOs was started using the facilities of the ESO/Very Large Telescope site at Cerro Paranal in Chile (P.I.: Barucci). More

[⋆] Based on observations obtained at the VLT Observatory Cerro Paranal of European Southern Observatory, ESO, Chile, in the framework of programs 178.C-0036.

[⋆⋆] Table 2 is only available in electronic form at http://www.aanda.org

Table 1. Observational conditions of the TNOs and Centaurs spectroscopically investigated.

Object	Date	UT	Δ [AU]	*r* [AU]	α [°]	$T_{\rm exp}$ [s]	airm.	Solar An. (airm.)	Slope [%/(10^3 Å)]
CENTAURS									
5145 Pholus	2008 Apr. 12	05:57:44	21.214	21.864	2.0	2600	1.21	Ld102−1081 (1.15)	48.6 ± 0.7
10199 Chariklo	2008 Feb. 04	07:57:47	13.301	13.395	4.2	900	1.10	Ld102−1081 (1.13)	10.4 ± 0.6
52872 Okyrhoe	2008 Feb. 04	06:33:30	4.879	5.800	3.8	1800	1.14	Ld102−1081 (1.13)	13.4 ± 0.6
55576 Amycus	2008 Apr. 12	03:43:14	15.206	16.056	2.0	2400	1.16	Ld102−1081 (1.15)	37.1 ± 0.9
120061 (2003 CO1)	2008 Apr. 12	04:48:44	10.180	11.122	1.8	2400	1.13	Ld102−1081 (1.15)	9.4 ± 0.6
2002 KY14	2008 Sep. 21	01:11:40	7.802	8.649	3.8	1200	1.25	Ld112−1233(1.12)	36.9 ± 0.7
2007 UM126	2008 Sep. 21	04:46:01	10.202	11.163	1.6	2400	1.10	Ld112−1233(1.12)	8.8 ± 0.7
2007 VH305	2008 Nov. 22	02:38:07	7.853	8.638	4.2	2400	1.18	Ld98−978 (1.20)	12.1 ± 0.7
2008 FC76	2008 Sep. 21	00:21:29	10.976	11.688	3.6	1800	1.29	Ld112−1233(1.12)	36.0 ± 0.7
2008 SJ236	2008 Nov. 22	00:53:58	5.522	6.364	5.0	4000	1.28	Ld93−101 (1.30)	20.9 ± 0.8
CLASSICALS									
20000 Varuna	2007 Dec. 04	06:41:41	42.606	43.392	0.8	2400	1.57	Hyades64 (1.41)	24.9 ± 0.6
120178 (2003 OP32)	2008 Sep. 21	02:26:48	40.545	41.365	0.8	2400	1.14	Ld112−1233(1.12)	0.9 ± 0.7
120348 (2004 TY364)	2008 Nov. 22	04:53:01	38.839	39.591	0.9	2400	1.27	Ld93−101 (1.30)	22.9 ± 0.7
144897 (2004 UX10)	2007 Dec. 04	01:10:32	38.144	38.836	1.0	2400	1.13	HD1368 (1.12)	20.7 ± 0.8
144897 (2004 UX10)	2007 Dec. 05	02:41:59	38.158	38.836	1.1	2400	1.19	Ld93101 (1.24)	19.2 ± 0.9
145453 (2005 RR43)	2007 Dec. 04	02:59:10	37.623	38.511	0.6	2400	1.12	HD1368 (1.12)	1.6 ± 0.6
174567 (2003 MW12)	2008 Apr. 12	07:17:41	47.318	47.968	0.9	3700	1.09	Ld102−1081 (1.10)	19.2 ± 0.6
RESONANTS									
42301 (2001 UR163)	2007 Dec. 05	01:10:23	49.625	50.308	0.8	2400	1.23	Ld93−101 (1.24)	50.9 ± 0.7
55638 (2002 VE95)	2007 Dec. 05	04:13:26	27.297	28.248	0.5	2400	1.21	Ld93−101 (1.24)	40.0 ± 0.7
90482 Orcus	2008 Feb. 04	05:25:24	46.901	47.807	0.5	2400	1.07	Ld102−1081 (1.11)	1.6 ± 0.6
208996 (2003 AZ84)	2008 Nov. 22	06:29:23	44.883	45.458	1.0	2800	1.30	Ld93−101 (1.30)	3.6 ± 0.6
2003 UZ413	2007 Dec. 04	04:42:24	41.171	42.004	0.7	2400	1.36	Hyades64 (1.41)	6.2 ± 0.6
2003 UZ413	2008 Sep. 21	05:46:16	41.469	42.163	1.0	2400	1.25	Ld112−1233(1.12)	5.0 ± 0.8
2003 UZ413	2008 Nov. 22	03:49:31	41.275	42.197	0.5	2400	1.15	Ld98−978 (1.17)	4.9 ± 0.7
SDOs									
42355 Typhon	2008 Apr. 12	01:07:02	16.892	17.650	2.2	1200	1.22	Ld102−1081 (1.15)	12.1 ± 0.8
44594 (1999 OX3)	2008 Sep. 21	03:22:39	22.023	22.889	1.3	2400	1.07	Ld110−361 (1.10)	36.2 ± 0.8
73480 (2002 PN34)	2007 Nov. 10	00:51:51	14.893	15.344	3.3	2800	1.22	LD115−871 (1.13)	15.8 ± 0.7
145451 (2005 RM43)	2007 Dec. 04	04:04:16	34.298	35.195	0.7	2400	1.15	HD1368 (1.12)	2.2 ± 0.7
2007 UK126	2008 Sep. 21	08:18:31	45.136	45.619	1.1	2400	1.07	Ld112−1233(1.12)	19.6 ± 0.7
DETACHED OBJECTS									
90377 Sedna	2008 Sep. 21	06:53:28	87.419	88.015	0.5	3600	1.20	Ld112−1233(1.12)	40.2 ± 0.9
120132 (2003 FY128)	2008 Apr. 12	02:32:57	37.477	38.454	0.3	2800	1.06	Ld102−1081 (1.10)	26.7 ± 1.0

Observational conditions: for each object we report the observational date and universal time (UT of the beginning of the exposure), the geocentric distance (Δ), the heliocentric distance (r), the phase angle (α), the total exposure time, the airmass (mean of the airmass value at the beginning and at the end of observation), the observed solar analogue stars with their airmass used to remove the solar contribution, and the spectral slope value computed in the 0.5−0.8 μm range. The TNOs and Centaurs observed in spectroscopy for the first time are in bold.

than 500 h were allocated to observe these objects in visible and near-infrared photometry-spectroscopy, and $V-R$ polarimetry from November 2006 until December 2008.

In this paper we report the results of the visible spectroscopy of TNOs and Centaurs performed with the instrument FORS2 at the VLT unit 1 *Antu* during the last two semesters of the LP (November 2007−November 2008). New visible spectra of 28 objects with $18.7 < V < 21.8$, were acquired, 15 of which were observed for the first time. A statistical analysis of the full data set of spectral slopes coming from this LP and from the literature is presented on a total sample of 73 TNOs and Centaurs.

2. Observations and data reduction

The data were obtained primarily during five runs in visitor mode on December 2007 and February, April, September, and November 2008. Only one object, 73480 (2002 PN34), was observed in service mode on November 10, 2007. All the details on the spectroscopic observations are given in Table 1. The spectra were obtained using a low-resolution grism (150 grooves/mm) with a 1 arcsec wide slit, covering the 4400−9300 Å wavelength range with a spectral resolution of about 200. The slit was oriented along the parallactic angle to minimise the effects of atmospheric differential refraction, which is also corrected by a system of two silica prisms up to an airmass of 1.4. The FORS2 detector is a mosaic of two 2K × 4K MIT/LL CCDs with pixel size 15 μm, corresponding to a pixel scale of 0.126″/px), used in a 2 × 2 binned mode and with the high-gain read-out mode (1.45 e^-/ADU).

During each night we also acquired bias, flat-field, calibration lamp (He-Ar), and several solar analogue star spectra at different intervals throughout the night. Spectra were reduced using normal data reduction procedures (see Fornasier et al. 2004a) with the software package Midas. The wavelength calibration was performed using helium, HgCd, and argon lamp spectral lines. The reflectivity of the objects was obtained by dividing their spectra by the spectrum of the solar analogue star closest in time and airmass, as reported in Table 1.

Spectra have been normalised to unity at 5500 Å and finally smoothed with a median filter technique, using a box width of 39 Å in the spectral direction for each point of the spectrum. Threshold was set to 0.1, meaning that the original value was replaced by the median value when this last differed by more than 10% from the original one. Finally, for each object we computed the slope S of the spectral continuum using a standard least squared technique for a linear fit in the wavelength range between 5000 and 8000 Å. The computed slopes and errors are listed in Table 1. The reported error bars take the 1σ uncertainty of the linear fit into account plus 0.5%/(10^3 Å) attributable to the use of different solar analogue stars.

Each night, immediately before spectral measurements, photometric data in the $V-R-I$ filters (except during the November and December 2007 runs, in which I filter observations were not taken) were obtained for each target, together with almost simultaneous photometric and spectroscopic observations in the near infrared with ISAAC and SINFONI instruments at VLT units 1 *Antu* and 4 *Yepun*. The results on V+NIR photometry are presented in Perna et al. (2009, in prep.), while the near infrared spectroscopic data are still under analysis.

The new spectra of the Centaurs and TNOs are shown in Figs. 1–5. In these figures we also plot the $V-R$ and $V-I$ (when available) colour indices converted to relative reflectance, colours that show nice agreement with the spectral gradient.

3. Results

We have obtained new spectra of 28 objects, 15 of which were observed in visible spectroscopy for the first time: 10 spectra of Centaurs (Figs. 1 and 2), 6 of classical TNOs (Fig. 3), 5 of resonants (4 plutinos plus 2001 UR163 which is in the 9:4 resonance with Neptune, Fig. 4), 5 scattered disk objects (SDOs) and two extended SDOs (Fig. 5). We distinguish the dynamical classes according to the Gladman et al. (2008) classification scheme. First of all, the wide variety in the spectral behaviour of both the Centaur and TNO populations is confirmed, since the spectral slopes span a wide range of colours, from grey to very red. All the objects have featureless spectra, with the exception of 10199 Chariklo and 42355 Typhon, whose spectra, showing faint absorption features, have already been investigated by Guilbert et al. (2009) and Alvarez-Candal et al. (2009). They are shown in this paper for completeness.

3.1. Centaurs

Six out of the 10 Centaurs observed have been spectroscopically observed for the first time (2007 UM126, 2007 VH305, 2008 SJ236, 2008 FC76, 2002 KY14 and 2003 CO1). All spectra are featureless except for 10199 Chariklo (discussed in Guilbert et al. 2009), and their spectral slopes range from 9 to 48%/(10^3 Å) (Figs. 1 and 2). For Chariklo, an absorption band centred at 0.65 μm, 0.3 μm wide and with a depth of 2% as compared to the continuum was identified on the February 2008 spectrum by Guilbert et al. (2009) and tentatively attributed to the presence of aqueous altered material on its surface. This detection confirms the possible feature of 1% depth reported by Alvarez-Candal et al. (2008) on a Chariklo spectrum acquired on March 2007.

The Centaurs' spectra are almost linear, but 4 objects (2008 SJ236, 2008 FC76, 2002 KY14 and 55576 Amycus) show a departure from a linear trend for wavelengths longer than 0.75 μm, as already noticed for some TNOs and Centaurs by Alvarez-Candal et al. (2008).

Comparing the spectral slopes of the objects previously observed in the literature (Table 2), we found a slightly higher slope value for 55576 Amycus, 10199 Chariklo, and 52872 Okyrhoe,

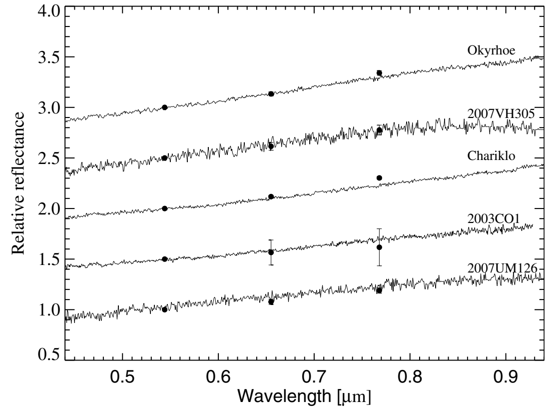

Fig. 1. Visible spectra of Centaurs. Spectra are shifted by 0.5 for clarity. The colour indices converted to spectral reflectance are also shown on each spectrum.

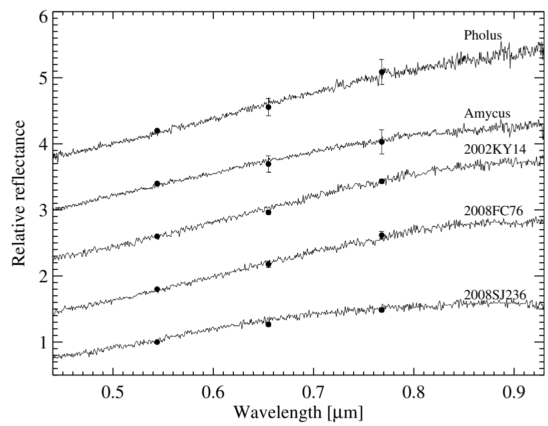

Fig. 2. Visible spectra of Centaurs. Spectra are shifted by 0.8 for clarity. The colour indices converted to spectral reflectance are also shown on each spectrum.

while for 5145 Pholus we find a value similar to the one published by Binzel (1992). Our spectral slopes are confirmed by the $V-R$ and $V-I$ colour indices obtained just before the spectroscopic observations (Figs. 1, 2). For 52872 Okyrhoe and 55576 Amycus, the difference in the spectral slopes are quite small and probably just related to the use of different solar analogue stars and/or to different observing and set-up conditions. For Chariklo, the different spectral behaviour shown both in the visible and near infrared regions was interpreted as coming from to surface heterogeneities (Guilbert et al. 2009).

3.2. Classical TNOs

The spectra of 6 classical TNOs are shown in Fig. 3, and all were observed in visible spectroscopy for the first time except 2005 RR43 and 2003 OP32, previously observed by Alvarez-Candal et al. (2008) and Pinilla-Alonso et al. (2008 and 2007). The spectral slopes range from 1 to 25%/(10^3 Å), and the values obtained in this work for 2005 RR43 and 2003 OP32 are in good agreement with those reported in the literature (Table 2). All the spectra are linear and featureless, and only 2004 UX10 shows a departure from linearity after 0.8 μm similar to what is seen on some Centaurs. 2004 UX10 was observed twice during the December 2007 run, and the two spectra are identical.

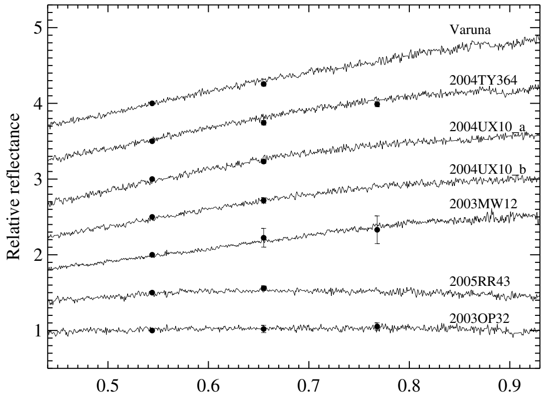

Fig. 3. Visible spectra of Classical TNOs. Spectra are shifted by 0.5 for clarity. The colour indices converted to spectral reflectance are also shown on each spectrum. 2004 UX10 was observed during two different nights: the spectrum labelled "a" was taken on 4 Dec. 2007, the one labelled "b" on 5 Dec. 2007.

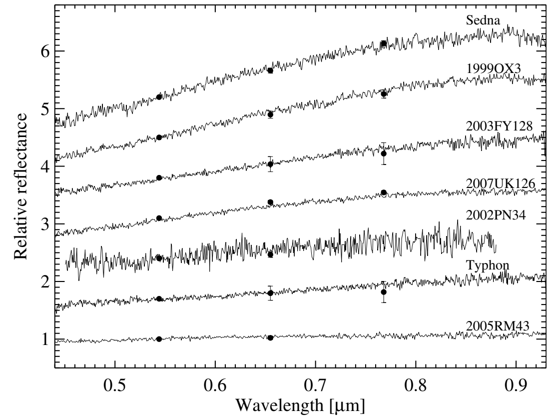

Fig. 5. Visible spectra of SDOs and detached objects (Sedna and 120132 2003 FY128). Spectra are shifted by 0.7 for clarity. The colour indices converted to spectral reflectance are also shown on each spectrum.

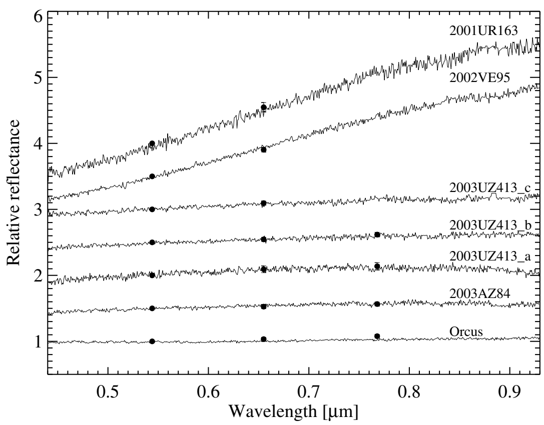

Fig. 4. Visible spectra of resonant TNOs. All are plutinos except 42301 (2001 UR163) which is in the 9:4 resonance with Neptune. We observed 2003 UZ413 during 3 different runs: the spectrum labelled "a" is from Sep. 2008, "b" from Nov. 2008, and "c" from Dec. 2007. Spectra are shifted by 0.5 for clarity. The colour indices converted to spectral reflectance are also shown on each spectrum.

Varuna was observed spectrophotometrically by Lederer & Vilas (1993) with 5 filters in the visible region. The spectral slope value estimated from their Fig. 1 is ~46%/(10^3 Å), very different from the one obtained here (24.9%/(10^3 Å), see Table 2). Jewitt & Sheppard (2002) measured a rotational period of 6.34 h and significant photometric variation (0.42 mag in *R*) for Varuna suggesting a triaxial shape (Lacerda & Jewitt 2007). The different spectral slope values may stem from heterogeneities on the surface of this large TNO.

3.3. Resonant TNOs

Figure 4 shows the spectra of the 5 resonant TNOs observed. All have featureless spectra, and their spectral slope values range from 1 to 40%/(10^3 Å) for the plutinos, while 42301 2001 UR163, populating the 9:4 resonance with Neptune, has a very steep spectral slope (51%/(10^3 Å)). Orcus, 2003 AZ84, and 55638 (2002 VE95) were observed previously. The new spectral slope values obtained for Orcus and 2003 AZ84 are in agreement with those in the literature (see Table 2), while the values are different for 55638 (2002 VE95) and it is possible that this object has a heterogeneous surface. Despite the similarity of 2003 AZ84 spectral slope values obtained in different observing runs, the new spectrum of 2003 AZ84 is featureless, while a weak band centred on 0.7 μm with a depth of about 3% with respect to the continuum and a width of more than 0.3 μm was reported by Fornasier et al. (2004a). This feature was also detected by Alvarez-Candal et al. (2008) on the January 2007 data acquired during this LP.

We processed the 3 available spectra of 2003 AZ84 (March 2003, January 2007, and November 2008) by removing a linear continuum, computed by a linear fit in the 0.46 and 0.88 μm wavelength range. The spectra after the continuum removal are plotted in Fig. 6: the new data on 2003 AZ84 do not show any absorption band, except for some small features that are clearly residuals of the background removal (in particular the O_2A band around 0.76 μm and the water telluric bands around 0.72 μm and 0.83 μm). It is possible that 2003 AZ84 has a heterogeneous surface composition. Its rotational period is 6.71 or 6.76 h for a single-peaked solution or 10.56 h for a double-peaked solution (Sheppard & Jewitt 2003; Ortiz et al. 2006). A small satellite 5 mag fainter than the primary is reported by Brown & Suer (2007) with HST observations. The satellite flux is only 1% of the primary flux, assuming a similar albedo value (0.12, Stansberry et al. 2008), so it is unlikely that it would affect the spectral behaviour of 2003 AZ84.

We observed 2003 UZ413 during three different runs because it is a peculiar TNO with estimated high density, a lightcurve amplitude of 0.13 ± 0.03 mag, and a fast rotational period of 4.13 ± 0.05 h (Perna et al. 2009), presently the second fastest rotator among TNOs after 136108 Haumea, which has a rotational period of 3.9155 ± 0.0001 h (Lacerda et al. 2008). The 3 spectra were obtained in December 2007, September 2008, and November 2008. Since the December 2007 observations were taken very close in time (1 day apart) to the determination of 2003 UZ413 rotational period, we can derive their position on the lightcurve precisely, that is at 0.64 of the phase curve (see Fig. 5 in Perna et al. 2009), on the second peak. Using the current accuracy in the rotational period determination, the 2008 September and November observations are located at 0.49 (just after the first minimum) and 0.78 (just before the second minimum) of the phase curve, respectively (but with some uncertainty as the observations were obtained far away from the time of the rotational period determination). Our observations

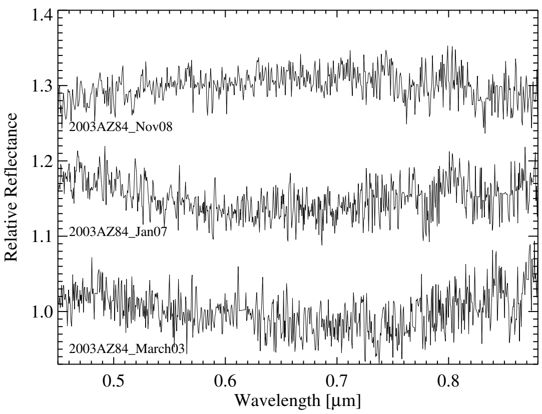

Fig. 6. Visible spectra of 2003 AZ84 taken during 3 different observing runs, after continuum slope removal. No indication of the band seen in the March 2003 and Jan. 2007 data appears in the spectrum obtained on Nov. 2008.

span less than 1/3 of the rotational period and therefore less than 1/3 of the surface. The 2008 September and November spectra have very similar spectral slope values (5.0 and 4.9%/(10^3 Å), respectively), while the 2007 December spectrum has a slightly higher value (6.2%/10^3 Å). Although the 3 values are within the uncertainties, the higher spectral gradient corresponding to the spectrum acquired at the peak of the lightcurve could indicate surface inhomogeneity. It is worth noting that the very fast spinning Haumea shows evidence of surface heterogeneity (Lacerda et al. 2008, 2009). Further observations covering the whole rotational period of 2003 UZ413 are needed to confirm that the spectral variation on its surface is real and that it may display surface variability.

3.4. SDOs and detached objects

The spectra of the 7 SDOs and detached objects are shown in Fig. 5. The objects 145451 (2005 RM43), 73480 (2002 PN34), and 2007 UK126 were spectroscopically observed for the first time. The spectral slope values range from 2 to 40%/10^3 Å. For the objects previously observed in the literature, there is good agreement for the spectral slope of Sedna, while for Typhon, 2003 FY128, and above all 44594 (1999 OX3), the values are different (Table 2). Our spectra agree with the colours converted to reflectance (Fig. 5), and likewise for the spectra already published in the literature with their associated broadband colours. It is possible that Typhon and 2003 FY128, which have rotational periods estimated to be longer than 5 and 7 h respectively (Dotto et al. 2008), and 1999 OX3 (period not yet determined) have inhomogeneous surface compositions.

For 42355 Typhon, a faint absorption feature, similar to that identified on Chariklo, was noticed by Alvarez-Candal et al. (2009). This band is centred on 0.62 μm with a depth of 3% as compared to the continuum, and is similar to the subtle broad feature reported previously by Alvarez-Candal et al. (2008) on the 2007 January spectrum of Typhon. The identified shallow broad feature resembles absorption bands detected on some main belt dark asteroids (Vilas et al. 1994; Fornasier et al. 1999), and is attributed to the presence of minerals on their surface produced by the aqueous alteration of anhydrous silicates.

4. Discussion

TNOs and Centaurs reveal an extraordinary spectral variety, as already noticed by several authors from the broadband photometry carried out on a larger sample of objects (Tegler et al. 2008; Doressoundiram et al. 2008, and reference therein). In the visible wavelength range, most of them have featureless and linear spectra, with spectral gradients from neutral-grey to very red. A few of them reveal some absorption bands: two very large bodies (Eris and Makemake, beside Pluto) show strong features due to methane ice (Brown et al. 2008, and reference therein); Haumea might have a band at 0.5773 μm, possibly due to O_2 ice that needs to be confirmed (Tegler et al. 2007); and five bodies seem to show faint absorption bands attributed to aqueous alteration processes. Two of these objects are Chariklo and Typhon, already discussed in the previous section. The other three bodies are 47932 (2000 GN171) and 38628 Huya (2000 EB173) (Lazzarin et al. 2003), and 208996 (2003 AZ84) (Fornasier et al. 2004a). For 47932 and Huya, the feature has never been confirmed (de Bergh et al. 2004; Fornasier et al. 2004a; Alvarez-Candal et al. 2008), even when observing more than half of the rotational period of 47932, and this was interpreted as the result of surface composition heterogeneities during the TNO's rotation.

For 2003 AZ84, the weak feature centred around 0.7 μm reported by Fornasier et al. (2004a) was also detected by Alvarez-Candal et al. (2008) on data acquired during this LP on January 2007, but is not confirmed in these more recent observations (Figs. 4 and 6). Again it is possible that the surface of this plutino is not homogeneous.

The features identified on these bodies, most of all on Typhon, Chariklo and 2003 AZ84, are very faint and look similar to those seen on some low albedo main belt asteroids that have been attributed to hydrated silicates. How aqueous alteration processes could have occurred in the outer solar System is not well understood, and it is also possible that some hydrated minerals formed directly in the solar nebula. A complete discussion about the possible effect of the aqueous alteration process on TNOs and Centaurs is reported in de Bergh et al. (2004).

For a better analysis of the spectral slope distribution for Centaurs and TNOs we collected all the visible spectral slopes obtained from spectroscopy available from this work and in the literature (Table 2). Including also the six classical TNOs 86047 (1999 OY3), 86177 (1999 RY215), 181855 (1998 WT31), 1998 HL151, 2000 CG105, and 2002 GH32, whose spectral slope gradient evaluated from spectrophotometry is presented in Ragozzine & Brown (2007, and reference therein), we get a sample of 20 Centaurs and 53 TNOs (14 resonants, 29 classicals, 6 SDO and 4 detached objects, including the dwarf planet Eris). For objects reported in Table 2 with more than one observation we used a weighted mean of the spectral slope values.

For a clearer analysis of the Centaurs and TNOs spectral slope distribution we show in Fig. 7 the number of objects as a function of spectral slope for the 4 distinct dynamical groups: Centaurs, resonants, classicals, and a group including both scattered and detached TNOs.

In Fig. 7 it is evident that there is a lack of very red objects in the classical TNOs investigated, as all have spectral slopes lower than 35%/10^3 Å, and they also show a lower spectral slope mean value compared to the other classes (Table 3). More than half of the classical population (51.7%) has $S < 13\%/10^3$ Å and is peaked at neutral-grey colours (mean slope value of 3.4%/10^3 Å), and the remaining part shows medium-red spectra with a mean slope value of 24.9%/10^3 Å.

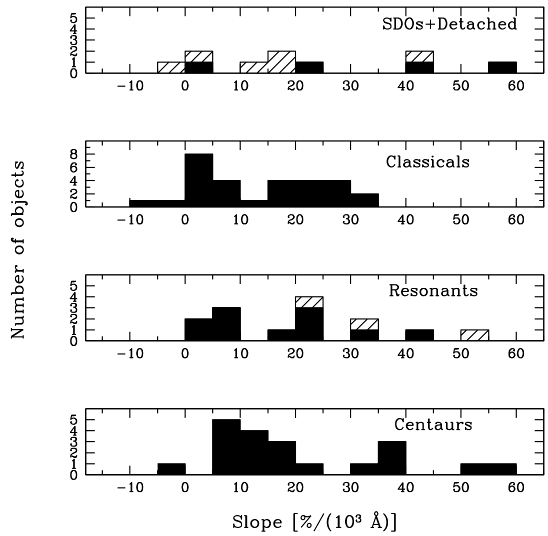

Fig. 7. Distribution of TNOs and Centaurs as a function of the spectral slope. The sample comprises 20 Centaurs, 14 Resonants of which 11 are plutinos (black histogram), and 3 are in the resonances 11:2, 5:2 and 9:4 with Neptune (hatched areas), 29 Classicals, 6 SDOs (hatched areas) and 4 detached bodies.

The Centaurs, resonants, and SDOs-detached objects have very similar mean spectral slope values (Table 3), and most of them have neutral to moderately red slopes (~70% of the population of each class has $S < 24.0\%/10^3$ Å). Our limited dataset based on spectral slope does not clearly show a bimodal distribution for the Centaurs as seen with photometric colours on a larger sample by several authors (Tegler et al. 2008, and references therein).

The whole sample (TNOs+Centaurs) has a mean slope value of $17.9\%/10^3$ Å. The majority of the bodies (54 out of 73, that is 74% of the sample) has $S < 25\%/10^3$ Å, 17.8% of the sample has $25 < S < 40\%/10^3$ Å, and only 8.2% has a very red spectral slope value ($S > 40\%/10^3$ Å). About 20% of the bodies show neutral to grey spectral behaviour ($-2 < S < 5\%/10^3$ Å).

It has been claimed that the Kuiper Belt is a possible source of Jupiter Trojans, which would have been formed there and then trapped by Jupiter in the L4 and L5 Lagrangian points during planetary migration (Morbidelli et al. 2005). Fornasier et al. (2007) analysed a sample of 146 Jupiter Trojans (68 L5 and 78 L4) for which visible spectroscopy was available, and calculated an average slope of $9.15 \pm 4.19\%/10^3$ Å for objects populating the L5 swarm and $6.10 \pm 4.48\%/10^3$Å for the L4 ones. A comparison between the spectral slope distribution of Jupiter Trojans (Fig. 14 in Fornasier et al. 2007) and of Centaurs-TNOs (Fig. 7) shows that the Trojans' distribution is very narrow and distinguishable from that of Centaurs-TNOs. The Trojans' spectral gradient is similar only to the neutral-grey to moderately red objects in the Centaurs and TNOs population. The lack of red objects in the Trojan population compared to Centaurs and TNOs might reflect either an intrinsic different planetesimal composition with increasing heliocentric distances or a diverse degree of surface alteration and/or a different collisional history.

4.1. Statistical analysis

We ran a Spearman rank correlation (Spearman 1904) to look for possible correlations between spectral slope values (S) and orbital elements (inclination i, eccentricity e, and semimajor axis a) or absolute magnitude H inside the classical, resonant, and Centaur classes. The function calculating the Spearman correlation gives a two-element vector containing the rank correlation coefficient (ρ) and the two-sided significance of its deviation from zero (P_r). The value of ρ varies between −1 and 1: if it is close to zero this means no correlation, if $|\rho|$ is close to 1 then a correlation exists. The significance is a value in the interval $0 < P_r < 1$, and a low value indicates a significant correlation. We consider a strong correlation to have $P_r < 0.01$ and $|\rho| > 0.6$, and a weak correlation to have $P_r < 0.05$ and $0.3 < |\rho| < 0.6$.

For the 29 classical TNOs, we find an anticorrelation between S and i and a weaker anticorrelation between S and e (Table 4 and Figs. 8, 9). The anticorrelation between S and i was mentioned in Tegler & Romanishin (2000), first investigated by Trujillo & Brown (2002) and then by several

Table 3. Mean spectral slope values and standand deviation of TNOs and Centaurs.

Class	Mean [%/ (10³ Å)]	Std deviation [%/ (10³ Å)]
Centaurs	20.5	15.1
Classicals	13.8	12.1
Resonants	20.8	15.6
SDOs & Detached	21.1	18.3
all TNOs & Centaurs	17.9	14.8

Table 4. Spearman correlation.

Class	ρ	P_r	n
Centaurs			
S vs. i	–0.00451293	0.98495	20
S vs. e	0.430989	0.0578041	20
S vs. a	0.0691989	0.771903	20
S vs. H	0.398494	0.0818076	20
S vs. q	–0.0910117	0.702757	20
Classicals			
S vs. i	**–0.641537**	**0.000176407**	**29**
S vs. e	**–0.510963**	**0.00461781**	**29**
S vs. a	–0.109633	0.571303	29
S vs. H	–0.0892836	0.64510	29
S vs. q	0.430648	0.0196961	29
Resonants			
S vs. i	–0.393407	0.164032	14
S vs e	**0.767033**	**0.00136768**	**14**
S vs. a	0.560440	0.0371045	14
S vs. H	0.382838	0.176678	14
S vs. q	0.142857	0.626118	14
SDOs			
S vs. i	–0.542857	0.265703	6
S vs e	**–0.885714**	**0.0188455**	**6**
S vs. a	–0.657143	0.156175	6
S vs. H	0.0857143	0.871743	6
S vs. q	–0.0857143	0.871743	6
Detached Objs			
S vs. i	–0.200000	0.800000	4
S vs. e	0.00000	1.00000	4
S vs. a	–0.400000	0.600000	4
S vs. H	0.800000	0.200000	4
S vs. q	–0.400000	0.600000	4

Spearman correlation results of the spectral slope S, orbital parameters (inclination i, eccentricity e, semimajor axis a, perihelion q), and absolute magnitude H. ρ is the Spearman rank correlation, P_r is the significance level, and n the number of objectsused in the statistical analysis. Strongest correlations are in bold.

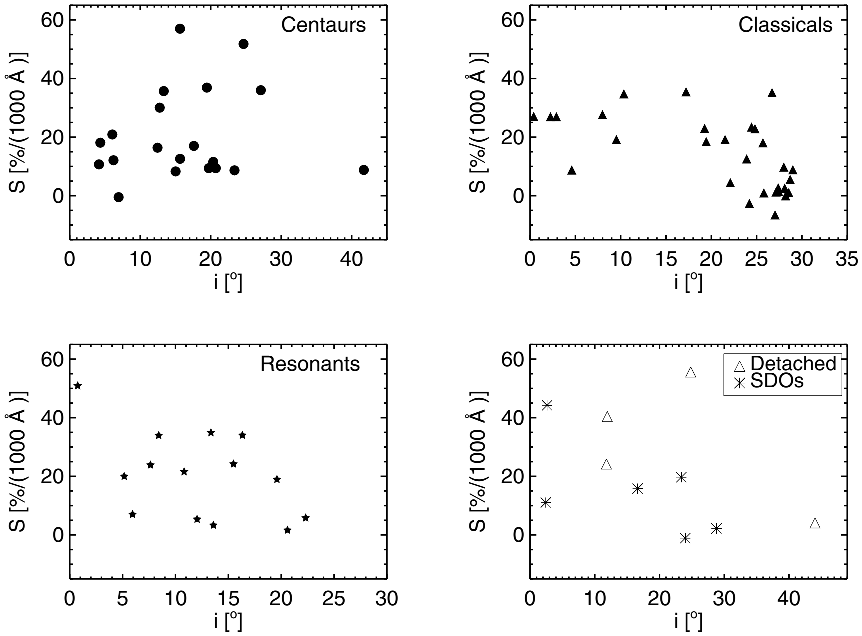

Fig. 8. Spectral slope versus orbital inclination. The sample comprises 20 Centaurs, 14 Resonants, 29 Classicals, 6 SDOs, and 4 detached bodies.

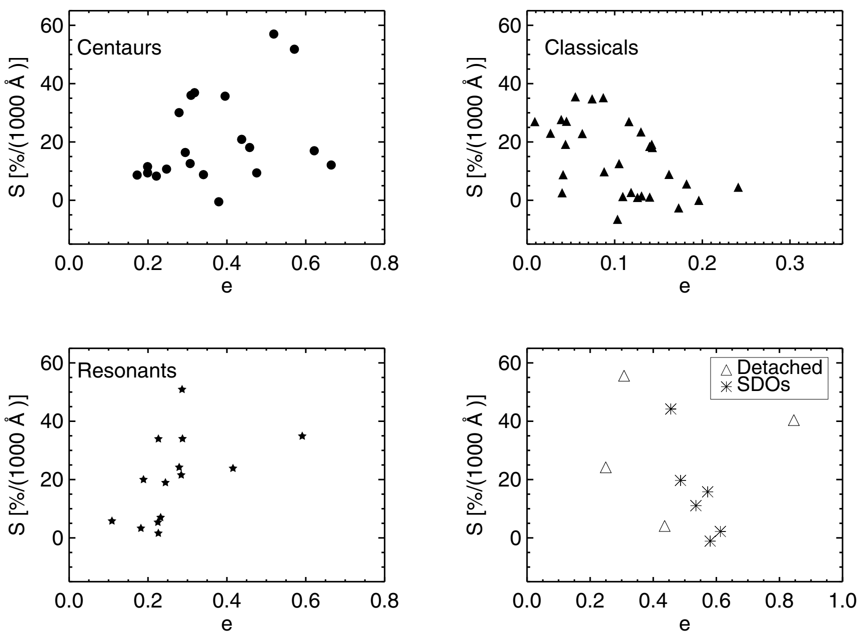

Fig. 9. Spectral slope versus orbital eccentricity. The sample comprises 20 Centaurs, 14 Resonants, 29 Classicals, 6 SDOs, and 4 detached bodies.

authors (see Doressoundiram et al. 2008, and references therein). This strong anticorrelation has also been recently confirmed by Santos-Sanz et al. (2009) and Peixinho et al. (2008) on a sample of 73 and 69 classical TNOs, respectively, investigated in photometry. Nevertheless, Peixinho et al. (2008) find that the optical colours are independent of inclination below $i \sim 12°$ and that they provide no evidence of a change in the $B - R$ colour distribution at the boundary between dynamically hot and cold populations (at $i \sim 5°$). Our smaller sample of classical TNOs has a gap in the inclination distribution for $\sim 10 < i < 17°$. If we consider the 7 objects with $i < 10.4°$, there is effectively no correlation between S and i ($\rho = 0.198206$ and $P_{\rm r} = 0.993299$), while the bodies with $i > 10.4°$ show an anticorrelation between S and i that is weaker than the one found for the entire sample ($\rho = -0.503106$ and $P_{\rm r} = 0.017000$), so our spectral data independently confirm the result by Peixinho et al. (2008) that classical TNOs with $i < 12°$ show no correlation between surface colour and inclination.

Classical TNOs with $e > 0.14$ have neutral to grey slopes, and there is a lack of red bodies (Fig. 9). The anticorrelation between S and e in the classical TNOs might be related to the weak correlation found between S and the perihelion distance q (Table 4). These correlations are mainly driven by the hot population (25 out of the 29 objects in the sample have $i > 5°$), so we can conclude that hot classicals show a neutral/blue spectral behaviour for increasing values of i and e, and they are also located at short perihelion distances. Similar results have been obtained by Santos-Sanz et al. (2009) analysing colours versus orbital elements. They interpreted the correlation between perihelion distances and colours as support for colouring scenarios: blue objects may be the results of resurfacing by fresh ices due to sublimation of volatiles or by micrometeoroid bombardment, as these mechanisms are more efficient at smaller perihelion distances.

The 5 Centaurs in the sample with inclination lower than 10° have $S < 21\%/10^3$ Å, while for those with higher inclination we distinguish 2 groups: one (9 bodies) with $8 < S < 17\%/10^3$ Å and one (6 bodies) with $30 < S < 57\%/10^3$ Å (Fig. 8). Nevertheless, no correlation is found between S and i, or with other parameters, except a weak one between S and e (Table 4). For the resonant TNOs, there is a strong correlation between S and e (Table 4). Objects with high eccentricity tend to be redder than those in low eccentricity orbits; that is, the spectral slope tends to increase with eccentricity. If we exclude the 3 non plutino objects, the correlation becomes weaker ($\rho = 0.681818$ and $P_r = 0.020843$).

The stronger correlation found inside the whole sample is for the SDOs: spectral slope decreases with increasing eccentricity (Fig. 9), as shown by the anticorrelation between S and e (Table 4), but we must be careful as our sample of 6 SDOs is too small to be statistically significant. This strong correlation was also found by Santos-Sanz et al. (2009) on a larger sample (25) of SDOs.

Both Centaurs and Resonants tend to have higher slope values with increasing eccentricity, and this trend is opposite to what is seen for SDOs. Analysing the colour−colour correlations, Peixinho et al. (2004) found some resemblance between the Centaur and Plutino distributions, and they also found that the correlations for these two classes is opposite to those of SDOs. They suggest that Centaurs might have mainly originated from the Plutino population, not from SDOs, and that the mechanism changing the surface spectral behaviour might be similar for Centaurs and Plutinos. This interpretation is strengthened by the similar $S - e$ correlation between the Centaurs and Plutinos, and by the $S - e$ anticorrelation for SDOs found here.

5. Conclusions

In this work we have presented new visible spectra for 18 TNOs and 10 Centaurs obtained in the framework of a LP devoted to the investigation of these pristine bodies. The main results obtained may be summarised as follows.

- Our data confirm the diversity in the surface composition of the Centaur and TNO populations, with a spectral slope gradient ranging from ∼1 to 51%/10^3 Å.
- Absorption features: all the new spectra are featureless, excluding 10199 Chariklo and 42355 Typhon, which show faint broadband absorptions centred at 0.62−0.65 μm, tentatively attributed to phyllosilicates. These two objects are fully discussed in two separate papers (Guilbert et al. 2009; Alvarez-Candal et al. 2009).
- The new spectrum obtained of the plutino 2003 AZ84 is featureless, while a faint broadband feature possibly attributed to hydrated silicates was previously reported by Fornasier et al. (2004a,b) and Alvarez-Candal (2008), so we cannot confirm an aqueous alteration action on its surface, but we cannot exclude that 2003 AZ84 simply has a heterogeneous surface composition.
- Spectral heterogeneity: comparing the spectral slope values of the objects obtained here with those available in the literature, we found important differences for a few objects, in particular for 10199 Chariklo, 20000 Varuna, 44594 (1999 OX3), and 120132 (2003 FY128). This variability on the spectral behaviour may stem from surface heterogeneities. We observed the fast-rotating (period of 4.13 ± 0.05 h, Perna et al. 2009) plutino 2003 UZ413 during 3 different runs. We found that the slope of the spectrum acquired on the second maximum of the lightcurve is higher than the two slopes obtained near the minima, even if the differences are not greater than the uncertainties. Further observations covering the whole rotational period of 2003 UZ413 are needed to confirm if the spectral variation on its surface is real and if this object may display surface variability.
- Spectral slope distribution: we combined the new data presented here with the visible spectra published in the literature (coming mainly from the 2 LPs devoted to TNOs and Centaurs carried out at ESO). The total sample contains 20 Centaurs and 53 TNOs. After analysing the spectral slope distribution of Centaurs, classicals, resonants, and SDOs-detached bodies, we found a lack of very red objects in the classical population, as all have spectral slope values <35%/10^3 Å, with the lowest mean value (∼14%/10^3 Å) in the dynamical classes investigated. The Centaur population is dominated (70%) by bluish to grey or moderately red objects but also comprises very red objects, with spectral slopes greater than 40%/10^3 Å. Neththeless, very red objects are a minority in the Centaur and TNO populations (8%), while most of them (74%) have spectral slope values <25%/10^3 Å.
- Statistical analysis: running a Spearman rank order analysis, we confirm a strong anticorrelation between the spectral slope and inclination for the classical TNOs, of a weak anticorrelation between S and e, and of a weak correlation between S and the perihelion distance. Our sample mainly contains objects in the hot population ($i > 5°$), which thus show neutral/blue spectral behaviour for increasing values of i and e. Nevertheless, we do not observe a change in the slope distribution between the hot and cold populations, but we do find that objects with $i < 12°$ show no correlation between spectral slope and inclination. This result independently confirms the finding by Peixinho et al. (2008) on the colour-inclination relation for classical TNOs. We found a strong correlation between S and e for resonant bodies, a similar but weaker one for Centaurs, while for SDOs we confirm the anticorrelation between S and e found by Santos-Sanz et al. (2009), even though it must be noted that our sample is very limited.

Acknowledgements. We thank the anonymous referee for his/her useful comments in the reviewing process.

References

Alvarez-Candal, A., Fornasier, S., Barucci, M. A., de Bergh, C., & Merlin, F. 2008, A&A, 487, 741
Alvarez-Candal, A., Barucci, M. A., Merlin, F., et al. 2009, A&A, in press
Barucci, M. A., Lazzarin, M., & Tozzi, G. P. 1999, AJ, 117, 1929
Barucci, M. A., Cruikshank, D. P., Dotto, E., et al. 2005, A&A, 439, 1
Barucci, M. A., Merlin, F., Dotto, E., Doressoundiram, A., & de Bergh, C. 2006, A&A, 455, 725
Binzel, R. P. 1992, Icarus, 99, 238
Boehnhardt, H., Tozzi, G. P., Birkle, K., et al. 2001, A&A, 378, 653
Brown, M. E. 2008, The Largest Kuiper Belt Objects, in The Solar System beyond Neptune, ed. A. Barucci, H. Boehnhardt, D. Cruikshank, & A. Morbidelli (Tucson: Univ. of Arizona Press), 335
Brown, M. E., & Suer, T. A. 2007, ed. D. W. E. Green, IAU Circ., 8812, 1
de Bergh, C., Boehnhardt, H., Barucci, M. A., et al. 2004, A&A, 416, 791
Doressoundiram, A., Boehnhardt, H., Tegler, S. C., et al. 2008, Color Properties and Trends of the Transneptunian Belt, in The Solar System beyond Neptune, ed. A. Barucci, H. Boehnhardt, D. Cruikshank, & A. Morbidelli (Tucson: Univ. of Arizona Press), 91
Dotto, E., Perna, D., Barucci, M. A., et al. 2008, A&A, 190, 829

Fitzsimmons, A., Dahlgren, M., Lagerkvist, C. I., Magnusson, P., & Williams, I. P. 1994, A&A, 282, 634
Fornasier, S., Lazzarin, M., Barbieri, C., & Barucci, M. A. 1999, A&A, 135, 65
Fornasier, S., Doressoundiram, A., Tozzi, G. P., et al. 2004a, A&A, 421, 353
Fornasier, S., Dotto, E., Barucci, M. A., & Barbieri, C. 2004b, A&A, 422, 43
Fornasier, S., Dotto, E., Hainaut, O., et al. 2007, Icarus, 190, 622
Gladman, B., Marsden, B. G., & VanLaerhoven, C. 2008, Nomenclature in the outer Solar System, in: The Solar System Beyond Neptune, ed. M. A. Barucci, H. Boehnhardt, D. Cruikshank, & A. Morbidelli (Tucson: Univ. of Arizona Press), 43
Guilbert, A., Barucci, M. A., Brunetto, R., et al. 2009, A&A, 501, 777
Jewitt, D. C., & Sheppard, S. S. 2002, AJ, 123, 2110
Lacerda, P. 2009, AJ, 137, 3404
Lacerda, P., & Jewitt, D. C. 2007, AJ, 133, 1393
Lacerda, P., Jewitt, D. C., & Peixinho, N. 2008, AJ, 135, 1749
Lazzarin, M., Barucci, M. A., Boehnhardt, H., et al. 2003, AJ, 125, 1554
Lederer, S. M., & Vilas, F. 2003, Earth, Moon, and Planets, 92, 193
Licandro, J., di Fabrizio, L., Pinilla-Alonso, N., et al. 2006a, A&A, 457, 323
Licandro, J., Pinilla-ALonso, N., Pedani, M., et al. 2006b, A&A, 445, 35
Luu, J. X., & Jewitt, D. C. 1996, AJ, 111, 499
Luu, J. X., & Jewitt, D. C. 1998, ApJ, 494, 117
Marchi, S., Lazzarin, M., Magrin, S., & Barbieri, C. 2003, A&A, 408, L17
Morbidelli, A., Levison, H. F., Tsiganis, K., & Gomes, R. 2005, Nature, 435, 462
Ortiz, J. L., Gutierrez, P. J., Santos-Sanz, P., Casanova, V., & Sota, A. 2006, A&A, 447, 1131
Peixinho, N., Boehnhardt, H., Belskaya, I., et al. 2004, Icarus, 170, 153
Peixinho, N., Lacerda, P., & Jewitt, D. 2008, AJ, 136, 1837
Perna, D., Dotto, E., Barucci, M. A., et al. 2009, A&A, accepted for publication
Pinilla-Alonso, N., Licandro, J., Gil-Hutton, R., & Brunetto, R. 2007, A&A, 468, 25
Pinilla-Alonso, N., Licandro, J., & Lorenzi, V. 2008, A&A, 489, 455
Pinilla-Alonso, N., Brunetto, R., Licandro, J., & Gil-Hutton, R. 2009, A&A, 496, 547
Ragozzine, D., & Brown, M. E. 2007, AJ, 134, 2160
Santos-Sanz, P., Ortiz, J. L., Barrera, L., & Boehnhardt, H. 2009, A&A, 494, 693
Sheppard, S. S., & Jewitt, D. C. 2003, Earth, Moon, and Planets, 92, 207
Spearman, C. 1904, The proof and measurements of associations between two things, AM. J. Psychol., 57, 72
Stansberry, J., Grundy, W., Brown, M., et al. 2008, Physical Properties of Kuiper Belt and Centaur Objects: Constraints form the Spitzer Space Telescope, in The Solar System Beyond Neptune, ed. M. A. Barucci, H. Boehnhardt, D. Cruikshank, & A. Morbidelli (Tucson: Univ. of Arizona Press), 161
Tegler, S. C., & Romanishin, W. 2000, Nature, 6807, 979
Tegler, S. C., Grundy, W. M., Romanishin, W., et al. 2007, AJ, 133, 526
Tegler, S. C., Bauer, J. M., Romanishin, W., & Peixinho, N. 2008, Colors of Centaurs, ed. A. Barucci, H. Boehnhardt, D. Cruikshank, & A. Morbidelli (Tucson: Univ. of Arizona Press), 105
Trujillo, C. A., & Brown, M. E. 2002, AJ, 566, 125
Vilas, F., Jarvis, K. S., & Gaffey, M. J. 1994, Iron Alteration Minerals in the Visible and Near-Infrared Spectra of Low Albedo Asteroids, Icarus, 109, 274

5.6 Observations avec le télescope spatial HERSCHEL

J'ai participé comme co-investigatrice au programme clé *TNOs are Cools : a survey of the Transneptunian region* (PI T. Mueller) qui a obtenu environ 370 heures d'observation pour les OTNs et les Centaures avec Herschel, le plus grand télescope spatial dédié à l'astronomie dans les domaines infrarouge et submillimétrique. Le programme est en cours et a comme but l'observation d'un échantillon considérable d'OTNs et de Centaures (environ 140) avec les instruments PACS (principalement, bandes d'observation centrées à 70, 100 et 160 micron) et SPIRE (bandes centrées à 250, 350 et 500 micron).
Mon rôle est consacré principalement à l'analyse des données de SPIRE, et à leur interprétation (ajoutant les données issues de Herschel-Pacs et celles de SPITZER-MIPS ou WISE) avec des modèles thermiques standards (STM et NEATM). La mesure de l'émission submillimétrique de ces objets permet la détermination de leur taille et de leur albédo, et de contraindre certains paramètres comme la rugosité, la porosité, l'inertie thermique.
Les premiers résultats concernent une dizaine d'objets (Müller et al. 2010) de 100 à 1300 km de diamètre dont les albédos s'étalent de 0,05 (objets sombres) à 0,7 (objets brillants). L'observation de la courbe de lumière thermique de la planète naine (136108) Haumea a permis de confirmer que l'objet était allongé (Lellouch et al. 2010). Les observations de (90482) Orcus et (136472) Makemake ont été combinées avec les observations dans l'infrarouge obtenues avec l'observatoire spatial Spitzer, montrant que la surface de Makemake est hétérogène, mais pas celle d'Orcus (Lim et al. 2010). Beaucoup d'autres données sont en cours d'analyse et d'interprétation et seront bientôt publiées.

Chapitre 6

Perspectives scientifiques

Notre compréhension de l'évolution du Système Solaire, ainsi que ses implications sur la formation des planétésimaux, précurseurs des planètes, est devenue un objectif majeur en sciences planétaires au cours des dernières années. Les petits corps du Système Solaire constituent les restes des essaims de planétésimaux qui se sont formés au cours des premières phases de l'accrétion des planètes. L'étude de leurs propriétés physiques et de leurs compositions de surface doit donc nous renseigner sur la formation et l'évolution du Système Solaire.
L'étude des petits corps du Système Solaire est aujourd'hui en plein essor grâce à l'exploration continue des missions spatiales et aux nombreuses campagnes observationnelles au sol.

Mon activité de recherche est basée principalement sur la caractérisation des propriétés physiques des petits corps du Système Solaire, géocroiseurs, astéroïdes, Troyens, Centaures et transneptuniens. Dans le futur, je vais continuer mes recherches sur ces objets, mais je vais également beaucoup m'investir dans l'étude des comètes et noyaux cométaires, grâce aux données qui viendront de la mission Rosetta, et, dans un futur plus lointain, dans l'étude de la surface de la planète Mercure qui sera survolée par la mission BepiColombo.

Mes travaux s'appuient largement sur les observations obtenues avec les télescopes au sol et dans l'espace, sur la modélisation de la composition physico-chimique, sur la modélisation thermique et sur l'analyse statistique. En perspective, ma recherche va se développer principalement sur les axes suivants :

- Continuer l'exploitation des données de la caméra OSIRIS et l'activité de calibration de l'instrument, afin de pouvoir garantir les meilleures performances possibles pour la rencontre avec la comète 67P en 2014. Je vais m'investir largement dans un futur très proche dans l'étude des noyaux et coma cométaires afin de développer les connaissances et les outils nécessaires pour l'interprétation des données uniques sur 67P qui seront prises par la mission Rosetta.
- Etudier les géocroiseur, avec des observations de caractérisation des propriétés physiques de cette population et des cibles des missions spatiales en particulier ; observations *in situ* et retour d'échantillons grâce à la mission de la NASA OSIRIS-REX, dont je suis scientifique associée, et, si sélectionnée par l'ESA, grâce à la mission MarcoPolo-R, dont je suis co-investigatrice
- la planète Mercure : étudier sa surface, les processus d'interaction surface-vent solaire, les processus d'altération de surface. Cette activité sera basée essentiellement sur les données qui arriveront, après 2020, de la mission BepiColombo et de l'instrument Symbio-Sys, dont je suis co-investigatrice
- analyse des propriétés thermiques des Centaures et des Transneptuniens sur la base des observations avec le télescope Herschel, qui sont en cours et qui donneront un aperçu

unique sur un grand échantillon (environ 140 objets) de petits corps du Système Solaire externe. En perspective future, utilisation de l'interféromètre ALMA pour étudier encore plus d'objets lointains dans le domaine millimétrique-submillimétrique. En parallèle, je continuerai l'activité de caractérisation et de modélisation des propriétés de surface avec des observations au sol en photométrie, polarimétrie et spectroscopie, en particulier des gros OTNs
- Mesures en laboratoires de météorites, de minéraux et de mélanges de glaces pour étudier les effets d'altération de surface et les changements des spectres des échantillons en fonction de plusieurs paramétres comme par exemple la taille de grains et la température. Ceci est nécessaire pour pouvoir contraindre la composition de surface des différents petits corps observés et les processus qui peuvent les altérer. Cette activité sera fondamentale en support des observations *in situ* ou à partir de l'orbiteur des nombreuses missions spatiales en cours ou proposées dédiées aux petits corps du Système Solaire.
- Observations multi-longueurs d'onde d'astéroïdes, géocroiseurs et Troyens pour en caractériser les propriétés de surface, en étudier les corrélations, établir leur région d'origine, et donner des contraintes sur les conditions physico-chimiques et thermiques des différentes régions du Système Solaire

Cette activité est évidement très vaste et s'appuiera largement sur de nombreuses collaborations nationales et internationales.

6.1 Mission Rosetta : rendez-vous avec la comète 67P

Bien que la mission Rosetta soit maintenant en hibernation, les équipes des différents instruments travaillent pour définir l'orbite et la distance autour de la comète 67P, et préparer les séquences observationnelles qui permettront la caractérisation du noyau de la comète et l'identification du site d'atterrissage du *lander Philae*.
La sonde sera entièrement réactivée en janvier 2014, avant la manœuvre de rendez-vous avec la comète. Elle se placera alors en orbite autour de Churyumov-Gerasimenko, tandis que la comète poursuivra sa trajectoire à travers le Système Solaire interne.
Rosetta permettra une étude unique de la structure interne du noyau de la comète, l'analyse de la nature et de la composition minéralogique, chimique et isotopique, notamment de sa composante organique et de l'interaction du noyau avec le vent et la pression de radiation solaire.
Pendant 6 mois, Rosetta sera chargée de cartographier la surface du noyau de la comète de façon très précise pour préparer le choix du site d'atterrissage. En novembre 2014, l'atterrisseur sera éjecté de la sonde à une faible altitude et se posera en douceur sur le noyau. Philae fera ses mesures *in situ* pendant au moins une semaine. Tandis que l'atterrisseur mènera ses investigations et après l'achèvement de cette partie de la mission, la sonde Rosetta restera en orbite autour de la comète pour l'étudier longuement lorsqu'elle se rapprochera du périhélie et commencera à développer une activité cométaire. Ce sera la première fois qu'une sonde observera de près les modifications d'une comète à l'approche du Soleil, c'est-à-dire lorsque se forment la chevelure et les queues d'ions et de poussière.
Je compte donc commencer à m'investir sur l'étude des noyaux et comas cométaires afin de développer les connaissances et les outils nécessaires pour l'interprétation des données uniques sur la comète 67P. Avec le système d'imagerie OSIRIS nous pourrons jouer un rôle fondamental non seulement pour la sélection du site d'atterrissage de Philae, mais également pour obtenir les premiers résultats scientifiques sur la forme et la structure du noyau, ses propriétés rotationnelles, dériver les champs de pesanteur et les moments d'inertie, étudier la topographie superficielle et identifier les processus physiques qui ont influencé la structure de surface, étudier les paramètres

physiques du régolithe extérieur, la couleur et la minéralogie de la surface et déterminer le degré d'hétérogénéité du noyau.
Au fur et à mesure que la comète s'approchera du Soleil, la caméra OSIRIS permettra d'étudier la structure du noyau, les processus d'érosion dans les régions actives, les hétérogénéités éventuelles. Elle permettra aussi de déterminer le taux de perte de masse du noyau et les forces non-gravitationnelles, d'identifier et de mesurer toutes les sources de dégagement de poussière et leur variation en fonction du temps, de suivre les structures dans la coma et leur évolution dynamique. Au niveau du gaz, la caméra WAC a des filtres étroits dédiés à l'étude des émissions des gaz, donc on pourra déterminer les taux de production des différentes molécules et leur évolution temporelle.

Nous continuons aussi l'exploitation des données de la caméra OSIRIS, et nous sommes en train de développer un modèle photométrique de Lutétia pour corriger dans les images les effets dus à la géométrie et aux conditions d'illumination et pour pouvoir analyser les variations d'albédo et spectrales sur une petite échelle. Cette opération s'est avérée beaucoup plus longue que prévu à cause de la grande vitesse de la rencontre et des variations importantes de conditions géométriques et d'illumination entre les images.

6.2 Les géocroiseurs : observations au sol et *in situ* : missions OSIRIS-REX et MARCO POLO-R

La population des géocroiseurs (NEOs) est composée d'astéroïdes (NEAs) et de comètes dormantes ou éteintes ayant des orbites avec un périhélie q<1.3 UA et un aphélie Q>0.98 UA. La durée de vie estimée pour les NEOs est d'environ 10^7 ans avant qu'ils ne s'écrasent sur le Soleil, qu'ils soient éjectés du Système Solaire ou qu'ils impactent une planète. Ceci implique que les NEOs observés à l'heure actuelle ne peuvent être des corps ayant orbité parmi les planètes telluriques depuis la formation du Système Solaire, et que leur population a des sources de réapprovisionnement : la plus grande partie vient de la ceinture d'astéroïdes, en particulier de zones de résonance avec Jupiter, et 20% des NEOs sont des comètes dormantes ou éteintes.
Etant des impacteurs potentiels de notre planète, de nombreuses campagnes observationnelles sont dédiées à la découverte, au suivi et à la caractérisation de leurs propriétés de surface. Leur étude est cruciale : i) pour analyser les relations entre la population des NEOs et les autres populations de petits corps du Système Solaire (astéroïdes de la ceinture principale, comètes et météorites) ii) pour étudier l'origine des NEOs et leur évolution ; iii) pour comprendre les processus d'altération de surface.
Deux astéroïdes de la classe S ont déjà été survolés par les missions spatiales NEAR de la NASA (Eros) et HAYABUSA de la JAXA (Itokawa). L'étude de ces objets est aujourd'hui en plein essor et vise en particulier les géocroiseurs primitifs, c'est-à-dire les NEOs appartenant aux classes C, B, F, P, qui ont conservé la plus grande mémoire de la composition initiale du milieu dans lequel nos planètes se sont formées. Les trois plus grandes agences spatiales mondiales ont proposé des missions ambitieuses visant à l'étude et au retour d'échantillon de géocroiseurs primitifs : OSIRIS-REX pour la NASA, MarcoPolo-R pour l'ESA et Hayabusa 2 pour la JAXA.

La mission de la NASA OSIRIS-REX (Origins Spectral Interpretation Resource Identification Security Regolith Explorer) vient d'être sélectionnée par la NASA dans le cadre du programme New Frontiers pour l'étude du géocroiseur (101955) 1999 RQ36. Cette mission (Principal Investigator : L. Lauretta, Université d'Arizona, USA) a pour objectif d'étudier l'astéroïde de type B 1999 RQ36 et de ramener sur Terre un échantillon d'environ 60 grammes pour l'analyser en

laboratoire. OSIRIS-Rex sera lancée en septembre 2016 pour un rendez-vous avec la cible en 2020, et un retour d'échantillon de cet astéroïde en septembre 2023. Cet astéroïde géocroiseur est aussi susceptible d'entrer un jour en collision avec la Terre (1 chance sur 1800 en 2182).
Ma demande comme scientifique associée à la mission vient d'être acceptée par l'équipe de la NASA. En même temps, je suis co-investigatrice de la mission MarcoPolo-R (PI A. Barucci), sélectionnée pour une étude de faisabilité dans le cadre des missions M3 du programme Cosmic Vision de l'ESA. Cette mission a également comme objectif principal le retour d'échantillons d'un astéroïde géocroiseur primitif. La cible de MarcoPolo-R devrait être un géocroiseur binaire (l'astéroïde 175706 1996FG3), ayant un satellite en orbite, d'autant plus intéressant car les interactions gravitationnelles avec leur compagnon permettent des migrations de régolithe et donc le rafraîchissement de la surface qui se traduit par une variation des signatures spectrales.
Ces missions fourniront des informations cruciales pour répondre aux questions suivantes : 1) Quels sont les processus qui se produisent dans le Système Solaire jeune et qui accompagnent la formation des planètes ? 2) Quelles sont les propriétés physiques et l'évolution des planétésimaux qui ont formé les planètes terrestres ? 3) Est-ce que les géocroiseurs de classe primitive contiennent du matériau pré-solaire inexistant dans les météorites ? 4) Quelles sont la nature et l'origine de la matière organique dans les astéroïdes primitifs et comment peuvent-ils nous éclairer sur l'origine des molécules nécessaires à la vie ?

Le retour d'échantillons d'objets primitifs est fondamental car leur analyse fournira des informations cruciales pour expliquer comment notre Système Solaire s'est formé, et pour déterminer si ces petits corps ont pu contribuer à l'apport des ingrédients nécessaires à la vie sur Terre.

6.3 La mission BepiColombo : la planète Mercure

Mercure est la planète la plus proche au Soleil et pour cela très difficile à survoler. Une longue période d'oubli s'est écoulée entre la première visite de Mercure par une sonde spatiale (Mariner 10 en 1974-1975) et la suivante, celle de la mission américaine Messenger en 2011. L'ESA, en collaboration avec l'agence spatiale japonaise JAXA, est en train de préparer le lancement de la mission BepiColombo, pierre angulaire du programme spatial européen dédié à l'étude de Mercure. L'ESA a réalisé l'orbiteur planétaire (MPO : Mercury Planetary Orbiter) qui sera dédié à l'étude de la surface, de la composition et de l'exosphère de la planète, la JAXA a fourni l'orbiteur magnétosphérique (MMO : Mercury Magnetospheric Orbiter), qui sera focalisé sur l'étude du champ magnétique de Mercure, sur l'interaction du vent solaire avec la possible magnétosphère, sur l'environment ionosphérique et sur l'exosphère. La mission BepiColombo avec ses 2 modules sera lancée par une fusée Soyouz depuis le Centre Spatial Guyanais en août 2015. Six ans de voyage interplanétaire seront nécessaires avant que la mission se positionne autour de Mercure en 2020. Les deux orbiteurs se sépareront pour mener leurs missions respectives d'une durée nominale d'un an.

Depuis 2005 je suis co-investigatrice de l'instrument Symbio-Sys, une des expériences sélectionnées sur l'orbiteur MPO. Symbio-Sys est un imageur intégré issu d'un consortium à maîtrise italienne (PI E. Flamini de l'agence spatiale italienne) incluant un spectromètre imageur (VIHI = Visual and Infrared Hyper-spectral Imager), une caméra stéréographique (STC = Stereo Channel), et une caméra à haute résolution (HRIC = high resolution channel). Les 3 instruments ont une électronique commune. VIHI fera de l'imagerie spectrale ($400 - 2000$ nm) de la surface de Mercure. L'objectif est de faire la cartographie minéralogique complète de la planète avec une résolution spatiale < 500m et une résolution spectrale < 10nm. La caméra HRIC obtiendra des images avec une résolution allant jusqu'à 5 m/pixel, et la caméra STC donnera la cartographie de la planète avec une résolution spatiale ≥ 50 m/pixel.

Grace à l'expérience que j'ai acquise dans le traitement des données de spectroscopie visible et infrarouge à partir d'observations au sol et dans le traitement d'images à basse et haute résolution spatiale avec le système d'imagerie OSIRIS à bord de Rosetta, je compte m'investir dans l'analyse, l'interprétation et l'exploitation des données de spectroscopie issues de l'instrument VIHI et d'imagerie venant de la caméra STC, en étroite collaboration avec A. Doressoundiram, collègue au LESIA et Co-PI de VIHI, et G. Cremonese, Co-PI de STC.
Les images fournies par la caméra STC permettront de cartographier la surface de la planète en 3D, d'étudier les phénomènes de cratérisation, d'analyser les processus de volcanisme et de tectonique de la surface.
VIHI nous donnera des spectres du visible au proche infrarouge avec une résolution spatiale dans l'intervalle 100-375 mètres, selon la position sur l'orbite, nous permettant de mieux comprendre la composition superficielle de la planète, les processus de différentiation et de chauffage ainsi que les effets de l'altération spatiale qui amènent à la maturation-vieillissement des surfaces, dû à l'environnement très dur de Mercure. On pourra donc comparer la composition de surface de Mercure avec celle de la Lune et de certains astéroïdes, comme ceux de type igné qui ont subi des températures élevées. Ceci nous permettra de comprendre les processus de formation des planétésimaux dans la région interne du disque protoplanétaire.

6.4 Caractérisation des propriétés physico-chimiques des OTNs et Centaures

Le programme clé *TNOs are Cools : a survey of the Transneptunian region* (PI T. Mueller) est en cours et a pour but la mesure de la taille, de l'albédo, et des propriétés thermophysiques d'un grand échantillon (environ 140) d'objets transneptuniens et de Centaures. Les observations sont faites à 70, 100 et 160 micron avec l'instrument PACS, et pour les objets les plus brillants (une douzaine) aussi à 250, 350 et 500 micron avec l'instrument SPIRE. Les objets sont aussi observés avec des télescope au sol pour en déterminer la magnitude absolue, information très importante pour la modélisation thermique, pour obtenir la fonction de phase et, lorsque c'est possible, pour obtenir des spectres (ou des couleurs) qui nous renseignent sur la possible composition de surface.
Pour le programme Herschel, mon rôle est consacré principalement à l'analyse des données de SPIRE, et à leur interprétation avec des modèles thermiques standards (STM et NEATM), mais aussi à l'analyse statistique et à la recherche des corrélations entre les propriétés thermiques et la composition de surface, les couleurs, les paramètres orbitaux, la taille des objets. L'étude du flux thermique multilongueurs d'onde, grâce à la combinaison des observations de SPIRE et PACS avec celles de SPITZER et WISE, permet aussi d'étudier la variation de l'émissivité avec la longueur d'onde. Celle-ci est considérée constante dans les modèles (on prend une valeur de 0,9), mais de nombreux petits corps montrent une forte diminution de l'émissivité de la surface avec la longueur d'onde. Ce phénomène suggère que les premiers millimètres de la surface deviennent transparents, ce qui laisse passer le flux thermique issu des couches les plus profondes. Des processus de diffusion multiple de petits grains de moins de 100 microns de taille pourraient être responsables de ce phénomène. Les résultats préliminaires montrent que certains OTNs et Centaures ont aussi une baisse importante de l'émissivité avec la longueur d'onde.
En combinant les résultats issus des observations HERSCHEL avec les données au sol obtenues par le Large Programme et d'autres campagnes observationnelles dédiées aux OTNs et aux Centaures, nous obtiendrons un aperçu unique des propriétés physico-chimiques et thermiques de ces objets. Nous pourrons donc :

1) Déterminer la taille, l'albédo, et les propriétés thermophysiques des objets, qui donnent des contraintes sur le type de surface : la température de surface et l'inertie thermique nous permettent de distinguer si une surface a une composition riche en glace plutôt que rocheuse ; l'émissivité donne des contraintes sur la taille des grains, et le paramètre η (*beaming factor*) nous renseigne sur la rugosité.
2) Déterminer la distribution en taille et en albédo des OTNs, pour la totalité des objets et pour les différents groupes, et étudier ainsi le rôle des collisions.
3) Faire une analyse statistique et rechercher de possibles corrélations entre :
albédo-couleur et albédo-spectre, pour avoir des indications sur la composition de surface et sur les effets d'altération de celle-ci ; albédo - propriétés orbitales, corrélation qui peut nous renseigner sur leur évolution dynamique et sur les processus de space weathering (on s'attend par exemple à ce que les objets subissant le plus de collisions soient les plus brillants suite à un renouvèlement de leur surface) ;
4) pour les 5 objets dont on dispose d'une courbe de lumière thermique : distinguer les effets dus à la forme de ceux dus aux variations d'albédo, déterminer s'il y a de grandes structures à la surface, déterminer l'orientation de l'axe de rotation et l'inertie thermique.
5) Beaucoup d'OTNs binaires sont en cours d'observation avec HERSCHEL, et on pourra en déduire la structure et la composition interne et étudier les mécanismes de formation.
6) Utiliser la valeur de l'albédo obtenue par Herschel afin d'améliorer l'interprétation des spectres obtenus pendant le large programme sur les OTNs-Centaures et mieux contraindre la composition de surface avec les modèles de transfert radiatif de Hapke et Shkuratov (l'albédo étant un paramètre d'entrée très important).

Au delà des observations HERSCHEL, je vais continuer l'activité de caractérisation au sol des ces objets, ciblés sur les gros transneptuniens-planètes naines et ceux découverts récemment. Le but est d'obtenir des spectres avec le plus grand rapport signal sur bruit possible pour analyser les espèces chimiques comme le méthanol et le méthane présentes à la surface de plusieurs objets, et d'en étudier les évolutions saisonnières, comme pour la planète naine Pluton. Ces espèces volatiles permettront de nous renseigner en profondeur sur les mécanismes d'évolution de ces objets dénués d'atmosphère dense.
Je souhaite aussi continuer les observations en polarimétrie des grands OTNs pour contraindre leurs propriétés de surface (rugosité, porosité).

6.5 Mesure en laboratoire d'échantillons de météorites, de minéraux et de mélanges de glaces

La spectroscopie des petits corps nous permet d'obtenir des spectres à partir desquels nous souhaitons comprendre et contraindre la composition de surface des objets. Pour cela il est très important de disposer de bases de données spectrales sur les minéraux, les météorites et les glaces afin de pouvoir les comparer avec les astéroïdes, Centaures et OTNs et procéder à la modélisation des surfaces de ces derniers.
En effet, la comparaison entre le spectre d'une météorite et celui d'un astéroïde est limitée par plusieurs effets : nous observons globalement un astéroïde alors qu'en laboratoire nous pouvons (ou devons) effectuer des mesures sur des échantillons de météorites de taille de quelques centimètres ou dizaines-centaines de micron ; la préparation de mesures d'échantillons en laboratoire peut altérer les météorites et ne pas reproduire les conditions physiques des matériaux à la surface d'un astéroïde ; les météorites peuvent provenir de la surface aussi bien que de la partie interne

du corps parent, suite aux collisions, alors que nous pouvons étudier seulement la surface des astéroïdes ; l'altération de surface des astéroïdes peut introduire des biais lors d'une comparaison directe avec le spectre d'une météorite.
Pour l'interprétation des petits corps du Système Solaire externe on utilise surtout les modèles de transfert radiatif qui nécessitent la connaissance des constantes optiques des matériaux. Les modèles de composition de surface ont pour but d'affiner nos connaissances sur la composition chimique de surface (abondance et taille relative des composés et agencement des composés entre eux, par exemple). La base de données sur les constantes optiques des glaces et des mélanges de glaces et d'autres composés est, elle aussi, limitée, et les effets d'irradiation ont été testés jusqu'à présent seulement sur quelques composés purs.

Dans le futur, je souhaite m'investir dans les mesures en laboratoires car je me suis aperçue qu'il y a souvent un manque de données qui limite ensuite les modèles et l'interprétation de la composition de surface des petits corps.
Notre équipe a entamé plusieurs collaborations avec différents laboratoires, notamment avec : a) le LASp (Experimental Astrophysics Laboratory), de Catania, Italie : le laboratoire est équipé d'une chambre à vide, et d'un système d'irradiation par ions et protons. Plusieurs spectromètres sont opérationnels dans les gammes de longueur d'onde de 190 nm à 200 microns ; b) le laboratoire de l'Observatoire de Capodimonte, Naples, Italie, qui est équipé d'un spectromètre et d'un bolomètre permettant d'effectuer des mesures en réflectance jusqu'à 1 mm ; c) le laboratoire de Planétologie de Grenoble qui est spécialisé dans la mesure en réflectance des mélanges de glaces et la mesure de constantes optiques.
Je suis particulièrement intéressée par de nouvelles mesures sur les météorites, les minéraux et les mélanges de glaces qui nous aident à comprendre les effets du space weathering sur différents types de matériaux, car le vent solaire, les rayons cosmiques et les micro-impacts peuvent changer les propriétés spectrales de manière différente selon la composition (un assombrissement et un rougissement progressif du spectre pour les silicates, mais une diminution de la pente spectrale pour de fortes altérations de certains matériaux organiques).
En particulier, vu le manque de données, je souhaite m'investir sur la caractérisation des sous-espèces produites par irradiation de mélanges de glace qui sont créées à la surface des objets dénués d'atmosphère dans le Système Solaire.

6.6 Propriétés physiques des astéroïdes primitifs

La récente découverte de la glace d'eau à la surface des astéroïdes Thémis et Cybèle et la découverte de plusieurs comètes de la ceinture principale (*main belt comets*) nous montrent qu'il y a une continuité entre les populations d'astéroïdes et les comètes et que la distinction entre les deux n'est pas toujours simple et nette. Certains astéroïdes de la ceinture principale pourraient développer une coma et une activité cométaire s'ils s'approchaient plus au Soleil. La recherche d'espèces dites volatiles comme la glace d'eau dans les petits corps a des implications importantes pas seulement pour comprendre la formation et l'évolution du Système Solaire mais aussi pour l'émergence de la vie sur Terre, car une partie de l'eau terrestre aurait pu être amenée par des astéroïdes et des comètes. Dans le futur, je souhaite continuer à m'investir dans l'étude des astéroïdes de types primitifs (C, B, F, P, D), en support aussi des missions spatiales acceptées ou proposées vers des géocroiseurs primitifs. Une activité de recherche que j'avais entamée et que je souhaite approfondir est celle dédiée au processus d'altération aqueuse dans la ceinture principale. Ce processus est très important pour comprendre la composition et l'évolution chimique et physique du Système Solaire primordial. Il est dû à l'eau liquide qui agit comme solvant et produit des matériaux similaires aux phyllosilicates (les sulfates, les oxydes, les hydroxydes et

les carbonates). Ce processus produit des absorptions caractéristiques, dans la région visible et dans le proche infrarouge, sur les spectres des astéroïdes primitifs.
Le but est d'acquérir de nouvelles données multi-longueur d'onde et avec un grand rapport signal sur bruit afin de détecter et caractériser les possibles bandes d'absorption. De nouvelles observations dans la région à 3μm sont en cours aussi bien dans la région visible que dans le proche infrarouge. Ceci, couplé avec les données disponibles dans la littérature et les toutes récentes mesures d'albédo et de propriétés thermiques par le télescope WISE, nous permettra une étude statistique poussée et la recherche de corrélations entre l'altération aqueuse et les paramètres orbitaux, l'albédo et la taille des objets. Des études spectrales à différentes phases rotationnelles de plusieurs astéroïdes primitifs sont en cours pour rechercher si leur composition de surface est hétérogène.
Je souhaite en particulier entamer une étude spectroscopique d'une partie des membres de la famille de Thémis pour rechercher de la glace d'eau et des minéraux hydratés sur leur surface. La famille de Thémis, composée surtout d'astéroïdes primitifs (classe B et P), peut être un réservoir important de glace d'eau dans la ceinture principale externe, et les études dynamiques et spectroscopiques montrent qu'elle semble être aussi la source de certaines comètes de la ceinture principale (133P, 238P et 176P).
En parallèle, un programme d'observation avec l'instrument HIFI du télescope HERSCHEL vient d'être approuvé pour détecter le dégazage de la glace d'eau par sublimation sur 24 Thémis. Ces observations permettront de confirmer la présence de la glace d'eau, d'en estimer le taux de production et d'en contraindre l'abondance à la surface de Thémis.

Bibliographie

Alvarez-Candal A., Fornasier S., Barucci A., De Bergh C., Merlin F., 2008, A&A 487, 741

Barucci M.A, Fulchignoni M., Fornasier S., et al., 2005a, A&A 430, 313

Barucci M.A., Belskaya, I. N., Fulchignoni, M., Birlan, M. 2005b, Astron. Journal 130, 1291

Barucci A., Fornasier S., Dotto E., et al., 2008a, A&A 477, 665

Barucci M.A., Merlin F., Guilbert, A., et al., 2008b, A&A 479, L13

Barucci M.A., Alvarez-Candal A., Merlin F., et al. 2011, Icarus 214, 297

Beaugé, C., Roig, F., 2001, Icarus 53, 391

Belskaya I., Bagnulo S., Muinonen K., et al., 2008, A&A 479, 265

Belskaya I., Fornasier S., Krugly Yu. N., et al., 2010a, A&A 515, 29

Belskaya I., Bagnulo S., Barucci A., et al., 2010b, Icarus 210, 472

Birlan M., Barucci M. A., Vernazza P., et al.,2004, New Astronomy 9, 343

Brunetto, R., & Roush, T.L., 2008, A&A 481, 879

Burbine T.H., McCoy T.J., Nittler L., et al., 2002, Meteorit. Planet. Sci. 37, 1233

Carry B., Kaasalainen M., Leyrat C., et al, 2010. A&A 523, 94.

Clark, B. E., Bell, J. F., et al., 2000, Meteoritics & Plan. Science 35, 41

Clark B.E., Bus S.J., Rivkin A.S., et al., 2004, J. Geophys. Res. 109, E02001

Cloutis E. A., Gaffey M. J., Jackowski T. L., Reed, K. L. 1986, J. Geoph. Res., 91, 11641

Dalle Ore C., M., Barucci A., Emery J. P., et al., 2009, A&A 501, 349

De Bergh C., Boehnhardt H., Barucci M. A., et al, 2004, A&A 416, 791

Delsanti A., Merlin F., Guilbert-Lepoutre, A. et al., 2010, A&A 520, id.A40

De Luise F., Dotto E., Fornasier S., et al. 2010, Icarus 209, 586

DeMeo F., Barucci M. A., Merlin F., et al. 2010, A&A 521, id.A35

Doressoundiram A., Peixinho N., de Bergh C., et al., 2002, Astron. Journal 124, 2279

Doressoundiram A., Peixinho, N., Moullet A., et al., 2007, Astron. Journal 134, 2186

Dotto E., Fornasier S., Barucci M.A.,.et al., 2006, Icarus 183, 420

Dotto E., Perna D., Barucci A., et al., 2008, A&A 490, 829

Dotto E., Perna D., Fornasier S., et al, 2009, A&A 494, L29

Duncan M. J. & Levison, H. F. 1997, Science 276, 1670

Emery, J.P., Brown, R.H., 2003, Icarus 164, 104

Emery, J.P., Brown, R.H., 2004, Icarus 170, 131

Emery, J.P., Cruikshank, D.P., Van Cleve, J., 2006, Icarus 182, 496.

Fornasier, S., Lazzarin, M., 2001, Icarus 152, 127

Fornasier, S., Barucci M.A., Binzel R.P., et al. 2003, A&A 398, 327

Fornasier S., Dotto E., Marzari F.,et al. 2004a, Icarus 172, 221

Fornasier S., Doressoundiram A., Tozzi G.P., et al. 2004b, A&A 421, 353

Fornasier S., Dotto E., Barucci M.A., Barbieri, C., 2004c, A&A 422, L43

Fornasier S., Belskaya I., Fulchignoni M., Barucci M. A., Barbieri C., 2006a, A&A 449, L9

Fornasier S., Belskaya I., Shkuratov Yu.G, P., et al., 2006b, A&A 455, 371

Fornasier S., Marzari, F, Dotto, et al. 2007a, A&A 474, 29

Fornasier S., Dotto E., Hainaut O., et al. 2007b, Icarus 190, 622, A&A 398, 327

Fornasier S., Migliorini A., Dotto E., Barucci M.A., 2008, Icarus 196, 119

Fornasier S., Barucci A., De Bergh C., et al., 2009, A&A 508, 457

Fornasier S., Clark B. E., Dotto E., et al., 2010, Icarus 210, 655

Fornasier S., Clark B. E., Dotto E., 2011a, Icarus 214, 131

Fornasier S., Mottola S., Barucci M. A., Sierks H., Hviik S., 2011b, A&A 533, L9.

Fulchignoni, M., Birlan, M., Barucci, M. A. 2000, Icarus, 146, 204

Gaffey, M. J., Burbine, T. H., Piatek, J. L., et al., 1993, Icarus 106, 573

Gladman B., Marsden B. G., VanLaerhoven, C., 2008, in : The Solar System Beyond Neptune, ed. M. A. Barucci, H. Boehnhardt, D. Cruikshank, & A. Morbidelli (Tucson : Univ. of Arizona Press), 43

Gil-Hutton R., Licandro J., Pinilla-Alonso N., Brunetto R., 2009, A&A 500, 909

Grimm, R.E., McSween, H.Y., 1993, Science 259, 653

Guilbert A., Barucci A., Brunetto R., et al., 2009, A&A 501, 777

Harris, A. W., Young, J. W., Bowell, E., et al. 1989, Icarus, 77, 171

Hapke, B., 1981, J. Geophys. Res., 86, 4571

Hapke, B., 1993, Theory of reflectance and emittance spectroscopy, Topics in Remote Sensing, Cambridge, UK : Cambridge University Press

Jorda L., Lamy P. L., Faury G., et al., 2008, A&A 487, 1171

Jewitt, D.C., Luu, J.X., 1990, Astron. Journal 100, 933

Jewitt, D.C., Luu, J.X., 2004, Nature 432, 731

Keller H. U., Barbieri C., Koschny D., et al., 2010, Science 327, 190

Keller H.U., Küppers M., Fornasier S., et al., 2007, Icarus 191, 241

Küppers M., Bertini I., Fornasier S., et al., 2005, Nature 437, 987

Lamy P. L., Jorda L., Fornasier S., et al., 2008a, A&A 487, 1187

Lamy P. L., Kaasalainen M., Lowry S., et al., 2008b, A&A 487, 1179

Lamy P. L., Groussin O., Fornasier S., et al., 2010, 516, A74

Leyrat C., Fornasier S., Barucci A., et al., 2010. Planetary and Space Science 58, 1097

Lellouch E., Kiss C., Santos-Sanz P., et al., 2010, A&A 518, L147

Levison, H., Shoemaker, E.M., Shoemaker, C.S., 1997, Nature 385, 42

Li, J. Y., Bodewits, D., Feaga, L. M., et al. 2011, Icarus 216, 640

Lim T. L., Stansberry J., Müller T. G., et al., 2010,A&A 518, L148

Küppers M., Mottola S., Lowry S. C., et al., 2007, A&A 462, L13

Lupisko, D.F., Belskaya, I.N., 1989, Icarus 78, 395

Marchis F., Hestroffer D., Descamps P., Berthier J., et al., 2006, Nature 439, 565

Marzari, F., Farinella, P., Vanzani, V., 1995, A&A 299, 267

Marzari, F., Farinella, P., Davis, D.R., et al., 1997, Icarus 125, 39

Marzari, F., Scholl, H., Murray, C., Lagerkvist, C., 2002. In : Bottke Jr., W.F., Cellino, A., Paolicchi, P., Binzel, R.P. (Eds.), Asteroids III. Univ. of Arizona Press, Tucson, pp. 725

McFadden, L. A., Wellnitz, D. D., Schnaubelt, M., et al., 2001, Meteoritics & Plan. Science 36, 1711

Merlin F., Alvarez-Candal A., Delsanti A., et L., 2009. Astron. Journal 137, 315

Merlin F., Barucci A., De Bergh C., et al., 2010, Icarus 208, 945

Morbidelli A., Levinson H. F., Tsiganis K., Gomes R., 2005, Nature 435, 462

Morbidelli A., Levinson H. F., Gomes, R., 2008, in : The Solar System Beyond Neptune, ed. M. A. Barucci, H. Boehnhardt, D. Cruikshank, & A. Morbidelli (Tucson : Univ. of Arizona Press), 275

Moroz, L.V., Arnold, G., Korochantsev, A.V., Wasch, R., 1998, Icarus 134, 253

Moroz, L., Baratta, G., Strazzulla, G., et al., 2004, Icarus 170, 214

Müller T. G., Lellouch E., Stansberry J., et al., 2010, A&A 518, L146

Ockert-Bell M. E., Clark B. E., Shepard M. K., et al., 2010. Icarus 210, 674.

Perna D., Barucci A., Fornasier S. et al., 2010, A&A, 510, A53

Rivkin A.S., Howell E.S., Britt D.T., et al., 2000, Icarus 117, 90

Scott E.R.D., Taylor, G.J., Newsom, H.E., et al., 1989, In : Binzel, P.R., Gehrels, I., Matthews, M.S. (Eds.), Asteroids II. Univ. of Arizona Press, Tucson, pp. 701

Shepard, M.K., et al, 2008, Icarus 195, 184

Shepard, M.K. et al., 2010, Icarus 208, 221

Shimazu, H., Teresawa, T., 1995, Journal of Geophys. Research 100, 16923

Shkuratov Y., Starukhina L., Hoffmann H., Arnold G., 1999, Icarus 137, 235

Shoemaker, E.M., Shoemaker, C.S., Wolfe, R.F., 1989. In : Binzel, P.R., Gehrels, I., Matthews, M.S. (Eds.), Asteroids II. Univ. of Arizona Press, Tucson, pp. 487

Sierks H., Lamy P., Barbieri C., et al., 2011, Science 334, 487

Snodgrass C., Tubiana, C., Vincent J.B, et al., 2010, Nature 467, 814

Tegler S. C., & Romanishin, W., 2000, Nature 6807, 979

Tholen, D.J., Barucci, M.A., 1989, In : Binzel, R.P., Gehrels, T., Matthews, M.S. (Eds.), Asteroids II. Univ. of Arizona Press, Tucson, pp. 298

Vilas, F., Hatch, E.C., Larson, S.M. et al., 1989, Icarus 102, 225

Vilas, F., Jarvis, K.S., Gaffey, M.J., 1994, Icarus 109, 274

Zolensky M.E., Krott A., Benedix, G., 2008, Reviews in Mineralogy and Geochemistry 68, 345

Sonia Fornasier : Curriculum Vitæ

CURRICULUM VITÆ ET STUDIORUM

Sonia Fornasier

Nom : Fornasier
Prenom : Sonia
État civil : mariée, épouse Panuzzo, un enfant
Date de naissance : 31 mai 1972
Nationalité : Italienne
Adresse professionelle : Observatoire de Paris-LESIA, 5 Place J. Janssen, 92195 Meudon cedex, France *Tel.* : +33-0145077746
e-mail : sonia.fornasier@obspm.fr

SITUATION ACTUELLE

depuis 2006 : Maître de conférence à l'Université Paris Diderot-Paris 7, titularisée en Septembre 2007.
Laboratoire de rattachement : Laboratoire d'études spatiales et d'instrumentation en Astrophysique (LESIA), UMR CNRS 8109, Observatoire de Paris

CURSUS UNIVERSITAIRE ET FORMATION

- **1997** : *Laurea* en Astronomie (équivalence DEA obtenue de l'Université P7) de l'Université des Études de Padoue, le 25 octobre 1997 avec la note : 107/110.
  Titre de la thèse : Recherche spectroscopique des produits de l'altération aqueuse dans les astéroïdes primitifs.
  Sous la direction de : Pr. Cesare Barbieri, Dr. Monica Lazzarin

- **nov. 1999 -dec. 2002** doctorat en Sciences et Technologies Spatiales à l'Université des études de Padoue, et, en cotutelle, Doctorat (III cycle) d'Astrophysique et Méthodes associées, école doctorale Astronomie et Astrophysique d'Ile de France, de l'Université Denis Diderot, Paris VII.
  Titre des travaux : Caractérisation Scientifique de la Wide Angle Camera et étude Physique des petits corps du Système Solaire, thèse faite sous la direction de Pr. Maria Antonietta Barucci et Pr. Cesare Barbieri.
  Soutenance : 18 Décembre 2002 à Padoue, Italie ; j'ai obtenu le **Doctorat d'Astrophysique et Méthodes associées** de l'Université Denis Diderot, avec **mention très honorable**, et le **Doctorat en Science et Technologie spatiales** de l'Université de Padoue.

ACTIVITÉS PROFESSIONNELLES PASSÉES

- Avril –Décembre 1998 : CDD de recherche pour l'étude, avec le logiciel Opticad, de la réflectivité des matériaux des surfaces éclairées du Soleil dans le milieu spatial mené au Département d'Astronomie et au centre de Sciences et Activités Spatiales (CISAS) de l'Université de Padoue, Italie, sous la direction du Pr. Barbieri
- 11 Janvier 1999 –10 Janvier 2000 : CDD avec l'Université des Etudes de Padoue, Italie, comme fonctionnaire technicienne (VIII statut), avec comme tâche de recherche : "Calibrations photométriques de la Wide Angle Camera pour la mission spatiale Rosetta"
- 01 Décembre 2002– 30 Juin 2003 : CDD de 7 mois du type Assegno di ricerca avec l'Université de Padoue pour une activité de recherche sur le sujet : l'étude des petits corps du Système Solaire.
- 01 Juillet 2003– 30 Juin 2005 : CDD (bourse post-doctorale) de 2 ans avec l'Université de Padoue pour une activité de recherche sur le sujet : étude physique des petits corps du Système Solaire
- 07 Juillet 2005 – 31 Octobre 2005 : CDD avec l'Université de Padoue pour une activité de recherche sur l'étude du système pour la suppression de la lumière diffuse pour l'instrument QUANTEYE de l'ESO, projet de recherche Astronomie quantiste sur le télescope OWL
- 01 Janvier 2006 – 31 août 2006 : CDD de recherche avec l'Université de Padoue-CISAS (financé par le contrat avec l'agence spatiale Italienne (ASI) n. I/032/05/0) sur le sujet : Calibration Photométrique et astrométrique de l'instrument OSIRIS-WAC (mission Rosetta).
- Dès Septembre 2006 : Maître de Conférence à l'Université de Paris Diderot (titularisée en Septembre 2007)

INTÉRÊTS ET EXPERIENCES SCIENTIFIQUES

- Caractérisation des propriétés de surface des astéroïdes de la ceinture principale, des géocroiseurs et des petits corps du Système Solaire externe : Troyens de Jupiter, Centaures et trans-neptuniens
- Large expérience d'observations au sol (en spectroscopie, photométrie et polarimétrie) avec plusieurs télescopes (télescopes VLT, NTT, 1.52m et 2.2m de l'European Southern Observatory (ESO), La Silla et Paranal, Chile ; 3.0m IRTF Nasa télescope, Hawaii, USA ; WHT et TNG télescopes de l'European Northern Observatory (ENO), La Palma, Espagne ; télescopes 1.2m et 1.8m, Observatoire Astrophysique d'Asiago, Italie
- Observation au sol et caractérisation des propriétés physiques des astéroïdes cibles des missions spatiales (Rosetta et Dawn) ; en particulier, cette activité a permis à l'ESA de choisir les deux cibles les plus intéressantes pour la mission Rosetta : Steins et Lutetia.
- Étude des processus d'altération aqueuse sur les astéroïdes de la ceinture principale.
- Comparaison entre astéroïdes et météorites et recherche des possibles corps parents des météorites.
- Analyse statistique et corrélations entre les différentes populations des petits corps
- Modélisation physico-chimique de la surface des petits corps
- Etude des propriétés thermiques par observations en spectroscopie et photométrie dans la région infrarouge d'astéroïdes, de géocroiseurs et de Centaures et OTNs, avec l'instrument IRS du télescope spatial SPITZER et avec les instruments PACS et SPIRE du télescope HERSCHEL. Modélisation thermique de leur surface.

- Analyse du type Ray-Tracing et simulations optiques du système de baffling (système pour la suppression de la lumière diffuse) de la Wide Angle Camera de la Mission spatiale Rosetta.
- Mesure goniophotométrique des surfaces et caractérisation de la Bi Directional Reflectance Function (BDRF) des matériaux.
- Co-investigateur de l'instrument OSIRIS de la mission Rosetta ; participation à l'activité de calibration de l'instrument, et responsable des calibrations photométriques en vol d'OSIRIS. Réduction, analyse et élaboration des données astronomiques du système d'imagerie OSIRIS dans une collaboration internationale.
- Co-investigateur de l'instrument SYMBIOSYS pour la mission spatiale de l'ESA Bepi Colombo

RESPONSABILITÉS SCIENTIFIQUES

- **Co-investigatrice du système d'imagerie OSIRIS (dès 2004) de la mission ROSETTA (ESA) et responsable des calibrations photométriques en vol**. L'instrument OSIRIS comprends 2 caméras (WAC et NAC), et il est issu d'un consortium de 9 instituts de 6 pays différents. Avant et pendant ma thése, j'ai longuement travaillé sur l'instrument OSIRIS, avec l'étude de son système complexe de suppression de la lumière diffuse, la caractérisation des propriétés optiques de certains matériaux et vernis utilisés dans les caméras WAC et NAC d'OSIRIS, et la partecipation active aux phases de calibration de l'instrument faites au MPS de Lindau, Allemagne.
  Après le lancement de Rosetta, j'ai participé à la préparation et à l'analyse des observations des astéroïdes Steins et Lutétia (2008-2010) : calcul du temps de pose, stratégie observationnelle, écriture OIOR (orbiter instrument operations requests), analyse et interprétation des données. Pour le survol de Lutétia j'ai été la coordinatrice du groupe de travail sur la composition et les propriétés photométriques de l'astéroïde. Je participe également aux différents groupes de travail sur l'étude des astéroides et du noyau et coma de la comète.
  Mon travail a été reconnu par l'agence spatiale européenne (ESA), qui m'a donné une distinction honorifique (ESA-AWARD) attestant l'*outstanding contribution* à la mission spatiale Rosetta.
- Dès 2005 : **Co-investigatrice de l'ensemble instrumental SIMBIO-SYS (caméras et spectromètre) embarqué sur la sonde BepiColombo/Mercury Planetary Orbiter (ESA)**. J'étais responsable des calibrations scientifiques de la caméra stéréo STC (réalisée en Italie) de l'instrument SIMBIO-SYS, tâche que j'ai dû abandonner suite à mon recrutement en France (vu l'impossibilité de pouvoir suivre de près les phases de réalisation et calibration instrumentales faites en Italie).
- **Investigatrice principale et co-investigatrice de plusieurs programmes d'observations avec des télescopes au sol** (VLT, NTT, TNG, IRTF, CFH,..) dédiés à la photométrie, polarimétrie et spectroscopie dans le visible et le proche infrarouge des petits corps du Système Solaire
- 2007-2009 : Co-investigatrice de la mission Marco Polo proposée à l'ESA pour le programme d'exploration spatiale Cosmic Vision (M2)
- Dès 2008 : **Co-investigatrice d'un programme d'observations (key program)** 'TNOs are cool ' dédié à l'étude des OTNs et Centaures **avec le télescope spatial HERSCHEL (ESA)**
- 2006-2008 : **Co-investigatrice des 3 programmes d'observations** dédiés à l'étude de 13 géocroiseurs et des astéroïdes cibles de la mission Rosetta (2867 Steins et 21 Lutétia)

avec le télescope spatial SPITZER (NASA)

- Dès 2010 : **Co-investigatrice de la mission Marco Polo-R** sélectionnée par l'ESA pour la phase d'étude de faisabilité dans le cadre du programme d'exploration spatiale Cosmic Vision-M3
- Dès 2010 : **Co-investigatrice de la mission Binary Asteroid in situ Explorer (BASiX)** proposées à la NASA pour le programme Discovery 2010
- **Scientifique associé à la mission de la NASA OSIRIS-REX**
- dès 2006 : **Co-investigatrice des projets Quantum Optics for Astronomy (PI Barbieri, Univ. de Padoue, Italie), et Quantum properties of light and astronomy (projet d'excellence approuvé par la fondation Cariparo**, Italie, avec un financement de 290000 Euro) qui ont mené à la réalisation de 2 instruments (AQUEYE pour le télescope 1.8m d'Asiago et IQUEYE pour le télescope 3.5m NTT de l'ESO) dédiés à l'astronomie quantique (précision temporelle <1ns).
- **Responsable d'un projet pour jeunes chercheurs financé par l'Université de Padoue** pour l'année 2000 (montant 10 kEuro) sur l'étude des propriétés de réflectance et la diffusivité des matériaux pour des applications spatiales et astronomiques
- 2006-2011 : **Responsable scientifique de l'équipe petits corps du LESIA pour la demande annuelle de financement PNP** (programme national de planétologie) à l'Institut national des Sciences de l'Univers. Nos demandes ont étés financées chaque année (montant 9-13 KEuro par an).
- **Rapporteur pour les revues scientifiques** : Icarus, Astronomy and Astrophysics, Planetary and Space Science, New Astronomy, Journal of Quantitative Spectroscopy and Radiative Transfer

RESPONSABILITÉS ADMINISTRATIVES ET COLLECTIVES

Université

- Membre nommé du Conseil National des Universités, section 34 (dès 2011)
- Membre du conseil scientifique de l'UFR de physique de l'Univ. Paris Diderot (dès janvier 2012)
- Membre du jury du concours pour un poste de maître de conférences sur Formation et évolution des planètes à l'Université de Paris 7, section CNU 34 (Avril 2010)

Organisation de colloques

- Organisatrice du colloque "Osiris calibrations" (mission Rosetta), Meudon (10 janvier 2008)
- Organisatrice du colloque "Rosetta fly-bys", Paris (11-12 janvier 2008)
- Organisatrice du colloque "21 Lutetia : results from the OSIRIS instrument", Paris (1-2 mars 2011)
- Membre du comité local du colloque "Earth-Moon relationships", à Padoue, Italie (8-10 Novembre 2000)

- Membre du comité local du colloque "Quantum Astronomy Instrument for OWL (OwerWhelmingly Large Telescope)", à Padoue, Italie (22-23 mars 2005)
- Membre du comité local du colloque "International Symposium Marco Polo and other Small Body Sample Return Missions", Paris, Université Paris 7, mai 2009
- Membre du comité local du colloque Regolith in the Solar System, Meudon, Déc. 2010

RAYONNEMENT

- La commission Asteroids Meteors and Comets (ACM) a nommé l'astéroïde 13248 (1998 MT37) Fornasier en juillet 2002, comme reconnaissance de mon activité sur l'étude des petits corps.
- Distinction honorifique de l'agence spatiale européenne (ESA-AWARD) pour l'*outstanding contribution* à la mission spatiale Rosetta
- *Reviewer* pour les revues scientifiques : Icarus, Astronomy and Astrophysics, Planetary and Space Science, New Astronomy, Journal of Quantitative Spectroscopy and Radiative Transfer
- Membre de la commission 15 'Physical studies of comets and minor planets', division III (Planetary systems sciences) de l'Union astronomique internationale (IAU)

Invitation dans des universités étrangères

- Scientifique invitée à plusieurs reprises à l'Université de Padoue, Italie, dans le cadre du programme EUROPLANET de *personnel exchange* (2004-2009).
- Scientifique invitée à l'ESO (European Southern Observatory), Santiago, Chili en Janvier-Février 2006
- Scientifique invitée au MPS pour les calibrations de l'instrument OSIRIS (juin-septembre 2002), et pour l'exploitation des données pendant les survoles de Rosetta avec la Terre, Mars, Steins, Lutétia et les observations de la comète Tempel 1 (Juillet 2005, Février et Novembre 2007, Septembre 2008, Juillet 2010)
- Avril 2011 : Scientifique invitée au Centre d'études spatiales CISAS de l'Univ. de Padoue
- Plusieurs séminaires invités sur les petits corps et la mission Rosetta (Institut Max Planck MPS, Allemagne, Observatoire de Monte Porzio, Rome, Italie, Université de Bologne, Italie, Université de Padoue, Italie, Univ. *Pontificia Universidad Catolica*, Chili, Institute d'Astrophysique des Canaries, Espagne, ESO-european southern observatory, Santiago, Chili)

Jury de thèse

- Membre du jury de thèse de DOCTORAT en « Astronomie et Astrophysique » de l'Ile de France de M. Dan Alin NEDELCU, titre de la thèse : Modélisation dynamique et spectroscopique des astéroïdes : applications aux géocroiseurs et aux cibles de missions spatiales (23/09/2010)
- Membre du jury de thèse de DOCTORAT en Astronomie de l'Université de Padoue, Italie, de M. Mesa Dino, titre de la thèse : Planet detection with SPHERE and EPICS (11/04/2011)
- Membre du jury de thèse de DOCTORAT en Astronomie de l'Université de Padoue, Italie, de M. Verroi Enrico, titre de la thèse : Very fast photon counting photometers for astronomical applications (11/04/2011)

ACTIVITÉS D'ENSEIGNEMENT

Niveau L1

TD pour le cours de physique –PCEM (440 heures pendant les années 2006-2009) sur la mécanique, la dynamique, l'hydrodynamique, l'hydrostatique, la thermodynamique et les ondes.

TP de physique mécanique (60 h, année 2008-2009) sur l'optique, la mécanique, et les écoulements granulaires et fluides

TP de 'Physique expérimentale' (156 h, années 2009-2012) ; il s'agit de projets expérimentaux permettant l'étude d'un ou de plusieurs phénomènes liés à la mécanique, l' hydrodynamique, l'optique, l'électromagnétisme ou la thermodynamique.

TP de 'Panorama de la physique moderne' (148 h, années 2009-2012) et séminaires d'introduction au cours (1,5 heure chaque année) sur la thématique Astronomie et Astrophysique. Ce cours est une introduction à des thématiques de la physique moderne que les étudiants approfondiront dans leurs études.

Tous ces cours ont été donnés à l'Université de Paris 7 - Paris Diderot

Niveau L2

75 heures d'enseignement en TD et TP au cours de Physique II (dédié à l'optique et à l'électromagnétisme) du diplôme universitaire d'Astronomie de l'Université de Padoue, Italie (responsable du cours : Pr. R. Stagni-C. Pernechele), années 2003-2006.

Niveau L3

Cours d'Astronomie (10 heures d'enseignement) pour le diplôme universitaire d'Astronomie (responsable du cours Pr. C. Barbieri) à l'Université de Padoue, Italie, année 2002-2003

Cours d'Astronomie et Astrophysique (12 heures d'enseignement) pour le diplôme universitaire d'ingénieur aérospatial (responsable du cours Pr. C. Barbieri) à l'Université de Padoue, Italie

Niveau MASTER M2

Cours sur les 'Planètes, satellites et petits corps du Système Solaire' du master M2 d'Astronomie et Astrophysique de l'Observatoire de Paris (67,5 heures, années 2009-2012)

TD et TP pour le cours de méthodologie sur le 'Traitement des données astronomiques en imagerie et spectroscopie' du master M2 d'Astronomie et Astrophysique, parcours Dynamique des Systèmes Gravitationnels, de l'Observatoire de Paris (88 heures, années 2010-2012)

Formation à distance

Cours pour le Diplôme d'Université à distance d' Astronomie et Mécanique Céleste de l'Observatoire de Paris (25 heures, année 2011-2012).

ENCADREMENT DE STAGES UNIVERSITAIRES ET DE THÈSES

Stages niveau L3

- 2011 : Co-directrice avec Pr. M. Fulchignoni du stage de L3 magistère- Univ. Paris Diderot de M. Alan Loh (titre : 21 Lutétia : études des cratères d'impact et datation)

Stages niveau M1

- 2007 : Co-directrice avec Pr. M. Fulchignoni du stage d'Adeline Gicquel (Intercomparaison

des petits corps du Système Solaire extérieur) pour le Master M1 du magistère de physique de l'Université de Paris 7 - Denis Diderot
- 2008 : Co-directrice avec Pr. M. Fulchignoni du stage de Jennyfer Claudel (Surface morphologies of asteroids visited by space missions : hints for Rosetta targets data interpretation) pour le Master M1 Sciences de l'Univers et Technologies Spatiales de l'Observatoire de Paris
- 2011 : Directrice du stage de M. Rudy Colomba pour le Master M1 -Physique de la matière et ses applications (PMA) de Paris Diderot (Titre : Etude du processus d'altération aqueuse)

Stages niveau M2

- 2003 : Directrice du stage (équivalent M2) d'Alessandra Gregnanin du département d'Astronomie de l'Université de Padoue, sur le sujet : Caractérisation des filtres de la Wide Angle Camera de la mission spatiale Rosetta
- 2009 : Directrice du stage de Remi Soave (Analyse et interprétation de données spectrales de 55 astéroïdes de type M et X) pour le Master M2 de Planétologie de l'Université de Paris 6 Marie Curie

Encadrement de thèses

2004-2007 : Co-encadrement à 35% avec M. Barucci et C. Barbieri de la thèse de doctorat (cotutelle Italie-France) d'Alessandra Migliorini : Etude physique des petits corps du Système Solaire. Le co-encadrement a eu lieu quand j'étais en CDD de recherche post-doctorale à l'Université de Padoue, Italie, jusqu'en Aoôt 2006, puis en France. J'ai encadré Mme Migliorini sur les observations en spectroscopie visible et proche infrarouge, sur l'analyse et interprétation des données spectroscopiques des astéroïdes de type E, sur la modélisation de la composition superficielle des astéroïdes. Le travail a mené à la publication de 3 articles dans des revues à comité de lecture. Elle est actuelement en CDD à l'IASF , Rome, Italie.

2007-2009 : Co-encadrement à 33% avec M. Barucci et E. Dotto de la thèse de doctorat (cotutelle Italie-France) de Davide Perna : "Propriétés physiques des astéroïdes cibles de la mission spatiale Rosetta, et des petits corps du Système Solaire externe". J'ai surtout suivi la partie d'encadrement des observations aux télescopes, analyse et interprétation des données en photométrie et spectroscopie des TNOs, Centaures, et des 2 astéroïdes cibles de Rosetta, sur le développement des méthodes d'analyse multivariée (G-mode) pour la classification taxonomique des TNOs et Centaures. Le travail a mené à la publication de plusieurs articles (10) dans des revues à comité de lecture. M. Perna est actuellement post-doc à l'Observatoire de Naples.

2007-2010 : Co-encadrement à 25% avec M. Barucci et R. Binzel de la thèse de doctorat de Francesca DeMeo : La variation compositionnelle des petits corps à travers le Système Solaire. J'ai encadré Mlle DeMeo sur la partie réduction et analyse des données photométriques et spectroscopiques, et sur le développement des modèles de composition de surface. Plusieurs travaux (7) issus de la thèse de Mlle DeMeo ont étés publiés dans des revues scientifiques. Elle est actuellement post-doc au MIT, Etats Unis.

Encadrement Post-doctoral

-2009-2011 : Encadrement à 60% du post-doc (bourse CNES) de Cédric Leyrat, Ph.D., sur les aspects de modélisation photométrique des astéroïdes 2867 Steins et 21 Lutétia survolés par la mission spatiale Rosetta. M. Leyrat a eu un poste comme astronome-adjoint au CNAP-Observatoire de Paris à partir de septembre 2011.

Autres activités d'encadrement
-2010-2011 : Encadrement d'un projet de TIPE (travail d'initiative personnelle encadré) sur La luminosité des astéroïdes pour des élèves en classe préparatoire scientifique
-2011-2012 : Encadrement d'un projet de TIPE sur les "Risques liés aux astéroïdes géocroiseur" pour des élèves en classe préparatoire scientifique

DIFFUSION SCIENTIFIQUE

-Interviews accordées à la presse audiovisuelle lors d'événements astronomiques comme le survol de Steins et Lutétia par la mission Rosetta ou la découverte de géocroiseurs potentiellement dangereux (France 3, Radio France)
-Participation aux événements dédiés au grand public comme les journées du patrimoine, la fête de la science
-Plusieurs conférences pour le grand public sur la mission Rosetta, les Centaures et les trasneptuniens et les astéroïdes

PUBLICATIONS

- Articles dans des revues à comité de lecture : 84 (dont 15 comme premier auteur)
- Présentations invitées dans des colloques internationaux avec publication des actes : 2
- Communications dans des colloques internationaux : > 90
- Publications dans des bases de données (NASA-Planetary Data System) : 3

Liste des publications

Publications dans des revues à comité de lecture

1. **Fornasier S.**, Lazzarin M., Barbieri C., Barucci M. A., 1999. *Spectroscopic comparison of aqueous altered asteroids with CM2 carbonaceous chondrite meteorites.* Astronomy and Astrophysics S. S. 135, 65–73.
2. Doressoundiram A., Weissman P. R., Fulchignoni M., Barucci M. A., Le Bras A., Colas F., Lecacheux J., Birlan M., Lazzarin M., **Fornasier S.**, Dotto E., Barbieri C., Sykes M. V., Larson S., Hergenrother C., 1999. *4979 Otawara : Flyby target of the Rosetta mission.* Astronomy and Astrophysics 352, 697–702.
3. Barbieri C., **Fornasier S.**, Lazzarin M., Marchi S., Rampazzi F., Verani S., Cremonese G., Ragazzoni R., Dolci M., Benn C. R., Mendillo M., Baumgardner J., Chakrabarti S., Wilson J., 2001. *Lunam 2000 (Lunar Atmosphere Mission).* Earth, Moon, and Planets 85, 487.
4. **Fornasier S.**, Lazzarin M., 2001. *E-Type Asteroids : Spectroscopic Investigation on the 0.5 micron Absorption Band.* Icarus 152, 127.
5. Lazzarin M., **Fornasier S.**, Barucci M. A., Birlan M., 2001. *Groundbased investigation of asteroid 9969 Braille, target of the spacecraft mission Deep Space 1.* Astronomy and Astrophysics L. 375, 281.
6. Barucci M. A., Boehnhardt H., Dotto E., Doressoundiram A., Romon J., Lazzarin M., **Fornasier S.**, de Bergh C., Tozzi G. P., Delsanti A., Hainaut O., Barrera L., Birkle K., Meech K., Ortiz J. L., Sekiguchi T., Thomas N., Watanabe J., West R. M., Davies J. K., 2002. *Visible and near-infrared spectroscopy of the Centaur 32532 (2001 PT13). ESO Large Program on TNOs and Centaurs : First spectroscopy results.* Astronomy and Astrophysics 392, 335.
7. Doressoundiram A., Peixinho N., de Bergh C., **Fornasier S.**, Thebault P., Barucci M. A., Veillet C., 2002. *The Color Distribution in the Edgeworth-Kuiper Belt.* Astronomical Journal 124, 2279.
8. **Fornasier S.**, Barucci M.A., Binzel R.P., Birlan M., Fulchignoni M., Barbieri C., Bus S.J., Harris A.W., Rivkin A.S., Lazzarin M., Dotto E., Michalowski T., Doressoundiram A., Bertini I., Peixinho N., 2003. *A portrait of 4979 Otawara, target of the Rosetta Space Mission.* Astronomy and Astrophysics 398, 327-333.
9. Doressoundiram A., Tozzi G.P., Barucci M.A., Boehnhardt H., **Fornasier S.**, Romon J., 2003. *ESO Large Program on TNOs and Centaurs : Spectroscopic investigation of Centaur 2001 Bl41 and trasneptunian objects (26181) 1996 GQ21 and (26375) 1999 DE9.* Astronomical Journal 125, 2721-2727.

10. Boehnhardt H., Barucci M. A., Delsanti A., de Bergh C., Doressoundiram A., Romon J., Dotto E., Tozzi G. P., Lazzarin M., **Fornasier S.**, Peixinho N., Hainaut O., Davies J. K., Roussellot P., Barrera L., Birkle K., Meech K., Ortiz J. L., Sekiguchi T., Watanabe J., Thomas N., West R. M., 2003. *Results from the Eso Large Program on Transneptunian Objects and Centaurs.* Earth Moon and Planets 92, 145–156.
11. Birlan M., Barucci M. A., Vernazza P., Fulchignoni M., Binzel R. P., Bus S. J., Belskaya I., **Fornasier S.**, 2004. *Near-IR spectroscopy of asteroids 21 Lutetia, 89 Julia, 140 Siwa, 2181 Fogelin, and 5480 (1989 YK8), potential targets for the Rosetta mission ; remote observing campaign on IRTF.* New Astronomy 9, 343–351.
12. De Bergh C., Boehnhardt H., Barucci M. A., Lazzarin M., **Fornasier S.**, Romon-Martin J., Tozzi G.P., Doressoundiram A., Dotto E., 2004. *Aqueous altered silicates at the surface of two Plutinos ?* Astronomy and Astrophysics 416 791–798.
13. Binzel R. P., Bus S. J., Harris A. W., Rivkin A. S., **Fornasier S.**, 2004. *Spectral Observation for Near-Earth Objects including potential target 4660 Nereus : Results from Meudon Remote observations at the NASA Infrared Telescope Facility (IRTF).* Planetary and Space Science 52, 291–296.
14. **Fornasier S.**, Doressoundiram A., Tozzi G.P., Barucci M.A., Boehnhardt H., de Bergh C., Delsanti A., Davies J., Dotto E., 2004. *ESO Large Program on Physical Studies of Trans-Neptunian Objects and Centaurs : final results of the visible spectroscopic observations.* Astronomy and Astrophysics 421, 353-363.
15. **Fornasier S.**, Dotto E., Barucci M.A., Barbieri, C., 2004. *Water ice on the surface of the large TNO 2004 DW.* Astronomy and Astrophysics 422, L43–L46.
16. Cremonese G., Capria M. T., Achilli V., Angrilli F., Baggio P., Barbieri C., Baumgardner J., Bistacchi N., Capaccioni F., Caporali A., Casanova I., Debei S., Forlani G., **Fornasier S.**, Hunten D., Ip W. H., Lazzarin M., Longhi I., Marinangeli L., Marzari F., Massironi M., Masson P., Mendillo M., Pain B., Preti G., Ragazzoni R., Raitala J., Salemi G., Sgavetti M., Sprague A., Suetta E., Tordi M., Verani S., Wilson J. K., Wilson L., 2004. *MEMORIS : a wide angle camera for the BepiColombo mission.* Advances in Space Research 33, 2182-2188.
17. **Fornasier S.**, Dotto E., Marzari F., Barucci M.A., Boehnhardt H., Hainaut O., de Bergh, C., 2004. *Visible spectroscopic and photometric survey of L5 Trojans : investigation of dynamical families.* Icarus 172, 221–232
18. Barucci M. A., Fulchignoni M., **Fornasier S.**, Dotto E., Vernazza P., Birlan M., Binzel R. P., Carvano J., Merlin F., Barbieri C., Belskaya I., 2005. *Asteroid target selection for the new Rosetta mission baseline : 21 Lutetia and 2867 Steins.* Astronomy and Astrophysics 430, 313–317.
19. Barucci M. A., Cruikshank D. P., Dotto E., Merlin F., Poulet F., Dalle Ore C., **Fornasier S.**, de Bergh, C., 2005. *Is Sedna another Triton ?* Astronomy and Astrophysics 439, L1–L4.
20. Belskaya I.N., Shkuratov Yu. G, Efimov Yu. S, Shakhovskoy N. M., Gil-Hutton R., Cellino A., Zubko E. S., Ovcharenko A. A., Bondarenko S. Yu., Shevchenko V. G., **Fornasier S.**, Barbieri C., 2005. *The F-type asteroids with small inversion angles of polarization.* Icarus 178, 213–221
21. Küppers M., Bertini I., **Fornasier S.**, Gutierrez P., Hviid S., Jorda L., Keller H. U., Knollenberg J., Koschny D., Kramm R., Lara L. M., Sierks H., Thomas T., Barbieri C., Lamy P., Rickman H., Rodrigo R., 2005. *Evidence for a Large Dust/Ice Ratio in the Nucleus of Comet 9P/Tempel 1.* Nature 437, 987-990.

22. **Fornasier S.**, Belskaya I., Fulchignoni M., Barucci M. A., Barbieri C., 2006. *First albedo determination of 2867 Steins, target of the Rosetta mission.* Astron. Astrophys, 449, L9-L12.
23. **Fornasier S.**, Belskaya I., Shkuratov Yu.G, Pernechele C., Barbieri C., Giro E., Navasardyan H., 2006. *Polarimetric survey of asteroids with the Asiago telescope.* Astronomy and Astrophysics 455, 371-377.
24. Dotto E., **Fornasier S.**, Barucci M.A.,.et al., 2006. *The surface composition of Jupiter Trojans : Visible and near-infrared survey of dynamical families.* Icarus 183, 420-434.
25. Vernazza Pierre, Birlan Mirel, Rossi A., Dotto E., Nesvorny D., Brunetto R., **Fornasier S.**, Fulchignoni M., Renner S.. 2006. *Physical characterization of the Karin family.* Astronomy and Astrophysics 460, 945–951
26. Doressoundiram A., Peixinho, N., Moullet A., **Fornasier S.**, Barucci A., Beuzit J.-L., Veillet C. , 2007. *The Meudon Multicolor Survey (2MS) of Centaurs and Trans-Neptunian Objects : From Visible to Infrared Colors.* Astronomical Journal 134, 2186-2199.
27. **Fornasier S.**, Dotto E., Hainaut O., Marzari F., Boehnhardt H., De Luise F., Barucci M.A., 2007. *Visible spectroscopic and photometric survey of Jupiter Trojans : final results on dynamical families.* Icarus 190, 622-642
28. **Fornasier S.**, Marzari, F, Dotto, E., Barucci M.A., Migliorini, A., 2007. *Are the E-type asteroids (2867) Steins, a target of the Rosetta mission, and NEA (3103) Eger remnants of an old asteroid family ?* Astronomy and Astrophysics 474, 29-32
29. Barbieri C., Dravins D., Occhipinti T., Tamburini F., Naletto G., Deppo V. Da, **Fornasier S.**, D'Onofrio M., Fosbury R. A. E., Nilsson R., Uthas H, 2007. *Astronomical applications of quantum optics for extremely large telescopes.* Journal of Modern Optics 54, 191-197.
30. De Luise F., Perna D., Dotto E., **Fornasier S.**, Belskaya I., Boattini A., Valsecchi G. B., Milani A., Rossi A., Lazzarin M., Paolicchi P., Fulchignoni M., 2007. *Physical investigation of the potentially hazardous Asteroid (144898) 2004 VD17.* Icarus 191, 628-635.
31. Forbrich J., Preibisch Th., Menten K. M., Neuhäuser R., Walter F. M., Tamura M., Matsunaga N., Kusakabe N., Nakajima Y., Brandeker A., **Fornasier S.**, Posselt B., Tachihara K., Broeg C., 2007. *Simultaneous X-ray, radio, near-infrared, and optical monitoring of young stellar objects in the Coronet cluster.* Astronomy and Astrophysics 464, 1003-1013.
32. Keller H. U., Barbieri C., Lamy P., ..,**Fornasier S.**, et al., 2007. *OSIRIS The Scientific Camera System Onboard Rosetta.* Space Science Reviews 128, 433-506.
33. Keller H.U., Küppers M., **Fornasier S.**, Gutierrez P. J., et al., 2007. *Observations of Comet 9P/Tempel 1 around the Deep Impact event by the OSIRIS cameras onboard Rosetta.* Icarus 191, 241-257.
34. Keller H.U., Küppers M., **Fornasier S.**, Gutierrez P. J., et al., 2007. *Observations of Comet 9P/Tempel 1 around the Deep Impact event by the OSIRIS cameras onboard Rosetta.* Icarus 187, 87-103.
35. Küppers M., Mottola S., Lowry S. C., A'Hearn Michael F., Barbieri C., Barucci A., **Fornasier S.**, Groussin O., Gutiérrez P., Hviid S. F., Keller H. U., Lamy P., 2007. *Determination of the light curve of the Rosetta target asteroid (2867) Steins by the OSIRIS cameras onboard Rosetta.* Astronomy and Astrophysics 462, L13-L16.
36. **Fornasier S.**, Migliorini A., Dotto E., Barucci M.A., 2008. *Visible and near infrared spectroscopic survey of E-type asteroids, including 2867 Steins, a target of the Rosetta mission.* Icarus 196, 119-134

37. Barucci A., **Fornasier S.**, Dotto E., Lamy P. L., Jorda L., Groussin O., Brucato J. R., Carvano Jorge M., Alvarez A., Cruikshank D., Fulchignoni M., 2008. *Asteroids 2867 Steins and 21 Lutetia : surface composition from far infrared observations with the Spitzer space telescope.* Astronomy and Astrophysics 477, 665-670
38. Belskaya I., Bagnulo S., Muinonen K., Barucci A., Tozzi G. P., **Fornasier S.**, Kolokolova L., 2008. *Polarimetry of the dwarf planet (136199) Eris.* Astronomy and Astrophysics 479, 265-269
39. Alvarez-Candal A., **Fornasier S.**, Barucci A., De Bergh C., Merlin F., 2008. *Visible spectroscopy of the new ESO large program on trans-Neptunian objects and Centaurs. Part 1.* Astronomy and Astrophysics 487, 741-748
40. Bagnulo S., Belskaya I., Muinonen K., Tozzi G. P., Barucci A., Kolokolova L., **Fornasier S.**, 2008. *Discovery of two distinct polarimetric behaviours of trans-Neptunian objects.* Astronomy and Astrophysics 491, L33–L36.
41. Carvano J. M., Barucci A., Delbó M., **Fornasier S.**, Lowry S., Fitzsimmons A., 2008. *Surface properties of Rosetta's targets (21) Lutetia and (2867) Steins from ESO observations.* Astronomy and Astrophysics 479, 241-248.
42. Dotto E., Perna D., Barucci A., Rossi A., De Bergh C., Doressoundiram A., **Fornasier S.**, 2008. *Rotational properties of Centaurs and Trans-Neptunian Objects. Lightcurves and densities.* Astronomy and Astrophysics 490, 829-833.
43. Jorda L., Lamy P. L., Faury G., Weissman P., Barucci A., **Fornasier S.**, Lowry S., Toth I., Küppers M., 2008. *Asteroid 2867 Steins. I. Photometric properties from OSIRIS/Rosetta and ground-based visible observations.* Astronomy and Astrophysics 487, 1171-1178.
44. Lamy P. L., Jorda L., **Fornasier S.**, Groussin O., Barucci A., Carvano J.M., Dotto E., Fulchignoni M., Toth I., 2008. *Asteroid 2867 Steins. III. Spitzer Space Telescope observations, size determination, and thermal properties.* Astronomy and Astrophysics 487, 1187-1193.
45. Lamy P. L., Kaasalainen M., Lowry S., Weissman P., Barucci A., Carvano J. M., Choi Y.-J., Colas F., Faury G., **Fornasier S.**, Groussin O., Hicks M. D., Jorda L., Kryszczynska A., Larson S., Toth I., Warner B., 2008. *Asteroid 2867 Steins. II. Multi-telescope visible observations, shape reconstruction, and rotational state.* Astronomy and Astrophysics 487, 1179-1185.
46. Barbieri C., Naletto G., Occhipinti T.,..,**Fornasier S.**, et al., 2009. *AquEYE, a single photon counting photometer for astronomy.* Journal of Modern Optics 56, 261–272.
47. Belskaya I., **Fornasier S.**, Krugly Yu. N., 2009. *Polarimetry and BVRI photometry of the potentially hazardous near-Earth Asteroid (23187) 2000 PN9* . Icarus 201, 167-171.
48. De Bergh C., Barucci A., Merlin F., **Fornasier S.**, Doressoundiram A., Brunetto R., 2009. *Carbonaceous Compounds at the Surface of Transneptunian Objects and Centaurs.* Meteoritics and Planetary Science Supplement 72, 5102.
49. Demeo F., **Fornasier S.**, Barucci A., Perna D., Protopapa Silvia, Alvarez-Candal A., Delsanti A., Doressoundiram A., Merlin F., De Bergh C., 2009. *Visible and near-infrared colors of Transneptunian objects and Centaurs from the second ESO large program.* Astronomy and Astrophysics 493, 283–290.
50. **Fornasier S.**, Barucci A., De Bergh C., Alvarez-Candal A., Demeo F., Merlin F., Perna D., Guilbert A., Delsanti A., Dotto E., Doressoundiram A., 2009. *Visible spectroscopy of the new ESO large programme on trans-Neptunian objects and Centaurs : final results.* Astronomy and Astrophysics 508, 457-465.

51. Guilbert A., Barucci A., Brunetto R., Delsanti A., Merlin F., Alvarez-Candal A., **Fornasier S.**, De Bergh C., Sarid G., 2009. *A portrait of Centaur 10199 Chariklo*. Astronomy and Astrophysics 501, 777-784.
52. Merlin F., Alvarez-Candal A., Delsanti A., **Fornasier S.**, Barucci A., Demeo F., De Bergh C.,Doressoundiram A.,Quirico E.,Schmitt B.,2009. *Stratification of Methane Ice on Eris' Surface*. Astronomical Journal 137, 315-328.
53. Perna D., Dotto E., Barucci A., Rossi A., **Fornasier S.**, De Bergh C., 2009. *Rotations and densities of trans-Neptunian objects*. Astronomy and Astrophysics 508, 451-455.
54. Dalle Ore C., M., Barucci A., Emery J. P., Cruikshank D. P., Dalle Ore L. V., Merlin F., Alvarez-Candal A., De Bergh C., Trilling D. E., Perna D., **Fornasier S.**, Mastrapa R. M. E., Dotto E. , 2009. *Composition of KBO (50000) Quaoar*. Astronomy and Astrophysics 501, 349–357.
55. Dotto E., Perna D., **Fornasier S.**, Belskaya I., Barucci A., Shevchenko V. G., Krugly Yu. N., Gaftonyuk N. M., Tereschenko I. A., Scipioni F., De Luise F., 2009. *Photometric and spectroscopic investigation of 2867 Steins, target of the Rosetta mission. Ground-based results prior to the Rosetta fly-by*. Astronomy and Astrophysics 494, L29–L32.
56. Müller, T. G., Lellouch E.l, Böhnhardt, H, .., **Fornasier S.**, et al., 2009. *TNOs are Cool : A Survey of the Transneptunian Region*. Earth Moon and Planets 105, 209-219
57. Naletto G., Barbieri C., Occhipinti T., .., **Fornasier S.**, et al., 2009. *Iqueye, a single photon-counting photometer applied to the ESO new technology telescope*. Astronomy and Astrophysics 508, 531–539.
58. Protopapa S., Alvarez-Candal A., Barucci A., Tozzi G. P., **Fornasier S.**, Delsanti A., Merlin F., 2009. *ESO large program about transneptunian objects : surface variations on (47171) 1999 TC36*. Astronomy and Astrophysics 501, 375–380.
59. Belskaya I., Bagnulo S., Barucci A., Muinonen K., Tozzi G. P., **Fornasier S.**, Kolokolova L., 2010. *Polarimetry of Centaurs (2060) Chiron, (5145) Pholus and (10199) Chariklo*. Icarus 210, 472–479.
60. Belskaya I., **Fornasier S.**, Krugly Yu. N., Shevchenko V. G., Gaftonyuk N. M., Barucci A., Fulchignoni M., Gil-Hutton R., 2010. *Puzzling asteroid 21 Lutetia : our knowledge prior to the Rosetta fly-by*. Astronomy and Astrophysics 515, 29–37.
61. Carry B., Kaasalainen M., Leyrat C., Merline W. J., Drummond J. D., Conrad A., Weaver H. A., Tamblyn P. M., Chapman C. R., Dumas C., Colas F., Christou J. C., Dotto E., Perna D., **Fornasier S.**, Bernasconi L., Behrend R., Vachier F., Kryszczynska A., Polinska M., Fulchignoni M., Roy R., Naves R., Poncy R., Wiggins P., 2010. *Physical properties of the ESA Rosetta target asteroid (21) Lutetia. II. Shape and flyby geometry*. Astronomy and Astrophysics 523, 94–100.
62. Demeo F., Barucci A., Merlin F., Guilbert-Lepoutre A., Alvarez-Candal A., Delsanti A., **Fornasier S.**, De Bergh Catherine., 2010. A spectroscopic analysis of Jupiter-coupled object (52872) Okyrhoe, and TNOs (90482) Orcus and (73480) 2002 PN34 . Astronomy and Astrophysics 521, 35–41.
63. **Fornasier S.**, Clark B. E., Dotto E., Migliorini A., Ockert-Bell Maureen E., Barucci A., 2010. *Spectroscopic survey of M-type asteroids*. Icarus 210, 655–673.
64. Merlin F., Barucci A., De Bergh C., **Fornasier S.**, Doressoundiram A., Perna D., Protopapa S., 2010. *Surface composition and physical properties of several trans-neptunian objects from the Hapke scattering theory and Shkuratov model*. Icarus 208, 945–954.

65. Perna D., Dotto E., Lazzarin M., Magrin S., Fulchignoni M., Barucci A., **Fornasier S.**, Marchi S., Barbieri C., 2010. *Inhomogeneities on the surface of 21 Lutetia, the asteroid target of the Rosetta mission. Ground-based results before the Rosetta fly-by.* Astronomy and Astrophysics 513, L4.
66. Perna D., Barucci A., **Fornasier S.**, Demeo F., Alvarez-Candal A., Merlin F., Dotto E., Doressoundiram A., De Bergh C., 2010. *Colors and taxonomy of Centaurs and trans-Neptunian objects.* Astronomy and Astrophysics 510, A53.
67. Alvarez-Candal A., Barucci A., Merlin F., De Bergh Catherine, **Fornasier S.**, Guilbert A., Protopapa S., 2010. *The trans-Neptunian object (42355) Typhon : composition and dynamical evolution.* Astronomy and Astrophysics 511, A35.
68. Clark B. E., Ziffer J., Campins H., Rivkin A. S., Hiroi T., Barucci A., Fulchignoni M., Binzel R. P., **Fornasier S.**, Demeo F., Ockert-Bell M. E., Licandro J., Mothe Diniz T., 2010. *Spectroscopy of B-type asteroids : Subgroups and meteorite analogs.* Journal of Geophysical Research (Planets) 115, 06005.
69. De Luise F., Dotto E., **Fornasier S.**, Barucci A., Pinilla-Alonso N., Perna D., Marzari F., 2010. *A peculiar family of Jupiter Trojans : The Eurybates.* Icarus 209, 586–590.
70. Keller H. U., Barbieri C., Koschny D., . . . ,**Fornasier S.**, et al., 2010. *E-Type Asteroid (2867) Steins as Imaged by OSIRIS on Board Rosetta.* Science 327, 190–193.
71. Lamy P. L., Groussin O., **Fornasier S.**, Jorda L., Kaasalainen M., Barucci A., 2010. *Thermal properties of asteroid 21 Lutetia from Spitzer Space Telescope observations.* Astronomy and Astrophysics 516, A74.
72. Leyrat C., **Fornasier S.**, Barucci A., Magrin S., Lazzarin M., Fulchignoni Marcello, Jorda L., Belskaya I., Marchi S., Barbieri C., Keller U., Sierks H., Hviid S., 2010. *Search for Steins' surface inhomogeneities from OSIRIS Rosetta images.* Planetary and Space Science 58, 1097–1106.
73. Lellouch E., Kiss C., Santos-Sanz P., Müller T. G., **Fornasier S.**,et al., 2010. *"TNOs are cool" : A survey of the trans-Neptunian region. II. The thermal lightcurve of (136108) Haumea.* Astronomy and Astrophysics 518, L147.
74. Lim T. L., Stansberry J., Müller T. G., ..,**Fornasier S.**, et al., 2010. *"TNOs are Cool" : A survey of the trans-Neptunian region . III. Thermophysical properties of 90482 Orcus and 136472 Makemake.* Astronomy and Astrophysics 518, L148.
75. Müller T. G., Lellouch E., Stansberry J., .., **Fornasier S.**, et al., 2010. "TNOs are Cool" : A survey of the trans-Neptunian region. I. Results from the Herschel science demonstration phase (SDP). Astronomy and Astrophysics 518, L146.
76. Ockert-Bell M. E., Clark B. E., Shepard M. K., Isaacs R. A., Cloutis E. A., **Fornasier S.**, Bus S. J. , 2010. *The composition of M-type asteroids : Synthesis of spectroscopic and radar observations.* Icarus 210, 674–692.
77. Shestopalov D. I., Golubeva L. F., McFadden L. A., **Fornasier S.**, Taran M. N., 2010. *Titanium-bearing pyroxenes of some E asteroids : Coexisting of igneous and hydrated rocks.* Planetary and Space Science 58, 1400–1403.
78. Groussin O., Lamy P., **Fornasier S.**, Jorda L., 2011. *The properties of asteroid (2867) Steins from Spitzer Space Telescope observations and OSIRIS shape reconstruction.* Astronomy and Astrophysics 529, A73.
79. **Fornasier S.**, Clark B. E., Dotto E., 2011a. *Spectroscopic survey of X-type asteroids. Icarus* 214, 131–146.

80. Barucci M. A., Alvarez-Candal A., Merlin F., Belskaya I. N., de Bergh C., Perna D., DeMeo F., **Fornasier S.**, 2011. *New insights on ices in Centaur and Transneptunian populations.* Icarus 214, 297–307.

81. **Fornasier S.**, Mottola S., Barucci M. A., Sierks H., Hviik S., 2011b. *Photometric observations of asteroid 4 Vesta by the OSIRIS cameras onboard the Rosetta spacecraft.* Astronomy and Astrophysics 533, L9.

82. Sierks H., Lamy P., Barbieri C.,..**Fornasier S.**, et al., 2011. *Images of Asteroid 21 Lutetia : A Remnant Planetesimal from the Early Solar System.* Science 334, 487

83. Santos-Sanz P., Lellouch E., **Fornasier S.**, Kiss C., Pal A., Müller T. G., Vilenius E., Stansberry J., Mommert M., Delsanti A., Mueller M., Peixinho N., Henry F., Ortiz J. L., Thirouin A., Protopapa S., Duffard R., Szalai N., Lim T., Ejeta C., Hartogh P., Harris A. W., Rengel M., 2012. *"TNOs are Cool" : A Survey of the Transneptunian Region IV. Size/albedo characterization of 15 scattered disk and detached objects observed with Herschel Space Observatory-PACS.* Astronomy and Astrophysics, en presse.

84. Baurcci M.A., Merlin F., Perna D., Alvarez-Candal A., Müller T., Mommert M., Kiss C., **Fornasier S.**, Santos-Sanz P., Dotto E., 2012. The extra red plutino (55638) 2002 VE95. Astronomy and Astrophysics, en presse.

Presentation en conférences et congrès

1. Lazzarin M., **Fornasier S.**, Barbieri C., Barucci A., 1999. *Spectroscopic comparison of aqueous altered asteroids with CM2 carbonaceous chondrite meteorites.* Meeting *Asteroids, Comets and Meteors*, Cornell University, Ithaca, NY, July 1999.

2. Cremonese G., Barbieri C., Baruffolo A., Bernardi F., **Fornasier S.**, Ghedina A., Lazzarin M., Marchetti E., Ragazzoni R., 1999. *Speckle interferometry of asteroids with the 3.5m TNG.* Meeting *Asteroids, Comets, Meteors*, Cornell Univ., Ithaca, New York, July 1999.

3. **Fornasier S.**, Pernechele C., Barbieri C., 1999. *The Asiago Observatory's reflectogoniometer*, 31^{o} Annual Meeting of the Division for Planetary Science of the A.A.S., *Bull. A.A.S.*, **31**, 5007.

4. Lazzarin M., **Fornasier S.**, Barbieri C., Di Martino M., 1999. *Spectroscopic investigation of asteroid targets of spacecraft missions Rosetta and Deep Space 1.* 31^{o} Annual Meeting of the Division for Planetary Science of the A.A.S., *Bull. A.A.S.*, **31**, 1106.

5. Doressoundiram A., Weissman P.R., Fulchignoni M., Barucci M.A., Le Bras A., Colas F., Lecacheux J., Birlan M., Lazzarin M., **Fornasier S.**, Dotto E., Barbieri C., Sykes M.V., Larson S., Hergenrother C., 1999. *Physical and chemical properties of 4979 Otawara.* 31^{o} Annual Meeting of the Division for Planetary Science of the A.A.S., *Bull. A.A.S.*, **31**, 5912.

6. Debei S., Angrilli F., Barbieri C., Bianchini G., Da Deppo V., De Cecco M., **Fornasier S.**, Guizzo G., Naletto G., Ragazzoni R., Saggin B., Tondello G., Zaccariotto M., Brunello P., Peron F., 1999. *The Wide Angle Camera for the Rosetta Mission.* 31^{o} Annual Meeting of the Division for Planetary Science of the A.A.S.,*Bull. A.A.S.*, **31**, 5948.

7. Brunello P., Peron F., **Fornasier S.**, Barbieri C., 2000. *Baffling system for the Wide Angle Camera (WAC) of Rosetta Mission. SPIE Proceedings*, **4093**, 79–88.

8. Barbieri C., Cremonese, G., **Fornasier S.**, Lazzarin M., Marchi S., Ragazzoni R., Rampazzi F., Verani S., Benn C., Mendillo M., Baumgartner J., Wilson J., Chakrabarti S., Dolci M., 2000. *LUNAM (Lunar Atmosphere Mission). Conference Earth-Moon Relationships*, 8/10 November 2000, Accademia Galileiana - Padova, Italy.

9. Cremonese G., Achilli V., Barbieri C., Caporali A., Capria M. T., Colangeli L., Forlani **Fornasier S.**, Lazzarin M., Marzari F., Marinangeli L., Naletto G., Palumbo P., Ragazzoni R., Salemi G., Verani S., 2001. *A Wide Angle Camera for Bepi Colombo. Workshop on Mercury : Space Environment, Surface, and Interior*, October 4-5, 2001, abstract n. 8023.
10. Barbieri C., Lazzarin M., Marchi S., **Fornasier S.**, Verani S., Cremonese G., Ragazzoni R., Benn C., Dolci M., Mendillo M., Baumgardner J., Chakrabarti S., 2001. *Lunam 2000 (Lunar Atmosphere Mission)*, *European Geophysical Society*, Nizza, March 2001.
11. Cremonese G., Ragazzoni R., Barbieri C., Lazzarin M., **Fornasier S.**, Verani S., Marzari F.,Naletto G., Caporali A., Achilli V., Salemi G., Capaccioni F., 2001. *Wide Angle Camera for Bepi Colombo. European Geophysical Society*, Nizza, March 2001.
12. Barbieri C., Lazzarin M., Verani S., Rampazzi F., **Fornasier S.**, Ragazzoni R., Cremonese G., Mendillo M., Baumgardner J., Chakrabarti S., Cook T., Wilson J., 2001. *Lunam 2000 (Lunar Atmosphere Mission)*, *ASI workshop on the International Space Station*, Torino, Italy, May 2001.
13. Lazzarin M., **Fornasier S.**, Barucci M.A., Barbieri C., 2001. *Low resolution spectroscopic survey of main belt asteroids : looking for aqueous alteration products.* Congresso *Asteroids 2001 : from Piazzi to the 3rd millenium*, Palermo, Italy, June 2001.
14. Lazzarin M., Di Martino M., Marchi S., **Fornasier S.**, Barucci M.A., Dotto E., Barbieri C., 2001. *Visible and Near Infrared Investigation of Near Earth Asteroids.* Congresso *Asteroids 2001 : from Piazzi to the 3rd millenium*, Palermo, Italy, June 2001.
15. Doressoundiram A., Peixinho N., Barucci M. A., **Fornasier S.**, Blancho S., 2001. *Meudon Multicolor Survey of Outer Solar System Objects.* 33^o Annual Meeting of the Division for Planetary Science of the A.A.S.,*Bull. A.A.S.*, **33**, 1201.
16. Debei S., **Fornasier S.**, Ramous P., Barbieri C., Da Deppo V., Brunello P., Peron F., 2001. *The Wide Angle Camera of Rosetta Mission : design and manufacturing of an innovative baffling system for an aspherical optics telescope. SPIE* proceedings, **4498**, 324–334.
17. Lazzarin M., Barbieri C., Marchi S., **Fornasier S.**, 2002. *Cofin 1998-2000 : Near Infrared spectroscopy of Near Earth Objects*, meeting *SAIT*, 10-12 April 2002, Padova.
18. **Fornasier S.**, Barucci M. A., Binzel R. P., Fulchignoni M., Birlan M., Barbieri C., Lazzarin, M., Doressoundiram A., Dotto, E., Peixinho N., 2002. *A portrait of 4979 Otawara, target of the Rosetta space mission.* Meeting *Asteroids, Comets, Meteors*, Berlin, Germany, July 2002.
19. Peixinho N., Doressoundiram A., De Bergh C., **Fornasier S.**, Thebault P., Barucci M. A., Veillet, C, 2002. *Meudon Multicolor Survey of Outer Solar System Objects : Trends and Correlations.* Meeting *Asteroids, Comets, Meteors*, Berlin, Germany, July 2002.
20. Lazzarin M., Marchi S., Barucci M.A., **Fornasier S.**, Barbieri C., 2002. *Visible and Near Infrared Spectroscopy of Near Earth Objects.* Meeting *Asteroids, Comets, Meteors*, Berlin, Germany, July 2002.
21. Barucci M. A., Boehnhardt H., de Bergh C., Dotto E., Doressoundiram A., Lazzarin M., Romon J., Tozzi G. P., **Fornasier S.**, Barrera L., Birkle K., Delsanti A., Hainaut O., Meech K., Ortiz J. L., Sekiguchi T., Thomas N., Watanabe J., West R. M., 2002. *Visible and Infrared spectroscopy of Centaurs and TNOs. from ESOs Large Programm.* Meeting *Asteroids, Comets, Meteors*, Berlin, Germany, July 2002.
22. De Bergh C., Boehnhardt H., Barucci M. A., Lazzarin M., Romon-Martin J., **Fornasier S.**, 2002. *About the weak signatures detected in visible spectra of two plutinos.* Meeting *Asteroids, Comets, Meteors*, Berlin, Germany, July 2002.

23. Barbieri C., **Fornasier S.**, Verani, S., Ragazzoni R., Barilli M., Paolinetti R, Romoli A., Della Torre A., Mendillo M., Baumgardner J., 2002. *PLEXISS : a coronograph for imaging the lunar atmosphere from the International Space Station. SPIE*, **4767**, 106–113.

24. **Fornasier S.**, Barucci M. A., Binzel R. P., Birlan M., Fulchignoni M., Barbieri C., Bus S. J., Harris A. W., Rivkin A. S., Lazzarin, M., Dotto, E., Erikson A., Michalowsky T., Doressoundiram A., Bertini I., Peixinho N., 2002. *Spectrophotometric observations of 4979 Otawara, target of the Rosetta space mission.* 34^o Annual Meeting of the Division for Planetary Science of the A.A.S., *Bull. A.A.S.*, **34**, 1411.

25. Barucci M. A., Boehnhardt H., Dotto E., Lazzarin M., Romon J., de Bergh C., Doressoundiram A., Tozzi G. P., **Fornasier S.**, Davies J., Peixinho N., Barrera L., Birkle K., Delsanti A., Hainaut O., Meech K., Ortiz J. L., Sekiguchi T., Thomas N., Watanabe J., West R. M., 2002. *ESO Large Program : Results from Visible and Infrared spectroscopy of Centaurs and TNOs.* 34^o Annual Meeting of the Division for Planetary Science of the A.A.S., *Bull. A.A.S.*, **34**, 707.

26. Naletto G., Da Deppo V., Nicolosi P., Zambolin P., Barbieri C., **Fornasier S.**, 2003. *Calibration of the Wide Angle Camera for the Rosetta Mission : Preliminary Results on the Flight Model. SPIE*, **4954**, 375–384.

27. Barbieri C., **Fornasier S.**, Verani S., Bertini I., Lazzarin M., Rampazzi, F., Cremonese G., Ragazzoni R., Marzari F., Angrilli F., Bianchini G. A., Debei S., Dececco M., Guizzo G., Parzianello G., Ramous P., Saggin B., Zaccariotto M., Da Deppo V., Naletto G., Nicolosi G., Pelizzo M. G., Tondello G., Brunello P., Peron F., 2003. *The Wide Angle Camera of the ROSETTA Mission*, *Memorie della Societa Astronomica Italiana*, **74**, 434–435

28. **Fornasier S.**, 2003. *Aqueous alteration on minor bodies of the Solar System. Proceeding of the V Italian meeting of Planetary Science*, Gallipoli, Italy, 2003, pp. 139–142

29. Gregnanin A., **Fornasier S.**, Barbieri C., 2003. *Visible spectroscopy of minor bodies from the 1.22m Asiago telescope. Proceeding of the V Italian meeting of Planetary Science*, Gallipoli, Italy, 2003, pp. 143–146

30. Barbieri C, **Fornasier S.**, Cremonese G., Bertini I., Fulle M., Magazzù A., 2003. Observations of the new Rosetta targets. *Workshop on the new Rosetta targets*, Capri, Italy, October 2003.

31. Barucci M. A., Boehnhardt H., Doressoundiram A., Dotto E., de Bergh C., Tozzi G. P., Lazzarin M., **Fornasier S.**, Davies J., Delsanti A., LP Team, 2003. *Visible and near-infrared spectroscopy of Centaurs and TNOs : update of the ESO Large Program.* 35^o Annual Meeting of the Division for Planetary Science of the A.A.S., *Bull. A.A.S.*, **35**, 39.02.

32. Birlan M., Vernazza P., Barucci M. A., Fulchignoni M., Binzel R. P., Bus S. J., **Fornasier S.**, 2003. *Near-IR spectroscopy of new asteroid targets for the Rosetta mission.* 35^o Annual Meeting of the Division for Planetary Science of the A.A.S., *Bull. A.A.S.*, **35**, 34.14.

33. Fulchignoni M., Barucci A., **Fornasier S.**, Dotto E., Vernazza P., Birlan M., Carvano J. M., Merlin F., Belskaya I. 2867 Steins and 21 Lutetia : the Rosetta mission asteroid targets. In Bulletin of the American Astronomical Society. 2004, vol. 36, pp. 1130

34. Barbieri C., **Fornasier S.**, Cremonese G., Bertini I., Fulle M., Magazzú A. Observations of the new Rosetta targets. In The New Rosetta Targets. Observations, Simulations and Instrument Performances. 2004, vol. 311, pp. 53

35. Da Deppo V., Naletto G., Nicolosi P.,.., **Fornasier S.**, et al., preliminary calibration results of the wide angle camera of the imaging instrument OSIRIS for the Rosetta mission. In 5th International Conference on Space Optics. 2004, vol. 554, pp. 191-198
36. Dotto E., **Fornasier S.**, Barucci A., Boehnhardt H., Hainaut O., Marzari F., Licandro J., De Bergh C.. Visible and near-infrared spectroscopic survey of Jupiter Trojan asteroids : investigation of dynamical families. In Bulletin of the American Astronomical Society. 2004, vol. 36, pp. 1139
37. Barucci A., Cruikshank D. P., Dotto E., Merlin F., Poulet F., Dalle Ore C., **Fornasier S.**, De Bergh C.. Nitrogen and Methane Ices on the Surface of Sedna ?. In Bulletin of the American Astronomical Society. 2005, vol. 37, pp. 744
38. Vernazza P., Fulchignoni M., Birlan M., Dotto E., Rossi A., **Fornasier S.**, Marzari F., Nesvorny D. Spectroscopic characterization of the Karin family. In Bulletin of the American Astronomical Society. 2005, vol. 37, pp. 644
39. Dotto E., **Fornasier S.**, Barucci A., Licandro J., Boehnhardt H., Hainaut O., Marzari F., De Bergh Catherine, De Luise F. Jupiter Trojans : a Survey of Members of Dynamical Families. In Bulletin of the American Astronomical Society. 2005, vol. 37, pp. 623
40. Barbieri C., **Fornasier S.**, Bertini I., et al. First Results from the Wide Angle Camera of the ROSETTA Mission. Memorie della Società Astronomica Italiana Supplement 2005 , v.6, p.28
41. Keller H. U., Küppers M., Hviid S., Sierks H., Barbieri C., **Fornasier S.**, et al. Deep Impact observations by the scientific imaging system OSIRIS of the Rosetta mission. Bulletin of the American Astronomical Society, Vol. 37, p.709
42. Cavadore C., Elst E. W., Lagerkvist C.-I.,..**Fornasier S.**, et al. Minor Planet Observations [809 European Southern Observatory, La Silla]. Minor Planet Circulars, 2005, vol. 5435
43. Barbieri C., Da Deppo V., D'Onofrio M., Dravins D., **Fornasier S.**, et al. QuantEYE, the quantum optics instrument for OWL. In The Scientific Requirements for Extremely Large Telescopes. 2006, vol. 232, pp. 506-507
44. Dotto E., **Fornasier S.**, Barucci A., Hainaut O., Boehnhardt H., Licandro J., Marzari F., De Bergh C., De Luise F. Jupiter Trojans : The Physical Properties Of Members Of Dynamical Families. In Bulletin of the American Astronomical Society. 2006, vol. 38, pp. 595
45. Keller H. U., Küppers M., Rengel M., **Fornasier S.**, Cremonese G., Gutierrez P., Ip W. H., Knollenberg J., Jorda L. Observations of comet 9P/Tempel 1 around the Deep Impact event with the OSIRIS cameras on Rosetta. In 36th COSPAR Scientific Assembly. 2006, vol. 36, pp. 2382
46. Küppers M., Keller H. U., Hviid S. F., Mottola S., **Fornasier S.**, Barbieri C., Barucci Antonella, Gutierrez P., Lamy P. L. Determination Of The Light Curve Of Rosetta Target Asteroid 2867 Steins With The Osiris Narrow Angle Camera Onboard Rosetta. In Bulletin of the American Astronomical Society. 2006, vol. 38, pp. 596
47. Lamy P. L., Barucci A., Jorda L., Lowry S., Carvano Jorge M., **Fornasier S.**, Groussin O., Kaasalainen M. Visible and infrared observations of Asteroid Steins, a target of the Rosetta mission. In 36th COSPAR Scientific Assembly. 2006, vol. 36, pp. 3351
48. Lamy P. L., Jorda L., **Fornasier S.**, Kaasalainen M., Lowry S., et al. Visible and Infrared Observations of Asteroid 2867 Steins, a target of the Rosetta Mission. In Bulletin of the American Astronomical Society. 2006, vol. 38, pp. 59.09

49. Cremonese G., Capria M. T., Barbieri, C., .., **Fornasier S.**, et al. The stereo channel (STC) of the SIMBIO-SYS instrument for the BepiColombo mission to Mercury. Memorie della Società Astronomica Italiana Supplement 2006, v.9, p.173
50. Naletto G., Barbieri C., Dravins D., .., **Fornasier S.** et al., QuantEYE : a quantum optics instrument for extremely large telescopes. Ground-based and Airborne Instrumentation for Astronomy. Edited by McLean, Ian S. ; Iye, Masanori. Proceedings of the SPIE, Volume 6269, pp. 62691W, 2006
51. De Luise F., Dotto E., **Fornasier S.**, Lazzarin M., Perna Davide, Perozzi E., Rossi A., Valsecchi G. B. Study for potential candidates for a Sample Return Spase Mission to a Near Earth Object. Memorie della Societa Astronomica Italiana, 2007, vol. 78, 604.
52. Barucci A., Merlin F., Guilbert A., bf Fornasier S., et al. Characterization of TNOs' Surface Properties : Preliminary Results of a Large VLT Programme. In AAS/Division for Planetary Sciences Meeting Abstracts. 2007, vol. 39, pp. 49.02
53. Merlin F., Alvarez A., Barucci A., Delsanti A., bf Fornasier S., De Bergh C. Spectrum of Eris from 0.5 to 2.4 Microns. Clues for a Stratified Surface. In AAS/Division for Planetary Sciences Meeting Abstracts. 2007, vol. 39
54. Peixinho N., Doressoundiram A., Moullet A., bf Fornasier S., Barucci A., Beuzit J., Veillet C. Visible and Infrared Colors of Centaurs and TNOs from the Meudon Multicolor Survey (2ms). In American Astronomical Society Meeting Abstracts. 2007, vol. 210
55. Perna D., Dotto E., De Luise F., Barucci A., Fulchignoni M., **Fornasier S**. Physical Properties of 21 Lutetia, Target of the Esa Space Mission Rosetta. In AAS/Division for Planetary Sciences Meeting Abstracts. 2007, vol. 39
56. Dotto E., Perna D., Barucci A., De Bergh C., Doressoundiram A., **Fornasier S**. Rotational Properties of Centaurs and KBOs. In AAS/Division for Planetary Sciences Meeting Abstracts. 2007, vol. 39
57. Demeo F., **Fornasier S.**, Barucci A., et al., 2008. Visible and Near-Infrared Colors of KBOs and Centaurs from the Second ESO Large Program. LPI Contributions, 2008, vol. 1405, pp. 8189
58. Merlin F., Alvarez-Candal A., Delsanti A., Quirico E., Schmitt B., **Fornasier S.**, Barucci A., Demeo F., De Bergh C., Doressoundiram A. Icy Surface Properties of the Dwarf Planet Eris. LPI Contributions, 2008, vol. 1405, pp. 8141
59. Alvarez-Candal A., **Fornasier S.**, Barucci M. A., de Bergh, C., Merlin, F., 2008. New ESO-Large Program on TNOs : First Visible Spectroscopic Results. LPI Contribution 2008, vol. 1405, pp. 8001
60. Vernazza P., Binzel R. P., Rossi A., Birlan M., **Fornasier S.**, Fulchignoni M., Renner S., 2008. Physical Characterization of Very Young Asteroid Families. LPI Contribution 2008, vol. 1405, pp. 8044.
61. **Fornasier S.**, Migliorini A., Dotto E., Barucci M. A. 2008. Spectroscopic Survey of E-Type Asteroids, Including 2867 Steins, a Target of the Rosetta Mission. LPI Contribution 2008, vol. 1405, pp. 8045
62. Lamy P. L., Barucci A., **Fornasier S.**, et al.. A Portrait of Asteroid 2867 Steins from Visible and Infrared Observations with Ground- and Space-Based Telescopes. LPI Contribution 2008, vol. 1405, pp.8163
63. Perna D., Dotto E., Barucci A., Rossi A., De Bergh C., Doressoundiram A., **Fornasier S.**. Rotational Properties of Centaurs and Trans-Neptunian Objects : Results from the ESO Large Program. LPI Contributions, 2008, vol. 1405, pp. 8110

64. Müller T. G., Lellouch E., Böhnhardt H., ...,**Fornasier S.** et al. 2008. Hershel open time key programme : TNOs are Cool : A survey of the transneptunian region. LPI Contributions, 2008, vol. 1405, pp. 8080.
65. Belskaya I., Bagnulo S., Barucci A., Muinonen K., Tozzi G. P., **Fornasier S.**, Kolokolova L. Polarimetric Properties of Transneptunian Objects and Centaurs. In Bulletin of the American Astronomical Society. 2008, vol. 40, pp. 482
66. Belskaya I., Bagnulo S., Barucci A., Muinonen K., Tozzi G. P., **Fornasier S.**, Kolokolova L. Polarimetry of Transneptunian Objects and Centaurs with VLT. LPI Contribution 2008, vol. 1405, pp. 8172
67. Merlin F., Barucci A., **Fornasier S.**, De Bergh C., Perna D., Doressoundiram A., Delsanti A. Surface Analyses Of The Centaur Echeclus And Trans-neptunian Objects.. In Bulletin of the American Astronomical Society. 2008, vol. 40, pp. 482
68. Perna D., Dotto E., Barucci A., Rossi A., De Bergh C., Doressoundiram A., **Fornasier S**. Light Curves and Densities of Centaurs and Trans-Neptunian Objects from the ESO Large Program. In Bulletin of the American Astronomical Society. 2008, vol. 40, pp. 483
69. De Luise F., Dotto E., **Fornasier S.**, Barucci A., Perna D., Marzari F. The Nature of the Eurybates Family. In Bulletin of the American Astronomical Society. 2008, vol. 40, pp. 438
70. DeMeo F., **Fornasier S.**, Barucci A., et al. Visible and Near-infrared Colors of TNOs from the Second ESO Large Program. In Bulletin of the American Astronomical Society. 2008, vol. 40, pp. 482
71. McFadden L. A., A'Hearn M. F., Ammannito E., ...,**Fornasier S.** et al. Coordinated Laboratory Studies of Aubrite Meteorites for Rosetta flyby of Asteroid 2867 Steins. In Bulletin of the American Astronomical Society. 2008, vol. 40, pp. 509
72. **Fornasier S.**, Dotto E., Hainaut O., Marzari F., Boehnhardt H., de Luise F., Barucci M. A., de Bergh, C. Spectroscopy and Photometry of Jupiter Trojans V1.0. NASA Planetary Data System, EAR-A-EMMI-3-FORNASIER-V1.0, 2008
73. Guilbert A., Barucci A., Brunetto R., ...,**Fornasier S.** et al. A Portrait of Centaur 10199 Chariklo. In AAS/Division for Planetary Sciences Meeting Abstracts. 2009, vol. 41
74. Perna D., **Fornasier Sonia**, Barucci A., et al. Colors and Taxonomy of Tnos and Centaurs. In AAS/Division for Planetary Sciences Meeting Abstracts. 2009, vol. 41
75. Barucci M.A., **Fornasier S.**, Alvarez-Cantal A., De Bergh C., Merlin F., Demeo F., Dumas C. Surface Properties of TNOs : Preliminary Statistical Analysis. In AAS/Division for Planetary Sciences Meeting Abstracts. 2009, vol. 41
76. Barbieri C., Naletto G., Verroi E., ...,**Fornasier S.** et al. First Results of AQuEye, a Precursor 'Quantum' Instrument for the E-ELT. In Science with the VLT in the ELT Era. 2009, pp. 249
77. Clark B. E., Ziffer J., Nesvorny D., ...,**Fornasier S.** et al.Spectroscopy of B-Type Asteroids : Subgroups and Meteorite Analogs. In AAS/Division for Planetary Sciences Meeting Abstracts. 2009, vol. 41
78. Dalle Ore C. M., Barucci A., Emery J. P., ...,**Fornasier S.** et al. Composition of KBO (50000) Quaoar. In American Astronomical Society Meeting Abstracts. 2009, vol. 214
79. Hviid S. F., **Fornasier S.**, Vernazza Pierre, et al. Rosetta Fly-by of Asteroid 2867 Steins : Phase Function from the OSIRIS Imaging System. In Bulletin of the American Astronomical Society. 2009, vol. 40, pp. 558

80. Küppers Michael, **Fornasier S.**, Schroder S., et al., Photometric Properties of Asteroid (2867) Steins in the Near-UV to Near-IR Spectral Range from Images Obtained with the OSIRIS Cameras on Rosetta. In AAS/Division for Planetary Sciences Meeting Abstracts. 2009, vol. 41
81. Küppers Michael, Keller, H.U., **Fornasier S.**, et al., Observations of Comet 9P/Tempel 1 and Deep Impact by the OSIRIS Cameras onboard Rosetta. In Deep Impact as a World Observatory Event : Synergies in Space, Time, and Wavelength. 2009, pp. 29
82. Leyrat C., Jorda L., **Fornasier S.**, Fulchignoni M., et al., Exploring Potential Surface Heterogeneity of the Asteroid Steins observed from the Rosetta OSIRIS Instrument. In AAS/Division for Planetary Sciences Meeting Abstracts. 2009, vol. 41
83. **Fornasier S.**, Clark B. E., Dotto E., Migliorini Alessandra, Ockert-Bell Maureen E., Barucci Antonella. Spectroscopic survey of M type asteroids. In European Planetary Science Congress 2010, 19-25 septembre 2010, Rome. EPSC absctracts, 2010
84. **Fornasier S.**, Barucci A., Belskaya I., Fulchignoni M.. A portrait of the Rosetta targets 2867 Steins and 21 Lutetia. In European Planetary Science Congress 2010, 19-25 septembre 2010, Rome. EPSC absctracts, 2010 (communication invitées).
85. **Fornasier S.**, Barbieri C., Barucci A., Da Deppo V., De Léon J., et al.. Surface Physical Properties of (21) Lutetia : Results from OSIRIS Observations During the Rosetta Fly-by. In Bulletin of the American Astronomical Society. 2010, vol. 42, pp. 1032
86. DeMeo F., Barucci A., Alvarez-Candal A., De Bergh C., **Fornasier S.**, Merlin F., Perna D., Belskaya I. Surface properties of icy transneptunian objects from the second ESO large program. In IAU Symposium. 2010, vol. 263, pp. 186-191
87. Dotto E., Perna D., De Luise F., .., **Fornasier S.**, et al. Low Delta-v Near Earth Objects : A Survey Of Suitable Targets For Space Missions. In Bulletin of the American Astronomical Society. 2010, vol. 42, pp. 1053
88. Hviid S. F., Barbieri C., Barucci A., .., **Fornasier S.**, et al. Overview of the Rosetta Fly-by of 21-Lutetia as Observed by the OSIRIS Camera System. In Bulletin of the American Astronomical Society. 2010, vol. 42, pp. 1043
89. Keller H. U., Schröder S. E., Hviid S. F., .., **Fornasier S.**, et al. OSIRIS Observations of Asteroid 21 Lutetia : Geomorphology and Colour Variegation. In Bulletin of the American Astronomical Society. 2010, vol. 42, pp. 1044
90. Leyrat C., Sierks H., Barbieri C.,.., **Fornasier S.**, et al. Spatial Variations of Spectral Properties of (21) Lutetia as Observed by OSIRIS/Rosetta. In Bulletin of the American Astronomical Society. 2010, vol. 42, pp. 1044
91. Ockert-Bell M. E., Clark B. E., Shepard M. K., Issacs R. A., Cloutis E. A., **Fornasier S.**, Bus S. J. The Composition of M-type Asteroids : Synthesis of Spectroscopic and Radar Observations.. In Bulletin of the American Astronomical Society. 2010, vol. 42, pp. 1073
92. Santos-Sanz P., Lellouch E., **Fornasier Sonia**, Kiss C., Müller T. G., Lacerda P. Dwarf planets observations with Herschel Space Observatory. In Bulletin of the American Astronomical Society. 2010, vol. 42, pp. 1013
93. Vincent, J.B., Marchi, S., Besse, S., ..**Fornasier Sonia**, et al., 2011. Physical Properties of Craters on Asteroid (21) Lutetia. Lunar and Planetary Science Conference No. 1608, p.2417

Rapports têchniques

- Brunello P., Peron F., **Fornasier S.**, Barbieri C., 2000. *Description of the WAC baffling system*, UPD-TN-171/D, OSIRIS internal technical report, March 2000
- **Fornasier S.**, Barbieri, C., Polato, P., Rossi, G., 2001. *Optical characterization of WAC coatings and materials.* RO-RIS-UPD-TN-172/D, OSIRIS internal technical report, April 2001.
- **Fornasier S.**, Barbieri, C., Bertini, I., 2004. *Evaluation of the cleanliness of the cometary environment*, WP-230 for ASTRIUM contract on the Wide Angle Camera of the OSIRIS imaging system on Rosetta mission
- **Fornasier S.**, Naletto G., Da Deppo V., Gregnanin A., 2004. *Properties and performance of the baffling system of the Wide Angle Camera*, WP-220B for ASTRIUM contract on the Wide Angle Camera of the OSIRIS imaging system on Rosetta mission
- Naletto G., Gregnanin A., **Fornasier S.**, Da Deppo V., 2004. *WAC filters calibration : pin-hole defects mappings (positions, dimensions, intensity) on UV filters flat images.* WP-220 for ASTRIUM contract on the Wide Angle Camera of the OSIRIS imaging system on Rosetta mission